dc_1961_21

MITOCHONDRIAL SUBSTRATE-LEVEL PHOSPHORYLATION: FROM SALVAGING HYPOXIC CELLS TO A PROMISING CANCER TARGET

Hungarian Academy of Sciences

Doctoral Dissertation

Dr. Christos Chinopoulos

Semmelweis University

Institute of Biochemistry and Molecular Biology

Department of Biochemistry

Budapest, 2022

PROLOGUE

I entered the world of research in 1993 upon invitation by prof. Tretter László to join the group led by prof. Ádám Veronika. After spending one year trying to establish the method for measuring acetylcholine release from isolated nerve terminals, I arrived to the conclusion that all of my data were artifacts. This led me to assemble a dossier which I -perhaps arrogantly- named “Christos *vs* luminol-enhanced chemiluminescence” and showed it to my superiors; although we did not discuss it thoroughly, they made it clear that I had a strong case, approved of my perseverance and assigned to me another project; it was this incident that led me to commit myself to science.

TABLE OF CONTENTS

INTRODUCTION

In the present dissertation I will argue about the critical role of mitochondrial substrate-level phosphorylation as a means of ATP production within the matrix, preventing mitochondria from becoming cytosolic ATP consumers during respiratory arrest. Having said that, I should emphasize that the original intend, *i.e.* the hypotheses tested upon commencing of this work in 2007 were different from the research directive outlined in the past few years up to this day. Initially, biochemical pathways were sought that damage or salvage tissues experiencing metabolic stress; it was later realized that some of the salvaging pathways could serve the needs of neoplasia mindful that tumor cells are forced to thrive under adverse micronenvironmental conditions encompassing hypoxia.

In 2007 we aimed to elucidate the components of the mitochondrial permeability transition pore (mPTP), a multi-component protein complex comprising a mega-channel that disrupts mitochondrial integrity (Halestrap and Brenner, 2003). The adenine nucleotide translocase (ANT) was considered a structural -or at least modulatory- constituent in mPTP assembly. Mindful that the mitochondrial membrane potential ($\Delta\Psi m$) is also a parameter influencing mPTP and that ANT operation is electrogenic, I was interested in the relation of $\Delta\Psi m$ and ANT activity as they both affect pore opening. Exhaustive literature search yielded that there are no easy methods for measuring ANT activity as a function of $\Delta\Psi m$, so the task was clear: develop an ANT kinetic assay. In (Chinopoulos et al., 2009) we described the methodology to measure mitochondrial ADP-ATP exchange rate (scheme 1), and correlate this rate as a function of $\Delta\Psi m$ and ΔpH. The participation of the ANT in mPTP has been proven by the group of Molkentin (Karch et al., 2019), (Bround et al., 2020). The full list of protein(s) constituting the mPTP is/are still unknown.

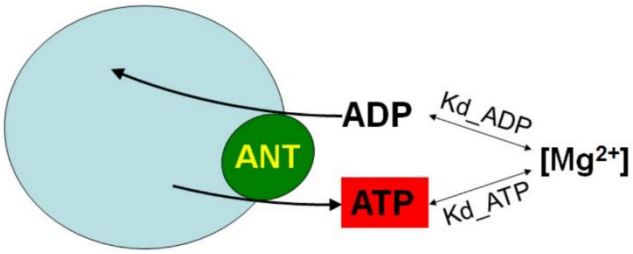

Scheme 1. ADP-ATP exchange rate mediated by the ANT embedded in mitochondria (depicted as cyan disc) could be quantified by measuring the rate of change in $[Mg^{2+}]$ concentration; the method is based on the differential affinities (Kd) of ADP and ATP for Mg^{2+}. The method was described in (Chinopoulos et al., 2009), modified for use in permeabilized cells and/or tissue homogenates in (Kawamata et al., 2010) and further improved in (Chinopoulos et al., 2014).

Upon describing the above technique (Chinopoulos et al., 2009), we sought to adapt this method for measuring ANT activity in environments with competing reactions that interconvert adenine nucleotides, such as in permeabilized cells that harbor phosphorylases and kinases, ion pumps exhibiting substantial ATPase activity and myosin ATPase activity. We therefore tested the inclusion of BeF_3^- and Na_3VO_4 to media containing digitonin-permeabilized cells that inhibit all ATP-ADP utilizing reactions, except the ANT-mediated mitochondrial ATP-ADP exchange. An advantage of this modification was that mitochondria that may have been also permeabilized by digitonin do not contribute to ATP consumption by the exposed F_1F_o-ATPase, due to its sensitivity to BeF_3^- and Na_3VO_4. With this assay, ADP-ATP exchange rate mediated by the ANT in permeabilized cells (Kawamata et al., 2010) was measured for the entire range of mitochondrial membrane potential titrated by stepwise additions of an uncoupler, and expressed as a function of citrate synthase activity per total amount of protein. In (Chinopoulos et al., 2014), the method was further refined by which the reliability of $[Mg^{2+}]$ conversion to [ATP] and [ADP] was much improved.

Having established the method for measuring ADP-ATP exchange rate mediated by the ANT, two new perspectives were envisaged: i) to compile a computational model for the ATP-ADP steady-state exchange rate mediated by the ANT *versus* mitochondrial membrane potential dependence for the purpose of predicting kinetic rates, and ii) provide theoretical values of free matrix [ATP] and [ADP].

Indeed, through a collaboration set with Dr. Eugeniy Metelkin and Prof. Oleg Demin we published a model of ATP-ADP steady-state exchange rate mediated by the ANT using data obtained from isolated rat liver mitochondria (Metelkin et al., 2009). In addition to providing several predictions (see Results section), this work serves as a complete ATP phosphorylation model that could be incorporated in future versions of larger and more complex models of mitochondrial functions, such as those described elsewhere (Beard, 2005), (Wu et al., 2007).

Subsequently, by establishing i) the methodology for measuring ADP-ATP exchange rate mediated by the ANT and ii) the model predicting ANT operation and matrix adenine nucleotide levels, we addressed the effect of cyclophilin D binding on F_o-F_1 ATP synthase on mitochondrial ATP output. Approximately one year before publishing our results, the group of Lippe showed that cyclophilin D binds to and decreases the activity of F_0F_1-ATP synthase in submitochondrial particles and permeabilized mitochondria, decreasing both ATP synthesis and hydrolysis rates (Giorgio et al., 2009). In (Chinopoulos et al., 2011) we not only reaffirmed these findings in *intact* mitochondria, but also showed that the modulation of F_0F_1-ATP synthase by cyclophilin D did not change the ANT-mediated adenine nucleotide flux rates. We concluded that in mitochondria exhibiting intact inner membranes, the absence of cyclophilin D or inhibition of its binding to F_0F_1-ATP synthase by cyclosporin A affects matrix adenine nucleotides levels but not the ANT.

From then on, the established methodologies and knowledge obtained set stage for a new research directive; specifically, we aimed to understand the "paradoxical" finding by which in respiration-inhibited mitochondria, addition of an ANT vs F_0F_1-ATPase inhibitor (carboxyatractyloside versus oligomycin) yielded an increase *vs* a decrease in $\Delta\Psi$m; this was at odds with the current "dogma", as it was universally believed that respiration-inhibited mitochondria exhibit F_0F_1-ATPase reversal, meaning that they hydrolyze -instead of generate- ATP, and that this ATP comes from an extramitochondrial source, primarily glycolysis. This was a totally unexpected and serendipitous finding, because it was a "product" of not having oligomycin at hand that day and using carboxyatractyloside instead to confer collapse in $\Delta\Psi$m, which was not observed. Eventually, in (Chinopoulos et al., 2010) we published that when the electron transport chain is compromised, the F_0F_1-ATPase reverses and the membrane potential is maintained as long as matrix substrate-level phosphorylation (mSLP) substantiated by succinate CoA ligase is functional, without a concomitant reversal of the ANT (scheme 2).

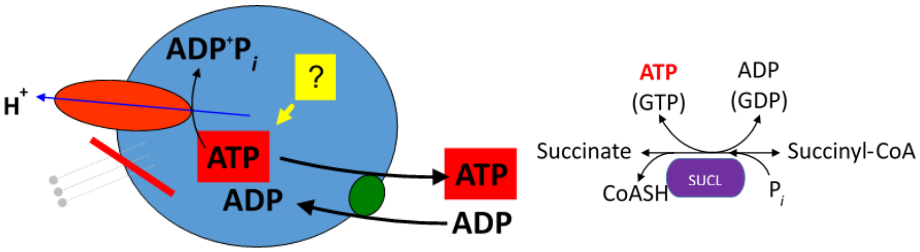

Scheme 2. When the ETC is inhibited (red dash) in mitochondria (blue disc), the paradox (yellow question mark) arose as of what could provide ATP to the F_0F_1-ATPase (orange oblong) while the ANT (green disc) is still expelling ATP from the matrix. The reaction catalyzed by succinate-CoA ligase (SUCL, right panel) provides ATP even when the respiratory chain is inhibited.

Further on, mindful of the role of mSLP substantiated by succinate CoA ligase in respiration-deficient mitochondria in maintaining organellar ATP output, the question arose how important succinyl-CoA provision was to this enzyme. To this end, in (Kiss et al., 2013) we examined mSLP in transgenic mice lacking subunits of KGDHC, the multienzyme complex generating succinyl-CoA and demonstrated ATP consumption in respiration-impaired isolated and *in situ* neuronal somal mitochondria. Consequently, we proposed that KGDHC-associated pathologies are a result of the inability of respiration-impaired mitochondria to rely on "in-house" mitochondrial ATP reserves.

Mindful of the reaction catalyzed by KGDHC converting α-ketoglutarate, CoASH and NAD^+ to succinyl-CoA, NADH and CO_2, the question arose as to the source of NAD^+ when the electron transport chain is dysfunctional. It is a textbook definition that NADH generated in the citric acid cycle is oxidized by complex I, resupplying NAD^+ to the cycle. In the absence of oxygen or when complexes are not functional, an excess of NADH in the matrix is expected. Yet, our previous reports showed that without NADH oxidation by complex I of the respiratory chain, substrate-level phosphorylation was operational and supported by succinyl-CoA (Chinopoulos et al., 2010), (Kiss et al., 2013), implying KGDHC activity. In (Kiss et al., 2014) we reported that during anoxia or pharmacological blockade of complex I, mitochondrial diaphorases oxidized matrix NADH supplying NAD^+ to KGDHC which in turn yielded succinyl-CoA, thus supporting mSLP (see figure 8.7, page 214). Diaphorases are flavoenzymes catalyzing the oxidation of reduced pyridine nucleotides by endogenous or artificial electron acceptors. They are collectively referred to as 'DT diaphorases' because of their reactivity with both DPNH (NADH) and TPNH (NADPH) discovered by the group of Lars Ernster (Conover and Ernster, 1960). Such a diaphorase has also been identified in parallel by Märki and Martius, called "vitamin K reductase" (Maerki and Martius, 1961) and later confirmed to be the same enzyme (Ernster et al., 1962). 'Quinone reductases' with properties similar to the enzymes described by Ernster and colleagues also appears in earlier literature by Wosilait and colleagues (Wosilait and Nason, 1954), (Wosilait et al., 1954), as well as a microsomal "TPNH-neotetrazolium diaphorase", described by Williams and colleagues (Williams et al., 1959), and a 'brain diaphorase' by Giuditta and Strecker (Giuditta and Strecker, 1959), (Giuditta and Strecker, 1961). Finally, a 'menadione reductase' has been reported by Koli and colleagues (Koli et al., 1969).

A direct extension of the study published in (Kiss et al., 2014) was the work using $Nqo1^{-/-}$ vs wild-type littermate mice. Nqo1 (NAD(P)H:quinone oxidoreductase isoform 1) is a diaphorase known to localize in mitochondria, among several other intracellular compartments (Radjendirane et al., 1998). In (Ravasz et al., 2018), we showed that in rotenone-treated, isolated liver mitochondria, 2-methoxy-1,4-naphtoquinone (MNQ) was preferentially reduced by matrix Nqo1 yielding NAD^+ to KGDHC, supporting mSLP. The results led to the conclusions that i) MNQ is a Nqo1-preferred substrate, and ii) in the presence of suitable quinones, mitochondrially-localized diaphorases other than Nqo1 support NADH oxidation when complex I is inhibited. This also confirmed that complex I bypass can occur by quinones reduced by intramitochondrial diaphorases oxidizing NADH, thus supporting mSLP. Ultimately, this work may assist in elucidating structure-activity relationships of redox-active quinones with diaphorase enzymes.

Up to this point, our work pointed to the direction that mSLP substantiated by succinate CoA ligase is critical for maintaining matrix adenine nucleotide levels during respiratory arrest, preventing mitochondria from importing and hydrolysing ATP. To this end, provision of NAD^+ by matrix diaphorases and -depending on the substrate- Nqo1 to KGDHC was also shown to be critical. Experimental results were strongly suggestive of the above claims, but unequivocal proof was lacking. In (Kacso et al., 2016) we bolstered our claims further by generating transgenic mice deficient in succinate CoA ligase expression and also experimenting on human fibroblasts from patients with no succinate CoA ligase activity.

Succinate-CoA ligase (SUCL), also known as succinyl coenzyme A synthetase, or succinate thiokinase is a heterodimer enzyme composed of an invariant α subunit encoded by *SUCLG1* and a substrate-specific β subunit, encoded by either *SUCLA2* or *SUCLG2*. This dimer combination results in either an ATP-forming (EC 6.2.1.5) or a GTP-forming SUCL (EC 6.2.1.4). ΔG of either reaction is ~0.07 kJ/mol and therefore, reversible (Li et al., 2013). SUCL is located in the mitochondrial matrix catalyzing the conversion of succinyl-CoA and ADP (or GDP) to CoASH, succinate and ATP (or GTP) (Lambeth et al., 2004). Being at the intersection of several metabolic pathways (Tretter et al., 2016), it is not surprising

that its deficiency leads to pleiotropic pathology which is also influenced by the tissue-specific expression of its subunits: SUCLA2 is strongly expressed in skeletal muscle, brain and heart, whereas SUCLG2 is barely detected in brain and muscle, but robustly expressed in liver and kidney (Lambeth et al., 2004). Furthermore, in the human brain SUCLA2 is exclusively expressed in the neurons, whereas SUCLG2 is only found in cells forming the microvasculature (Dobolyi et al., 2015a), (Dobolyi et al., 2015b). To date, 51 patients have been reported with SUCLA2 deficiency (Gungor et al., 2016), (Elpeleg et al., 2005), (Jaberi et al., 2013), (Lamperti et al., 2012), (Matilainen et al., 2015), (Morava et al., 2009), (Navarro-Sastre et al., 2012), (Nogueira et al., 2015), (Ostergaard et al., 2007b), (Maas et al., 2016), (Carrozzo et al., 2016), and 21 patients with SUCLG1 deficiency, due to different mutations (Carrozzo et al., 2016). Patients with *SUCLG1* mutations may have an extremely severe phenotype with antenatal manifestations of the disorder, severe acidosis with lactic aciduria in the first day of life and death within 2–4 days (Ostergaard, 2008), or a phenotype similar to those of patients with *SUCLA2* mutations. Mutations in the *SUCLG2* gene have not been reported so far, and may be incompatible with life. SUCLA2 deficiency (MIM ID#612073) has an incidence of 1 in 1,700 in the Faroe Islands due to a founder effect, and a carrier frequency of 1 in 33 (Ostergaard et al., 2007b). More recently, evidence of two founder mutations in the Scandinavian population have also been put forward (Carrozzo et al., 2016). The symptoms comprise hypotonia, muscle atrophy, hyperkinesia, severe hearing impairment and postnatal growth retardation. Neuroimaging findings comprise demyelination, central and cortical atrophy including atrophy of the basal ganglia (Ostergaard et al., 2007b), (Carrozzo et al., 2007). Some of the patients fulfill the criteria for Leigh syndrome (Ostergaard, 2008). Urine and plasma methylmalonic acid, C3-carnitine and C4-dicarboxylic carnitine (the latter likely to be a mixture of succinyl- and methylmalonyl carnitine ester) are elevated (Ostergaard, 2008), (Ostergaard et al., 2007b) while there are no abnormalities related to liver functions. Median survival is 20 years (Carrozzo et al., 2016); the longest documented survival is 45 years (Morava et al., 2009). It is being hypothesized that, patients with missense mutations in *SUCLA2* (or *SUCLG1*) may exhibit some residual SUCL activity which is associated with longer survivals; however, given the small number of patients and the lack of expression studies providing direct experimental evidence of residual activity, such postulations must be interpreted cautiously (Carrozzo et al., 2016). Heterozygous relatives of patients with SUCLA2 deficiency are asymptomatic (Ostergaard, 2008), (Ostergaard et al., 2007b). Given the role of SUCL in maintaining mtDNA content, SUCLA2 deficiency patients suffer from mtDNA depletion in muscle (Ostergaard, 2008), (Ostergaard et al., 2007b), (Navarro-Sastre et al., 2012). Data from heart and brain biopsies are not available. mtDNA depletion has also been reported in fibroblasts but only from some patients (Carrozzo et al., 2007), or only after serum deprivation (Miller et al., 2011). mtDNA depletion would influence many targets in mitochondria, including the electron transport complexes of the respiratory chain creating a bioenergetic insufficiency that could in turn impair energy-dependent mechanisms. Indeed, respiratory chain enzyme analysis show decreased complex I, III and IV activity, whereas complex II, which is encoded exclusively by nDNA genes shows normal activity (Ostergaard et al., 2007b), (Carrozzo et al., 2016). There are no data available regarding ETC activities from brain tissue. In fibroblasts, a slightly decreased complex IV activity has been reported (Ostergaard et al., 2007b).

Until approximately 2015, our work established the critical importance of succinate-CoA ligase in providing ATP in the matrix through mSLP when ETC components are inhibited. We were therefore interested if this phenomenon was just an “experimenter-induced artifact” or it could unfold in an actual pathophysiological setting. Relevant to this, in 2013 the group led by Hiller reported that itaconic acid is produced in cells of macrophage lineage (Michelucci et al., 2013); this was interesting to us, because it was known for over 60 years that itaconate is oxidized in the citric acid cycle (Adler et al., 1957) forming pyruvate and acetyl CoA (Wang et al., 1961); this obviously implied that its catabolism passes through succinate-CoA ligase; however, at the time, the identity of succinate-CoA ligase (referred to as

"succinate-activating enzyme", or "P enzyme") and its role in substrate-level phosphorylation was not yet known (Sanadi et al., 1954), (Labbe et al., 1965), (Ottaway et al., 1981). In (Nemeth et al., 2016) we investigated the possibility that itaconate exerts an effect on adenine (or guanine) nucleotide production in the mitochondrial matrix via succinate-CoA ligase. Indeed, itaconate was thwarting mSLP either by pushing the reversible reaction of succinate-CoA ligase towards itaconyl-CoA formation associated with ATP (and GTP) hydrolysis, and/or creating a “CoASH trap”, thus impeding KGDHC operation, the enzyme feeding succinate-CoA ligase with succinyl-CoA (see figure 11.4, page 146).

Having demonstrated that itaconate exerts an effect in mSLP, we reasoned that perhaps other endogenous metabolites passing through succinate-CoA ligase may affect mSLP. 4-Aminobutyrate, also known as 4-aminobutanoate, γ-aminobutyrate or more frequently, GABA, is most widely known as the predominant inhibitory or excitatory neurotransmitter in the adult versus neonate brain, respectively (Cherubini et al., 1991). Since its discovery (Udenfriend, 1950), (Roberts and Frankel, 1950), (Awapara et al., 1950), GABA has been increasingly recognized to participate in processes other than neurotransmission as it is present in many organs other than the brain, such as pancreas, testes, gastrointestinal tract, ovaries, placenta, uterus and adrenal medulla (Gladkevich et al., 2006), (Garry et al., 1987). Most notably though, very high concentrations of GABA have been found in the livers of all animal species reported, particularly humans (White and Sato, 1978), reviewed in (Minuk, 1993). Normally, GABA is only catabolized but very little synthesized in the liver, and it originates from the intestinal flora (Minuk, 1993) finding its way through the portal system; however, hepatic lobular GABA synthesis increases >300% following partial hepatectomy (Minuk, 1993). Relevant to this, the high GABA concentration in liver has been implicated in the pathophysiology of hepatic encephalopathy (Schafer and Jones, 1982). Furthermore, GABA has been long known to operate as a signaling molecule in dendritic cells (Wolff et al., 1978) and this was later confirmed in a variety of immune cells (reviewed in (Jin et al., 2013), act as a developmental signal during brain organogenesis (Owens and Kriegstein, 2002), and even inhibit mitophagy and pexophagy in mammalian cells of various tissues, in an mTOR-sensitive manner (Lakhani et al., 2014). Finally, GABA’s realm has been recently recognized to extent to *plantae*, playing a vital role as a plant-signaling molecule (Gilliham and Tyerman, 2016). In (Ravasz et al., 2017) we examined the effect of metabolites catabolized through the GABA shunt on mSLP. The rationale for this undertaking was that catabolism of GABA, succinic semialdehyde or GHB through the shunt should lead to elevation in matrix succinate concentration, shifting the equilibrium of the reversible reaction catalyzed by succinate-CoA ligase towards ATP (or GTP) hydrolysis, effectively negating mSLP (see figure 12.1, page 152).

In the same line of thought regarding itaconate and GABA metabolites, we investigated the effect of 2-ketobutyrate (2-KB) on mSLP. 2-KB is a common metabolic product of threonine, serine and methionine catabolism, all leading to production of succinyl-CoA. We reasoned that 2-KB catabolism would only negate the net ATP production from further succinyl-CoA catabolism through succinate-CoA ligase, without inhibiting the reaction. Indeed, in (Bui et al., 2019) we demonstrated that catabolism of 2-KB negates mSLP due to the ATP-consuming propionyl-CoA carboxylase step in rotenone-treated, isolated mouse liver and brain mitochondria (see figure 13.1, page 162).

The above results established the role of mSLP in rescuing mitochondria experiencing hypoxia or anoxia from becoming ATP sinks. Since mSLP is substantiated by the reaction catalyzed by succinate CoA ligase, an enzyme exhibiting strong tissue-dependent distribution (Lambeth et al., 2004), we were interested as to the cell-specific expression of succinate-CoA ligase subunits in human tissues. For this, the availability of human brain specimens from the Human Brain Tissue Bank maintained by Prof. Palkovits for which we gained access through Prof. Dobolyi, was instrumental. Because brain tissue is composed by many different cell types identifiable by suitable markers, it offers the opportunity of correlating cell

types with the expression of succinate-CoA ligase subunits. It is expected that those cells that exhibit succinate CoA ligase expression will be afforded with the capacity to withstand better hypoxic events. In (Dobolyi et al., 2015b) we published that the ATP-forming subunit SUCLA2 of succinate-CoA ligase is expressed exclusively in the neurons of the human brain. In (Dobolyi et al., 2015b) we also showed that SUCLG2 is very weakly expressed in the adult human brain, and this expression does not originate from the neurons. In a subsequent study published in (Dobolyi et al., 2015a) we reported that SUCLG2 exist only in cells forming the vasculature or its contents in the adult human brain.

The findings published in (Dobolyi et al., 2015b) and (Dobolyi et al., 2015a) showing that succinate CoA ligase exists only in the neurons of the adult human brain, begged the question: if the enzyme processing succinyl-CoA exhibits cell-specific expression, does the enzyme producing succinyl CoA follow the same pattern? This enzyme is the α-ketoglutarate dehydrogenase complex (KGDHC). KGDHC is a multi-subunit enzyme residing in the mitochondrial matrix (Maas and Bisswanger, 1990). It catalyzes the irreversible decarboxylation of α-ketoglutarate (αKg) to succinyl-CoA while reducing NAD^+ to NADH. Regulation of the complex and its overall impact on energy metabolism is reviewed in (Gibson et al., 2010) and (Starkov, 2013). More recently, the group of Gibson discovered that KGDHC serves as a trans-succinylase, adding succinyl moieties to lysines of proteins in an αKg-dependent manner (Gibson et al., 2015). Lysine succinylation is a widespread posttranslational modification occurring on thousands of lysines residing in hundreds of proteins distributed in the cytosol, nucleus and mitochondria (Zhang et al., 2011), (Weinert et al., 2013). In the work published in (Dobolyi et al., 2020) we showed that KGDHC-specific subunits are also absent from glial cells in the adult human brain cortex (see figure 16.19, page 225).

The absence of succinate-CoA ligase and KGDHC from glial cells in the adult human brain sparked a general interest regarding how much -if at all- do glial cells depend on oxidative metabolism. Our collaboration with Dr. Dobolyi and Prof. Palkovits continues to this day, mapping the cell-specific expression of mitochondrial enzymes in the adult human brain.

METHODS

Human brains (for (Dobolyi et al., 2015b)): Human brain samples were collected in accordance with the Ethical Rules for Using Human Tissues for Medical Research in Hungary (HM 34/1999) and the Code of Ethics of the World Medical Association (Declaration of Helsinki). Post mortem tissue samples were taken during brain autopsy. In addition, surgical brain samples were obtained from tissue removed during brain surgeries at the Department of Neurosurgery Medical School, University of Pécs in the framework of the Human Brain Tissue Bank, Budapest. For autopsy, brains were removed from the skull with a post mortem delay of 2–6 h. Prior written informed consent was obtained from the patients or from the next of kin for autopsies, which included the request to conduct neurochemical analyses. The protocols including analyses of tissue samples, were approved by institutional ethics committee of the Semmelweis University and the University of Pécs. The three surgical patients underwent the removal of brain tumors. The 11 subjects, whose brains were used in the autopsy study died without any known neurological or affective disorder. The medical history of the subjects was obtained from medical or hospital records, interviews with family members and relatives, as well as from pathological and neuropathological reports. All personal identifiers had been removed and samples were coded before the analyses of tissue. Surgically dissected freshly frozen temporal cortical samples from a 66 year old woman were used for RT-PCR and the development of in situ hybridization probes. In situ hybridization histochemistry was performed in temporal cortical samples from this patient as well as in the temporal cortex from a 64 year old woman. Immunolabeling was performed using frontal cortical sample of a 58

year old man and temporal cortical samples from the 64 year old and the 66 year old woman; tissue blocks of the latter two patients were also used for in situ hybridization histochemistry. Surgical samples that underwent immediate freezing for situ hybridization histochemistry or immediate fixation for immunolabeling were used in histochemical techniques, because they provided markedly superior results for visualizing *SUCLA2* expression and distribution as compared to post mortem samples. For western blotting, autopsy samples from different brain regions of 11 subjects were obtained by microdissection. Individual brain nuclei were microdissected from postmortem brains (that have been rapidly frozen on dry ice and stored at -80 °C) using the micropunch technique (Palkovits, 1973). Briefly, brains were cut as 1.0-1.5 mm thick coronal sections, and individual brain regions and nuclei were removed by special punch needles with an inside diameter of 1.0-3.5 mm, by using either a head magnifier or a stereomicroscope. The microdissected samples were collected in airtight plastic (Eppendorf) tubes and stored at -80 °C until further use. The temperature of brain sections and the microdissected samples was kept under 0 °C during the whole procedure. Human brains (for (Dobolyi et al., 2020)): Human brain samples were collected in accordance to the Ethical Rules for Using Human Tissues for Medical Research in Hungary (HM 34/1999) and the Code of Ethics of the World Medical Association (Declaration of Helsinki). Ethical permission for obtaining surgical brain material for the specific project has been obtained from the Medical Research Council of Hungary (No: 35302-5/2017/EKU), and is valid until June 30th, 2020. Post mortem tissue samples were taken during brain autopsy in the framework of the Human Brain Tissue Bank (HBTB), Budapest, Hungary. HBTB has been authorized by the Committee of Science and Research Ethic of the Ministry of Health of Hungary (No. 6008/8/2002/ETT) and the Semmelweis University Regional Committee of Science and Research Ethic (No. 32/1992/TUKEB). For autopsy, brains were removed from the skull with a post mortem delay of 2–6 h. Prior written informed consent was obtained from the patients or from the next of kin for autopsies which included the request to conduct neurochemical analyses. The protocols including analyses of tissue samples were approved by institutional ethics committee of the Semmelweis University. The surgical patients (all males) underwent the removal of brain tumors; samples were obtained from normal brain cortical tissue removed during clearing the path for accessing the area of the tumor. All patients survived the surgery. The subjects whose brains were used in the autopsy study died without any known neurological or affective disorder. The medical history of the subjects was obtained from medical or hospital records, interviews with family members and relatives, as well as from pathological and neuropathological reports. All personal identifiers had been removed and samples were coded before the analyses of tissue. Surgical samples underwent immediate fixation (immersed in ice-cold 4% paraformaldehyde in 0.1 M phosphate-buffered saline within a few seconds after their excision from the brain) for immunolabeling used in histochemical techniques. For western blotting, autopsy samples from 63 different brain regions of 11 subjects (7 females and 4 males) were obtained by microdissection. Individual brain nuclei were microdissected from postmortem brains (that have been rapidly frozen on dry ice and stored at -80 °C) using the micropunch technique (Palkovits, 1973). Briefly, brains were cut as 1.0-1.5 mm thick coronal sections, and individual brain regions and nuclei were removed by special punch needles with an inside diameter of 1.0-3.5 mm, by using either a head magnifier or a stereomicroscope. The microdissected samples were collected in Eppendorf tubes and stored at -80 °C until further use. The temperature of brain sections and the microdissected samples was kept under 0 °C during the whole procedure.

Tissue collection for immunolabeling: For immunocytochemistry, brains were cut into 5-10 mm thick coronal slices and immersion fixed in 4% paraformaldehyde in 0.1 M phosphate-buffered saline (PBS) for 3-5 days. Subsequently, the blocks were transferred to PBS containing 0.1% sodium azide for 2 days to remove excess paraformaldehyde. Then the blocks were placed in PBS containing 20% sucrose for 2 days for cryoprotection, after which the blocks were frozen and cut into 50 μm thick serial coronal

sections on a sliding microtome. Sections were collected in PBS containing 0.1% sodium azide and stored at 4 °C until further processing.

DAB immunolabeling of brain sections: Every fifth free-floating brain section of human temporal and frontal cortical blocks was immunostained for SUCLA2 and SUCLG2. The antibodies (at dilutions 1:80; 1:320; 1:1280; 1:5120) were applied for 48 h at room temperature, followed by incubation of the sections in biotinylated anti-rabbit secondary antibody (1:1000 dilution; Vector Laboratories, Burlingame, CA) and then in avidin-biotin-peroxidase complex (1:500; Vector Laboratories) for 2 h. Subsequently, the labeling was visualized by incubation in 0.02% 3,3-diaminobenzidine (DAB; Sigma), 0.08% nickel (II) sulfate and 0.001% hydrogen peroxide in PBS, pH=7.4 for 5 minutes. Sections were mounted, dehydrated and coverslipped with Cytoseal 60 (Stephens Scientific, Riverdale, NJ, USA).

Double labeling of SUCLA2 in brains sections: SUCLA2 was immunolabeled as for single labeling using 1:1000 dilution except for the visualization, which was performed with fluorescein isothiocyanate (FITC)-tyramide (1:8000) and H_2O_2 in 100 mM Trizma buffer (pH 8.0 adjusted with HCl) for 6 min. Subsequently, sections were placed in mouse anti-subunit d of the F_0-F_1 ATP synthase, (1:500), or mouse anti-S100, a marker of glial cells (1:500; Millipore, cat number MAB079-1) for 48 h at room temperature. The sections were then incubated in Alexa 594 donkey anti-mouse secondary antibody (1:500; Molecular Probes, Eugene, OR) for 2 h and washed. For the double labeling with Nissl staining, the sections were incubated in ´Neurotrace´ red fluorescent Nissl stain (Molecular Probes) diluted to 1:30 for 2 hours, and washed in PBS overnight. For double labeling with glial fibrillary acidic protein (GFAP), a marker of glial cells, the sections were first incubated in mouse anti-GFAP (1:300; Santa Cruz Biotechnology, Delaware, CA, USA; cat. number: sc-33673) and developed with FITC-tyramide amplification immunofluorescence as described above for SUCLA2. Then, the anti-SUCLA2 antiserum was used at a 1:350 dilution and visualized by Alexa 594 donkey anti-rabbit secondary antibody (1:500; Molecular Probes). Finally, all sections with fluorescent labels were mounted on positively charged slides (Superfrost Plus, Fisher Scientific, Pittsburgh, PA) and coverslipped in antifade medium (Prolong Antifade Kit, Molecular Probes).

Immunocytochemistry of cell cultures (for (Dobolyi et al., 2015b)): Fibroblasts or HEK293 cell cultures were first treated with 1 μM Mitotracker Orange (MTO) for 5 min in their culture media, at 37°C in 5% CO_2. Subsequent immunocytochemistry of the cultures was performed by fixing the cells with 4% paraformaldehyde in PBS for 20 min, followed by permeabilization by 0.1% TX-100 (in PBS) for 10 min and several washing steps in between with PBS at room temperature. Cultures were treated with 10% donkey serum overnight at 4 °C followed by bathing in 1% donkey serum and 1 μg/ml anti-SUCLA2 (Proteintech Europe Ltd, Manchester, UK, Cat. No. # 12627-1-AP) or 1 μg/ml anti-SUCLG2 (Abcam, Cambridge, UK, Cat. No # ab96172) for 1 hour at room temperature. Cells were subsequently decorated by using the appropriate Cy2- or Alexa 488-linked secondary antibody (1:4,000, donkey anti-rabbit, Jackson Immunochemicals Europe Ltd, Cambridgeshire, UK) in the presence of 1% donkey serum.

Western blotting (for (Dobolyi et al., 2015b)): Cultured fibroblasts were harvested by trypsinization. Frozen brain samples were thawn on ice in the presence of radioimmunoprecipitation assay buffer and a protease cocktail inhibitor containing: 0.5 mM 4-(2-aminoethyl) benzenesulfonyl fluoride hydrochloride, 150 nM Aprotinin, 1 μM E-64, 0.5 mM EDTA disodium, and 1 μM Leupeptin, and homogenized with a Teflon pestle. The suspensions were centrifuged once at 10,000 g for 10 min, and the proteins present in the supernatants were separated by sodium dodecyl sulfate – polyacrylamide gel electrophoresis (SDS-PAGE). Separated proteins were transferred to a methanol-activated polyvinylidene difluoride membrane. Immunoblotting was performed as recommended by the manufacturers of the antibodies. Rabbit polyclonals anti-SUCLG2 (Abcam, Cambridge, UK), and anti-SUCLA2 primary antibodies were used at concentrations of 1 μg/ml, and rabbit polyclonal anti-β actin

(Abcam) at 0.1 μg/ml. Immunoreactivity was detected using the appropriate peroxidase-linked secondary antibody (1:4,000, donkey anti-rabbit, Jackson Immunochemicals Europe Ltd, Cambridgeshire, UK) and enhanced chemiluminescence detection reagent (ECL system; Amersham Biosciences GE Healthcare Europe GmbH, Vienna, Austria).

siRNA and cell transfections: The ON-TARGETplus SMARTpool containing four different siRNA sequences, all specific to human KGDHC-specific components (see under "Results") and the corresponding non-targeting control (scrambled RNA), were designed by Thermo Scientific Dharmacon and synthesized by Sigma-Aldrich. HeLa cells were transfected with 100 nM of either siRNA or scrambled siRNA using Lipofectamine 2000 according to the manufacturer's instructions, 48 hours before immunocytochemistry.

RT-PCR: RNA was isolated from surgically dissected human temporal cortex and cultured human fibroblasts. The surgical brain tissue sample was quickly frozen on dry ice and kept at -80°C until RNA isolation. The fibroblasts were centrifuged and resuspended in PBS immediately before RNA isolation. Both the brain surgical samples and the fibroblasts were homogenized in Trizol^{R} Reagent (Invitrogen, Carlsbad, CA, USA) and RNA was isolated according to the manufacturer's instructions. After diluting RNA to 1 μg/μl, it was treated with Amplification Grade DNase I (Invitrogen) and cDNA was synthesized with a Superscript II reverse transcriptase kit (Invitrogen) according to the manufacturer's instructions. After 10-fold dilution, 2.5 μl of the resulting cDNA was used as template in PCR reactions performed with iTaq DNA polymerase (Bio-Rad Laboratories, Hercules, CA, USA) in total volumes of 12.5 μl under the following conditions: 95 °C for 3 min, followed by 35 cycles of 95 °C for 0.5 min, 60 °C for 0.5 min and 72 °C for 1 min. Primers were used at 300 nM final concentration for *SUCLA2* (primer pair A: CCAGCCAACTTCCTTGATGT and TCAGTGCCTTAGCATCATCG, primer pair B: TGCTGAGTCTCCTGAAGCAA and TCATCTTCCTGGGTCCAGTC**,** primer pair C: GCAGCAGAAAACATGGTCAA and CCATCGAGGCCAATGTAGTT), and *SUCLG2* (primer pair A: GAAGCTCTCGAGGCTGCTAA and GTCCATCAGAATTGCCAGGT, primer pair B: CCCTTTGGTGAAACTCCAGA and AATGATGGCACAGTTGACGA**,** primer pair C: GGTCCCAGGCAGTTCAATTA and TATCCAAGGCTTCAGCAACC, primer pair D: CATTGCCTGCTTTGTGAATG and AATGATGGCACAGTTGACGA). The calculated lengths of the PCR products are 235, 309, and 242 base pairs (bp) for human *SUCLA2* (1081-1315, 645-953, and 763-1004 bp of GenBank accession number NM_003850.2), and 279, 387, 366, and 211 bp for human *SUCLG2* (227-505, 758-1144, 105-470, and 934-1144 bp of GenBank accession number NM_001177599.1). The primers were chosen to generate probes that recognize all known RNA species for the particular gene. The resulting PCR products are intron-spanning, in order to detect potential genomic DNA contamination by its larger size. PCR products were run on gel and pictures were taken by a digital camera. Images were cropped and contrast was adjusted using the "levels" command in Adobe Photoshop CS 8.0.

Preparation of in situ hybridization probes: The PCR products using primer pairs A and B for both *SUCLA2* and *SUCLG2* were purified from gel in order to obtain non-overlapping probes to demonstrate specific labeling. The purified PCR products were inserted into TOPO TA cloning vectors (Invitrogen) and transformed chemically into competent bacteria according to the manufacturer's instructions. Plasmids were purified from 5-7 colonies and applied as templates in PCR reactions with the specific primer pairs to select plasmids containing specific inserts. A positive plasmid for each probe was applied as template in PCR reactions, using primer pairs specific for the probe and also containing T7 RNA polymerase recognition site (GTAATACGACTCACTATAGGGCGAATTGGGTA) added to the reverse primers. Finally, the identities of the cDNA probes were verified by sequencing them with T7 primers.

In situ hybridization histochemistry**:** Surgically dissected temporal cortical brain samples from 2 patients were quickly frozen on dry ice, and kept at -80°C. Serial coronal sections (12 μm thick) were cut using a

cryostat, mounted on positively charged slides (Superfrost Plus), dried, and stored at -80°C until use. [^{35}S]UTP-labeled riboprobes were generated from the DNA probes containing T7 RNA polymerase recognition sites using a MAXIscript transcription kit (Ambion, Austin, TX, USA). The preparation of tissue was performed using mRNA locator Kit (Ambion), according to the manufacturer's instructions. For hybridization, we used 80 µl hybridization buffer (mRNA locator Kit; Ambion) and labeled probes of 1 million DPM activity per slide. Washing procedures included a 30 min incubation in RNase A followed by decreasing concentrations of sodium-citrate buffer (pH=7.4) at room temperature and subsequently at 65^{o}C. Following successive dehydration and drying, the slides were dipped in 'NTB' nuclear track emulsion (Eastman Kodak, Rochester, NY, USA) and stored at 4°C for 3 weeks. Then the slides were developed and fixed with Kodak Dektol developer and Kodak fixer, respectively, counterstained with Giemsa, and coverslipped with Cytoseal 60 (Stephens Scientific). A cell was considered to express *SUCLA2* or *SUCLG2* if the number of autoradiography grains accumulated in a seemingly Gaussian distribution around a center was at least 3 times higher than the background level in an area corresponding to an average cell size (a circle with a diameter of 25 µm) in the same section. The background typically consisted of 1 -3 grains per cell.

Combination of in situ hybridization histochemistry with Nissl staining: Slide attached sections of fresh temporal cortical brain tissue were first processed for *in situ* hybridization, as described above. After development, the sections were stained with 0.1% cresyl-violet dissolved in PBS, and then immersed in 96% ethanol containing 0.01% acetic acid. Alternatively, the sections were incubated in ´Neurotrace´ red fluorescent Nissl stain (Molecular Probes,) diluted to 1:30 for 2 hours, washed in PBS overnight, and coverslipped in antifade medium (Prolong Antifade Kit, Molecular Probes). A cell was considered glial if it was dark labeled, and had a small diameter round-shape appearance. In turn, neurons exhibited less intense labeling, were larger and their shape was less regularly rounded. A cell was considered *SUCLA2*-expressing if it met the criteria described above for single label *in situ* hybridization histochemistry. A *SUCLA2*-expressing cell was considered Nissl-labeled if at least 70% of the area of the circle containing the accumulation of autoradiography grains contained Nissl labeling, and the center of the autoradiography grains was within the Nissl labeling.

Combination of in situ hybridization histochemistry with S100 immunohistochemistry: Slide-attached sections (20 µm thick) of fixed temporal cortical brain brains were first processed for *in situ* hybridization, as described above. Thus, tightly bound RNA-RNA pairs were already formed by the time immunohistochemistry was performed, immediately before dipping the slides into autoradiographic emulsion. In addition, the solutions used for perfusion and immunohistochemistry were prepared with DAPC-treated RNAse-free water, which ensured that the labeling intensity of the *in situ* hybridization histochemistry did not decrease significantly. The immunolabeling protocol for S100 was the same as that described above for double labeling immunohistochemistry. Immunoreactivity was visualized using DAB reactions, after which the *in situ* hybridization procedure was continued by dipping the slides into the emulsion. Each double labeling experiment included controls, which was carried out through the double labeling procedure without application of radioactive *in situ* hybridization probes. These controls demonstrated that the DAB signal did not induce an autoradiography signal. A *SUCLA2*-expressing cell was considered S100-immunopositive if at least 70% of the area of the circle containing the accumulation of autoradiography grains contained immunoreactivity for S100 and the center of the autoradiography grains was within the immunolabeled cell.

Image processing: The sections were examined using an Olympus BX60 light microscope equipped with bright-field, dark-field and fluorescence. Images were captured at 2048 x 2048 pixel resolution with a SPOT Xplorer digital CCD camera (Diagnostic Instruments, Sterling Heights, MI, USA) using a 4x objective for dark-field images, and 4-40x objectives for bright-field and fluorescent images. *Fluorescent sections*

were also evaluated using a Bio-Rad 2100 Rainbow Confocal System (Bio-Rad Laboratories, Inc, CA, USA). The contrast and sharpness of the images were adjusted using the “levels” and “sharpness” commands in Adobe Photoshop CS 8.0. Full resolution was maintained until the photomicrographs were finally cropped at which point the images were adjusted to a resolution of 300 dpi.

Analysis of double immunolabeling: Three 1 x 1 mm areas of double-labeled remote sections from each brain were randomly selected. The total number of SUCLA2-positive neurons with an identifiable cell nucleus and the number of double labeled cells was counted using a 20x objective of an Olympus BX60 light microscope equipped with fluorescent epi-illumination and a filter allowing for visualization of both green and red colors. Subsequently, the number of single labeled cells was also calculated in the area.

Isolation of non-synaptic mitochondria from rat brain: Non-synaptic mitochondria from adult rat brain were isolated on a Percoll gradient as described previously (Sims, 1990) with minor modifications, as described in (Chinopoulos et al., 2003) Male 300–350 gr Sprague-Dawley rats were used. All animal procedures were carried out according to the local animal care and use committee (Egyetemi Allatkiserleti Bizottsag) guidelines.

Isolation of synaptic mitochondria from rat brain: Synaptic mitochondria from adult rat brain were isolated as described previously (Brown et al., 2004) with major modifications: Forebrains of four rats were pooled and synaptosomes were obtained as described previously (Adam-Vizi and Ligeti, 1984); briefly, cortices obtained from forebrains were chopped and homogenized using a Teflon-glass homogenizer in ice-cold isolation buffer containing 0.32 M sucrose plus 5 mM Tris with pH adjusted to 7.4 (HCl). The cortex homogenate was centrifuged at 1,900 x g for 10 min, the pellet was discarded, and the supernatant was centrifuged at 13,300 x g for 20 min. The pellet was resuspended in 0.8 M sucrose plus 5 mM Tris (pH 7.4 adjusted with HCl) and centrifuged at 10,000 x g for 30 min. The upper fluffy layer was removed and the supernatant (synaptosomes) was diluted slowly with ice-cold distilled water to a concentration of 0.32 M (the pellet was discarded). Subsequently, the synaptosomes were pelleted by centrifugation at 31,000 x g for 20 min. The obtained pellet was suspended in a medium containing 225 mM mannitol, 75 mM sucrose, 5 mM Hepes, 1 mg/ml bovine serum albumin (fatty acid-free) and 1 mM EDTA with the pH adjusted to 7.4 using Tris. Chelating residual free Mg^{2+} with EDTA renders non-mitochondrial membranes exquisitely sensitive to disintegration by nitrogen cavitation. Synaptosomes (~1.5 ml of ~20 mg/ml) were placed inside a nitrogen cell disruption bomb (model 4639, Parr Instrument Company, Moline, IL, USA) precooled to 4 °C, and subjected to an initial pressure of 1,100 psi by delivering nitrogen to the bomb interior, under constant stirring. As nitrogen is dissolved within membranes, bomb pressure dropped by about 50-100 psi and further nitrogen was allowed to enter the bomb in order to reestablish a final value of 1,100 psi, which was maintained for 10 min. Following this time period, bomb pressure was decreased by opening the lower valve and ~0.8 ml of the sample was recovered and mixed with an equal volume of 30% Percoll containing 225 mM mannitol, 75 mM sucrose, 5 mM Hepes, and 1 mM EGTA (pH=7.4 using Tris) and layered on a preformed Percoll gradient (40 and 23%). Subsequently, the procedure was identical as described above for Percoll-purified mitochondria.

Isolation of mitochondria from rat and rabbit liver and heart: Mitochondria from rat heart and liver were isolated as detailed previously (Chinopoulos et al., 2005). Male 300–350 gr Sprague-Dawley rats and male 2-2.5 kg New Zealand albino rabbits were used. For all types of mitochondria protein concentration was determined using the Biuret assay.

Assessment of inner mitochondrial membrane integrity by measuring citrate synthase activity in non-solubilized mitochondria: Citrate synthase activity was measured as described by (Srere, 1969). 0.1 mg of mitochondria were added to a 2 ml medium containing 100 mM Tris-HCl, 0.36 mM acetyl-CoA, 0.1 mM dithionitrobenzoic acid (pH 8.0). The reaction was started by adding 0.5 mM oxaloacetate. Changes

in the absorbance at 412 nm due to 5-thio-2-nitrobenzoic acid formation were monitored in a GBC UV/VIS 920 spectrophotometer at 25 ^{o}C, under constant stirring. Activity was measured in the absence and in the presence of 0.1% Triton X-100 (v/v, dissolved in 100 mM Tris-HCl, pH 8.0), and calculated as μmol/min/mg protein assuming an extinction coefficient for 5-thio-2-nitrobenzoic acid, of εM= 14.15 $mM^{-1}*cm^{-1}$. Since the inner mitochondrial membrane is impermeable to both oxaloacetate and acetyl-CoA, the fraction of broken mitochondria was estimated from the amount of measured citrate synthase activity in the absence of Triton X-100, divided by the activity measured from mitochondria solubilized by this detergent.

Oxygen Consumption: Mitochondrial respiration was recorded at 37 °C with a Clark-type oxygen electrode (Hansatech, UK). Mitochondria (1 mg) were added to 2 ml of an incubation medium containing (in mM): KCl 8, K-gluconate 110, NaCl 10, Hepes 10, KH_2PO_4 10, EGTA 0.005, mannitol 10, $MgCl_2$ 1, N,N,N',N'-Tetramethyl-p-phenylenediamine (TMPD) 1, K-ascorbate 5, plus 0.5 mg/ml bovine serum albumin (fatty acid-free), pH 7.25. State 3 respiration was initiated by the addition of 2 mM K-ADP (stock titrated to pH=6.9 with KOH) to the incubation medium. State 4 respiration was initiated by the addition of 4 μM carboxyatractyloside (cATR).

Mg^{2+} fluorescence: Mitochondria (1 mg) were added to 2 ml of an incubation medium containing (in mM): KCl 8, K-gluconate 110, NaCl 10, Hepes 10, $KH_2PO_4$10, EGTA 0.005, mannitol 10, $MgCl_2$ 1, plus 0.5 mg/ml bovine serum albumin (fatty acid-free), pH 7.25, and 2 μM Magnesium Green $5K^{+}$ salt. The following three substrate combinations were used: i) 1 mM or 0.08 mM TMPD (as indicated) plus 5 mM K-ascorbate; or ii) 5 mM K-glutamate plus 5 mM K-malate; or iii) 5 mM K-succinate plus 1 μM rotenone. Magnesium Green (MgG) fluorescence was recorded in a PTI Deltascan fluorescence spectrophotometer at a 5 Hz acquisition rate, using 506 and 530 nm excitation and emission wavelengths, respectively. MgG exhibits an extremely high quantum yield (EM[MgG]=75,000 $M^{-1}*cm^{-1}$), therefore, slits were opened to widths of no more than 1 nm. Experiments were performed at 37 ^{o}C. 2 mM ADP was added, and the fluorescence (F) was recorded for 25 sec, followed by addition of 4 μM cATR. At the end of each experiment, minimum fluorescence (Fmin) was measured after addition of 4 mM EDTA, followed by the recording of maximum fluorescence (Fmax) elicited by addition of 20 mM $MgCl_2$. Free Mg^{2+} concentration ($[Mg^{2+}]f$) was calculated from the equation:

$$[Mg^{2+}]f = (Kd(F-Fmin)/(Fmax-F))-0.055 \text{ mM}, \quad \text{(Eq.1.1)}$$

assuming a Kd of 0.9 mM for the MgG- Mg^{2+} complex (Leyssens et al., 1996). The correction term -0.055 mM is empirical, and possibly reflects chelation of other ions by EDTA that have an affinity for MgG, and alter its fluorescence. This term was needed to obtain a reliable $[Mg^{2+}]$ estimate, as determined from calibration experiments using solutions with known, stepwise increasing, Mg^{2+} concentrations. An alternative means for converting MgG fluorescence to free $[Mg^{2+}]$ was by fitting the power function: f=y0+a*x^b to MgG fluorescence values obtained by stepwise additions of known amounts of Mg^{2+} to a medium containing mitochondria. Adventitious Mg^{2+} contaminating the medium prior to Mg^{2+} addition was considered very small and encompassed in the 'y0' constant of the power function. 'x' is for calculated free $[Mg^{2+}]$, 'a' and 'b' are constants and 'f' represents MgG fluorescence values.

Mitochondrial membrane potential (ΔΨm) determination: ΔΨm was estimated using fluorescence quenching of the cationic dye safranine O due to its accumulation inside energized mitochondria (Akerman and Wikstrom, 1976). Mitochondria (1 mg) were added to 2 ml of an incubation medium containing (in mM): KCl 8, K-gluconate 110, NaCl 10, Hepes 10, KH_2PO_4 10, EGTA 0.005, mannitol 10, $MgCl_2$ 1, plus 0.5 mg/ml bovine serum albumin (fatty acid-free), pH 7.25, and 5 μM safranine O. Substrate combinations used were as mentioned above. Experiments were performed at 37 ^{o}C. Fluorescence was recorded in a PTI Deltascan fluorescence spectrophotometer at a 5 Hz acquisition rate,

using 495 and 585 nm excitation and emission wavelengths, respectively. To convert Safranine O fluorescence into millivolts, a voltage-fluorescence calibration curve was constructed. To this end, Safranine O fluorescence was recorded in the presence of 2 nM valinomycin and stepwise increasing [K^+] (in the 0.2-120 mM range) which allowed calculation of ΔΨm by the Nernst equation assuming a matrix [K^+]=120 mM (Akerman and Wikstrom, 1976).

Estimation of ΔΨm from tetraphenylphosphonium (TPP^+) ion distribution was measured using a custom-made TPP^+-selective electrode (Kamo et al., 1979). For these experiments, the assay medium (identical to that for safranine O experiments) was supplemented with 2 μM TPP^+Cl^- and the mitochondrial protein concentration was 2 mg/ml. The electrode was calibrated by sequential additions of TPP^+Cl^-. Experiments were performed at 37 °C.

Fluorescein-tagged siRNA and cell transfections: The ON-TARGETplus SMARTpool containing four different siRNA sequences, all specific to murine Irg1 and the corresponding non-targeting control (scrambled siRNA), were designed by Thermo Scientific Dharmacon and synthesized by Sigma-Aldrich. All four siRNAs and the scrambled siRNA sequences were manufactured to contain a fluorescein tag on the 5' end of the 'sense' strand only. RAW264.7 cells were transfected with 100 nM of either siRNA or scrambled siRNA using Lipofectamine 2000 according to the manufacturer's instructions, twelve hours before a subsequent treatment with 5 μg/ml LPS, or vehicle. One day prior to transfections, cells were plated in their regular media (see above) in the absence of antibiotics. As such, lipofectamine and siRNA (or scrambled siRNA) were present for 24 hours and LPS for 12 hours prior to any subsequent measurements.

Irg1-FLAG plasmid transfections: pCMV6-FLAG-Irg1 overexpressing plasmid (4.2 μg, Mus musculus immune responsive gene 1 transfection-ready DNA, OriGene) was transfected into $5*10^6$ RAW-264.7 or COS7 cells cultures cells using Lipofectamine 2000 (Invitrogen) and further incubated for 24-48 hours.

Mitochondrial matrix pH (pHi) determination: pHi of liver mitochondria was estimated as described previously (Zolkiewska et al., 1993), with minor modifications. Briefly, mitochondria (20 mg) suspended in a 2 ml medium containing (in mM): 225 mannitol, 75 sucrose, 5 Hepes, and 0.1 EGTA (pH=7.4 using Trizma) were incubated with 50 μM BCECF-AM at 30 °C. After 20 min, mitochondria were centrifuged at 10,600 g for 3 min (at 4 °C), washed once and recentrifuged. The final pellet was suspended in 0.2 ml of the same medium devoid of EGTA and kept on ice until further manipulation. Fluorescence of hydrolyzed BCECF trapped in the matrix was measured in a Hitachi F-4500 spectrofluorimeter (Hitachi High Technologies, Berkshire, UK) in a ratiometric mode, using 450/490 nm excitation and 531 nm emission wavelengths, respectively. Buffer composition and temperature were identical to that used for both ΔΨm and Mg^{2+} fluorescence determinations. BCECF signal was calibrated using a range of buffers of known pH in the 6.8-7.8 range, and by equilibrating matrix pH to that of the experimental volume by 250 nM FCCP plus 10 μM nigericin.

Determination of ANT content: The ANT content of mitochondria was estimated from titration curves obtained by stepwise addition of cATR to isolated mitochondria during state 3 respiration, as described by Schonfeld (Schonfeld, 1990).

Preparation of cortical neurons: Primary cultures of cortical neurons were prepared from Sprague-Dawley rats (17th day in utero) as described in (Chinopoulos et al., 2004). All animal procedures were carried out according to the local animal care and use committee (Egyetemi Allatkiserleti Bizottsag) guidelines.

COS-7 cells cultures and transfection with the luciferase plasmids: Luciferases targeting the cytosol or nucleus were constructed by the group of Manfredi (Gajewski et al., 2003). COS-7 cells were grown on

175 cm^2 flasks in DMEM plus glutamine plus 10% fetal calf serum plus 1% streptomycin-penicillin. Upon reaching confluence (15-17·10^6 cells per flask), cultures were harvested by trypsinization and were transfected by electroporation according to the manufacturer's instructions (Amaxa Inc, Gaithersburg, MD, USA). Briefly, 3 μg of cytosol- or nuclear-targeted luciferase plasmid was electroporated into 5·10^6 cells in 100 μl electroporation medium. Then, ~70,000 transfected cells were seeded per 25 mm round coverslips pre-coated with poly-L-ornithine. Transfection efficiency was in the 25-40 % range, as verified by immunocytochemistry using a monoclonal antibody raised against luciferase protein from *Photinus pyralis* (10 μg primary mouse, Invitrogen, clone CS 17, IgG1 isotype). Images were evaluated using a Bio-Rad 2100 Rainbow Confocal System (Bio-Rad Laboratories, Inc, CA, USA)

Measurement of oxygen consumption and extracellular acidification rates in cultured cortical neurons: Oxygen consumption rate (OCR) and extracellular acidification rate (ECAR) measurements were performed on culture days 11-13 in an XF24 Extracellular Flux Analyzer (Seahorse Bioscience, North Billerica, MA) in a low buffering capacity medium containing (in mM) 120 NaCl, 3.5 KCl, 1.3 $CaCl_2$, 1 $MgCl_2$, 0.4 KH_2PO_4, 1.2 Na_2SO_4, 15 glucose at pH 7.4 at 37 ºC, as detailed previously (Gerencser et al., 2009b). To prevent excitotoxicity all experiments were performed in the presence of tetrodotoxin (1 μM), MK801 (10 μM), NBQX (10 μM) and nifedipine (1μM).

In situ determination of $\Delta\Psi m$ in neuronal and astrocytic mitochondria: Cortical cultures were grown in Lab-Tek 8-well chambered coverglasses (Nunc, Rochester, NY). $\Delta\Psi m$ was measured by wide-field fluorescence imaging. Briefly, the fluorescence of the mitochondrial potentiometric fluorescent dye tetramethylrhodamine methyl ester (TMRM; 7.5 nM) and an anionic plasma membrane potential indicator (PMPI) were followed in time over cell bodies. $\Delta\Psi m$ was calibrated to millivolts by modeling the redistribution of TMRM across the mitochondrial and plasma membranes (Nicholls, 2006) and PMPI across the plasma membrane (Gerencser et al., 2009a). Experiments were performed at 37 ºC in the medium used for OCR measurements above, supplemented by $NaHCO_3$ (5 mM), TES (20 mM) and tetraphenylboron (1 μM).

mtDNA content: Total DNA was isolated from 4 pooled tissues from each mouse group using QIAamp DNA Mini Kit (QIAGEN) following the manufacturer's instructions. Relative mtDNA content was quantified in triplicate by real time PCR using primers for cox1 (forward primer 5'-TGCTAGCCGCAGGCATTA C-3' reverse primer 5'-GGGTGCCCAAAGAATCAGAAC-3' and normalized against the nuclear encoded actinB gene (forward primer 5'GGAAAAGAGCCTCAGGGCAT-3' , reverse primer-5'-GAAGAGCTATGAGCTGCCTGA-3'), as previously described (Ylikallio et al., 2010). DNA was amplified in an ABI 7900 system as follows: 95°C for 10 min followed by 45 cycles of a two-stage temperature profile of 95°C for 15 sec and 60°C for 1 min.

Protein purification: The gene sequences for mature human SUCLG1 (residues 29-333, ~33.2 kDa, GenBank: CAG33420.1) and mature human SUCLG2 (residues 39-432, ~43.6 kDa, GenBank: AAH68602.1) were sequence optimized for expression in *E.coli*, synthesized, incorporated in pJ411 plasmids bearing kanamycin resistance, and sequence verified (DNA2.0, Newark, CA, USA). The native protein sequence in each case was supplemented with a C-terminal hexahistidine tag (GSHHHHHH). Each pJ411-SUCLG1/2 plasmid was transfected into inducible *E.coli* BL21 (DE3) strain and the bacteria were grown in Luria-Bertani medium at 37°C. Protein expression was induced with 1 mM isopropyl β-D-1-thiogalactopyranoside for 3 hours. The collected bacteria were sonicated in 10 ml lysis buffer (25 mM Tris (pH 8.5), 150 mM NaCl, 0.5 mg/ml lysozyme, 0.2% Triton X-100) per gram of wet pellet. Both proteins formed inclusion bodies when overexpressed, with minimal or no presence in the soluble fraction of the lysate. The proteins were purified in their unfolded state (7M urea, 200 mM NaCl) with affinity chromatography, after binding to Ni-Sepharose™ 6 Fast Flow resin (GE Healthcare). The eluates

were diluted 15-fold in 20 mM Tris (pH 8.5), 100 mM NaCl, the precipitated protein was removed, and the supernatants were dialyzed against the same buffer. The purity of the two proteins was assessed with SDS PAGE and the final protein concentrations were estimated using the bicinchoninic acid assay as detailed above. The protein stocks were aliquoted, flash-frozen in liquid nitrogen and stored at −80°C.

Electron transport chain complex and citrate synthase activity assays: Enzymatic activities of rotenone sensitive NADH CoQ reductase (Complex I), succinate cytochrome *c* reductase (complex II/III), succinate dehydrogenase (complex II, SDH), cytochrome *c* oxidase (COX complex IV) and citrate synthase (CS), a mitochondrial marker enzyme, were determined in isolated mitochondria as previously described (Saada et al., 2004), (Reisch and Elpeleg, 2007).

Determination of succinate-CoA ligase activity: ATP- and GTP-forming succinate-CoA ligase activity in isolated mitochondria was determined at 30 °C, as described in (Alarcon et al., 2002), with the modifications detailed in (Lambeth et al., 2004). Mitochondria (0.25 mg) were added in an assay mixture (2 ml) containing: 20 mM potassium phosphate, pH 7.2, 10 mM MgCl2, and 2 mM ADP or GDP. The reactions were initiated by adding 0.2 mM succinyl-CoA and 0.2 mM DTNB (5,5'-dithiobis(2-nitrobenzoic acid)) in quick succession. The molar extinction coefficient value at 412 nm for the 2-nitro-5-thiobenzoate anion formed upon reaction of DTNB with CoASH was considered as 13,600 M^{-1} cm^{-1}. Rates of 2-nitro-5-thiobenzoate formation were followed spectrophotometrically during constant stirring.

Determination of acylcarnitines: Multiple reaction monitoring transitions of butyl ester derivatives of acylcarnitines from dry bloodspots and stable isotope internal standards were analyzed by electrospray ionization-tandem mass spectrometry (MS-MS) using a Waters Alliance 2795 separations module coupled to a Waters Micromass quarto micro API mass spectrometer monitoring for acylcarnitines (Milford MA USA), as described in (Rashed et al., 1997).

Determination of Sucla2 mRNA by qRT-PCR: mRNA coding for Sucla2 was quantified by qPCR in two different laboratories using two different 'housekeeping' mRNAs for normalization, β-actin or proteasome 26S subunit, ATPase 4 (Psmc4). In both cases, total RNA was isolated from the organs (livers, hearts, brains) of at least four mice per age group and genotype (WT or $Sucla2^{+/-}$) with RNeasy Micro Kit (Qiagen, Hilden, Germany) according to the manufacturer's instructions. 1 µg RNA was reverse transcribed with QuantiTect Reverse Transcription Kit (Qiagen). Subsequently, quantitative Real-Time PCR (qRT-PCR) was carried out using predesigned TaqMan Gene Expression Assays (Thermo Fisher Scientific, Waltham, Massachusetts, USA): Sucla2 (Mm01310541_m1) and Actb (Mm00607939_s1). Real-time reaction was performed on a QuantStudio 7 Flex Real-Time PCR system (Applied Biosystem, Life Technologies, Carlsbad, California, USA) according to the manufacturer's protocol. Gene expression level was normalized to ß-actin. Fold change (FC) was calculated using the 2-ΔΔCt method [8]. Alternatively, expression level of Sucla2 mRNA was determined by real time PCR using TaqMan Gene Expression assay kit and 7500 Real Time PCR System (Applied Biosystems), using the TaqMan Gene Expression Assays, XS, Sucla2 (AB, 4331182, FAM/MGB-NFQ) kit. Measured values were normalized by using the TaqMan Gene Expression Controls, Psmc4 mouse (AB, 4448489, VIC-MGB) kit, as recommended by Applied Biosystems for standard gene expression experiments because of their design criteria.

Fluorescence Imaging: Imaging was performed on an Olympus IX-81 invert microscope equipped with a UAPO 20× air 0.75NA lens, a Lambda LS Xe-arc light source (175W), Lambda 10-2 excitation and emission filter wheels (Sutter Instruments, Novato, CA), a ProScan linear encoded xy-stage (Prior, Rockland, MA) and a Coolsnap HQ cooled digital CCD camera (Photometrics, Tucson, AZ; -30°C, 10 Mhz readout, low gain, 12 bit depth). Full frames at 4×4 binning (1.3 µm/pixel resolution) were taken in 3 minutes intervals. 12-30 view fields in 4-6 wells of the Lab-Tek chamber were recorded cyclically using the Multi

Dimensional Acquisition feature of the Metamorph 6.3 (Molecular Devices, Downingtown, PA). The filter sets given as excitation – dichroic mirror – emission in nm were: for PMPI 500/24 – 520LP (long pass) – 542/27 (all from Semrock, Rochester, NY); for TMRM: 555 – 475/560LP – 620/40 (all from Chroma, Rockingham, VT). The cross-talk of TMRM and PMPI emissions were eliminated by linear spectral unmixing of intensity traces in Mathematica 5.2 (Gerencser et al., 2009a).

Luciferase assay in COS-7 cells: For luciferase assays, 25 mm round coverslips with attached cells were incubated for 3 minutes in a medium containing: NaCl 120 mM, KCl 3.5 mM, Hepes-Na 20 mM, $MgCl_2$ 1 mM, $CaCl_2$ 1.3 mM, Glucose 15 mM (where indicated), pyruvate-Na 5 mM (where indicated, together with 2 mM 2-deoxyglucose) and iodoacetamide 250 μM, pH 7.38. Mitochondrial poisons and luciferin (1 mM) were added, and luminescence was measured in a Victor^3 Wallace plate reader luminometer (Perkin Elmer, Boston, MA, USA). Luminescence signals were recorded over a 60 min time interval, and results are shown as the area under the curve of the luminescence intensity.

Western blotting (for isolated mitochondria): Immunoblotting of solubilized mitochondria was performed as recommended by the manufacturers of the antibodies. Rabbit polyclonal to succinate-CoA ligase, ADP-forming, beta subunit (Proteintech Europe Ltd, Manchester, UK) primary antibody was used at 1:1,000. Mouse monoclonal to VDAC-1 (Calbiochem) was used at 1:20,000. Immunoreactivity was detected using the peroxidase-linked secondary antibodies (1:10,000, Jackson ImmunoResearch) and enhanced chemiluminescence detection reagent (ECL system, Amersham Biosciences GE Healthcare Europe GmbH, Vienna, Austria).

Cell-attached electrophysiological recordings: Patch pipettes were pulled from borosilicate glass to resistances of 6-8 MOhms. Pipette solution contained: KCl 120 mM, Hepes acid 20 mM, $MgCl_2$ 4 mM, $CaCl_2$ 1.3 mM, EGTA 5 mM, pH 7.38 tetrodotoxin 1 μM, MK801 12 μM, CNQX 10 μM, nimodipine 1 μM, charybdotoxin 100 nM, iberiotoxin 100 nM, apamin 0.5 μM, TRAM-34 1 μM, clotrimazole 100 nM, pH 7.4. Bath solutions contained: NaCl 120 mM, KCl 3.5 mM, Hepes-Na 20 mM, $MgCl_2$ 1 mM, $CaCl_2$ 1.3 mM, Glucose 15 mM, pH 7.38, tetrodotoxin 1 μM, MK801 12 μM, CNQX 10 μM, nimodipine 1 μM, iodoacetamide 250 μM and pinnacidil 100 μM. Cultured neurons were placed into a chamber and visualized under DIC in a non-perfused manner. Seal resistances of >10 GOhms were routinely obtained and patches remained stable for tens of minutes. Currents were acquired at 1 kHz amplified using an Axopatch 200B amplifier (Axon Instruments, Foster City, CA), digitized at a sampling rate of 10 kHz (Digidata 1322A, Axon Instruments), and recorded using pCLAMP 10 software (Axon Instruments). All recordings were done at ambient room temperature (~23°C).

Determination of α-ketoglutarate dehydrogenase activity*:* KGDHC activity in mouse liver and brain isolated mitochondria and isolated nerve terminals was measured fluorimetrically as detailed in (Starkov et al., 2004) with minor modifications. The reaction medium was composed of 20 mM HEPES, pH 7.8, 0.3 mM thiamine pyrophosphate, 50 μM $CaCl_2$, 0.2 mM $MgCl_2$, 5 mM α-ketoglutarate, 1 mM dithiothreitol and 0.5 mM NAD^+. The reaction was started by adding 0.12 mM CoASH to freeze-thawn mitochondria (0.1 mg/ml) or synaptosomes (0.5 mg/ml). Reduction of NAD^+ was followed at 435 nm emission after excitation at 340 nm. The extinction coefficient (ε340) of NADH fluorescence was considered as 6,220 $M^{-1}cm^{-1}$.

Culturing of myoblasts and preparation of myotubes: Mouse C_2C_{12} myoblasts (Blau et al., 1983) were cultured in DMEM containing 10% fetal bovine serum and antibiotic-antimycotic solution at 37°C in 5% CO_2. Cells were plated at 140,000 cells/well in 6 well tissue culture plates. To induce differentiation of myoblasts into myotubes, culture medium was replaced with differentiation medium containing DMEM and 2% horse serum when the cells reached >90% confluence. Fusion of myoblasts into elongated and multinucleated myotubes was evident in 3 to 4 days in differentiation medium. Myotubes were

processed on the 6th day for all subsequent experiments. Myotubes were washed once in phosphate-buffered saline and harvested with 0.1 ml of 0.25% trypsin-EDTA, inactivated by 0.9 ml calf serum, followed by centrifugation at 1,100 g for 2 minutes. Cells were washed once in a buffer containing, in mM: KCl 8, K-gluconate 110, NaCl 10, Hepes 10, KH_2PO_4 10, EGTA 0.005, mannitol 10, $MgCl_2$ 0.5-1.5 (where indicated) and 0.5 mg/ml bovine serum albumin (fatty acid-free), pH 7.25 without disturbing the pellet, prior to resuspension in 0.2 mL of the same buffer including, in mM: glutamate 5, malate 5, Ap5A 0.1, iodoacetamide 0.25, NaF 5, $BeSO_4$ 0.2 and Na_3VO_4 0.1.

Mitochondrial membrane potential (ΔΨm) determination in *in situ* mitochondria of permeabilized C_2C_{12} cells: ΔΨm was estimated using fluorescence quenching of the cationic dye safranine O due to its accumulation inside energized mitochondria (Akerman and Wikstrom, 1976). C_2C_{12} cells were treated exactly as described for free [Mg^{2+}] determination, except that MgG was replaced by 5 μM safranine O. Fluorescence was recorded in a Spectramax M5 plate reader at a 0.33 Hz acquisition rate (one acquisition every 2 sec plus 1 sec for mixing in between each acquisition), using 495 and 585 nm excitation and emission wavelengths, respectively. Experiments were performed at 37 °C.

Citrate synthase: Citrate synthase activity was measured as described by (Srere, 1969) with minor modifications. Briefly, 20 μl aliquots (~30 μg of protein) from the 0.2 ml cell suspensions that have been freeze-thawn were added to a 0.18 ml medium containing 20 mM Hepes pH 7.8, 0.5 mM oxaloacetate and 0.1 mM dithionitrobenzoic acid. The reaction was started after 3 min preincubation time by adding 0.36 mM acetyl-CoA. Changes in the absorbance at 412 nm due to 5-thio-2-nitrobenzoic acid formation were monitored in a Spectramax M5 plate reader at 25 °C. Activity was calculated as nmol/min/mg protein assuming an extinction coefficient for 5-thio-2-nitrobenzoic acid, of εM= 14,150 $M^{-1}*cm^{-1}$. The light path for 0.2 ml volume in the well of a 96 plate is 0.5 cm. Protein content was measured by the bicinchoninic acid assay using bovine serum albumin protein as standards and calibrating by a 3 parameter power function, $f=y_0+a*x^b$, where y_0 is background absorbance in the absence of protein, a and b are constants, and x is the amount of protein in the unknown samples.

Preparation of sodium orthovanadate (Na_3VO_4) and BeF_3^-: A 25 mM Na_3VO_4 solution was prepared in bi-distilled water. The pH was set to 8.7 with HCl, upon which the solution turned to yellow. This solution was boiled until colorless and allowed to cool to room temperature. pH was reassessed, and readjusted to pH 8.7 with HCl, upon which the solution returned again to yellow color. This solution was boiled again and this cycle was repeated until the solution remained colorless and at pH 8.7 after boiling and cooling. Finally, it was brought up to the initial volume with bi-distilled water and stored in aliquots at -80 °C. This treatment removes all decavanadate ions present in the Na_3VO_4 solution. Decavanadate induces mitochondrial membrane depolarization in addition to inhibiting oxygen consumption (Aureliano and Crans, 2009). Orthovanadate inhibits the oxidation of only disrupted mammalian mitochondria (Byczkowski et al., 1979). Likewise, fluoroberyllium nucleoside diphosphate complexes inhibit only the exposed F_1F_o-ATPase (Issartel et al., 1991). $BeSO_4$ and NaF are prepared as aqueous solutions of 0.2 M and 0.5 M respectively, without any additional modifications, and kept at +4 °C. BeF_3^- (among other combinations) is formed immediately in solution upon mixing $BeSO_4$ and NaF, provided that NaF is in excess. Vanadate, beryllium and fluoride salts are highly toxic to tissues and to the environment, and must be handled and disposed properly. The combination of orthovanadate and BeF_3^- will inhibit kinases, mutases, phosphatases, and ATPases (Climent et al., 1981), (Ray et al., 1990) . Some kinases though, will remain uninhibited, such as pyruvate kinase (Lord and Reed, 1990). In this respect, upon permeabilization of the cells one has to totally separate pyruvate kinase from its substrate, phosphoenol pyruvate, i.e. there must be no glucose present in the medium prior to permeabilization, and a few minutes lag time must be allowed prior to ADP-ATP exchange rate measurements in order for the remaining reactions by kinases to 'die-out'. The effect of 10 nM cATR blocking completely ADP-ATP

exchange rates signifies that all adenine nucleotide interconverting reactions have been rendered inoperable.

Determination of matrix adenine nucleotides by HPLC: 0.25 ml of 65 mg/ml rat liver mitochondria were added to 1 ml buffer with 5 mM glutamate and 5 mM malate or without substrates (but in the presence of 1 μM SF 6847) containing (in mM): KCl 8, K-gluconate 110, NaCl 10, Hepes 10, KH_2PO4 10, EGTA 0.005, mannitol 10, $MgCl_2$ 1, 0.5 mg/ml bovine serum albumin (fatty acid-free), pH 7.25, and 1 μM Cys A (to inhibit opening of the permeability transition pore that could lead to loss of matrical adenylate nucleotide pools) and 50 μM A_p5A for 3 min. Subsequently, 1 ml of this mixture was added to 1 ml of ice-cold perchloric acid (3 M), and allowed to deproteinise at 0 ^{0}C for 5 min. After, 2 ml of 1.5 M KOH and 0.5 M Tris was added, and allowed for the precipitate to form at 0 ^{0}C for 5 more min. Then 0.8 ml of the supernatant was spun at 25,000 g for 3 min at 4 ^{0}C, 0.6 ml was collected, adjusted to pH 6.5-6.7 with perchloric acid or KOH and Tris and respun at 25,000 g for 3 min at 4 ^{0}C to remove any remaining precipitate. Supernatants were immediately frozen with liquid nitrogen and kept at -70 ^{0}C for further use. The chromatographic separation of adenine nucleotides (AMP, ADP and ATP) were carried out using a C18 reversed-phase column (ODS Hypersyl, 250 mm x 4.6 mm i.d.; particle size 5 μm). The mobile phase was composed of 215 mM sodium dihydrogen phosphate, 2.3 mM tetrabutyammonium hydroxide, 4% acetonitrile, 0.4 % potassium hydroxide and the flow rate was 1 ml/min. The sample injection volume was 20 μl and during isocratic acquisition the components were monitored at 260 nm by a multiwavelength Jasco Pu-2075 Plus Intelligent UV detector connected to a Jasco Pu-2089 Quaternary Gradient pump and Rheodyne sample injector (Jasco, Gross-Umstadt, Germany). Calibration of the signals was performed by 'spiking' the samples with known amounts of AMP, ADP and ATP in a relevant range of concentrations.

Kinetic model of phosphorylation in mitochondria: Kinetic model of phosphorylation subsystem of mitochondrial oxidative phosphorylation includes quantitative description of the following processes: 1) ATP synthesis, catalyzed by ATP-ase/ATP-synthase (V_{SYN}); 2) electrogenic translocation of adenine nucleotides, catalyzed by the adenine nucleotide translocase (V_{ANT}); 3) electroneutral symport of inorganic phosphate and a proton, as catalyzed by the phosphate carrier; 4) electrogenic transport of protons from matrix to intermembrane space by electron transport chain (I-IV complexes) with generation of membrane potential (V_{O2}); 5) K^+, H^+ and other ions leaks across the mitochondrial inner membrane (V_{leak}). The transport and synthesis of adenylates can be represented by system of algebra-differential equations:

$$\begin{cases} \frac{d}{dt} D_i^t = -V_{SYN} + V_{ANT}, \\ T_i^t + D_i^t = A_i^t. \end{cases} \qquad (3a)$$

Here, T_i^t and D_i^t stand for concentrations of total ATP and ADP in mitochondrial matrix. Additionally, it is necessary to take into account the ionic balance in the system. The total ionic current can be represented as following:

$$I = F \cdot \left(20 \cdot V_{O2} - V_{leak} - 3 \cdot V_{SYN} - V_{ANT}\right)$$

Where "*I*" stands for total current (positive and negative) of ions transported across the inner membrane of mitochondria. The positive current direction is from matrix to intramembrane space. The integer

coefficients of the right hand side of second equation of the system (3) were chosen on the basis of the knowledge of number of charges transferred or leaked across the inner mitochondrial membrane:

- The electron transport chain transports 20 protons per O_2 molecule;
- F_0-F_1 ATPase transports 3 protons per one molecule of ATP synthesized;
- One cycle of transport by ANT leads to transport of one additional charge;

The ionic current across the membrane determines the changes in membrane potential.

$$I = C_m \frac{d\Delta\Psi_m}{dt}$$

Thus, the changes in membrane potential can be described as:

$$\frac{d\Delta\Psi_m}{dt} = \frac{F}{C_m}\left(20 \cdot V_{O2} - V_{leak} - 3 \cdot V_{SYN} - V_{ANT}\right) \quad (3b)$$

The equations 3a, 3b represent the full system describing the phosphorylation of mitochondria.

The following ion balances have been taken into account in the model:

1) Binding/dissociation of magnesium ions to adenylate nucleotides in mitochondrial matrix and outside of mitochondria to form the following complexes $MgADP^-$, $MgATP^{2-}$;

$$ATP^{4-} + Mg^{2+} = MgATP^{2-}, \quad K_{T,Mg} = \frac{T_i \cdot Mg_i}{MgT_i}, K_{T,Mg} = \frac{T_o \cdot Mg_o}{MgT_o} \quad (4)$$

$$ADP^{3-} + Mg^{2+} = MgADP^-, \quad K_{D,Mg} = \frac{D_i \cdot Mg_i}{MgD_i}, K_{D,Mg} = \frac{D_o \cdot Mg_o}{MgD_o} \quad (5)$$

Here, T_o and D_o stand for concentrations of free ATP and ADP outside of mitochondria. Values of dissociation constants are listed in Table 4.1.

2) Binding/dissociation of protons to inorganic phosphate to form following complexes $H_2PO_4^-, HPO_4^{2-}$ in mitochondrial matrix and outside of mitochondria

$$HPO_4^{2-} + H^+ = H_2PO_4^-, \quad K_{P,H} = \frac{P2_i \cdot H_i}{P1_i}, K_{P,H} = \frac{P2_o \cdot H_o}{P1_o} \quad (6)$$

Here, $P1_i$, $P2_i$ and $P1_o, P2_o$ are concentrations of twice-protonated and once-protonated inorganic phosphate in mitochondrial matrix and outside mitochondria, respectively. All these binding/dissociation processes are assumed to be at equilibrium.

On the basis of equations (4) and (5) we can express concentrations of free adenine nucleotide and their complexes with magnesium in terms of total concentrations of ADP (D_o^t, D_i^t) and ATP (T_o^t, T_i^t):

$$T_i = T_i^t \frac{1}{1+\frac{Mg_i}{K_{T,Mg}}} \qquad T_o = T_o^t \frac{1}{1+\frac{Mg_o}{K_{T,Mg}}}$$

$$MgT_i = T_i^t \frac{\frac{Mg_i}{K_{T,Mg}}}{1+\frac{Mg_i}{K_{T,Mg}}} \qquad MgT_o = T_o^t \frac{\frac{Mg_o}{K_{T,Mg}}}{1+\frac{Mg_o}{K_{T,Mg}}}$$

$$D_i = D_i^t \frac{1}{1+\frac{Mg_i}{K_{D,Mg}}} \qquad D_o = D_o^t \frac{1}{1+\frac{Mg_o}{K_{D,Mg}}} \qquad (7)$$

$$MgD_i = D_i^t \frac{\frac{Mg_i}{K_{D,Mg}}}{1+\frac{Mg_i}{K_{D,Mg}}} \qquad MgD_o = D_o^t \frac{\frac{Mg_o}{K_{D,Mg}}}{1+\frac{Mg_o}{K_{D,Mg}}}$$

Using equations (6) we can express concentrations of extramitochondrial $H_2PO_4^-, HPO_4^{2-}$ in terms of total concentration of inorganic phosphate (P_o^t)

$$P2_o = P_o^t \frac{1}{1+\frac{H_o}{K_{P,H}}}$$

$$P1_o = P^t \frac{\frac{H_o}{K_{P,H}}}{1+\frac{H_o}{K_{P,H}}} \qquad (8)$$

The Pi/H carrier of mitochondria catalyzes the electroneutral symport of twice protonated phosphate and proton: $\left(H_2PO_4^-\right)_o + H_o^+ = \left(H_2PO_4^-\right)_i + H_i^+$. The V_{max} of inorganic phosphate transport is much higher than the rates of adenylates transport and synthesis (Coty and Pedersen, 1974) and K_m is much lower than the concentrations of *Pi in* or *out* of matrix. Thus, the phosphate transport does not limit oxidative phosphorylation at physiological conditions. According to the rapid-equilibrium approximation we can express concentrations of matrix $H_2PO_4^-, HPO_4^{2-}$ in terms of extramitochondrial phosphate concentration and *pH* values in mitochondrial matrix and extramitochondrial space:

$$K_{eq}^{P/H} = \frac{P1_o \cdot H_o}{P1_i \cdot H_i}$$

So, taking into account the stoichiometry 1:1 and electroneutrality of Pi/H transport we can conclude $K_{eq}=1$, so we can express the following:

$$P1_i = P1_o \cdot \frac{H_o}{H_i}$$

$$P2_i = P1_i \frac{K_{P,H}}{H_i} \qquad (9)$$

Here H_i and H_o are proton concentrations in mitochondrial matrix and outside of mitochondria:

$$H_o = 10^{3-pH_o}\, mM$$
$$H_i = 10^{3-pH_i}\, mM$$

The rate equation of the ATP-synthase reaction is based on a minimal kinetic scheme for ATP synthesis - hydrolysis (Demin et al., 1998):

$$V_{SYN} = c_{SYN} \cdot V_{\max}^{SYN} \exp\left(n_{SYN}\chi\phi\right)\left(\frac{H_o}{K_{Ho}^{SYN}}\right)^{n_{SYN}} \times$$
$$\times \frac{1}{K_{MgD}^{SYN} \cdot K_{P1}^{SYN}} \frac{MgD_i \cdot P1_i - MgT_i \cdot K_{eq}^{SYN} \cdot \exp\left(-n\phi\right) \cdot \left(\frac{H_o}{H_i}\right)^{-n}}{1 + \frac{MgD_i \cdot P1_i}{K_{MgD}^{SYN} \cdot K_{P1\ i}^{SYN}}\left(\frac{H_o}{K_{Ho}^{SYN}}\right)^{n_{SYN}} + \frac{MgT_i}{K_{MgT}^{SYN}}\left(\frac{H_i}{K_{Hi}^{SYN}\exp\left(\chi_n\phi\right)}\right)^{n_{SYN}}} \qquad (10)$$

Here, $\phi = -\frac{F\Delta\psi}{RT}$ and $K_{eq}^{SYN} = K_{hyd}^{SYN}\frac{K_{T,Mg}}{K_{D,Mg}} \cdot \frac{10^{-7+3}}{10^{-7+3}+K_{P,H}}$

Values of all parameters of the equation except c_{SYN} are taken from (Demin et al., 1998) and (Demin et al., 2001) and listed in Table 4.1 and references therein. c_{SYN} is a dimensionless correction factor characterizing activity of ATP-synthase in the particular mitochondria preparation. This factor has been estimated through the fitting of the model to experimental data presented in (Metelkin et al., 2009). The rate equation for adenine nucleotide translocation has been derived in (Metelkin et al., 2006):

$$v_{ANT} = c_{ANT} \cdot \frac{1}{\Delta^{ANT}}\left(k_2^{ANT} q^{ANT} \frac{T_i \cdot D_o}{K_{Do}^{ANT}} - k_3^{ANT} \frac{D_i \cdot T_i}{K_{To}^{ANT}}\right),$$
$$\Delta^{ANT} = \left(1 + \frac{T_o}{K_{To}^{ANT}} + \frac{D_o}{K_{Do}^{ANT}}\right)\left(D_i + q^{ANT} \cdot T_i\right), \qquad (11)$$

Here,

$$q^{ANT} = \frac{k_3^{ANT} K_{Do}^{ANT}}{k_2^{ANT} K_{To}^{ANT}} \exp(\phi),$$
$$K_{Do}^{ANT} = K_{Do}^{ANT,0} \exp(3\delta_D \phi),$$
$$K_{To}^{ANT} = K_{To}^{ANT,0} \exp(4\delta_T \phi),$$
$$k_2^{ANT} = k_2^{ANT,0} \exp\{(-3a_1 - 4a_2 + a_3)\phi\},$$
$$k_3^{ANT} = k_3^{ANT,0} \exp\{(-4a_1 - 3a_2 + a_3)\phi\}$$

Values of all parameters of the equation except c_{ANT} are taken from (Metelkin et al., 2006) and listed in Table 4.1 and references therein. Value of c_{ANT} refers to the *apparent* (not true) concentration of ANT dimers per mg of total mitochondrial protein. Indeed, values for $k_2^{ANT,0}$ and $k_3^{ANT,0}$ have been estimated (see (Metelkin et al., 2006) for details) on the basis of the experimental data measured on proteoliposomes. This means that the values of the rate constants are underestimated because some of ANT proteins may be damaged in that experiment. Consequently, to use the equation of ANT activity it is necessary to estimate c_{ANT} for the given mitochondria suspension. In this way the values of:

$$k_{ANT+}^0 = k_2^{ANT,0} \cdot c_{ANT}$$

and

$$k_{ANT-}^0 = k_3^{ANT,0} \cdot c_{ANT}$$

can be considered as "true" direct and reversed activities of ANT at zero membrane potential. Only these values characterize the given suspension of mitochondria but not the value of c_{ANT} itself. Thus, c_{ANT} has been estimated through the fitting of the model to experimental data presented in this paper (see Results and Discussion section).In order to describe generation/consumption of membrane potential it is necessary to take into account a variety of processes of ion exchanges and leaks catalyzed by different enzymes and transporters. Several models have been published serving this purpose (for an example see (Demin et al., 1998)). However, to simulate ATP synthesis just in respiration states II, III, IV, a detailed description is obviously redundant. In our study, a simple empirical description of membrane potential of generation/consumption was used. Indeed, we assumed that oxygen consumption rate (V_{O2}) and rate of ion leaks through the inner mitochondrial membrane were given by following equations:

$$V_{O2} = \frac{k_{O2}}{1 + K_{O2} \exp(\beta_{O2}\phi)}$$

$$V_{leak} = k_{leak} \exp(\beta_{leak}\phi)$$

There are 5 parameters in these equations. The values of the parameters (Table 4.1) were chosen in such a way to fit experimentally measured dependence of O_2 consumption on electric potential difference depicted in Fig. 4.4A and to allow the model to describe values of respiratory rate at states II, III and IV. Indeed, our model was verified against following experimental data: State III corresponds to V_{O2}= 216 nmol/min/mg, ΔΨm= -145 mV. State II corresponds to V_{O2}=19 nmol/min/mg, ΔΨm=-170 mV. State IV (induced by cATR) corresponds to V_{O2}=17 nmol/min/mg, ΔΨm=-170 mV.

Table 4.1. **The parameters of the model**

Parameter	**Value**	**Comment**	**Source**

pH_o	7.25	*pH* in experimental volume	Measured or given value
pH_i	7.30	*pH* in matrix under phosphorylating conditions	
Mg_o^t	1 mM	Total magnesium concentration in experimental volume	
V_o	2 ml	Experimental volume	
P_o^t	10 mM	Total [Pi] concentration in experimental volume	
T_o^t, D_o^t	Dependent on experimental conditions	Concentration of adenine nucleotides (ATP, ADP) in experimental volume	
Mg_i^{2+}	0.35 mM	Buffered magnesium concentration in the matrix	(Corkey et al., 1986)
$A_i^t = T_i^t + D_i^t$	12 mM	Total concentration of adenylates (ATP+ADP) in the matrix; (see (Hagen et al., 2003)).	(Hagen et al., 2003), (Joyal et al., 1995), (Austin and Aprille, 1984), (Nosek et al., 1990), (Rulfs and Aprille, 1982)
$K_{P,H}$	$6.31 \cdot 10^{-5}$ mM	Dissociation constant for H^+ and phosphate	Calculated from pKa=7.2
$K_{T,Mg}$	0.114 mM	Dissociation constant for Mg^{2+} and ATP	(Chinopoulos et al., 2009)
$K_{D,Mg}$	0.906 mM	Dissociation constant for Mg^{2+} and ADP	
K_{hyd}^{SYN}	$2.23 \cdot 10^{8}$ mM	Equilibrium constant of ATP hydrolysis	Calculated from $\Delta G_0'$=-30.5 kJ/mole (Rosing and Slater, 1972)
c_{ANT}	$4.8 \cdot 10^{1}$ nmol/ mg	effective coefficient	Estimated on the basis of fitting of the model against our data
$k_2^{ANT,0}$	10.8 min^{-1}	Constant of direct ANT exchange	(Metelkin et al., 2006)
$k_3^{ANT,0}$	21.0 min^{-1}	Constant of reverse ANT exchange	
$K_{To}^{ANT,0}$	0.057 mM	Dissociation constant of ATP and ANT	
$K_{Do}^{ANT,0}$	0.051 mM	Dissociation constant of ADP and ANT	

a_1	0.268	Parameters of ANT electrostatic profile	
a_2	-0.205		
a_3	0.187		
δ_T	0.070		
δ_D	0.005		
c_{SYN}	22	Correction factor of ATP-synthase in mitochondria	Estimated on the basis of fitting of the model against our data
n_{SYN}	3	H^+/ATP ratio	(Ferguson, 2000)
χ	0.9	Parameters of H^+-ATP-synthase electrostatic profile	
χ_n	0.1		
$V_{\max}^{SYN}$	$1.2 \cdot 10^{-4}$ nmol/min/mg	Parameters of H^+-ATP-synthase model	(Demin et al., 1998)
K_{Ho}^{SYN}	$3 \cdot 10^{-5}$ mM		
K_{Hi}^{SYN}	$1 \cdot 10^{-6}$ mM		
K_{MgD}^{SYN}	$5.56 \cdot 10^{-3}$ mM		
K_{P1}^{SYN}	$3.55 \cdot 10^{-1}$ mM		
K_{MgT}^{SYN}	$9.26 \cdot 10^{-1}$ mM		
F	$9.64 \cdot 10^4$ C·mol^{-1}	Faraday constant	
R	8.31 J·mol^{-1}·K^{-1}	Universal gas constant	
T	310 K	Temperature	Measured
C_m	$7.8 \cdot 10^{-6}$ F/mg	Capacitance of inner mitochondrial membrane	(Reich and Rohde, 1983)
k_{O2}	250 nmol/min/mg	The empirical coefficients of membrane potential generation	Fitted to experimental data
K_{O2}	$1.45 \cdot 10^{-12}$		
β_{O2}	0.36		
k_{leak}	0.438 nmol/min/mg	The empirical coefficients of membrane leak description	
β_{leak}	1.05		

RESULTS

1. Development of a kinetic assay of mitochondrial ATP-ADP exchange rate mediated by the ANT

The adenine nucleotide translocase (ANT) catalyzes the reversible exchange of ADP for ATP with a 1:1 stoichiometry across the inner mitochondrial membrane. It is the most abundant among mitochondrial carrier family proteins, and in the heart it accounts for as much as 10% of all inner mitochondrial membrane proteins (Nury et al., 2006) (Pebay-Peyroula and Brandolin, 2004). In humans, there are 4 known isoforms (Palmieri, 2004), (Dolce et al., 2001), all encoded by nuclear DNA (Dahout-Gonzalez et al., 2006), (Nury et al., 2006). Prior to the more recent discovery of the 4th isoform (ANT-4), it was shown that rodents lack ANT-3 (T2) (Levy et al., 2000) (Dummler et al., 1996) but possess ANT-1 (T1) and ANT-2 (T3), sharing a sequence homology of 97-98%, at the amino acid level (Levy et al., 2000). Besides the canonical role of ANT as an adenine nucleotide exchanger which brings ADP into mitochondria to support respiration while simultaneously supplying cytosolic energy-consuming processes with ATP, this protein has many other roles in both physiological and pathological conditions. ADP/ATP exchange through ANT is reversible (Metelkin et al., 2006); therefore, in cells in which mitochondrial respiration is compromised, ATP could enter mitochondria to be hydrolyzed by the –also reversible- F_o-F_1 ATPase. This process can maintain an appreciable protonmotive force (pmf) in the absence of a functional respiratory chain (Scott and Nicholls, 1980), however, not exceeding the reversal potential of the F_o-F_1 ATPase (see below). In addition to transporting nucleotides, ANT is also a major conduit of the "proton leak" (Brand et al., 1994), a passage of protons back into the matrix which bypasses the F_o-F_1 ATPase and causes mild uncoupling.

The kinetic assay of mitochondrial ATP-ADP exchange was based on the concept that the ANT transports Mg^{2+}-free adenine nucleotides. Since the nucleotides exhibit different affinities for Mg^{2+}, by following [Mg^{2+}] concentration one could deduce the absolute [ATP] and [ADP] concentrations using standard binding equations. The abundance of ANT in mitochondria ensures that the changes in [ATP] and [ADP] concentrations are sufficiently large so that the changes in [Mg^{2+}] concentration are detactable.

1.1. Rationale for using particular buffer and substrate compositions

The ATP-ADP exchange rate was determined in intact isolated mitochondria and the incubation medium was designed to enhance the specificity and reproducibility of the method. The main modifications, as compared to 'standard' compositions employed elsewhere in studies with isolated mitochondria (Chinopoulos et al., 2003), were (i) the replacement of a large fraction of [Cl^-] with gluconate, (ii) the use of 10 mM KH_2PO_4, and (iii), where indicated, the high concentration (1 mM) of TMPD. Concerning the estimation of the initial ANT activity rates and the steady-state ATP-ADP exchange rates and their differences, the reader is referred to a recent comprehensive review by Klingenberg (Klingenberg, 2008).

Total [Cl^-] in the buffer was ~20 mM, being within the physiological range of intracellular [Cl^-] for all tissues used as a source of mitochondria in our study. ANT is inhibited at high [Cl^-]; 140 mM Cl^- inhibits ANT activity by ~35%, while with 140 mM gluconate this is only ~7% (Gropp et al., 1999). The combination of [Cl^-] and [gluconate] used in our buffer is unlikely to cause substantial inhibition of ANT activity while maintaining isoosmolarity. Furthermore, we found that mitochondria kept in 20 mM [Cl^-] exhibit similar respiration rates and membrane potential, but significantly lower steady-state rates of ROS formation, when compared to mitochondria exposed to 140 mM [Cl^-] (Chinopoulos et al., 2009). The phosphate (Pi) concentration in our assay medium was 10 mM for the following reasons: There are two Pi carrier isoforms in mitochondria with Km values for Pi (on the external membrane surface) of 2.2 and 0.78 mM, respectively (Palmieri, 2004). The high concentration of phosphate achieves 81.97 % and

92.76 % saturation of the low and high-affinity Pi carrier, respectively. At lower concentrations extramitochondrial Pi becomes rate-limiting for oxidative phosphorylation (Tager et al., 1983), while at saturating [Pi] the rate of Pi transport greatly exceeds the net rate of ATP synthesis (Ligeti et al., 1985). At [Pi] ≤ 3 mM ATP formation is largely dependent on the F_0-F_1 ATPase. Finally, Pi has been shown by mathematical modeling to play a significant role in stimulating both oxidative phosphorylation and tricarboxylic acid cycle (Wu et al., 2007), as originally proposed by Bose (Bose et al., 2003). 10 mM KH_2PO_4 did not affect free [Mg^{2+}] measured by Magnesium Green (Chinopoulos et al., 2009). This is partly because at pH=7.25, KH_2PO_4 dissociates to $H_2PO_4^-$ and HPO_4^{2-} (pK_2=7.21) and neither of these ions form a precipitation with Mg^{2+} (PO_4^{3-} is the only component that forms $Mg_3(PO_4)_2$ precipitate, but this ion is essentially not present at this pH (pK_3=12)). On the other hand, Mg^{2+} also forms soluble coordination compounds with phosphate anions (preferably with HPO_4^{2-}). However, chelation of Mg^{2+} by HPO_4^{2-} in the low millimolar range is negligible, since the textbook definition of the dissociation constant for the [Mg^{2+}- HPO_4^{2-}] complex is 210 mM although a much lower value has been reported elsewhere (Wu et al., 2007). The substrates TMPD (in most cases 1 mM) plus ascorbate were chosen for the following reasons: at concentrations >0.4 mM TMPD supports direct transfer of electrons to cytochrome oxidase (Sagi-Eisenberg and Gutman, 1979), (Crinson and Nicholls, 1992), thus, the availability of cytochrome c (or of any upstream component of the respiratory chain) as an electron donor is no longer rate limiting. This is advantageous, because due to harsh isolation conditions, the outer membrane of isolated mitochondria is frequently damaged, leading to a partial loss of cytochrome c (Wojtczak et al., 1972). In addition, ATP-ADP steady-state exchange rates mediated by the ANT of various types of mitochondria can be normalized to their respective cytochrome oxidase activities. The use of TMPD plus ascorbate also eliminates a possible confounding factor, due to the binding of either ADP or ATP to the matrix-facing domain of subunit IV of cytochrome oxidase regulating its' activity in a pmf-independent manner (Kadenbach and Arnold, 1999). This mechanism of respiratory control does not operate when mitochondria are fueled by TMPD plus ascorbate (Arnold and Kadenbach, 1997). This is important for our assay using intact mitochondria, because ATP-mediated inhibition of cytochrome oxidase would decrease pmf, the ultimate driving force for ANT-mediated ADP/ATP exchange. Furthermore, it has been shown that the fraction of ANT molecules which form functional dimers, and hence contribute to the flux control coefficient of ANT, is maximum if TMPD plus ascorbate is used to support mitochondrial respiration, as compared to other substrate combinations (Faustin et al., 2004). The importance of including bovine serum albumin in the assay medium is two-fold: firstly, albumin binds both fatty acids and their coenzyme A esters, that can inhibit ANT activity (Wojtczak and Zaluska, 1967), (Morel et al., 1974); secondly, fatty acids exhibit uncoupling properties plus inhibitory effects on respiratory chain components (Wojtczak and Schonfeld, 1993) that decrease pmf –particularly with succinate as a substrate (Tretter et al., 2007). Finally, the use of 1 mM total [Mg^{2+}] yields 0.32-0.6 mM free [Mg^{2+}] (depending on the type and amount of adenine nucleotide present in the extramitochondrial medium, see below), which is within the physiological range of cytosolic free [Mg^{2+}] (Rodriguez-Zavala and Moreno-Sanchez, 1998), (Rutter et al., 1990), (Jung et al., 1997).

1.2. Establishment of [Mg^{2+}] measurement by MgG fluorescence and determination of Kd for Mg^{2+} bound to ADP or ATP

The 'core' of the method for estimating ATP-ADP steady-state exchange rate lies in a reliable estimation of free [Mg^{2+}] in the range of 0.1-1 mM. Our calibration of MgG fluorescence using Eq. 1.1: ($[Mg^{2+}]_f$ =(K_d(F-F_{min})/(F_{max}-F))-0.055 mM) gave reasonable estimates of free [Mg^{2+}] ($[Mg^{2+}]_f$); in figure 1.1A, curve (a) shows the calibrated signal of MgG fluorescence upon adding 0.1 mM $MgCl_2$ boluses (arrows) to a solution initially devoid of Mg^{2+}. Because all Mg^{2+}-sensitive dyes also bind Ca^{2+} (MgG has a K_d=4.7 μM for

Ca^{2+}), we tested the response of MgG fluorescence to consecutive boluses of 1 μM $CaCl_2$ (figure 1S.1A, curve (b)). In the presence of 1 mM $MgCl_2$ MgG fluorescence, and hence the calculated free [Mg^{2+}] (curve (b)), was only marginally affected by boluses of $CaCl_2$. Note, that in our buffer the contaminating free [Ca^{2+}] is ~150 nM, as measured by fura-6F (K_d=2.47 μM (Chinopoulos et al., 2003), and fura 2 (K_d=0.225 μM in the presence of Mg^{2+}).

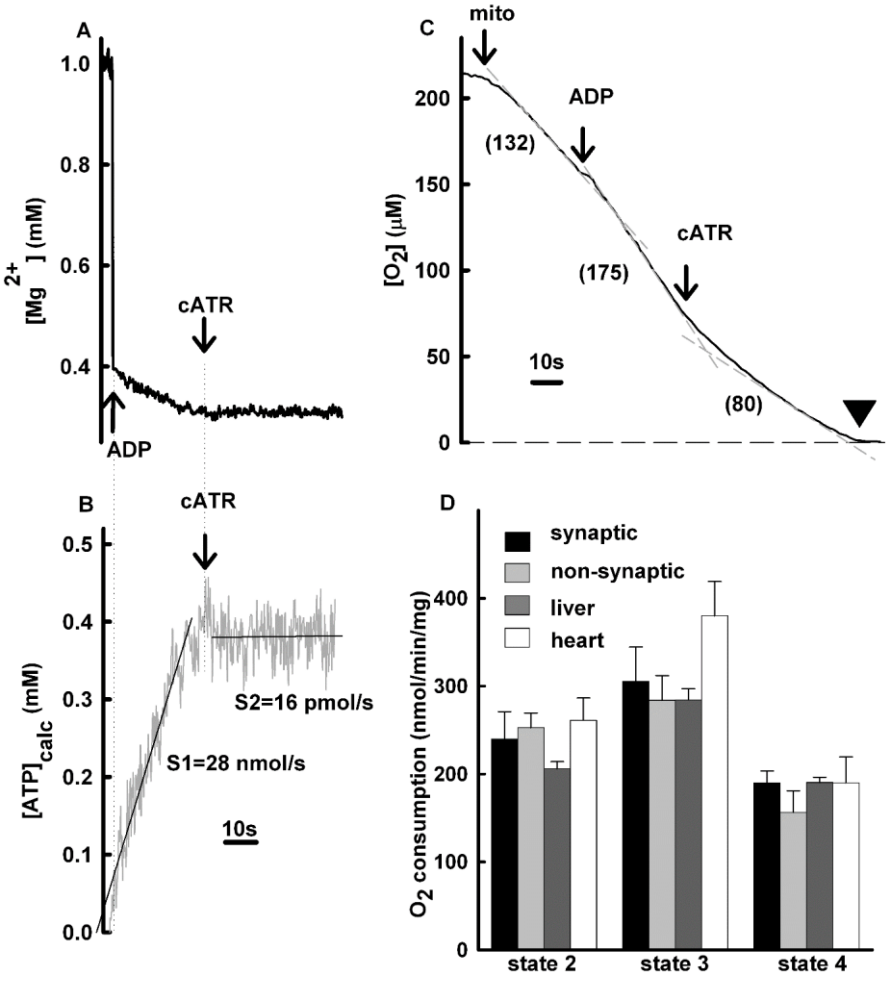

Figure 1.1. ***Estimation of ATP release and verification of [O_2] during the experimental time frame. A:*** *Reconstructed time course of free [Mg^{2+}], calculated from MgG fluorescence using Eq.1.2. Less than 50 seconds prior to the start of the trace 1 mg of non-synaptic mitochondria was added to a 2-ml medium containing 50 μM AP_5A, 1 mM TMPD, 5 mM ascorbate, 1 mM $MgCl_2$, and 2 μM Magnesium Green 5K$^+$ salt. 2 mM ADP and 4 μM carboxy-atractyloside (cATR) were added where indicated (arrows).* ***B****: Time course of $[ATP]_t$ appearing in the medium, calculated from the data in panel A using Eq.1.5. S1 and S2 are slopes obtained by linear regression (r^2=0.918 for S1, S.E. of the fit=0.01). Panels A and B are aligned on the x-axis (time, sec).* ***C****: Time course of [O_2], measured with a Clark electrode in an open chamber. 1 mg of heart mitochondria, 2 mM ADP, and 4 μM cATR were sequentially added, as indicated (arrows), to a 2-ml medium which contained 50 μM AP_5A, 1 mM TMPD, 5 mM ascorbate, and 1 mM $MgCl_2$. Rates of respiration (μM/min) are given in parentheses.* ***D****: Rates of O_2 consumption in various states of respiration, for the types of mitochondria used in this study (expressed as nmol of O_2 consumed/mg of mitochondrial protein/min). State 2 (1 mM TMPD + 5 mM ascorbate, no ADP), State 3 (substrates plus ADP), State 4 (addition of 4 μM cATR).*

For the calculation of [ATP] from free [Mg^{2+}] (see Eq. 1.5, below), the apparent K_d values (at our pH of 7.25 and our temperature of 37°C) of Mg^{2+} for ADP and ATP are required. These can be calculated from

the room-temperature values of the proton dissociation constants of ATP (or ADP) and the association constants of ATP^{4-} and $ATPH^{3-}$ (or ADP^{3-} and $ADPH^{2-}$) for Mg^{2+}, by taking into account the dependencies of these parameters on temperature – all these parameters have been estimated previously by others (Phillips et al., 1963), (Phillips et al., 1966). However, differing values have been reported for these constants in different studies, while our calculation of [ATP] from free [Mg^{2+}] (Eq. 5) is non-linear in nature, and even small differences in K_d could result in large errors in [ATP] estimates. Therefore, we directly determined the apparent K_d of Mg^{2+} for ADP (K_{ADP}) and for ATP (K_{ATP}) under our conditions by stepwise titration of Mg^{2+} with the respective nucleotide (figure 1S.1B, C). ADP and ATP were added in 0.25 mM and 0.2 mM boluses, respectively, to a medium containing a total concentration of 1 mM Mg^{2+} and the free [Mg^{2+}] was measured using MgG. To obtain K_d values, free [Mg^{2+}] versus total [nucleotide] plots (Fig. 1S.1B,C; *dots*) were fitted by least squares (Fig. 1S.1B,C; *solid lines*) to the binding equation

$$[Mg^{2+}]_f = 0.5 \cdot \left([Mg^{2+}]_t - K_d - [L]_t + \sqrt{\left([Mg^{2+}]_t - K_d - [L]_t\right)^2 + 4K_d[Mg^{2+}]_t} \right), \qquad \text{(Eq. 1.2)}$$

where $[Mg^{2+}]_t$ is the total [Mg^{2+}] (1 mM), $[L]_t$ is the total concentration of added ADP or ATP, and K_d is the fitted value of K_{ADP} or K_{ATP}, respectively. From our fits we obtained estimates of K_{ADP}=0.906 ± 0.023 mM (Fig. 1S.1B), and K_{ATP}=0.114 ± 0.005 mM (Fig. 1S.1C). As a comparison, using Martell and Smith's and Fabiato A. and Fabiato F.'s constants (Fabiato and Fabiato, 1979) predicts apparent K_d values of K_{ADP}=0.739 mM, and K_{ATP}=0.060 mM – in reasonable agreement with our measured values.

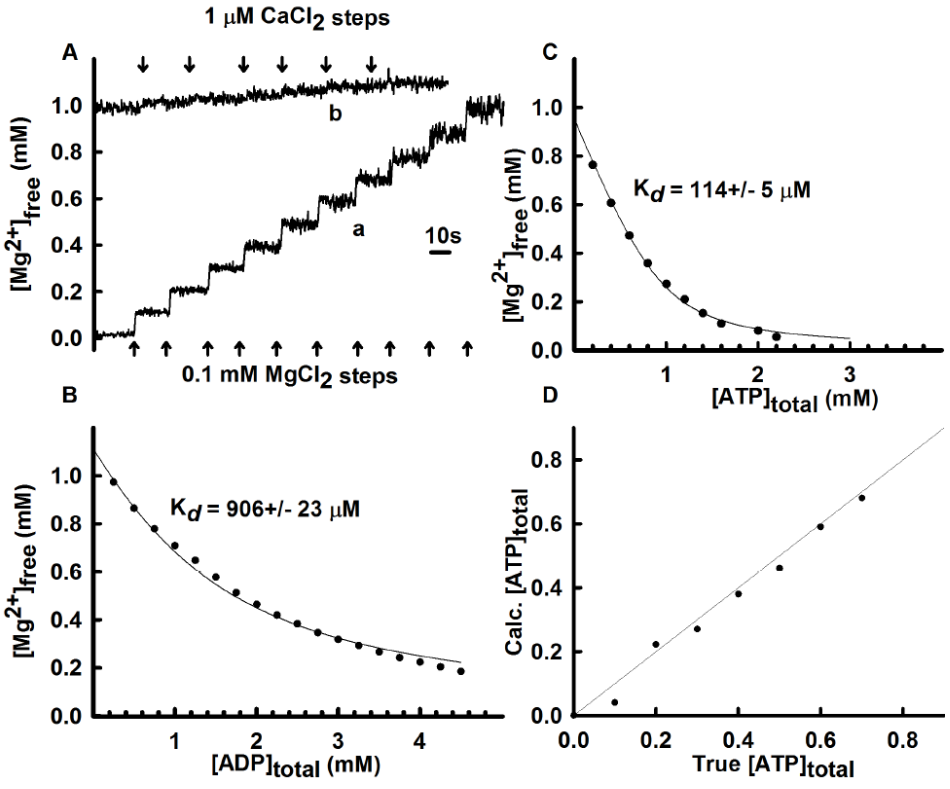

Figure 1S.1. ***Dependence of MgG fluorescence on $[Mg^{2+}]_f$ and $[Ca^{2+}]_f$ and determination of K_d for Mg-AdNucl complexes. A:*** *Reconstructed time courses of free [Mg^{2+}], calculated from MgG fluorescence using Eq.1.2. In curve '**a**', 0.1 mM $MgCl_2$ boluses were added, where indicated (arrows), to a 2-ml medium (see Materials and Methods for composition) initially devoid of Mg^{2+}, containing 2 μM MgG 5K^+ salt. In curve '**b**', 1 mM $MgCl_2$ was already present in the medium at the onset, and 1 μM $CaCl_2$ boluses were added where indicated (arrows).* ***B**: Determination of K_d of ADP for Mg^{2+} by sequential addition of 18 boluses of ADP (0.25 mM each) while recording MgG fluorescence. Dots illustrate calculated free [Mg^{2+}] after each bolus. The solid line is a fit to Eq.1.2, yielding the K_d value shown.* ***C**: Determination of K_d of ATP for Mg^{2+} by sequential addition of 10 ATP boluses (0.2 mM each). Details are as in B. All panels (A, B, C) share the same y-axis, i.e. $[Mg^{2+}]_f$ (mM).* ***D**: Plot of calculated $[ATP]_t$ values as a function of true $[ATP]_t$.*

1.2.1 Evaluation of ATP-ADP steady-state exchange rate by calculating the total [ATP] released from measured free extramitochondrial [Mg^{2+}]

Addition of 2 mM ADP to a medium containing mitochondria, AP_5A (diadenosine pentaphosphate, adenylate kinase inhibitor), substrates, 1 mM $MgCl_2$, and 2 μM MgG causes an immediate drop in free [Mg^{2+}], from 1 mM to ~0.39 mM (figure 1.1A), which is in agreement with the calculated value (0.3939 mM) considering the K_{ADP} value estimated above (figure 1S.1B and Eq. 1.2). Under these conditions oxidative phosphorylation is initiated and for the next 25 sec is maintained, while ADP is replaced in the medium with ATP. Because ATP binds Mg^{2+} with a higher affinity than does ADP, this process is reflected by a further gradual decline in the free [Mg^{2+}] (figure 1.1A). Addition of 4 μM cATR, a specific inhibitor of ANT, immediately stops this progressive decrease in free [Mg^{2+}] (figure 1.1A), consistent with the fact that under these conditions the ANT is the sole mediator of ADP/ATP exchange. cATR binds to ANT with a very high affinity (K_d=10^{-8} M); because this binding is non-competitive (unlike for atractyloside), ADP even in high concentrations cannot overcome the inhibition (Vignais et al., 1971). Since one molecule of cATR binds to one ANT dimer, and mitochondrial preparations contain 0.24-1.8 nmol of ANT per mg protein (depending on the tissue (Forman and Wilson, 1983), (Rossignol et al., 2000) plus our own estimates, see below), 4 μM cATR is sufficient to inhibit all molecules of ANT in our mitochondrial suspension (1 mg of mitochondrial protein per 2 ml). Free [Mg^{2+}] also ceased to decline upon addition of 10 μM oligomycin. Including the adenylate kinase inhibitor AP_5A into the medium is essential; Mg^{2+}, which is present in the assay medium, activates adenylate kinase which exhibits an appreciable activity in some tissues. Significant production of ATP by this enzyme, upon addition of 2 mM ADP, would result in overestimation of ATP-ADP steady-state exchange rate mediated by the ANT. When AP_5A was omitted from the medium, we indeed observed a faster decrease in free [Mg^{2+}] upon ADP addition and free [Mg^{2+}] continued to fall (although at a lower rate) even after addition of cATR (not shown). To convert measured $[Mg^{2+}]_f$ into total [ATP] in the medium ($[ATP]_t$), we assumed that in our medium the system

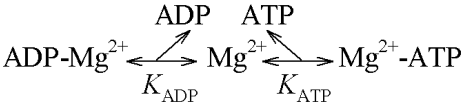

is at equilibrium at any moment. This is a fair assumption, as the rate of Mg^{2+} binding to, and unbinding from, nucleotides is faster than the rate of ATP/ADP exchange across mitochondrial membranes (diffusion of ions in solution is several orders of magnitude faster than any conformational transitions of proteins). Thus, at any moment, $[Mg^{2+}]_t$ in the medium is distributed between three equilibrium pools, free, ADP-bound, and ATP-bound:

$$[Mg^{2+}]_t = [Mg^{2+}]_f + \frac{[Mg^{2+}]_f [ADP]_t}{K_{ADP} + [Mg^{2+}]_f} + \frac{[Mg^{2+}]_f [ATP]_t}{K_{ATP} + [Mg^{2+}]_f}$$, (Eq. 1.3)

where $[ADP]_t$ and $[ATP]_t$ are the total concentrations of ADP and ATP, respectively, in the medium.

Because the ANT exchanges ADP for ATP at a 1:1 stoichiometry, $[ADP]_t$+$[ATP]_t$ remains constant in the extramitochondrial compartment throughout the experiment. In particular, at any time point

$$[ADP]_t = [ADP]_t(t=0) + [ATP]_t(t=0) - [ATP]_t,$$ (Eq. 1.4)

where $[ADP]_t(t=0)$ and $[ATP]_t(t=0)$ are $[ADP]_t$ and $[ATP]_t$ in the medium at time zero (2 mM and 0 mM, respectively - our ADP stock solution exhibited negligible contamination with ATP). Substituting $[ADP]_t$ from the latter equation into Eq. 1.3, and rearranging Eq. 1.3 to express $[ATP]_t$ we get

$$[ATP]_t = \left(\frac{[Mg^{2+}]_t}{[Mg^{2+}]_f} - 1 - \frac{[ADP]_t(t=0) + [ATP]_t(t=0)}{K_{ADP} + [Mg^{2+}]_f} \right) \Bigg/ \left(\frac{1}{K_{ATP} + [Mg^{2+}]_f} - \frac{1}{K_{ADP} + [Mg^{2+}]_f} \right)$$ (Eq. 1.5).

Equation 1.5 is available for download at: https://semmelweis.hu/biokemia/en/research/christos-lab/antactivity/. To verify the reliability of the $[ATP]_t$ estimates obtained using Eq. 1.5 and measured values of $[Mg^{2+}]_f$, we applied the above algorithm to a series of solutions with known $[ATP]_t$ (Fig. 1.1D). To this end, 0.1 mM ATP boluses were added in a stepwise fashion to a 2-ml aliquot of our bath solution containing 2 mM ADP and MgG. After each ATP bolus $[Mg^{2+}]_f$ was determined from MgG fluorescence using Eq. 1.2; and [ATP]t was estimated using Eq. 1.5 in which $[ADP]_t(t=0)+[ATP]_t(t=0)$ was set to 2 mM+*i**0.1 mM (*i*=1, 2, ...7) for the trial following the *i*th ATP bolus. A plot of calculated $[ATP]_t$ values as a function of true $[ATP]_t$ for this series of experiments (Fig. 1S.1D) convinced us that we could predict $[ATP]_t$ in the medium with reasonable accuracy.

1.3 Estimation of ATP release in isolated mitochondria

In our assays of ATP-ADP exchange rate mediated by the ANT we could confidently apply Eq. 1.5 of the supplementary material (using $[Mg^{2+}]_t$ =1 mM, $[ADP]_t(t=0)$=2 mM, $[ATP]_t(t=0)$=0 mM, K_{ADP}=0.906 mM, and K_{ATP}=0.114 mM) to directly convert the recorded time course of [Mg2+]f into the time course of $[ATP]_t$ in the medium (Fig. 1.1B). The fitted slope of this time course (Fig. 1.1B, slope=S1) during conversion of ADP into ATP by mitochondria reflects ATP-ADP exchange rate mediated by the ANT; S2 is the slope fitted after blocking ANT operation with cATR. For all subsequent estimations of ATP-ADP exchange rate, S2 has been subtracted from S1. The standard error of the slopes given by the linear regression analysis were in the 0.01 range and this is further assisted by the ability of the method to operate at high acquisition rate; this in turn enables performing the linear regression on larger number of data points and therefore, even though the data look noisy, the slope of the fit provides a robust determination of ATP production rate. For some of the experiments, the calculated initial [ATP]t values were not exactly zero, but in the range of ~0.01-0.04 mM. In these cases, we arbitrarily readjusted the calculated [ATP]t time course to make it start from zero.

1.4 Verification of the maintenance of mitochondrial respiration within the experimental time frame

Even though the experiments are performed in an open chamber, 1 mg of mitochondria in a 2 ml volume would consume dissolved O_2 within a few minutes, especially when 1 mM TMPD plus 5 mM ascorbate is used, a combination that gives very high rates of respiration (figure 1.1D). Furthermore, oxidative phosphorylation depends on oxygen tension at values lower than 100 μM [O_2] (Wilson et al., 1979). In order to ensure that recordings of free $[Mg^{2+}]$ are performed in mitochondria not depleted from oxygen, respiration measurements were also performed under the same conditions. As evident from figure 1.1C, which shows the time course of oxygen consumption by heart mitochondria, there remained sufficient

oxygen in the medium within our experimental time frame of <40 s, and importantly prior to the addition of cATR (Fig. 1.1C), to keep cytochrome oxidase saturated. The black arrowhead in Figure 1.1C indicates the time point at which [O_2] has reached the lower sensitivity limit of the Clark electrode, which is near the Km for O_2 of cytochrome oxidase. Among the types of mitochondria used, those isolated from heart exhibited the highest respiratory rates (figure 1.1D). As cATR was given 25 sec after the addition of ADP, we conclude that our experiments were not limited by oxygen depletion.

1.5 Validation of the ATP-ADP exchange rate mediated by the ANT technique

In (Chinopoulos et al., 2009) we described the method for determining the ATP-ADP exchange rate mediated by the ANT in intact, metabolically competent isolated mitochondria. The same principle should also be applicable to purified ANT protein reconstituted in liposomes (Kramer, 1986); indeed, this has been adapted by the group of Pohl (Kreiter et al., 2020). Because the protocol includes only a single addition of a substance (ADP), this method has the potential for a high-throughput drug screening. The principle of the method is the measurement of the rate of the cATR-sensitive decline in free [Mg^{2+}] in the extramitochondrial compartment upon exchange of ADP with ATP. Total [ATP] in the medium is then calculated from free [Mg^{2+}] using Eq.1.5; and ATP-ADP steady-state exchange rate mediated by the ANT is expressed as total [ATP] appearing in the medium per unit time per amount of protein. This technique is viable due to fact that ANT does not transport Mg-ADP or Mg-ATP (Klingenberg, 2008), (Kramer, 1980) unlike the ATP-Mg^{2+}/P_i carrier (Aprille, 1993), and is specific for this exchanger because all other known nucleotide transporters are insensitive to inhibition by cATR (Vozza et al., 2004), (Dolce et al., 2001), (Fiermonte et al., 2004), (Palmieri et al., 2001), (Shin et al., 2000). A conceivable limitation of our method could be the transport of Mg^{2+} across the inner mitochondrial membrane, as well as the transport of adenine nucleotides by carriers other than ANT. A mitochondrial Mg^{2+} efflux pathway of unknown molecular identity activated by cAMP has been proposed (Romani et al., 1991), but remained unconfirmed (Altschuld et al., 1994). In mammalian mitochondria, the only proven mechanisms of Mg^{2+} transport across the inner mitochondrial membrane are: i) the ATP- Mg^{2+}/Pi carrier (Aprille, 1993) and ii) a homologue of the Mrs2 protein originally described in yeast which mediates an electrophoretic uptake of Mg^{2+} (Kolisek et al., 2003). Mrs2p is also found in mice but it exhibits a low level of transcription (Zsurka et al., 2001). Concerning (i), free [Ca^{2+}] in our media was ~150 nM which prevents the ATP-Mg^{2+}/Pi carrier from operation (Nosek et al., 1990). Furthermore, the activity of the ATP- Mg^{2+}/Pi carrier (which can also exchange ADP unbound to Mg^{2+} for $HPO4^{2-}$ (Nosek and Aprille, 1992) is many-fold lower than that of the ANT (Aprille, 1993). To address the possible presence of Mg^{2+} transport through some Mrs2p homologue in our mitochondria, the following experiment was performed: mitochondria were incubated in a medium in the presence of substrates and cATR, but in the absence of Mg^{2+} plus 20 μM EDTA to chelate contaminating Mg^{2+}; 1 mM $MgCl_2$ was added and the rate of [Mg^{2+}] decline was recorded in the presence or absence of 0.2 μM SF 6847. As measured by MgG fluorescence, the rate of decline in free extramitochondrial [Mg^{2+}] was small, and not significantly affected by the presence of the uncoupler (0.00055 and 0.000462 mM/min/mg protein, respectively, in the absence and presence of the uncoupler). In contrast, the rates of decline in free extramitochondrial [Mg^{2+}] due to ADP/ATP exchange are many fold higher, depending on the type of mitochondria used. Based on the very low rates of decline in free extramitochondrial [Mg^{2+}] and the lack of effect of the electrophoretic capacity of mitochondria, it is safe to assume that in our conditions the Mrs2p – if present – contributes only insignificantly to Mg^{2+} transport. This is in agreement with the fact that in our hands cATR abolished all changes in free [Mg^{2+}] (Fig. 1.1A, B), again indicating that the ANT is the only significant means for altering extramitochondrial free [Mg^{2+}], as a result of ATP-ADP concentration changes. When ANT molecules are reconstituted in liposomes, and there is only one of the nucleotides present in the extra-

or intraliposomal compartment, then unidirectional transport can occur (Gropp et al., 1999). Otherwise, in metabolically competent isolated mitochondria, the concerted exchange of one ADP for one ATP per ANT dimer is obligatory, ensured by the strong positive cooperativity in the binding of the two nucleotides (Duyckaerts et al., 1980), (Barbour and Chan, 1981). The high concentration of ADP used ([ADP] falls from a 2 mM starting value to ~1.5 mM until the addition of cATR) serves two purposes. First, it ensures that ANT is saturated at all times, as its K_m for ADP is between 1-100 μM (Pfaff et al., 1969), (Akerboom et al., 1977), (Halestrap and Brenner, 2003), (Palmieri, 2004). In the presence of Mg^{2+}, the consensus is that the Km for ADP is 4 μM (Abramov and Duchen, 2005). Second, State 3 respiration strongly depends on [ADP] at concentrations below 0.3 mM (Jacobus et al., 1982), but becomes insensitive to [ADP] above 0.5-1 mM (Kay et al., 2000). Therefore, the rate of State 3 respiration remains constant throughout the relevant part of our assay (Fig. 1.1C).

1.6 Comparison of the present method to previously established methods for determination of ATP-ADP exchange rate mediated by the ANT

Several methods for ATP-ADP steady-state exchange rate mediated by the ANT determination have been described in the past. Some of these directly measure ADP and/or ATP by 1) thin-layer chromatography (Pedersen and Catterall, 1979), 2) high-performance liquid chromatography (Hartwick and Brown, 1975), or 3) using radioactive nucleotides (Duee and Vignais, 1969a). Others employ coupled reactions which yield an end-product that can be detected either fluorimetrically by 4) monitoring the reduction of $NADP^+$ which occurs in the presence of glucose, hexokinase, glucose-6-phosphate dehydrogenase and effluxed ATP (Williamson and Corkey, 1979), (Passarella et al., 1988) or 5) luminometrically, detecting chemiluminescence upon ATP-dependent oxidation of luciferin, catalyzed by firefly luciferase (Lemasters and Hackenbrock, 1979). Furthermore, there are techniques which employ fluorescent derivatives of nucleotides (method 6) to evaluate the rate of release of the fluorescent molecule upon ANT-mediated exchange for ADP (Block et al., 1986). To complement these functional assays, the amount of ANT protein can be estimated using (method 7) a fluorescent derivative of atractyloside, or, exploiting the 1:1 stoichiometry of binding of the inhibitor to the translocase, by (method 8) stepwise titration of State 3-mitochondria with cATR until respiration is completely inhibited (Schonfeld, 1990). Among these, only methods 4, 5 and perhaps 6 are on-line measurements, while the rest are end-point assays (although a satisfactory time resolution can be obtained using a large number of samples as detailed by (Brandolin et al., 1990). Methods 1 and 2 require expertise in specialized equipment, while method 3 requires handling of radioactive material, conditions which may render these methods cumbersome to use. However, it must be noted that these are all very sensitive assays which require small amounts of mitochondrial protein. Methods 6 and 7 rely on materials which are not commercially available, and are therefore not appealing to the broader scientific community. Method 5, if used as an on-line method, suffers from several drawbacks. First, the lack of constant proportionality between ATP concentration and luminescence, caused by product inhibition of the luciferase reaction by oxyluciferin, renders this method at best semi-quantitative. Second, for reliable estimation of the kinetics of ATP formation, the endogenous ATP concentration prior to the assay has to be determined. Third, the required use of a low ionic strength medium and room temperature restricts experiments to conditions which are nowhere near physiological. Fourth, the necessity to maintain $[O_2]$ below 50 μM, needed to avoid significant drifts in luminescence, adds extra effort to any application of this method. Nevertheless, some of the disadvantages of this method have been overcome by various modifications (Wibom et al., 1990). Method 4 has two disadvantages. First, there are two mediating coupled reactions which may affect stoichiometry through product (glucose-6-phosphate) inhibition of hexokinase. Second, the measured signal -NADP(H) autofluorescence- precludes the simultaneous measurement of

this mitochondrial parameter, plus the stimulation of mitochondrial respiration by addition of ADP affects the NAD(P)H steady state. For a comprehensive appraisal of methods to measure ATP-ADP exchange rates in mitochondria and reconstituted systems, the reader is referred to a recent review by Martin Klingenberg (Klingenberg, 2008). The advantage of the method described in our study is that it provides kinetic information at a high acquisition rate while it does not suffer from the drawbacks described for methods 4, 5 and 6. In addition, our method can be combined with simultaneous recording of further mitochondrial parameters using other types of fluorescent dyes. As an example, MgG fluorescence has been used to report changes in intracellular [ATP] in cardiomyocytes combined with simultaneous recording of NAD(P)H autofluorescence and mitochondrial membrane potential using JC-1 (Leyssens et al., 1996). A disadvantage of our method is that it requires relatively large amounts of protein (1 mg per experiment was used here, although for mitochondria which exhibit high rates of ADP/ATP exchange 0.25 mg mitochondrial protein could be sufficient). Theoretically, special cuvettes with very small internal volumes (as low as 100 μl) could be employed to decrease the amount of protein required; however, in such cases care should be taken that mitochondria do not run out of dissolved O_2 during the experiment, should the application demand full pmf. On the other hand, 1 mg of total mitochondrial protein contains an estimated 2-12 μg of ANT protein, depending on the source tissue. Thus, in a liposome system using purified ANT, protein amounts in the low μg range should yield exchange rates in the order shown in this study, albeit lower, since transporters in reconstituted systems are prone to disorientation and partial loss of functionality. Also, this method is not applicable for cases in which a very high concentration of Ca^{2+} (>10 μM, when at least 1 mM Mg^{2+} is present) is necessary, such as investigation of the Ca^{2+}-induced mitochondrial permeability transition (Chinopoulos et al., 2003); MgG has a Km of 4.7 μM for Ca^{2+}, and substantial Ca^{2+} binding would alter the fluorescent signal and invalidate the calculation of free [Mg^{2+}] using Eq.1.1. Obviously, the method cannot be applied in the case where the integrity of the inner mitochondrial membrane has been breached to the extent that passage of adenine nucleotides in and out of the matrix occurs freely, bypassing the obligatory exchange by the ANT. Finally, the method described here is not applicable if one needs to exclude Mg^{2+} from the media; relevant to this, the necessity of including Mg^{2+} in the buffer could be a drawback because divalent cations (Me^{2+}) which exhibit a considerable affinity for adenine nucleotides cause a decrease in the ATP-ADP steady-state exchange rate, exactly because of the formation of Me^{2+}-ADP and Me^{2+}-ATP complexes (Kramer, 1980). However, the increase in the ADP-ATP steady-state exchange rate observed in the absence of Mg^{2+} compared to the rate recorded in the presence of Mg^{2+} can only be experimentally shown, and bears no pathophysiological relevance, as there are no conditions in situ in which cytosolic Mg^{2+} is absent. By the same token, the ADP-ATP exchange rate mediated by the ANT is strongly dependent on the $[Mg^{2+}]_f$, and it is therefore modulated by the relative concentrations of extramitochondrial $[Mg^{2+}]_t$ and its chelators, [ADP] and [ATP]. This is demonstrated in figure 1.2.

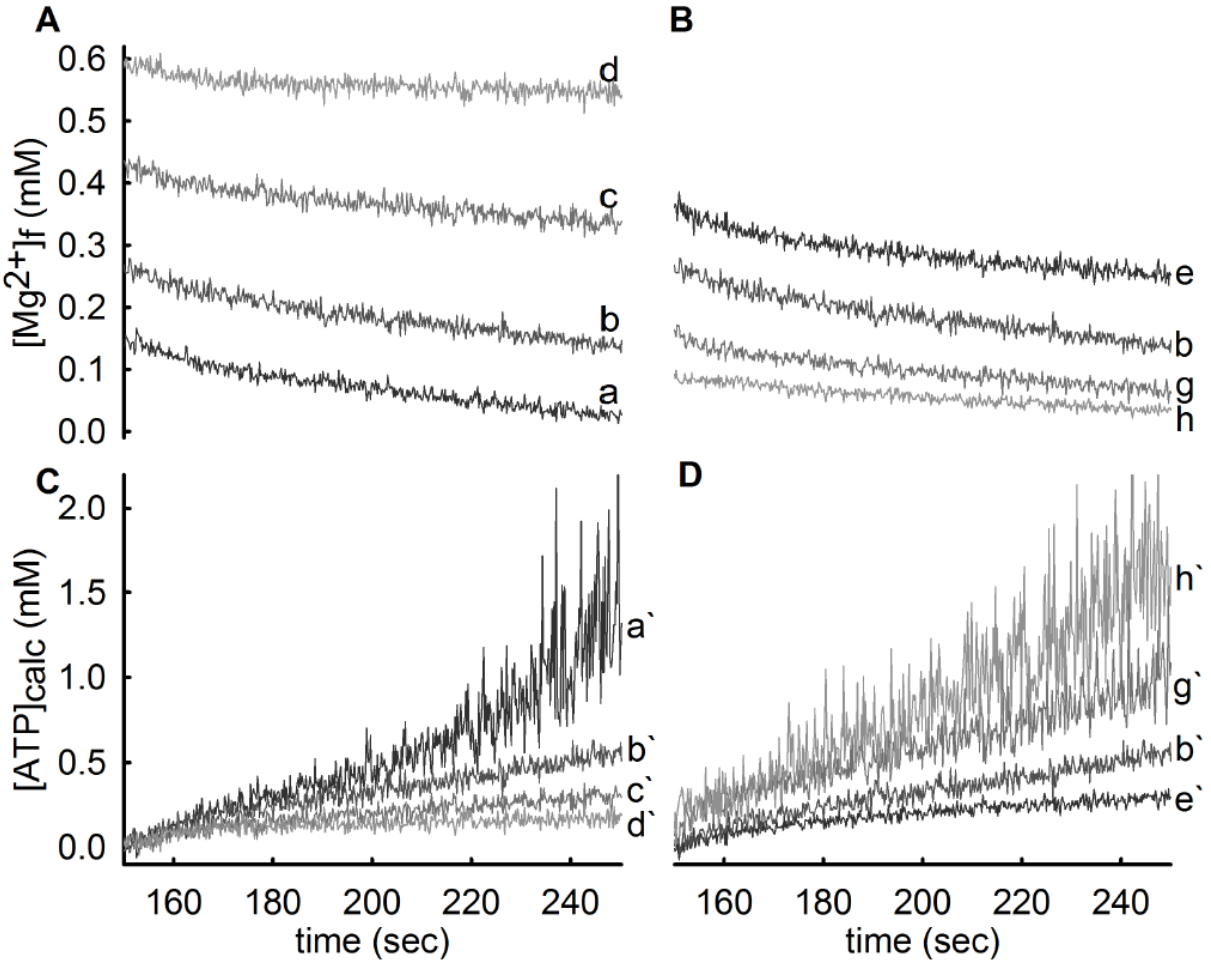

Figure 1.2. ***Dependence of $[Mg^{2+}]_f$ and ADP-ATP exchange rate on $[Mg^{2+}]_t$ and total [ADP].*** *1 mg of liver mitochondria was added to a 2-ml medium containing 50 μM AP_5A, 5 mM K-glutamate, 5 mM K-malate, 2 μM Magnesium Green 5K⁺ salt, and $MgCl_2$ at concentrations as detailed below ($[Mg^{2+}]_t$). ADP was added at 150 sec in concentrations as indicated below.* ***A, B:*** *Reconstructed time course of free $[Mg^{2+}]$, calculated from MgG fluorescence, aligned on the y-axis ($[Mg^{2+}]_f$, mM).* ***C, D****: Time courses of corresponding $[ATP]_t$ appearing in the medium, calculated from the data in panels* ***A*** *and* ***B*** *using Eq.1.5, (aligned on the y-axis, $[ATP]_{calc}$, mM), indicated as a`, b`, c`, d`, e`, b`, g` and h`. All panels are aligned on the x-axis (time, sec). Concentrations of $[Mg^{2+}]_t$ (in mM, already present in the medium) were as follows: a: 0.25, b: 0.5, c: 0.75, d: 1. In panel* ***A****, 1 mM ADP was added at 150 sec, while $[Mg^{2+}]_t$ was varied. In panel* ***B****, media contained 0.5 mM $MgCl_2$ and the amount of ADP added was varied as follows (in mM): e: 0.5, b: 1, g: 2, h: 4.*

In these experiments, rat liver mitochondria were energized with glutamate plus malate and $[Mg^{2+}]_f$ was recorded in media with increasing concentrations of $[Mg^{2+}]_t$ (0.25, 0.5, 0.75 and 1 mM, panel A), and adding 1 mM ADP at 150 sec, or keeping $[Mg^{2+}]$t constant (at 0.5 mM) and altering the amount of added ADP (0.5, 1, 2, and 4 mM, panel B). In panel A, it is shown that this produced initial $[Mg^{2+}]$f of 0.127, 0.27, 0.429 and 0.6 mM, for a, b, c, and d, respectively. In panel B this produced initial $[Mg^{2+}]$f of 0.358, 0.27, 0.175 and 0.100 mM, for e, b, g, and h, respectively. For both A and B panels, corresponding ADP-ATP exchange rates are given in panels C and D respectively, as a`, b`, c`, d`, e`, f`, g` and h`. As shown in panels C and D, the lower the initial $[Mg^{2+}]$f, the higher the ADP-ATP exchange rate. However, that comes at the expense of increased noise of the calculated [ATP] appearing in the medium, due to the nature of the Eq.1.5, when $[Mg^{2+}]$f approaches <0.1 mM values. This is a potential limitation of the method, if one

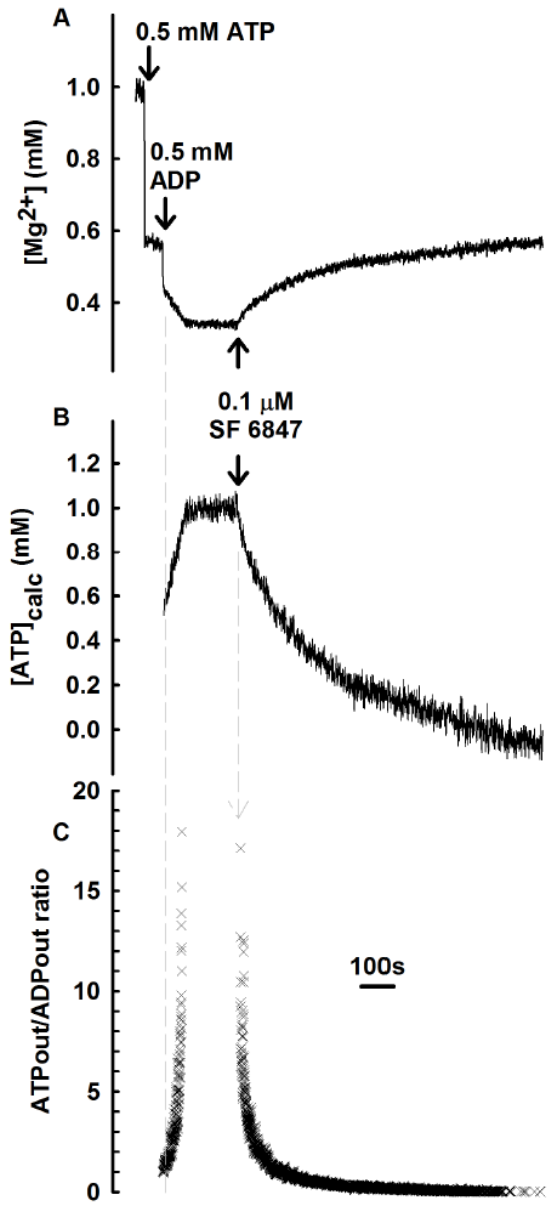

wishes to investigate the ADP-ATP exchange rate at $[Mg^{2+}]f$ below ~0.1 mM. A decrease in the signal-to-noise ratio will be inevitable if the initial $[Mg^{2+}]t$ is too small, or the amount of ADP added is large enough to diminish $[Mg^{2+}]f$ below ~0.1 mM. The effect of gradually decreasing of $[Mg^{2+}]f$ as a result of ADP-ATP exchange and its effect on this exchange is hard to implement, because although there is a slight initial exponential "splay" during the first 10 sec, this is associated with an inherent decrease in $\Delta\Psi m$ of ~25 mV (see figure 1.3A), and the causal relationship of ADP-ATP exchange rate to $\Delta\Psi m$ is evident in figure 1.6E. However, for the duration of the first 150 sec of ADP-ATP exchange, the rate of [ATP] appearing in the medium fits well with a linear regression (figure 1.1B). Therefore, the effect of the gradual change of $[Mg^{2+}]f$ and [ADP]o cannot be discerned while the ANT is in operation. Nonetheless, the results depicted in figure 1.2 panels C and D in which the rate of [ATP] appearing in the medium increases by increasing the initially added [ADP] or by decreasing the initially added $[Mg^{2+}]t$, revitalize a decades-old debate, whether free Mg^{2+} affects ADP-ATP exchange rate mediated by the ANT per se, and not just through chelation of ADP only (Kramer, 1980). Alternatively, the Km of the ANT may be higher than the currently held consensus values, which fluctuate around 0.004 mM (Klingenberg, 2008). As a third –yet unexplored- possibility, ADP may be activating ANT or recruiting more ANT molecules to the mitochondrial inner membrane, see (Rossignol et al., 2000). An additional limitation of our method related to the amount of ADP and Mg^{2+} required in order to achieve satisfactory reproducibility, is reflected in the inability to determine the Km of the ANT for ADP or ATP. In order to determine the Km of the ANT, diluted suspensions of mitochondria are required (~0.07 mg/ml), concentrations of ADP in the 0.001-0.1 mM range, and concentration of Mg^{2+} in the ~4 mM range. The reasons for such conditions are explained in (Pfaff et al., 1969), rendering our assay beyond reliable reproducibility, exactly because of the very dilute amount of functional ANTs, low ADP and high Mg^{2+}. For example, addition of 0.25 mM ADP causes a 0.1097 mM decrease in $[Mg^{2+}]f$.

Figure 1.3. ***Reversibility of the ANT and estimation of extramitochondrial ATP/ADP ratio.*** *Reconstructed time course of free $[Mg^{2+}]$, calculated from MgG fluorescence using Eq. 1.2.* ***A****: 1 mg of liver mitochondria was added to a 2-ml medium containing 50 μM AP_5A, 5 mM K-glutamate, 5 mM K-malate, 1 mM $MgCl_2$, and 2 μM Magnesium Green 5K⁺ salt. 0.5 mM ATP and 0.5 mM ADP were added where indicated. After consumption of ADP, there is no further alteration in free $[Mg^{2+}]$. Upon addition of 0.1 μM SF 6847 a progressive elevation in free $[Mg^{2+}]$ is observed reflecting a decrease in extramitochondrial ATP and concurrent increase in ADP. This reaction process continues until ATP is consumed.* ***B****: Time course of $[ATP]_t$ in the medium, calculated from the data in panel A using Eq.1.5.* ***C****: Time course of $[ATP]_t/[ADP]_t$ in the medium, calculated from the data in panel B as described in the text. Panels A, B and C are aligned on the x-axis (time, sec).*

Since the current consensus it that the Km of ANT for ADP is ~ 0.004 mM, in order to verify that with our method, [ADP] had to be added in that range. However, that would produce a reduction in $[Mg^{2+}]f$ smaller than the noise of the fluorescence signal. It is improbable that the method described in our manuscript can provide a reliable estimate in the low micromolar range of [ADP] values. This stems from the Km value of MgG for Mg^{2+}, which is 0.9 mM. This allows for reliable conversion of MgG fluorescence to $[Mg^{2+}]$ in the 0.1-2.5 mM range. This is depicted in the figure 1S.2, where a calibration curve is shown (sequential additions of 0.1 mM $MgCl_2$ to media containing mitochondria in the presence of ADP plus cATR). In panel A of the figure 1S.2, the raw trace of MgG fluorescence is shown. In panel B, a calibration curve is constructed for the entire set of data shown in panel A using a power function as described in the materials and methods. In the inset of the figure 1S.2B, a calibration curve of the first 6 additions of the same calibration curve is shown that fits well with a linear regression.

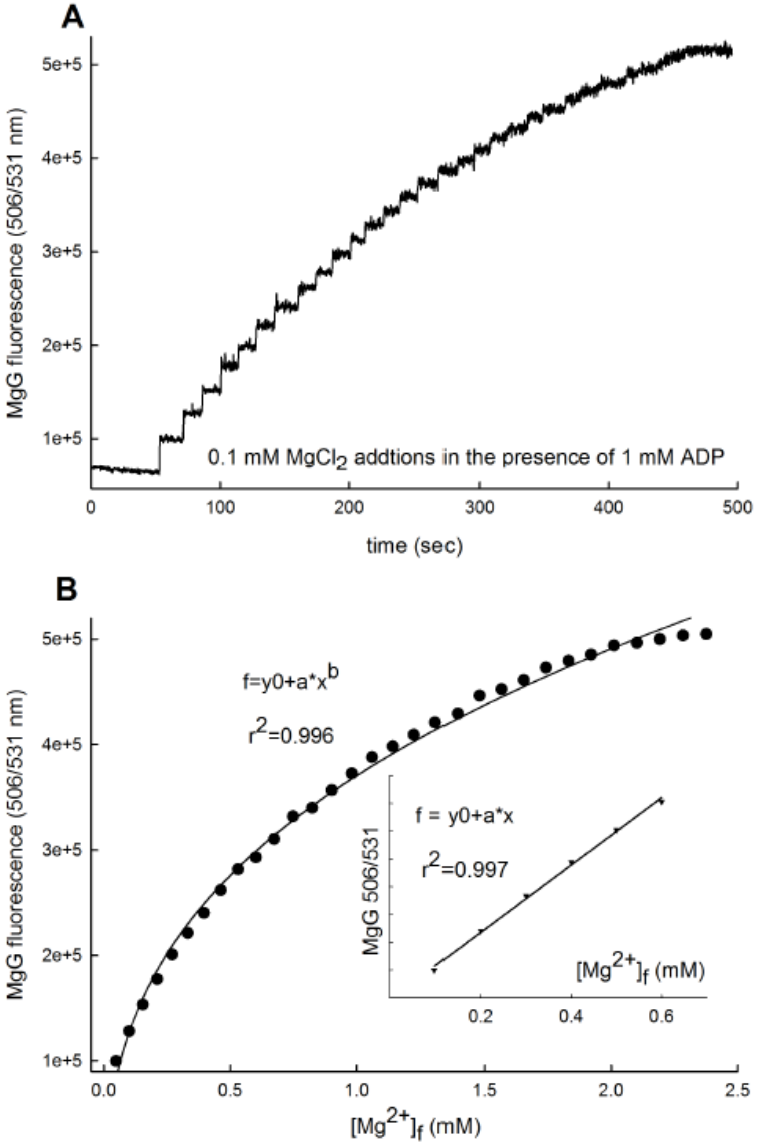

Figure 1S.2. Dependence of MgG fluorescence on $[Mg^{2+}]_f$ in the presence of 1 mM ADP, mitochondria and cATR. ***A****: Raw MgG fluorescence as a function of time. 0.1 mM $MgCl_2$ boluses were added to a 2-ml medium (see Materials and Methods for composition) initially devoid of Mg^{2+}, containing 2 µM MgG $5K^+$ salt.* ***B****: Conversion of MgG fluorescence shown in panel A to $[Mg^{2+}]_f$, in the 0.1-2.5 mM range using a calibration curve as described in the Materials and Methods. The inset of panel B shows a linear regression of the first 6 additions of $MgCl_2$ of the same calibration curve.*

1.7 Measurement of ANT in the reverse mode and estimation of the extramitochondrial ATP/ADP ratio

As mentioned above, mitochondria with a non-functional respiratory chain become ATP consumers, maintaining an appreciable pmf by pumping protons out of the matrix through the F_0-F_1 ATPase, at the expense of ATP hydrolysis. Under these conditions, the ANT reverses, bringing ATP into the matrix in exchange for ADP, driven by a $\Delta\Psi m$ less negative than ~-100 mV. ANT reversal can also be achieved in the presence of ATP by application of an uncoupler. Consumption of ATP by mitochondria in the presence of uncouplers is a well characterized phenomenon (Budd and Nicholls, 1996). We chose to test the uncoupler SF 6847 (Terada, 1981), as opposed to the more widely used FCCP, CCCP, or 2,4-dinitrophenol, because i) SF 6847 was the only

uncoupler that did not quench MgG fluorescence up to a concentration of 1 μM, while 0.1 μM was sufficient to completely depolarize 1 mg of mitochondria. (SF 6847 is also appropriate to use with Calcium Green, a Ca^{2+}-sensitive dye, while all the other uncouplers tested also quenched Calcium Green fluorescence (unpublished observations); this is not unexpected as both Calcium Green and Magnesium Green are fluorescein derivatives); ii) the uncoupling effect of SF 6847 is resistant to cATR (Skulachev, 1998); this is important because many types of uncouplers act by inducing a proton translocation through the ANT (Lou et al., 2007), possibly jeopardizing its ability to translocate adenine nucleotides. Figure 1.3 illustrates the effect of SF 6847 on ATP-ADP steady-state exchange rate mediated by the ANT. Addition of the uncoupler reversed both the time course of free [Mg^{2+}] (Fig. 1.3A), and that of [ATP]t in the extramitochondrial space (Fig. 1.3B) demonstrating mitochondrial ATP uptake by the ANT. As a further parameter of potential interest, our method also immediately yields the time course of the ATP/ADP ratio in the experimental volume (e.g., Fig. 1.3C). This is because the summed concentration of ATP and ADP in the extramitochondrial compartment ([ATP]t+[ADP]t) is known at the onset and remains constant throughout the experiment. Therefore, [ADP]t at any time point is given by ([ATP]t(t=0)+[ADP]t(t=0))-[ATP]t, which affords calculation of [ATP]t/[ADP]t (Fig. 1.3C). Values after consumption of ADP (corresponding to plateau phase of [ATP]t) are not plotted as they would reflect division by 0.

1.8 Correlation of ATP-ADP exchange rate by the ANT to ADP-induced mitochondrial membrane depolarization and state 3 respiration

Due to the electrogenic nature of the ANT (a net negative charge is exported in each ADP^{3-} import/ATP^{4-} export cycle) and because ATP formation is coupled to the flow of protons back into the matrix, initiation of state 3 respiration by addition of ADP to mitochondria is associated with a transient depolarization. This depolarization persists as long as mitochondria undergo oxidative phosphorylation. On the other hand, $\Delta\Psi m$ contributes to the driving force for the ANT (Alexandre et al., 1978), (Klingenberg, 1980), (Metelkin et al., 2006). Therefore, we were interested to temporally correlate ADP-induced depolarization to ATP-ADP steady-state exchange rate mediated by the ANT. As shown in figure 1.4, addition of 1 mM ADP to mitochondria causes a depolarization of 25 mV (panel A). The repolarization phase correlates with the transition from state 3 to state 4 respiration (indicating ADP consumption, panel B), as well as to cessation of changes in [ATP]t appearing in the medium (panel C). The fact that the oxygen consumption and $\Delta\Psi m$ time course correlate with the calculated [ATP] time course provides additional assurance of the validity of the method.

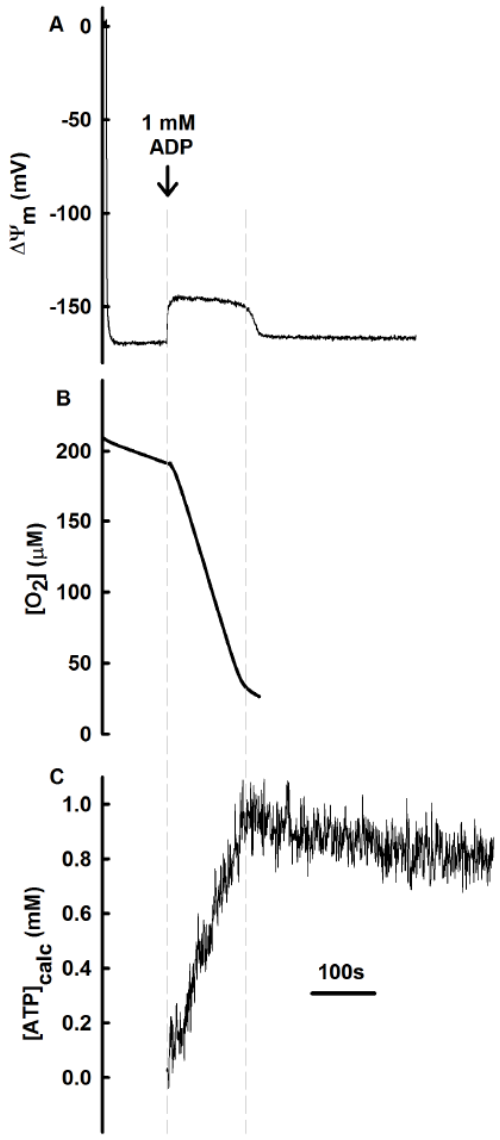

Figure 1.4. ***ATP-ADP exchange rate mediated by the ANT and O_2 consumption during ADP-induced depolarization. A:*** *Reconstructed time course of $\Delta\Psi_m$, calculated from safranine O fluorescence. 1 mg of liver mitochondria was added to a 2-ml medium and energized by 5 mM K-glutamate plus 5 mM K-malate. 1 mM ADP was added where indicated, causing a ~25 mV depolarization. Upon consumption of ADP, $\Delta\Psi_m$ returns to baseline level (-170 mV).* ***B****: Time course of [O_2], measured with a Clark electrode in a closed chamber, using type of mitochondria and conditions as for (**A**).* ***C****: Time course of $[ATP]_t$ in the medium. In (**B**) and (**C**) the same type of mitochondria and experimental conditions were used as in (**A**).*

1.9 'Normalization' of ATP-ADP exchange rate mediated by the ANT to the degree of inner mitochondrial membrane integrity

So far, the method describing the assessment of ATP-ADP exchange rate mediated by the ANT, depends on the compartmentalization of the dye, i.e. MgG must remain in the extramitochondrial medium (the $5K^+$ salt of MgG does not penetrate intact bilayers). Furthermore, the intactness of the inner mitochondrial membrane is also crucial for nucleotide translocation, as in its absence there is no pmf to drive i) ATP/ADP exchange and ii) ATP formation by the F_0-F_1 ATPase. ATP-ADP exchange rate mediated by the ANT, expressed as the concentration of ATP appearing in the extramitochondrial medium per unit time per mg of mitochondrial protein, is therefore underestimated due to the presence of a fraction of damaged mitochondria (possessing a leaky inner membrane), since the latter contribute to the amount of protein but not to nucleotide translocation. We estimated the fraction of leaky mitochondria in our preparation by measuring the fractional activity of citrate synthase (a matrix enzyme) in the medium. To this end, two membrane-impermeable substrates, oxaloacetate and acetyl-CoA were added to the medium, and citrate synthase activity was measured. This activity was then divided by total citrate synthase activity (figure 1.5A, top panel), determined by repeating the measurement in the presence of 0.1% Triton X-100 which disrupts membranes. The resulting fraction is an index of the fraction of broken mitochondria (figure 1.5A, bottom panel, grey shaded bars), while the complementary fraction indicates the fraction of intact mitochondria (figure 1.5A, bottom panel, white bars) to which ATP-ADP exchange rate mediated by the ANT could be normalized. Figure 1.5B shows this rate normalized to the amount of intact mitochondrial protein, for each type of mitochondria fuelled by 1 mM TMPD plus 5 mM ascorbate. Significantly lower activities were found in liver, and even more so in heart, as compared to brain mitochondria. Because ATP-ADP steady-state exchange rate mediated by the ANT is driven by pmf, which is different depending on the substrate used for supporting respiration (Lee et al., 1996), ATP-ADP exchange rate is also expected to depend on this variable. We indeed obtained differences (figure 1.5C)

for non-synaptic mitochondria fuelled by different substrate combinations. However, these did not reach statistical significance, except when compared to mitochondria assayed in the complete absence of substrates.

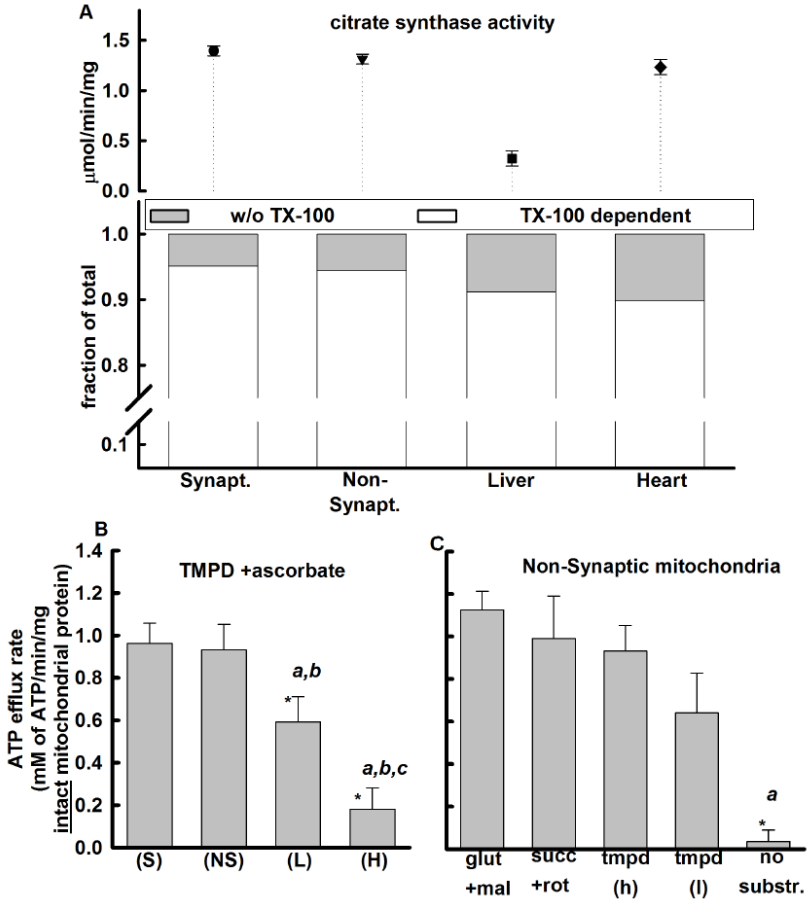

1.10 Relationship of ATP-ADP exchange rate mediated by the ANT to cytochrome oxidase activity

When 1 mM TMPD plus 5 mM ascorbate are used as substrates for mitochondrial respiration, cytochrome oxidase is the only site at which protons are pumped out of the matrix to generate $\Delta\Psi m$ which drives oxidative phosphorylation and ultimately ADP/ATP exchange. Consequently, cytochrome oxidase, the F_0-F_1 ATPase, and the ANT remain the only players to control the overall respiratory flux. The amount of ATPases in mitochondria of

*Figure 1.5. N**ormalization of ATP-ADP steady-state exchange rate mediated by the ANT to inner mitochondrial intactness. A**: Citrate synthase activity in the medium was measured for each type of mitochondrial preparation in the absence and in the presence of 0.1% Triton X-100. The top panel shows the absolute values (µmol/min/mg protein) of total citrate synthase activity, measured in the presence of 0.1% Triton X-100. In the bottom panel gray bars indicate the fractional activity in the absence of detergent (normalized to the total activity shown in the top panel); white bars plot the complementary ("TX-100 dependent") fraction. **B**: ATP-ADP exchange rate mediated by the ANT in different types of mitochondria, normalized to the amount of intact mitochondrial protein estimated from data shown in A. (S): synaptic, (NS): non-synaptic, (L): liver, (H): heart mitochondria. Mitochondria were fuelled by 1 mM TMPD plus 5 mM ascorbate. a,b: significantly different from synaptic and non-synaptic mitochondria (p<0.001); c: significantly different from liver mitochondria (p=0.003). **C**: Normalized ATP-ADP steady-state exchange rate mediated by the ANT in non-synaptic mitochondria fuelled by a variety of mitochondrial substrates. tmpd(h) designates 1 mM TMPD; tmpd(l) designates 0.08 mM TMPD. a, significantly different from all other conditions (p<0.03).*

various origin could differ significantly (Rossignol et al., 2000). Therefore, we caution that the relative contributions of the F_0-F_1 ATPase and the ANT to the differences in ATP efflux rates among mitochondria of different origin cannot be further dissected. By the same token, using TMPD plus ascorbate the respiratory flux of the cytochrome oxidase (and consequently of the ATPase and the ANT) likely changes (Brand et al., 1994). However, cytochrome oxidase activity can be directly measured. This enzyme exhibits robust tissue-specific kinetic properties (Patel and Katyare, 2005); for this and the previous

reason, it makes sense to compare ATP-ADP exchange rates with the respective cytochrome oxidase activity (Forman and Wilson, 1983) from various types of mitochondria. Nonetheless, no correlation between ATP-ADP exchange rates and cytochrome oxidase activity were observed.

1.11 Correlation of ATP-ADP steady-state exchange rate mediated by the ANT to $\Delta\Psi m$

As seen in figures 1.6A and B, mitochondria energized with TMPD plus ascorbate, were challenged by increasing concentrations of the uncoupler SF 6847. Both potentiometric dyes (Safranine O and TMRM) exhibited spikes of depolarization followed by spontaneous repolarization, sometimes unrelated to the addition of uncoupler (curves a). This created an obstacle for the subsequent correlation of ATP-ADP steady-state exchange rate mediated by the ANT to clamped $\Delta\Psi m$, but it was not observed if mitochondria were energized by glutamate plus malate (curves b). Therefore, in subsequent experiments, mitochondria were energized with glutamate and malate, and the step size of the uncoupler concentration was increased so as to produce depolarization up to ~-100 mV (panel c). In parallel experiments, ATP-ADP steady-state exchange rate mediated by the ANT was measured from mitochondria pretreated with the same amount of uncoupler in the 0-60 nM range. Calculated values of ATP-ADP steady-state exchange rate mediated by the ANT were plotted versus the applied dose of the uncoupler (panel D). From the data shown in panels C and D we could reconstruct the dependence of ATP-ADP steady-state exchange rate mediated by the ANT on $\Delta\Psi m$ (panel E). The open circles symbols represent the $\Delta\Psi m$ values reached 20 sec after addition of ADP. In similar conditions, rat liver mitochondria during state 3 and 4 produce similar $\Delta\Psi m$ values (e.g. see (Azzu et al., 2008)) as opposed to other kind of mitochondria, such as from pig heart (Bose et al., 2003).

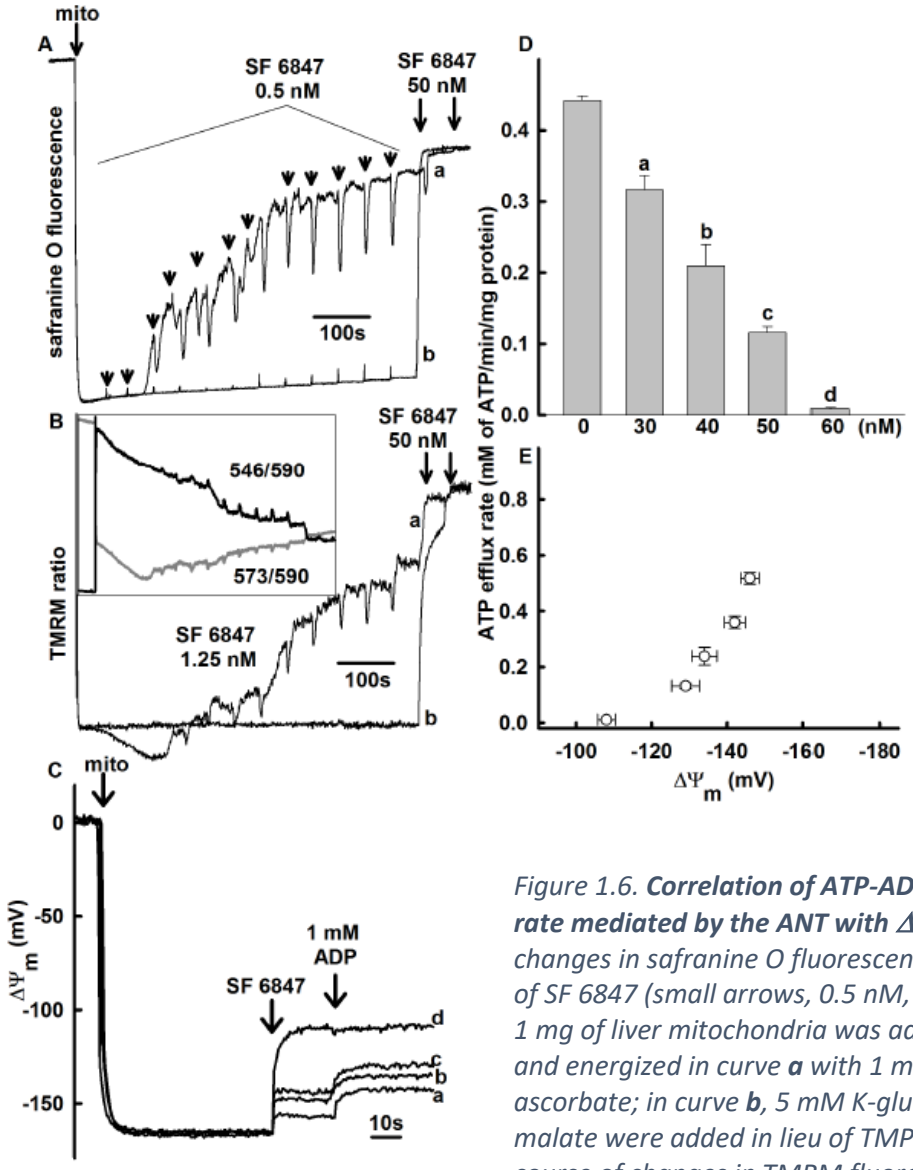

Figure 1.6. ***Correlation of ATP-ADP steady-state exchange rate mediated by the ANT with $\Delta\Psi_m$. A:*** *Time course of changes in safranine O fluorescence, in response to addition of SF 6847 (small arrows, 0.5 nM, long arrows 50 nM each); 1 mg of liver mitochondria was added to a 2-ml medium and energized in curve* ***a*** *with 1 mM TMPD plus 5 mM K-ascorbate; in curve* ***b****, 5 mM K-glutamate and 5 mM K-malate were added in lieu of TMPD+ascorbate.* ***B:*** *Time course of changes in TMRM fluorescence ratio, in response to addition of SF 6847 (small arrows, 1.25 nM each, long arrows 50 nM each); conditions identical as in (****A****). Inset: Time courses of individual TMRM fluorescence of 546/590 and 573/590 wavelengths used to derive the TMRM ratio shown in curve* ***a*** *of the same figure.* ***C****: Time course of changes in $\Delta\Psi_m$, as calculated from safranine O fluorescence. 1 mg of liver mitochondria was added to a 2-ml medium and energized with 5 mM K-glutamate plus 5 mM K-malate. SF 6847 was added where indicated in 30 (a), 40 (b), 50 (c) or 60 (d) nM concentration. 1 mM ADP was added where indicated. (****D****). Bar graph of the ATP-ADP exchange rate mediated by the ANT measured using the same type of mitochondria and conditions as in (****C****) vs the amount of uncoupler used to pretreat the mitochondria.* ***E****: Plot of ATP-ADP exchange rate mediated by the ANT vs $\Delta\Psi_m$ in liver mitochondria depolarized to various voltages, constructed from the data in panels (****C****) and (****D****). The $\Delta\Psi_m$ values represent the values obtained after addition of ADP.*

BCECF ratio fluorescence to the pH of the extracellular volume. Note also that the presence of 60 nM SF 6847, a concentration that brings a complete collapse of $\Delta\Psi$m does not alter matrix pH significantly. Note also that at least in our experimental conditions, ΔpHmax is only ~0.11. In panel B, a correlation of measured $\Delta\Psi$m during state 3 is depicted as a function of matrix pH, in the absence (black circles) or presence of uncoupler at various concentrations. Note that at higher pH values than 7.35 (pHout=7.25), state 4 to state 3 transition causes smaller depolarization, while the opposite is observed for matrix pH values more acidic than 7.35. This is in good

1.12 Correlation of ATP-ADP steady-state exchange rate mediated by the ANT to $\Delta\Psi$m clamped at various matrix pH values

The ANT transports the deprotonated form of adenine nucleotides (Metelkin et al., 2006). We were therefore interested in how does the ATP-ADP exchange rate depends on pH. In figure 1.7A, we show a correlation diagram based on measuring of matrix pH by calibrated

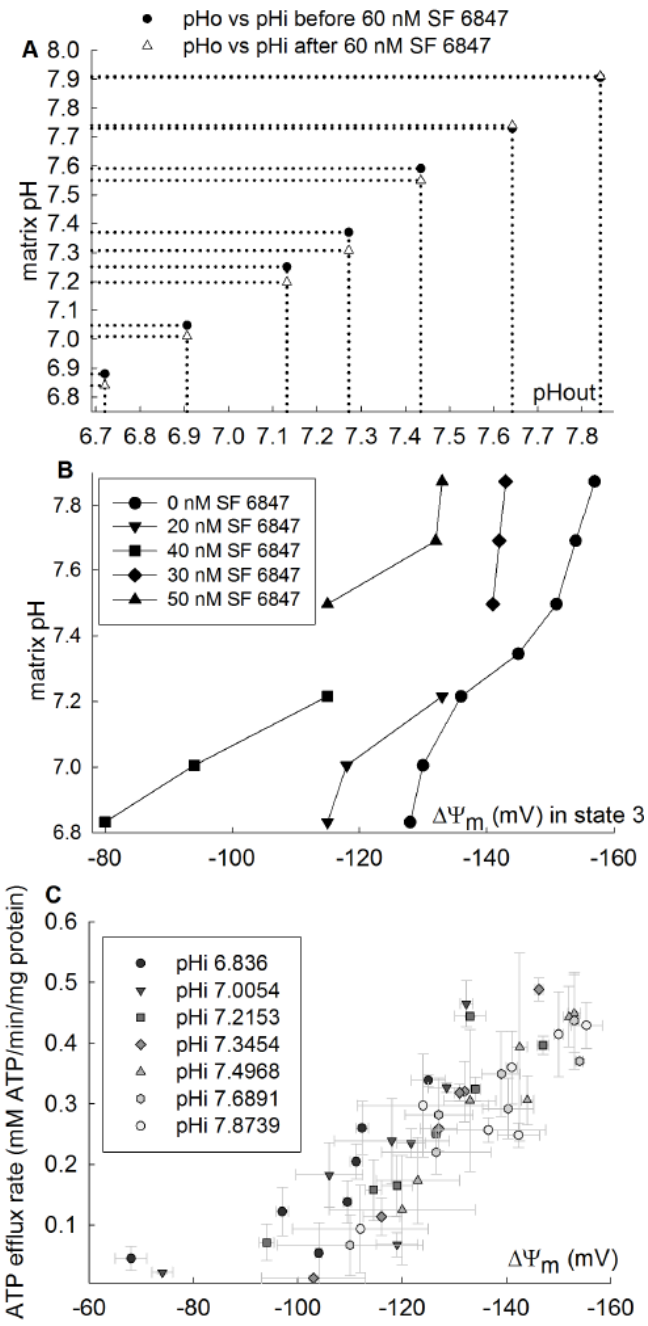

Figure 1.7. ***Correlation ATP-ADP steady-state exchange rate mediated by the ANT with $\Delta\Psi_m$ at various matrix pH values. A:*** *correlation of matrix pH to the pH of the experimental volume, before and after collapse of $\Delta\Psi_m$ by SF 6847.* ***B:*** *Correlation of matrix pH to clamped values $\Delta\Psi_m$ by titration with SF 6847 during state 3.* ***C****: Correlation of ATP-ADP steady-state exchange rate mediated by the ANT with $\Delta\Psi_m$ clamped at various matrix pH values by manipulation of the pH of the experimental volume.*

agreement with a mitochondrial energetics model described recently by the group of Beard (Wu et al., 2007). In the same panel, it is also apparent that smaller amount of uncoupler is required at pHin< 7.35 to cause depolarization than at pHin > 7.35. This is because the efficiency of any protonophoric uncoupler (U) exhibits pH dependence. SF 6847 possesses a pKa=6.5. By increasing the pH, one increases the amount of the dissociated, U- form of uncoupler outside mitochondria, thereby more uncoupler is needed to maintain the same level of uncoupling (proton flux), as U- form does not accumulate in mitochondria. By decreasing the pH the opposite is observed – increasing of the UH form, so less uncoupler is needed. In panel C, the ATP-ADP exchange rate mediate by the ANT for various matrix pH values is depicted as a function of $\Delta\Psi$m. For panel C, the dissociation constants of the adenine nucleotides for Mg^{2+} for the quantification of ATP-ADP exchange rates have been re-estimated for each pH value (not shown). Likewise, calibrations of safranine O for the same pH range exhibited no deviations among different pH buffer values in the -170 -40 mV range.

1.13 Estimation of the molecular turnover number of the ANT

Using previously published values and our own estimates of the total amount of ANT protein found in mitochondria of various origins (0.2-0.24 nmole ANT per mg of total mitochondrial protein in liver (Winkler and Lehninger, 1968), (Forman and Wilson, 1983), 1.2 nmole in heart (Halestrap and Brenner, 2003), 1.44 nmole in brain non-synaptic mitochondria (our estimate) and 1.37 nmole in synaptic mitochondria (our estimate), we can calculate the rates of ADP/ATP exchange per ANT molecule. The calculated values of the ATP/ADP turnover rates for the ANT are between 82 s^{-1} and 99 s^{-1} in liver, 23 s^{-1} in brain (synaptic mitochondria), 22 s^{-1} in brain (non-synaptic), but only 5 s^{-1} in heart. It is of note, that by using substrates such as glutamate and malate as opposed to TMPD plus ascorbate, heart mitochondria exhibit much

higher ANT molecular turnover numbers. These values correspond to the 'forward' mode of transport of the ANT and are valid at 37 °C, pHo 7.25, with TMPD (1 mM) plus ascorbate (5 mM) as substrates at a $\Delta\Psi m$ of -163 ± 3 mV (liver mitochondria), -165 ± 2 mV (heart mitochondria), -168 ± 3 mV (synaptic mitochondria), and -167 ± 3 mV (non-synaptic mitochondria) in the presence of 1 mM total extramitochondrial Mg^{2+}.

2. The ANT kinetic assay can be applied in permeabilized cells

In (Chinopoulos et al., 2009) we described a method to measure ADP-ATP exchange rates in isolated mitochondria by recording the changes in free extramitochondrial [Mg^{2+}] reported by a Mg^{2+}-sensitive fluorescent indicator, exploiting the differential affinity of ADP and ATP to Mg^{2+}. Subsequently, we published a modification of this method suited for following ADP-ATP exchange rates in environments with competing reactions by including BeF_3^- and Na_3VO_4 in the media (Kawamata et al., 2010).

2.1 Rationale for developing a modification of the ADP-ATP exchange assay for permeabilized cells

In isolated mitochondria, the only other reaction that interconverts adenine nucleotides in the experimental volume is that catalyzed by adenylate kinase, residing in the intermembrane space of mitochondria (Chinopoulos et al., 2009), but this is effectively inhibited by P^1,P^5-di(adenosine-5') pentaphosphate (AP_5A) (Lienhard and Secemski, 1973). A creatine kinase isoform that also resides in the intermembrane space remains inoperable for as long as there is no creatine or its phosphate derivatives present in the medium. However, in permeabilized cells there are a number of additional reactions that interconvert adenine nucleotides, such as the Na^+/K^+ ATPase, the plasmalemmal and endoplasmic Ca^{2+} ATPase, and in contractile cells the myosin ATPase, in addition to a gamut of phosphorylases, phosphatases and kinases. Reactions interconverting adenine nucleotides other than the ANT invalidate the binding equations that are applied on recordings of free [Mg^{2+}] for calculating ADP-ATP exchange rates of mitochondria (Chinopoulos et al., 2009). In order to apply the method described in (Chinopoulos et al., 2009) to permeabilized cells, one must inhibit all competing adenine nucleotide interconverting reactions, except the ANT. BeF_3^- and vanadium compounds has been successfully used for over 40 years in many applications as inhibitors of ADP and/or ATP utilizing reactions (Baukrowitz et al., 1994), (Cantley et al., 1977), (Davies and Hol, 2004), (Gordon, 1991), (Mukherjee, B. et al., 2004), (Robinson et al., 1986), (Werber et al., 1992). In (Kawamata et al., 2010) we demonstrated a modification of the original method developed for measuring ADP-ATP exchanges in isolated mitochondria so that it can be applied in permeabilized cells, using BeF_3^- and Na_3VO_4.

2.2. Gaining access to in situ ANT while inhibiting other adenine nucleotide interconverting reactions

In order to gain access to the cell interior and deliver known amounts of ADP, Mg^{2+}, the membrane-impermeable $5K^+$ salt of the Mg^{2+}-sensitive fluorescent indicator, Magnesium Green, BeF_3^-, Na_3VO_4, AP_5A and mitochondrial substrates (the creatine kinase inhibitor iodoacetamide is membrane-permeable) without compromising the inner mitochondrial membrane integrity, the following experiment was performed, as shown in figure 2.1A: Oxygen consumption of C_2C_{12} cells was recorded in cytosol-mimicking media (the composition of which is described in Materials and Methods) and using succinate as a mitochondrial respiratory substrate (2 mM) and ADP (2 mM), both being impermeable to the cell membrane. Stepwise additions of digitonin increased oxygen consumption rates, signifying permeabilization of the cell membrane and provision of entry points for succinate and ADP to the *in situ* mitochondria. Upon reaching a sufficiently high concentration of digitonin, the detergent decreased oxygen consumption rates, indicative of either disrupting the i) inner mitochondrial membrane integrity and/or ii) outer mitochondrial membrane integrity causing a leak of cytochrome c. The concentration of digitonin that produced the highest rate of oxygen consumption was chosen for all further experiments.

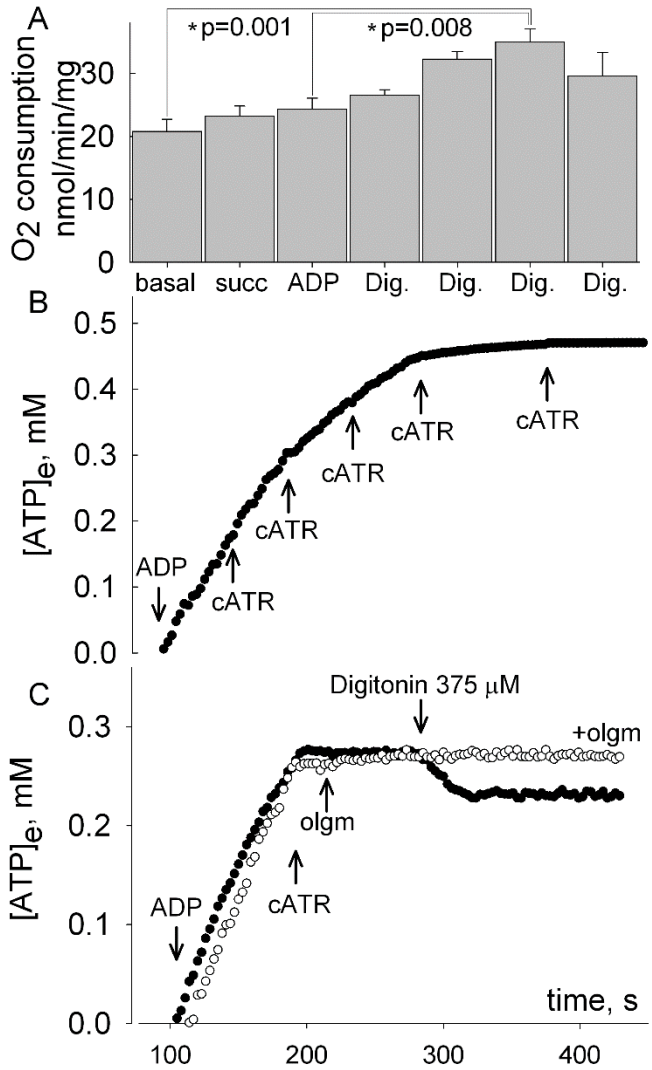

Figure 2.1. ***Validating the method for permeabilized cells upon gaining access to cell interior. A:*** *Mitochondrial respiration of C_2C_{12} cells; succ: succinate, 2 mM, ADP: 2 mM, Dig.: digitonin 1 μl of 2.5 mM.* ***B:*** *Time course of $[ATP]_e$ in the medium, calculated from $[Mg^{2+}]_{free}$ as described in the main text. Effect of stepwise addition of 2 nM cATR to permeabilized cells.* ***C:*** *Time courses of $[ATP]_e$ appearing in the medium, calculated from $[Mg^{2+}]_{free}$ as described in the main text. Effect of high concentration of digitonin on in situ mitochondria with inhibited ANT. In the trace formed by black circles, only ADP, cATR and digitonin were added where indicated. In the trace formed by the open circles, oligomycin (olgm) was also added where indicated. Panels* ***B*** *and* ***C*** *share the same x-axis.*

In the subsequent experiment shown in figure 2.1B, digitonin-permeabilized C_2C_{12} cells were incubated in cytosol-mimicking media in the presence of BeF_3^-, Na_3VO_4, AP_5A and iodoacetamide. Addition of ADP resulted in a gradual emergence of ATP in the medium. Subsequent stepwise additions of 2 nM cATR resulted in a complete halt of ATP rise in the media after 5 additions, amounting to 10 nM cATR. That attests to the fact that the ANT was the only entity mediating ADP-ATP exchanges in these permeabilized cells using this cocktail of inhibitors. Although using this methodology the amount of ANT can be estimated, this amount must be considerably higher than the K_i of cATR for the transporter. Since this K_i is in the 1-10 nM range, which is similar to the amount of cATR required to block ADP-ATP exchanges completely, the estimation of the

amount of ANT for the amount of cells/*in situ* mitochondria that are present in the well would be overestimated. For the same reason, the molecular turnover number of the ANT cannot be estimated using such a low amount of cells/*in situ* mitochondria. During the digitonin permeabilization, it is conceivable that a small (due to digitonin titration during oxygen consumption experiments) but undetermined fraction of *in situ* mitochondria would also be permeabilized. This should have exposed the hydrolytic part of the F_1F_o-ATPase that in deenergized-permeabilized mitochondria would result in vigorous ATP hydrolysis. To address this possibility, a large bolus of digitonin (10 times higher amount than the optimal concentration for selective cell membrane permeabilization) was added to already permeabilized cells in which their mitochondria have been allowed to phosphorylate 0.285 mM of ADP to ATP, followed by inhibiting their ANT with 1 μM cATR. As seen in figure 1C (black circles), addition of 0.375 mM digitonin that is expected to permeabilize all *in situ* mitochondria, resulted in an initial gradual decrease in ATP that halted within 30-40 seconds. We interpret this lag as the time required for BeF_3^- and orthovanadate to interrupt the ATP hydrolysis cycle of the F_1F_o-ATPase by binding in place of the released hydrolysis product, inorganic phosphate. Accordingly, if oligomycin (olgm) was added after cATR (open circles), there was no gradual decrease in ATP upon subsequent addition of 0.375 mM digitonin. This experiment demonstrates that the gradual decrease in ATP that halted within 30-40 seconds was sensitive to oligomycin, thus it was attributed to the hydrolytic action of the exposed F_1F_o-ATPase.

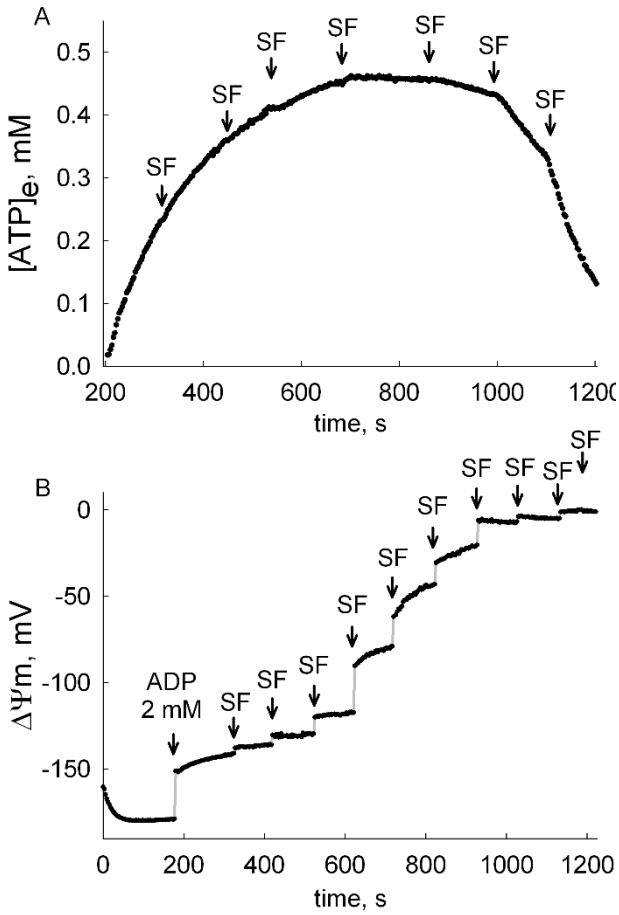

Figure 2.2. ***Estimation of ADP-ATP exchange rates and ΔΨm in permeabilized cells. A:*** *Time course of $[ATP]_e$ in the medium, calculated from $[Mg^{2+}]_{free}$ as described in the main text. Effect of membrane depolarization to various voltages by stepwise addition of 10 nM SF 6847.* ***B:*** *Reconstructed time course of ΔΨm, calculated from safranine O fluorescence. Permeabilized cells were challenged initially by 2 mM ADP, followed by stepwise additions of 10 nM SF 6847.*

2.3 Estimation of ADP-ATP exchange rates in permeabilized cells as a function of mitochondrial membrane potential

Among many bioenergetic parameters elaborated in (Metelkin et al., 2009), mitochondrial ADP-ATP exchange rate depends steeply on ΔΨm. It is therefore imperative to provide ADP-ATP exchange rates mediated by the ANT as a function of ΔΨm. In figure 2.2 panel A, we show the experiment where permeabilized cells were incubated in cytosol-mimicking media in the presence of BeF_3^-, Na_3VO_4, AP_5A and iodoacetamide, and Magnesium Green fluorescence was recorded over time, calibrated to free $[Mg^{2+}]$, and calculated to extramitochondrial ATP, ($[ATP]_e$). Addition of ADP resulted in a gradual emergence of $[ATP]_e$. Subsequent stepwise additions of the uncoupler SF 6847 (10 nM each) resulted in a progressive decrease in the rate of $[ATP]_e$, that leveled off upon addition of the fourth SF 6847 pulse. At this point, the ANT operated at its "reversal potential", E_{rev_ANT}, a ΔΨm value

during which there is no net transport of adenine nucleotides across the inner mitochondrial membrane (Chinopoulos et al., 2010). Further additions of the uncoupler dropped $\Delta\Psi m$ to a sufficiently low level that resulted in reversal of the ANT, and conversion of mitochondria to ATP consumers (Chinopoulos and Adam-Vizi, 2010a), (Chinopoulos et al., 2010). In figure 2.2 panel B, permeabilized cells were incubated in cytosol-mimicking media using the same cocktail of inhibitors, and $\Delta\Psi m$ was estimated by using fluorescence quenching of the cationic dye safranine O which accumulates inside energized mitochondria (Akerman and Wikstrom, 1976). As shown, addition of ADP caused a moderate depolarization. Subsequent stepwise addition of the uncoupler SF 6847 (10 nM each) caused a stepwise dissipation of $\Delta\Psi m$. In isolated mitochondria, safranine O fluorescence can be calibrated to $\Delta\Psi m$ by applying the Nernst equation assuming a matrix $[K^+]$=120 mM and recording safranine O fluorescence in the presence of 2 nM valinomycin and stepwise additions of $[K^+]$ in the 0.2-120 mM range (Akerman and Wikstrom, 1976).

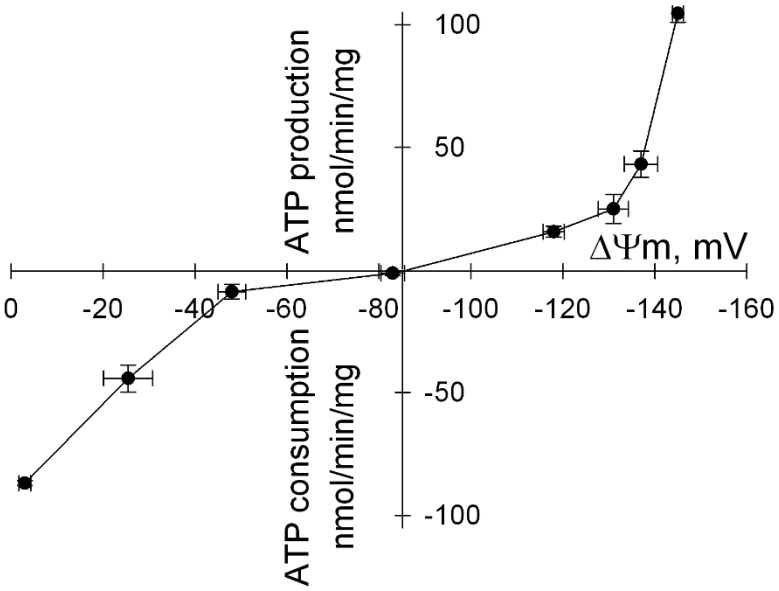

Figure 2.3. ***ADP-ATP exchange rate/ΔΨm profile of in situ mitochondria of permeabilized cells.*** *Plot of ATP–ADP exchange rate mediated by ANT versus ΔΨm in in situ mitochondria of C_2C_{12} permeabilized cells depolarized to various voltages by increasing amounts of SF 6847; constructed from the data of 3 independent experiments performed as described in figure 2.2.*

This technique is not reproducible in permeabilized cells. Hereby, we have adopted three assumptions, in order to arbitrarily convert safranine O fluorescence to mV: i) minimum fluorescence was considered as -180 mV, ii) maximum fluorescence was considered as 0 mV, and iii) safranine O fluorescence increases linearly upon dissipation of $\Delta\Psi m$. Although these assumptions are in good agreement with a large body of literature, we cannot overemphasize that this is only an arbitrary approximation. Nevertheless, using this approximation, E_{rev_ANT} falls well within calibrated values for isolated mitochondria (Chinopoulos et al., 2010). By linear regression analysis of the ADP-ATP exchange rates of *in situ* mitochondria of permeabilized cells plotted as a function of $\Delta\Psi m$ titrated by stepwise additions of an uncoupler, we derived the "ADP-ATP exchange rate/$\Delta\Psi m$" profile depicted in figure 2.3, showing an average plot of 3 independent experiments. By analogy of a current-voltage relationship of a channel (Offner, 1991) or a transporter (Gadsby and Nakao, 1989), this graph depicts the rate of transfer of an adenine nucleotide phosphorylated group per mg protein per unit time, as a function of the potential that exists across the membrane through which the phosphorylation group transfer takes place. However, if one is to compare different cell types, or samples of the same cell type but with manipulated mitochondria, comparisons must be made for the same amount of mitochondria. One intrinsic mitochondrial parameter that is representative of the amount of mitochondria in a cell is citrate synthase activity. In our hands, citrate synthase specific activity of C_2C_{12} cells was 436 ± 13 nmol/min/mg protein. By comparison, isolated mitochondria from skeletal muscle exhibit 8-10 times higher citrate synthase specific activity (Chess et al., 2009), (Rasmussen et al., 2003), (Winder et al., 1975), which is in a good agreement with 8-10 times higher ADP-ATP exchange rates in similar type of mitochondria (Chinopoulos et al., 2009).

3. Measurement of ADP-ATP exchange in relation to membrane potential and oxygen consumption in mitochondria with improved calibration

Above, the method was shown to measure ADP-ATP exchange rates in isolated or *in situ* mitochondria of permeabilized cells; below a modification of this method is described by improving a calibration step minimizing errors introduced during conversion of the dye-emission signal to free extramitochondrial [Mg^{2+}] and further to ATP. Basically, the conversion of dye emission signal to [Mg^{2+}], and subsequently to ATP, was priorly calibrated by obtaining the maximal fluorescence signal with excess [Mg^{2+}] and the minimal fluorescence by the addition of the cation chelator, EDTA. However, because Magnesium Green is a fluorimetric dye with single excitation and emission, it is subject to the potential pitfalls of non-ratiometric dyes related to variations in dye concentration and/or bleaching. In practice, this introduced variability in the measurement of ADP-ATP exchange rate and a better calibration was required. Step-by-step instructions of the improved calibration protocol applied in permeabilized cells and measured simultaneously to oxygen consumption have been published in (Chinopoulos et al., 2014) and appear below:

3.1 K_d determination of ATP and ADP for Mg^{2+}

First, one should measure the apparent K_d values of ADP for Mg^{2+} and ATP for Mg^{2+} for the pertaining conditions (media, temperature, ionic strength, type and amount of cells, etc), steps 1-7.

1) Cells resuspended in 2 ml of buffer C are added to a chamber of an Oroboros Oxygraph-2k. The presence of cATR and oligomycin in the buffer is only required for the K_d determination. Magnesium Green fluorescence is recorded by the O2k-Fluorescence LED2-Module at a 1 Hz acquisition rate. Experiments are performed at 37 ^oC. Digitonin and Magnesium Green $5K^+$ salt (MgGr; 1 μM) are subsequently added to the chamber.

2) MgGr fluorescence signal is recorded upon stepwise additions of 0.1 mM $MgCl_2$ for a total of 10 additions (about 50 sec of recording time per addition). This is shown in figure 3.1A, on the *left* side of the dashed line.

3) Continuing in same cells in the chamber, add 0.25 mM ADP in subsequent steps for a total of 19 steps (about 50 sec of recording time per addition). This is shown in figure 3.1A, on the *right* side of the dashed line.

4) Likewise, in a new cell preparation, repeat Steps 1- 3, but with 11 additions of 0.2 mM ATP instead of ADP, also shown in figure 3.1A.

5) Convert the MgGr signal of both left and right part of figure 3.1A to free [Mg^{2+}]. To do this, plot the steady-states of MgGr after each addition of $MgCl_2$ (as seen in the left part of figure 3.1A) on the y-axis as a function of [Mg^{2+}] (x-axis) and apply the following fit equation (you can use either trace): f=y0+a*(1-exp(-b*x)). This is an exponential rise to maximum equation with a 3 parameter function, where y0, a, and b are coefficients. The results are shown in figure 3.1B.

6) Calibrate the right part of figure 3.1A, using the coefficients y0, a, and b determined from step 5, shown in figure 3.1B, by solving the following exponential function for x: x=(-1/b)*ln(1-((f-

y0)/a)). After calibration of MgGr signals obtained in figure 3.1A, it should look like figure 3.1C. If calibration was performed correctly, the left parts of both traces should be almost identical.

7) Next, from the calibrated right part of figure 3.1C, the K_d of ADP for Mg^{2+} and the K_d of ATP for Mg^{2+} is estimated by fitting the following equation with the least squares method to the data points:

$$[Mg^{2+}]_f = 0.5 \cdot \left([Mg^{2+}]_t - K_d - [L]_t + \sqrt{\left([Mg^{2+}]_t - K_d - [L]_t\right)^2 + 4K_d[Mg^{2+}]_t} \right),$$

where $[Mg^{2+}]_t$ is the total $[Mg^{2+}]$ (1 mM), $[L]_t$ is the total concentration of added ADP (or ATP). The fitted curves are shown in figure 3.1D for both ADP and ATP. The K_d determined are K_d _ADP= 0.914 $^{+/-}$ 0.028 mM, and K_d _ATP=0.147 $^{+/-}$ 0.008 mM. Since K_d values are now known for the pertaining experimental conditions, ADP-ATP exchange rates can be calculated from the MgGr recordings.

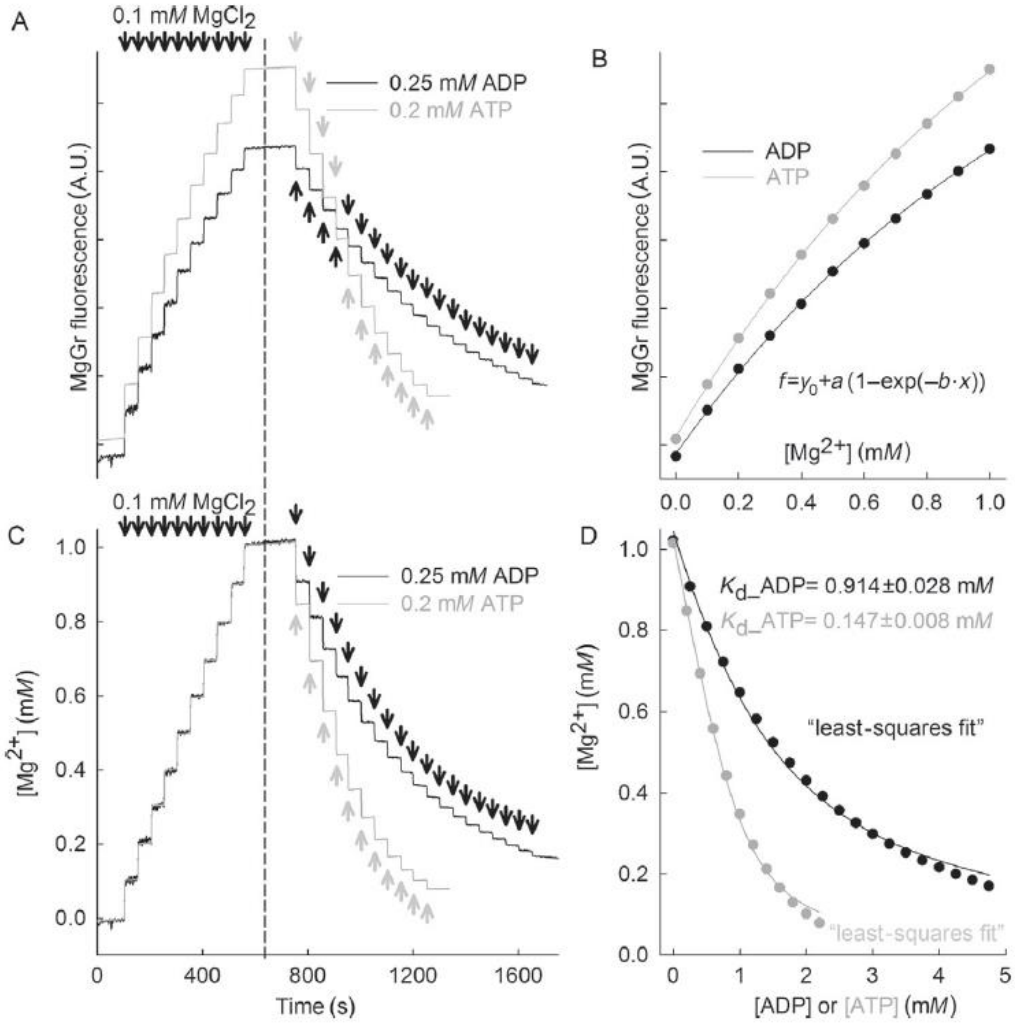

Figure 3.1. ***Magnesium green fluorescence calibration and estimation of K_d of ATP and ADP for Mg^{2+}.*** ***A****: Reconstructed time-recordings of MgGr raw fluorescence traces in permeabilized HEK293 cells as a function of extramitochondrial $[Mg^{2+}]$ (left part of the traces), and as a function of extramitochondrial ADP or ATP (right parts of the traces).* ***B****: MgGr fluorescence changes are dependent on extramitochondrial $[Mg^{2+}]$.* ***C****: Calibrated time-recordings of extramitochondrial $[Mg^{2+}]$ (left part of the traces), and as a function of extramitochondrial ADP and ATP (right parts of the traces) are shown.* ***D****:*

Calibrated extramitochondrial Mg^{2+} plots as a function of ADP or ATP are shown, from which we estimated K_d of ADP and ATP for Mg^{2+} using the least squares method to fit the data.

3.2 $[Mg^{2+}]_{free}$ determination from Magnesium Green fluorescence in permeabilized cells and conversion to ADP-ATP exchange rate

1) Add 1.1 μM of MgGr in 1.8 ml of buffer B. Record MgGr fluorescence for a few minutes and allow the signal to stabilize. In the meantime, harvest cells by trypsinization as elaborated above. Cells are washed once with buffer A and then resuspended in 0.2 ml of buffer B.

2) Upon addition of cells to the measuring chamber, wait 3 minutes and resume recording. After 2 minutes, add a known amount of ADP; we suggest 2 mM ADP. When ADP is added, the fluorescence signal will drop, as shown in figure 3.2A. Subsequently, the uncoupler SF 6847 is added to the chamber in 10 nM increments (~100 seconds between each interval); this will be used later on to correlate the ATP efflux rates with membrane potential changes, see below. It is important to use SF 6847 and not the more widely used FCCP, CCCP, or 2,4-dinitrophenol, because SF 6847 is the only uncoupler that does not quench Magnesium Green fluorescence up to a concentration of 1 μM.

3) Figure 3.2B shows the free $[Mg^{2+}]$ calibrated from MgGr raw fluorescence. One may notice that initial total $[Mg^{2+}]$ was measured to be 1.1486 mM, i.e. not exactly 1 mM, which was the actual amount added into the chamber. After the addition of 2 mM ADP, free $[Mg^{2+}]$ was measured to attain the value of 0.5553 mM, i.e. not the exact value of 0.3958 mM, which is what would be expected. The value of 0.3958 mM was derived from the equation below:

$$[\mathrm{Mg}^{2+}]_\mathrm{f} = 0.5 \cdot \left([\mathrm{Mg}^{2+}]_\mathrm{t} - K_\mathrm{d} - [L]_\mathrm{t} + \sqrt{\left([\mathrm{Mg}^{2+}]_\mathrm{t} - K_\mathrm{d} - [L]_\mathrm{t}\right)^2 + 4K_\mathrm{d}[\mathrm{Mg}^{2+}]_\mathrm{t}} \right)$$

where $[Mg^{2+}]_t$ is the total $[Mg^{2+}]$ (1 mM), [L]t is the total concentration of added ADP (or ATP), and K_d is the fitted value of K_{ADP} or K_{ATP}, respectively. These errors stem from the fact that MgGr is not a ratiometric dye, and thus it is subject to the pitfalls elaborated above. It is therefore necessary to adjust the whole trace shown in figure 3.2B so that the value just prior to addition of 2 mM ADP is 1 mM $[Mg^{2+}]$ (the total), and the first value of $[Mg^{2+}]$ after the addition of 2 mM ADP is 0.3958 mM. From figure 3.1B, it is apparent that the relation between free $[Mg^{2+}]$ and MgGr fluorescence signal in the 0-0.5 mM range is fairly linear. Thus, one may apply a series of simple arithmetic operations to correct the errors: the difference between the measured total $[Mg^{2+}]$ (1.1486 mM) and the measured first value of $[Mg^{2+}]$ after the addition of 2 mM ADP (0.5553 mM) is 0.5933 mM, while the difference between the actual total $[Mg^{2+}]$ (1 mM) and the expected first value of $[Mg^{2+}]$ after the addition of 2 mM ADP (0.3958 mM) is 0.6042 mM; therefore, the measured changes in free $[Mg^{2+}]$ are underestimated by a factor of 0.6042/0.5553=1.01837. Thus, the whole trace of figure 3.2B is multiplied by 1.01837. This would generate a trace in which the value of $[Mg^{2+}]$ just prior to addition of 2 mM ADP is 1.169 mM (the estimated total), and the first value of $[Mg^{2+}]$ after the addition of 2 mM ADP is 0.5655 mM (not shown). By subtracting the difference of 1.169-1=0.169 mM from this whole trace, the final trace should look like the one depicted in figure 3.2C. Note that in the trace shown in figure 3.2C the value just prior to addition of 2 mM ADP is 1 mM $[Mg^{2+}]$ (the total), and the first value of $[Mg^{2+}]$ after the addition of 2 mM ADP is 0.3958 mM. The trace depicting the estimated $[Mg^{2+}]$ has therefore been corrected, and the conversion to ATP appearing in th medium can now be applied, as shown in the next step.

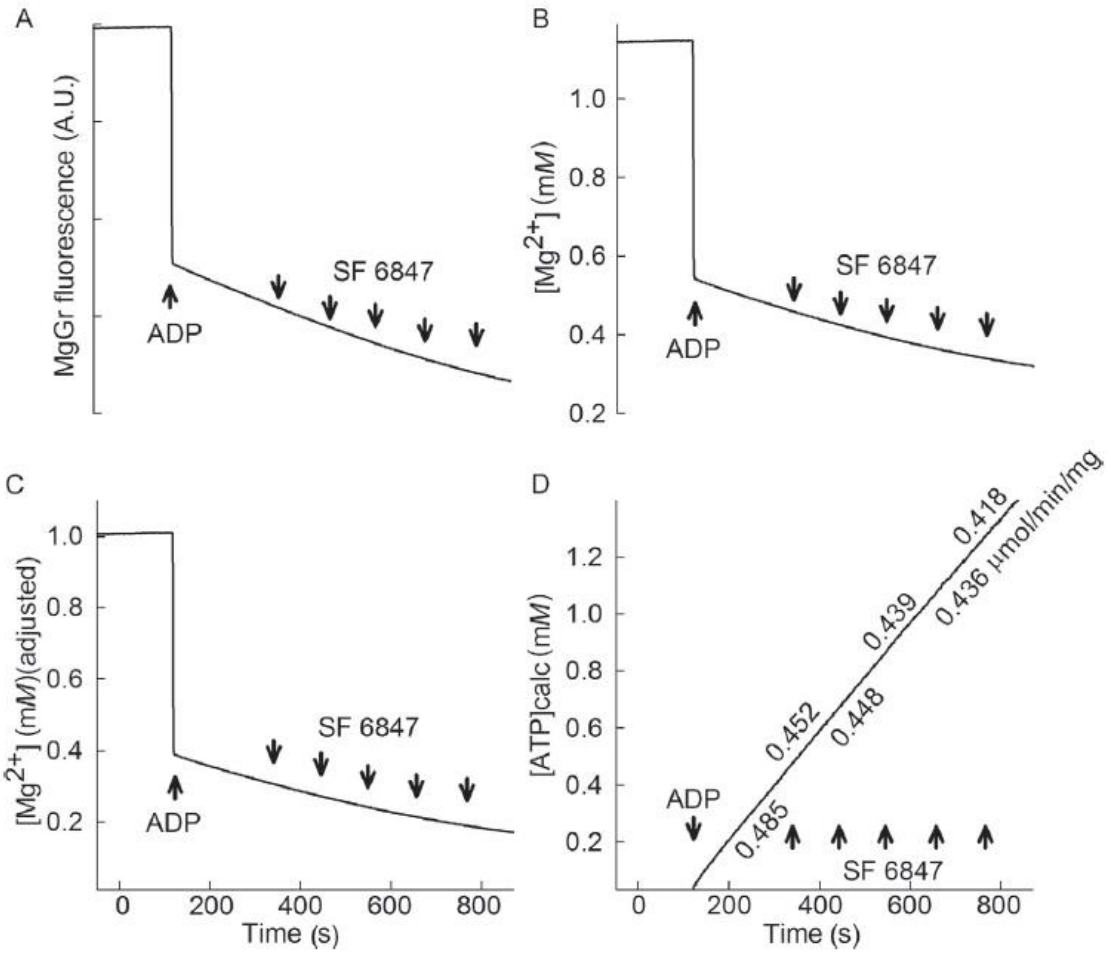

Figure 3.2. ***Determination of extramitochondrial [Mg^{2+}] and conversion to ATP****. **A**: Reconstructed time recording of MgGr raw fluorescence in permeabilized HEK293 cells upon addition of 2 mM ADP (where indicated), followed by incremental 10 nM additions of the uncoupler SF 6847. **B**: Calibrated time recording of extramitochondrial [Mg^{2+}] obtained from panel 2A. **C**: Corrected calibrated trace of panel 2B, as described in the text. **D**: Calculated amount of ATP appearing in the medium converted from panel 2C. The rate of ATP appearing in the medium is indicated in µmol/min/mg protein.*

4) We convert the corrected [Mg^{2+}] values to ATP appearing in the medium, using the equation below:

$$[\mathrm{ATP}]_t = \left(\frac{[\mathrm{Mg}^{2+}]_t}{[\mathrm{Mg}^{2+}]_f} - 1 - \frac{[\mathrm{ADP}]_t(t=0) + [\mathrm{ATP}]_t(t=0)}{K_{\mathrm{ADP}} + [\mathrm{Mg}^{2+}]_f} \right) \Bigg/ \left(\frac{1}{K_{\mathrm{ATP}} + [\mathrm{Mg}^{2+}]_f} - \frac{1}{K_{\mathrm{ADP}} + [\mathrm{Mg}^{2+}]_f} \right)$$

The rate of ATP appearing in the medium can be calculated by making a linear regression for the ATP values as a function of time, as shown in figure 3.2D.

3.3 Mitochondrial membrane potential (ΔΨm) determination in in situ mitochondria of permeabilized cells

ΔΨm is estimated using fluorescence quenching of the cationic dye safranin O due to its accumulation inside energized mitochondria (Akerman and Wikstrom, 1976), also taking into account the considerations discussed in (Perevoshchikova et al., 2009) and (Figueira et al., 2012).

1) Cells are treated exactly as described for free [Mg^{2+}] determination, except that MgGr is replaced by 5 μM safranin O.

2) Fluorescence is recorded in an Oroboros Oxygraph-2k at a 1 Hz acquisition rate, using the 495 nm excitation and 585 nm emission wavelengths. Experiments are performed at 37 ^{o}C. After the baseline signal has stabilized, 2 mM ADP is added to the chamber and fluorescence is allowed to stabilize. The raw signal of safranin O fluorescence is shown in figure 3.3A.

3) After addition of ADP, $\Delta\Psi$m is further depolarized stepwise by addition of 10 nM SF 6847 until the signal after depolarization becomes stable (~100 sec). Safranin O fluorescence is converted to mV (figure 3.3B) using the Nernst equation and assuming a matrix [K^+]=120 mM, which was determined by a voltage-fluorescence calibration curve of safranin O fluorescence in the presence of 2 nM valinomycin and increasing [K^+] (0.2-120 mM; (Akerman and Wikstrom, 1976)). An important note is that cancer cells express very variable levels of IF-1 (Sanchez-Arago et al., 2013), which inhibits the ATP-hydrolytic function of the ATPase, thus hindering reversal rates. Therefore, it is not recommended to study ATP *influx* rates in mitochondria from cancer cells, i.e. at very depolarized values. The method is suitable for studying cancer mitochondria during ATP synthesis.

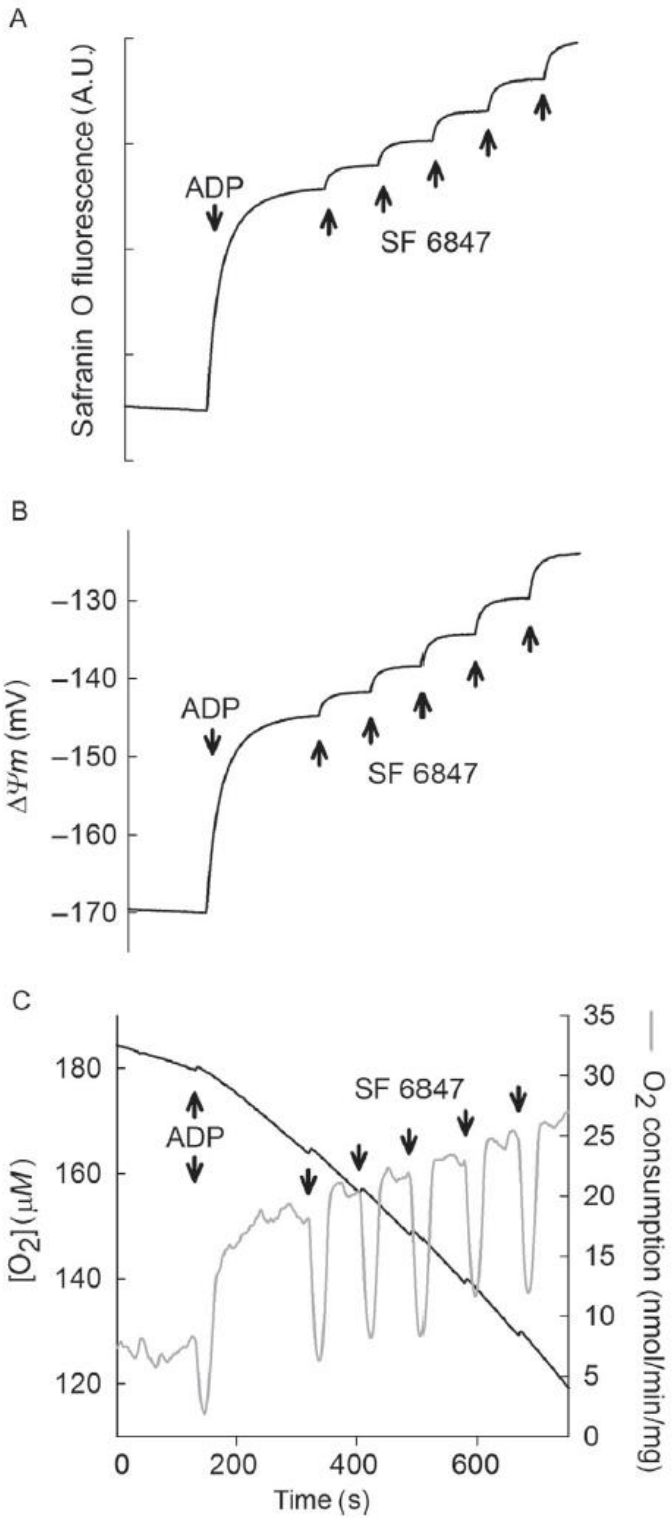

Figure 3.3. ***Mitochondrial membrane potential and oxygen consumption determination in permeabilized cells. A:*** *Reconstructed time recording of Safranin O raw fluorescence in permeabilized HEK293 cells upon addition of 2 mM ADP (where indicated), followed by incremental 10 nM additions of the uncoupler SF 6847.* ***B****: Calibrated time recording of $\Delta\Psi$m obtained from panel 3A.* ***C****: Reconstructed time recording of oxygen concentration in the medium (black trace) and oxygen flux (grey trace) recorded simultaneously with either MgGr signal (panel 2A) or Safranin O signal (panel 3A).*

3.4 Mitochondrial respiration

Oxygen consumption is simultaneously measured with Safranin O reflecting $\Delta\Psi$m or MgGr fluorescence reflecting ADP-ATP exchange rates in the same samples polarographically using the Oxygraph-2k. Oxygen concentration (black trace of figure 3.3C) and oxygen flux (grey trace of figure 3.3C) expressed as pmol·s^{-1}·mg^{-1}; negative time derivative of oxygen concentration, divided by tissue mass per volume and corrected for instrumental background oxygen flux arising from oxygen consumption of the oxygen sensor and back-diffusion into the chamber) were recorded using DatLab software (Oroboros Instruments). From the above measured parameters, one is able to estimate the rate of ATP appearing in the medium as a function of $\Delta\Psi$m or oxygen consumption rate.

4. Modeling of ATP-ADP steady- state exchange rate mediated by the adenine nucleotide translocase in isolated mitochondria

The model (Metelkin et al., 2009) represents the system of three ordinary differential equations and the basic components included are the ANT, the F_0-F_1 ATPase, and the phosphate carrier. The model reproduces quantitatively the relation of mitochondrial membrane potential to the ATP-ADP steady-

state exchange rate mediated by the ANT operating in the forward mode, with the assumption that the phosphate carrier functions under rapid equilibrium. Furthermore, the model can simulate the kinetics of experimentally measured data on mitochondrial membrane potential titrated by an uncoupler. Verified predictions imply that the ADP influx rate is highly dependent on the mitochondrial membrane potential, and in the [0 -100] mV range it is close to zero due to extremely low matrical ATP values. In addition to providing theoretical values of free matrical ATP and ADP, the model explains the diminished ADP-ATP exchange rate in the presence of nigericin, a condition in which there is hyperpolarization of the inner mitochondrial membrane at the expense of the mitochondrial DeltapH gradient. The kinetic model of mitochondrial phosphorylation described below consists of: i) the adenine nucleotides exchange model across the mitochondrial membrane by (Metelkin et al., 2006), ii) the model of F_0-F_1 ATPase developed previously by (Demin et al., 1998), iii) the simple steady-state model of phosphate carrier and iv) the empirical description of membrane potential formation and ions leak across the inner mitochondrial membrane.

4.1 Correlation of ATP-ADP steady-state exchange rate mediated by the ANT to $\Delta\Psi$m

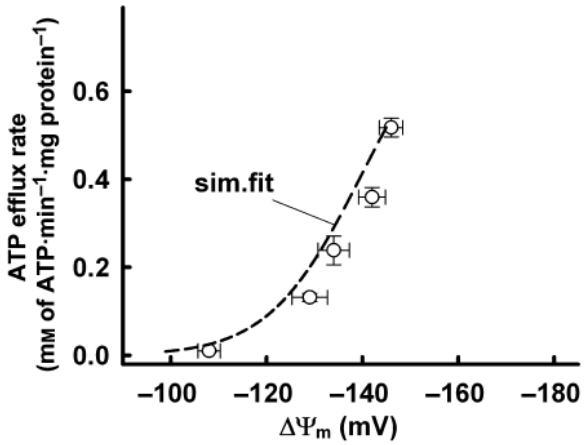

Figure 4.1. ***Correlation of ATP-ADP steady-state exchange rate mediated by the ANT with $\Delta\Psi$m.*** *Plot of ATP-ADP exchange rate mediated by the ANT vs $\Delta\Psi$m in liver mitochondria depolarized to various voltages by different amount of SF 6847. The dashed line represents the result of the model described in the text.*

Data for Fig. 4.1 were obtained from the recently published paper by us (Chinopoulos et al., 2009). Open circles symbols represent the $\Delta\Psi$m values reached 20 s after addition of ADP in the presence of increasing concentration of SF 6847 as detailed in (Chinopoulos et al., 2009). SF 6847 is a protonophoric uncoupler that dissipates $\Delta\Psi$m in a dose-dependent manner, by allowing re-entry of protons into the matrix, bypassing F_0-F_1 ATP synthase (Terada, 1975). The dotted line shows the result of the modeling after estimation of the unknown parameters. The conditions of the described set of experimental data (namely the low concentration of ATP in volume) prevent the reverse functioning of ANT. In that case the model shows the synthesis of ATP occurs at potential from -100 mV or higher. It is important to notice that in this range the mitochondrial ATP production does not saturate; that means that, within a physiological range the ATP production is controlled by ΔΨm**.** At the membrane potential values from 0 mV to -100 mV the rate of ATP production by mitochondria is close to zero.

4.2 Calibration of the kinetic model of phosphorylation in mitochondria

There are two parameters of the kinetic model whose values cannot be estimated on the basis of *in vitro* data measured for purified enzymes, namely: i) the activity of ATP synthase (c_{SYN}) and ii) the amount of ANT (c_{ANT}) for a given tissue. These parameters characterize particular suspension of mitochondria (type of animal, organ, experimental procedure) and require experimental data measured on this mitochondrial suspension to be identified. To estimate these two parameters we have fitted our model

against the dependence of ATP-ADP steady-state exchange rate mediated by the ANT on $\Delta\Psi$m (Fig. 4.1 open cycles) and dependence of these rates on *cATR*, the non-competitive blocker of the ANT (Fig. 4.2, filled cycles) measured on suspension of mitochondria respiring on glutamate and malate. Values of c_{SYN} and c_{ANT} have been chosen (see Table 4.1) in such a way as to provide minimal deviation between experimental data (circles) and model generated curve. As a criterion of fitness, the following function was used:

$$f\left(k_j, K_j\right) = \sum_i^n \left(\frac{v_i - \tilde{v}_i}{v_i} \right)^2 \quad (1)$$

Here, n is the total number of the experimental points, $\tilde{v}_i$ is the experimentally measured value of the ATP-ADP steady-state exchange rate mediated by the ANT and v_i is the value of the ATP-ADP steady-state exchange rate mediated by the ANT calculated on the model at a point corresponding to the experimental ones. To estimate values of unknown parameters the relative error of the model ($\sqrt{f/n}$) has been minimized. This procedure was performed in the DBSolve 7 package using the Hooke-Jeeves method (Mogilevskaya et al., 2009).

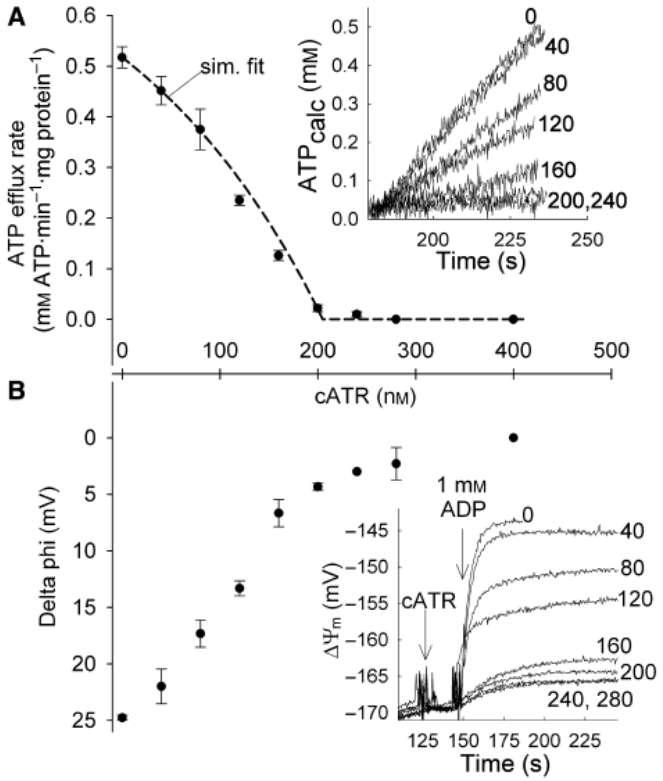

Figure 4.2. ***Titration of ATP-ADP steady-state exchange rate mediated by the ANT with cATR and correlation with $\Delta\Psi$m. A:*** *ATP-ADP steady-state exchange rate mediated by the ANT determined as a function of cATR concentration. Dashed-line: simulation fit as described in the text.* ***A, inset:*** *A representative experiment showing the calculated [ATP] appearing in the extramitochondrial medium after addition of ADP, in the presence of cATR (in the concentrations indicated in the inset figure, in nM).* ***B:*** *Delta phi represents the difference of $\Delta\Psi$m before and after addition of 1 mM ADP to liver mitochondria pretreated with cATR of the same concentration range as in panel (**A**).* ***B, inset:*** *A representative experiment showing the addition of cATR (in the concentrations indicated in the inset figure, in nM) on $\Delta\Psi$m, as indicated in inset of panel B. Data on panels A and B are shown as S.E.M. from 4 independent experiments.*

4.3 Nigericin decreases ATP-ADP steady-state exchange rate mediated by the ANT

Nigericin is an ionophore that mediates electrically neutral exchange of potassium ions for protons, eliminating the *pH* gradient across the mitochondrial membrane and causing a compensatory increase in $\Delta\Psi$m (Shavit and San Pietro, 1967), (Reed, 1979).

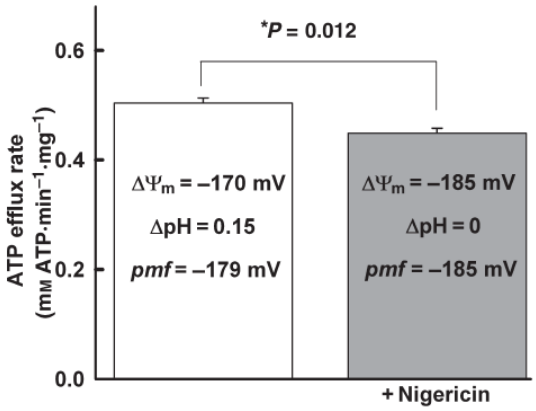

Figure 4.3. ***Effect of nigericin on ATP-ADP steady-state exchange rate mediated by the ANT.*** *Bar graph of ATP-ADP steady-state exchange rate mediated by the ANT in the absence (white bar) and presence (grey bar) of 10 μM nigericin. Pmf shown in the bars was calculated as follows: pmf=ΔΨm-60ΔpH (at 37 °C). Data are shown as S.E.M. from 4 independent experiments.*

As seen in Fig. 4.3, nigericin (10 μM) decreased the ATP-ADP steady-state exchange rate mediated by the ANT significantly, even though it hyperpolarized mitochondria by 15 mV. This is also predicted by the model. We have explained this finding in terms of a decrease in *Pi* flux through the inner mitochondrial membrane, due to collapse of *ΔpH* by nigericin. This means that a decrease in [*Pi*], in turn reducing ATP synthase activity, contributes more to steady state phosphorylation rate than the increase of electric potential and corresponding increase in ATP-ADP steady-state exchange rate mediated by the ANT. As also seen in Fig. 4.3, the calculated values of *pmf* in the presence of nigericin are higher than those in the absence of the ionophore. The calibration of the safranine O fluorescence signal may be unreliable in the very high polarized range, >-170 mV (Akerman and Wikstrom, 1976); attempts to produce higher membrane potentials (such as by addition of nigericin to fully charged mitochondria) result in deviations from a straight line. This is presumably due to the fact that estimated extramitochondrial K^+ is considered as *added* K^+. Thus, $\Delta\Psi$m will be overestimated at the point where the concentration of added K^+ approaches that of K^+ that has leaked out from the mitochondria.

4.4 Predictions of the kinetic model of phosphorylation in mitochondria: matrical ATP and ADP values and the dependence of Pi on ΔpH

On the basis of the model developed above and verified against experimental data measured on isolated mitochondria, we have calculated the dependence of matrical concentrations of ADP and ATP as function of electric potential difference across the inner mitochondrial membrane. As shown in Fig. 4.4A, predictions of our model correspond to experimentally measured (open circles) dependence of O_2 consumption (V_{O2} in the model) on electric potential difference ($\Delta\Psi$m). Moreover, our model predicts that concentrations of ADP and ATP (Fig. 4.4B) at State III ($\Delta\Psi$m is about -145 mV) are equal to 8.7 mM and 3.3 mM, respectively and transition from State III to State IV ($\Delta\Psi$m is about -170 mV) reverses the order of the concentrations to 2.2 mM for ADP and 9.8 mM for ATP. In order to compare these predicted values to experimental data, we measured matrical ATP and ADP concentrations from mitochondrial matrix extracts by HPLC. Representative traces of HPLC raw data (absorbance at 260 nm versus retention time), is shown in Fig. 4.4C. AMP, ADP and ATP have been resolved on the basis of different retention times through the HPLC column, identified and calibrated by “spiking” the samples with known amounts of AMP, ADP and ATP, individually.

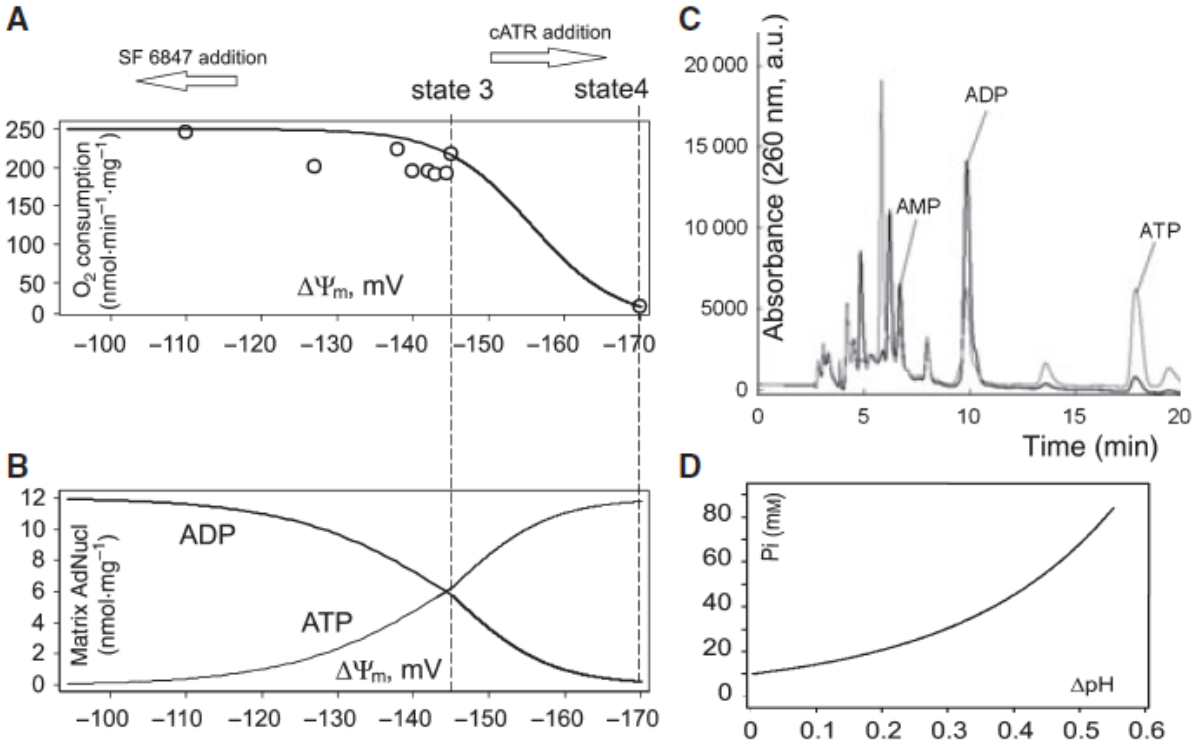

Figure 4.4. ***Steady-state simulations of main characteristics of mitochondria using the model described in the text. Panels A, B:*** *Experimental conditions have been simulated by assigning the following values to model parameters: ATPout=0 mM, Pout=10 mM, pHout=7.25, pHin=7.35, Mgin=0.35 mM, Mgouttotal=1 mM. State III corresponds to addition of ADP to the experimental volume (ADPout= 1 mM). The state IV corresponds to addition of cATR at high concentration (full inhibition of ANT). The uncoupling by SF 6847 (left part of curves) corresponds to increase of parameter k_{leak} in the model. A: The dependence of membrane potential generation rate in terms of O2 consumption rate. B: Model predicted dependence of steady-state concentrations of matrical ADP, ATP on electric potential difference in the -85 – 170 mV $\Delta\Psi$m interval. C: Representative traces of HPLC raw data (from n=4), for the following metabolic conditions: Black line: mitochondria probed without substrates, in the presence of 1 μM SF 6847. Grey line: mitochondria energized with glutamate 5 mM and malate 5 mM. D: Model predicted dependence of matrical phosphate concentration on difference in the pH between matrix and extramitochondrial space at the following values of model parameters: ADPout=1 mM, ATPout=0 mM, Pout=10 mM, pHout=7.25*

Assuming 1 microliter of matrix volume for every mg mitochondrial protein, we estimated the following values: At 0 mV (no substrates, in the presence of 1 μM SF 6847), rat liver mitochondria have, in mM: AMP: 3.64 ± 0.34, ADP: 8.23 ± 0.65, ATP: 0.51 ± 0.05. At -170 mV (mitochondria energized with glutamate 5 mM + malate 5 mM, rat liver mitochondria have, in mM: AMP: 2.57 ± 0.67, ADP: 2.98 ± 0.41 (predicted 2.2 mM), ATP: 7.11 ± 1.55 (predicted 9.8 mM). Concerning measuring matrical ATP and ADP values during state 3, this requires addition of ADP to the mitochondrial suspension, followed by conversion of ATP. That creates a technical challenge, since the matrical volume is 2,000 times smaller than the experimental volume, and therefore matrical adenylates concentrations are many fold lower than that appearing in the extramitochondrial compartment. Such obstacles have been addressed by centrifuging mitochondria while phosphorylating through lipid layers, thus excluding as much as possible the water-soluble extramitochondrially located nucleotides, with or without accounting for nucleotides residing in the intermembrane space that would be carried along the lipid layer (e.g. silicon oil). For isolated rat liver mitochondria and using experimental procedures similar –if not identical- to ours, other investigators report a wide range of matrical ATP/ADP ratios during state 3, ranging from 0.01 to 4.5

(Soboll et al., 1978), (Heldt et al., 1972), (Letko et al., 1980) or in the 8-12 range (Wilson et al., 1982), (Wilson et al., 1983). For mitochondria *in situ* or *in vivo* most investigators agree in the 1-3 ratio range (Schwenke et al., 1981), (Soboll et al., 1984), (Soboll et al., 1980). Those studies that do not pass isolated mitochondria through silicone oil or do not make corrections for intermembrane space adenine nucleotide retentions, report matrix ATP/ADP ratios towards the higher values (Shrago et al., 1977). Also, it is possible that results obtained after separation of intra-and extramitochondrial compartments are not relevant because of the time used for the separation process and possible interconversion of adenine nucleotides even in the presence of inhibitors (Pfaff and Klingenberg, 1968). Furthermore, a great part of the matrix adenine nucleotides is bound to proteins (Albano et al., 2002), a notion supported by the fact that rat liver mitochondria retain more than 50% of their total adenine nucleotide content after permeabilization by toluene (Matlib et al., 1977). Because of this potential binding of adenine nucleotides to intramitochondrial proteins (Boyer, 2001), (Senior et al., 2000), (Jault and Allison, 1994), (Harris et al., 1973) the relationship between the measured total ATP/ADP ratio to *free* intramitochondrial ATP/ADP ratio is difficult to predict. Previous data by Vignais show that a large fraction (75-80%) of the ATP produced by phosphorylation of added ADP within the inner mitochondrial membrane is released into the matrix space before being transported out from the mitochondria; only a small part (20-25%) is released directly outside the mitochondria without penetrating the matrix space (Vignais et al., 1975). It is therefore inferred that there are separate intramitochondrial pools of adenine nucleotides, one near the ANT-ATPase, and another located in the bulk of the matrix. The notion of matrix microcompartmentation of adenine nucleotides emanated from several laboratories (Vignais et al., 1975), (Murthy and Pande, 1985), (Vignais, 1976), (Hamman and Haynes, 1983), (Out et al., 1976), but is not accepted unequivocally by several investigators in the field (Heldt and Pfaff, 1969), (Hartung et al., 1983). Furthermore, microcompartmentation implies the existence of an ATP "synthasome", (ATPase:Pi transporter:ANT in 1:1:1 ratio) and that is at odds with an estimated ratio of ANT/Pi-transporter of 4. The ability of our model to calculate concentrations of intramitochondrial nucleotides on the basis of $\Delta\Psi$m value, and values of extramitochondrial ADP and ATP makes it possible to use the model as tool kit for study of responses of the intramitochondrial characteristics to external influences (Chinopoulos and Adam-Vizi, 2010a). Furthermore, one more prediction which we have derived on the basis of the model is the dependence of intramitochondrial concentration of Pi on ΔpH. As shown at Fig. 4.4D concentration of matrix Pi can be increased substantially due to increase in ΔpH.

4.5 Predictions of the direct-reverse profile of ADP-ATP exchange by the ANT as a function of $\Delta\Psi$m

Mitochondria with a non-functional respiratory chain become ATP consumers, maintaining an appreciable *pmf* by pumping protons out of the matrix through the F_0-F_1-ATPase, at the expense of ATP hydrolysis. Under these conditions, the ANT reverses, bringing ATP into the matrix in exchange for ADP, driven by a $\Delta\Psi$m less negative than ~-100 mV (Metelkin et al., 2006). The directionality of the ANT is thermodynamically governed by the concentrations of free nucleotides (ATP^{4-} and ADP^{3-}) across the inner mitochondrial membrane according to the equation (11).

The concentrations of free ATP^{4-} and ADP^{3-} can be estimated as follows:

$$L = \left(L_t \Big/ \left(1 + \frac{Mg^{2+}}{K_{M,app}} \right) \right) \Big/ \left(1 + \frac{H^+}{K^H} \right) \quad (2).$$

Here *L* denotes ATP^{4-}, L_t denotes total measured ATP concentration (i.e., ATP^{4-}+ $ATP\text{-}H^{3-}$+$ATP\text{-}Mg^{2-}$+ATP-H-Mg^{-}), and Mg^{2+} is *free* magnesium. K_H is the dissociation constant for the reaction $ATP\text{-}H^{3-} \leftrightarrow ATP^{4-} + H^{+}$, and $K_{M,app}$ is the apparent dissociation constant of MgATP we have measured at pH=7.25 and T=37°C. Similarly, the concentration of free ADP^{3-} can also be obtained using Eq. 1.2, with *L* denoting ADP^{3-}, L_t denoting total ADP concentration (i.e., ADP^{3-}+ $ADP\text{-}H^{2-}$+$ADP\text{-}Mg^{-}$+ADP-H-Mg), and $K_{M,app}$ is the apparent dissociation constant of MgADP we have measured at pH=7.25 and T=37°C. However, the values for K_H and $K_{M,app}$ might be hard to determine for the conditions found inside the matrix. On the basis of the kinetic model, we can estimate the steady state directionality of the ANT on the basis of any given values of ATP_o, ADP_o and $\Delta\Psi m$ (Fig. 4.5A). Relevant to this, it would be useful to construct an experimentally-derived $\Delta\Psi m$ vs ADP-ATP exchange rate profile for the 0-100 mV range, however, it is difficult to establish the relation of $\Delta\Psi m$ to ATP consumption rates, because upon exceeding the reversal potential of the ANT (indicated by a dotted line in Fig. 4.5B), $\Delta\Psi m$ is not clamped at relatively steady states (Fig. 4.5B, grey curves).

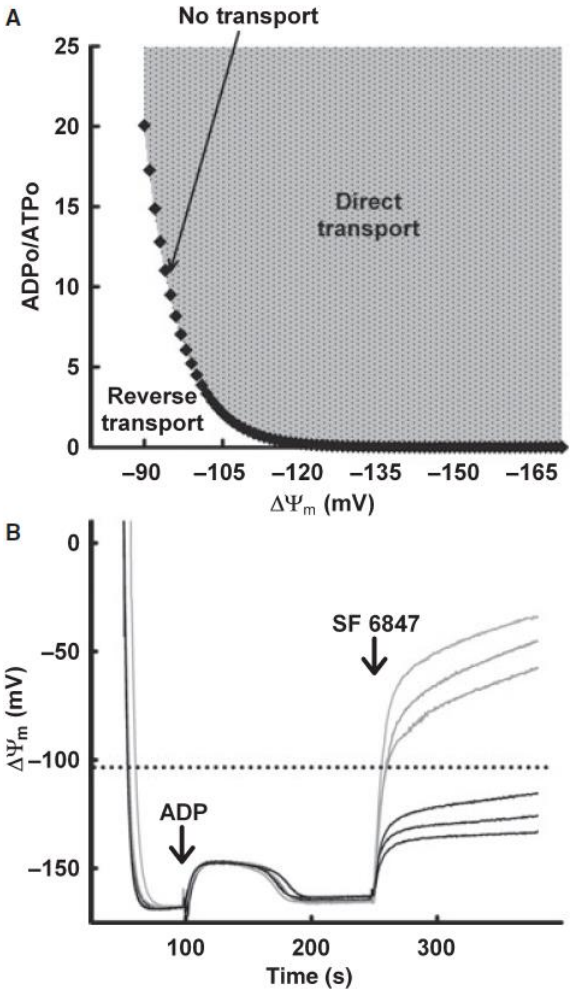

Figure 4.5. ***Forward – reverse profile of ATP-ADP transport and effect of bioenergetic inhibition on ΔΨm. A****: Diagram of directionality of nucleotide transport in mitochondria. Each point of the curve corresponds to the values of ADP_{out}/ATP_{out} and $\Delta\Psi m$ providing "zero" steady state flux of adenine nucleotides. Areas above and below the curve correspond to the values of ADP_{out}/ATP_{out} and $\Delta\Psi m$ assigning direct and reverse transport of ATP-ADP exchange, respectively.* ***B****: Reconstructed time course of $\Delta\Psi m$, calculated from safranine O fluorescence. 1 mg of liver mitochondria was added to a 2-ml medium and energized by glutamate and malate. 1 mM ADP was added where indicated, causing a ~25 mV depolarization. Upon consumption of ADP, $\Delta\Psi m$ returns to approximate baseline level. Increasing concentrations of SF 6847 (10, 20, 30 nM for the lower three black lines from bottom to top, 50, 60, 70 nM for the upper three grey lines, from bottom to top) are subsequently administered where indicated. The dotted line represents the reversal potential of the ANT.*

4.6 Kinetic behavior of the model resulted from consecutive addition of uncoupler and ADP

$\Delta\Psi m$ has been shown to fluctuate as a function of time (Kindmark et al., 2001), (Duchen et al., 1998), (O'Reilly et al., 2003), (Gerencser and Adam-Vizi, 2005); therefore, we sought to formulate our model in order it to be capable of simulating the time dependent response of mitochondria to different $\Delta\Psi m$ values. Titration of $\Delta\Psi m$ to different values was achieved by different doses of uncoupler SF 6847 and ADP. To test applicability of our model for description of time response, we have calculated time dependencies of electric potential difference resulted from consecutive addition of uncoupler and ADP

to mitochondria at State II, and have compared the results of calculation with experimental data presented in (Chinopoulos et al., 2009).

As shown in Fig. 4.6A, the model calculated dependence of ΔΨm on time corresponds to experimental data (open symbols). The period of time from 0 to 70 seconds corresponds to state II of mitochondria (ADP_{out}=0 mM). Different concentrations of uncoupler (30 (a), 40 (b), 50 (c), or 60 (d) nM) have been added where indicated. ADP (2 mM) was added after SF 6847, where indicated. As shown in this figure, the model simulates the steady-state membrane potential sufficiently well, without any fittings of parameters. There is only a slight difference in kinetics upon uncoupler addition at high doses. To predict the response of mitochondria at State II to consecutive addition of uncoupler and ADP we have calculated the time response of ATP efflux (Fig. 4.6B), O_2 consumption rate (Fig. 4.6C) and total matrix ADP concentration (Fig. 4.6D). Time response kinetics of ΔΨm, ATP efflux rate, O_2 consumption rate and ADP in matrix resulted from uncoupler or ADP addition depicted in Fig. 4.6 can be characterized by two features: transition time from one steady-state to another, and levels of the steady-states. Difference between steady state before and after uncoupler/ADP addition maybe characterized by their amplitude. As shown in Fig. 4.6, the transition time from one steady-state to another for all characteristics is less than 10 s. As shown in Fig 4.6A, 4.6C and 4.6D, the amplitude of time response of electric potential difference, O_2 consumption rate and total matrix ADP concentration increases with elevation of uncoupler concentration. On the contrary, the

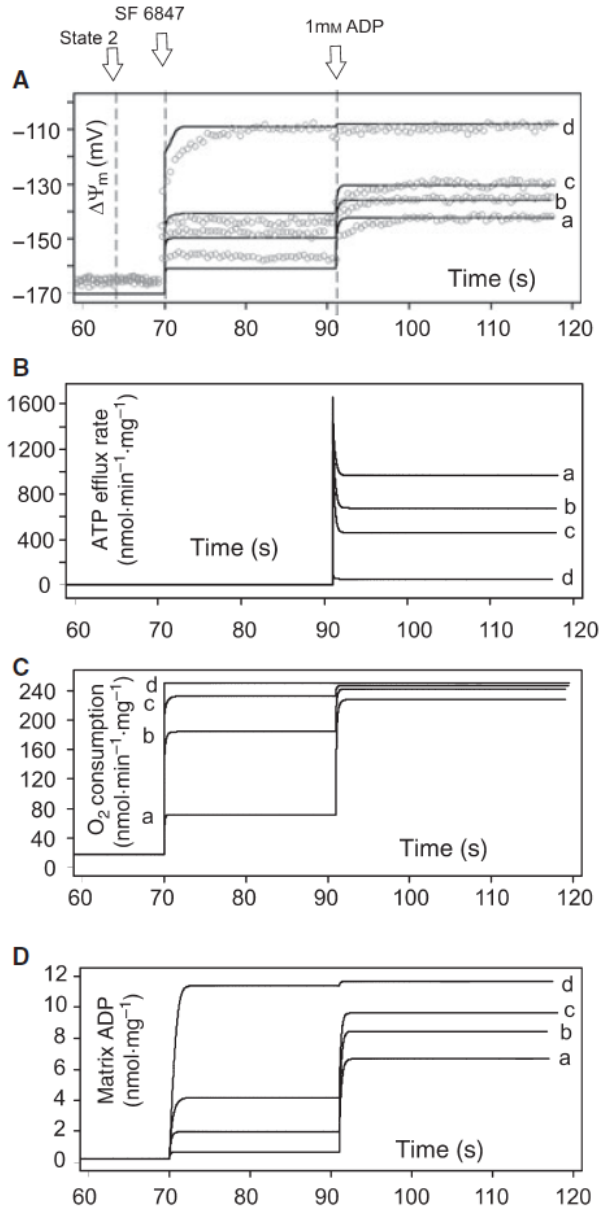

Figure 4.6. ***The kinetics of main characteristics of mitochondria. A:*** *Dependence of electric membrane potential versus time. Solid black lines indicate the kinetics of mitochondrial membrane potential. Open symbols indicate the calibrated ΔΨm data.* ***B:*** *Dependence of ATP efflux rate versus time.* ***C:*** *Time dependence of O_2 consumption rate.* ***D:*** *The kinetics of total matrix ADP concentration. The model parameters have been chosen in such a way as to simulate experimental data presented in Fig. 1 for different doses of uncoupler. Experimental conditions have been simulated by assigning the following values to model parameters: ATP_{out}=0 mM, P_{out}=10 mM, pH_{out}=7.25, pH_{in}=7.35, Mg_{in}=0.35 mM, Mg_{out}^{total}=1 mM. The initial period (0 – 70 seconds) describes steady state corresponding to state II of mitochondria (ADP_{out}=0 mM). After 70 seconds, different doses of uncoupler SP 6847 have been added. At time 90 seconds, the ADP has been added to the experimental volume. Letters* ***a, b, c, d*** *correspond to different uncoupler doses: 30 (a), 40 (b), 50 (c), or 60 (d) nM.*

amplitude of time response of $\Delta\Psi m$ (Fig. 4.6A), V_{O2} (Fig. 4.6C), ATP efflux rate (Fig. 4.6B) and matrix ADP (Fig. 4.6D) after ADP (2mM) addition gradually decreases with increasing of the uncoupler concentration.

5. Modulation of F_o-F_1 ATP synthase activity by cyclophilin D regulates matrix adenine nucleotide levels but not the ANT

In (Chinopoulos et al., 2011) we showed that the modulation of F_0F_1-ATP synthase by cyclophilin D did not change the ANT-mediated adenine nucleotide flux rates; this was attributed to the ~2.2 times lower flux control coefficient of the F_0F_1-ATP synthase than that of ANT, deduced from measurements of adenine nucleotide flux rates in intact mitochondria. These findings were further supported by our kinetic model, suggesting that a ~30% change in F_0F_1-ATP synthase activity in fully energized or fully deenergized mitochondria affects ADP-ATP exchange rate mediated by the ANT in the range of 1.38-1.7%.

5.1 ADP-ATP exchange rates in intact mitochondria and ATP hydrolysis rates in permeabilized mitochondria from cyclophilin D knock-out (CYPD KO) mice

We investigated the ADP-ATP exchange rate mediated by the ANT in intact isolated WT and CYPD KO mouse liver mitochondria, both in the presence and absence of cyclosporin A (an inhibitor of cyclophilin D (Basso et al., 2008)), in the -130 -160 mV ΔΨm range, titrated by the uncoupler SF 6847 using different concentrations, and at 0 mV produced by a maximal dose of the uncoupler. We compared these ADP-ATP exchange rates mediated by the ANT to those obtained by direct ATP hydrolysis rates by the F_0F_1-ATP synthase in mitochondria that have been permeabilized by alamethicin. Mitochondria were energized by succinate (5 mM) and glutamate (1 mM). ADP was added (2 mM), and small amounts of the uncoupler SF 6847 was subsequently added (10-30 nM) in order to reduce ΔΨm to not more than -130 mV, while ΔΨm was recorded as time courses from fluorescence changes due to redistribution of safranine O across the inner mitochondrial membrane. In parallel experiments, ATP efflux rates were calculated from measuring extramitochondrial changes in free [Mg^{2+}], by the method developed by the candidate (Chinopoulos et al., 2009) exploiting the differential affinity of ADP and ATP to Mg^{2+}. ADP-ATP exchange rates as a function of ΔΨm in the -130 -160 mV range, comparing mitochondria isolated from the livers of WT versus CYPD KO mice is shown in figure 5.1, panel A. As shown, there was no difference in ATP efflux-ΔΨm profile of the WT compared to CYPD KO mice. Likewise, when mitochondria were completely depolarized by 1 μM SF 6847 (figure 5.1, panel B), no statistical significant difference was observed between mitochondria isolated from WT and CYPD KO mice during ATP influx, irrespective of the presence of cyclosporin A in the medium.

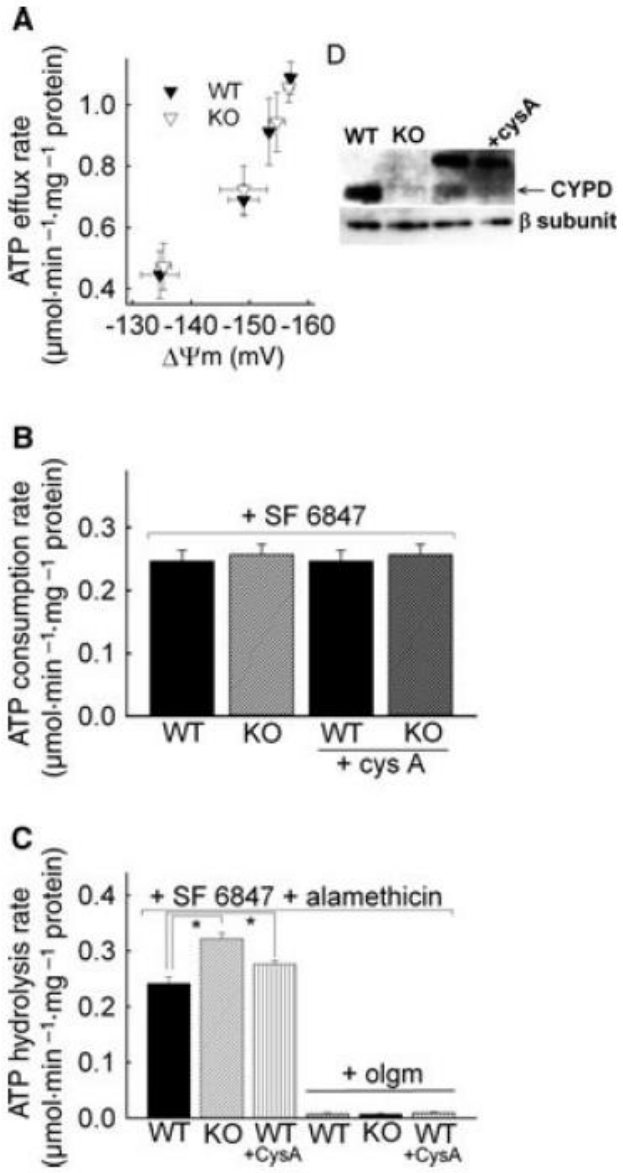

Figure 5.1. ***ADP-ATP exchange rates in intact mitochondria and ATP hydrolysis rates in permeabilized mitochondria; CYPD binds on F_0F_1-ATP synthase, in a cys A-inhibitable manner in intact mouse liver mitochondria. A****: ATP efflux rates as a function of $\Delta\Psi m$ in intact, energized mouse liver mitochondria isolated from WT and CYPD KO mice.* ***B****: Bar graphs of ATP consumption rates in intact, completely deenergized WT and CYPD KO mouse liver mitochondria, and effect of cyclosporin A.* ***C****: Bar graphs of ATP hydrolysis rates in permeabilized WT +/- cys A and CYPD KO mouse liver mitochondria, and effect of oligomycin (olgm). *, significant, (Tukey's test, $p<0.05$).* ***D****: Lanes 1 and 2 represent CYPD-WT and KO mitochondria respectively (0.85 µgr each). Lanes 3 and 4 represent co-precipitated samples of cross-linked intact mitochondria, treated with 1% digitonin, prior to cross-linking. For lane 4, mitochondria were additionally treated with cys A, prior to cross-linking. Upper panel is a western blot for CYPD, lower panel for the β subunit of F_0F_1-ATP synthase.*

However, if mitochondria were subsequently permeabilized by alamethicin (20 µg), mitochondria isolated from CYPD KO mice exhibited a 30.9 ± 1.3% faster ATP hydrolysis rate than WT littermates. The effect of cyclosporin A was only 14.3 %, but nonetheless, statistically significant (p=0.027). This ATP hydrolysis rate was 96.7% sensitive to oligomycin, thus affording the assumption that it was almost entirely due to the F_0F_1-ATP synthase. In order to provide further assurance that in intact mitochondria the binding of CYPD to F_0F_1-ATP synthase occurs and is inhibitable by cyclosporin A (cys A) we incubated mitochondria with the membrane-permeable cross-linker 3-3'-dithiobis[sulfosuccinimidylpropionate] (DSP) in the absence or presence of cys A, extracted proteins with 1% digitonin (Giorgio et al., 2009), immunoprecipitated with anti-Complex V antibodies, and finally tested immunocaptured proteins for the presence of CYPD using the β subunit of the F_0F_1-ATP synthase as loading control. As shown in figure 5.1, panel D, digitonin-treated, cross-linked samples pulled down CYPD (lane 3), and cys A reduced the amount of CYPD bound to F_0F_1-ATP synthase (lane 4). In lane 1, mitochondria from the liver of a CYPD-WT mouse and in lane 2 mitochondria from the liver of a CYPD-KO mouse were loaded (0.85 µgr each), serving as a positive and negative control for the CYPD blot, respectively. It is to be noted that only in the immunoprecipitates a band of higher molecular weight than CYPD was present, most likely due to reaction of the secondary antibody with the light chains of the immunoglobulins used for immunoprecipitation. From the results shown in panel D of figure 5.1, we deduce that the CYPD- F_0F_1-ATP synthase interactions can be observed in intact mitochondria, and that cys A disrupts these interactions.

5.2 Prediction of alterations in ADP-ATP exchange rate mediated by the ANT caused by alterations in matrix ATP and ADP levels, due to changes in F_0F_1-ATP synthase activity by kinetic modeling

Using the model developed by us in (Metelkin et al., 2009), we were able to calculate the changes in T_i and D_i, (free matrix ATP and ADP concentrations, respectively) assuming an increase in F_0F_1-ATP synthase activity by 30%, (due to CYPD ablation), and estimate the impact on ADP-ATP exchange rate mediated by the ANT for pre-defined values of $\Delta\Psi$m. Such values of $\Delta\Psi$m were chosen, as depicted in figure 5.1A, that were obtained by addition of the uncoupler SF 6847 in different concentrations. The increase in ADP-ATP exchange rate mediated by the ANT due to a 30% increase in F_0F_1-ATP synthase activity was in the range of 1.38-7.7%. Percentage change increased for more depolarized $\Delta\Psi$m values. At 0 mV, during which both the ANT and the F_0F_1-ATP synthase operate in reverse mode, the increase in ADP-ATP exchange rate mediated by the ANT drops to 1.7%. It is to be noted, that the greatest increase in ADP-ATP exchange rate mediated by the ANT calculated at -134 mV (7.7%) occurs during the lowest ADP-ATP exchange rate (figure 5.1A). It is therefore, least likely to observe a statistical significance in adenine nucleotide flux rates from mitochondria obtained from WT versus CYPD KO littermates. The above calculations afford the assumption that a 30% increase in F_0F_1-ATP synthase activity will lead to an insignificant increase (1.38-1.7%) in ADP-ATP exchange rate mediated by the ANT, in maximally polarized (forward mode of both ANT and ATPase) and maximally depolarized (reverse mode of both ANT and ATPase) mitochondria.

5.3 Flux control coefficients of ANT and F_0F_1-ATP synthase for adenine nucleotide flux rates

In order to strengthen the predictions of the model with experimental evidence on the pertaining conditions elaborated above, we measured the flux control coefficients of the reactions catalyzed by the ANT and the F_0F_1-ATP synthase separately, on ADP-ATP flux rates from energized intact mitochondria. This coefficient is defined, for infinitesimally small changes, as the percent change in the steady state rate of the pathway divided by the percent change in the enzyme activity causing the flux change. The flux control coefficient for ANT and most other mitochondrial bioenergetic entities have been measured in a variety of conditions, but on respiration rates, not adenine nucleotide flux rates (Wilson et al., 1979), (Moreno-Sanchez et al., 1991), (Wisniewski et al., 1993), (Tager et al., 1983). Although no individual step was found to be 'rate-limiting' (i.e. having a flux control coefficient equal to 1), the regulatory potential of any particular step is quantitated by its control coefficient. During State 3, ANT exhibits a control coefficient of ~0.4 (Kholodenko, 1984). At 10 mM extramitochondrial P_i, the phosphate carrier exhibits a flux control coefficient of <0.1, and this is also reflected by the predictions of the model assuming that the carrier operates in rapid equilibrium. The model predictions shown above would be strengthened if the flux control coefficient of the ANT is sufficiently higher than that of the F_0F_1-ATP synthase, for adenine nucleotide flux rates. The determination of the flux control coefficients (FCCs) was performed by measuring ATP efflux rates, correlating it to the difference of $\Delta\Psi$m before and after addition of ADP (2 mM) to WT and CYPD KO mitochondria, and calculated on the basis of steady-state titration data by catr and olgm. The activities of ANT and F_0F_1-ATP synthase were calculated taking into account the strong irreversible inhibition of ANT and F_0F_1-ATP synthase by their respective inhibitors (Kacser and Burns, 1979), (Heinrich and Rapoport, 1974) :

$$a_{ANT} = \frac{CATRm - CATR}{CATRm},$$

where *CATR* is the concentration of CATR added, *CATRm* is the minimal concentration of CATR that corresponds to maximum ANT inhibition (205 nM of CATR). a_{ANT} is the activity of ANT normalized to initial activity (from 0 to 1). A similar equation was used for F_0F_1-ATP synthase activity performing calculations with 35 nM of olgm for OLGMm.

$$a_{ATPsyn} = \frac{OLGMm - OLGM}{OLGMm}$$

The logarithmic values of ATP flux vs. activities were plotted as shown in panel C of figure 5.2 and analyzed by linear regression. The FCC values were estimated as the coefficients of the linear regression according to the definition:

$FCC_{ANT} = \frac{\partial \ln(V_{ANT})}{\partial \ln(a_{ANT})}$, and likewise for the F_0F_1-ATP synthase.

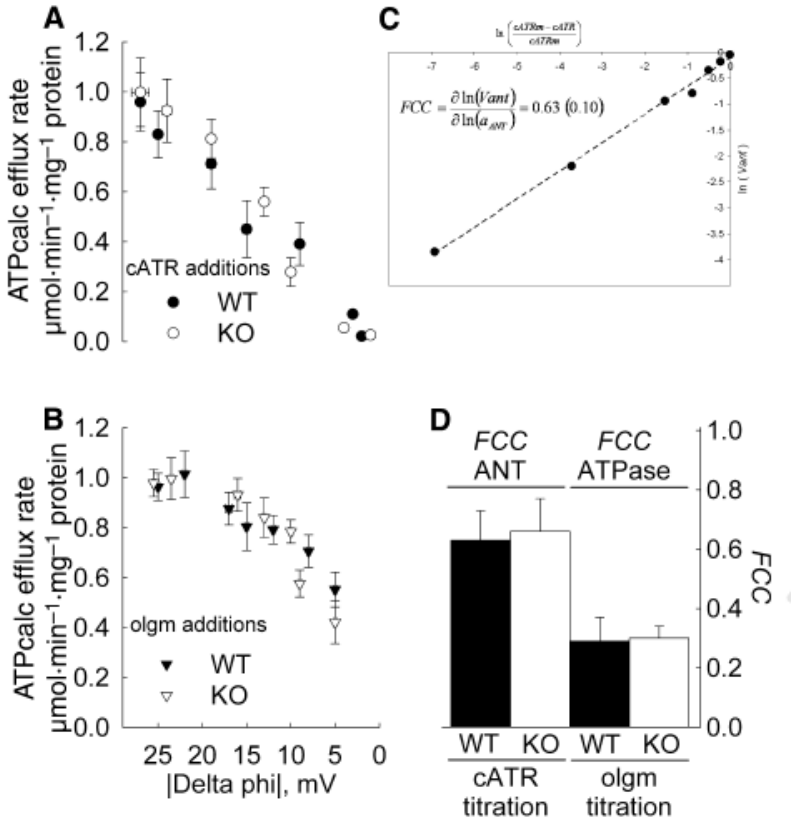

A similar ADP/ATP exchange rate versus ΔΨm profile had been observed in rat liver mitochondria, shown in (Chinopoulos et al., 2010). The calculated FCC values are shown in panel D of figure 5.2. As shown, the FCC of both WT and CYPD KO ANT is ~2.2 times higher than that of the F_0F_1-ATP synthase.

Figure 5.2. ***Determination of flux control coefficients of ANT and F_0F_1-ATP synthase for adenine nucleotide flux rates. A****: ATP-ADP steady-state exchange rate mediated by ANT as a function of Delta phi, for various carboxyatractyloside (catr) concentrations. The points represent the additions of 0, 40, 80, 120, 160, 200, 240 and 280 nM of catr. Data shown as black circles were obtained from WT liver mitochondria. Data shown as open circles were obtained from CYPD KO liver mitochondria.* ***B****: ATP-ADP steady-state exchange rate mediated by ANT as a function of Delta phi, for various oligomycin (olgm) concentrations. The points represent the additions of 0, 5, 10, 15, 20, 25, 30 and 35 nM of olgm. Data shown as black triangles were obtained from WT liver mitochondria. Data shown as open triangles were obtained from CYPD KO liver mitochondria. Panels* ***A*** *and* ***B*** *share the same Delta phi axis. Delta phi represents the difference of $\Delta\Psi m$ before and after addition of 2 mM ADP to liver mitochondria (using 1 mM total $MgCl_2$) pretreated with catr or olgm at the above sub-maximal concentrations.* ***C****: The dependence of ATP transport flux on ADP-ATP exchange rate mediated by the ANT (log values). The black circles represent the measured values from WT mitochondria, shown in panel* ***A****. The dashed line represents a linear regression analysis.* ***D****: Values of flux control coefficients of ANT and F_0F_1-ATP synthase for ADP-ATP exchange rates, for WT and CYPD KO mice mitochondria, calculated by linear regression analysis as depicted in panel* ***C,*** *from the data shown in panels* ***A*** *and* ***B****.*

5.4 Effect of altering matrix pH on adenine nucleotide exchange rates

It can be argued, that since the uncoupler acidified the matrix, this may have directly affected CYPD binding to the inner membrane by means of decreasing matrix P*i* concentration –which could in turn affect CYPD binding to F_0F_1-ATP synthase- and decreased binding of the inhibitory protein IF-1 to ATPase. IF1 is a naturally occurring protein that inhibits the consumption of ATP by a reverse-operating F_0F_1-ATP synthase (Pullman and Monroy, 1963), (Campanella et al., 2008), especially during acidic conditions (Rouslin and Broge, 1996), (Rouslin and Broge, 1993). IF1 would inhibit ATP hydrolysis independent of the CYPD- F_0F_1-ATP synthase interaction, and as such mask activation of ATP hydrolysis due to CYPD ablation or displacement by cyclosporin A. ΔpH across the inner mitochondrial membrane is inversely related to the amount of Pi in the medium (Klingenberg and Rottenberg, 1977), (Chance and Mela, 1966), and in the presence of abundant P_i, ΔpH is in the 0.11-0.15 range (Vajda et al., 2009), (Chinopoulos and Adam-Vizi, 2010b).

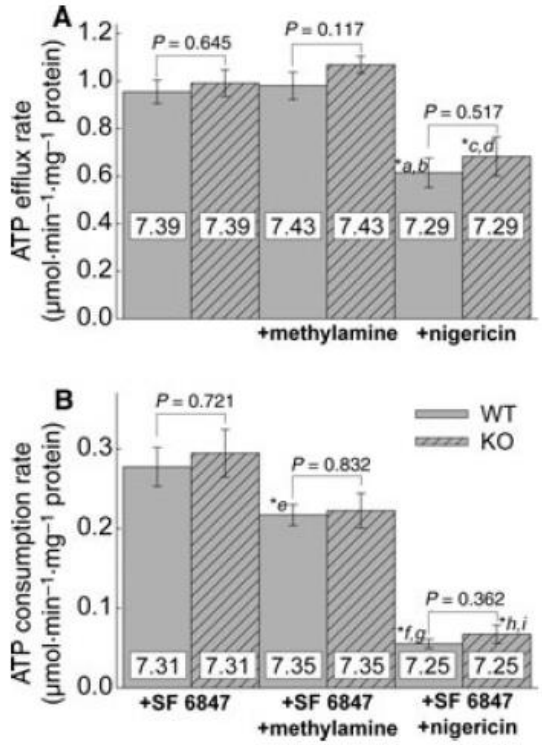

Accordingly, at pH_o=7.25, pH_{in} in our hands was 7.39 +/- 0.01, far from the 6.8 pH optimum of IF-1. However, IF-1 also binds to the F_0F_1-ATP synthase at pH higher than 6.8, promoting the dimerization of two synthase units (Dominguez-Ramirez et al., 2006), thus modulating ATP synthesis (Bisetto et al., 2007). Therefore, we manipulated matrix pH during the application of the uncoupler, and recorded ATP influx and efflux rates. The acidification produced by the uncoupler was either minimized by methylamine (60 μM), or exacerbated by nigericin (1 μM), as also described in (Vajda et al., 2009). Matrix pH is shown in the white boxes within the grey bars, for the conditions indicated in the x-axis of the figure 5.3. As seen in figure 5.3B, ATP consumption rates were not statistically significantly different between WT and CYPD KO mitochondria, in which the uncoupler-induced acidification has been altered by either

Figure 5.3. ***ATP efflux (A) and consumption (B) rates in WT and CYPD KO (striped bars) mitochondria as a function of matrix pH.*** *Matrix pH is shown in the white box within each bar for the respective condition indicated in the x-axis. a*, significant from WT control. b* significant from WT + methylamine. c*, significant from KO control. d* significant from KO + methylamine. e*, significant from WT +SF 6847. f*, significant from WT +SF 6847. g*, significant from WT +SF 6847 + methylamine. h*, significant from KO +SF 6847. i*, significant from KO +SF 6847 + methylamine.*

methylamine or nigericin (n=8, for all data bars). No differences were also observed for ATP efflux rates, in fully polarized mitochondria (figure 5.3A). The effect of nigericin decreasing ATP efflux rate in mitochondria even though it yielded a higher membrane potential (at the expense of ΔpH) has been explained in (Metelkin et al., 2009). Methylamine did not affect $\Delta\Psi m$, though in the concomitant presence of SF 6847, it decreased ATP consumption rates as compared to the effect of SF 6847 alone (figure 5.3B). Nigericin also decreased ATP consumption rates (figure 5.3B).

5.5 CYPD decreases reverse H^+ pumping rate through the F_0F_1-ATPase in partially energized intact mitochondria

In order to demonstrate the ability of CYPD to modulate F_0F_1-ATP synthase -mediated ATP hydrolysis rates, we de-energized intact mouse liver mitochondria by substrate deprivation in the presence of rotenone, followed by addition of 2 mM ATP, while recording $\Delta\Psi m$ and compared the WT ± cyclosporin A versus CYPD KO mice. Under these conditions, due to the sufficiently low $\Delta\Psi m$ values prior to ATP addition, ANT and F_0F_1-ATP synthase operate in the reverse mode. Provision of exogenous ATP leads to ATP influx to mitochondria, followed by its hydrolysis by the reversed F_0F_1-ATP synthase that in turn pumps protons to the extramitochondrial compartment, establishing $\Delta\Psi m$ to an appreciable extent. In this setting, the ability of the F_0F_1-ATP synthase to pump protons out of the matrix represents the only component opposing the action of an uncoupler. Mindful that CYPD binds to F_0F_1-ATP synthase only in the presence of phosphate (Giorgio et al., 2009), we performed the below experiments in the presence and absence of 10 mM P_i.

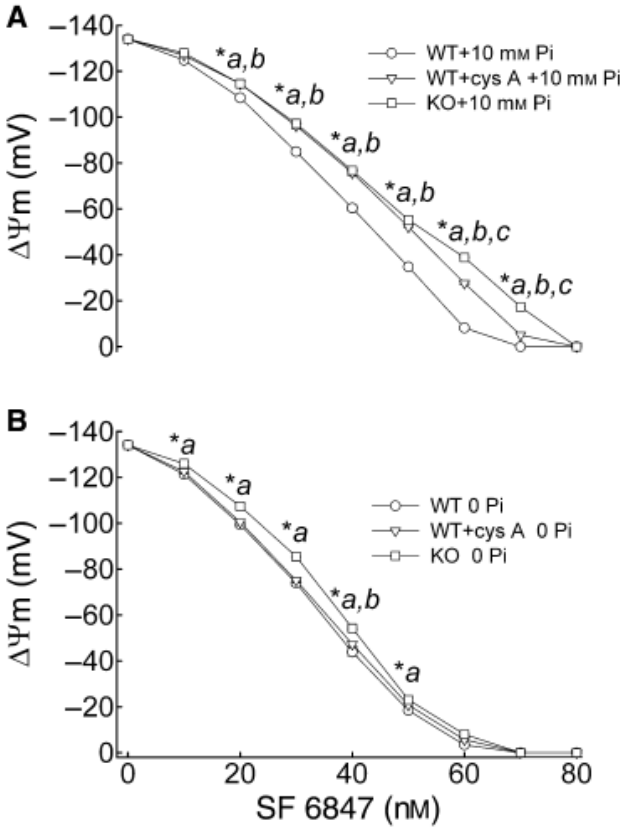

As shown in figure 5.4 panel A, in the presence of 10 mM P_i, mitochondria isolated from the livers of CYPD KO mice resisted more the uncoupler-induced depolarization (open quadrangles), than those obtained from WT littermates (open circles). Cyclosporin A also exhibited a similar effect on WT mitochondria (open triangles) but not on KO mice. These results also attest to the fact that a possible acidification-mediated IF1 binding on F_0F_1-ATP synthase, in turn masking the relief of inhibition by CYPD, could not account for the lack of effect on adenine nucleotide flux rates in intact mitochondria, as shown above. In the absence of exogenously added P_i, this effect was much less pronounced, figure 5.4 panel B; however, during endogenous ATP hydrolysis in intact mitochondria, it is anticipated that there can be a significant production of P_i in the vicinity of the ATPase within the matrix.

Figure 5.4. ***Effect of CYPD on F_0F_1-ATPase-mediated H^+ pumping due to ATP hydrolysis in intact mitochondria. A****: Safranine O fluorescence values converted to mV in intact, de-energized WT and CYPD KO mitochondria by substrate deprivation and rotenone, subsequently energized by exogenous addition of 2 mM ATP (with 1 mM total $MgCl_2$ in the buffer), as a function of uncoupler dose (0-80 nM), in the presence of 10 mM P_i in the medium.* ***B****: same as in* ***A****, but in the absence of P_i from the medium. *a, statistically significant, KO significantly different from WT; *b, statistically significant, WT +cys A significantly different from WT; *c, statistically significant, KO significantly different from WT+cys A (Tukey's test, p<0.05).*

5.6 CYPD ablation or its inhibition by Cyclosporin A increases the rate of respiration stimulated by arsenate in intact mitochondria

Regarding the CYPD–F_0F_1-ATP synthase interaction and how it affects the efficiency of oxidative phosphorylation, we measured mitochondria respiration. CYPD ablation or inhibiting the CYPD with cyclosporin A had no effect on State 4 and State 3 respiration rates and did not affect ADP:O and respiratory control ratios. Therefore, CYPD interaction with F_0F_1-ATP synthase does not translate to changes in the efficiency of oxidative phosphorylation of exogenously added ADP. However, it still may affect the phosphorylation state of endogenous adenine nucleotides present in the matrix of mitochondria. To test this hypothesis, we investigated the effect of AsO_4 on the rate of respiration of CYPD KO and WT mitochondria. This approach is based on a well-studied "uncoupling" effect of AsO_4 explained by its ability to substitute for P*i* in the F_0F_1-ATP synthase catalyzed reaction of phosphorylation of ADP. However, the AsO_3-ADP bond is easily and non-enzymatically water-hydrolysable, which forces a futile cycle of phosphorylation of matrix ADP by F_0F_1-ATP synthase and stimulates respiration (ter Welle and Slater, 1967), (Crane and Lipmann, 1953), (Wadkins, 1960). In these experiments, mitochondria were resuspended in a buffer supplemented with substrates and 0.2 mM EGTA but without Pi and ADP. AsO_4 was titrated to produce the maximum stimulation of the State 4 respiration, which was observed at 4 mM AsO_4. The maximum rate of oxygen consumption was obtained by supplementing the respiration medium with 400 nmol ADP. We found that CYPD KO mitochondria exhibited ~10% higher rates of AsO_4 stimulated respiration than WT mitochondria, with no changes in the maximum rates of respiration. As anticipated, a similar effect was observed with WT mitochondria treated with cyclosporin A, which stimulated their AsO_4-stimulated respiration to the level of CYPD KO mitochondria. (Table 2).

6. Forward operation of adenine nucleotide translocase during F_0F_1-ATPase reversal: critical role of matrix substrate-level phosphorylation

Having established the methodology for measuring ADP-ATP exchange mediated by the ANT and the model for mitochondrial phosphorylation as a function of membrane potential, we sought to investigate the finding by which addition of an ANT vs F_0F_1-ATPase inhibitor (carboxyatractyloside versus oligomycin) yielded an increase *vs* a decrease in $\Delta\Psi m$ in respiration-inhibited mitochondria. In (Chinopoulos et al., 2010), by using thermodynamic assumptions and computer modeling we showed that mitochondrial membrane potential can be more negative than the reversal potential of the ANT while more positive than that of the F_0F_1-ATPase.

6.1 Thermodynamic assumptions and computer modeling of ANT and F_0F_1-ATPase directionalities, and general considerations

The mitochondrial F_0F_1-ATPase is able to synthesize as well as to hydrolyze ATP (Rouslin et al., 1986), (McMillin and Pauly, 1988), (Petronilli et al., 1988), (Rouslin et al., 1990). Since nucleotide phosphorylation/dephosphorylation takes place on the matrix side of the ATP synthase, obviously, only ADP and ATP present in the matrix participate in the production/consumption process. Extramitochondrial adenine nucleotides can contribute to the matrical adenine nucleotide pool only through the adenine nucleotide translocase (ANT), and, by a minor fraction, through the ATP-Mg/Pi carrier (Aprille, 1993). Both ANT and F_0F_1-ATPase catalyze reversible processes; their directionality is governed by $\Delta\Psi m$, and their respective "reversal potential" (E_{rev}), the latter determined by the

concentrations of the participating reactants. For ANT, this is referred to as E_{rev_ANT}, for the F_0F_1-ATPase as E_{rev_ATPase} and the values (in mV) are given by Eqs.6.1-2:

$$E_{\mathrm{rev\_ANT}} = \frac{2.3RT}{F} \cdot \log\left[\left([\mathrm{ADP}^{3-}]free_{\mathrm{out}} \cdot [\mathrm{ATP}^{4-}]free_{\mathrm{in}}\right) \Big/ \left([\mathrm{ADP}^{3-}]free_{\mathrm{in}} \cdot [\mathrm{ATP}^{4-}]free_{\mathrm{out}}\right)\right] \quad \text{(Eq. 6.1)}$$

$$E_{\mathrm{rev\_ATPase}} = -(316/n) - \left(\frac{2.3RT}{F}/n\right) \cdot \log\left[[\mathrm{ATP}^{4-}]free_{\mathrm{in}} \Big/ \left([\mathrm{ADP}^{3-}]free_{\mathrm{in}} \cdot [\mathrm{P}^{-}]_{\mathrm{in}}\right)\right] - \frac{2.3RT}{F} \cdot (\mathrm{pH_o} - \mathrm{pH_i}) \quad \text{(Eq. 6.2)}$$

$$[\mathrm{P}^{-}]_{\mathrm{in}} = [\mathrm{P}_{\mathrm{total}}]_{\mathrm{in}} \Big/ \left(1 + 10^{\mathrm{pH_i} - \mathrm{pK_{a2}}}\right) \quad \text{(Eq. 6.3)}$$

where “o” or “out” signifies outside the matrix, “i” or “in” inside the matrix, “*n*” is the H^+/ATP coupling ratio, R is the universal gas constant 8.31 $J \cdot mol^{-1} \cdot K^{-1}$, F is the Faraday constant $9.64 \cdot 10^4$ $C \cdot mol^{-1}$, T is temperature (in Kelvin), $[P^-]$ is the free phosphate concentration given by Eq. 6.3, where pK_{a2}=7.2 for phosphoric acid. When $\Delta\Psi m$ is more negative than E_{rev_ATPase} and E_{rev_ANT}, ATP is synthesized in the matrix and ANT operates in the “forward” mode translocating ADP into- and ATP out of the matrix. With $\Delta\Psi m$ less negative than E_{rev_ATPase} and E_{rev_ANT}, ATP is hydrolyzed and ANT operates in the “reverse” mode, transporting ATP into- and ADP out of the matrix. It is apparent from Eq.6.1 and 6.2 that alterations in $[ATP^{4-}]_{in}$ and $[ADP^{3-}]_{in}$ alter E_{rev_ATPase} and E_{rev_ANT}. In fact, these would change inversely; a decrease in $[ATP^{4-}]_{in}/[ADP^{3-}]_{in}$ ratio would shift E_{rev_ATPase} towards more positive and E_{rev_ANT} towards more negative values, and *vice versa*. $[ATP^{4-}]_{in}/[ADP^{3-}]_{in}$ ratio is a variable element being dependent on the current metabolic demand under physiological conditions. In addition, other parameters may also exhibit wide fluctuations; phosphate (Wu et al., 2008), the coupling ratio “n” (Tomashek and Brusilow, 2000), (Cross and Muller, 2004) and ΔΨm “flickering”, the latter could be greater than 100 mV (Duchen et al., 1998), (O'Reilly et al., 2003), (Gerencser and Adam-Vizi, 2005). Decrease in ΔΨm due to electron transport chain (ETC) inhibition or to an increase in the inner membrane permeability stops ATP synthesis and allows the ATP synthase to reverse, (reviewed in (Chinopoulos and Adam-Vizi, 2010a)), leading to bioenergetic failure in cells. Depletion of ATP produced in glycolysis due to an i.e. overly-stimulated plasmalemmal Na^+/K^+ ATPase is a crucial element in the development of energy crisis, which should involve the reverse operation of ANT. However, it is a realistic assumption that ΔΨm could be in a range where ANT and F_0F_1-ATPase function in opposite direction, in particular under pathological conditions involving a decrease in the $[ATP^{4-}]_{in}/[ADP^{3-}]_{in}$ ratio. Therefore, the question arises whether mitochondria are able to hydrolyze matrical ATP without the assistance of ANT. In this respect alternative ATP sources potentially available in mitochondria are to be considered. In the mitochondrial matrix, two reactions are capable of substrate-level phosphorylation; the mitochondrial phosphoenolpyruvate carboxykinase (PEPCK), and the succinate-CoA ligase (SUCL or succinate thiokinase or succinyl-CoA synthetase). Mitochondrial PEPCK is thought to participate in the transfer of the phosphorylation potential from the matrix to cytosol and *vice versa* (Lambeth et al., 2004), (Ottaway et al., 1981), (Lambeth, 2002), (Wilson et al., 1983). SUCL catalyses the reversible conversion of succinyl-CoA and ADP or GDP to CoASH, succinate and ATP or GTP (Johnson et al., 1998). The enzyme is a heterodimer, being composed of an invariant α subunit encoded by *SUCLG1*, and a substrate-specific β subunit, encoded by either *SUCLA2*

or *SUCLG2*. This dimer combination results in either an ADP-forming SUCL (A-SUCL, EC 6.2.1.5) or a GDP-forming SUCL (G-SUCL, EC 6.2.1.4).

6.2 Computational estimations of E_{rev_ATPase} and E_{rev_ANT}

From Eqs. 6.1 and 6.2, the concentration of free ATP^{4-} ([*L*]) can be obtained by Eq. 6.4:

$$[L] = \left([L]_t \Big/ \left(1 + \frac{[Mg^{2+}]_{free}}{K_{M,app}} \right) \right) \Big/ \left(1 + \frac{10^{(-pH)}}{K_H} \right)$$, (Eq. 6.4)

where $[L]_t$ is the total ATP concentration i.e., $[ATP^{4-}]+[ATP\text{-}H^{3-}]+[ATP\text{-}Mg^{2-}]+[ATP\text{-}H\text{-}Mg^{-}]$, K_H is the dissociation constant for the reaction $ATP\text{-}H^{3-} \leftrightarrow ATP^{4-} + H^+$ and $K_{M,app}$ is the apparent dissociation constant of MgATP measured at pH=7.25 and T=37°C (Chinopoulos et al., 2009). Similarly, the concentration of free ADP^{3-} can also be obtained using Eq. 6.4 ([*L*], free $[ADP^{3-}]$; $[L]_t$, total ADP concentration i.e., $[ADP^{3-}]+[ADP\text{-}H^{2-}]+[ADP\text{-}Mg^{-}]+[ADP\text{-}H\text{-}Mg]$; $K_{M,app}$, apparent dissociation constant of MgADP measured at pH=7.25 and T=37°C (Chinopoulos et al., 2009)). The values for K_H and $K_{M,app}$ might be difficult to determine for the conditions found inside the matrix, and we assume that they are not different from those found outside the matrix. Because the matrix $[Mg^{2+}]$ and pH_i are only slightly different from the extramitochondrial $[Mg^{2+}]$ and pH_o (Chinopoulos et al., 2009), it is assumed that both ANT and the F_0F_1-ATPase handle the measured free [ATP] and [ADP].

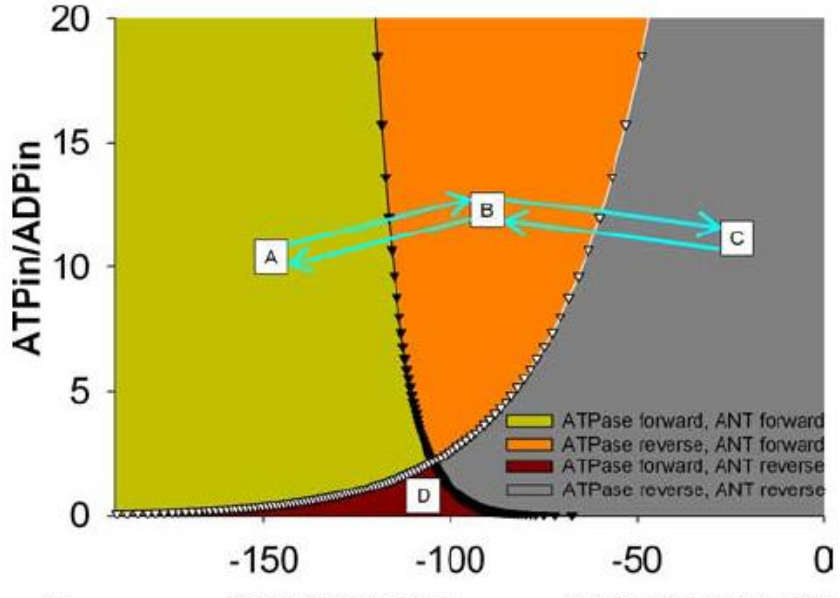

In Fig.6.1 we computed E_{rev_ANT} (white triangles) and E_{rev_ATPase} (black triangles) for a range of free $[ATP]_{in}$ and $[ADP]_{in}$ as an input to Eq. 6.1 and 6.2. It follows from Fig. 6.1 that during progressive depolarization of mitochondria, ΔΨm could be in a range ("B" in Fig. 6.1) where the F_0F_1-ATPase is reversed, but ANT still functions in the forward

Figure 6.1. ***Computational estimation of E_{rev_ANT} and E_{rev_ATPase} at different free $[ATP]_{in}/[ADP]_{in}$ ratios.*** *Black triangles represent the E_{rev_ATPase}; white triangles of E_{rev_ANT}. These values were computed for $[ATP]_{out}$= 1.2 mM, $[ADP]_{out}$= 10 μM, P_{in}= 0.02 M, n=3.9, pHi= 7.38, pHo= 7.25.*

mode. For the estimations other parameters were assumed to be static, specifically those of $[ATP]_{out}$, $[ADP]_{out}$, $[Pin]_{in}$, n, pH_i and pH_o. Some of these values have been chosen on the basis of reports on cytosolic estimations or computational predictions (Mannella et al., 2001).

6.3 Directionality of the function of F_0F_1-ATPase and ANT in isolated mitochondria during respiratory chain inhibition

To demonstrate that F_0F_1-ATPase could indeed hydrolyze ATP without the assistance of the reverse operation of ANT in mitochondria, a prediction emerging from the model shown in Fig. 6.1, experiments

were performed on isolated liver mitochondria compromised by targeted ETC inhibition. We measured $\Delta\Psi$m and addressed the effect of carboxyatractyloside (cATR) or oligomycin (olgm), specific ANT and F_0F_1-ATPase inhibitors, respectively (Fig. 6.2).

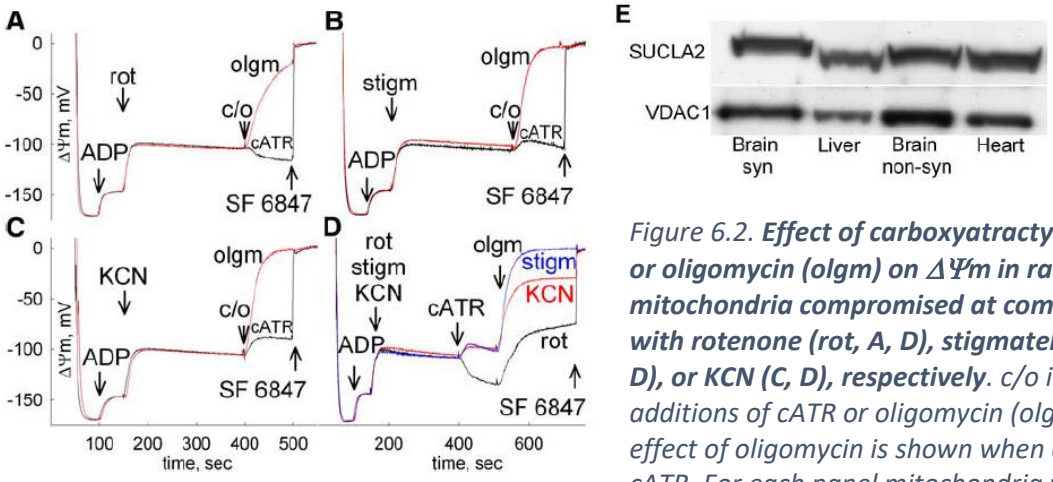

Figure 6.2. ***Effect of carboxyatractyloside (cATR) or oligomycin (olgm) on $\Delta\Psi$m in rat liver mitochondria compromised at complex I, III or IV with rotenone (rot, A, D), stigmatellin (stigm, B, D), or KCN (C, D), respectively****. c/o indicates additions of cATR or oligomycin (olgm). In* ***D****, the effect of oligomycin is shown when added after cATR. For each panel mitochondria were allowed to be fully charged by glutamate plus malate and state 3 respiration was induced by 1 mM ADP prior to addition of the respiratory chain inhibitors. At the end of experiments, 200 nM SF 6847 was added to achieve complete depolarization.* ***E****: Western blot of rat brain synaptic, liver, brain non-synaptic and heart mitochondria for SUCLA2 and VDAC1.*

State 3 respiration in glutamate plus malate-supported mitochondria was initiated by ADP (1 mM) depolarizing mitochondria by ~25 mV, then complex I, III, or IV were inhibited by the specific inhibitors, rotenone (1 μM), stigmatellin (1.25 μM) and KCN (1 mM), respectively, which led to a clamp of $\Delta\Psi$m to ~-100 mV. Subsequent addition of cATR (black traces) caused a moderate repolarization in mitochondria inhibited by rotenone at complex I (Fig. 6.2A and D), and a minor depolarization when complex III or complex IV was inhibited by stigmatellin (Fig. 2B, D) or KCN, respectively (Fig. 6.2C, D). This implied that at ~-100 mV, the ANT was only minimally functional or it did not reverse. This is in accordance with the ADP-ATP steady-state exchange activity/$\Delta\Psi$m relationship shown recently (Metelkin et al., 2009), (Chinopoulos et al., 2009). In contrast, when oligomycin (red traces) was added instead of cATR, an immediate depolarization was observed, implying that ATPase was reversed. Oligomycin also caused an abrupt depolarization when added after cATR (Fig. 6.2D) indicating that F_0F_1-ATPase could function in reverse, even when ANT is blocked. Lack of extramitochondrial ATP consumption under identical conditions is also shown in the figure 6.S.2D). Obviously, under the conditions shown in Fig. 6.2, ATP was available in the matrix from sources other than ANT. To address whether ATP-forming SUCL is present in mitochondria, we performed Western blots of rat liver, brain (synaptic and non-synaptic) and heart mitochondria and observed *SUCLA2* immunoreactivity using VDAC isoform 1 immunoreactivity as a reference in these mitochondria (Fig. 6.2E).

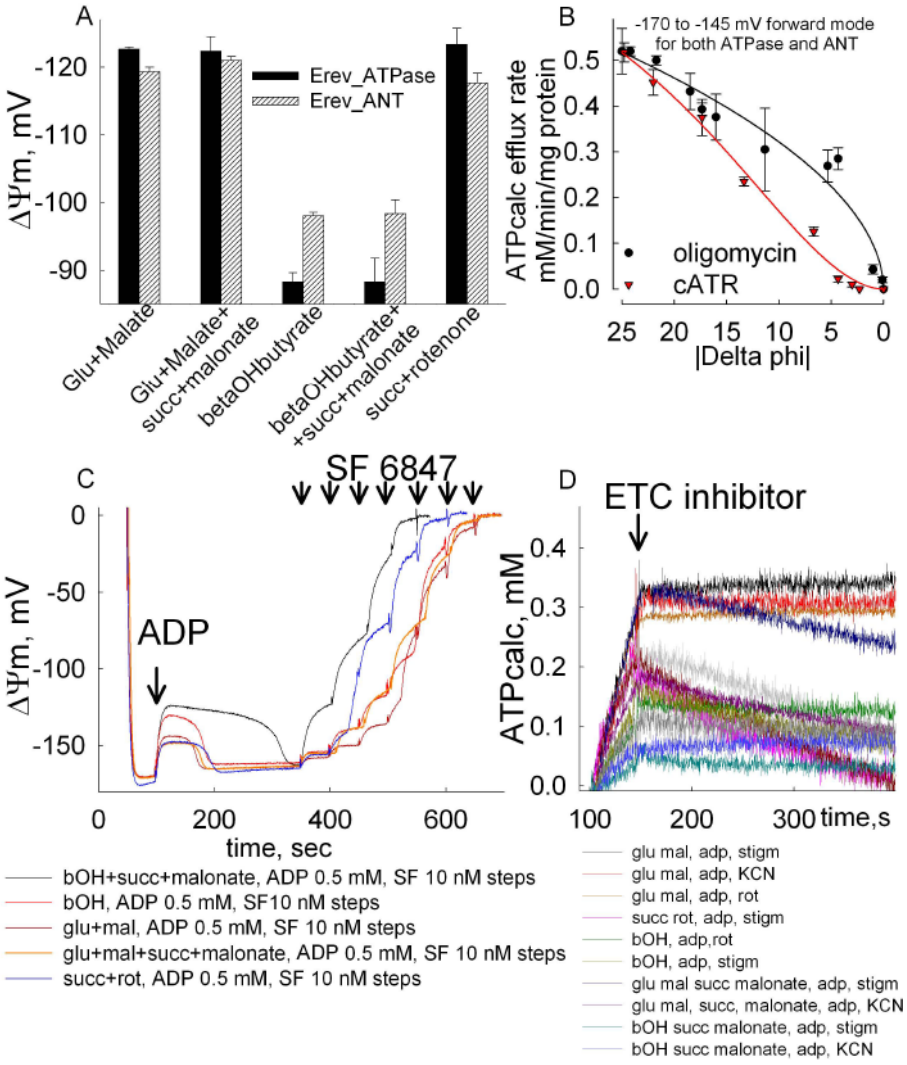

Figure 6.S.2. ***Dependence of Erev_ATPase, Erev_ANT and ADP-ATP exchange rate on substrates combinations****.* ***A****: Bar plot of Erev_ATPase and Erev_ANT for various substrate combinations.* ***B****: ATP-ADP steady-state exchange rate mediated by ANT as a function of Delta phi. Delta phi represents the difference of $\Delta\Psi_m$ before and after addition of 1 mM ADP to liver mitochondria pretreated with cATR or oligomycin at sub-maximal concentrations.* ***C****: Reconstructed time course of $\Delta\Psi_m$, calculated from safranine O fluorescence. 1 mg of liver mitochondria was added to a 2-ml medium and energized by substrates as indicated in the y-axis. 1 mM ADP was added where indicated, causing a ~25 mV depolarization. Upon consumption of ADP, $\Delta\Psi_m$ returns to approximate baseline level. 10 nM steps of SF 6847 are subsequently administered where indicated.* ***D****: Reconstructed time course of calculated ATP appearing in the medium after the addition of 1 mM ADP to rat liver mitochondria respiring on various substrates, and the effect of an ETC inhibitor (rotenone, or stigmatellin, or KCN).*

In the experiments depicted in panels 6.2A-D, respiration of liver mitochondria was maintained by glutamate plus malate, which support operation of SUCL towards the formation of succinate plus ATP. If ATP generated by SUCL is critical for driving the reverse operation of F_0F_1-ATPase, then mitochondria supported by substrates that favor the formation of succinyl-CoA and ADP in the SUCL-mediated reaction are expected to behave differently when challenged with ETC inhibitors. To test this hypothesis, we performed experiments shown in Fig. 6.3. When succinate was given after cATR to mitochondria supported by glutamate and malate in the presence of rotenone (Fig. 3A, trace a), mitochondria were repolarized due to activation of the ETC via complex II. When ETC was inhibited distal from complex II, by KCN (trace b) or stigmatellin (trace c), succinate induced an immediate loss of $\Delta\Psi$m. Under this condition, succinate was shifted towards succinyl-CoA and ADP (plus P_i) formation decreasing matrix ATP levels, and $\Delta\Psi$m could no longer be maintained in the absence of ANT reversal. Essentially similar results were obtained in mitochondria compromised by stigmatellin or KCN when succinate plus malonate were present together with glutamate and malate from the start of the experiments, (Fig. 6.3B, traces b and d).

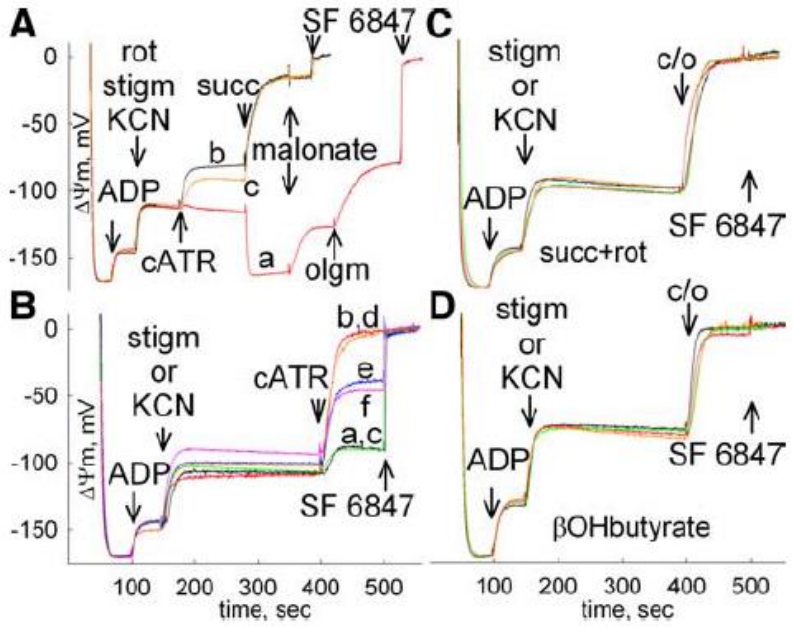

In these conditions, malonate prevents succinate from being shuttled towards fumarate formation by succinate dehydrogenase, leaving no other option for succinate but to follow the succinyl-CoA ligase reaction towards succinyl-CoA and ADP (plus P_i) formation. In mitochondria where SUCL was partially inhibited by propionate (Stumpf et al., 1980) in the presence of stigmatellin or KCN, addition of cATR induced further depolarization (Fig. 6.3B, traces

Figure 6.3. ***The effect of carboxyatractyloside (cATR) or oligomycin (olgm) on ΔΨm of mitochondria compromised at complex I, III, or IV in the presence of different substrate combinations****. **A**: 1 mM ADP was given where indicated to mitochondria polarized by glutamate plus malate, and subsequently, complex I, III, or IV was compromised by rotenone (trace a), stigmatellin (trace c), or KCN (trace b), respectively; cATR was added where indicated. Subsequently, succinate (5 mM) was administered, followed by malonate (10 mM), where indicated. In trace a, olgm was also added after malonate. **B**: Mitochondria were allowed to be fully charged in the presence of the following substrate combinations: glutamate plus malate (traces a, c), glutamate plus malate plus succinate plus malonate (traces b ,d), or glutamate plus malate plus propionate (traces e, f). Stigmatellin was given for traces a, e, and b; KCN was given in lieu of stigmatellin for traces c, f, and d. **C, D**: Mitochondria were polarized by succinate plus rotenone (**C**) or β-OH butyrate (**D**). 1 mM ADP was given where indicated, and subsequently, complex III, or IV was compromised by stigmatellin, or KCN, respectively; cATR or olgm was added where indicated (c/o). At the end of all experiments, 200 nM SF 6847 was added to achieve complete depolarization.*

e, f, as compared to traces a, c, where no propionate was present) indicating that decrease in SUCL function involves ANT reversal. With alternative substrates, such as succinate plus rotenone (Fig. 6.3C), β-OH butyrate (Fig. 6.3D) or β-OH butyrate plus succinate and malonate, which do not support ATP generation in the SUCL-mediated reaction, ΔΨm collapsed by both oligomycin and cATR added after inhibiting ETC by stigmatellin or KCN. E_{rev_ATPase} and E_{rev_ANT} have been estimated for the various substrate combinations used for Fig. 6.2 and 6.3. In line with the above experiments, ATP efflux rates mediated by ANT were much slower with substrates unfavoring substrate-level phosphorylation than with those substrate combinations, which allow substrate-level phosphorylation.

6.4 Addressing the role of IF-1 on the directionality of F_0F_1-ATPase and ANT in isolated rabbit heart and liver mitochondria

There is a naturally occurring protein, termed Inhibitor protein IF-1, that inhibits the consumption of ATP by the F_0F_1-ATPase (Pullman and Monroy, 1963). Such a mechanism would pose the obvious implication that upon extensive mitochondrial depolarization, the ATPase would not reverse. That would lead to lack of elevation of matrical [ADP] and decrease in [ATP], disfavoring ANT reversal. To address the contribution of IF-1 in these conditions, we compared mitochondria from rabbit heart to rabbit liver, to rat heart and rat liver. Rabbit heart exhibits the highest expression of IF-1 with the highest affinity for the ATPase, while rabbit liver exhibits very low expression of IF-1, almost similar to rat liver and heart, that exhibits low affinity for the ATPase (Rouslin and Broge, 1996), (Rouslin et al., 1995), (Rouslin and Broge, 1990), (Rouslin, 1987).

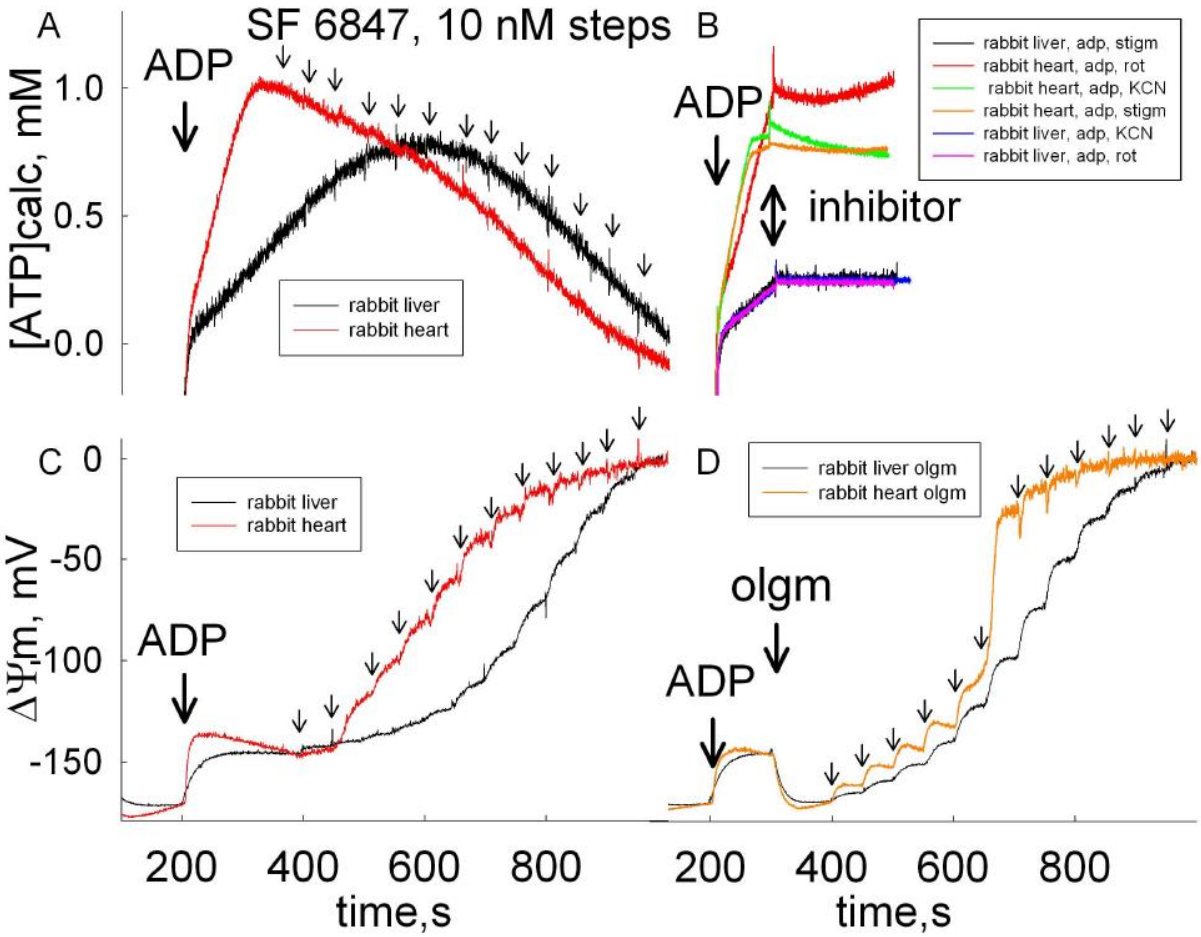

Figure 6.S.4. ***Comparison of the effect of graded depolarization by SF 6847 on the ATP/ADP exchnage in rat liver, rat heart, rabbit liver and rabbit heart mitochondria. A:*** *Reconstructed time course of calculated ATP appearing in the medium after the addition of 1 mM ADP to rabbit liver vs rabbit heart mitochondria respiring on glutamate plus malate, and the effect of stepwise addition of SF 6847.* ***B****: Reconstructed time course of calculated ATP appearing in the medium after the addition of 1 mM ADP to rabbit liver vs rabbit heart mitochondria respiring on glutamate plus malate, and the effect of and ETC inhibitor (rotenone, stigmatellin or KCN, as indicated).* ***C****: Reconstructed time course of $\Delta\Psi m$ calculated from safranine O fluorescence after the addition of 1 mM ADP to rabbit liver vs rabbit heart mitochondria respiring on glutamate plus malate, and the effect of stepwise addition of SF 6847.* ***D****: Reconstructed time course of $\Delta\Psi m$ calculated from safranine O fluorescence after the addition of 1 mM ADP to rabbit liver vs rabbit heart mitochondria respiring on glutamate plus malate, followed by the addition of oligomycin (olgm) and the effect of stepwise addition of SF 6847.*

As shown in figure 6.S.4, mitochondria from rabbit liver and heart were allowed to respire on glutamate plus malate and ADP was given where indicated, while recording ATP efflux-influx rates (A) and $\Delta\Psi$m (C). Subsequently, several 10 nM additions of SF 6847 were added, up to complete collapse of $\Delta\Psi$m.

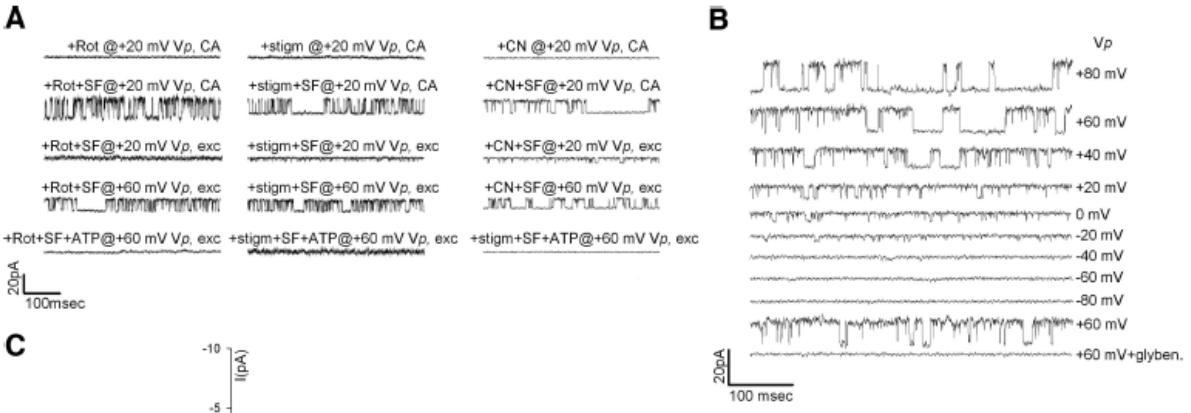

Figure 6.4. ***Single-channel recordings in the cell-attached or excised inside-out patch mode of cultured cortical neurons, challenged by ETC inhibitors****.* ***A****: Single channel recordings in the presence of rotenone (rot), stigmatellin (stigm) or NaCN (CN) +/- SF 6847 (SF) in the presence of 0.25 mM iodoacetamide and 0.1 mM pinnacidil among other plasma membrane channel inhibitors as described under "Materials and Methods". Vp: pipette potential. CA: cell-attached. exc: excised.* ***B****: Single channel recordings in the -80 +80 mV pipette potential range; glyben: glybenclamide.* ***C****: Current-voltage relationship of the unitary conductance of channels appearing after application of stigmatellin and SF 6847 in the cell-attached mode.*

From panel 6.4A, it is apparent that rabbit liver mitochondria exhibited symmetric ATP production and consumption rates, as opposed to mitochondria from rabbit heart that exhibited diminished rates of ATP consumption, compared to ATP production. That implied impaired ATP consumption processes, consistent with an inhibition of the ATPase by IF-1. This notion is further supported by the finding that the difference in $\Delta\Psi$m depolarization by SF 6847 in rabbit heart and liver mitochondria in the absence of oligomycin is greater than in the presence of oligomycin (added after ADP), since in the presence of oligomycin the effect of IF-1 is irrelevant (figure 6.S.4, panels C and D). Nevertheless, inhibition of the respiratory chain by rotenone, stigmatellin or KCN (all given after ADP) did not cause a reversal of ANT in either mitochondria isolated from rabbit liver and heart, respiring on glutamate plus malate (figure 6.S.5). From this finding we inferred that the action of IF-1 would not confound the ANT reversal profile upon inhibition of the respiratory chain. Indeed, as shown in figure 6.S.5, experiments comparing rabbit liver to rabbit heart mitochondria and performed similar to those shown in figure 6.2A, B and C, exhibit the same pattern: addition of catr to mitochondria inhibited at complex I, III, or IV, by rotenone, stigmatellin, or KCN, respectively causes a small decrease in $\Delta\Psi$m or even repolarization, revealing slight or no reversal of the ANT. Addition of olgm in lieu of catr caused an abrupt depolarization, consistent with a reversal of ATPase. However, addition of catr on rabbit liver mitochondria inhibited by KCN showed an almost maximal depolarization (figure 6.S.5F).

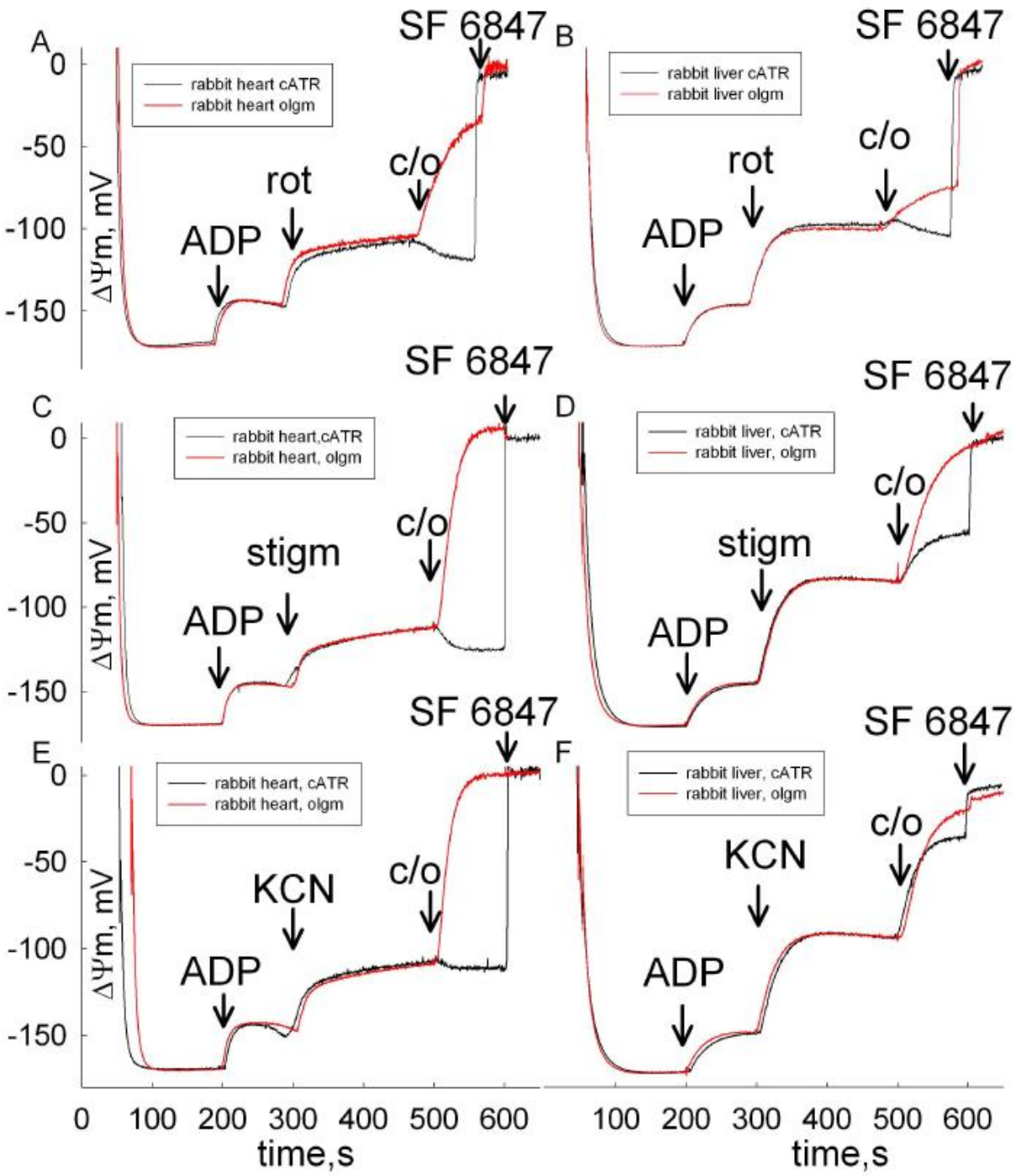

Figure 6.S.5. ***The effect of catr or oligomycin on ΔΨm in rabbit heart or liver mitochondria with a compromised respiratory chain at complex I, III, or IV by rotenone, stigmatellin, or KCN, respectively.*** *All mitochondria were energized by glutamate plus malate and 1 mM ADP was given where indicated.* ***A, C, E****: Rabbit heart mitochondria.* ***B, D, F****: Rabbit liver mitochondria. At the end of all experiments, 200 nM SF 6847 is added to achieve complete depolarization.*

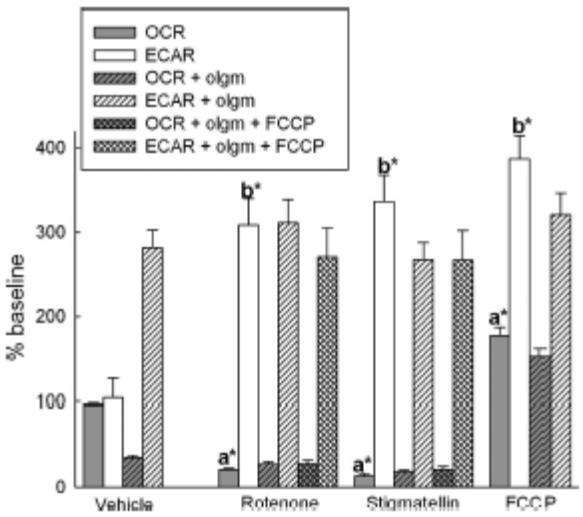

Figure 6.5. ***Effect of rotenone or stigmatellin on oxygen consumption and extracellular acidification rates in rat cortical cultures with or without oligomycin (olgm)****. Oxygen consumption rate (OCR) and extracellular acidification rate (ECAR) were determined in a microplate format respirometry/pH assay. Solid bars indicate mean ± sem of OCR (gray) and ECAR (white), normalized to resting conditions, after mixing vehicle, rotenone (2 μM), stigmatellin (1.2 μM) or FCCP (1 μM) to the assay medium. Hatched bars indicate the above conditions in the presence of oligomycin (2 μg/ml), and cross hatched bars after addition of FCCP (1 μM). Data are from four independent cell culture preparations, n=10-12 wells per condition. *a and *b, p<0.05 significance by ANOVA and Tukey's post-hoc test as compared the vehicle treatment for OCR and ECAR assays, respectively.*

6.5 K(ATP) channel activity in cell-attached mode as an ATP sensor assay during metabolic inhibition in cultured cortical neurons

Next, we wanted to address whether a reversal of F_0F_1-ATPase without a parallel reversal of ANT suggested by our modeling (Fig. 6.1) and found in isolated mitochondria (Fig. 6.2 and 6.3) may operate also in *in situ* mitochondria in a cellular model. For this, we detected changes in the cytosolic ATP level by recording, in cell-attached mode, the activity of K(ATP) channels, which open upon a decrease in the cytosolic ATP level. We chose cortical neurons in culture, because they exhibit K(ATP) channels (Ohno-Shosaku and Yamamoto, 1992), (Tang and Tong, 1995). In this assay, plasmalemmal K(ATP) channels were rendered hypersensitive to changes in the cytosolic ATP level by 0.1 mM pinnacidil, a sensitizing compound (Sasaki et al., 2001). Creatine kinase was inhibited by the membrane-permeable inhibitor, iodoacetamide (0.25 mM), which is important for the K(ATP) channel cytosolic ATP biosensor assay, because the enzyme buffers changes in cytosolic ATP and ADP levels. At 0.25 mM, creatine kinase of isolated brain mitochondria was completely inhibited. As shown in Figure 6.4A, application of either rotenone, stigmatellin or NaCN alone failed to result in K(ATP) channel activity (top traces). The holding potential of the pipette (V*p*) was +20 mV, resulting in plasma membrane potential of a -60-80 mV, in the cell-attached mode. This is because the plasma membrane potential of the cells prior to application of the mitochondrial toxins was in the -40-60 mV range (estimated by current-clamp in the whole-cell mode). The cocktail used in the measurement contained inhibitors of inward-rectifying channels other than K(ATP) channel which are not sensitive to [ATP] alterations (Bajic et al., 2002). The presence of channel inhibitors also served the purpose of minimizing the Na^+ load and the cytosolic ATP consumption by the Na^+/K^+ ATPase. Subsequent application of the uncoupler decreased the plasma membrane potential even further, clamping it in the -10-30 mV range. Therefore, after addition of the uncoupler, the holding potential of the cell would be in the -30-50 mV range. Subsequent excision of the patch would result in holding the ruptured inside-out patch to +20 mV (therefore -20 mV outside), but that yielded very low single channel current amplitudes, buried in the background noise. Elevation of the holding potential to +60 mV reproduced K(ATP) channel activity, which is abundant due to the absence of ATP from the extracellular medium; accordingly, while in the inside-out configuration, application of ATP closed the channels immediately. A gap-free recording at various holding potentials in the cell-attached configuration is shown in Figure 6.4B. In Figure 6.4C, a current/voltage relationship for K(ATP) single channel conductance is shown, exhibiting inward rectification. The inward rectification, single-channel amplitude, burst-like openings, sensitivity to ATP

and glybenclamide, provide enough assurance that the patches contained authentic K(ATP) channels, and therefore the reporting channel activity was indeed a biosensor assay of cytosolic ATP levels. Collectively, the patch clamp experiments in the cell-attached mode showed channel activity only in the presence of an uncoupler. ETC inhibition alone in the *in situ* mitochondria failed to induce plasmalemmal K(ATP) channel activity implying that cytosolic ATP level if altered, was below the detection level of the K(ATP) channels. Since buffering of cytosolic ATP-ADP inter-conversions by creatine kinase were inhibited, there are two alternative but non-mutually excluding explanations for the lack of decline in the ATP level: i) cytosolic ATP was not consumed by mitochondria with impaired ETC, and ii) mitochondria consumed cytosolic ATP but a rebound increase in glycolytic ATP output compensated adequately, therefore cytosolic ATP level remained unchanged. In order to check for a possible rebound increase in glycolytic ATP production, i.e. a Pasteur effect, we investigated the acidification rates of the extracellular space in parallel with O_2 consumption rates in cortical cultures, which together reliably reflect the glycolytic activity.

6.6 Extracellular acidification rates, O_2 consumption and $\Delta\Psi m$ in cultured cortical neurons and astrocytes

Cultured cortical neurons and astrocytes were exposed to rotenone (2 μM), stigmatellin (1.2 μM) or NaCN (5 mM), with or without oligomycin (2 μg/ml) for 3 minutes, then the change in the extracellular acidification rate (ECAR; shown as normalized ΔpH) was measured in comparison to the basal rates (Fig. 6.5). All of these tested inhibitor combinations, except for cyanide, triggered a 150-250% increase in the acidification rates. In the presence of cyanide a gradual, but significant alkalinization of the low buffering capacity medium (optimized for the ECAR assay) was found, which may be the result of the volatility of HCN. ECAR results from glycolytic lactate and mitochondrial carbonic acid production (Choi et al., 2009), which is typical in the case of FCCP. However, in the presence of oligomycin or rotenone/stigmatellin, when the respiration is strongly suppressed (Fig. 6.5), acidification is mainly due to glycolysis. Rotenone or stigmatellin did not trigger stronger acidification than oligomycin, suggesting that either mitochondria do not use cytosolic ATP, or glycolysis runs at maximal capacity under these conditions. FCCP added after rotenone or stigmatellin did not trigger further acidification, supporting the latter scenario, but not negating the former. Oligomycin strongly attenuated basal respiration, suggesting that the basal proton leak is very small (olgm-stigm)/(basal-stigm)= (35-20.5)/(100-20.5) = 18.2%, thus the basal ATP turnover is accountable for 81.8% of the mitochondrial respiration. This small proton leak is expected to be further decreased when $\Delta\Psi m$ is partially depolarized in the presence of rotenone (Porter, 2001). In separate experiments $\Delta\Psi m$ was determined in intact cultured cortical neurons and astrocytes using fluorescence microscopy. TMRM and PMPI fluorescence of whole cell bodies were followed in time and $\Delta\Psi m$ was determined in millivolts by deconvoluting the fluorescence intensity time lapses taking in account the slow, potential-dependent redistribution of the probes. Rotenone (2 μM) or stigmatellin (1.2 μM) depolarized *in situ* mitochondria in cortical neurons to ~-85mV from the assumed resting potential (-150 mV, (Scott and Nicholls, 1980)) and subsequent addition of oligomycin (2 μg/ml) induced further depolarization (Fig.6.6A, B). In contrast, the ANT inhibitor bongkrekic acid (BKA; 50 μM, cATR was not used due to its inability to penetrate the cell membrane) first transiently increased mitochondrial polarization, which was followed by a delayed depolarization to a similar level observed with oligomycin. Importantly, depolarization in the presence of BKA exhibited asynchrony between cells and 24% of BKA-treated cells retained the more polarized $\Delta\Psi m$ for the next 30 min (n=233). In contrast, oligomycin treated cells depolarized synchronously. The BKA-evoked transient repolarization of the $\Delta\Psi m$ in the presence of rotenone or stigmatellin can be explained by the alleviation of ATP turnover on a forward working ANT, or by a decrease in proton leak. Mitochondria of BKA- and oligomycin-treated

neurons had essentially the same ΔΨm (-147.9±2.4 mV, n=6 view fields (196 cells) and -146.3±3.2 mV, n=5 (179 cells), respectively, see supplemental figures 6 and 7 in (Chinopoulos et al., 2010), figures are too large to be included in the present dissertation format).

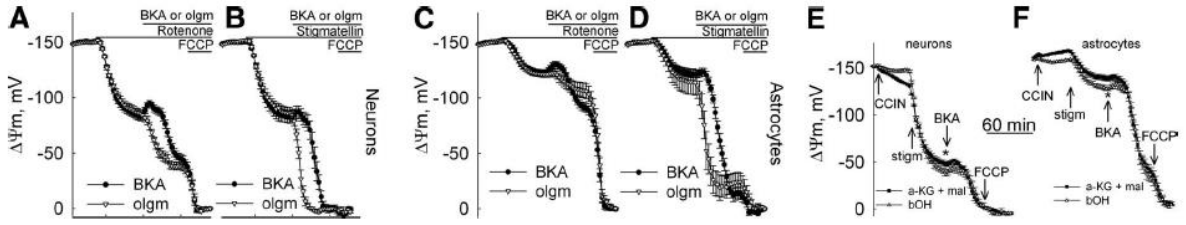

Figure 6.6. ***Effect of bongkrekic acid (BKA), oligomycin (olgm) and a metabolic condition not supporting succinate thiokinase reaction on the rotenone- or stigmatellin-evoked depolarization of ΔΨm in cultured rat cortical neurons (A, B, E), astrocytes (C, D, F)****. ΔΨm was followed in intact cells with fluorescence microscopy using the potentiometric probes PMPI and TMRM. ΔΨm was calculated as millivolts by a compartment model-based, dynamic calibration of single cell fluorescence intensities (see supplementary material). (A-D) BKA (50 μM; black circles), oligomycin (2 μg/ml; open triangles), rotenone (2 μM), stigmatellin (1.2 μM), FCCP (1 μM) were added by mixing into the assay medium containing 15 mM glucose, and were present as indicated by bars. (E,F) CCIN 500 μM was added together with (R)-β-OH-butyrate (5 mM; black squares) or with α-ketoglutarate plus L-malate (both 5 mM; open triangles) in the presence of 5 mM glucose, as marked by "CCIN". The following additions were performed as described above. *, p<0.05 significance by Student t-test. Data were pooled from 3-5 independent cell culture preparations, and data points represent the mean ± SEM of n=6-9 view fields containing 200-300 neurons or 80-150 astrocytes per condition.*

In separate experiments, the effect of oligomycin (2 μg/ml) or BKA (50 μM) on the respiration of cortical neurons were also identical; the basal respiration was decreased to 35.8±3.7% (n=8 wells) and 35.9±3.9% (n=6 wells) of the control, respectively, as measured ~10 minutes after drug addition using the XF24 Extracellular Flux Analyzer. Both in the presence of oligomycin and BKA, mitochondria were in state 4 with identical ΔΨm and respiration rates, therefore the proton leak was identical, and could not be responsible for the repolarization observed with BKA. Moreover, in the presence of ETC inhibition, when ΔΨm is diminished, the extent of contribution of proton leak to ΔΨm is 3-12 times smaller than that obtained in fully charged mitochondria (Porter, 2001). The existence of a subpopulation of cells, which maintained the repolarized ΔΨm in the presence of rotenone or stigmatellin plus BKA for a longer period of time suggests, that these cells are able to maintain ΔΨm without hydrolyzing cytosolic ATP. Assaying astrocytes that were present in the cortical cultures for ΔΨm yielded qualitatively similar results, (Fig. 6.6C and D). Next, mitochondrial pyruvate uptake was inhibited by α-cyano-4-hydroxy-cinnamate (CCIN, 500 μM), and (R)-β-OH-butyrate (5 mM) or α-ketoglutarate (5 mM) plus L-malate (5 mM) were provided as mitochondrial substrates, both in the presence of 5 mM glucose. The first combination does not support ATP generation in the SUCL-mediated reaction (as shown above; Fig. 6.3C), and this resulted in a significantly larger drop of ΔΨm upon stigmatellin addition (Fig. 6.6E,F *), then the latter combination, by 8.6±6.6 mV in neurons and by 10.7±4.4 mV in astrocytes. See raw fluorescence data and additional control experiments in supplemental figures 6 and 7 in (Chinopoulos et al., 2010), figures are too large to be included in the present dissertation format).

6.7 Cytosolic and nuclear ATP pools during ETC inhibition in COS-7 cells

In order to further test the hypothesis that extramitochondrial ATP depletion may not occur during ETC inhibition, we transfected COS-7 cells with plasmids encoding firefly luciferases that target the cytosol or nucleus, and performed a bioluminescence assay of intracellular [ATP] originating from the respective compartments, during metabolic inhibition. COS-7 cells were used due to high transfection efficiencies compared to those obtained from primary cells probed in different experiments. The targeting of the luciferases was specific for the intended compartments (Fig. 6.7A-B, insets). All experiments were performed in the presence of 0.25 mM iodoacetamide to block buffering and spatial transmission of phosphorylation potential (Dzeja et al., 2002). Two metabolic conditions were considered: i) supplying cells with glucose, therefore, both glycolysis and mitochondria contributed to cytosolic and nuclear ATP pools, and ii) replacing glucose with 2-deoxyglucose plus pyruvate, a condition in which only mitochondria maintained ATP production. As

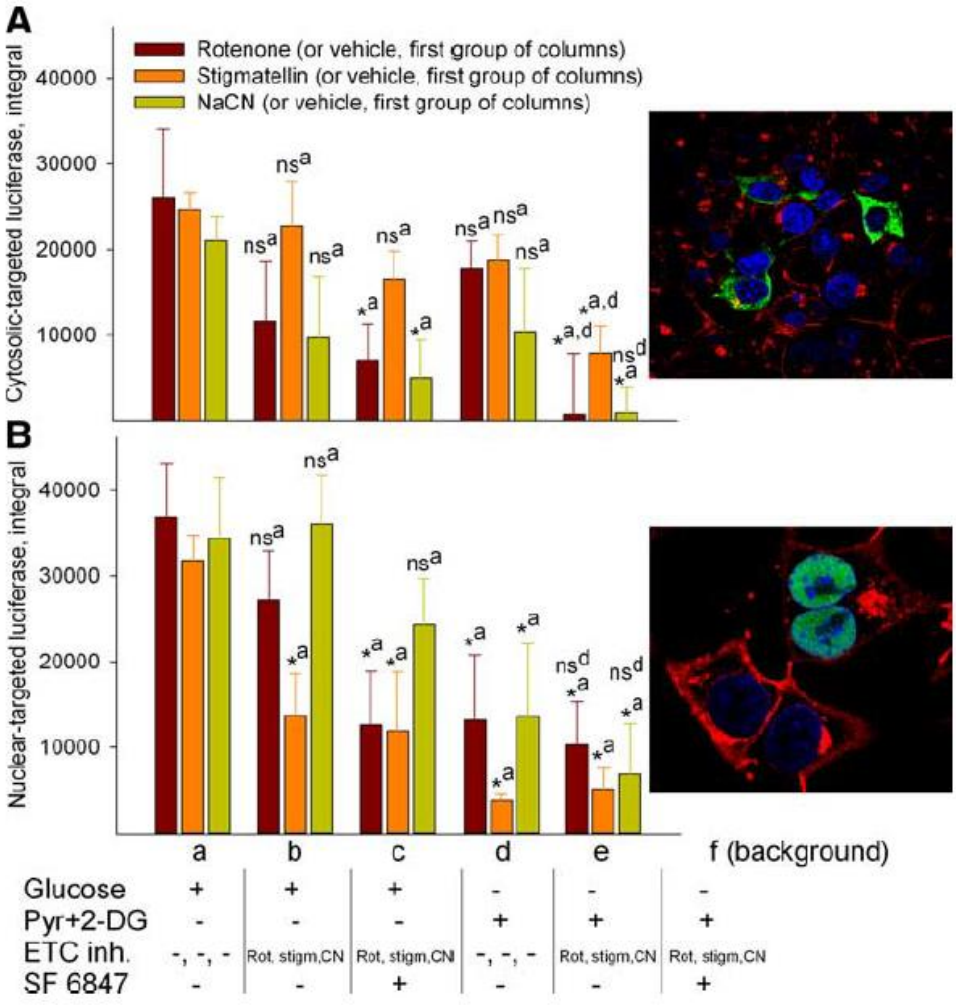

Figure 6.7. ***Bar graph of integrals of luciferin/luciferase assisted ATP luminescence in COS-7 cells during various metabolic conditions, transfected with cytosolic- or nuclear-targeted luciferases****. **A**: Integral of cytosol-targeted firefly luciferase luminescence signal, for various metabolic conditions as shown below the graph. glc: glucose (15 mM); pyr: pyruvate (5 mM); 2-DG: 2-deoxyglucose (2 mM); ETCinh: ETC inhibitor. **B**: Same as in **A**, but for nuclear-targeted luciferase. For background subtraction the following metabolic condition (f) was used in both A and B: no glucose + SF6847 + ETC inhibitor + pyruvate + 2-DG. Data were pooled from 3 independent cell culture preparations; *, p<0.05 significance by ANOVA and Tukey's post-hoc test as compared to the vehicle treatment. Insets: confocal micrographs (0.65 μm z-sections) of luciferase targeted to the cytosol (upper) or to the nucleus (lower), stained by with Alexa 647 agglutinin (prior to permeabilization) that decorates the plasma membrane and the Golgi apparatus (red), DAPI for the nucleus (blue) and antibodies raised against the luciferase (green).*

shown in Fig. 6.7A, in the presence of glucose, the addition of rotenone or NaCN decreased cytosolic ATP level, but this failed to reach statistical significance. Concomitant presence of the uncoupler SF 6847 led to a further drop in $[ATP]_{cyt}$ that reached statistical significance. However, in the absence of glucose, where glycolysis is unable to mount a Pasteur effect, the cytosolic ATP level was dropped by the inhibitors. Concomitant presence of the uncoupler SF 6847 led to a further drop of $[ATP]_{cyt}$, and this condition served as the "background" for baseline subtraction of the luciferase signal. Considering $[ATP]_{nucl}$ (panel 6.7B), the addition of either rotenone or NaCN did not result in a significant drop in $[ATP]_{nucl}$ levels compared to the absence of the ETC inhibitor, but the effect of stigmatellin was significant. The decrease of $[ATP]_{nucl}$ under conditions of glycolysis plus uncoupling or presence of an ETC inhibitor or absence of glycolysis are in accord with the interpretation of results obtained by (Gajewski et al., 2003), showing that $[ATP]_{nucl}$ pool may become depleted faster than the $[ATP]_{cyt}$ pool. This could suggest that in intact cells certain compartments are in preferential contact with mitochondria for the transfer of phosphorylation potential. From the above experiments we concluded that in COS-7 cells inhibition of the respiratory chain may not lead to uniform consumption of cytosolic and/or nuclear ATP.

7. The negative impact of α-ketoglutarate dehydrogenase complex deficiency on matrix substrate-level phosphorylation

In (Kiss et al., 2013) we showed ATP consumption in respiration-impaired isolated and *in situ* neuronal somal mitochondria from transgenic mice with a deficiency of either dihydrolipoyl succinyltransferase (DLST) or dihydrolipoyl dehydrogenase (DLD) that exhibit a 20-48% decrease in KGDHC activity. Import of ATP into the mitochondrial matrix of transgenic mice was attributed to a shift in the reversal potential of the ANT towards more negative values due to diminished mSLP, causing the translocase to reverse prematurely. Immunoreactivity of all three subunits of succinyl-CoA ligase and maximal enzymatic activity were unaffected in transgenic mice as compared to wild-type littermates. Therefore, decreased matrix substrate-level phosphorylation was due to diminished provision of succinyl-CoA. These results were further corroborated by the finding that mitochondria from wild-type mice respiring on substrates supporting substrate-level phosphorylation exhibited ~30% higher ADP-ATP exchange rates compared to those obtained from $DLST^{+/-}$ or $DLD^{+/-}$ littermates.

7.1 KGDHC: general considerations and potential link to brain pathologies; rationale for implicating mSLP

The α-ketoglutarate dehydrogenase complex (KGDHC) is an enzyme consisting of multiple copies of three subunits: α-ketoglutarate dehydrogenase (E1k or KGDH, E.C. 1.2.4.2), dihydrolipoyl succinyltransferase (E2k or DLST, E.C. 2.3.1.61) and dihydrolipoyl dehydrogenase (E3 or DLD, E.C. 1.8.1.4). It participates in the tricarboxylic acid (TCA) cycle where it irreversibly catalyzes the conversion of α-ketoglutarate, CoASH and NAD^+ to succinyl-CoA, NADH and CO_2. A decline in KGDHC activity has been associated with a number of neurodegenerative diseases; however, activity decline is not universal for all TCA cycle enzymes (Bubber et al., 2005), (Gibson et al., 2010), (Bubber et al., 2011). In search of an association between a decrease in KGDHC activity and incidence of neurodegeneration, two transgenic mouse strains have been generated, one lacking the DLST subunit (Yang, L. et al., 2009), and the other lacking the DLD subunit (Johnson et al., 1997). Disruption of both alleles of either gene results in perigastrulation lethality; heterozygote mice exhibit no apparent behavioral phenotypes. A deficiency in the DLD or DLST subunit has been shown to cause increased vulnerability to mitochondrial toxins modeling neurodegenerative diseases (Yang, L. et al., 2009), (Klivenyi et al., 2004), (Browne and Beal,

2002), and to result in reduced numbers of neural progenitor cells in the hippocampi of adult mice (Calingasan et al., 2008). In transgenic mice carrying human mutations prompting them to develop amyloid deposits, DLST deficiency aggravates amyloid plaques burden (Dumont et al., 2009). Additionally, increased levels of the lipid peroxidation marker, malondialdehyde, was found in $DLD^{+/-}$ (Klivenyi et al., 2004) but not $DLST^{+/-}$ mice (Calingasan et al., 2008). KGDHC is known to generate reactive oxygen species (ROS), and $DLD^{+/-}$ mice exhibited diminished rates of ROS production (Starkov et al., 2004), (Tretter and Adam-Vizi, 2004). Although the above considerations establish a link between KGDHC deficiency and brain pathology, they stop short in identifying the molecular mechanism(s) underlying the propensity for neurodegeneration. So far, the focus of this association has been biased towards diminished provision of reducing equivalents and excess production of reactive oxygen species. In (Kiss et al., 2013) we demonstrated that in KGDHC-deficient mice the decreased provision of succinyl-CoA diminishes matrix substrate-level phosphorylation resulting in impaired mitochondrial ATP output and consumption of cytosolic ATP by respiration-impaired mitochondria, in line with our previous predictions (Chinopoulos et al., 2010).

7.2 Effect of cATR on $\Delta\Psi$m during respiratory inhibition if isolated brain mitochondria from WT, $DLD^{+/-}$, $DLST^{+/-}$ and $DLD^{+/-}/DLST^{+/-}$ mice

As shown in figure 7.2, $\Delta\Psi$m was measured by safranine O fluorescence in Percoll-purified brain mitochondria obtained from WT, $DLD^{+/-}$, $DLST^{+/-}$ and $DLD^{+/-}/DLST^{+/-}$ mice. Based on experiments performed first with liver mitochondria where yields were high, (supplementary figures 1-5 in (Kiss et al., 2013), figures are too large to be included in the present dissertation format) specific substrates and their combinations were selected to investigate brain mitochondria where much lower yields are typically obtained. The sequence of additions, identical for all panels, was the following: mitochondria were allowed to polarize, followed by the addition of 2 mM ADP, where indicated. ADP would depolarize mitochondria to a variable level depending on the substrate combinations (Chinopoulos et al., 2009). After 50 sec during which a substantial amount of ADP has been converted to ATP, complex I was inhibited by rotenone (1 μM) which 'clamped' $\Delta\Psi$m in the -83 -99 mV range again depending on substrate combinations. After an additional 150 sec, cATR (2 μM) was added. Towards the end of each experiment the uncoupler SF 6847 (1 μM) was added in order to completely depolarize mitochondria; this would assist in the calibration of the safranine O signal. In all panels of figure 7.2, it is evident that addition of cATR to respiration-impaired mitochondria obtained from WT mice resulted in the gain of $\Delta\Psi$m, indicating that the ANT was operating in forward mode. On the other hand, addition of cATR to respiration-impaired mitochondria obtained from $DLD^{+/-}$, (panel C), and $DLD^{+/-}/DLST^{+/-}$ (panels B and D) mice resulted in the loss of $\Delta\Psi$m, implying that the ANT was operating in reverse mode. Therefore, for the corresponding substrates, respiration-impaired mitochondria of KGDHC-deficient mice imported extramitochondrial ATP. Addition of succinate to any substrate combination in brain mitochondria of WT or KGDHC-deficient mice resulted in cATR-induced depolarization, attributed to the shifting of the succinyl-CoA ligase equilibrium towards ATP consumption, (supplementary figures 1-5 in (Kiss et al., 2013), figures are too large to be included in the present dissertation format). No swelling was observed under any circumstances (supplementary figures 8-9 in (Kiss et al., 2013), figures are too large to be included in the present dissertation format); therefore, the losses of $\Delta\Psi$m were not due to opening of

the permeability transition pore. For other substrate combinations, additions of cATR to KGDHC-deficient mitochondria was either causing less repolarization (panels A, E and I for $DLD^{+/-}$ and panels B and J for $DLST^{+/-}$) than WT littermates, no difference compared to WT (panel F), or no effect (panels G and H, red and green traces, respectively); in the latter case this means that the values of $\Delta\Psi m$ and Erev_ANT were identical. Results obtained using the cATR 'biosensor' test imply that using substrate combinations supporting substrate-level phosphorylation in mitochondria obtained from KGDHC

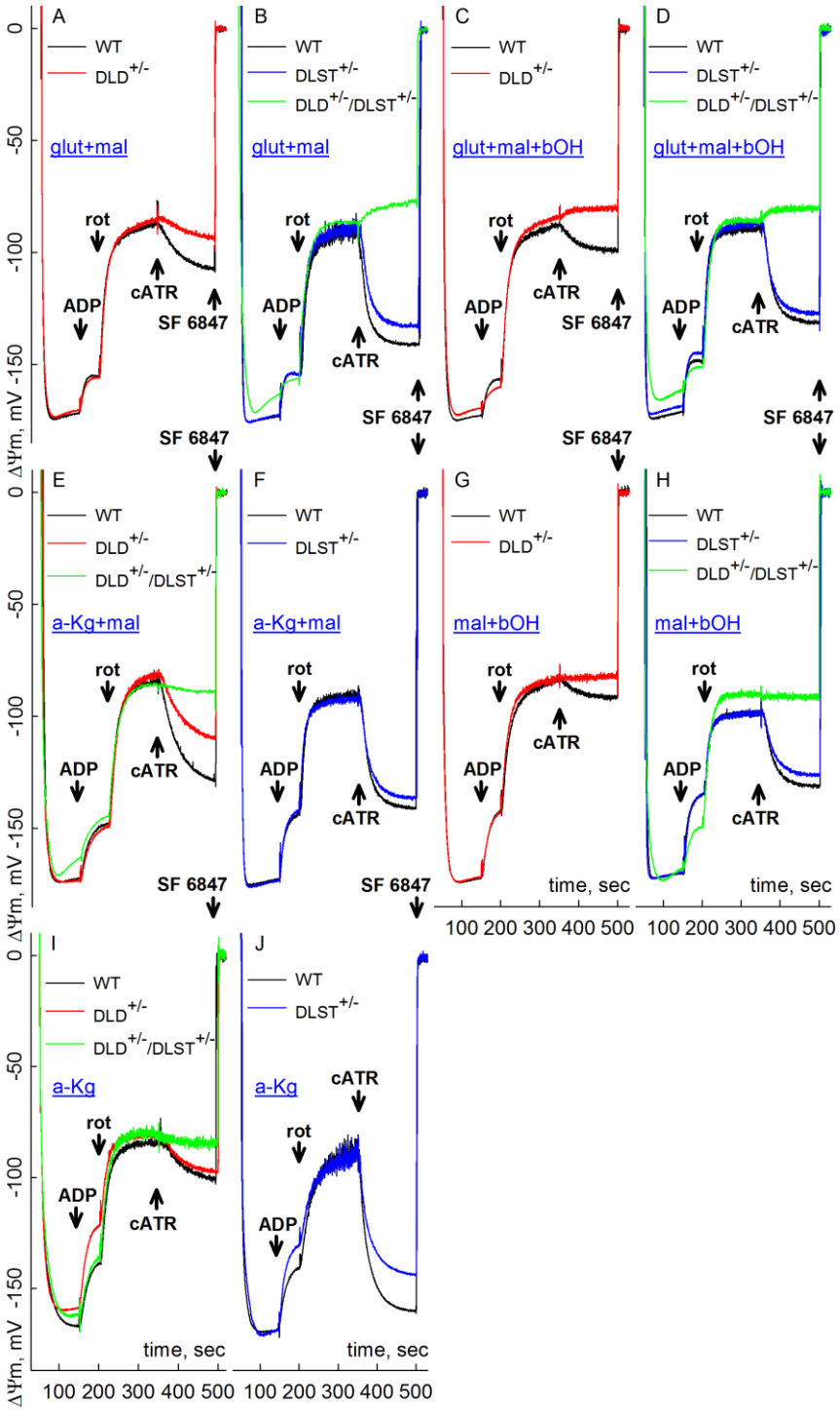

Figure 7.2. Effect of carboxyatractyloside (cATR, 2 μM) on ΔΨm of mouse brain mitochondria of WT, $DLD^{+/-}$, $DLST^{+/-}$ or $DLD^{+/-}/DLST^{+/-}$ double transgenic mice compromised at complex I by rotenone (1 μM), in the presence of different substrate combinations. ADP (2 mM) was added where indicated. Substrate concentrations were: glutamate (glut, 5 mM), malate (mal, 5 mM), β-hydroxybutyrate, (bOH, 2 mM), α-ketoglutarate, (a-Kg, 5 mM). At the end of all experiments 1 μM SF 6847 was added to achieve complete depolarization. The WT mice compared with the $DLD^{+/-}$ littermate mice are of C57BL/6 genetic background. The WT mice compared with the littermate $DLST^{+/-}$ mice are of C57BL/6 and 129SV/EV hybrid genetic background. $DLD^{+/-}$ / $DLST^{+/-}$ double transgenic mice are of either C57BL/6 only or C57BL/6 and 129SV/EV hybrid genetic background. Because of this background heterogeneity, some of the traces from WT mice appear in several panels in order to match as littermates of the KGDHC-deficient mice.

transgenic mice compared to those from WT littermates, either i) Erev_ANT values were more negative, and/or ii) matrix ATP/ADP ratios were lower. Besides the function of the ANT, matrix ATP/ADP ratios are primarily (but not exclusively) affected by the reversible mechanisms producing or consuming ATP. In the mitochondrial matrix the two most significant

contributors are the F_0-F_1 ATP synthase and the ATP-forming succinyl-CoA ligase. The GTP-forming succinyl-CoA ligase still contributes to the matrix ATP pools due to the concerted action of nucleoside diphosphokinase, converting GTP and ADP to GDP and ATP (Kadrmas et al., 1991). The activity of the F_0-F_1 ATP synthase but not of succinyl-CoA ligase strongly depends on $\Delta\Psi$m (Metelkin et al., 2009), (Demin et al., 1998), (Chinopoulos et al., 2011). We therefore investigated ATP efflux and respiration rates from fully energized mitochondria of WT, DLD$^{+/-}$, DLST$^{+/-}$ and DLD$^{+/-}$/DLST$^{+/-}$ mice for various substrates in the absence of confounding factors, such as respiratory inhibition that would lead to membrane depolarization.

7.3 ATP efflux rates in brain mitochondria from WT, DLD$^{+/-}$, DLST$^{+/-}$ and DLD$^{+/-}$/DLST$^{+/-}$ mice

In figure 7.3, ATP efflux rates of isolated brain mitochondria obtained from WT, DLD$^{+/-}$, DLST$^{+/-}$ and DLD$^{+/-}$/DLST$^{+/-}$ transgenic mice is shown. In DLST$^{+/-}$ liver mitochondria all substrates and their combinations yielded lower ATP efflux rates than WT littermates. It is evident that in KGDHC-deficient brain mitochondria those substrates and their combinations supporting substrate-level phosphorylation yielded lower ATP efflux rates than WT littermates (glut+mal, α-Kg, α-Kg+mal). From these results we conclude that mitochondria deficient in DLD and/or DLST subunit of KGDHC may exhibit diminished ATP efflux rates depending on substrates used. For those substrate combinations that do not support substrate-level phosphorylation (mal+bOH) there was no difference in the ATP efflux rates among WT and KGDHC-deficient liver mitochondria. However, the substrate combination glut+mal+bOH also did not show a statistically significant difference in ATP efflux rates among WT and KGDHC-deficient mice, nor for glut+mal for DLST$^{+/-}$ vs WT mice or α-Kg+mal for DLD$^{+/-}$ vs WT mice.

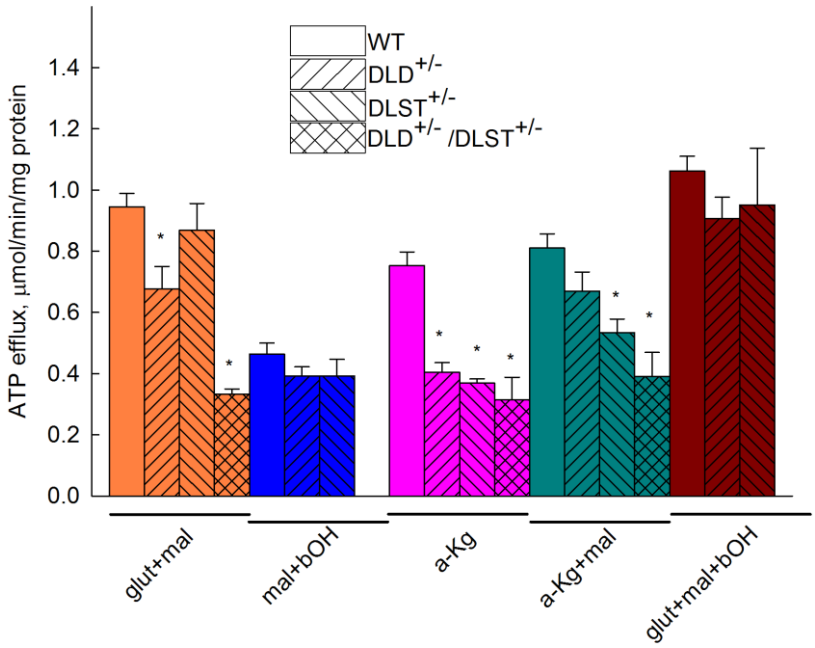

*Figure 7.3. ATP efflux rates of isolated brain mitochondria of WT, DLD$^{+/-}$, DLST$^{+/-}$ and DLD$^{+/-}$/ DLST$^{+/-}$ mice as a function of various substrate combinations. Substrate concentrations were: glutamate (glut, 5 mM), malate (mal, 5 mM), β-hydroxybutyrate, (bOH, 2 mM), α-ketoglutarate, (a-Kg, 5 mM), *, statistically significant, p<0.05 (one-way ANOVA followed by Dunnett's test post-hoc analysis if comparing three or more groups; control: results obtained from WT mice). p values for the various substrate combination groups are as follows: glut+mal: <0.001; a-Kg: <0.001; a-Kg+mal: <0.001.*

7.4 Respiration rates in isolated brain mitochondria from WT, DLD$^{+/-}$, DLST$^{+/-}$ and DLD$^{+/-}$/DLST$^{+/-}$ mice

In order to investigate the possibility of cATR-induced alterations in $\Delta\Psi$m being due to membrane leaks, we measured mitochondrial respiration. Respiration rates were measured during state 2, state 3

induced by a small bolus of ADP (0.1 mM), state 4 (upon phosphorylation of the entire amount of ADP), state 3 re-induced by a large bolus of ADP (2 mM), state 4 induced by cATR, and uncoupled respiration induced by SF 6847 (50 nM for brain and 170 nm for liver mitochondria). Experiments were performed for isolated brain and liver (supplementary figure 7 in (Kiss et al., 2013), figure is too large to be included in the present dissertation format) mitochondria from WT, $DLD^{+/-}$, $DLST^{+/-}$ and $DLD^{+/-}/DLST^{+/-}$ transgenic mice for all substrate combinations. Each substrate combination was repeated 4-6 times on independent occasions. Quantitative data in bar graph format is shown in figure 7.4. It is evident that in KGDHC-deficient brain mitochondria several substrates and their combinations supporting substrate-level phosphorylation yielded lower respiration rates than WT littermates (glut+mal, glut+mal+AcAc, α-Kg, α-Kg+mal, glut+mal+bOH, glut). From these results we concluded that mitochondria deficient in DLD and/or DLST subunit of KGDHC exhibited diminished respiration rates. For those substrates and their combinations that support only weakly substrate-level phosphorylation (mal, mal+bOH, mal+AcAc, pyr, pyr+asp) there was no difference in the respiration rates among WT and KGDHC-deficient brain mitochondria. These data are in congruence with the ATP efflux data shown in figure 7.3. Furthermore, state 2 respiration and state 4 respiration (whether induced after phosphorylation of the entire bolus of ADP given or induced by cATR) was not statistically significantly different for any substrate combination among WT and KGDHC-deficient mice, arguing against a possible contribution from leaks to the changes in membrane potential shown in figure 7.2.

7.5 Effect of BKA during respiratory inhibition of in situ synaptic and neuronal somal mitochondria from WT and transgenic mice

In the above experiments using isolated mitochondria, the choice of substrate was a controlled variable; we therefore addressed if the differences in ANT directionalities can be demonstrated among WT and transgenic mice in *in* situ mitochondria, where substrate is an uncontrolled variable. For this purpose, isolated nerve terminals (synaptosomes) and cultured cortical neurons were prepared from the brains of WT, $DLD^{+/-}$, $DLST^{+/-}$ and $DLD^{+/-}/DLST^{+/-}$ mice. Also, BKA was used to inhibit the ANT instead of cATR, because the former can penetrate the plasma membrane, but the latter cannot. The same principles as detailed above apply here for identifying whether *in situ* synaptic mitochondria consume extramitochondrial ATP or not. The experimental protocol for the synaptosomes was the following, (figure 7.5): synaptosomes were incubated in an extracellular-like buffer, supplemented with 15 mM glucose as the sole energy substrate, and $\Delta\Psi m$ was measured by TMRM fluorescence . Addition of the uncoupler SF 6847 at the end of each experiment causing the complete collapse of $\Delta\Psi m$ assisted in the normalization of the TMRM signal of all traces. In this *in situ* mitochondrial model, mitochondria respire, albeit sub-maximally (Tretter and Adam-Vizi, 2007b). Application of the complex I inhibitor, rotenone (1 μM, panels A, C) or the complex III inhibitor, stigmatellin (1.2 μM, panels B, D) caused a significant depolarization. Subsequent addition of oligomycin (10 μg/ml, panels A, C, red traces) caused a nearly complete collapse of $\Delta\Psi m$, implying that *in situ* mitochondria relied on ATP hydrolysis by the F_0-F_1 ATPase. However, addition of BKA in lieu of oligomycin led to a robust repolarization in WT, $DLD^{+/-}$ and $DLST^{+/-}$ mice (black and green traces of panels A, and C), implying that the ANT was still operating in the forward mode. Only in synaptosomes prepared from $DLD^{+/-}/DLST^{+/-}$ double transgenic mice did BKA cause almost no repolarization (blue trace of panel C), followed by a delayed minor depolarization.

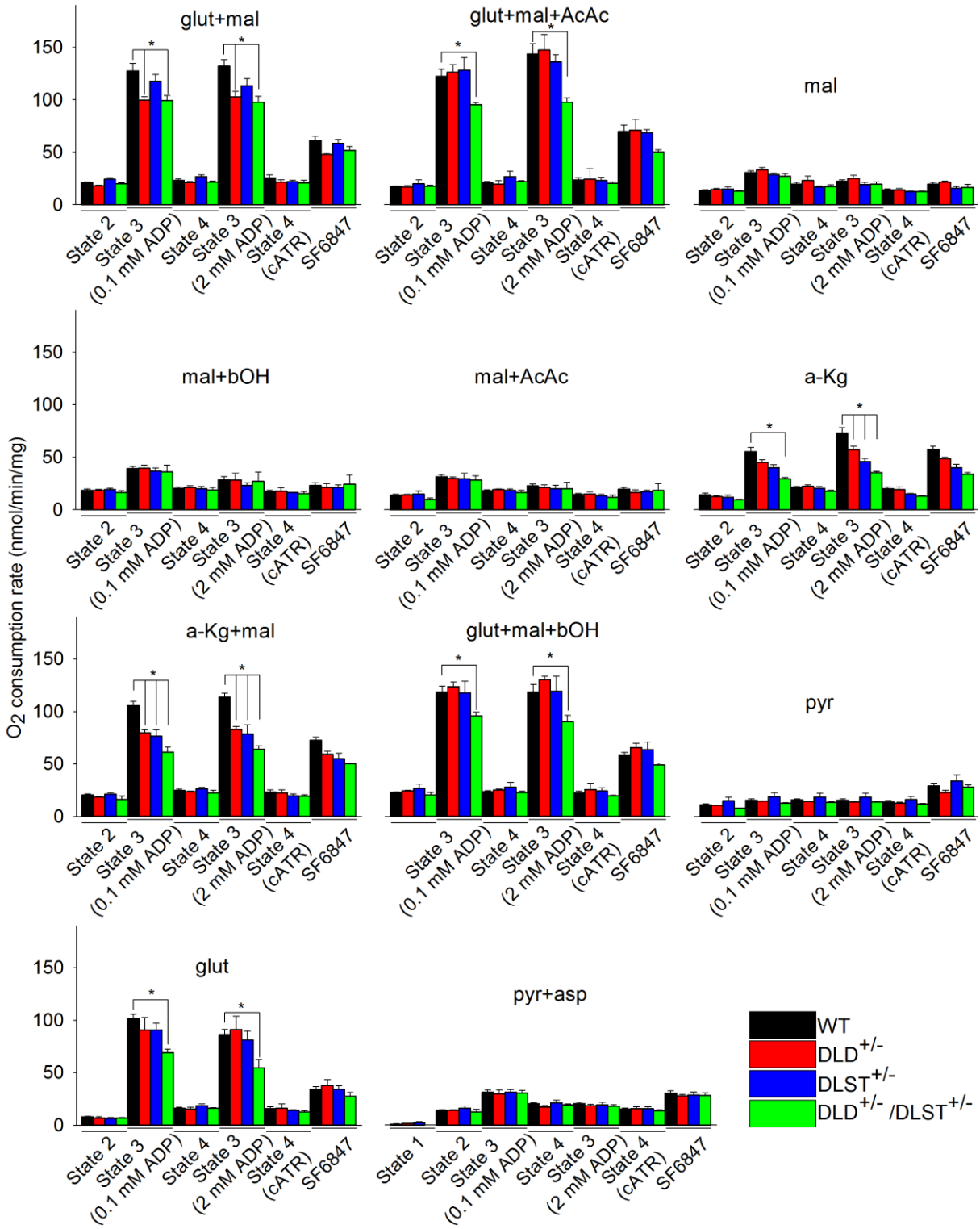

*Figure 7.4. Respiration rates of isolated brain mitochondria of WT, DLD$^{+/-}$, DLST$^{+/-}$ and DLD$^{+/-}$/ DLST$^{+/-}$ mice for various substrate combinations indicated in the panels. Substrate concentrations were: glutamate (glut, 5 mM), malate (mal, 5 mM), acetoacetate, (AcAc, 0.5 mM), β-hydroxybutyrate, (bOH, 2 mM), α-ketoglutarate (a-Kg, 5 mM), pyruvate (pyr, 5 mM), aspartate (asp, 5 mM). At the end of each experiment, 50 nM SF 6847 was administered. *, statistically significant, p<0.05 one-way ANOVA followed by Dunnett's test post-hoc analysis; control: results obtained from WT mice. p-values were as follows: glut-mal: 0.1 mM ADP bolus: 0.002, 2 mM ADP bolus: 0.002; glut-mal-AcAc: 0.1 mM ADP bolus: 0.026, 2 mM ADP bolus: 0.006; α-Kg: 0.1 mM ADP bolus: 0.002, 2 mM ADP bolus: <0.001; α-Kg-mal: 0.1 mM ADP bolus: < 0.001, 2 mM ADP bolus: <0.001; glut+mal+bOH: 0.1 mM ADP bolus: 0.021, 2 mM ADP bolus: 0.015; glut: 0.1 mM ADP bolus: 0.011, 2 mM ADP bolus: 0.022. State 1 (no mitochondria, no substrates) is shown only in panel (pyr+asp, bottom middle panel).*

This implied that in double transgenic animals, net adenine nucleotide flux through the ANT of rotenone-treated *in situ* synaptic mitochondria is near zero, and perhaps importing minor amounts of synaptoplasmic ATP into the matrix. Synaptosomes of WT mice inhibited by stigmatellin did not exhibit BKA-induced repolarization (black traces of panels B and D), neither those obtained from $DLD^{+/-}$, $DLST^{+/-}$ and $DLD^{+/-}/DLST^{+/-}$ mice (green and blue traces of panels B and D). It must be emphasized that KGDHC determinations from synaptosomal preparations (shown in figure 7.7) also involve enzymes from contaminating isolated mitochondria, the extent of which cannot be reliably estimated from the various transgenic mouse colonies. So therefore, the results obtained from the TMRM measurements of *in situ* mitochondria from the isolated nerve terminals cannot be reliably correlated to the extent of maximal KGDHC activity from the exact same mitochondria. Results obtained from cultured cortical neurons are shown in figure 7.6.

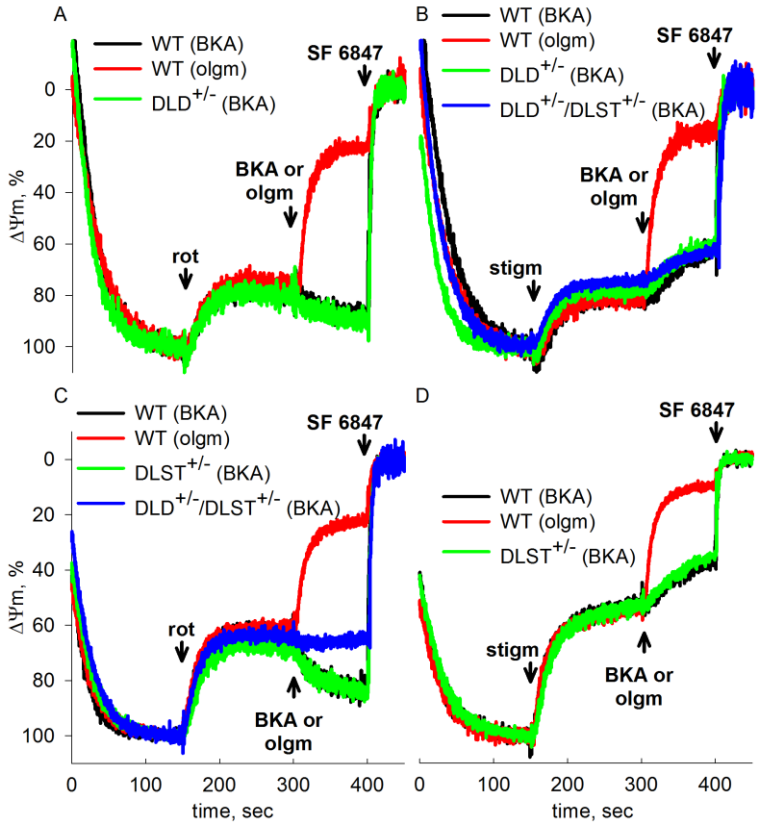

Neurons of $DLST^{+/-}$ versus WT mice were compared in panels A and B and neurons of $DLD^{+/-}$ versus WT mice in panel C and D. For all panels the experimental paradigm was similar to that applied for synaptosomes. Cultures were bathed in an extracellular-like buffer, supplemented with 15 mM glucose as the sole substrate, and $\Delta\Psi m$ was measured by TMRM fluorescence. Addition of the uncoupler SF 6847 at the end of each experiment causing the complete collapse of $\Delta\Psi m$ assisted in the normalization of the TMRM signal of all traces. Rotenone (1 μM) or stigmatellin (1.2 μM) was applied where indicated to inhibit *in situ* mitochondrial respiration, causing a significant depolarization.

Figure 7.5. Effect of bongkrekic acid (BKA), oligomycin (olgm) on the rotenone- or stigmatellin-evoked depolarization of $\Delta\Psi m$ in isolated nerve terminals of WT vs $DLD^{+/-}$ mice (A, B), or WT vs $DLST^{+/-}$ (C, D) or $DLD^{+/-}/DLST^{+/-}$ mice (B, D). $\Delta\Psi m$ was followed using the potentiometric probe TMRM. BKA (20 μM); oligomycin (olgm 10 μg/ml), rotenone (rot, 1 μM); stigmatellin (stigm, 1.2 μM). At the end of each experiment, 1 μM SF 6847 was added to achieve complete depolarization.

Subsequent addition of oligomycin (10 μg/ml) caused a nearly complete collapse of $\Delta\Psi m$ (green traces), implying that respiration-impaired *in situ* mitochondria relied on ATP hydrolysis by the F_0-F_1 ATPase. However, when *in situ* mitochondria were inhibited by rotenone, subsequent addition of BKA in lieu of oligomycin led to a repolarization in WT cultures (panels A and C, black traces), unlike in cultures obtained from $DLD^{+/-}$ and $DLST^{+/-}$ mice where a depolarization was observed (panels A and C, red traces). This implied that respiration-impaired *in situ* neuronal somal mitochondria of $DLD^{+/-}$ and $DLST^{+/-}$ mice were consuming extramitochondrial ATP. Application of stigmatellin in lieu of rotenone caused a large depolarization, and subsequent addition of BKA in either WT or transgenic mice neurons did not confer any repolarization (panels B and D, black traces). The results obtained from *in situ* somal neuronal

mitochondria using stigmatellin are supported by results obtained from Percoll-purified (that consist of both somal neuronal and astrocytic) mitochondria, where a very large depolarization was observed.

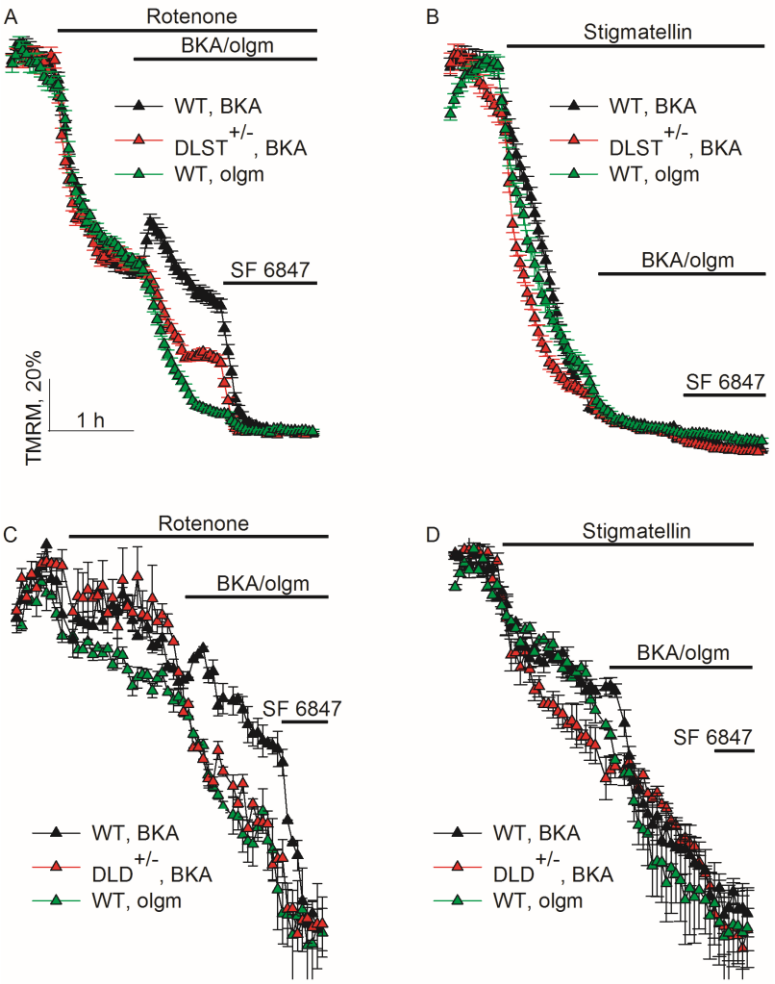

Figure 7.6. Effect of bongkrekic acid (BKA), oligomycin (olgm) on the rotenone or stigmatellin-evoked depolarization of $\Delta\Psi m$ in cultured mouse cortical neurons of WT vs DLST$^{+/-}$ mice (A, B), or WT vs DLD$^{+/-}$ mice (B, D). $\Delta\Psi m$ was followed in intact cells with confocal (A, B) or epifluorescence (C, D) microscopy using the potentiometric probe TMRM. BKA (20 μM; black triangles), oligomycin (10 μg/ml; green triangles), rotenone (1 μM, or stigmatellin 1.2 μM, where indicated, red triangles). Data were pooled from 13 cell culture preparations. Data points obtained by epifluorescent imaging represent the mean ± SEM of 2 view fields per well containing 50-60 neurons per condition. Data points obtained by confocal imaging represent the mean ± SEM of 3 view fields per well containing 90-120 neurons per condition. At the end of each experiment, 5 μM SF 6847 was added to achieve complete depolarization.

7.6 KGDHC and succinyl-CoA maximal activities in tissues from WT and transgenic mice

Succinyl-CoA ligase has been reported to co-precipitate with KGDHC (Porpaczy et al., 1983); therefore, alterations in KGDHC due to genetic manipulations could have an impact on succinyl-CoA ligase. To address this possibility, we measured KGDHC activity and succinyl-CoA ATP-and GTP-forming activities in isolated liver and brain mitochondria and synaptosomes obtained from WT, and transgenic mice, as well as immunoreactivities of all three subunits of succinyl-CoA ligase. We were unable to measure KGDHC and succinyl-CoA ligase activity from cultured neurons, due to limitations on the available tissue (i.e. neurons from one pup brain was sufficient to cover a single Lab-Tek chamber). Succinyl-CoA ligase is a heterodimer enzyme, composed of an invariant α subunit encoded by SUCLG1 and a substrate-specific β subunit, encoded by either SUCLA2 or SUCLG2. This dimer combination results in either an ATP-forming SUCL (EC 6.2.1.5) or a GTP-forming SUCL (EC 6.2.1.4). Results on KGDHC activities are shown in figure 7.7, panel A (isolated brain mitochondria), panel C (synaptosomes), and panel E (isolated liver mitochondria). Immunoreactivities of SUCLG1, SUCLG2 and SUCLA2 from the same tissues are shown in figure 7.7, panels F and G. As shown in panel A and consistent with reports published before (Yang, L. et al., 2009), (Starkov et al., 2004), KGDHC activity of DLD$^{+/-}$ and DLST$^{+/-}$ brain mitochondria was reduced by 20-48 %, compared to WT littermates. KGDHC activity of double transgenic DLD$^{+/-}$/DLST$^{+/-}$ brain and liver isolated mitochondria was reduced by 62%

and 50%, respectively. On the contrary, succinyl-CoA ATP- or GTP-forming maximal activities were not different between WT and transgenic mice. This is in accordance to the findings regarding immunoreactivities of the subunits of the succinyl-CoA ligase enzyme, showing no differences between WT and any KGDHC transgenic mice, panels F and G. These results strongly suggest that the impact of genetic manipulations of KGDHC on matrix substrate-level phosphorylation is solely due to decreased provision of succinyl-CoA.

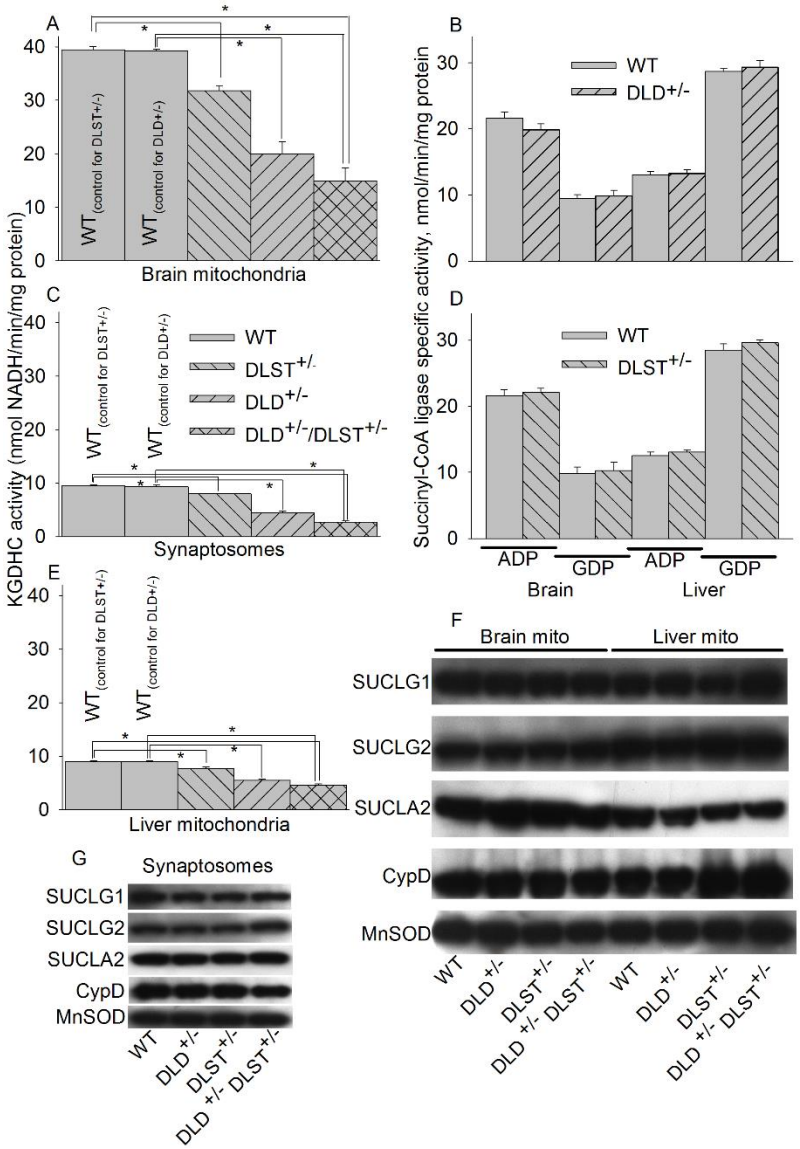

7.7 Predictions of matrix ATP/ADP ratios for each substrate combination used for isolated brain mitochondria from WT vs KGDHC-deficient mice, after inhibition by rotenone

From the $\Delta\Psi m$ values extracted from figure 7.2, the cATR-induced de- or repolarization for each substrate combination indicating the directionality of the ANT we can predict the range of matrix ATP/ADP ratios for these conditions after inhibition of complex I of the respiratory chain. These predictions are depicted in figure 7.8; panel A for mitochondria from WT mice, panel B for mitochondria from $DLD^{+/-}$ mice, panel C for mitochondria from $DLST^{+/-}$ mice and panel D for mitochondria from $DLD^{+/-}$ /$DLST^{+/-}$ mice. Substrates are indicated by a single letter as detailed in the legend. For each substrate combination found in the orange

Figure 7.7. Enzymatic activities of KGDHC, Succinyl-CoA ligase and immunoreactivities of the subunits of the latter enzyme in isolated liver and brain mitochondria and synaptosomes. ***A, C, E****: KGDHC activities of isolated brain mitochondria, synaptosomes and isolated liver mitochondria, respectively of WT, $DLST^{+/-}$, $DLD^{+/-}$, and $DLD^{+/-}$/$DLST^{+/-}$transgenic mice. *, statistically significant, p<0.05 (1-way ANOVA followed by Dunnett's test post-hoc analysis).* ***B, D****: Succinyl-CoA ligase activities (ATP- and GTP-forming) of isolated liver and brain mitochondria of WT vs $DLD^{+/-}$, and WT vs $DLST^{+/-}$ mice, respectively.* ***F, G****: Immunoreactivities of SUCLG1, SUCLG2, SUCLA2 subunits of Succinyl-CoA ligase, cyclophilin D (CypD), and Manganese Superoxide Dismutase (MnSOD) of isolated brain and liver mitochondria (F) and synaptosomes (G) of WT, $DLD^{+/-}$, $DLST^{+/-}$, and $DLD^{+/-}$/$DLST^{+/-}$ mice.*

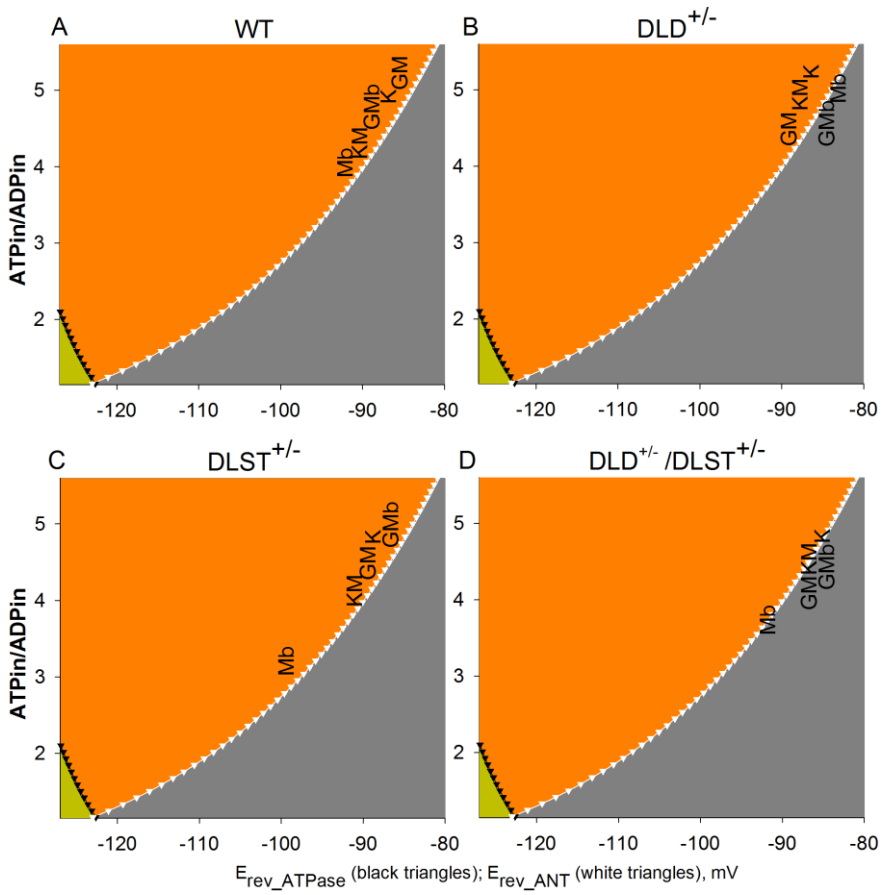

Figure 7.8. Predicted ranges of matrix ATP/ADP ratios (ATP/ADPin) for each substrate combination used for brain mitochondria from WT vs KGDHC-deficient mice, after inhibition by rotenone; glutamate (G), malate (M), β-hydroxybutyrate, (b), α-ketoglutarate, (K). For each substrate combination found in the 'B' (orange) space, the range of values that the matrix ATP/ADP ratio may attain is from Erev_ANT for the respective membrane potential and upwards. If the substrate combination is found in the 'C' (grey) space, the range of values that the matrix ATP/ADP ratio may attain is from Erev_ANT for the respective membrane potential until theoretical zero.

(B) space, matrix ATP/ADP ratio may have a value from Erev_ANT for the respective membrane potential and upwards. If the substrate combination is found in the grey (C) space, the matrix ATP/ADP ratio may have a value from Erev_ANT for the respective membrane potential until theoretical zero. As shown in figure 7.8 for brain mitochondria, and in (supplementary figure 10 in (Kiss et al., 2013), figure is too large to be included in the present dissertation format) for liver mitochondria, several substrate combinations supporting substrate-level phosphorylation appear in the orange (B) space in WT mice, while the substrate combinations appear in the grey (C) space in KGDHC-deficient mice. Substrate combinations that disfavor substrate-level phosphorylation appear exclusively in the grey (C) space for both WT and KGDHC-deficient mice.

8 Mitochondrial diaphorases as NAD^+ donors to segments of the citric acid cycle that support substrate-level phosphorylation yielding ATP during respiratory inhibition

In (Kiss et al., 2013) we showed that when the electron transport chain is dysfunctional, provision of succinyl-CoA by the α-ketoglutarate dehydrogenase complex (KGDHC) is crucial for maintaining the function of succinyl-CoA ligase yielding ATP, preventing the adenine nucleotide translocase from reversing. Subsequently, in (Kiss et al., 2014) we showed that under these conditions mitochondrial diaphorases provide NAD^+ to KGDHC in turn yielding succinyl-CoA, thus supporting mitochondrial substrate-level phosphorylation.

8.1 Diaphorases: general considerations

DT diaphorase (EC 1.6.5.2, formerly assigned to EC 1.6.99.2) catalyzes a two-electron reductive metabolism (unlike other NAD(P)-linked quinone reductases (Iyanagi and Yamazaki, 1970a)) detoxifying quinones and their derivatives; several isoforms have been identified (Long and Jaiswal, 2000), (Vasiliou et al., 2006); among them, NQO1 and NQO2 have been most extensively characterized (Long and Jaiswal, 2000). A striking difference between these two is that NQO2 uses dihydronicotinamide riboside (NRH) while NQO1 utilizes NAD(P)H as an electron donor (Wu et al., 1997), (Zhao et al., 1997). NQO1 has been found to localize not only in the cytosol, but also in mitochondria from several tissues (Ernster et al., 1962), (Dong et al., 2013), (Eliasson et al., 1999), (Edlund et al., 1982), (Conover and Ernster, 1962), (Lind and Hojeberg, 1981). Mitochondrial diaphorase corresponds to 3-15% of total cellular activity and is localized in the matrix, since it reacts only with intramitochondrial reduced pyridine nucleotides, but is inaccessible to those added from the outside (Conover and Ernster, 1960), (Conover and Ernster, 1963). However, it must be emphasized that mitochondrial diaphorase activity may not be exclusively due to NQO1; other mitochondrial enzymes also exhibit diaphorase-like activity as a moonlighting function; for example, the isolated DLD subunit of KGDHC exhibits diaphorase activity and it is known to exist in the matrix as such, without being part of the KGDH complex (Massey, 1960), (Reed and Oliver, 1968), (Bando and Aki, 1992).

8.2 Identifying mitochondria as extramitochondrial ATP consumers during anoxia

As elaborated in (Chinopoulos et al., 2010) and (Kiss et al., 2013), to label a mitochondrion as an extramitochondrial ATP consumer its $\Delta\Psi$m, matrix ATP/ADP ratio, and *reversal potentials* of F_0-F_1 ATP synthase and ANT (*the $\Delta\Psi$m values at which there is no ATP generation nor hydrolysis for the former and no net transfer of ADP–ATP across the inner mitochondrial membrane for the latter*) must be determined, which is an extremely challenging experimental undertaking. Mindful that the reversal potential of the F_0-F_1 ATP synthase is more negative than that of the ANT (Chinopoulos et al., 2010), (Chinopoulos, 2011b), (Chinopoulos, 2011a), meaning that whenever the ANT has reversed, the ATP synthase works in reverse too, it is simpler and equally informative to examine the effect of an ANT inhibitor on $\Delta\Psi$m during ADP-induced respiration. Since one molecule of ATP^{4-} is exchanged for one molecule of ADP^{3-} (both nucleotides being Mg^{2+}-free and deprotonated) by the ANT, the exchange is electrogenic (Klingenberg, 2008). Therefore, during forward mode of the ANT, abolition of its operation by a specific inhibitor such as carboxyatractyloside (cATR) leads to an increase in $\Delta\Psi$m, whereas during the reverse mode of ANT, the same condition leads to a loss of $\Delta\Psi$m. In (Kiss et al., 2014) we used this method in isolated mitochondria subjected to true anoxic conditions and/or specific inhibitors of the electron transport chain, while sources of NAD^+ for KGDHC were being sought.

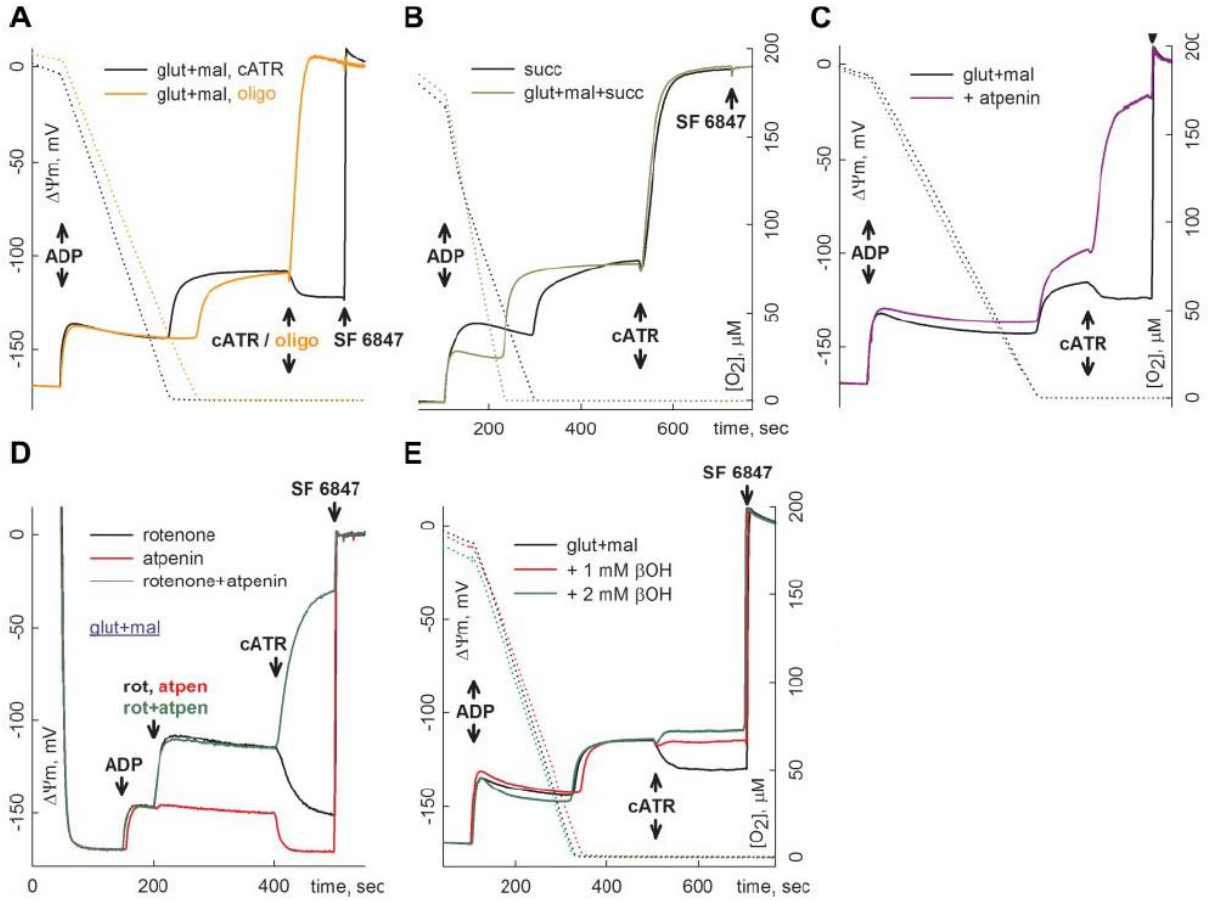

Figure 8.1. Reconstructed time courses of safranine O signal calibrated to $\Delta\Psi m$ (solid traces), and parallel measurements of oxygen concentration in the medium (dotted traces) in isolated mouse liver mitochondria. Effect of carboxyatractyloside (cATR, 2 μM) or oligomycin (oligo, 5 μM) on $\Delta\Psi m$ during anoxia (A, B, C, E) or during compromised respiratory chain by poisons (D), in the presence of different substrate combinations. ADP (2 mM) was added where indicated. Substrate concentrations were: glutamate (glut, 5 mM), malate (mal, 5 mM), succinate (succ, 5 mM), β-hydroxybutyrate, (βOH, 1 or 2 mM as indicated). Substrate concentrations were the same for all subsequent experiments shown below. At the end of each experiment 1 μM SF 6847 was added to achieve complete depolarization (except for the orange trace in panel A, where 250 nM SF 6847 was added).

Time-lapse recordings of safranine O fluorescence reflecting ΔΨm while measuring oxygen concentration in the same sample was achieved by using the recently developed O2k-Fluorescence LED2-Module of the Oxygraph-2k (Oroboros Instruments, Innsbruck, Austria). Mitochondria were allowed to deplete the oxygen dissolved in the air-sealed chamber and additions of chemicals through a tiny-bore hole did not allow reoxygenation of the buffer from the ambient atmosphere. Safranine O is known to increase state 4 respiration (Valle et al., 1986), decrease maximum Ca^{2+} uptake capacity and exhibit an appreciable non-specific binding component if used at concentrations above 5 µM (Chinopoulos and Adam-Vizi, 2010b). However, at concentrations below 5 µM, calibration of the safranine O fluorescence signal to ΔΨm deviates significantly from linearity, thereby more complex fitting functions are required, decreasing the faithfulness of the conversion. Therefore, for our experiments we used 5 µM of safranine O at the expense of diminishing the respiratory control ratio by approximately one unit (from 7.5 to 6.5 using glutamate and malate), but the signal-to-noise ratio was optimal and the calibration of the fluorescence signal to ΔΨm highly reproducible. TPP^+ appeared to be less toxic than safranine O in terms of an effect on mitochondrial respiration; however, the signal-to noise ratio was not as satisfactory as that obtained from safranine O, and it could not be improved by

increasing the concentration of TPP^+ (from a total 2 to a total 6 μM). The non-specific binding component of safranine O to mitochondria is determined by the mitochondria/safranine O ratio; by using 5 μM of safranine O for 2 mg of mitochondria the non-specific component is within 10% of the total safranine O fluorescence signal, estimated by the increase in fluorescence caused by the addition of a detergent to completely depolarized mitochondria. As such, it was accounted for, during the calibration of the fluorescence signal to $\Delta\Psi m$. The result of a typical experiment is shown in figure 8.1. Mouse liver mitochondria (2 mg) were added in 4 ml of buffer containing substrates indicated in the panels, and allowed to fully polarize (solid traces). State 3 respiration was initiated by ADP (2 mM) depolarizing mitochondria by ~25 mV; with a respiration rate of ~60 nmol/min/mg mitochondria run out of oxygen within 5-6 min as verified by recording 'zero' levels of dissolved oxygen in the chamber at ~400 sec (dotted traces). Anoxia also coincided with the onset of an additional depolarization leading to a clamp of $\Delta\Psi m$ at ~-100 mV. In mitochondria respiring on glutamate and malate, i.e. substrates that support substrate-level phosphorylation, subsequent addition of cATR (figure 8.1, panel A, black solid trace) caused a moderate repolarization. This implied that at ~-100 mV, the ANT was still operating in the forward mode, in accordance with the ADP-ATP steady-state exchange activity/$\Delta\Psi m$ relationship shown recently (Metelkin et al., 2009), (Chinopoulos et al., 2009). In contrast, when the specific F_0-F_1 ATP synthase inhibitor oligomycin (figure 1, panel A, orange solid trace) was added instead of cATR, an immediate depolarization was observed, implying that F_0-F_1 ATP synthase was working in reverse and generated the residual $\Delta\Psi m$. This depolarization was complete, since further addition of the uncoupler SF 6847 (250 nM) yielded no further depolarization. Obviously, under the conditions shown in figure 8.1A, ATP was available in the matrix from sources other than ANT. Our previous results (Chinopoulos et al., 2010), (Kiss et al., 2013) showed that under this condition, ATP was supplied by matrix substrate-level phosphorylation mediated by succinyl-CoA ligase. This was further validated by the experiments shown in panels 8.1B and 8.1C: in panel B, mitochondria respiring on succinate alone (black trace) or glutamate plus malate plus succinate (olive green trace), both conditions being unfavorable for substrate-level phosphorylation by succinyl-CoA ligase (succinate would 'push' this reversible reaction towards ATP or GTP hydrolysis), reacted to cATR with an immediate and complete depolarization in anoxia. Likewise, in the presence of 2 μM atpenin A5, a specific inhibitor of succinate dehydrogenase (Miyadera et al., 2003) causing accumulation of succinate in the matrix, cATR induced depolarization in mitochondria that had been previously respiring on glutamate plus malate and were subject to anoxia (figure 8.1, panel C, lilac trace). In the presence of atpenin though, onset of anoxia was associated with a greater depolarization prior to addition of cATR, thus it is possible that the value of $\Delta\Psi m$ exceeded the value of the reversal potential of the ANT (Erev_ANT). However, when the electron transport chain was rendered inoperable by rotenone in lieu of anoxia, $\Delta\Psi m$ values were identical prior to addition of the ANT inhibitor (figure 8.1, panel D, compare black with green trace), but loss of $\Delta\Psi m$ implying ANT reversal in the presence of atpenin A5 was verified by cATR. From the above experiments we concluded that in true anoxic conditions the ANT could be maintained in forward mode implying active matrix substrate-level phosphorylation in isolated mitochondria, similar to the previously published paradigms with a poisoned respiratory chain (Chinopoulos et al., 2010), (Kiss et al., 2013). Furthermore, the results obtained in (Kiss et al., 2013) showing that provision of succinyl-CoA by KGDHC is critical for matrix substrate-level phosphorylation implies an emerging demand of NAD^+ for KGDHC, a concept that is at odds with the idea that in anoxia there is shortage of NAD^+ in the mitochondrial matrix. Indeed, figure 8.1 panel E shows that after elevating matrix NADH/NAD^+ ratio by 1 or 2 mM β-hydroxybutyrate (leading to NADH -and acetoacetate- formation through the reaction catalyzed by β-hydroxybutyrate dehydrogenase) cATR-induced a small depolarization, compared to near repolarization in panels 8.1E, 8.1A and 8.1C (black traces). The same effect with β-hydroxybutyrate was found in mitochondria with

poisoned respiratory chain (Kiss et al., 2013). These results underline the importance of NAD^+ for establishing the conditions for the forward operation of ANT during anoxia.

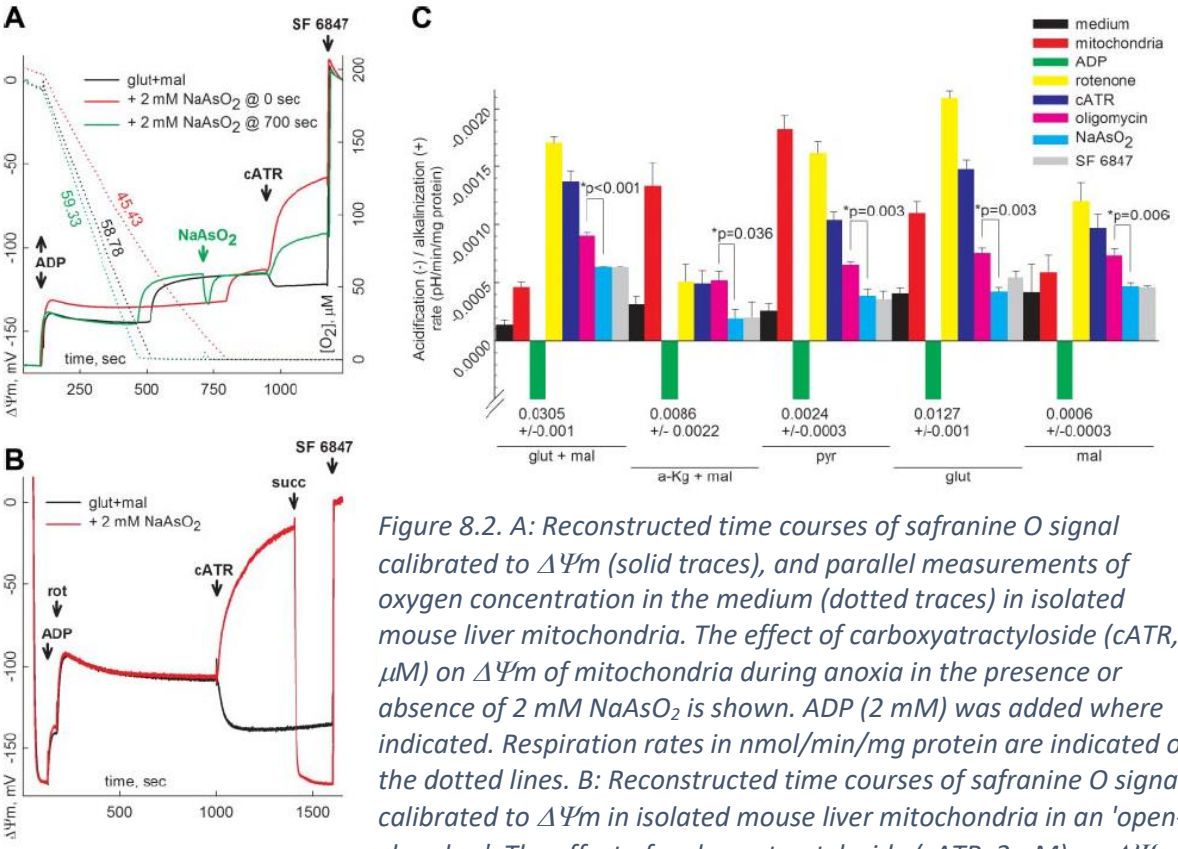

Figure 8.2. A: Reconstructed time courses of safranine O signal calibrated to $\Delta\Psi m$ (solid traces), and parallel measurements of oxygen concentration in the medium (dotted traces) in isolated mouse liver mitochondria. The effect of carboxyatractyloside (cATR, 2 μM) on $\Delta\Psi m$ of mitochondria during anoxia in the presence or absence of 2 mM $NaAsO_2$ is shown. ADP (2 mM) was added where indicated. Respiration rates in nmol/min/mg protein are indicated on the dotted lines. B: Reconstructed time courses of safranine O signal calibrated to $\Delta\Psi m$ in isolated mouse liver mitochondria in an 'open-chamber'. The effect of carboxyatractyloside (cATR, 2 μM) on $\Delta\Psi m$ of mitochondria treated with rotenone (rot, 1 μM, where indicated) in the presence or absence of 2 mM $NaASO_2$ (2 mM, red trace) is shown. ADP (2 mM) was added where indicated. At the end of each experiment 1 μM SF 6847 was added to achieve complete depolarization. C: Bar graph of rates of acidification in the suspending medium of mitochondria respiring on various substrate combinations indicated in the panel upon addition of different bioenergetic poisons.

8.3 The importance of NAD^+ for a maintained operation of KGDHC during anoxia or respiratory chain inhibition

In (Kiss et al., 2014) we further addressed the importance of a maintained operation of KGDHC requiring supply of NAD^+ in mitochondria during anoxia using arsenite, which enters intact mitochondria in an energy-dependent manner (Harris and Achenjang, 1977) and inhibits PDHC and KGDHC (Clark and Land, 1979). When mitochondria respire on glutamate plus malate, an effect of arsenite could be attributed to inhibition of KGDHC. Safranine O fluorescence and oxygen concentration in the medium where mitochondria underwent anoxia or drug-induced respiratory inhibition was recorded. As shown in figure 2, panel A, the fully polarized mitochondria in the presence of glutamate and malate were depolarized by ~25 mV by ADP (2 mM, solid black and green traces) consuming within ~6 min the total amount of oxygen present in the medium (dotted black and green traces) leading to an additional depolarization to ~-100 mV. Respiration rates are indicated in the panel, in nmol/min/mg protein. The transient repolarization upon addition of 2 mM sodium arsenite ($NaAsO_2$) at 700 sec was due to the high volume of the addition (0.08 ml), which contained a significant amount of dissolved oxygen. This is seen as a

minor elevation in oxygen concentration (figure 8.2 panel A, dotted green line near 700 sec) which quickly subsided as it was consumed by mitochondria and was also associated with a re-establishment of $\Delta\Psi m$ to ~-100 mV. Subsequent addition of cATR to mitochondria treated with $NaAsO_2$ (figure 8.2 panel A, green solid trace) initiated a drop in $\Delta\Psi m$ as opposed to a moderate repolarization observed in the absence of arsenite (figure 8.2 panel A, black solid trace). cATR also caused a depolarization when arsenite was present in the medium prior to addition of mitochondria (figure 8.2 panel A, red solid trace), which as expected, was associated with a diminished rate of respiration (figure 8.2 panel A, red dotted trace) leading to a prolongation until complete anoxia was achieved. cATR also caused a depolarization when arsenite was present in the medium prior to mitochondria (figure 8.2 panel B, red trace), in which electron transport was halted by inhibiting complex I with rotenone (rot). Subsequent addition of succinate (succ, 5 mM) fully restored $\Delta\Psi m$ indicating that mitochondria were capable of electron transport from complex II when complex I was blocked, in the presence of arsenite. Finally, the effect of arsenite was investigated on the rate of acidification in weakly-buffered media, in which mitochondria were treated with a specific set of inhibitors. The concept of this experiment relies on the fact that mitochondria are net CO_2 producers acidifying the medium due to the following equilibria: $CO_2 + H_2O \leftrightarrow H_2CO_3 \leftrightarrow H^+ + HCO_3^-$. Depending on the substrate(s) combined with targeted inhibition of bioenergetic entities, one may deduce the role of arsenite-inhibitable targets. Mitochondria were suspended in a weakly-buffered medium containing different substrates as indicated in figure 8.2, panel C. Acidification is indicated as an upward-pointing bar, alkalinization as a downward-pointing bar. The sequence of additions were: medium (black), mitochondria (2 mg, red), ADP (2 mM, green) rotenone (1 μM, yellow), cATR (2 μM, blue), oligomycin (5 μM, magenta), $NaAsO_2$ (2 mM, cyan), and SF 6847 (1 μM, grey). With substrate combinations bypassing PDHC (glutamate plus malate, α-ketoglutarate plus malate, or glutamate alone -all at 5 mM-) arsenite caused a statistically significant decrease in acidification in mitochondria pretreated with rotenone, cATR and oligomycin. We assumed that in mitochondria in which complex I is blocked by rotenone, the ANT and the F_0-F_1 ATP synthase are blocked by cATR and oligomycin, respectively, the arsenite-inhibitable acidification may only stem from KGDHC generating CO_2. The CO_2 production by KGDHC in respiration-impaired mitochondria suggested the availability of NAD^+. Mindful of the above results we sought for NAD^+ sources in mitochondria other than that produced by complex I and considered the possibility of NAD^+ provision by mitochondrial diaphorases.

8.4 The effect of diaphorase inhibitors on bioenergetic parameters

As mentioned above, diaphorase activity is attributed to flavoproteins designated as NQOs; depending on the organism several isoforms and their polymorphisms have been identified (Long and Jaiswal, 2000) and (Vasiliou et al., 2006). Among these, NQO1 and NQO2 have been most extensively characterized

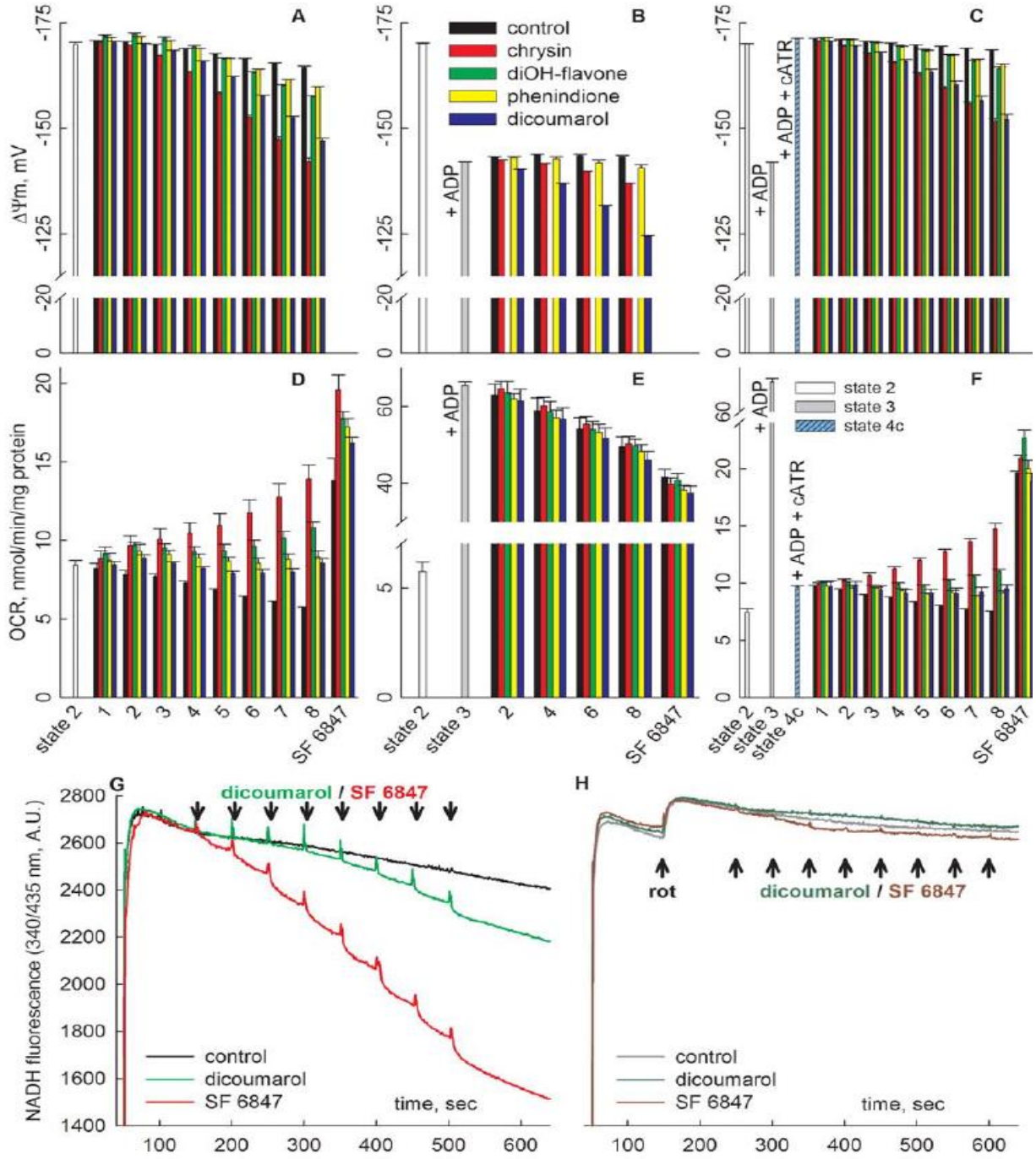

Figure 8.S.1. A-F: Bar graphs of the effect of diaphorase inhibitors (colour-coded within panel B) on ΔΨm (panels A, B and C) and oxygen consumption rates (OCR, panels D, E and F) under state 2 (panel A), state 3 (+2 mM ADP, panel B) or state 4 (+2 mM ADP + 2 μM cATR, panel C) conditions. G, H: Reconstructed time courses of NADH autofluorescence in isolated mouse liver mitochondria in the absence (panel G) and presence of 1 μM rotenone (panel H), and the effect of dicoumarol applied consecutively in 1.25 μM concentrations or that of SF 6847 in 10 nM concentrations, as indicated by the arrows. Panels G and H share the same y-axis.

(Vasiliou et al., 2006). Although NQO1 is not in the list of mouse or human mitochondrial proteins (MitoCarta) (Pagliarini et al., 2008) and it was also suggested not to localize in mitochondria of certain human cancers (Winski et al., 2002), it has been found in mitochondria from different tissues (Dong et al., 2013), (Bianchet et al., 2004), (Eliasson et al., 1999). To address the contribution of mitochondrial

diaphorases to provision of NAD^+ for KGDHC reaction in anoxia, we used an array of pharmacological inhibitors; however, all of them exhibit uncoupling properties at high concentrations (Conover and Ernster, 1962), (Martius and Nitz-Litzow, 1953). The potential uncoupling effect of an inhibitor would be confounding, because in its presence $\Delta\Psi m$ could become less negative than Erev_ANT leading to ANT reversal (Chinopoulos et al., 2010); in this case, its impact could not be distinguished from a genuine effect on the diaphorases. Therefore, we first determined the concentration-range in which their uncoupling effects were negligible. As shown in supplemental figure 8.S.1, the dose-dependent effect of four different NQO1 inhibitors, -chrysin, 7,8-dihydroxyflavone hydrate (diOH-flavone), phenindione, and dicoumarol- have been compared to a vehicle (black bars) on $\Delta\Psi m$ in mitochondria respiring on glutamate and malate (panel A), after addition of 2 mM ADP (panel B), and after the addition of cATR (panel C), while simultaneously in the same samples rates of oxygen consumption were also recorded (panels D, E and F, for state 2, state 3 and state 4c (induced by cATR), respectively). Supplemental figure 8.S.1 shows the effects of eight consecutive additions of chrysin, (2.5 μM each: red bars); diOH-flavone (5 μM each: green bars); phenindione (2.5 μM each: yellow bars) and dicoumarol (1.25 μM each: blue bars). From the bar graphs it is apparent that all diaphorase inhibitors exhibited a concentration range in which they had no significant uncoupling effect. That was for chrysin ≤ 5 μM, for phenindione ≤ 20 μM, and for dicoumarol ≤ 5 μM. diOH-flavone showed a significant quenching effect on the safranine O signal during state 3 respiration, thus only its effect on oxygen consumption rate was evaluated to establish the safe use at a concentration below 20 μM. Finally, the effect of diaphorase inhibitors was compared to that of the uncoupler SF 6847 in decreasing NADH signals in intact isolated mitochondria. Such an experiment (for dicoumarol) is demonstrated in supplemental figure 8.S.1, panels G and H. Mouse liver mitochondria (1 mg) were allowed to fully polarize in a medium containing glutamate and malate, then either vehicle (control) or 1.25 μM dicoumarol or 10 nM SF 6847 were added where indicated. As shown in supplemental figure 8.S.1, panel G, while SF 6847 dose-dependently decreased NADH fluorescence, dicoumarol 1.25-5 μM was without an effect. The changes in NADH fluorescence shown in panel G were largely controlled by complex I, because in the presence of rotenone (panel H), responses to dicoumarol and SF 6847 were almost completely dampened.

8.5 The effect of diaphorase inhibitors on ANT directionality in anoxic or rotenone-treated mitochondria

Having established the concentration range of the diaphorase inhibitors exhibiting no appreciable uncoupling activity, we wanted to determine their effects in the 'biosensor' test addressing the direction of the operation of ANT by recording the effect of cATR on $\Delta\Psi m$ in respiration-impaired mitochondria, when they are exquisitely dependent on matrix substrate-level phosphorylation (Chinopoulos et al., 2010). The rationale behind these experiments was that, diaphorases might be responsible for providing NAD^+ to KGDHC, which in turn is important for generating succinyl CoA for substrate-level phosphorylation. The experimental conditions for figure 8.3, panels A-D, were essentially similar to those shown for figure 8.1, again demonstrating changes of $\Delta\Psi m$ in response to cATR. The anoxia also coincided with the onset of a depolarization leading to a clamp of $\Delta\Psi m$ to ~-100 mV. As shown in figure 8.3, panels A, B, C, and D black solid traces, addition of cATR in mitochondria made anoxic caused a repolarization, implying a forward operation of the ANT in spite of the lack of oxygen. However, in the presence of diaphorase inhibitors (concentration and color-coding detailed in panel A) cATR induced depolarization (solid traces) without affecting the rate of respiration (figure 8.3, panels A, B, C, and D, dotted traces), implying ANT reversal. Likewise, in the presence of diaphorase inhibitors (concentration and color-coding detailed in panel E) rotenone-treated mitochondria (figure 8.3, panels E, F, G and H, red and orange traces) responded with depolarization to cATR, as compared to their vehicles showing cATR-induced repolarizations (black and grey traces). From these results we concluded that diaphorases

were likely to provide NAD^+ to KGDHC that in turn supported substrate-level phosphorylation via generating succinyl-CoA during anoxia or inhibition of complex I by rotenone. In order to quasi-quantify the extent of contribution of NAD^+ emanating from the mitochondrial diaphorases that can be utilized by KGDHC during anoxia, we compared the rates of cATR-induced depolarizations (mV/sec) in the presence of diaphorase inhibitors to the rate of cATR-induced depolarization in the presence of 2 mM $NaAsO_2$. From the data obtained with 20 μM diOH-flavone, 5 μM dicoumarol, 5 μM chrysin and 20 μM phenindione, we inferred that mitochondrial diaphorases contributed 26, 41, 37 and 81% to the matrix NAD^+ pool during anoxia, respectively.

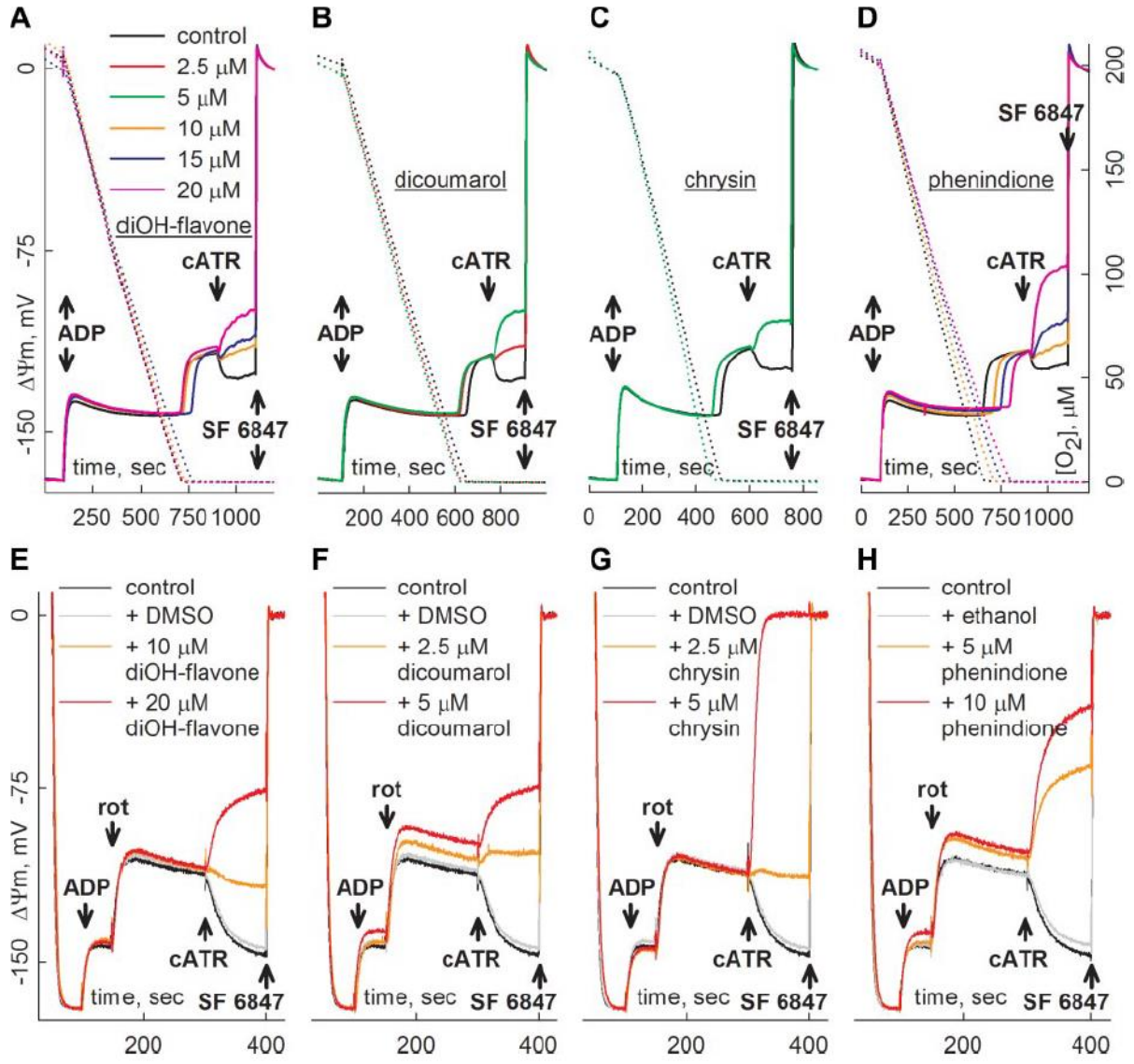

Figure 8.3. Reconstructed time courses of safranine O signal calibrated to $\Delta\Psi m$ (solid traces), and parallel measurements of oxygen concentration in the medium (dotted traces) in isolated mouse liver mitochondria supported by glutamate and malate. The effect of diaphorase inhibitors (doses are color-coded within panel A) on cATR-induced changes of $\Delta\Psi m$ during anoxia (A-D) or under complex I inhibition by rotenone (E-H). Grey traces in panels E-H show the effect of vehicles (either DMSO or ethanol). At the end of each experiment 1 μM SF 6847 was added to achieve complete depolarization.

8.6 The effect of diaphorase substrates on ANT directionality of respiration-impaired mitochondria due to anoxia or rotenone

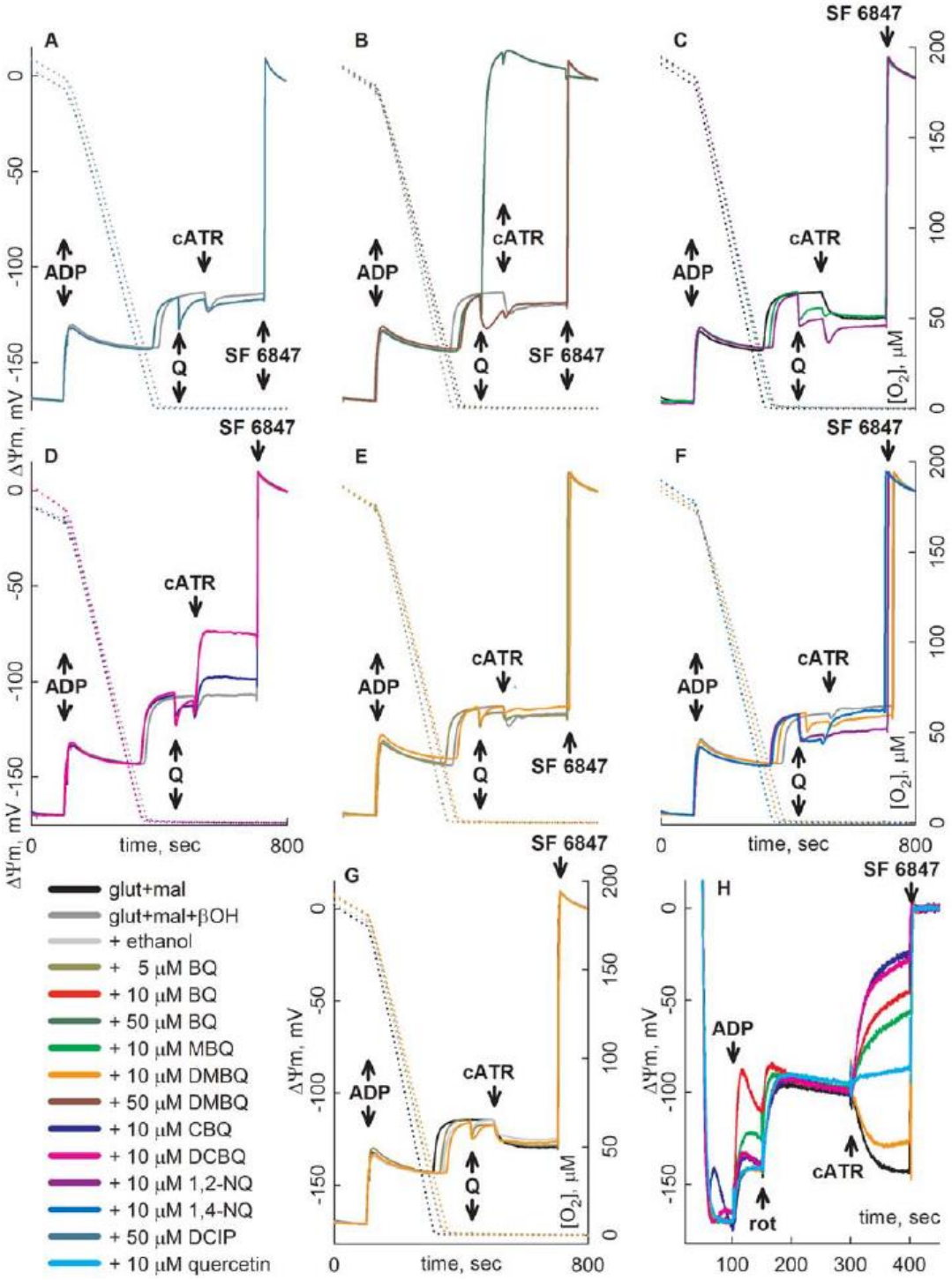

Figure 8.S.2. A-G: Reconstructed time courses of safranine O signal calibrated to $\Delta\Psi m$ (solid traces), and parallel measurements of oxygen concentration in the medium (dotted traces) in isolated mouse liver mitochondria, demonstrating the effect of diaphorase substrates on cATR-induced changes of $\Delta\Psi m$ during anoxia. Diaphorase substrates are colour-coded as indicated in the figure. H: Reconstructed time courses of safranine O signal calibrated to $\Delta\Psi m$ in isolated mouse liver mitochondria, demonstrating the effect of diaphorase substrates on cATR-induced changes of $\Delta\Psi m$ after complex I inhibition by rotenone. At the end of each experiment 1 μM SF 6847 was added to achieve complete depolarization.

To strengthen the above conclusion, next we performed the 'biosensor' test in the presence of known diaphorase substrates in mitochondria undergoing respiratory inhibition by anoxia or rotenone. Diaphorase activity mediated by NQO1 exhibits lack of substrate- and electron donor specificity because its active site can accommodate molecules of varying size and structure (Faig et al., 2001), therefore, various types of quinoid compounds and their derivatives can be processed by the isolated enzyme (Lind et al., 1990). Furthermore, it is also able to react with different dyes, nitro compounds and some inorganic substances (Lind et al., 1990). The mitochondrial matrix is a quinone-rich environment, containing several coenzyme Qs with variable side-chains. Of course, NQO1 exhibits unequal affinities for them, but it is reasonable to assume that some coenzyme Qs are in the millimolar concentration range and could be substrates for NQO1. We tested 14 different diaphorase substrates: menadione (vitamin K3, 10 μM), phylloquinone (vitamin K1, 10 μM), menaquinone (vitamin K2, 10 μM), duroquinone (DQ, 10-100 μM), mitoquinone (mitoQ, 0.5 μM), p-benzoquinone (BQ, 10 μM), methyl-p-benzoquinone (MBQ, 10 μM), 2,6-dimethylbenzoquinone (DMBQ, 10-50 μM), 2-chloro-1,4-benzoquinone (CBQ, 10 μM), 2,6-dichloro-1,4-benzoquinone (DCBQ, 10 μM), 1,2-naphthoquinone (1.2-NQ 10 μM), 1,4-naphthoquinone (1.4-NQ 10 μM), 2,6-dichloroindophenol (DCIP, 50 μM), and 2-(3,4-dihydroxyphenyl)-3,5,7-trihydroxy-4H-chromen-4-one (quercetin, 10 μM). In concentrations exhibiting no uncoupling or other side-effects on $\Delta\Psi m$ or rate of respiration, mouse liver mitochondria were treated with ADP and cATR similarly to that demonstrated in figure 8.1. As shown in figure 8.4 panels A-C (and supplemental figure 8.S.2), when using different substrate combinations supporting respiration, addition of cATR caused repolarization except when glutamate plus malate plus β-hydroxybutyrate were used (panel C, black solid trace), a substrate combination that limits the availability of NAD^+ during anoxic conditions. In this paradigm, dose-dependent addition of duroquinone during anoxia led to cATR-induced repolarization (panel C, colored solid traces). Addition of menadione had no effect (panel A, solid orange trace), while mitoQ even abolished the cATR-induced repolarization (panel B, solid green trace). By contrast, when respiratory inhibition was achieved by rotenone instead of anoxia, duroquinone, menadione and mitoQ resulted in a strong cATR-induced repolarization (figure 8.4, panels D-H). This effect of menadione (vitamin K3) was not shared by vitamins K1 (phylloquinone) and K2 (menaquinone), as shown in panels G and H, respectively. The variable effects of a host of other quinones in this paradigm are shown in figure 8.S.2. Furthermore, since safranine O may also be a substrate for diaphorases due to its structural similarity to Janus Green B, which is a genuine diaphorase substrate (Giuditta and Strecker, 1963), redistribution of tetraphenylphosphonium (TPP) as an index of $\Delta\Psi m$ was also measured as an alternative, using a TPP electrode, (figure 8.4, panel I). Mitochondria were allowed to polarize by glutamate and malate then ADP (2 mM) was added, followed by rotenone that led to a depolarization. Addition of cATR induced a repolarization, like in the above experiment indicating that safranine O is unlikely to be a diaphorase substrate. From these results we concluded that mitochondrial diaphorases were not saturated by endogenous quinones and were likely providing NAD^+ to KGDHC that in turn yielded succinyl-CoA supporting substrate-level phosphorylation during anoxia or inhibition of complex I by rotenone. Furthermore, there appeared to be a clear distinction between true anoxia and rotenone-induced respiratory inhibition; in anoxia, menadione and mitoQ were not effective in conferring cATR-induced repolarization.

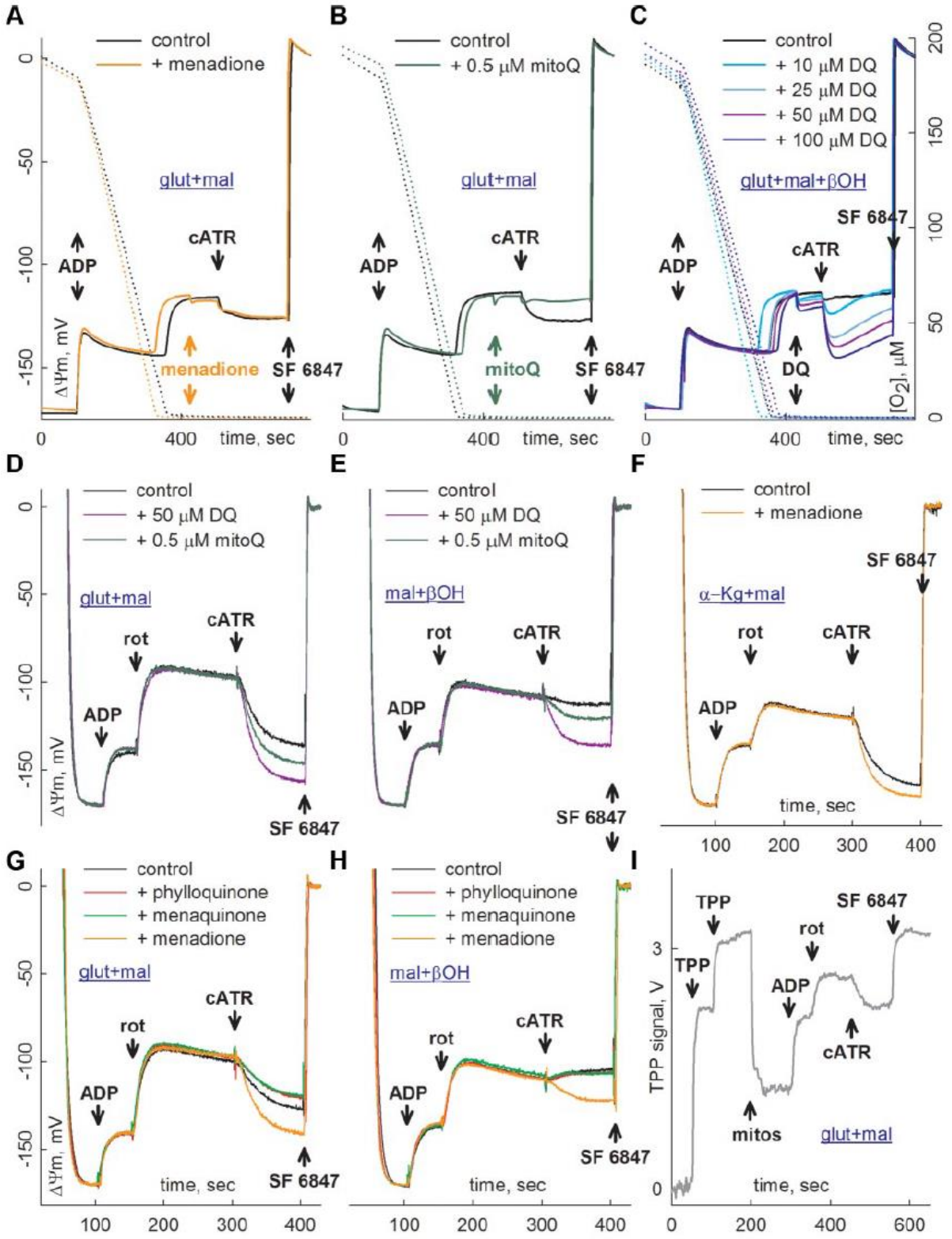

Figure 8.4. Reconstructed time courses of safranine O signal calibrated to ΔΨm (solid traces), and parallel measurements of oxygen concentration in the medium (dotted traces) in isolated mouse liver mitochondria demonstrating the effect of diaphorase substrates on cATR-induced ΔΨm changes during anoxia (A, B, C) or complex I inhibition by rotenone (D-H). Substrate combinations are indicated in the panels. I: Reconstructed time course of TPP signal (in Volts) in isolated mouse liver mitochondria supported by glutamate and malate. Additions were as indicated by the arrows. At the end of each experiment 1 μM SF 6847 was added to achieve complete depolarization.

8.7 The role of complex III in re-oxidizing diaphorase substrates

To address the discrepancy that emerged from the results obtained with rotenone-treated vs anoxia-treated mitochondria in respect to the effect of diaphorase substrates, we inhibited mitochondrial respiration with stigmatellin, a specific inhibitor of complex III. The rationale behind this relies on several reports pointing to complex b of complex III as being capable of re-oxidizing substrates that are reduced by mitochondrial diaphorases (Conover and Ernster, 1962), (Colpa-Boonstra and Slater, 1958), (Dedukhova et al., 1986), (Kolesova et al., 1991), (Kolesova et al., 1993), (Ernster et al., 1969).

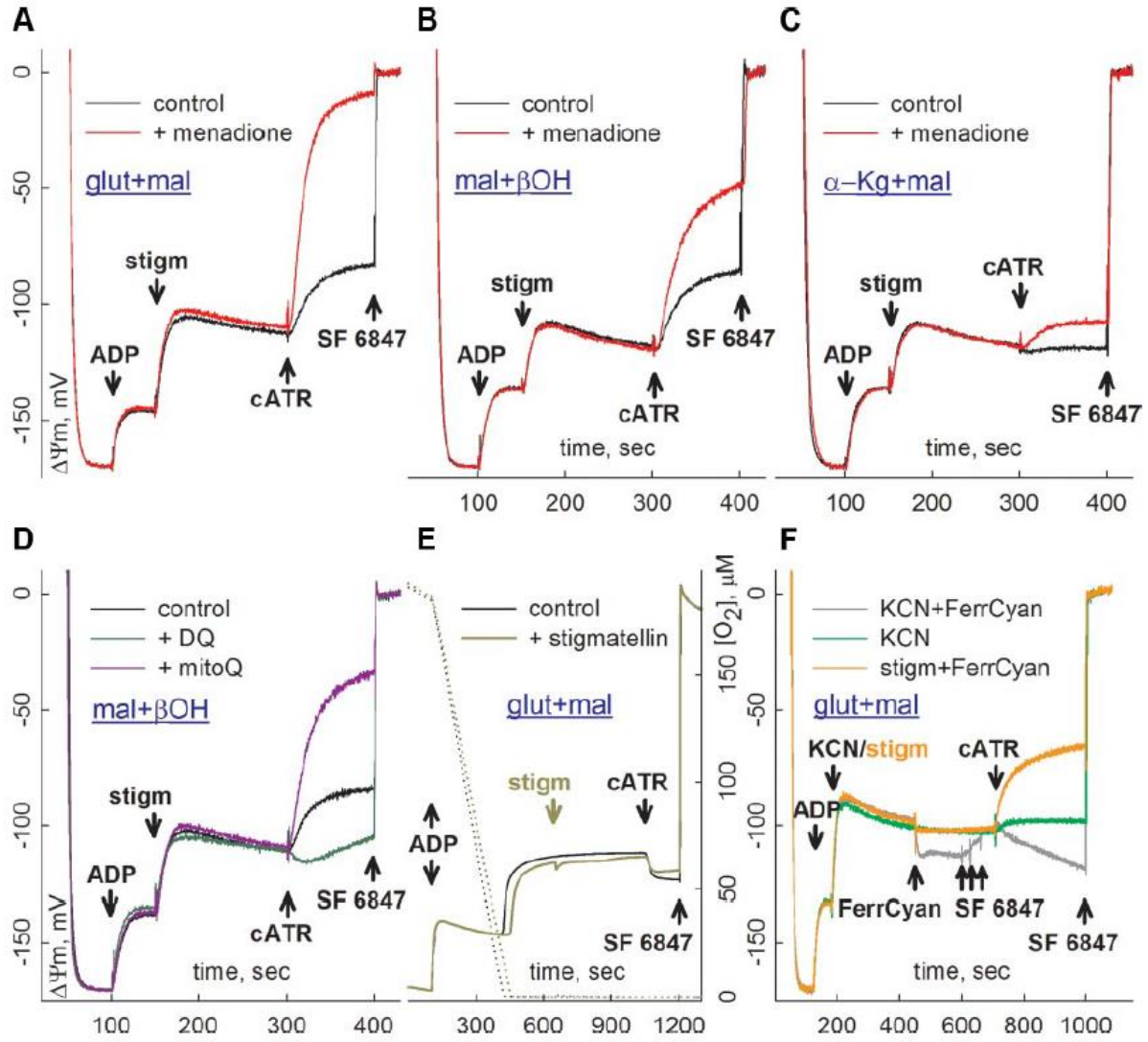

Figure 8.5. The effect of diaphorase substrates (menadione: 10 μM, DQ: 50 μM, mitoQ: 0.5 μM) on cATR-induced changes of ΔΨm after complex III inhibition by stigmatellin or complex IV by KCN. Reconstructed time courses of safranine O signal calibrated to ΔΨm in isolated mouse liver mitochondria and oxygen consumption (panel E, dotted lines) are shown. Mitochondria respired by different substrates as shown in the panels. Additions were as indicated by the arrows. At the end of each experiment 1 μM SF 6847 was added to achieve complete depolarization. FerrCyan: ferricyanide.

As shown in figure 8.5, panels A-D, in mouse liver mitochondria respiring on different substrate combinations indicated in the panels, state 3 respiration initiated by ADP (2 mM) was arrested by 0.8 μM stigmatellin (stigm), leading to a clamp of ΔΨm to ~-100 mV. Subsequent addition of cATR (figure 8.5, panels A, B and C, black solid traces) conferred a depolarization to variable extent, depending on

the substrates used, indicating that functional complex III was required for the forward operation of ANT when it relied on ATP generated by substrate-level phosphorylation. The lack of re-oxidation of the reduced diaphorase substrate by complex III is likely to reflect in the result showing that the presence of menadione (panels A, B and C, red traces) or mitoQ (panel D, lilac trace), but not duroquinone (panel D, green trace), conferred a more robust cATR-induced depolarization. In mitochondria undergoing respiratory arrest by anoxia (panel E), addition of stigmatellin (olive green trace) did not result in cATR-induced depolarization. However, while respiratory arrest of mitochondria achieved by inhibiting complex IV with KCN (1 mM) yielded a very small change in $\Delta\Psi$m by cATR (panel F, green trace), co-presence of $K_3[Fe(CN)_6]$ (FerrCyan, 1 mM), which can oxidize cytochrome c due to its higher redox potential (~400 mV *vs* 247-264 mV for cytochrome c (Flatmark, 1967), (Gopal et al., 1988)) led to a cATR-induced repolarization (panel F, grey trace). This effect was abolished by stigmatellin (panel F, orange trace). When FerrCyan was used, it was necessary to titrate $\Delta\Psi$m back to the same levels as in its absence, hence SF 6847 (5 nM boluses) were added where indicated (panel F, grey trace). From the above experiments we concluded that stigmatellin was negating the beneficial effect of diaphorase substrates assisting in cATR-induced repolarization emphasizing the involvement of complex III in mitochondria with respiratory inhibition by rotenone or anoxia. Evidently not all diaphorase substrates assisted in preventing mitochondria from being extramitochondrial ATP consumers, which meant that not all of them could be processed by either the diaphorases, and/or re-oxidized by complex III. Relevant to this, it is well known that vitamins K1, K2 and Q_{10} do not react with the isolated diaphorase (Preusch and Smalley, 1990), (Haefeli et al., 2011), (Ernster et al., 1962); furthermore, while numerous compounds have been shown to react readily with purified diaphorase (Ernster et al., 1962), (Lind et al., 1990), there is specificity in the oxidation of the reduced quinone by the respiratory chain (Conover and Ernster, 1962). Indeed, menadione and duroquinone were previously shown to be processed by the mitochondrial diaphorases and re-oxidized by complex III (Conover and Ernster, 1962), (Kolesova et al., 1991).

8.8 Lack of the role of diaphorase in the regeneration of NAD^+ during anoxia in mitochondria from pigeon liver

The diaphorase activity described for rodent and human tissues has been reported to be absent in the liver and breast muscle of pigeons (*Columba livia domestica*) (Maritius and Strufe, 1954). We therefore reasoned that in mitochondria obtained from pigeon tissues, the diaphorase inhibitors and substrates would exert no effect. As shown in figure 8.6, panels A-D (black traces), pigeon liver mitochondria respiring on different substrates were repolarized by cATR added after ADP and rotenone indicating an ATP generation from the forward operation of the ANT. The lack of diaphorase involvement in this effect was confirmed by the results that menadione failed to cause a more robust cATR-induced repolarization (panels A-C, red traces), and none of the diaphorase inhibitors caused cATR-induced depolarization (figure 8.6, panel D). Accordingly, duroquinone (DQ) was without an effect on cATR-induced changes in $\Delta\Psi$m of mitochondria during anoxia (figure 8.6, panel E). These results support the conclusion that the effects of diaphorase substrates and inhibitors observed in mouse liver mitochondria were likely mediated through genuine diaphorase activity. Furthermore, it is also apparent that in the absence of a diaphorase, pigeon liver mitochondria were still able to maintain the KGDHC-succinyl-CoA ligase axis sustaining substrate-level phosphorylation. Indeed, in figure 8.6, panel F it is shown that the addition of succinate to pigeon mitochondria reverted the cATR-induced changes in $\Delta\Psi$m during anoxia from a repolarization to a depolarization. Furthermore, in pigeon liver mitochondria addition of atpenin A5 - which is expected to lead to a built-up of succinate in the mitochondrial matrix also led to a cATR-induced depolarization during anoxia (figure 6, panel G, red trace).

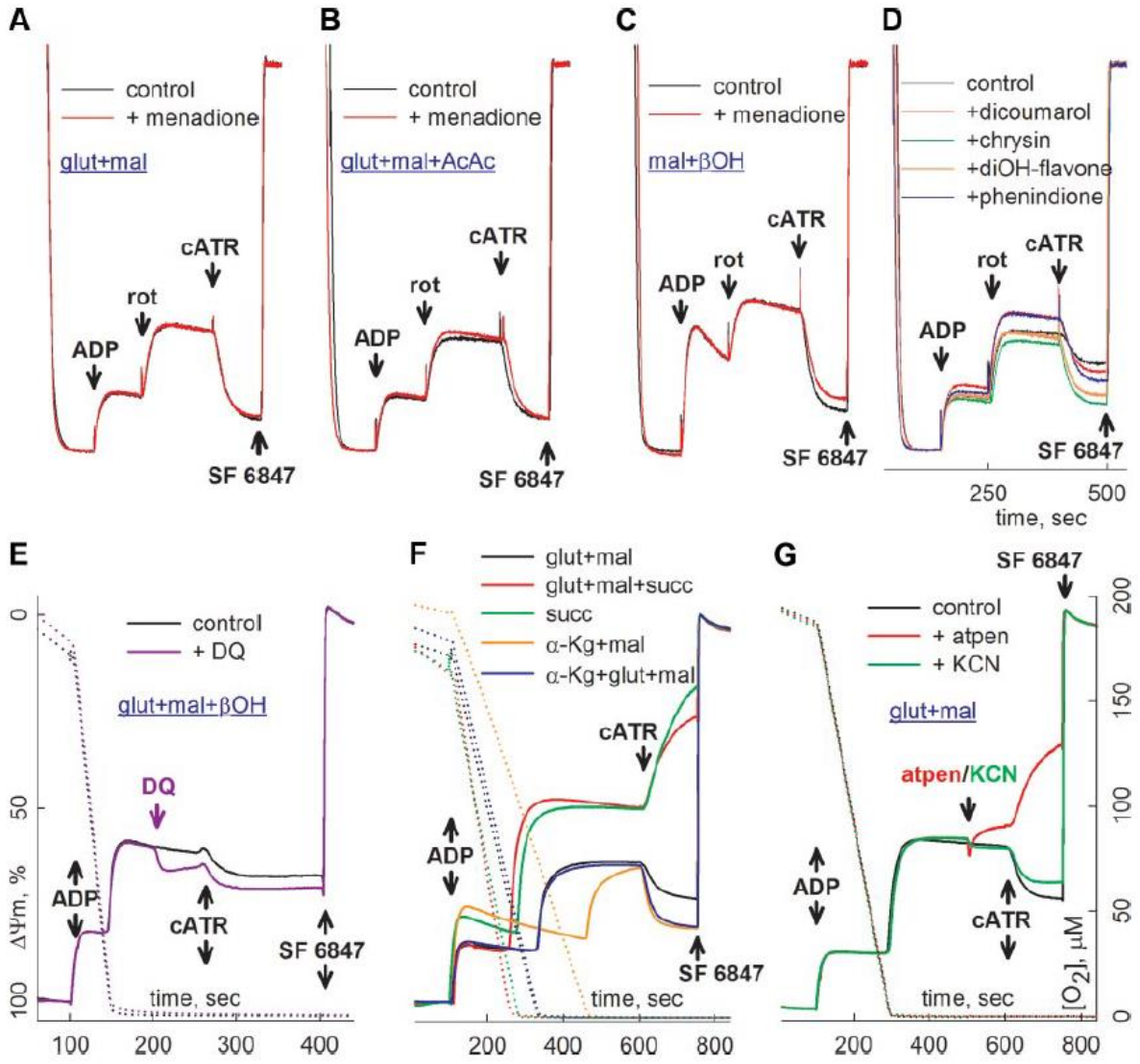

Figure 8.6. A-C: Reconstructed time courses of safranine O signal calibrated to percentage (solid traces, the y-axis of all panels is the same as shown for panel E) reflecting $\Delta\Psi m$ in isolated pigeon liver mitochondria, demonstrating the effect of various mitochondrial and diaphorase substrates on cATR-induced changes of $\Delta\Psi m$ after complex I inhibition by rotenone using different respiratory substrates as indicated in the panels. For D, diaphorase inhibitors were present as indicated (dicoumarol: 5 μM, chrysin: 5 μM, diOH-flavone: 20 μM, phenindione: 10 μM), and mitochondria were supported by glutamate and malate. Oxygen concentrations in the medium (dotted traces) were measured in panels E, F and G. The effect of duroquinone (DQ, 50 μM) is shown in panel E; that of various substrates in panel F, and that of the inhibitors atpenin A5 and KCN in panel G. At the end of each experiment 1 μM SF 6847 was added to achieve complete depolarization.

8.9 Alternative sources for NAD^+ provision in mitochondria during respiratory arrest

From the above data it is apparent that mitochondrial diaphorases are not the sole providers for NAD^+ during anoxia or respiratory inhibition by poisons. An obvious possibility for NAD^+ generation would be the malate dehydrogenase (MDH) reaction favoring malate formation from oxaloacetate (Chinopoulos, 2013), however, this is very difficult to address. We have compared wild-type C57BL/6J mice with another strain expressing an isoform of MDH, which yielded insignificantly smaller activity ($MDH2^b$), but we observed no differences (not shown). A 'transgenic' or 'silencing' approach for MDH inherently

suffers from the pitfall that this enzyme exhibits an extremely high activity compared to other enzymes of the citric acid cycle; therefore, one would expect to require very substantial decreases in activity in order to observe an impact on NAD^+ provision. The fact that there are no MDH specific inhibitors hindered the ability of studying the extent of contribution of MDH in our protocols.

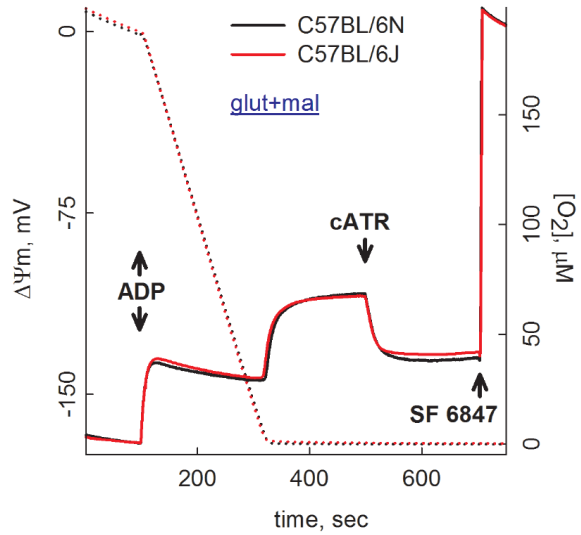

Figure 8.S.3. Reconstructed time courses of safranine O signal calibrated to $\Delta\Psi m$ (solid traces), and parallel measurements of oxygen concentration in the medium (dotted traces) in isolated liver mitochondria from C57Bl/6J vs 6N mice, on cATR-induced changes of $\Delta\Psi m$ during anoxia.

To address the extent of contribution of a proton-translocating transhydrogenase reversibly exchanging $NADP^+$ and NAD^+ to NADH and NADPH, respectively (Jackson, 1991) which may potentially serve as a source of matrix NAD^+, we compared mitochondria obtained from C57Bl/6N versus C57BL/6J mice, because in the latter strain the gene coding for the transhydrogenase is absent (Toye et al., 2005), (Freeman et al., 2006). Although the catalytic site of the transhydrogenase for oxidation and reduction of the nicotinamide nucleotides is facing the matrix, extramitochondrial pyridine nucleotides are also required; however, those released from broken mitochondria in our samples may have been sufficient for the exchange to materialize. As shown in figure 8.S.3, cATR-induced repolarization after anoxia in liver mitochondria from C57Bl/6N mice (black trace) was virtually indistinguishable from mitochondria obtained from C57BL/6J mice (red trace). From this result we concluded that in our isolated mitochondria preparations, provision of NAD^+ by the transhydrogenase is not a viable possibility. However, it remains as an option *in vivo*, at least in organisms expressing the transhydrogenase.

9. Reduction of 2-methoxy-1,4-naphtoquinone by mitochondrially-localized Nqo1 yielding NAD^+ supports substrate-level phosphorylation during respiratory inhibition

Above, it was elaborated that when NADH oxidation by complex I is inhibited by rotenone or anoxia, mitochondrial diaphorases yield NAD^+, provided that suitable quinones are present (Kiss et al., 2014). In (Ravasz et al., 2018) by using $Nqo1^{-/-}$ vs WT littermate mice we showed that in rotenone-treated, isolated liver mitochondria, 2-methoxy-1,4-naphtoquinone (MNQ) was preferentially reduced by matrix Nqo1 yielding NAD^+ to KGDHC, supporting mSLP. This process was sensitive to inhibition by specific diaphorase inhibitors. Reduction of idebenone and its analogues MRQ-20 and MRQ-56, menadione, mitoquinone and duroquinone were unaffected by genetic disruption of the Nqo1 gene.

9.1 Determination of NAD(P)H oxidation and quinone reduction capacity in cytosolic extracts vs permeabilized mitochondria from the livers of WT and Nqo1$^{-/-}$ mice

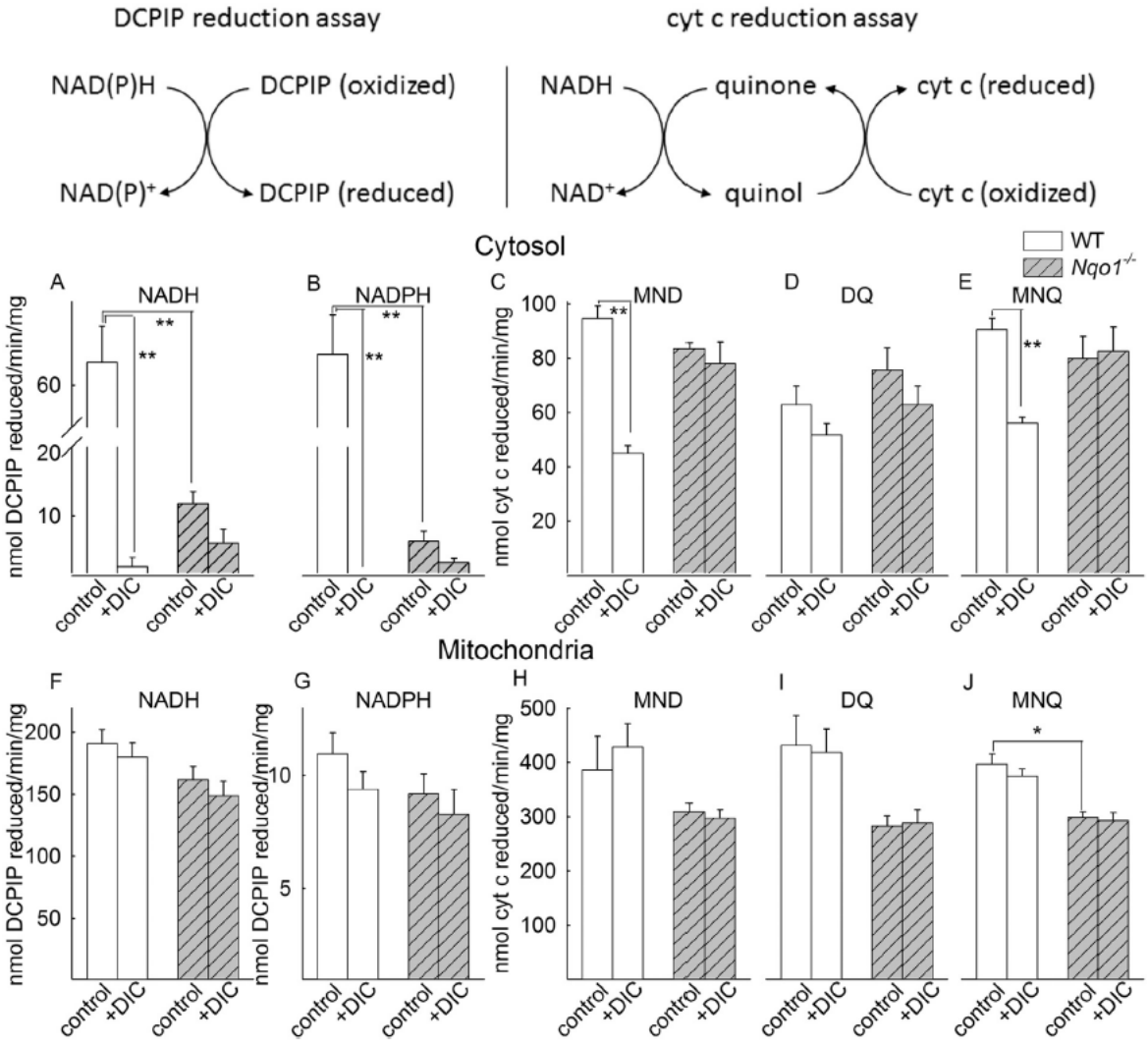

Figure 9.1. ***Determination of diaphorase activity in cytosolic extracts vs permeabilized mitochondria from the livers of WT and Nqo1$^{-/-}$ mice.*** *Schemes of the reactions involved in the two different methodologies are depicted on the top of the figure. Upper-row panels (**A-E**) depict data obtained from cytosolic extracts. Lower-row panels (**F-J**) depict data obtained from permeabilized mitochondria. White bars signify data from WT mice, grey-hatched bars from Nqo1$^{-/-}$ mice. Panels **A, B, F and G** depict data obtained by the DCPIP reduction method using NADH or NADPH as indicated in the panels. Panels **C, D, E, H, I** and **J** depict data obtained by the cytochrome c reduction method using menadione (MND, 10 μM), duroquinone (DQ, 10 μM) or 2-methoxy-1,4-naphtoquinone (MNQ, 10 μM) as indicated in the panels, in the presence of NADH. All samples were measured in the absence (control) or presence of 10 μM dicoumarol (DIC). Student's t-test; * implies p<0.05. ** implies p<0.001.*

The extent of contribution of Nqo1 to overall diaphorase activity in mouse liver was measured using two different methods: i) by determining the dicoumarol-sensitive rates of DCPIP reduction during either NADH or NADPH oxidation and ii) by determining the dicoumarol-sensitive rates of cytochrome c reduction using various quinones in the presence of NADH. The principles of these two methodologies are depicted in the top schemes in figure 9.1. Data obtained from WT and Nqo1$^{-/-}$ mice were pooled and

compared. Nqo1$^{-/-}$ mice have been developed by the group of Jaiswal (Radjendirane et al., 1998). As shown in figure panel 9.1A, the presence of 10 μM dicoumarol (DIC) decreased DCPIP reduction to nearly zero when using NADH in cytosolic extracts from the livers of WT mice. When NADPH was used instead of NADH, DCPIP reduction was 100% eliminated by dicoumarol (figure panel 9.1B, white bars). These two results confirm that the cytosolic NAD(P)H-dependent diaphorase activity is almost 100% sensitive to dicoumarol. By repeating these experiments but using cytosolic extracts from the livers of Nqo1$^{-/-}$ mice (grey hatched bars) it is obvious that diaphorase activity is largely –but not exclusively- due to Nqo1. This methodology relies on the ability of diaphorases (including Nqo1) to reduce DCPIP; however, different diaphorases exhibit different affinities for electron acceptors, thus we measured cytochrome c reduction rates in the presence of various quinones (as electron acceptors), which were later used for other experiments. As shown in figure panels 9.1C, D and E, the rates of cytochrome c reduction and their sensitivities to dicoumarol varied in the presence of menadione (MND), duroquinone (DQ) or 2-methoxy-1,4-naphtoquinone (MNQ), using cytosolic extracts from the livers of WT mice. Using this methodology, a statistically significant decrease in diaphorase activity was demonstrated only by using MND and MNQ. On the other hand, dicoumarol failed to decrease diaphorase activity in cytosolic extracts obtained from the livers of Nqo1$^{-/-}$ mice. The finding that in the hepatic cytosols of Nqo1$^{-/-}$ mice higher diaphorase activities were observed using the cytochrome c reduction method vs the DCPIP reduction method reflects the fact that other diaphorases are present in this compartment, which are not dicoumarol-sensitive and exhibit higher affinities for redox-active compounds other than DCPIP. To investigate the extent of contribution of mitochondrial Nqo1 to overall diaphorase activity, the same experiments were performed using freeze-thawn isolated mitochondria from the livers of WT and Nqo1$^{-/-}$ mice, in the presence of 2 μM rotenone. As shown in figure panel 9.1F, the presence of 10 μM DIC decreased DCPIP reduction to a small and not significant level, despite the extremely high DCPIP reduction rate in the presence of NADH, in both types of mitochondria isolated from the livers of WT and Nqo1$^{-/-}$ mice. When NADPH was used in lieu of NADH, a ~20 times lower rate of DCPIP reduction was recorded, which was also minorly sensitive to DIC. These findings reflect the presence of DCPIP reduction mechanisms dependent on NADH but not NADPH in mitochondria, a concept which is not at odds with the very rich redox matrix environment and its dependence on NADH/NAD$^+$ ratio. Exclusive mitochondrial Nqo1 activity can be calculated by subtracting the [control minus DIC-insensitive] DCPIP reduction rate obtained from WT mice minus the [control minus DIC-insensitive] rate obtained from Nqo1$^{-/-}$ mice for either NADH or NADPH. This calculation yielded evanescently small amounts (<1 nmol) of DCPIP reduced per minute per mg protein in mitochondria, which is in agreement with an average estimation of <15% of total (Conover and Ernster, 1962), (Ernster et al., 1962), (Stein and Kaplan, 1958), (Williams et al., 1959), (Dong et al., 2013). By using the cytochrome c reduction method with various quinones in freeze-thawn isolated mitochondria, a very high reduction rate was recorded for all quinones tested (figure panels 9.1H, I and J). Notably, if MNQ was the used quinone, there a statistically significant difference in diaphorase activity was observed by comparing WT with Nqo1$^{-/-}$ mice (figure panel 9.1J). When quinones other than MNQ were used, mitochondria from Nqo1$^{-/-}$ mice also showed diminished rates of cytochrome c reduction compared to those obtained from WT mice, albeit these differences did not reach statistical significance. As for the results obtained from cytosolic extracts, the mitochondrial matrix also harbors other than Nqo1 diaphorases which are also not dicoumarol-sensitive and exhibit higher affinities for redox-active compounds other than DCPIP.

9.2 Effect of quinones on NADH oxidation capacity of intact liver mitochondria from WT and Nqo1$^{-/-}$ mice

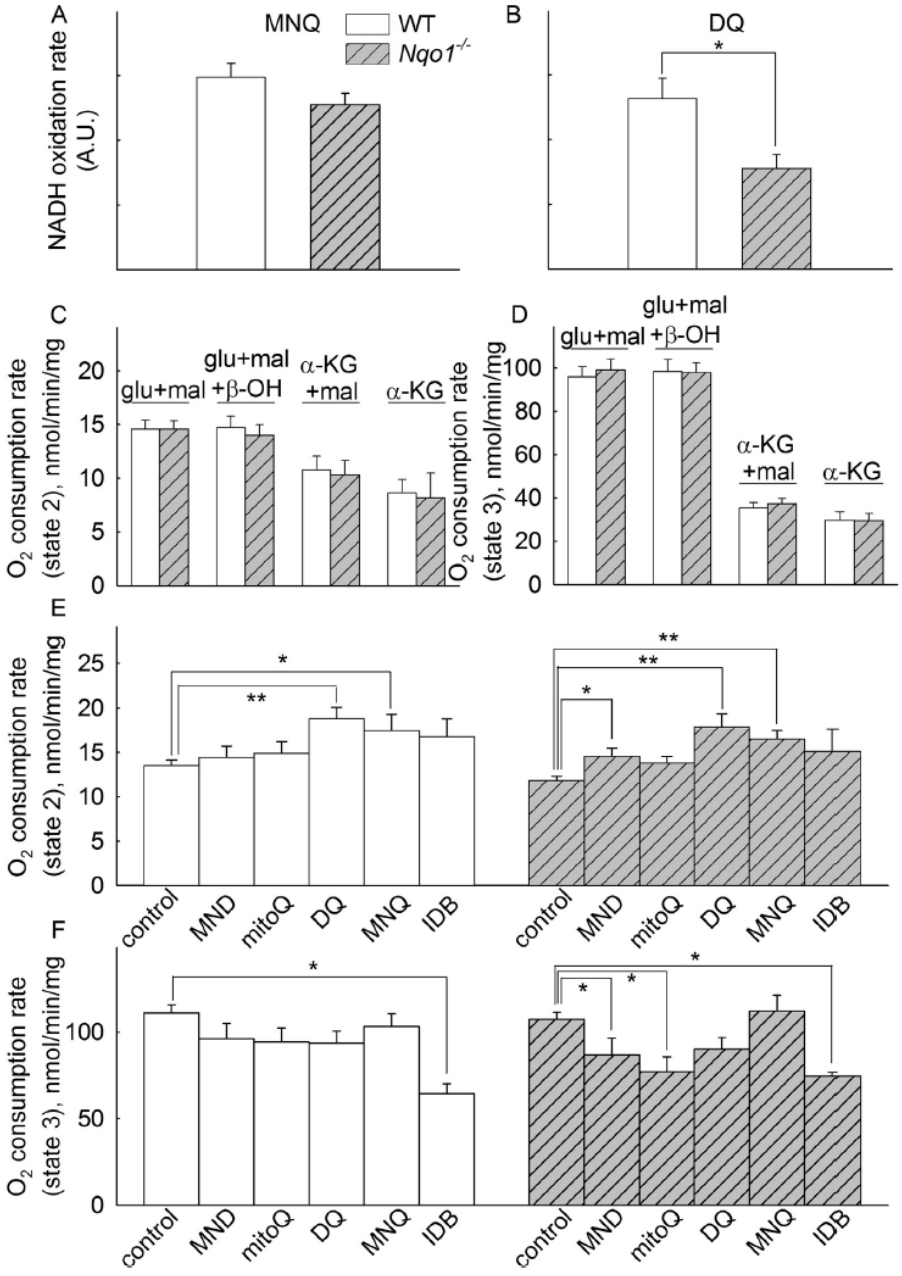

To examine the extent of contribution of mitochondrial Nqo1 on mitochondrial NADH oxidation capacity, the impacts of MNQ and DQ on NADH oxidation in intact mitochondria from the livers of WT and Nqo1$^{-/-}$ mice was investigated. As shown in figure panels 9.2A and 9.2B, addition of either MNQ and DQ caused NADH oxidation in mitochondria from WT (white bars) and Nqo1$^{-/-}$ (grey hatched bars) mice. The rates of NADH oxidation of mitochondria from Nqo1$^{-/-}$ mice were, however, lower than those from WT mice, and statistical significance was reached only in the case of DQ. These results imply that mitochondrial diaphorases other than Nqo1 can contribute to NADH oxidation supported by exogenous quinones, and that MNQ is rather a preferential substrate for Nqo1.

Figure 9.2. ***Effect of quinones on NADH oxidation (A, B) and respiratory capacity (C, D, E, F) of intact liver mitochondria from WT and Nqo1$^{-/-}$ mice****. White bars signify data from WT mice, grey-hatched bars from Nqo1$^{-/-}$ mice. The concentrations of quinones used for panels* ***A*** *and* ***B*** *were: 2-methoxy-1,4-naphtoquinone (MNQ): 100 μM; duroquinone (DQ): 0.2 mM. For panels* ***C*** *and* ***D*** *the concentrations of substrates were as follows: glutamate (glu): 5 mM; malate (mal): 5 mM; β-hydroxybutyrate (β–OH): 2 mM, α-ketoglutarate (α-Kg): 5 mM. The effect of quinones on mitochondria respiring on glutamate and malate and β-hydroxybutyrate is depicted on panels* ***E*** *(state 2) and* ***F*** *(state 3). The concentrations of quinones used for panels* ***E*** *and* ***F*** *were: menadione (MND): 10 μM; mitoquinone (mitoQ): 0.5 μM; duroquinone (DQ): 0.1 mM; 2-methoxy-1,4-naphtoquinone (MNQ): 10 μM; idebenone (IDB): 10 μM. Student's t-test (comparing two groups) or ANOVA on Ranks (comparing three or more groups); * implies p<0.05. ** implies p<0.001.*

9.3 Effect of quinones on respiratory capacity of intact mitochondria from WT and Nqo1$^{-/-}$ mice

Nqo1$^{-/-}$ mice are known to exhibit lower levels of nicotinamide nucleotides in their tissues (Gaikwad et al., 2001), (Iskander et al., 2005) which could affect the function of several NAD^+-dependent proteins (Asher et al., 2001) and as an extension of this, the overall process of mitochondrial respiration. However, as shown in figure panels 9.2C and 9.2D, by using four different substrate combinations (glutamate and malate, glutamate and malate and β-hydroxybutyrate, α-ketoglutarate and malate, α-ketoglutarate) all being NADH-linked substrates, no differences in either state 2 or state 3 respiration was observed in intact liver mitochondria from WT vs Nqo1$^{-/-}$ mice. Thus, our respiratory capacity data do not reflect a potential impact of diminished levels of nicotinamide nucleotides in the livers of NQO1$^{-/-}$ mice compared to controls. To examine the extent of contribution of mitochondrial Nqo1 on mitochondrial respiration as a function of exogenous quinones (in the presence of glutamate and malate and β-hydroxybutyrate), the impact of various quinones on oxygen consumption rates was investigated. As shown in figure panels 9.2E and 9.2F, some quinones led to a statistically significant increase vs decrease in state 2 and state 3 respiration, respectively, consistent with previous reports that some exhibit mitochondrial toxicities on recognized targets other than Nqo1 (Giorgio et al., 2012), (James et al., 2005). What is also apparent from figure panels 9.2C-F is that the respiratory control ratio (RCR) of ~8.5 (for glutamate and malate and β-hydroxybutyrate) for liver mitochondria obtained from both WT and Nqo1$^{-/-}$ mice affords the assurance that the lack of statistically significant difference in RCR between them is not due to poor mitochondrial quality that could potentially obliterate any variances.

9.4 Effect of targeted ETC inhibition on quinone-assisted respiration in intact mitochondria of WT and Nqo1$^{-/-}$ mice

When complex I is fully inhibited, respiration supported by quinones implies that they were reduced to the corresponding hydroquinone derivative which was later used by complexes III and IV. Quinone reduction may occur by many pathways such as dihydroorotate dehydrogenase (DHODH), glycerol-3-phosphate dehydrogenase (GPDH), electron-transferring-flavoprotein dehydrogenase (ETFDH), complex II, Nqo1 or other mitochondrial diaphorases. To interrogate the molecular entity reducing the quinones, we performed the following experiments: as shown in figure panel 9.3A, oxygen consumption rate of intact mitochondria was recorded, while ADP, rotenone, a quinone and inhibitors were sequentially added. Substrates (glutamate and malate) were already present in the medium. Dotted lines indicate oxygen concentration in the medium, and solid lines indicate oxygen consumption rate. Black line is a representative trace using liver mitochondria from WT mice, while red line represents a trace obtained by using Nqo1$^{-/-}$ mice. Briefly, state 2 respiration was recorded for 50 sec and then ADP (2 mM) was added leading to >8-fold increase in respiration rates. Subsequently, respiration was halted by the addition of rotenone (1 μM); the complete cessation of respiration is expected since, glutamate and malate are NADH-linked substrates, thus relying on NADH oxidation by complex I. Subsequently, a quinone was added (in panel A MNQ was added) which led to a small, but statistically significant increase in respiration. Then, the complex II inhibitor atpenin (atpn) was added that abolished this increase in respiration. Subsequently, the complex III and IV inhibitors stigmatellin and KCN, respectively, were added that led to no further decrease in respiration. The 'dip' in respiration rate upon addition of stigmatellin is artifactual, and it is due to brief introduction of oxygen in the air-tight chamber upon addition of the inhibitor through the syringe. Results from using menadione (MND), mitoQ, duroquinone (DQ), MNQ (10 μM), idebenone (IDB) and MNQ (50 μM) are

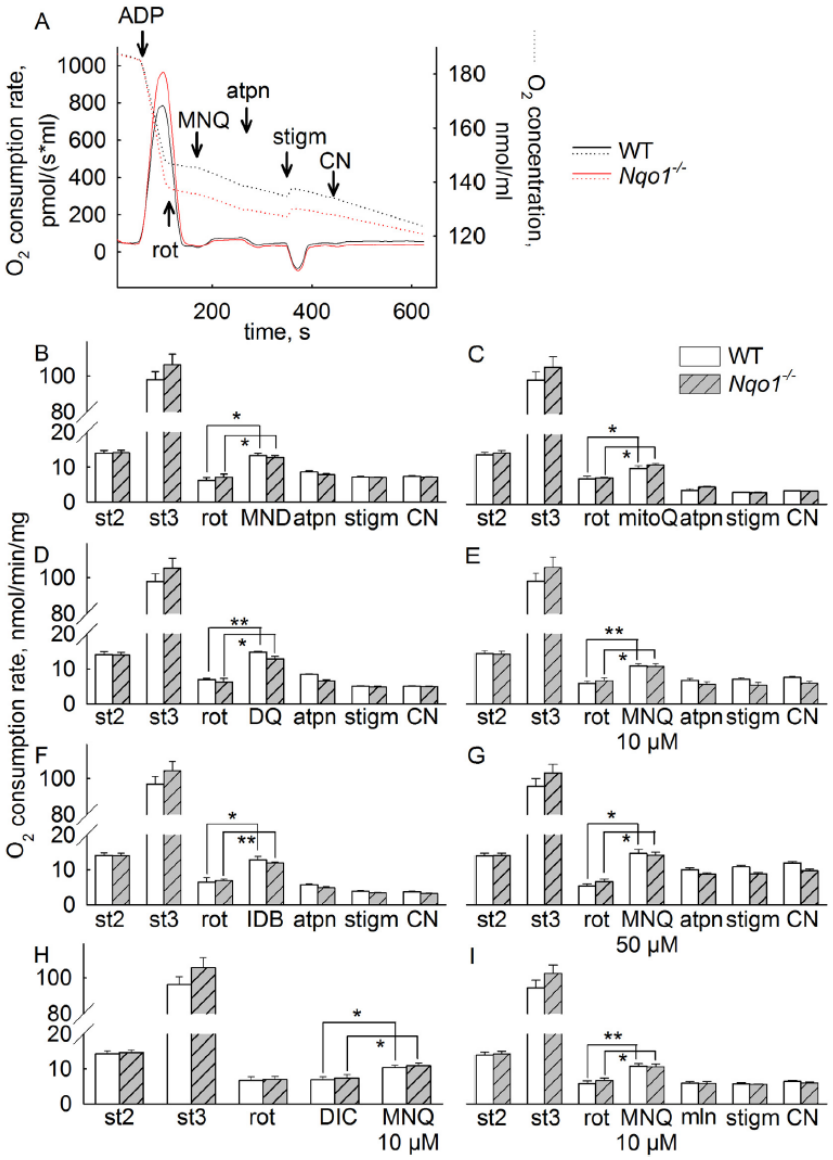

shown in figure panels 9.3B, C, D, E, F, and G, respectively. Those obtained from WT mice are depicted in white bars, and those from Nqo1$^{-/-}$ mice in grey hatched bars. As shown in figure panels 9.3B-G, addition of any quinone led to a statistically significant increase in respiration which was subsequently abolished by atpenin. The increase in respiration by MNQ in rotenone-treated mitochondria was also sensitive to inhibition by malonate, a competitive inhibitor of complex II, shown in figure panel 3I. To examine the contribution of dicoumarol-sensitive diaphorases in producing quinols for complex III supporting respiration, the effect of dicoumarol prior to addition of MNQ was tested. As shown in figure panel H, addition of dicoumarol after rotenone led to a protracted increase in respiration upon

Figure 9.3. ***Effect of targeted ETC inhibition on quinone-assisted respiration in intact mitochondria of WT and Nqo1$^{-/-}$ mice****. White bars or a black trace signify data from WT mice, grey-hatched bars or a red trace from Nqo1$^{-/-}$ mice. Panel* ***A*** *depicts a typical experiment recording oxygen concentration (dotted lines) and calculation of oxygen consumption rate (solid lines) in an air-tight chamber containing mitochondria and media as described in section 2.1.4. Panels* ***B-G*** *represent cumulated data of experiments performed as shown in panel* ***A****. Mitochondrial respiration was supported by 5 mM glutamate and 5 mM malate. The concentrations of quinones and inhibitors used were: menadione (MND): 10 µM; mitoquinone (mitoQ): 0.5 µM; duroquinone (DQ): 50 µM; 2-methoxy-1,4-naphtoquinone (MNQ): 10 or 50 µM as indicated in the panels; idebenone (IDB): 10 µM; rotenone (rot): 1 µM; atpenin (atpn): 1 µM; stigmatellin (stigm): 1 µM; KCN (CN): 1 mM; dicoumarol (DIC): 5 µM; malonate (mln): 5 mM. Student's t-test; * implies p<0.05. ** implies p<0.001.*

further addition of MNQ (compare figure panels 9.3H with 9.3E and 9.3I), albeit a statistically significant increase was recorded. Due to very low values of respiration after the addition of rotenone, statistical analysis comparing three groups (MNQ, MNQ+DIC, and MNQ+atpn) would require a very large number of experiments in order to reveal a statistical significance, and that was not performed. What is also apparent from all panels shown in figure 9.3 is that the absence of Nqo1 does not impact on

mitochondrial respiration supported by quinones in the presence of rotenone, and this was largely due to reduction of the quinones by complex II forming quinols, in turn supporting complexes III and IV.

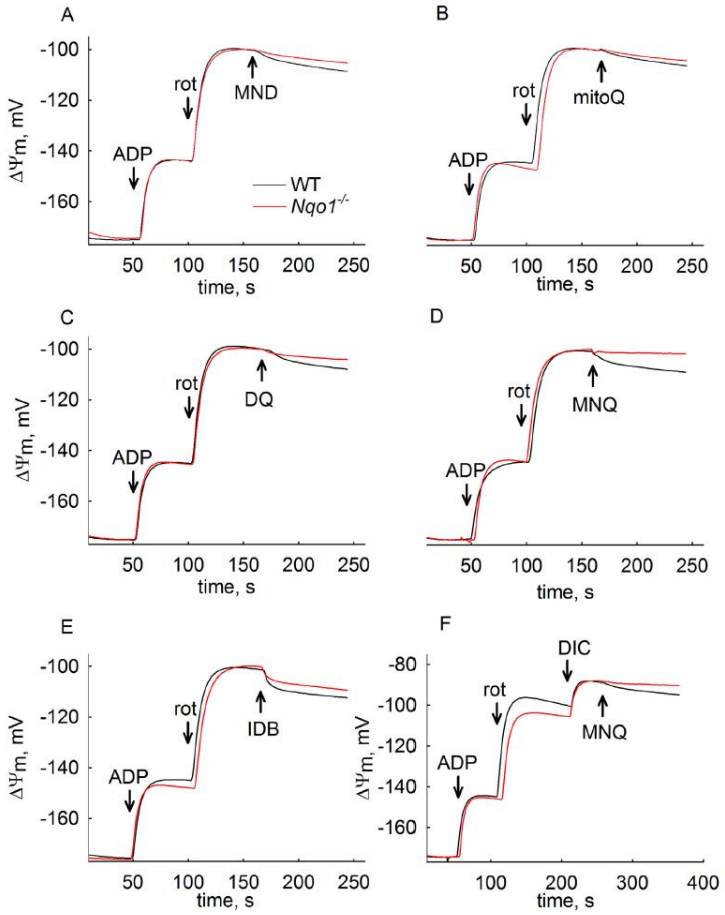

Figure 9.4. ***The contribution of mitochondrial Nqo1 on quinone-induced gain in ΔΨm in rotenone-treated mitochondria****. Reconstructed time courses of safranine O signal calibrated to ΔΨm in isolated liver mitochondria of WT (black traces) vs Nqo1$^{-/-}$ (red traces) mice respiring on 5 mM glutamate and 5 mM malate. ADP (2 mM) and rotenone (rot, 1 μM) were added where indicated. Quinones were added after rotenone where indicated. The concentrations of quinones used were: menadione (MND): 10 μM; mitoquinone (mitoQ): 0.5 μM; duroquinone (DQ): 50 μM; 2-methoxy-1,4-naphtoquinone (MNQ): 10 μM; idebenone (IDB): 10 μM; dicoumarol (DIC): 5 μM.*

9.5 The contribution of mitochondrial Nqo1 on quinone-induced gain in ΔΨm in rotenone-treated mitochondria

To address the extent of contribution of quinones generating ΔΨm and how much of this is due to Nqo1, we performed the following experiments: as shown in figure 9.4, membrane potential of liver mitochondria from WT (black traces) vs Nqo1$^{-/-}$ (red traces) mice was measured by calibrating safranine O fluorescence signals and the effect of sequential additions of the following compounds was recorded: mitochondria were allowed to fully polarize by using glutamate and malate (present in the medium prior to the addition of mitochondria); then, 2 mM ADP was added that led to a depolarization on the order of 25-30 mV. Subsequently, rotenone was added to inhibit complex I activity which led to a further depolarization, 'clamping' ΔΨm around -100 mV. The subsequent addition of a quinone the identity of which is written in the panels of figure 9.4 led to a small gain in ΔΨm in mitochondria from WT but not Nqo1$^{-/-}$ mice, except if the quinone was idebenone (IDB, figure panel 9.4E). In figure panel 9.4E, the effect of dicoumarol (DIC) is shown, which dampens the effect of MNQ on inducing ΔΨm gain (compare black traces in figure panels 9.4D with 9.4F).

9.6 Substrate-level phosphorylation supported by non-Nqo1 dicoumarol-sensitive mitochondrial diaphorases using endogenous quinones

In order to address the extent of contribution of mitochondrial Nqo1 providing NAD^+ to KGDHC yielding succinyl-CoA in turn supporting mSLP, we compared the adenine nucleotide translocase (ANT) directionalities of rotenone- and anoxia treated mitochondria from WT vs Nqo1$^{-/-}$ mice.

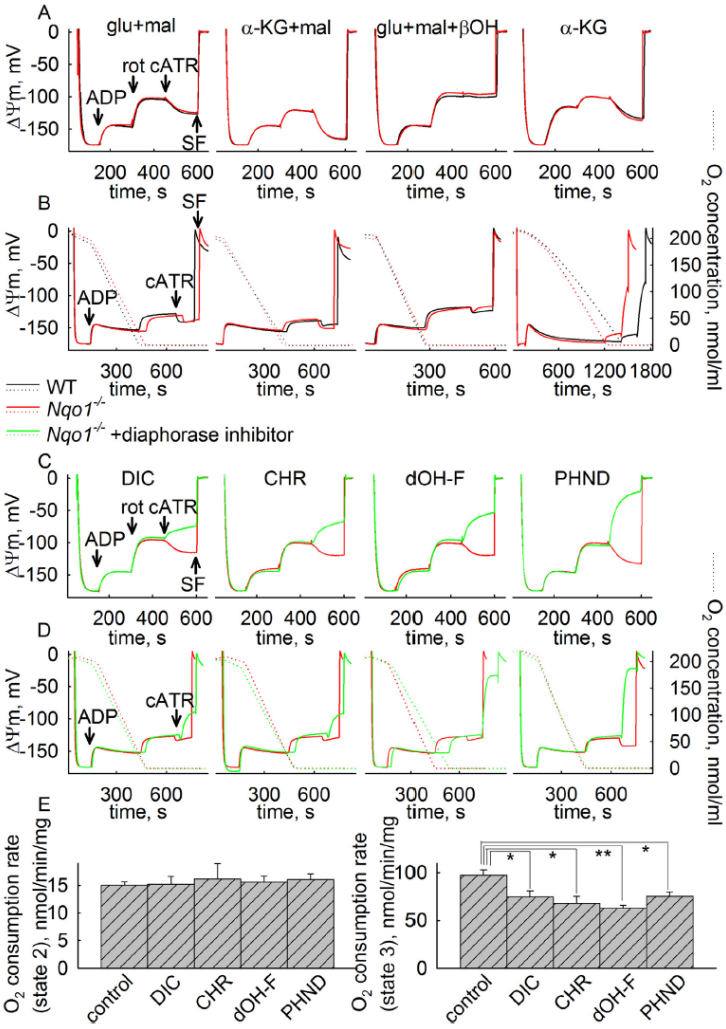

As shown in figure panels 9.5A (for rotenone-treatment) and 9.5B (anoxia), by using four different substrate combinations as for figure 9.2, mitochondria were initially allowed to fully polarize, while recording $\Delta\Psi m$; subsequently, ADP was added, which was allowed to be converted to ATP by respiring mitochondria. Then, respiration was halted either by rotenone (figure panel 9.5A) or upon consumption of all oxygen in the air-tight chamber (figure panel 9.5B). Subsequent inhibition of the adenine nucleotide translocase (ANT) by carboxyatractyloside (cATR) led to nearly identical changes in $\Delta\Psi m$ between WT and Nqo1$^{-/-}$, implying that mitochondrial Nqo1 is not critical for NAD^+ provision when mitochondria utilize endogenous quinones. However, even in mitochondria obtained from Nqo1$^{-/-}$ mice, the presence of dicoumarol or other diaphorase inhibitors (chrysin, dihydroxyflavone, phenindione, green traces in figure

Figure 9.5. ***Substrate-level phosphorylation supported by non-Nqo1 mitochondrial diaphorases using endogenous quinones and their sensitivity to diaphorase inhibitors****. Panel* ***A*** *shows reconstructed time courses of safranine O signal calibrated to $\Delta\Psi m$ in isolated liver mitochondria of WT (black traces) vs Nqo1$^{-/-}$ (red traces) mice treated with rotenone. ADP (2 mM) rotenone (rot, 1 μM) and carboxyatractyloside (cATR, 1 μM) were added where indicated on the left-most subpanel, and the same additions were made in all subsequent subpanels. Respiration substrates used are shown in the subpanels. Their concentrations were: glutamate (glu): 5 mM; malate (mal): 5 mM; β-hydroxybutyrate (β-OH): 2 mM, α-ketoglutarate (α-Kg): 5 mM. Panel* ***B*** *shows reconstructed time courses of safranine O signal calibrated to $\Delta\Psi m$ (solid traces) and parallel measurements of oxygen concentration in the medium (dotted traces) in isolated liver mitochondria of WT (black traces) vs Nqo1$^{-/-}$ (red traces) mice, and the effect of anoxia. Substrates were as in corresponding subpanels in panel* ***A****. Panels* ***C*** *and* ***D*** *depict the effect of diaphorase inhibitors in reconstructed time courses of safranine O signal calibrated to $\Delta\Psi m$ (solid traces) in isolated liver mitochondria of Nqo1$^{-/-}$ mice treated with rotenone or during anoxia. In red traces, inhibitors were absent. In green traces, diaphorase inhibitors were present as indicated in the panels, in the following concentrations: Dicoumarol (DIC): 5 μM; chrysin (CHR): 5 μM; dihydroxyflavone (dOH-F): 20 μM; phenindione (PHND): 10 μM. In panel* ***D*** *and all subpanels parallel measurements of oxygen concentration in the medium (dotted traces) are also shown. At the end of each experiment 1 μM SF 6847 was added to achieve complete depolarization. In panel* ***E****, the effect of diaphorase inhibitors as indicated in the panel (concentrations used as for panels* ***C*** *and* ***D****) on state 2 and state 3 respiration of liver mitochondria obtained from Nqo1$^{-/-}$ mice is shown. ANOVA on Ranks (comparing three or more groups); * implies p<0.05. ** implies p<0.001.*

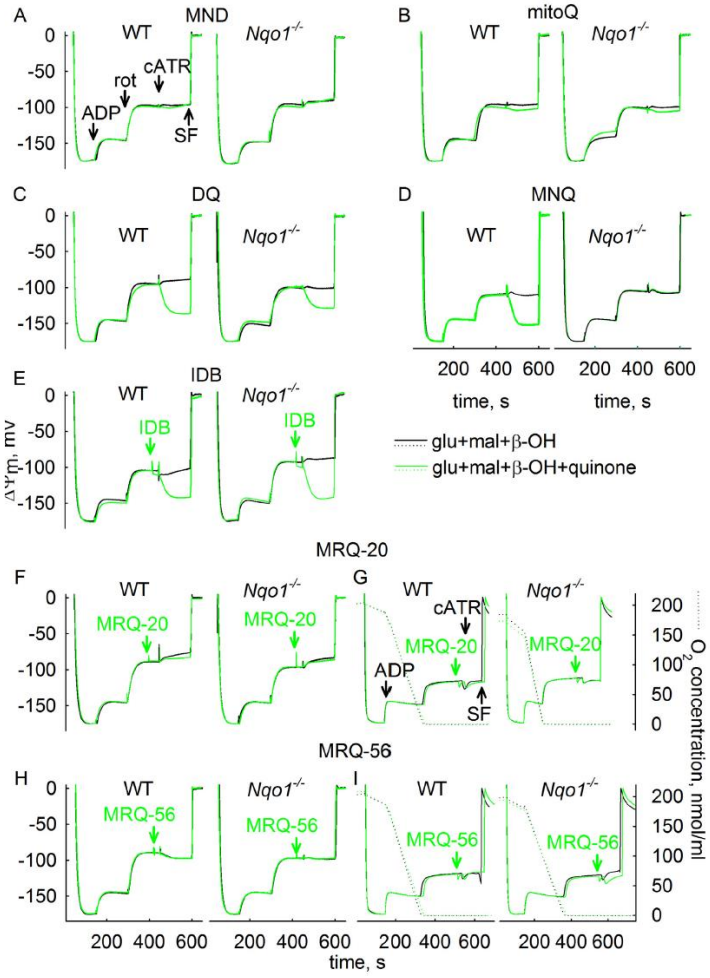

panel 9.5C) abolished mSLP, implying that some other diaphorase is responsible for this. Exactly as described for WT in (Kiss et al., 2014), diaphorase inhibitors worsened the cATR-induced changes in $\Delta\Psi m$ in anoxic mitochondria obtained from Nqo1$^{-/-}$ mice (figure panel 9.5D). Similar to the effect of diaphorase inhibitors on WT mitochondria, these compounds also moderately inhibited state 3 but not state 2 respiration (figure panel 9.5E), in mitochondria lacking Nqo1 expression.

9.7 MNQ supports mSLP preferably through Nqo1, in isolated mitochondria

The most important question of our study published in (Ravasz et al., 2018) was if mitochondrial Nqo1 is responsible for provision of NAD^+ to KGDHC yielding succinyl-CoA ultimately supporting mSLP as a function of exogenous quinones. To address this, we performed similar experiments as shown for the previous

Figure 9.6. ***Effect of diaphorase substrates on mSLP of liver mitochondria from WT and Nqo1$^{-/-}$ mice****. Panels* ***A-E****,* ***F*** *and* ***H*** *depict reconstructed time courses of safranine O signal calibrated to $\Delta\Psi m$ in isolated liver mitochondria of WT vs Nqo1$^{-/-}$ mice as indicated in the panels. ADP (2 mM) rotenone (rot, 1 μM), carboxyatractyloside (cATR, 1 μM) and idebenone (IDB, 10 μM) were added where indicated. Quinones (green traces) were used at the following concentrations: menadione (MND): 10 μM; mitoquinone (mitoQ): 0.5 μM; duroquinone (DQ): 50 μM; 2-methoxy-1,4-naphtoquinone (MNQ): 10 μM; idebenone (IDB): 10 μM; MRQ-20: 10 μM; MRQ-56: 10 μM. In panels* ***G*** *and* ***I*** *the effect of MRQ-20 and MRQ-56 is shown in mitochondria during anoxia. Parallel measurements of oxygen concentration in the medium are shown in dotted traces. Mitochondrial substrates were common for all experiments shown in the panels and were glutamate (glu, 5 mM) and malate (mal, 5 mM) and β-hydroxybutyrate (β-OH, 2 mM). At the end of each experiment 1 μM SF 6847 was added to achieve complete depolarization.*

figure, but mitochondrial substrates were glutamate and malate and β-hydroxybutyrate, a substrate combination in which by titrating β-hydroxybutyrate the mitochondrial NADH/NAD^+ ratio can be manipulated; as such, it is possible to achieve that by adding cATR after rotenone, no changes in $\Delta\Psi m$ can be observed because the value of this parameter is nearly identical to that of the reversal potential of the ANT (Chinopoulos, 2011a), (Chinopoulos, 2011b). This strategy was applied in liver mitochondria from WT and Nqo1$^{-/-}$ mice and as shown in figure panels 9.6A-F and 9.6H only MNQ did not show a rescue of mSLP in Nqo1$^{-/-}$ mitochondria (panel 9.6D, green and black trace), among all other quinones tested. This means, that NAD^+ provision by Nqo1 using MNQ as substrate, is preferably used for KGDHC

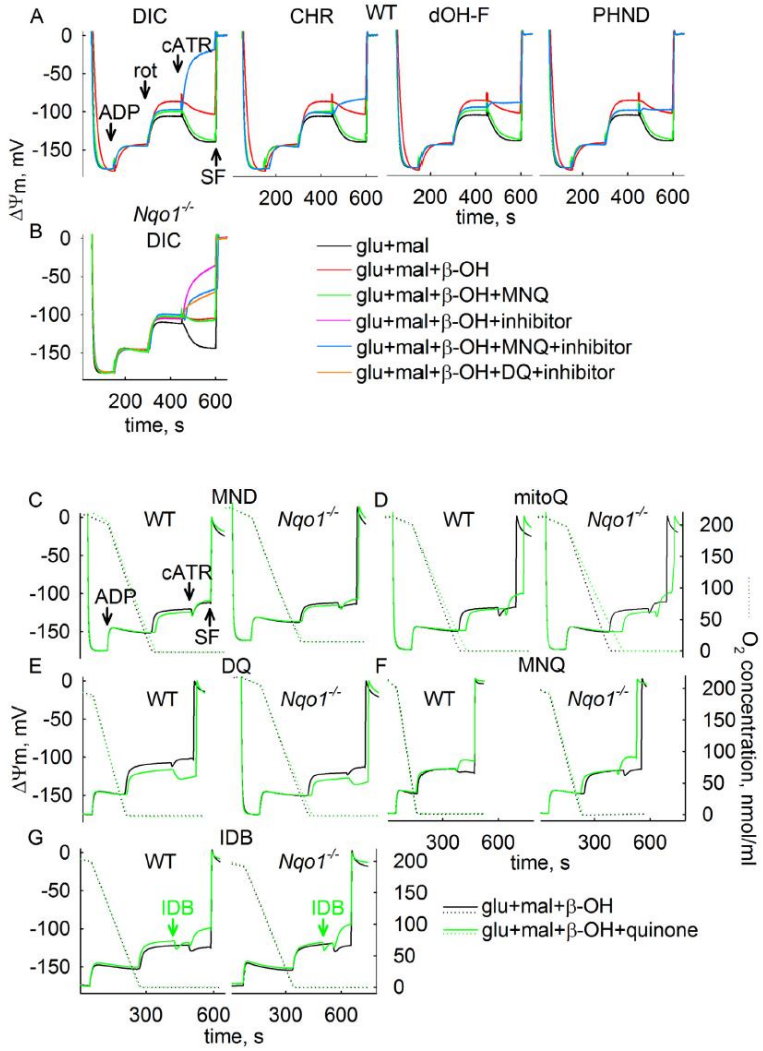

reaction forming succinyl-CoA, in turn supporting mSLP. The impact of idebenone analogues MRQ-20 and MRQ-56 on mSLP were also tested in anoxic mitochondria, and no effect of genetically deleting Nqo1 was found there either (figure panels 9.6G and 9.6I). Finally, just like for other diaphorase substrates, the effect of MNQ supporting mSLP in mitochondria from WT mice with an inhibited complex I by rotenone was sensitive to inhibition by several compounds tested, shown in figure panel 9.7A, respectively. To avoid trace clutter, in figure panel A the black, red, and green traces are identical for all subpanels. In a manner similar to that shown in (Kiss et al., 2014), quinones did not r escue mSLP in anoxic mitochondria, except for DQ (figure panels 9.7C-G).

Figure 9.7. ***Effect of diaphorase inhibitors on mSLP of liver mitochondria from WT and Nqo1$^{-/-}$ mice.*** *Panels **A** and **B** depict reconstructed time courses of safranine O signal calibrated to $\Delta\Psi m$ in isolated liver mitochondria of WT vs Nqo1$^{-/-}$ mice as indicated in the panels. ADP (2 mM) rotenone (rot, 1 μM) and carboxyatractyloside (cATR, 1 μM) were added where indicated. Mitochondrial substrates were common for all experiments shown in the panels and were glutamate (glu, 5 mM) and malate (mal, 5 mM) and β-hydroxybutyrate (β–OH, 2 mM). Inhibitors used are indicated in the panels, used in the following concentrations: Dicoumarol (DIC): 5 μM; chrysin (CHR): 5 μM; dihydroxyflavone (dOH-F): 20 μM; phenindione (PHND): 10 μM. When MNQ or DQ were additionally present, their concentrations were 10 μM. Panels **C-G** depict reconstructed time courses of safranine O signal calibrated to $\Delta\Psi m$ (solid lines) and parallel measurements of oxygen concentration in the medium (dotted lines) in isolated liver mitochondria of WT vs Nqo1$^{-/-}$ mice as indicated in the panels, and the effect of anoxia. ADP (2 mM) and carboxyatractyloside (cATR, 1 μM) were added where indicated. Quinones (green traces) were used at the following concentrations: menadione (MND): 10 μM; mitoquinone (mitoQ): 0.5 μM; duroquinone (DQ): 100 μM; 2-methoxy-1,4-naphtoquinone (MNQ): 10 μM; idebenone (IDB): 10 μM. At the end of each experiment 1 μM SF 6847 was added to achieve complete depolarization.*

9.8 Investigating the contribution of diaphorases including NQO1 to mSLP in HepG2 cells

To examine the extent of contribution of diaphorases including NQO1 to mSLP when mitochondria are in their natural environment, we used HepG2 cells. This cell line is known to express NQO1 at high levels (Erb et al., 2012). As shown in figure panel 9.8A, cells were permeabilized as described in (Kawamata et

al., 2010) and mSLP was evaluated by recording safranine O fluorescence signals converted to percentage and observing ANT directionality as a function of MNQ. Mitochondria were allowed to polarize by glutamate and malate and α-ketoglutarate (all at 5 mM); subsequently, ADP was added, leading to a physiological depolarization. Then, respiration was halted by rotenone leading to a further loss of ΔΨm.

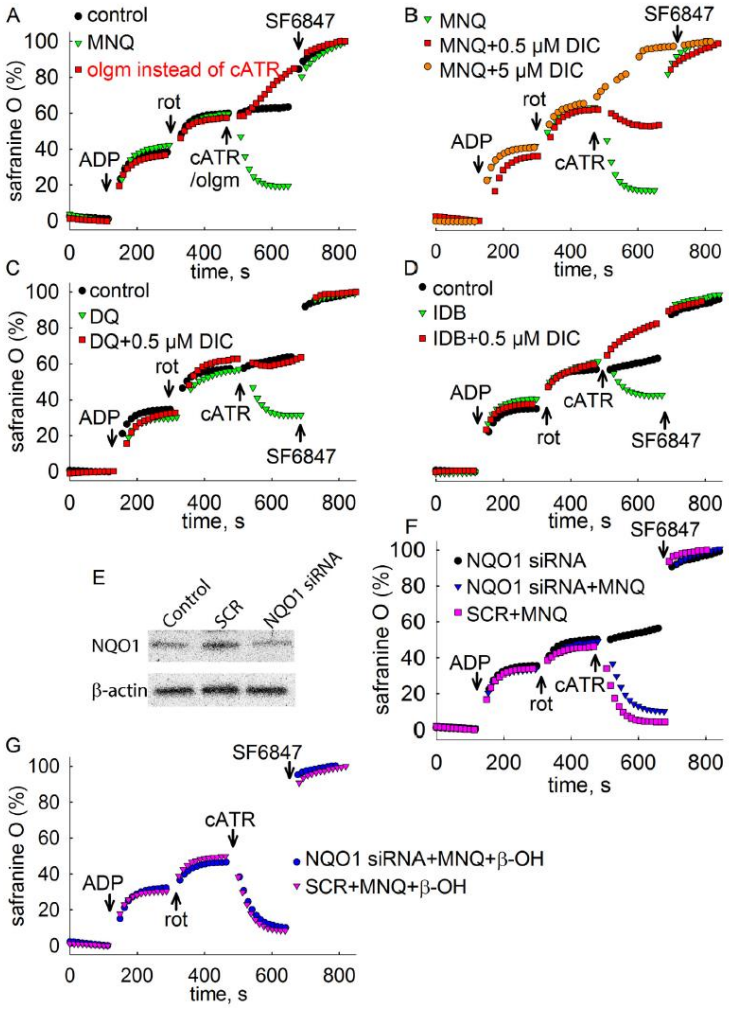

Subsequent inhibition of the ANT by carboxyatractyloside (cATR) led to unappreciable changes in safranine fluorescence, implying that HepG2 cells in permeabilized mode have lost some endogenous quinone (panel 9.8A, black circles), and ΔΨm is near the reversal potential of the translocase. By repeating the experiment but including MNQ (10 μM) in the media, *in situ* HepG2 mitochondria exhibited a robust cATR-induced repolarization (panel 9.8A, green triangles), implying a strong mSLP. By replacing cATR with oligomycin (olgm, 10 μM, panel 9.8A, red squares), a depolarization was evoked, confirming that the F_0-F_1 ATP synthase operated in reverse as a result of inhibition of complex I by rotenone. The effect of MNQ boosting mSLP in HepG2 cells through diaphorases was further supported by the finding that it was sensitive to inhibition by dicoumarol. As shown in figure panel 9.8B, the presence of 5

Figure 9.8. ***Effect of diaphorase substrates or inhibitors or siRNA directed against NQO1 on mSLP in permeabilized HepG2 cells.*** *All panels (except panel E) depict reconstructed time courses of safranine O signal expressed in percentage. ADP (2 mM) rotenone (rot, 5 μM) and carboxyatractyloside (cATR, 1 μM) or oligomycin (olgm, 10 μM) were added where indicated. Mitochondrial substrates were common for all experiments shown in the panels and were glutamate (5 mM) and malate (5 mM) and α-ketoglutarate (5 mM).β-hydroxybutyrate (β-OH, 4 mM) was additionally present in the experiments shown in panel G. Dicoumarol (DIC) was present at 5 or 0.5 μM concentration, as indicated in the panels. MNQ, DQ and IDB were at 10, 50 and 10 μM, respectively, present where indicated. Cells transfection with NQO1 siRNA or scramble (SCR) is described in section 2.1.9. At the end of each experiment 0.5 μM SF 6847 was added to achieve complete depolarization. In panel E, scanned images of Western blots of anti-NQO1 and β-actin for control, NQO1 siRNA and scramble (SCR)-transfected HepG2 cells is shown.*

μM dicoumarol (orange circles) or even 0.5 μM dicoumarol (red squares) abolished the effect of MNQ on boosting mSLP, i.e. cATR led to small repolarization or depolarization. The exact same effects were observed by replacing MNQ with duroquinone (DQ, 50 μM, panel 9.8C) or idebenone (IDB, 10 μM, panel 9.8D). Thus, from the experiments shown in figure panels 9.8A-D we concluded that quinones support

mSLP in a dicoumarol-sensitive manner, in permeabilized HepG2 cells. Of course, under these conditions it cannot be resolved if this effect was mediated by cytosolic and/or mitochondrial diaphorases. To address the extent of contribution of diaphorase activity attributed to NQO1, we transfected HepG2 cells with siRNA (or scramble RNA, SCR) directed against *NQO1*. As shown in the scanned western blots in figure panel 9.8E, by transfecting cells with siRNA against *NQO1* we were able to diminish NQO1 expression to a small extent. It is thus not surprising that by reducing NQO1 expression of this magnitude, an impact on mSLP supported by MNQ (figure panel 9.8F) cannot be observed, not even when β-OH is present in the media (4 mM) expected to increase matrix NADH/NAD^+ ratio (figure panel 9.8G), potentially weakening the ability of KGDHC to produce succinyl-CoA for succinate-CoA ligase. A similar phenomenon has been observed by the group of Gueven (Erb et al., 2012) where HepG2 cells transduced with lentivirus encoding *NQO1*-specific shRNA showed only a moderate reduction in rescuing ATP levels during rotenone treatment.

10 Two transgenic mouse models for β-subunit components of succinate-CoA ligase yielding pleiotropic metabolic alterations

In (Kacso et al., 2016) we addressed the concept that the directionality of succinate CoA ligase is critical for maintaining matrix adenine nucleotide levels during respiratory arrest, preventing mitochondria from importing and hydrolysing ATP that by i) generating two different transgenic mice colonies deficient in succinate CoA ligase expression and ii) experimenting on human fibroblasts from patients suffering from complete deletion of a critical subunit of succinate CoA ligase.

10.1 Succinate CoA ligase transgenic mice: general considerations

We generated transgenic mice lacking either one *Sucla2* or one *Suclg2* allele. Homozygous KO mice for either gene were never born. Results obtained from embryonic tissues of $Sucla2^{-/-}$ mice have been published in (Donti et al., 2014). In (Kacso et al., 2016) we quantitated the expression of SUCL subunits in mitochondria isolated from brains, hearts, and livers of 3-, 6- and 12 months old wild type and heterozygote mice. In the tissues of Sucla2 heterozygote mice we investigated respiration rates and membrane potential ($\Delta\Psi m$) for an array of mitochondrial substrates and various metabolic states, complex I, II, II/III and IV activities, as well as SLP during respiratory inhibition or true anoxia. SLP was further investigated during submaximal inhibition of SUCL by either itaconate or KM4549SC. We also compared mtDNA content, ATP-forming and GTP-forming SUCL activities, and blood levels of 20 carnitine esters. Furthermore, we cross-bred $Sucla2^{+/-}$ with $Suclg2^{+/-}$ mice, yielding double heterozygote $Sucla2^{+/-}$/$Suclg2^{+/-}$ mice, and investigated the expression of g1, g2 and a2 subunits, mtDNA content, blood carnitine esters and bioenergetic parameters.

10.2 Generation of Sucla2 mutant mice, Sucla2 mRNA quantification, SUCL subunit expression and enzymatic activities in WT vs $Sucla2^{+/-}$ mice

Mutant Sucla2 mice were generated using a gene-trapping technique (Hansen et al., 2008). Mice (strain C57BL/6N) were cloned from an ES cell line (IST10208H1; Texas A&M Institute for Genomic Medicine, TIGM). The ES cell clone contained a retroviral insertion in the Sucla2 gene (intron 4) identified from the TIGM gene trap database, and was microinjected into C57BL/6 albino host blastocysts to generate germline chimeras using standard procedures. The retroviral OmniBank Vector 76 contained a splice acceptor (Figure 10.1A) followed by a selectable neomycin resistance marker/LacZ reporter fusion

(bGeo) for identification of successful gene trap events further followed by a polyadenylation signal. Insertion of the retroviral vector into the Sucla2 gene led to the splicing of the endogenous upstream exons into this cassette to produce a fusion that leads to termination of further transcription of the

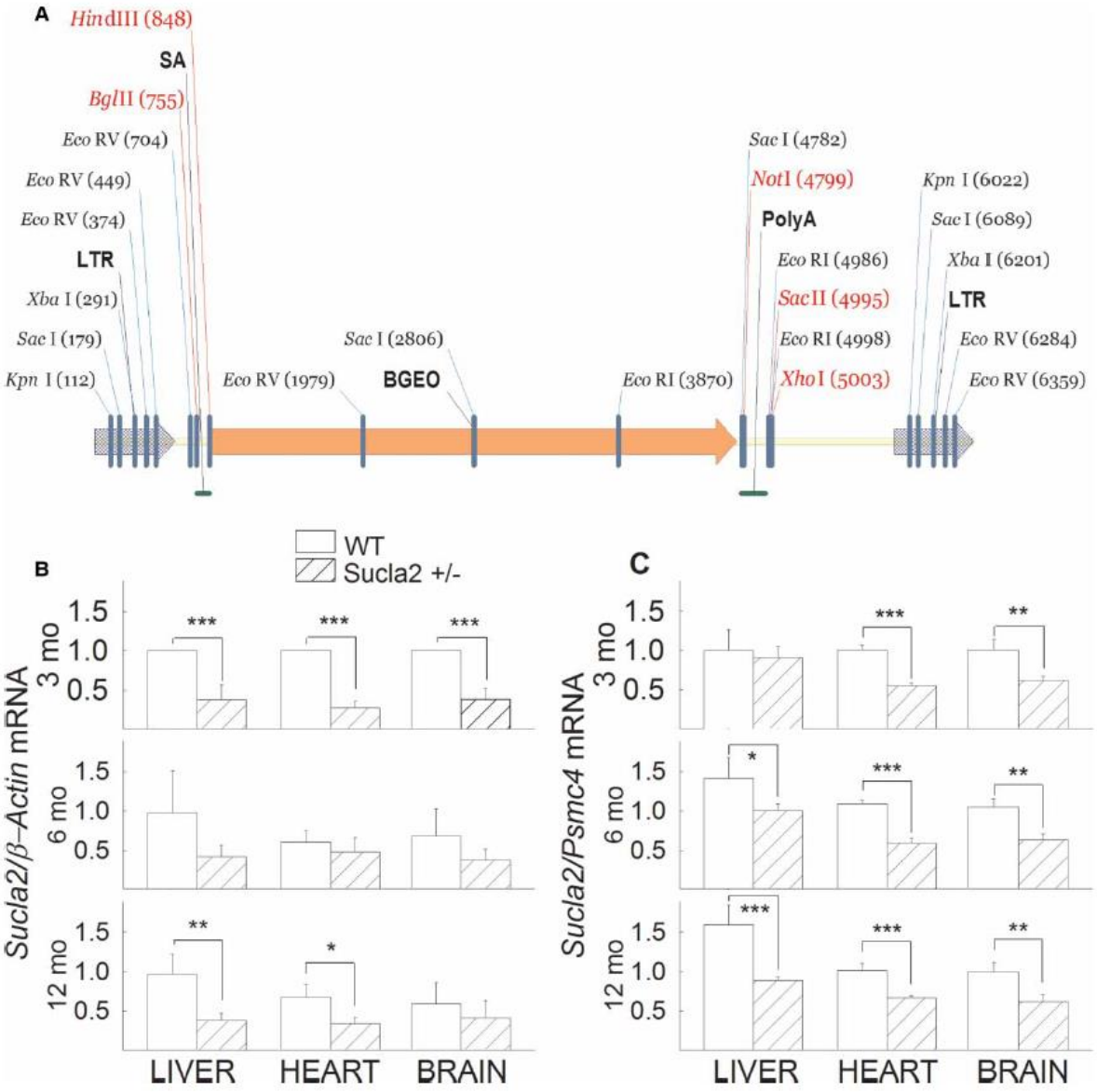

Figure 10.1. Generation of Sucla2 mutant mice and Sucla2 mRNA quantification. ***A****: Gene trap vector for generating Sucla2 mutant mice.* ***B****: Bar graphs of qPCR of Sucla2 mRNA ratioed to β-actin mRNA of 3-, 6- and 12 months old WT and Sucla2+/- mice from liver, heart and brain.* ***C****: Bar graphs of qPCR of Sucla2 mRNA ratioed to Psmc4 mRNA of 3-, 6- and 12 months old WT and Sucla2+/- mice from liver, heart and brain. * signifies p<0.05, ** p<0.01 and *** p<0.001. Data are S.E.M. from four different organs per animal group.*

endogenous Sucla2 exons downstream of the insertion. Chimeric males were bred to 129/SvEv females for germline transmission of the mutant Sucla2 allele. Total RNA was isolated from the livers, hearts and brains of 3-, 6-, and 12 months old WT and Sucla2$^{+/-}$ mice (four animals per group), and Sucla2 mRNA was quantified by qPCR, ratioed to β-actin (figure 10.1B) or Psmc4 expression (figure 10.1C). As shown in figures 10.1B and C, mRNA coding for Sucla2 was significantly decreased (26-71%) in the tissues obtained from Sucla2$^{+/-}$ mice, compared to those obtained from WT littermates. These results are in accordance to those obtained from immunodetection of Sucla2 subunit by Western blotting. These data

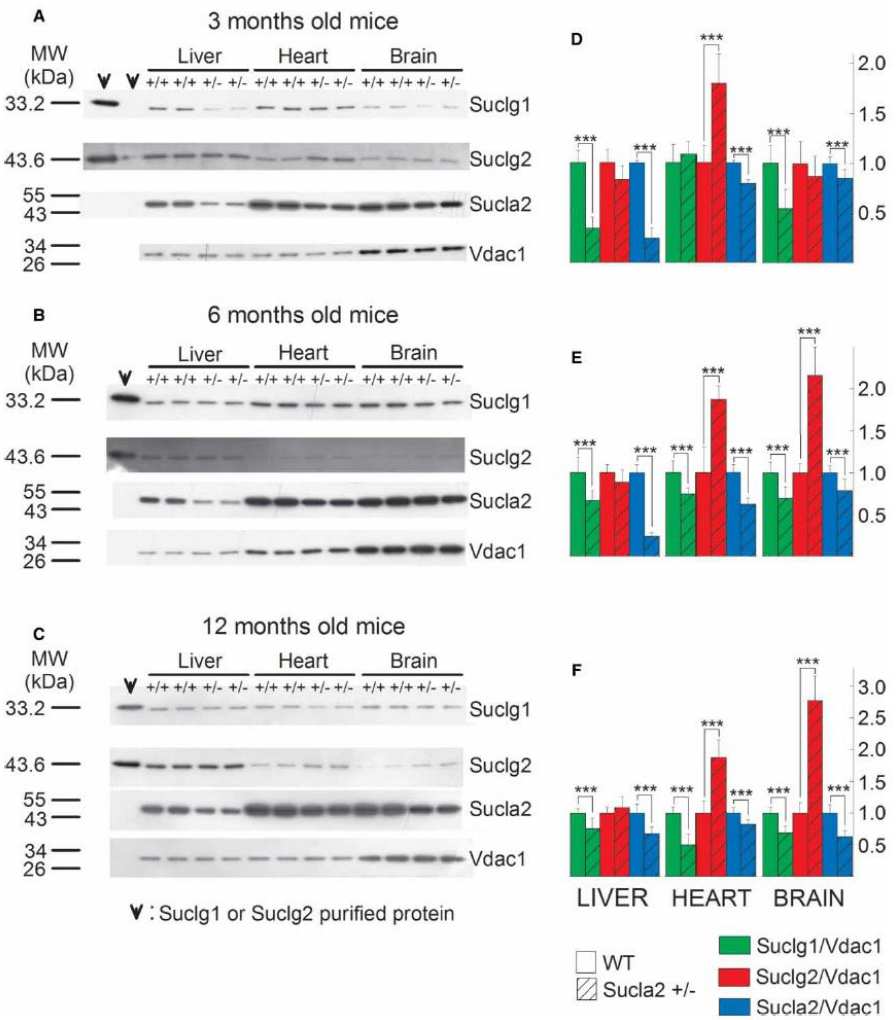

are depicted in figure 10.2. Mitochondria were prepared from the livers, hearts and brains of 3-, 6-, and 12 months old WT and Sucla2$^{+/-}$ mice and SUCLG1, SUCLA2, SUCLG2 and VDAC1 were immunodetected by Western blotting. Only 3.75 µg of purified mitochondria (pooled from mitochondria obtained from 8 organs per group) were loaded on each gel lane so as not to saturate the final ECL signals. Scanned images of representative Western blots are shown in figure 10.2A, B and C. As shown in the first two lanes of the left topmost panel in figure 10.2A, purified

Figure 10.2. SUCL subunit expression in WT vs Sucla2+/- mice. ***A, B, C****: Scanned images of Western blotting of purified SUCLG1 and SUCLG2 and mitochondria of 3-, 6- and 12 months old WT and Sucla2+/- mice from liver, heart and brain.* ***D, E, F****: Band density quantification of the scanned images shown in panels A, B, and C, respectively. Data were arbitrarily normalized to the average density of the first two bands of WT mice per organ. * signifies p<0.05, ** p<0.01 and *** p<0.001. Each Western blot lane contains mitochondria (except those containing the purified SUCLG1 or SUCLG2 proteins) pooled from two or four organs per animal group. Data shown in the bar graphs are S.E.M.*

recombinant SUCLG1 or SUCLG2 protein has been immunodetected. Purified protein has been loaded in the leftmost lane (30 ng) and in the adjacent right one (3 ng). In the remaining subpanels of figure 10.2A, B and C, 30 ng of either SUCLG1 or SUCLG2 was loaded. From the bands obtained from the purified proteins in relation to those obtained from the purified mitochondria, we deduce that i) the bands detected from the mitochondrial samples corresponding to slightly lower though nearly identical MW presumably due to the hexahistidine tags of the recombinant proteins, genuinely represent the sought proteins, and ii) the amount of either SUCLG1 or SUCLG2 in 3.75 µg of purified mitochondria corresponds to between 3-30 ng. The antibody directed against SUCLA2 protein has been validated in (Dobolyi et al., 2015b) using fibroblasts from a patient with *SUCLA2* deletion. Anti-VDAC1 was used as a loading control. As shown in figure panels 10.2A, B and C and from the quantification of the band densities in relation to that of VDAC1 shown in figure panels 10.2D, 10.2E and 10.2F, respectively, Sucla2$^{+/-}$ mice exhibited up to 76% decrease in Sucla2 expression, depending on the tissue and the age

of the mice. Concomitantly, Sucla2$^{+/-}$ mice exhibited up to 66 % reduction in Suclg1 protein, but also up to 177% increase in Suclg2 protein. In agreement with the above results regarding Suclg1/g2/a2 subunit quantification, ATP-forming activity of Sucla2$^{+/-}$ mice decreased, while GTP-forming activity increased, though only in heart mitochondria, for all ages (figure 10.3). From the above experiments we obtained the information that deletion of one *Sucla2* allele is associated with a decrease in Suclg1 expression and a rebound increase in Suclg2 expression, and this is reflected in reciprocal decrease *vs* increase in ATP-forming *vs* GTP-forming SUCL activity.

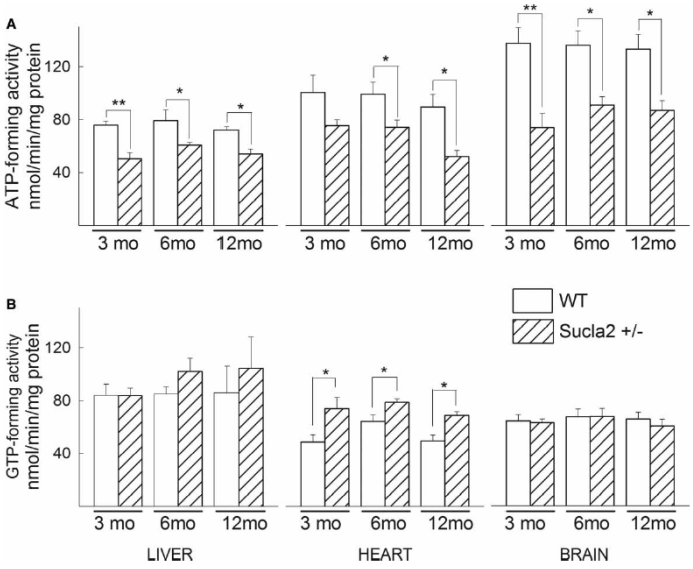

Figure 10.3. Bar graphs of ATP-forming SUCL activity from mitochondria of 3-, 6- and 12 months old WT (solid) and Sucla2+/- (striped) mice from liver, heart and brain. ***B****: Bar graphs of GTP-forming SUCL activity from mitochondria of 3-, 6- and 12 months old WT and Sucla2+/- mice from liver, heart and brain. * signifies p<0.05, ** p<0.01 and *** p<0.001. Data shown are S.E.M. from two or four pooled organs per animal group from four independent experiments.*

10.3 Generation of Suclg2 mutant mice, and characterization of SUCL subunit expression and enzymatic activities of WT vs Suclg2$^{+/-}$ mice

Mutant Suclg2 mice were generated using a gene-trapping technique (Araki et al., 2014), different than that for Sucla2 mutant mice. Mice (strain Albino B6) were cloned from an ES cell line (Ayu21-KBW131; Exchangeable Gene Trap Clones: EGTC). The ES cell clone contained a trap vector insertion in the Suclg2 gene (first intron) identified from the EGTC database, and was aggregated with morulae from ICR mice to generate germline chimeras using standard procedures. pU21-W (accession number: AB427140, 9333 bp) was a "promoter trap" vector with three stop codons which were arranged in upstream of the ATG of the beta-geo in all three frames, see figure 10.4A. Insertion of the trap vector into the Suclg2 gene led to the splicing of the endogenous upstream exons into this cassette to produce a fusion transcript that leads to termination of further transcription of the endogenous Suclg2 exons downstream of the insertion. Chimeric males were bred to C57BL/6N females for germline transmission of the mutant Suclg2 allele. To investigate the expression level of Suclg2 mRNA of Suclg2 heterozygote, the original ES cell line (Ayu21-KBW131: $^{+/-}$) was compared with the parental strain (KAB6: $^{+/+}$). mRNA was purified from parental ES cells ($^{+/+}$) and 21-KBW131 ($^{+/-}$). Suclg2 expression levels of these cells were analyzed by real time PCR using TaqMan Gene Expression Assays, XS, Suclg2 (AB, 4448892, FAM/MGB-NFQ) kit. Heterozygous ES cells showed almost half amount of Suclg2 mRNA compared to parent cells, figure 10.4B. Mitochondria were prepared from the livers, hearts and brains of 3-, 6-, and 12 months old WT and Suclg2$^{+/-}$ mice and SUCLG1, SUCLA2, SUCLG2 and VDAC1 were immunodetected by Western blotting. Scanned images of representative Western blots are shown in figure 10.5A, 10.5B and 10.5C. As shown in the first lane of the left topmost panel in figure 10.5A, purified recombinant SUCLG1 or SUCLG2 protein has been immunodetected. Purified protein has been loaded in the leftmost lane (30 ng). From the bands obtained from the purified proteins in relation to those obtained from the purified mitochondria, we deduce that i) the bands detected from the mitochondrial samples corresponding to slightly lower though nearly identical MW presumably due to

the hexahistidine tags of the recombinant proteins, genuinely represent the sought proteins, and ii) the amount of either SUCLG1 or SUCLG2 in 3.75 μg of purified mitochondria corresponds to slightly less than 30 ng.

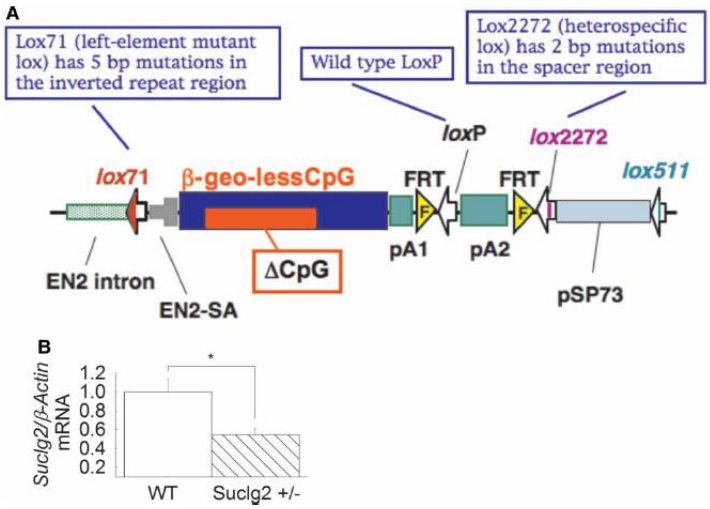

Figure 10.4. Generation of Suclg2 mutant mice and Suclg2 mRNA quantification. ***A****: Gene trap vector for generating Suclg2 mutant mice (adapted from http://egtc.jp/action/access/vector_detail?vector=pU-21W).* ***B****: Suclg2 heterozygote ES cell line (Ayu21-KBW131: +/-) was compared with parental strain (KAB6: WT). mRNA was purified from parental ES cells (+/+) and Suclg2 heterozygote (+/-). Suclg2 mRNA expression level were analyzed by real time PCR using TaqMan probe for Suclg2 (AB, 4448892, FAM/MGB-NFQ), and normalized by TaqMan probe for β-actin (AB, 4448489, VIC-MGB). *= 0.039. Data shown are S.E.M. from four independent experiments.*

Anti-VDAC1 was used as a loading control. As shown in figures 10.5A, B and C and from the quantification of the band densities in relation to that of VDAC1 shown in figure 10.5D, E, and F, respectively, Suclg2$^{+/-}$ mice exhibited an up to 56% decrease in Suclg2 expression, a mostly insignificant decrease in Suclg1 expression, and no rebound increase in Sucla2 expression. The variability in the decrease in Suclg2 (and Sucla2) expression in these transgenic mouse lines probably reflects the 'leakiness' of the mutant allele that could produce wild-type mRNAs by alternative splicing around the gene trap cassette, as it has been shown in several similar situations (Voss et al., 1998), (Gonzalez-Billault et al., 2000), (Salminen et al., 2000), (Pires-daSilva et al., 2001). From the above experiments we obtained the information that deletion of one *Suclg2* allele was not associated with the rebound effects as seen in the Sucla2$^{+/-}$ mice. Because of the lack of a rebound effect on Sucla2 expression in Suclg2$^{+/-}$ mice, in conjunction to the fact that SUCLG2 deficiency has never been reported in humans, this transgenic strain was further investigated only regarding respiration and SLP during chemical or true anoxia.

10.4 Characterization of SUCL subunit expression and enzymatic activities of Sucla2$^{+/-}$/Suclg2$^{+/-}$ double heterozygote mice

Since the deletion of one *Sucla2* allele led to a rebound increase in Suclg2 expression, we investigated the effect of combined loss of one allele from each *Sucla2* and *Suclg2* genes. Thus, we cross-bred Sucla2$^{+/-}$ mice with Suclg2$^{+/-}$ mice, which yielded viable Sucla2$^{+/-}$/Suclg2$^{+/-}$ offsprings. The results of Western blotting of mitochondria isolated from the brains, livers, hearts of 12 months old WT vs Sucla2$^{+/-}$/Suclg2$^{+/-}$ mice probing for SUCLG1, SUCLG2 and SUCLA2 (and VDAC1 as loading control) are shown in figure 10.6A. The quantification of the band densities in relation to that of VDAC1 is shown in figure 10.6B. As shown in figure 10.6B, deletion of one *Sucla2* allele still yields a rebound increase in Sucgl2 expression in liver, albeit protracted because these mice also lack one *Suclg2* allele. By the same token, the anticipated decrease (due to deletion of one *Suclg2* allele) in Suclg2 expression is lost, presumably because of the effect(s) of deletion of the *Sucla2* allele, antagonizing the diminution in expression of Suclg2. These results are also reflected from the measured ATP- and GTP-forming activities of WT vs

Sucla2$^{+/-}$/Suclg2$^{+/-}$ mice, shown in figures 10.6C, and 10.6D, respectively: ATP-forming activity is diminished in the double heterozygote mice compared to WT littermates due to loss of one *Sucla2* allele, however, GTP-forming activity remains unaffected, despite the loss of one *Suclg2* allele. From these experiments we deduce that the effect(s) of deleting one *Sucla2* allele upregulating Suclg2 expression are so dominant that adequately antagonize or even supersede the effect(s) of a concomitant loss of one *Suclg2* allele.

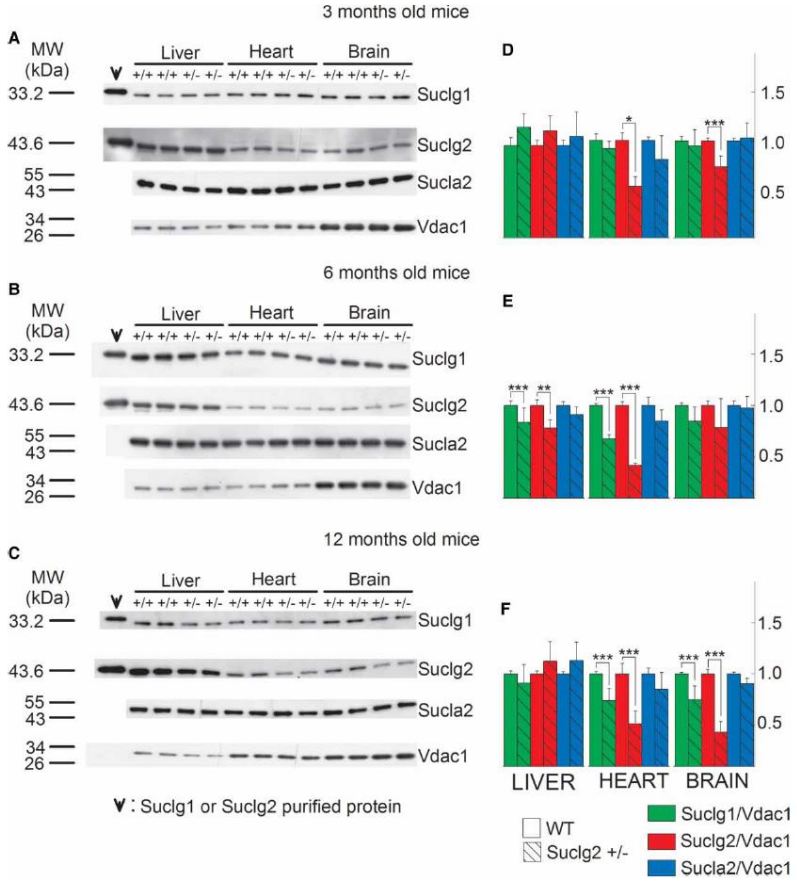

10.5 The effect of deleting one Sucla2 allele on mitochondrial respiration

Mitochondria were prepared from the livers, hearts and brains of 3-, 6-, and 12 months old WT and Sucla2$^{+/-}$ mice and state 2 and 3 (induced by addition of 2 mM ADP) of mitochondrial respiration was evaluated using an array of substrates, as indicated in the panels of figure 10.7. As shown in figure 10.7, with the exception of one combination for state 2 respiration and five combinations for state 3 respiration, the remaining 84 combinations of substrates per

Figure 10.5. SUCL subunit expression in WT vs Suclg2+/- mice. ***A, B, C****: Scanned images of Western blotting of purified SUCLG1 and SUCLG2 and mitochondria of 3-, 6- and 12 months old WT and Suclg2+/- mice from liver, heart and brain.* ***D, E, F****: Band density quantification of the scanned images shown in panels A, B, and C, respectively. Data were arbitrarily normalized to the average density of the first two bands of WT mice per organ. * signifies p<0.05, ** p<0.01 and *** p<0.001. Each Western blot lane contains mitochondria (except those containing the purified SUCLG1 or SUCLG2 proteins) pooled from two or four organs per animal group. Data shown in the bar graphs are S.E.M.*

tissue of origin per age of mice did not reveal statistically significant differences between WT and Sucla2$^{+/-}$ mice. From these experiments we concluded that a partial decrease in Sucla2 expression did not impact negatively on mitochondrial respiration to an appreciable extent. This lack of effect could be also explained by the rebound increases in Suclg2 expression and associated increases in GTP-forming SUCL activity that in turn could impact on mitochondrial ATP output through the concerted action of the nucleotide diphosphate kinase. In addition to this, it is possible that the flux control coefficient of SUCL regarding mitochondrial respiration is small enough so that inhibition of this enzyme to the extent observed hereby in the Sucla2$^{+/-}$ transgenic mice was insufficient to warrant a measurable effect on mitochondrial respiration.

10.6 The effect of deleting one Sucla2 allele on ΔΨm and SLP during inhibition of complex I by rotenone or true anoxia

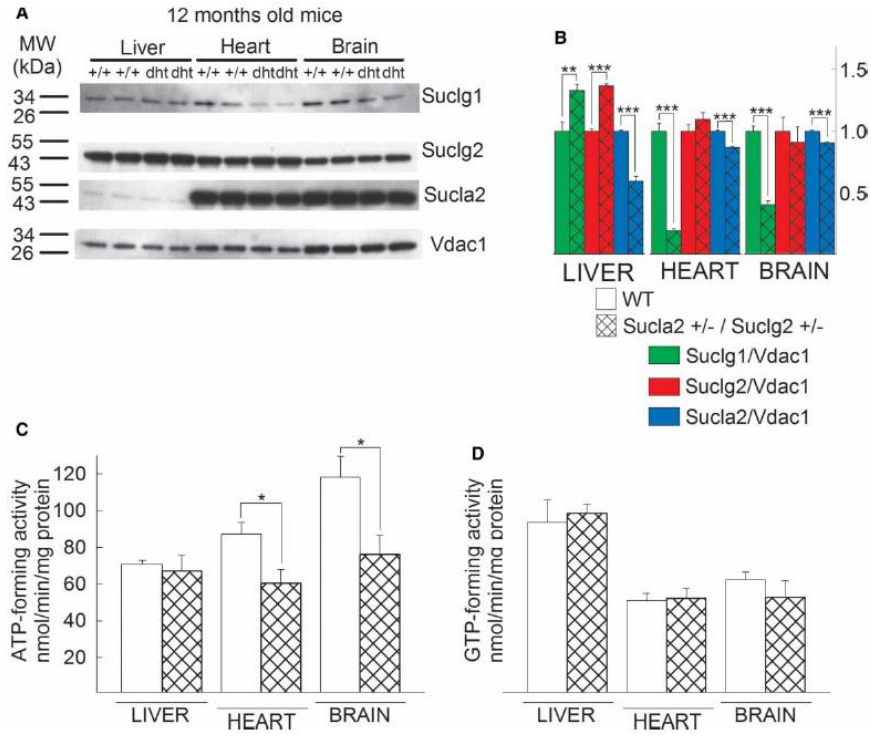

Figure 10.6. Characterization of SUCL subunit expression of Sucla2+/-/Suclg2+/- mice (dht: double heterozygote) and SUCL enzymatic activities. ***A****: Scanned images of Western blotting of 12 months old WT and Sucla2 +/- / Suclg2+/- mice from liver, heart and brain.* ***B****: Band density quantification of the scanned images shown in panel* ***A****. Data were arbitrarily normalized to the average density of the first two bands of WT mice per organ. * signifies p<0.05, ** p<0.01 and *** p<0.001. Each Western blot lane contains mitochondria pooled from two or four organs per animal group. Data shown in the bar graph are S.E.M.* ***C****: Bar graphs of ATP-forming SUCL activity from mitochondria of 12 months old WT (solid) and Sucla2+/-/Suclg2+/- (double striped) mice from liver.* ***D****: Bar graphs of GTP-forming SUCL activity from mitochondria of 12 months old WT (solid) and Sucla2+/-/Suclg2+/- (double striped) mice from liver. Data shown in panels C and D are S.E.M. from two or four pooled organs per group from four independent experiments.*

In (Kacso et al., 2016) we evaluated matrix SLP during either inhibition of complex I by rotenone or during anoxia. Mitochondria were prepared from the livers, hearts and brains of 3-, 6-, and 12 months old WT (black traces) and Sucla2$^{+/-}$ (red traces) mice and ΔΨm was evaluated using an array of substrates. Time-lapse recordings of safranine O fluorescence reflecting ΔΨm (while measuring oxygen concentration in the same sample) was achieved by using the recently developed O2k-Fluorescence LED2-Module of the Oxygraph-2k (Oroboros Instruments, Innsbruck, Austria). Mitochondria were allowed to deplete the oxygen dissolved in the air-sealed chamber and additions of chemicals through a tiny-bore hole did not allow re-oxygenation of the buffer from the ambient atmosphere. The sequences of additions were as follows: Mitochondria were added in 2 ml of buffer containing substrates as indicated in the panels, and allowed to fully polarize (solid traces). State 3 respiration was initiated by ADP (2 mM) depolarizing mitochondria; within a few minutes (depending on the substrates) mitochondria became anoxic as verified by recording 'zero' levels of dissolved oxygen in the chamber (dotted traces). Anoxia also coincided with the onset of an additional depolarization leading to a clamp of ΔΨm. Subsequent addition of cATR (1 μM) caused either a moderate re- or depolarization, implying that the ANT was operating in the forward- or reverse mode, respectively. Further addition of the uncoupler SF 6847 (1 μM) was subsequently used in order to cause a complete collapse of ΔΨm and assist in the calibration of the fluorescence signal. As shown in supplementary figures 10.1A, 10.1B, 10.1C, 10.2C and 10.2D, there were no differences between mitochondria from WT and Sucla2$^{+/-}$ mice. Likewise, when SLP was examined during inhibition of the

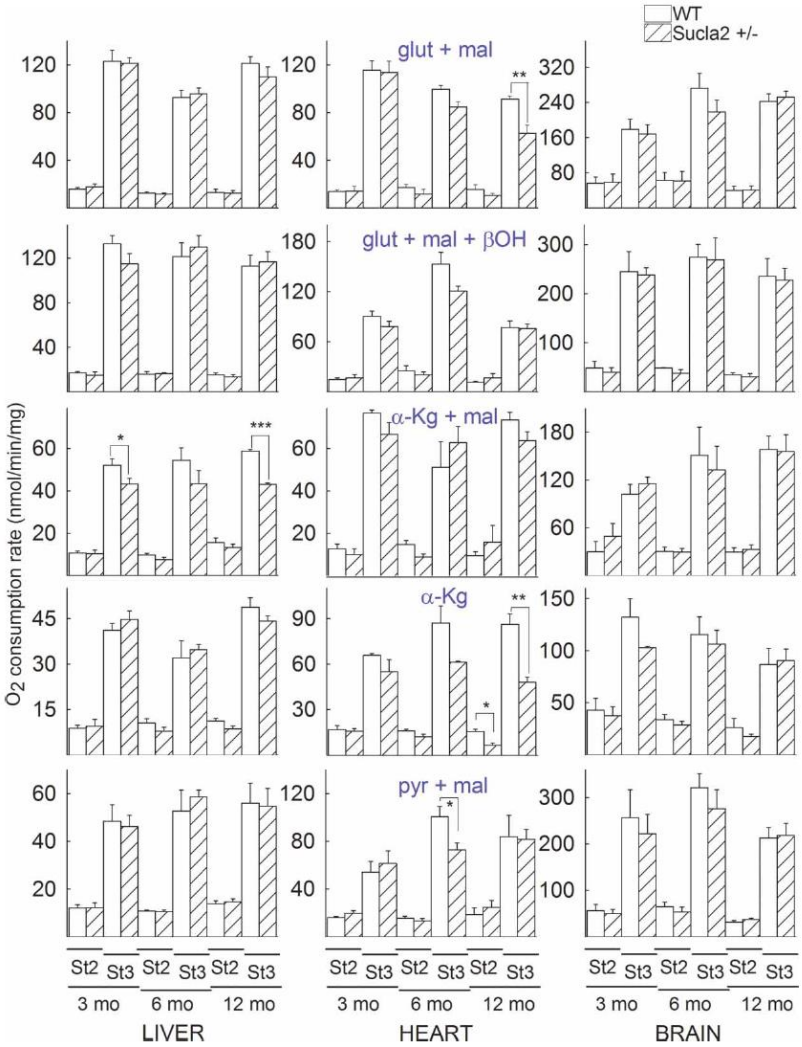

*Figure 10.7. Bar graphs of measurements of oxygen consumption in the medium containing isolated mitochondria of -3, 6- and 12 months old WT (solid) and Sucla2+/- (striped) mice from liver, heart and brain. Substrate combinations used as indicated in the panels, all at concentration of 5 mM, except β-hydroxybutyrate (βOH) that was 4 mM. St2: state 2 respiration; St3: state 3 respiration. * signifies p<0.05, ** p<0.01 and *** p<0.001. Data shown are S.E.M. from two or four pooled organs per animal group from four independent experiments.*

respiratory chain by rotenone instead of anoxia, no differences between WT and Sucla2$^{+/-}$ mice mitochondria were observed (supplementary figures 10.2A, 10.2B, 10.3A, 10.3B and 10.3C). Similarly to the results obtained from mitochondrial respiration, the lack of effect could be also explained by the rebound increases in Suclg2 expression and associated increases in GTP-forming SUCL activity that in turn could impact mitochondrial ATP output through the concerted action of the nucleotide diphosphate kinase or, it is possible that the flux control coefficient of SUCL regarding mitochondrial respiration is small enough so that inhibition of this enzyme to the extent observed hereby in the Sucla2$^{+/-}$ transgenic mice was insufficient to warrant a measurable effect. By the same token, no differences in mitochondrial respiration or SLP during chemical or true anoxia was observed by comparing Suclg2$^{+/-}$ versus WT littermate mice (supplementary figures 10.S.4, 10.S.5 and 10.S.6). By comparing WT vs Sucla2$^{+/-}$/Suclg2$^{+/-}$ double heterozygote mice, we also observed no difference in the ability of SLP to maintain ANT in the forward mode, with the exception of using glutamate + malate + β-hydroxybutyrate as substrates (a substrate combination that does not favor SLP) in liver mitochondria, where we obtained the full spectrum of results, ranging from maintenance of SLP, to its abolition (supplementary figure 10.S.7). However, a concomitant submaximal inhibition of SUCL by KM4549SC or itaconate (Nemeth et al., 2016) revealed that mitochondria obtained from Sucla2$^{+/-}$ mice are less able to perform SLP (figure 10.8A, 10.8B, and supplementary figures 10.S.8, 10.S.9 and 10.S.10). The argument that SUCLA2 is critical for SLP is also strengthened by the findings where, by applying the 'bio-sensor test' in permeabilized fibroblasts from a control subject vs a patient suffering from complete deletion of *SUCLA2* (Miller et al., 2011), the *in situ* mitochondria from the patient are unable to perform SLP during respiratory inhibition by rotenone (figure 10.8C).

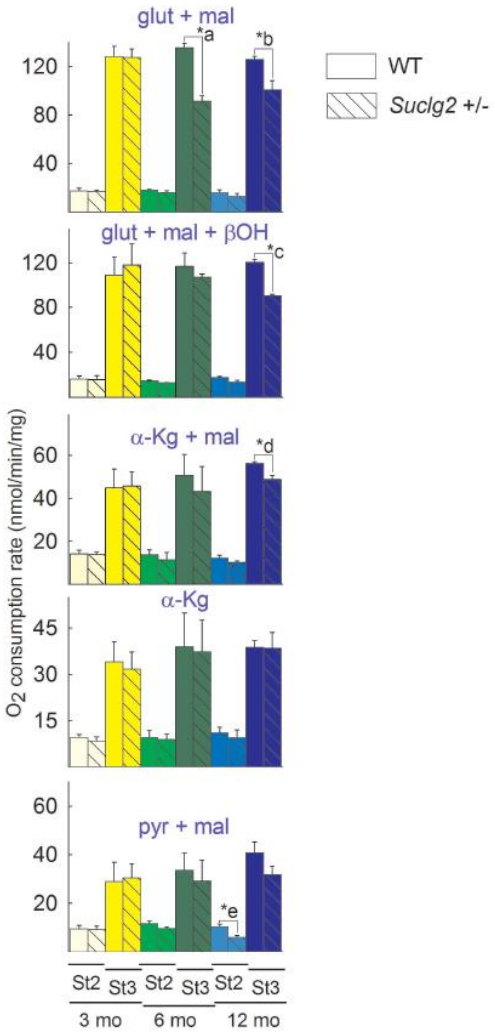

10.7 The effect of deleting one Sucla2 allele on ETC/CS

Mindful that some patients suffering from SUCLA2 deficiency exhibited decreases in the activities of electron transport chain complexes, we investigated the effect of deleting one *Sucla2* allele in mice on complex I, II, II/III and IV activities, ratioed to citrate synthase activity. As shown in figure 10.9, mitochondria from all tissues and all ages revealed no statistically significant differences between WT and Sucla2$^{+/-}$ mice. However, by comparing WT vs Sucla2$^{+/-}$/Suclg2$^{+/-}$ double heterozygote mice, there was a statistically significant increase in succinate dehydrogenase activity in heart mitochondria, echoing the results of Donti et al in Sucla2$^{-/-}$ mouse embryonic fibroblasts in (Donti et al., 2014).

10.8 The effect of deleting one Sucla2 allele on mtDNA

Because of the involvement of SUCL in the maintenance of mtDNA, we compared the amount of mtDNA in the tissues of WT vs Sucla2$^{+/-}$ mice. As shown in figure 10.10, relative mtDNA content from the livers, hearts and brains of 3-, 6- and 12 months old mice was quantitated by real time-PCR. It is evident that there is a moderate but statistically significant decrease in mtDNA in all tissues of 3 months old mice, and in the brains of 12 months old mice. Furthermore,

*Figure 10.S.4. Bar graphs of measurements of oxygen consumption in the medium containing isolated mitochondria of -3, 6- and 12 months old WT (solid) and Suclg2+/- (striped) mice from liver. Substrate combinations used as indicated in the panels, all at concentration of 5 mM, except β-hydroxybutyrate (β-OH) that was 4 mM. St2: state 2 respiration; St3: state 3 respiration. *a<0.001, *b=0.035, *c=0.001, *d=0.013, *e=0.022. Data shown are S.E.M. from at least four independent experiments.*

by comparing WT vs Sucla2$^{+/-}$/Suclg2$^{+/-}$ double heterozygote mice, there was a much greater statistically significant decrease in mtDNA in the livers and brains of double heterozygote mice, compared to wild-type littermates.

10.9 The effect of deleting one Sucla2 allele on blood carnitine esters

Finally, in view of the association of SUCL activity to the catabolism of a particular group of biomolecules converging to succinyl-CoA through propionyl-CoA and methylmalonyl-CoA which are in equilibrium with their carnitine esters, we measured the levels of 20 carnitine esters in the blood of mice. As shown in figure 10.11, there are statistically significant increases in 36 out of 63 comparisons of carnitine esters in the blood of Sucla2$^{+/-}$ mice from all age groups compared to that from WT mice, but also 6 occasions in which carnitine esters of Sucla2$^{+/-}$ mice is decreased compared to those of WT mice. What is also noteworthy is that although SUCLA2 deficiency in humans is associated with elevations of C3 and C4-DC

levels, in the Sucla2$^{+/-}$ mice there was elevation of several additional esters including those encompassing long-chain fatty acid chains (C16-OH, C18:1, C:18, and C18-OH).

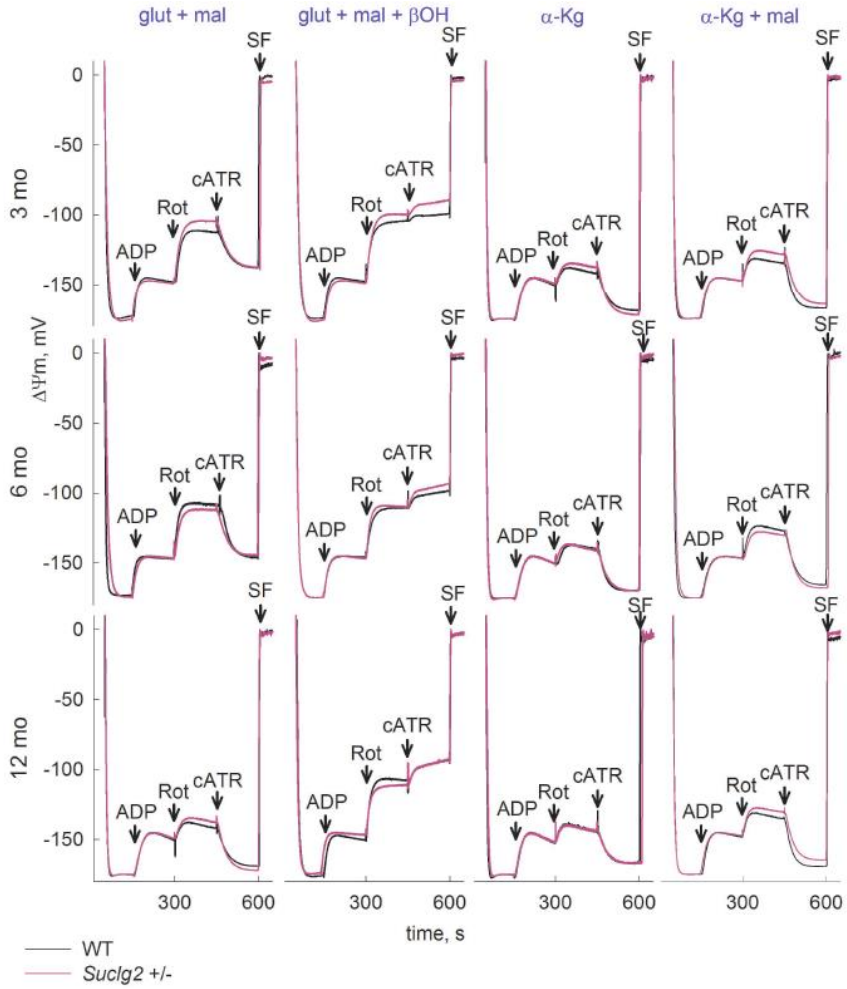

Figure 10.S.5. Reconstructed time courses of safranine O signal calibrated to $\Delta\Psi m$ in mitochondria of 12 months old WT (black) and Suclg2+/- (magenta) mice isolated from liver. ADP: 2 mM; carboxyatractyloside (cATR), 1 μM. Substrates are indicated in the panels; their concentrations were: glutamate (5 mM), malate (5 mM), α-ketoglutarate (α-Kg, 5 mM), beta-hydroxybutyrate (βOH, 4 mM). Rot: rotenone, 1 μM. At the end of each experiment 1 μM SF 6847 was added to achieve complete depolarization. Data shown are representative of at least four independent experiments.

This may be due to a plausible 'CoASH trap' in the form of succinyl-CoA, depleting mitochondria from CoASH which is critical for the entry and catabolism of long-chain fatty acids in mitochondria. Indeed, as seen in oxygen consumption experiments (figure 10.7) when using α-ketoglutarate as substrate, heart mitochondria (which are dependent on CoASH for optimal catabolism of fatty acids) of Sucla2$^{+/-}$ mice exhibited smaller state 2 and state 3 respiration rates than WT mice, implying that KGDHC activity may be impaired, possibly due to insufficient amounts of CoASH. Furthermore, by comparing WT vs Sucla2$^{+/-}$ /Suclg2$^{+/-}$ double heterozygote mice, there was a greater statistically significant increase in some carnitine esters of the blood of double heterozygote mice, compared to wild-type littermates.

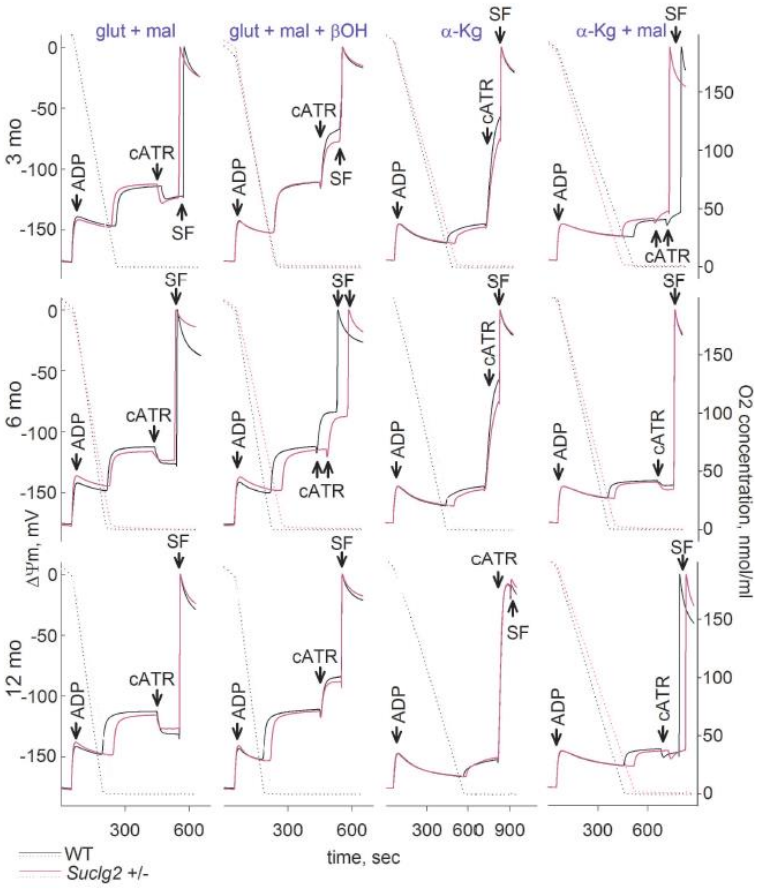

Figure 10.S.6. Reconstructed time courses of safranine O signal calibrated to $\Delta\Psi m$ (solid traces), and parallel measurements of oxygen concentration in the medium (dotted traces) in mitochondria of 3-, 6- and 12 months old WT (black) and Suclg2+/- (magenta) mice isolated from liver. ADP: 2 mM; carboxyatractyloside (cATR), 1 μM. Substrates are indicated in the panels; their concentrations were: glutamate (5 mM), malate (5 mM), α-ketoglutarate (α-Kg, 5 mM), beta-hydroxybutyrate (βOH, 4 mM). At the end of each experiment 1 μM SF 6847 was added to achieve complete depolarization. Data shown are representative of at least four independent experiments.

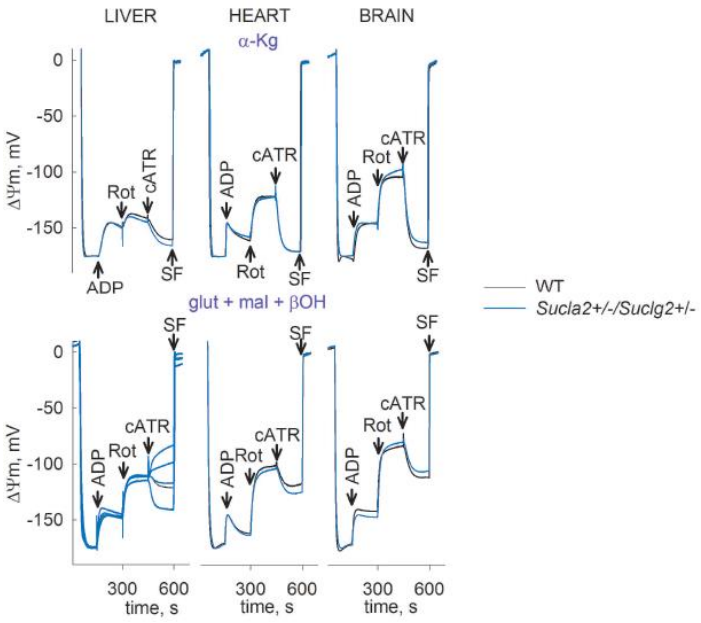

Figure 10.S.7. Reconstructed time courses of safranine O signal calibrated to $\Delta\Psi m$ in mitochondria of 12 months old WT (black) and Sucla2+/-/Suclg2+/- (blue) mice isolated from liver. ADP: 2 mM; carboxyatractyloside (cATR), 1 μM. Substrates are indicated in the panels; their concentrations were: glutamate (5 mM), malate (5 mM), α-ketoglutarate (α-Kg, 5 mM), beta-hydroxybutyrate (βOH, 4 mM). Rot: rotenone, 1 μM. At the end of each experiment 1 μM SF 6847 was added to achieve complete depolarization. Data shown are representative of at least four independent experiments.

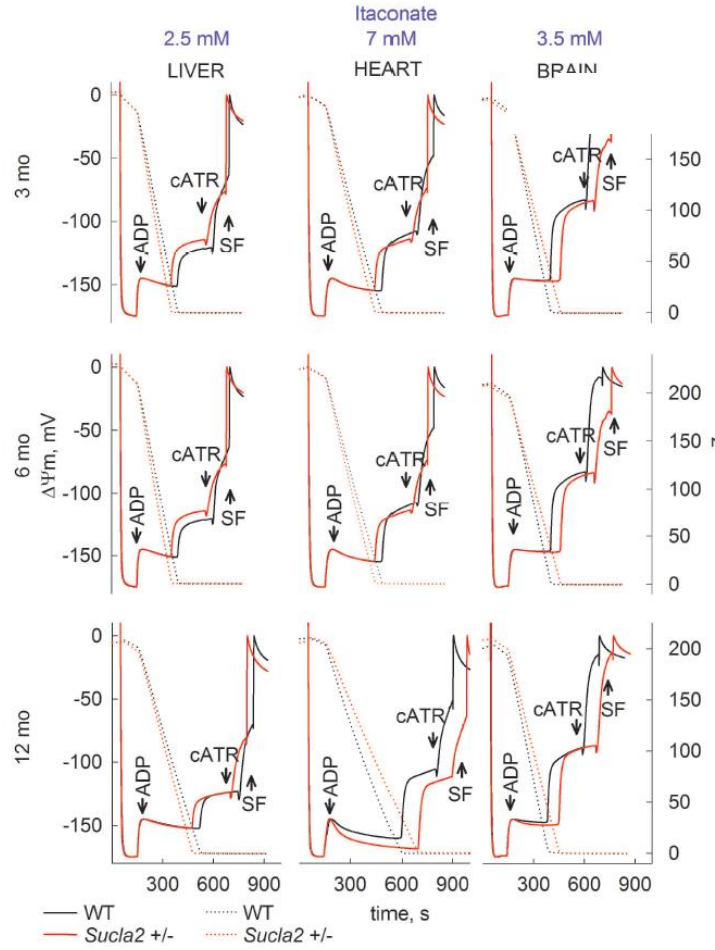

Figure 10.S.8. Reconstructed time courses of safranine O signal calibrated to $\Delta\Psi m$ (solid traces), and parallel measurements of oxygen concentration in the medium (dotted traces) in mitochondria of 3-, 6- and 12 months old WT (black) and Sucla2+/- (red) mice isolated from liver, heart and brain in the presence of itaconate (concentrations indicated in the panels). The concentration of itaconate was titrated so that the differences on substrate-level phosphorylation among WT and Sucla2 +/- mouse mitochondria were the greatest. ADP: 2 mM; carboxyatractyloside (cATR), 1 μM. At the end of each experiment 1 μM SF 6847 was added to achieve complete depolarization. Data shown are representative of at least four independent experiments.

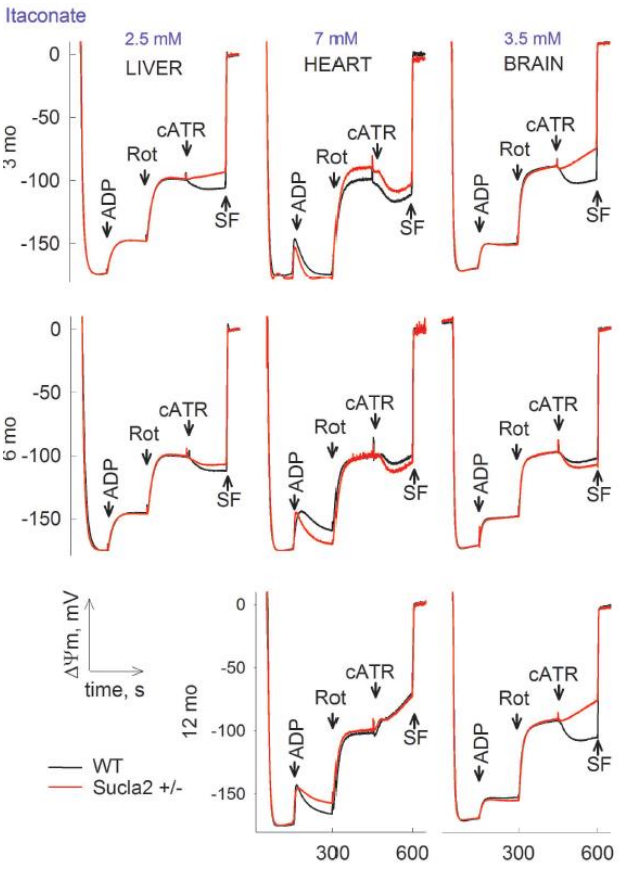

Figure 10.S.9. Reconstructed time courses of safranine O signal calibrated to $\Delta\Psi m$ (solid traces) of mitochondria from 3-, 6- and 12 months old WT (black) and Sucla2+/- (red) mice isolated from liver, heart and brain in the presence of itaconate (concentrations indicated in the panels). The concentration of itaconate was titrated so that the differences between WT and Sucla2+/- on substrate-level phosphorylation were the greatest. ADP: 2 mM; carboxyatractyloside (cATR), 1 μM. Rot: rotenone, 1 μM. At the end of each experiment 1 μM SF 6847 was added to achieve complete depolarization. Data shown are representative of at least four independent experiments.

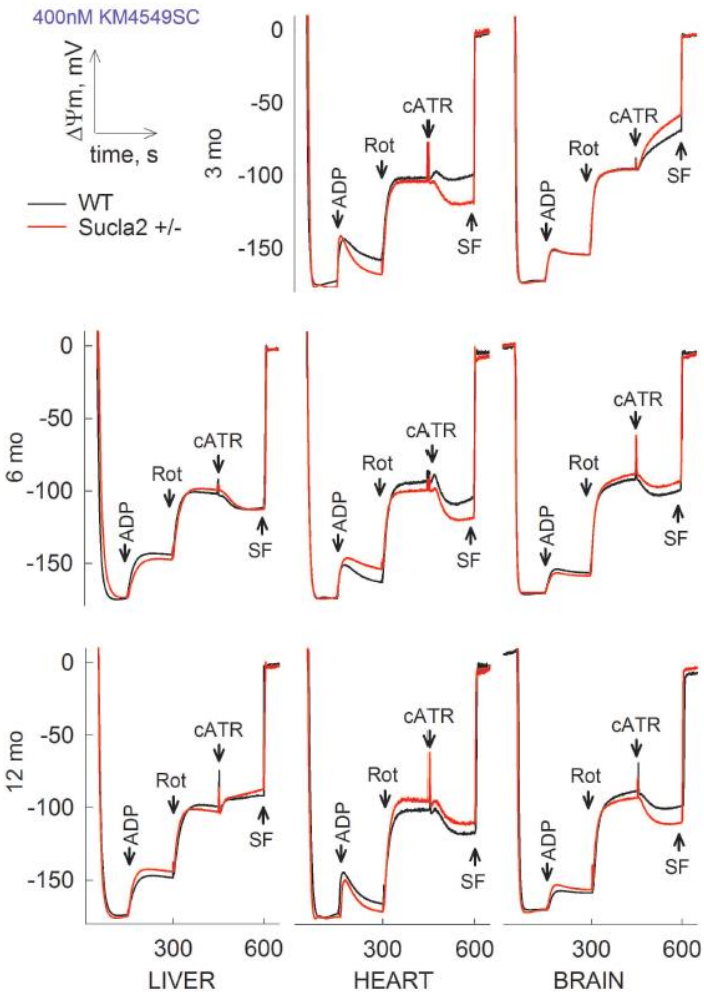

Figure 10.S.10. Reconstructed time courses of safranine O signal calibrated to $\Delta\Psi m$ (solid traces) of mitochondria from 3-, 6- and 12 months old WT (black) and Sucla2+/- (red) mice isolated from liver, heart and brain in the presence of 400 nM KM4549SC. ADP: 2 mM; carboxyatractyloside (cATR), 1 μM. Rot: rotenone, 1 μM. At the end of each experiment 1 μM SF 6847 was added to achieve complete depolarization. Data shown are representative of at least four independent experiments.

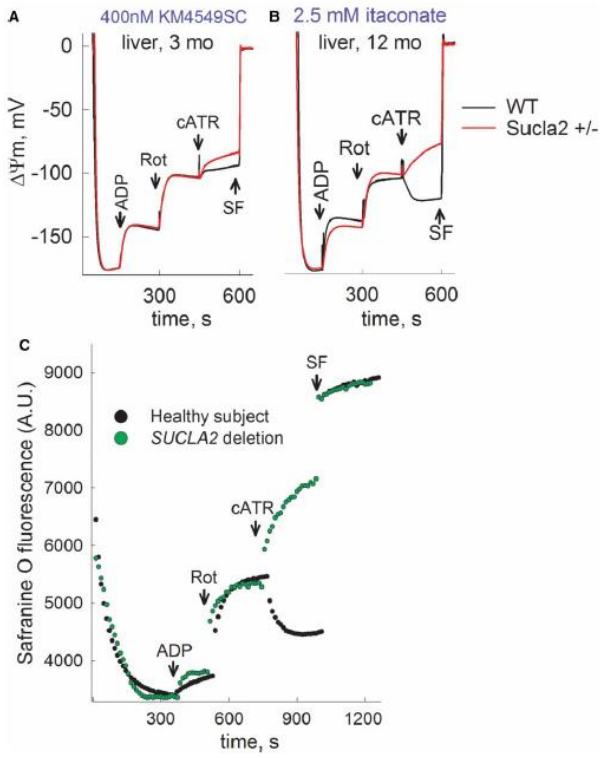

*Figure 10.8. Reconstructed time courses of safranine O signal calibrated to $\Delta\Psi m$ (solid traces), and parallel measurements of oxygen concentration in the medium (dotted traces) in mitochondria of 3- and 12 months old WT (black) and Sucla2+/- (red) mice isolated from liver, in the presence of (**A**) 400 nM KM4549SC or (**B**) itaconate (2.5 mM). ADP: 2 mM; carboxyatractyloside (cATR), 1 μM. Substrate concentrations were: glutamate (5 mM) and malate (5 mM). At the end of each experiment 1 μM SF 6847 was added to achieve complete depolarization. **C**: Reconstructed time course of safranine O signal from permeabilized fibroblasts of a control subject (black dots) and a patient suffering from complete SUCLA2 deletion (green dots). Rot: rotenone, 1 μM. Data shown are representative of at least four independent experiments.*

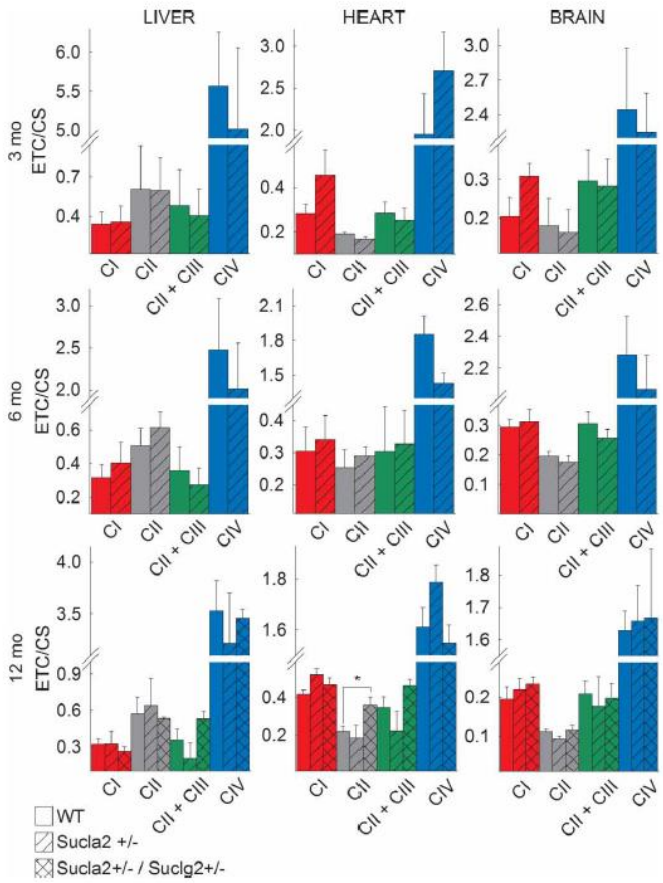

*Figure 10.9. Bar graphs of measurements of complex I, II, II+III and IV activities (ETC) ratioed to citrate synthase activity (CS) in isolated mitochondria of 3-, 6- and 12 months old WT (solid), Sucla2+/- (striped) mice from liver, heart and brain, and Sucla2+/-/Suclg2+/- (double striped) mice from livers of 12 month old mice. * signifies p<0.05. Data shown are S.E.M. from two or four pooled organs per animal group from four independent experiments.*

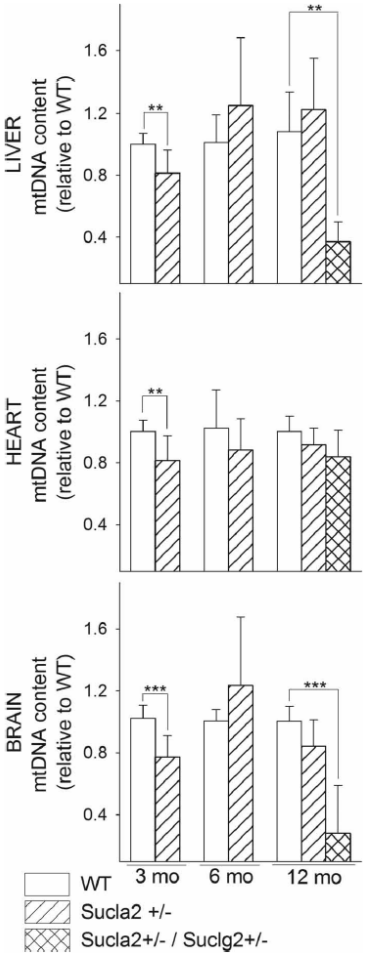

*Figure 10.10. Bar graphs of relative measurements of mtDNA content of livers, hearts and brains from 3-, 6- and 12 months old WT (solid) compared to that from Sucla2+/- (striped) mice, and Sucla2+/-/Suclg2+/- (double striped) mice from livers of 12 month old mice. ** signifies p<0.01 and *** p<0.001. Data shown are S.D. from four pooled organs per animal group from four independent experiments.*

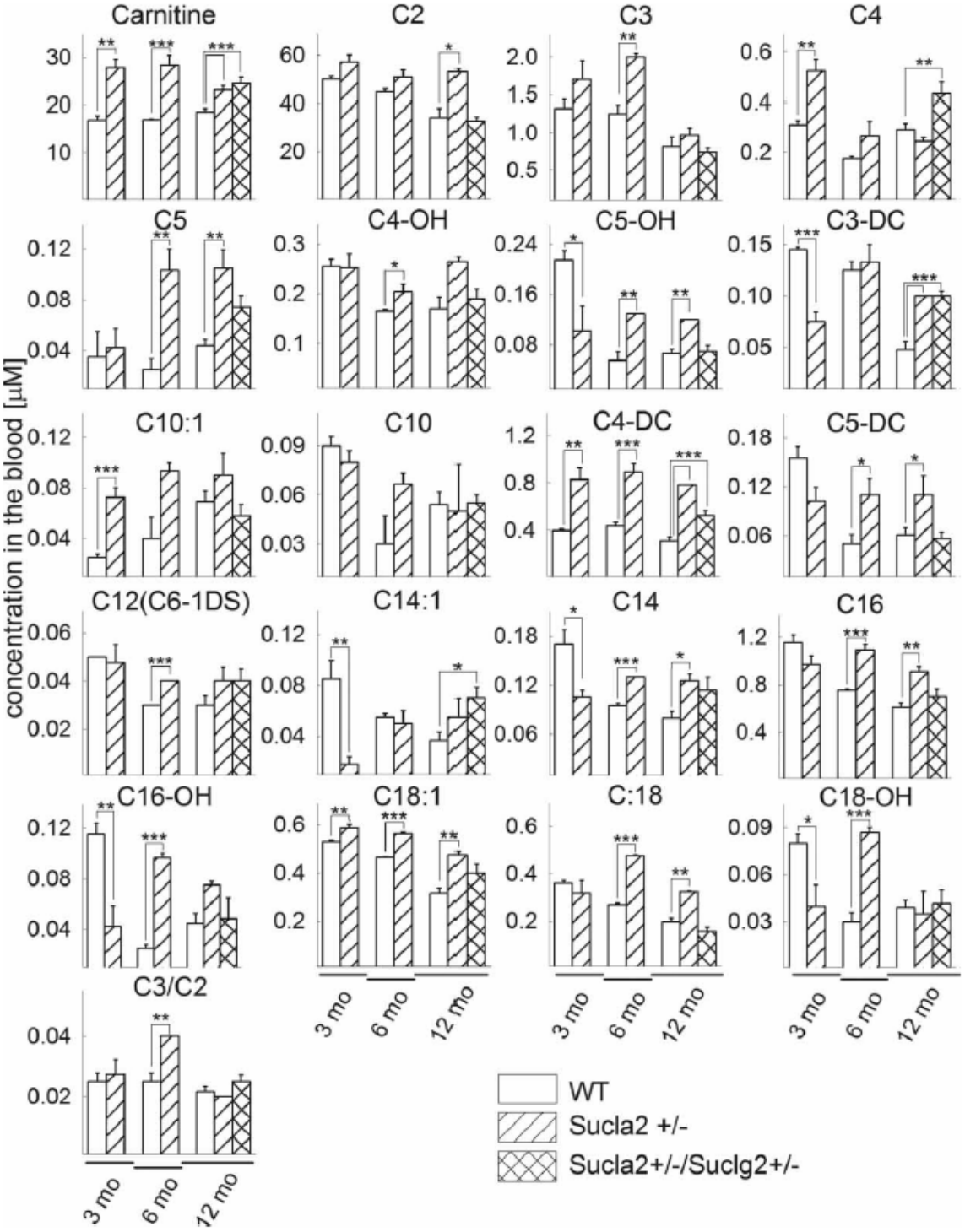

*Figure 10.11. Bar graphs of measurements of carnitine and its esters in the blood of 3-, 6- and 12 months old WT (solid) and Sucla2+/- (striped) mice and Sucla2+/-/Suclg2+/- (double striped) from 12 month old mice. * signifies p<0.05, ** p<0.01 and *** p<0.001. Data shown are S.E.M. from four blood draws per animal group from four mice each. Carnitine (free); C2(Acetyl); C3 (Propionyl); C4 (Butyryl/Isobutyryl); C5 (Isovaleryl/ 2-Methylbutyryl/ Pivaloyl); C4-OH (3-Hydroxybutyryl); C5-OH (3-Hydroxy isovaleryl/2-Methyl 3-hydroxybutyryl); C3-DC (Malonyl); C10:1 (Decenoyl); C10 (Decanoyl); C4-DC (Methylmalonyl/succinyl); C5-DC (Glutaryl); C12 (C6-1DS, Dodecanoyl); C14:1 (Tetradecenoyl); C14 (Myristoyl); C16 (Palmitoyl; C16-OH (3-Hydroxyhexadecenoyl); C18:1 (Oleyl); C18 (Stearoyl); C18-OH (3-Hydroxystearoyl).*

11 Abolition of mSLP by endogenous itaconate production in cells of murine macrophage lineage

In (Nemeth et al., 2016) we demonstrated that the increased itaconate production mediated by lipopolysaccharide (LPS)-induced stimulation of Irg1 in murine bone marrow-derived macrophages (BMDM) and RAW-264.7 cells abolishes mSLP.

11.1 Itaconate: general considerations

Itaconic acid (2-methylidenebutanedioic acid, methylenesuccinic acid, CAS registry number: 97-65-4) is an unsaturated dicarboxylic acid. It is produced in industrial scale from *cis*-aconitate by the extramitochondrial cis-aconitate decarboxylase, an enzyme encoded by the *cadA* gene in *Aspergillus terreus* (Steiger et al., 2013) and is used as a monomer for the production of a plethora of products including resins, plastics, paints, and synthetic fibers (Okabe et al., 2009), (Willke and Vorlop, 2001), reviewed in (Cordes et al., 2015). Itaconic acid has been identified in a small number of metabolomic studies of mammalian tissue specimens, such as activated macrophages, *Mycobacterium tuberculosis*-infected lung tissue, urine and serum samples and glioblastomas (Shin et al., 2011), (Kvitvang et al., 2011), (Wibom et al., 2010). Human and mouse macrophages produce itaconic acid from *cis*-aconitate through an enzyme exhibiting *cis*-aconitate decarboxylase activity, coded by the immunoresponsive gene 1 (*Irg1*, NM_001258406.1 for mice) (Michelucci et al., 2013). The latter finding confirmed earlier reports suggesting the presence of itaconate in macrophage-like tumor cell lines and primary murine macrophages in the low millimolar range (Strelko et al., 2011). The expression profile of Irg1 is reviewed in (Cordes et al., 2015). Irg1-mediated itaconate production contributes to the antimicrobial activity of macrophages by inhibiting isocitrate lyase, a key enzyme of the glyoxylate shunt (Patel and McFadden, 1978), (McFadden and Purohit, 1977). The glyoxylate shunt is not present in animals, but is essential for the survival of bacteria growing on fatty acids or acetate (Hillier and Charnetzky, 1981). Although the applications of itaconic acid and its derivatives extend to dental, ophthalmic, and drug delivery fields (Okabe et al., 2009), and in complexation with benzylammonium it is used to prepare water soluble coating for food packaging to reduce bacteria contamination, it does not enter the food chain to an appreciable degree. Still, it was shown to be extensively metabolized when administered *per os* to cats, dogs and murine animals (Booth et al., 1952), (Adler et al., 1957).

11.2 The effect of LPS on matrix SLP in macrophage cells

Cells of macrophage lineage express Irg1, the enzyme catalyzing the decarboxylation of *cis*-aconitate to itaconate, which is induced by lipopolysaccharide (LPS) (Michelucci et al., 2013), (Strelko et al., 2011). Prior to investigating the effect of LPS on mSLP in macrophage cells, we sought to establish the conditions in which we observe Irg1 expression. We investigated three types of macrophages: i) murine bone marrow-derived macrophages (BMDM), ii) macrophage-like RAW-264.7 cells and iii) murine thioglycollate-induced peritoneal macrophages (TIPM).

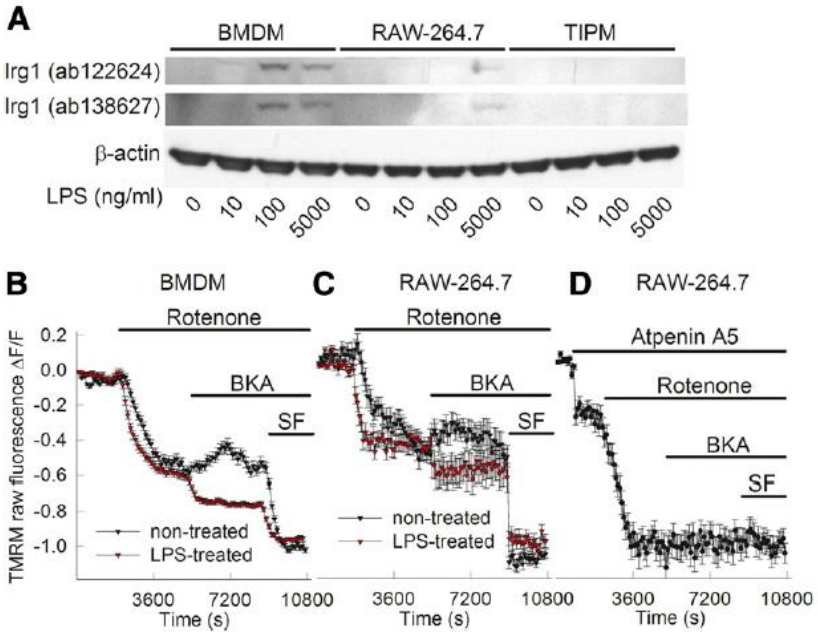

As shown in figure 11.1A, BMDM, RAW-264.7 and TIPM cells were challenged by different concentrations of LPS (0, 10, 100 and 5,000 ng/ml) for 12 hours, and subsequently probed for Irg1 expression by Western blot using two different antibodies, which were raised against different epitopes of the Irg1 protein. Cell types, concentration range and time frame for LPS treatment was chosen according to experimental data published elsewhere, using LPS in the low

Figure 11.1. LPS-treatment of macrophage cells induces Irg1 expression, abolishing in situ matrix SLP. A: Scanned western blot images of BMDM, RAW-264.7 and TIPM cells, non-treated versus LPS-treated (concentrations as indicated in the panel) for 12 hours for Irg1 (using two different antibodies raised against different epitopes of the Irg1 protein) and β-actin. LPS induces Irg1 expression in BMDM and RAW-264-7 cells at specific LPS concentrations, but not in TIPM cells. B, C: Effect of BKA on the rotenone-evoked depolarization of ΔΨm in cultured BMDM (B) and RAW264-7 (C) cells (non-treated, black triangles, versus LPS-treated, red triangles). ΔΨm was followed using the potentiometric probe TMRM. BKA, 20 μM. Rotenone, 5 μM. At the end of each experiment, 5 μM SF 6847 was added to achieve complete depolarization. Results shown in panel B are from an average of ~170 cells and from panel C from an average of ~30 cells (error bars: S.E.M). The experiments shown in panels B and C are representative of 4 independent experiments, each evaluating ~300 BMDM and ~120 RAW-264.7 cells, (untreated, versus LPS-treated, [5 μg/ml for 12 hours] in four individual chambered coverglasses (Lab-Tek). D: Effect of co-inhibition of complex I by 5 μM rotenone and complex II by 1 μM atpenin A5, followed by addition of BKA (20 μM) and SF 6847 (5 μM) in RAW-264.7 cells on TMRM fluorescence.

nano- to micromolar range, for 1-24 hours (Michelucci et al., 2013), (Strelko et al., 2011), (Hoebe et al., 2003), (Xaus et al., 2000), (Xu et al., 2012), (Kimura et al., 2009), (Hoentjen et al., 2005), (Liu et al., 2012). Equal loading of the wells was verified by probing for β-actin. As shown in the scanned blots of panel 11.1A, Irg1 expression was detected in BMDM and RAW-264.7 cells, but not in TIPM cells, with an excellent agreement among results obtained from the two different anti-Irg1 antibodies. Perhaps for TIPM cells a shorter or longer than 12 hours LPS treatment is required to induce *Irg1*. In BMDM cells, the blot using antibody ab122624 exhibited a very faint band for cells treated with 10 ng/ml LPS, while for both Irg1 blots band densities peaked for cells treated with 100 ng/ml; fair band densities were visible for cells treated with 5,000 ng/ml LPS. For RAW-264.7 cells, a band corresponding to Irg1 protein appeared only upon treatment with 5,000 ng/ml LPS. From the results obtained by Western blotting, we decided to investigate the effect of LPS at 5,000 ng/ml for 12 hours on matrix SLP in BMDM and RAW-264.7 cells. As shown in panels 11.1B and 11.1C for BMDM and RAW-264.7 cells respectively, we recorded the effect of the cell-permeable inhibitor of the ANT, bongkrekic acid (BKA, 20 μM) on TMRM fluorescence (reflecting $\Delta\Psi$m of *in situ* mitochondria) in the presence of rotenone (5 μM). Cultures were bathed in an extracellular-like buffer, supplemented with 15 mM glucose as the sole substrate, and TMRM fluorescence was recorded. Addition of the uncoupler SF 6847 (5 μM) at the end of each experiment causing the collapse of $\Delta\Psi$m assisted in the normalization of the TMRM signal of all traces.

As it has been extensively addressed in (Chinopoulos et al., 2010), (Kiss et al., 2013), (Chinopoulos, 2011b) the immediate effect of the ANT inhibitor BKA on TMRM fluorescence of rotenone-treated cells 'betrays' the directionality of the translocase at the time of the inhibition, implying the presence or absence of matrix SLP mediated by succinate-CoA ligase; BKA-induced repolarization during respiratory chain inhibition implies that succinate-CoA ligase was operating towards ATP (or GTP) formation; by the same token, BKA-induced depolarization during respiratory chain inhibition implies that succinate-CoA ligase was operating towards ATP (or GTP) consumption. As shown in figure 11.1B (for BMDM cells) and 11.1C (for RAW-264.7 cells), in non-treated cells (black triangles), BKA caused an increase in TMRM fluorescence, indicating a repolarization. However, in LPS-treated cells (red triangles), BKA caused a depolarization. From these experiments we suspected that treatment with LPS induced *Irg1* in BMDM and RAW-264.7 cells causing an increase in itaconate production that abolished matrix SLP. Itaconate is a weak competitive inhibitor of complex II -succinate dehydrogenase, SDH- leading to a build-up of succinate which shifts succinate-CoA ligase equilibrium towards ATP (or GTP) utilization thus thwarting SLP. We therefore investigated the effect of the known SDH inhibitor atpenin A5 on rotenone-treated macrophage cells (figure 11.1D). As expected, the concomitant inhibition of complex I by rotenone and complex II by atpenin A5 led to a complete collapse of $\Delta\Psi m$, and therefore BKA and SF 6847 exhibited no further loss of TMRM fluorescence; under these bioenergetic circumstances the ANT is completely reversed (Chinopoulos et al., 2010), (Kiss et al., 2013), (Chinopoulos, 2011b), (Chinopoulos, 2011a) and matrix SLP cannot be addressed.

11.3 The effect of transfecting cells with siRNA directed against Irg1 on matrix SLP during treatment with LPS

In order to verify that LPS treatment impaired matrix SLP by means of itaconate produced by Irg1, we performed silencing experiments directed against *Irg1* expression with siRNA. For these experiments we used RAW-264.7 cells which typically exhibit high transfection efficiencies (Degrandi et al., 2009), as opposed to primary cells such as BMDMs.

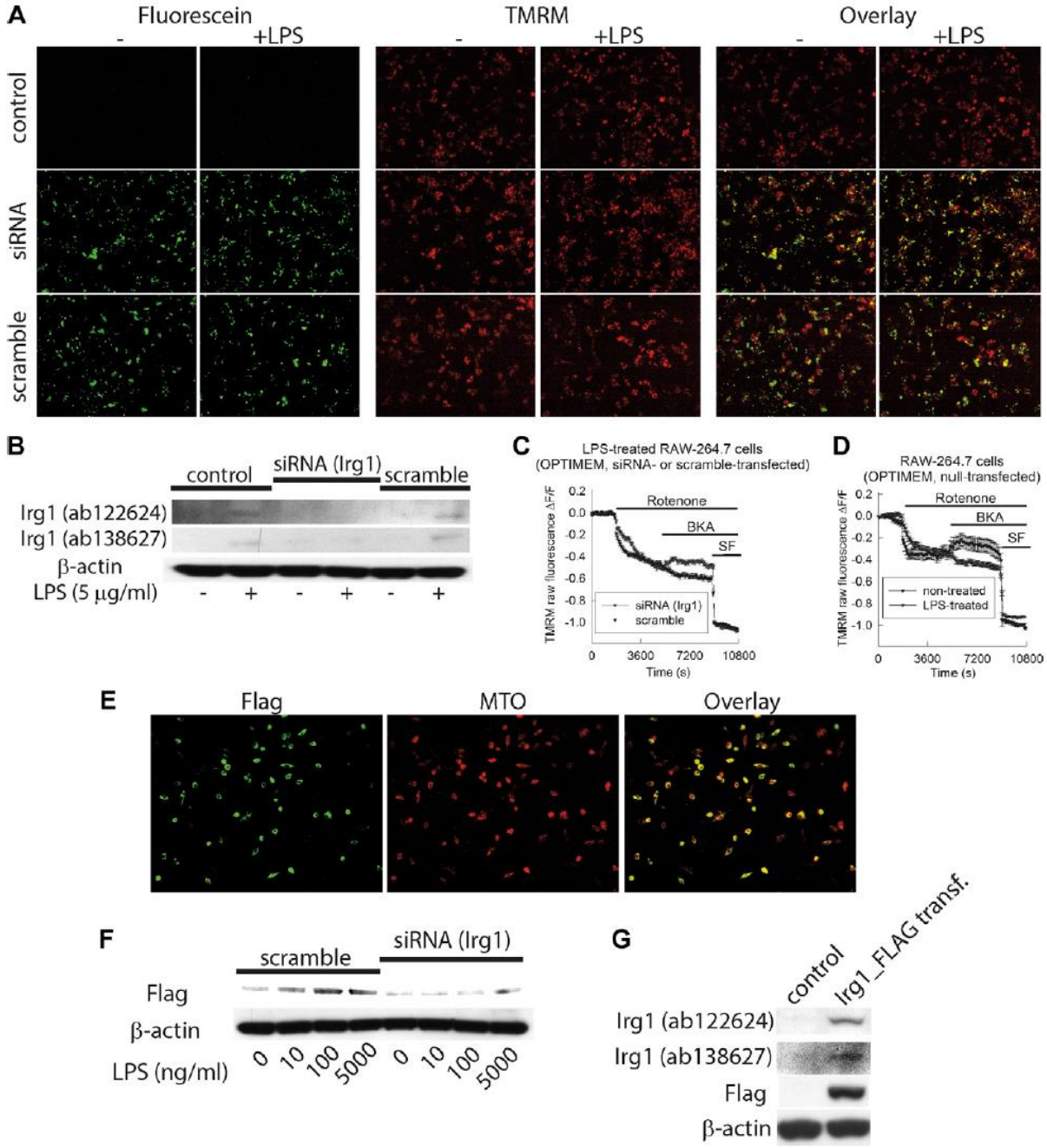

Indeed, as shown in figure 11.2A, fluorescein-conjugated siRNA or scrambled RNA decorated >90% of RAW-264.7 cells. The effect of siRNA and scrambled RNA transfecting RAW-264.7 cells on Irg1 expression level as a function of LPS treatment is shown in panel 11.2B. RAW-264.7 cells were divided in control, siRNA-transfected and scrambled RNA transfected tiers, and subdivided in i) no LPS treated versus ii) LPS (5 μg/ml) treated, as indicated in the panel 11.2B. Irg1 expression was probed by Western blot using the same two antibodies as in figure 11.1A. Equal loading of the wells was verified by probing for β-actin. As shown in panel 11.2B, control RAW-264.7 cells exhibited Irg1 expression upon LPS treatment, which was abolished by siRNA transfection directed against *Irg1*. Transfection with scrambled RNA did not result in abolition of *Irg1* expression. Similarly to panel 11.1A, in the scanned blots it is apparent that there is an excellent agreement of results obtained from the two different anti-Irg1 antibodies. We next compared the effect of siRNA versus scrambled RNA versus control in LPS-treated and untreated RAW-264.7 cells on matrix SLP, deduced from the directionality of the ANT during respiratory inhibition from TMRM fluorescence recordings. As shown in figure 11.2C, RAW-264.7 cells

Figure 11.2. Effect of transfecting cells with siRNA directed against Irg1 on matrix SLP during treatment with LPS. A: Epifluorescent images of fluorescein (tagging siRNA and scramble RNA) and TMRM-loaded (reflecting $\Delta\Psi m$) RAW-264.7 cells, and their overlays in the presence and absence of LPS (5 μg/ml for 12 hours). B: Scanned images of Western blots of RAW-264.7 cells transfected with siRNA directed against Irg1 or scramble RNA, further subcategorized in non-treated versus LPS-treated (5 μg/ml for 12 hours), for Irg1 (using two different antibodies raised against different epitopes of the Irg1 protein) and β-actin. C: Effect of BKA on the rotenone-evoked depolarization of $\Delta\Psi m$ in cultured RAW264-7 cells (LPS-treated, scramble RNA co-transfected, black triangles), versus LPS-treated, siRNA directed against Irg1 co-transfected (green triangles). D: Effect of BKA on the rotenone-evoked depolarization of $\Delta\Psi m$ in cultured RAW264-7 cells (non-treated, null-transfected, black triangles), versus LPS-treated, null-transfected (red triangles). $\Delta\Psi m$ was followed using the potentiometric probe TMRM. BKA, 20 μM. Rotenone, 5 μM. At the end of each experiment, 5 μM SF 6847 was added to achieve complete depolarization. Results shown in panels C and D are from an average of 63-192 cells (error bars: S.E.M). The experiments shown in panels C and D are representative of 4 independent experiments, evaluating 274-690 cells. E: Epifluorescent images of immunocytochemistry decorating Flag-expressing cells (transfected with the pCMV6-FLAG-Irg1 overexpressing plasmid, left) the mitochondrial network stained with MTO (middle) and the overlays (right). The fluorescence intensity depicted in the image showing the Flag-expressing cells has been 'thresholded' to expose only the Flag-expressing cells, due to a minor cross-talk of the secondary antibody fluorescence (used for FLAG immunocytochemistry) with the MTO. F: Scanned images of Western blots of RAW-264.7 cells transfected with siRNA directed against Irg1 or scramble RNA, co-transfected with the pCMV6-FLAG-Irg1 overexpressing plasmid and further subcategorized in non-treated versus LPS-treated (dose dependence indicated in the panel) for 12 hours, for the FLAG epitope and β-actin. G: Scanned images of Western blots of Cos-7 cells transfected with the pCMV6-FLAG-Irg1 overexpressing plasmid, for Irg1 (using two different antibodies raised against different epitopes of the Irg1 protein), the FLAG epitope and β-actin.

that have been transfected with scrambled RNA unaffecting *Irg1* expression, exhibited a BKA-induced depolarization (black triangles), due to the treatment by LPS. However, cells that have been transfected with siRNA directed against *Irg1*, exhibited a BKA-induced repolarization (green triangles). In figure 11.2D, RAW-264.7 cells that have undergone null-transfection treatment (neither siRNA nor scramble RNA, see under "Materials and Methods") with (red triangles) or without (black triangles) LPS exhibited similar responses as in figure 11.1C. From these experiments we concluded that LPS treatment caused a reversal in ANT activity of *in situ* rotenone-inhibited mitochondria due to activation of *Irg1* expression. Because the signal-to-noise ratio of the blots using both antibodies directed against Irg1 were admittedly small, which in turn could cast doubt on the efficiency of the siRNA treatment as judged by the western blot, we attempted to maximize Irg1 expression in cells where we could more reliably test the affinity of our antibodies, as well as siRNA treatment efficiency. For that, we transfected RAW-264.7 cells with a pCMV6-FLAG-Irg1 plasmid, known to yield high levels of Irg1 expression (Michelucci et al., 2013). The plasmid also encodes a FLAG region, for easier identification of the expressed protein by immuno-techniques. As shown in figure 11.2E, RAW-264.7 cells were identified by MTO labelling of their mitochondrial network and co-decorated with antibodies recognizing the FLAG. From the overlay of such images, we deduced that >90% of cells were successfully transfected with the plasmid. By using the same transfection protocols, we evaluated the efficiency of the siRNA versus scrambled RNA treatment in RAW-264.7 cells also treated dose-dependently with LPS, by western blot. As shown in figure 11.2F, RAW-264.7 cells tested positive for FLAG expression, and those that were co-transfected with the scrambled RNA against Irg1 exhibited a dose-dependent increase in FLAG expression; this is not surprising, because the CMV promoter (controlling the Irg1 expression in the pCMV6-FLAG-Irg1 plasmid) is known to be affected by LPS through TLR (Lee et al., 2004), which is present in the RAW cells. Moreover, co-transfection of RAW cells overexpressing FLAG-Irg1 with siRNA directed against *Irg1*

abolished the dose-dependent increase in FLAG expression by the LPS (right part of figure 11.2F). From these experiments we concluded that the siRNA could effectively diminish the expression of Irg1 in these cells. In order to address the quality of the anti-Irg1 antibodies, we transfected COS-7 cells with the pCMV6-FLAG-Irg1 plasmid exactly as for the RAW-264.7 cells. In these cells we then probed for Irg1 protein and the FLAG by western blot. The results are shown in figure 11.2G. As shown in figure 11.2G, only the transfected cells exhibited immunoreactivity for the anti-Irg1and the anti-FLAG antibodies. Anti-Irg1 ab122624 exhibited a slightly better signal-to-noise ratio as compared to blots shown in panels 11.1A and 11.2B, in line with an expected increased expression of Irg1 protein, but this was not apparent for antibody ab138627. From this experiment we concluded that the native Irg1 expression in BMDM and RAW-264.7 cells as induced by LPS occurs at lower levels than that compared to those cells that have been induced to overexpress Irg1 by the CMV promoter in the plasmid.

11.4 The effect of LPS treatment on oxygen consumption and extracellular acidification rates in macrophages

Cellular metabolism and macrophage functional polarization are intricately connected (Zhu et al., 2015); activation of TLR4 by LPS with numerous downstream effects extending to glycolytic and mitochondrial respiration pathways are known to occur (Tavakoli et al., 2013), (Everts et al., 2012), (Traves et al., 2012), (Garedew et al., 2010). We therefore examined the dose-dependent effect of LPS treatment in both BMDM and RAW-264.7 cells on oxygen consumption rates (OCR) and extracellular acidification rates (ECAR), the latter parameter partially reflecting glycolytic rates. It cannot be overemphasized that an additional potential source of extracellular protons is the production of CO_2 during mitochondrial substrate oxidation: CO_2 is hydrated to H_2CO_3, which then dissociates to HCO_3^- and H^+; the contribution of CO_2-produced acidification depends on the cell type and substrate, and may vary from 3% to 100% of the total acidification rate (Mookerjee et al., 2015). Therefore, measurements of extracellular acidification rates are bound to be affected by CO_2 production during mitochondrial substrate oxidation. However, as it will be shown below, increases in ECAR are associated with decreases in OCR, implying that alterations in ECAR are mostly due to changes in glycolytic fluxes, and not due to changes in CO_2 production during mitochondrial substrate oxidation. BMDM cells (panels 11.3B, D, F and H) and RAW-264.7 cells (panels 11.3A, C, E and G) were probed for OCR (figure 11.3, top panels) and ECAR (figure 11.3, bottom panels) under various, sequential metabolic conditions as indicated in the panels, in the presence and absence of glucose, and at different concentrations of LPS (0 [black-filled circles], 10 [red-filled triangles], 100 [green-filled squares] and 5,000 [yellow-filled diamonds] ng/ml, all for 12 hours). The 'Medium' contained 2 mM glutamine. As shown in figure 11.3C and 11.3D, addition of glucose resulted in a robust decrease in the basal level of respiration. This response is typical for macrophage cells upon activation of TLR, switching on aerobic glycolysis in addition to maintaining oxidative phosphorylation (Krawczyk et al., 2010), (Rodriguez-Prados et al., 2010), an effect that is also characteristic for tumor cells (Vander Heiden et al., 2009). Addition of 'Medium' in lieu of glucose (panels 11.3A and 11.3B) did not yield similar changes in OCR as glucose, thus serving as a 'vehicle' control. Subsequently, the inhibition of F_o-F_1 ATP synthase by oligomycin decreased further the OCR (panels 11.3C and 11.3D) and was used to assess oxygen consumption associated to ATP synthesis, and it was dissociated from the presence or absence of glucose (panels 11.3A and 11.3B).

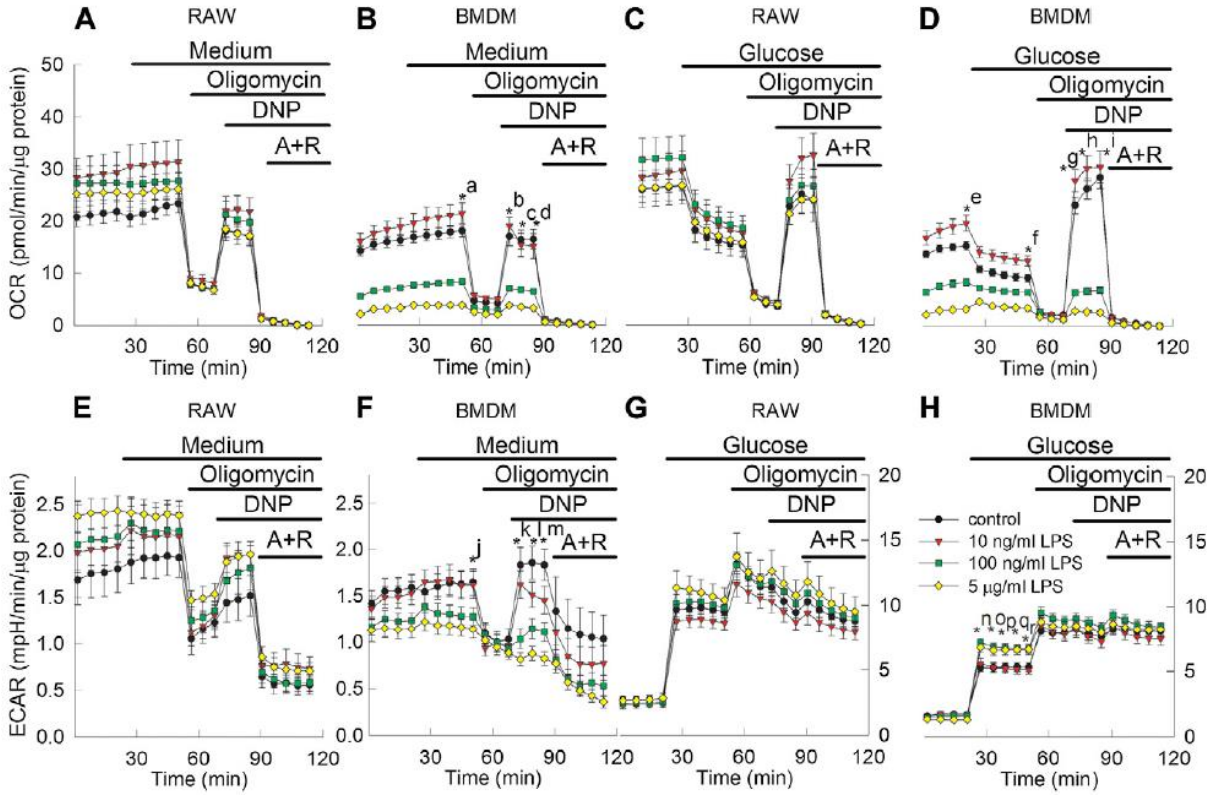

*Figure 11.3. Effect of LPS (concentrations indicated in panel H) on BMDM and RAW-264.7 cells on oxygen consumption (upper row panels) and extracellular acidification rates (bottom row panels) in the presence or absence of glucose, upon addition of various metabolic inhibitors. Oxygen consumption rate (OCR) and extracellular acidification rate (ECAR) were determined in a microplate format respirometry/pH assay using a Seahorse XF96 Analyzer. Glucose 10 mM, oligomycin 2 µM, DNP 100 µM, antimycin 1 µM, rotenone 1 µM. The 'Medium' contained 2 mM glutamine. Data are from three independent cell culture preparations, n=10-12 wells each containing ~ 25,000-50,000 RAW-264.7 cells or n=12-25 wells each containing ~50,000 BMDM cells. Panels A, B, C and D are aligned in the y-axis (OCR). Whenever error bars are not visible, it is because they are smaller than the symbol size. Data are presented as mean ± SEM; significant differences between groups of data were evaluated by one way ANOVA followed by Dunnett's posthoc analysis (control= no LPS treatment), with p < 0.05 considered as significant. *a, *b, *c, *d, *h, *i, *k, *l, *m, *n, *o, *p, *q, *r <0.001, compared to 100 ng/ml, 5 µg/ml LPS; *e, *f, *g <0.001 compared to 10 ng/ml, 100 ng/ml, 5 µg/ml LPS; *j =0.006 compared to 5 µg/ml LPS. All other data comparisons exhibited p values in the 0.143-0.676 range.*

Concomitantly, the increases in ECAR (panels 11.3G and 11.3H) upon the injection of glucose and oligomycin implied a shift in the metabolism from mitochondria to glycolysis. In the absence of glucose, changes in ECAR were miniscule (panels 11.3E and 11.3F) although still following the anticipated qualitative changes; uncoupling of BMDM cells by DNP led to statistically significant changes in ECAR, which were dose-dependently abolished by LPS (panel 3F). Uncoupling of the oxidative phosphorylation with DNP resulted in maximal respiration in both RAW-264.7 and BMDM cells (panels 11.3C and 11.3D, respectively); in RAW-264.7 cells, this was unaffected by LPS, at any concentration tested (panel 11.3C); on the other hand, the DNP-induced maximal respiration was dose-dependently abolished by LPS in BMDM cells (panel 11.3D). Along the same lines, LPS had a dose-dependent effect on increasing ECAR in BMDM (panel 11.3G) but not RAW-264.7 cells (panel 11.3H) upon injection of glucose. Co-application of antimycin A with rotenone (A+R) inhibiting mitochondrial Complex III and I, respectively, dramatically suppressed OCR in both cell types. What is also apparent from the above results is that RAW-264.7 cells

are more reliant on glycolysis for energy production than BMDM cells (compare OCR and ECAR basal rates between the cell types); this is probably because RAW-264.7 cells already exhibit maximal upregulation in glycolytic enzymes, as opposed to BMDM cells where an LPS effect in upregulating glycolysis further, in conjunction to inhibiting mitochondrial oxidation, can be demonstrated. This is not surprising, as RAW-264.7 cells are tumor-derived, and cancer cells are known to 'rewire' their bioenergetic pathways favouring a robust hypoxic response which results in upregulation of glycolysis (Zeng et al., 2015), (Riboldi et al., 2013). Mindful that no significant difference was observed in mitochondrial and glycolytic parameters between LPS-stimulated and non-stimulated RAW 264.7 cells, and that in the same cells LPS abolished SLP, we concluded that the effect of LPS on SLP was exclusively attributed to induction of *Irg1* yielding itaconate, and was not due to circumstantial bioenergetic effects involving glycolysis and/or oxidative phosphorylation. To elaborate further on the exact mechanism(s) by which itaconate is afforded the property of inhibiting SLP, we investigated the dose-dependent effect of exogenously added itaconate to isolated mitochondria, under defined metabolic conditions.

11.5 The pathway of itaconate metabolism in murine liver mitochondria

The details of itaconate metabolism in murine liver mitochondria have been the subject of scrutiny by the group of Henry A. Lardy (Wang et al., 1961); in order to illustrate the purpose of our experiments using isolated mitochondria, we first show a schematic representation of the relevant pathways merging with the part of the citric acid cycle and related metabolic reactions that involve SLP.

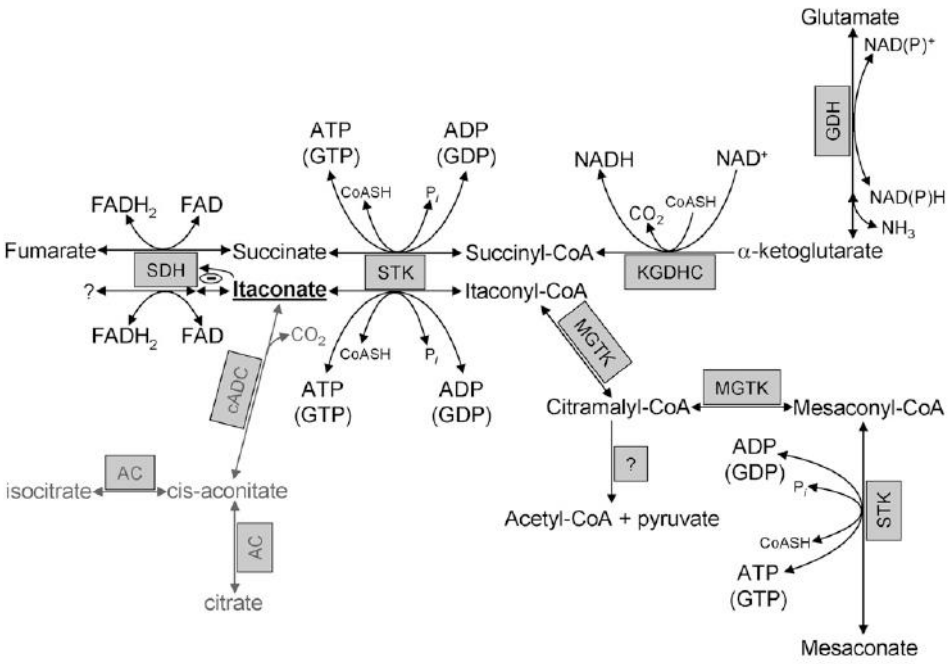

As shown in figure 11.4, itaconate (shown in bold, underlined text) arises from *cis*-aconitate, an intermediate of the aconitase (AC) reaction, but only in tissues where cis-aconitate decarboxylase (cADC) is expressed (Xiao et al., 2011). In the fungus *Aspergillus terreus*, cADC is an extramitochondrial

Figure 11.4. Schematic representation of itaconate and mesaconate metabolism in relation to a segment of the citric acid cycle and related reactions. SDH: succinate dehydrogenase; STK: succinate thiokinase (succinate-CoA ligase); KGDHC: α-ketoglutarate dehydrogenase complex; GDH: glutamate dehydrogenase; MGTK: methylglutaconase (methylglutaconyl-CoA hydratase); cADC: cis-aconitate decarboxylase; AC: aconitase (aconitate hydratase).

protein (Steiger et al., 2013); in mammalian cells, an iron-responsive element binding protein exhibiting aconitase activity has been found in the cytosol (Haile et al., 1992), however, in cells of macrophage

lineage (where itaconate is formed) cADC associates to mitochondria (Degrandi et al., 2009). *cis*-aconitate may arise from either isocitrate or citrate, since the reaction catalyzed by aconitase is reversible. Exogenously administered itaconate would be further metabolized only after entry into the mitochondria. Such entry is expected to occur through the dicarboxylate carrier (SLC25A10), although, to the best of our knowledge, this has not been verified. In the mitochondrial matrix, itaconate could weakly inhibit succinate dehydrogenase (SDH) in a competitive manner (Booth et al., 1952), (Adler et al., 1957), (Dervartanian and Veeger, 1964). The work of Lardy showed that itaconate would also become oxidatively catabolized in the citric acid cycle in a malonate-sensitive manner (Adler et al., 1957). However, due to the lack of hydrogen on the α-carbon of itaconate, a double bond cannot be formed; therefore it cannot be processed by SDH as such. Two possibilities by which itaconate is converted to products suitable for oxidation by the SDH could be envisaged: i) saturation of itaconate to methylsuccinate is the most likely scenario, in view of the fact that methylsuccinate is known to be processed by SDH (Abramov and Duchen, 2005), (Abramov and Duchen, 2008); ii) itaconate hydroxylation yielding hydroxymethyl-succinate is also a viable theoretical possibility, but to the best of our knowledge this has not been addressed. A possible decarboxylation or isomerisation of itaconate would yield products that cannot be further metabolized by SDH. On the other hand, in acetone extracts of murine liver mitochondria, itaconate metabolism was shown to occur extensively in the presence of ATP, Mg^{2+} and CoASH (Adler et al., 1957). Furthermore, in intact liver mitochondria and in the presence of ATP and Mg^{2+} but absence of oxygen, itaconate became thioesterified to itaconyl-CoA which was later converted to citramalyl-CoA through methylglutaconyl-CoA hydratase (Hilz et al., 1958) (EC 4.2.1.18, also known as methylglutaconase, MGTK). Citramalyl-CoA could be further converted to either mesaconyl-CoA by MGTK, or to acetyl CoA and pyruvate (Adler et al., 1957), (Wang et al., 1961). Mesaconyl-CoA can loose the CoASH in a reaction catalyzed by succinate-CoA ligase, forming mesaconate. This also means that mesaconate would exhibit similar effects on SLP as itaconate; however, mesaconate is much less potent than itaconate (Adler et al., 1957), probably because of a lower affinity of succinate-CoA ligase for mesaconate than for itaconate. Mindful of the above considerations, the metabolism of itaconate in mitochondria may hinder SLP since it proceeds at the expense of ATP (or GTP) hydrolysis. SLP can be investigated in intact isolated mitochondria with an inhibited respiratory chain using the 'biosensor test' described above.

11.6 Categorization of respiratory substrates used for isolated mitochondria

In the experiments detailed below, it is critical to use adequate substrate combinations to maintain mitochondrial respiration; some substrates support, and some do not support SLP. Glutamate and α-ketoglutarate are the two substrates that support SLP to the greatest extent. Malate alone has no effect, but it assists in the entry into mitochondria of other substrates including glutamate and α-ketoglutarate, thus indirectly supporting SLP. Acetoacetate (AcAc) is also without a direct effect on SLP; however, AcAc leads to NAD^+ regeneration through the reaction catalyzed by β-hydroxybutyrate dehydrogenase, that boosts SLP supported by glutamate (or α-ketoglutarate) yielding succinyl-CoA through the α-ketoglutarate dehydrogenase complex (KGDHC), see (Kiss et al., 2013) and (Kiss et al., 2014); succinate disfavours SLP.

11.7 The dose-dependent effect of itaconate on ANT directionality in rotenone-treated isolated mitochondria

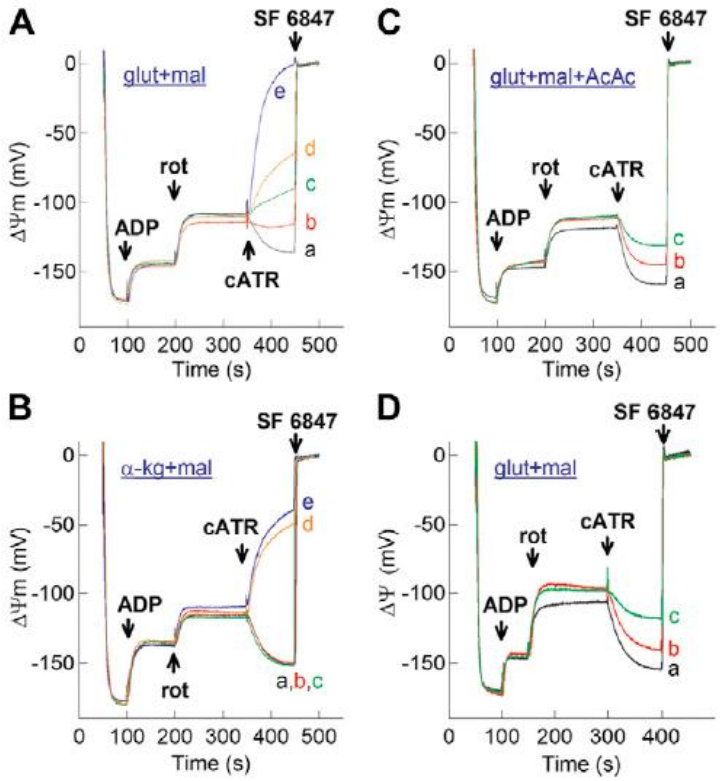

Figure 11.5. Reconstructed time courses of safranine O signal calibrated to ΔΨm in isolated mouse liver mitochondria supported by various substrates (indicated in the panels). The effect of cATR (2 μM) on ΔΨm of mitochondria treated with rotenone (rot, 1 μM, where indicated) in the presence or absence of itaconate (A, B, C) or mesaconate (D) is shown. ADP (2 mM) was added where indicated. Itaconate concentrations (present prior to addition of mitochondria) are as follows: for panel A: 'a': 0, 'b': 0.5 mM, 'c': 1 mM, 'd': 2 mM and 'e': 5 mM, for panel B: 'a': 0, 'b': 0.25 mM, 'c': 0.375 mM, 'd': 0.5 mM and 'e': 1 mM, for panel C: 'a': 0, 'b': 0.5 mM, 'c': 2 mM. Mesaconate concentrations in panel D are as follows: 'a': 0, 'b': 5 mM, 'c': 10 mM. At the end of each experiment 1 μM SF 6847 was added to achieve complete depolarization.

As shown in figure 11.5, ΔΨm was measured by safranine O fluorescence in mouse liver mitochondria and calibrated as described in (Chinopoulos et al., 2010). The sequence of additions, identical for each panel, was the following: mitochondria were allowed to polarize, followed by the addition of 2 mM ADP, which depolarized mitochondria to a variable level depending on the substrate combinations (Chinopoulos et al., 2009), indicated in the panels. After 100 sec during which a substantial amount of ADP has been converted to ATP, complex I was inhibited by rotenone which 'clamped' ΔΨm at ~-100 mV, again depending on the substrate combinations. After an additional 150 sec, cATR was added to block ANT. At the end of each experiment the uncoupler SF 6847 was added in order to completely depolarize mitochondria; this would assist in the calibration of the safranine O signal. In panel 11.5A, the effect of itaconate (always present in the media before addition of mitochondria, 'b': 0.5 mM, 'c': 1 mM, 'd': 2 mM and 'e': 5 mM) on the ANT operation is shown as compared to control 'a', for mitochondria supported by glutamate (5 mM) and malate (5 mM). It is evident that the forward operation of ANT observed in the control tends to be inhibited, even reversed in the presence of increasing concentration of itaconate, indicating an inhibitory action of this compound on SLP. Similar conclusion is drawn from experiments with other substrate combination. In panel 11.5B, the effect of itaconate ('b': 0.25 mM, 'c': 0.375 mM, 'd': 0.5 mM and 'e': 1 mM) versus control 'a' is shown for mitochondria supported by α-ketoglutarate (5 mM) and malate (5 mM). It is evident that with increasing concentrations of itaconate, cATR resulted in depolarization, compared to repolarization observed in the absence of this compound. Similar experiments with itaconate ('b': 0.5 mM, 'c': 2 mM) are shown in panel 11.5C for mitochondria supported by glutamate (5 mM) plus malate (5 mM) plus acetoacetate (AcAc, 0.4 mM). The latter result is consistent with the fact that AcAc increases [NAD^+] in the mitochondrial matrix, thus boosting succinyl-CoA production by KGDHC. In panel 11.5D, the effect of mesaconate ('b': 5 mM, 'c': 10 mM) versus control 'a' is shown, obtained in the presence of

glutamate (5 mM) and malate (5 mM). Consistent with the findings by Lardy (Adler et al., 1957), (Wang et al., 1961), mesaconate was much less potent than itaconate in exerting an impact on SLP. From the above results we concluded that itaconate abolished SLP in isolated mitochondria in which the respiratory chain was inhibited.

11.8 The effect of malonate on ANT directionality in rotenone-treated isolated mitochondria

Next, we investigated if the effect of itaconate was due to a mild inhibition of SDH leading to accumulation of succinate thus shifting the succinate-CoA ligase equilibrium towards ATP (or GTP) consumption, or due to consumption of ATP (or GTP) for itaconyl-CoA formation, and/or due to an ensuing 'CoA trap' in the form of itaconyl-CoA which could negatively affect the upstream supply of succinyl-CoA from the α-ketoglutarate dehydrogenase complex (21), in turn diminishing ATP (or GTP) formation through SLP by succinate-CoA ligase. Thus, we compared the effects of itaconate to that of malonate, a classical competitive inhibitor of SDH which is not metabolized by succinate-CoA ligase, for which it was necessary to titrate their concentrations so that they exhibit SDH inhibition to similar extent. As shown in figure 11.6A, the effect of itaconate (0.5-5 mM) versus malonate (panel 11.6B) was examined on state 2 (grey bars) and state 3 respiration (induced by 2 mM ADP, black bars) in mitochondria supported by 5 mM succinate in the presence of 1 μM rotenone. It is evident that 1 mM itaconate conferred a similar decrease in oxygen consumption as 125 μM malonate; likewise, 5 mM itaconate conferred a similar decrease in oxygen consumption as 500 μM malonate. Therefore, we deduced that itaconate was approximately eight to ten times less potent than malonate in

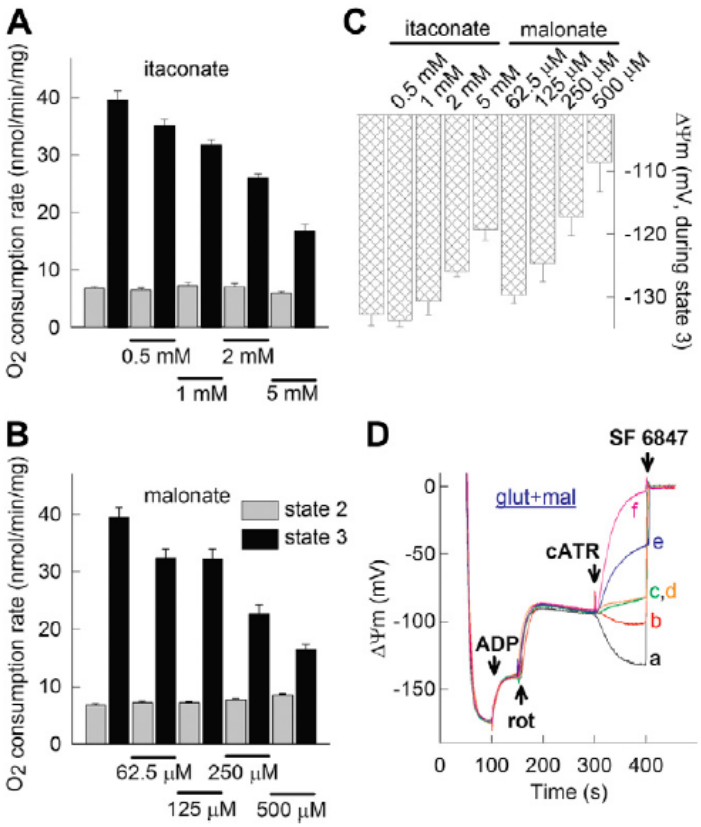

Figure 11.6. Bar graphs of the effect of itaconate (panel A) and malonate (panel B) on oxygen consumption rates expressed as nmol/min/mg protein (state 2, grey bars, state 3 induced by 2 mM ADP, black bars), in isolated mitochondria respiring on succinate (5 mM) in the presence of rotenone (1 μM). C: Bar graphs of the effect of itaconate and malonate on ΔΨm expressed in mV during state 3 (induced by 2 mM ADP), in isolated mitochondria respiring on succinate (5 mM) in the presence of rotenone (1 μM). Concentrations of itaconate and malonate are indicated in the panel. D: Reconstructed time courses of safranine O signal calibrated to ΔΨm in isolated mouse liver mitochondria supported by glutamate (5 mM) and malate (5 mM). The effect of cATR (2 μM) on ΔΨm of mitochondria treated with rotenone (rot, 1 μM, where indicated) in the presence of malonate is shown. ADP (2 mM) was added where indicated. Control trace 'a' is shown in black. Malonate concentrations (present prior to addition of mitochondria) are as follows: 'b': 0.0625 mM, 'c': 0.125 mM, 'd': 0.25 mM, 'e': 0.5 mM, and 'f': 5 mM. At the end of each experiment 1 μM SF 6847 was added to achieve complete depolarization.

inhibiting succinate-supported mitochondrial respiration. However, as shown in panel 11.6C, malonate, in concentrations exhibiting similar effect on O_2 consumption to those by itaconate, conferred greater ADP-induced depolarizations than itaconate in mitochondria supported by 5 mM succinate in the presence of 1 μM rotenone. The effect of malonate (added prior to mitochondria, supported by glutamate and malate) on cATR-induced changes in $\Delta\Psi m$ in the presence of rotenone is shown in panel 11.6D ('b': 0.0625 mM, 'c': 0.125 mM, 'd': 0.25 mM, 'e': 0.5 mM, and 'f': 5 mM malonate versus control 'a'). It is evident that malonate conferred cATR-induced depolarizations at concentrations in which they inhibit succinate-supported respiration to the same extent as itaconate. However, at the very same concentrations, malonate conferred greater ADP-induced depolarizations than itaconate in mitochondria respiring on succinate in the presence of rotenone. We could not demonstrate itaconate-mediated respiration as shown by Lardy; however, in their experiments mitochondria was incubated for several hours with itaconate, which might lead to sufficient conversion to a suitable product further oxidized by SDH. From the above results we concluded that the abolition of SLP by itaconate cannot be exclusively attributed to favouring itaconyl-CoA formation requiring ATP (or GTP) for the thioesterification, or to an ensuing 'CoA trap' in the form of itaconyl-CoA which could negatively affect the upstream supply of succinyl-CoA from the α-ketoglutarate dehydrogenase complex (Kiss et al., 2013), in turn diminishing ATP (or GTP) formation through SLP by succinate-CoA ligase, or to inhibition of complex II leading to a build-up of succinate which shifts succinate-CoA ligase equilibrium towards ATP (or GTP) utilization. Finally, it is worth considering that itaconate may also have exerted its effects on succinate oxidation by means of antagonizing with succinate for the same transporter(s), possibly the dicarboxylate carrier (SLC25A10), however, the means of itaconate transport have not been investigated.

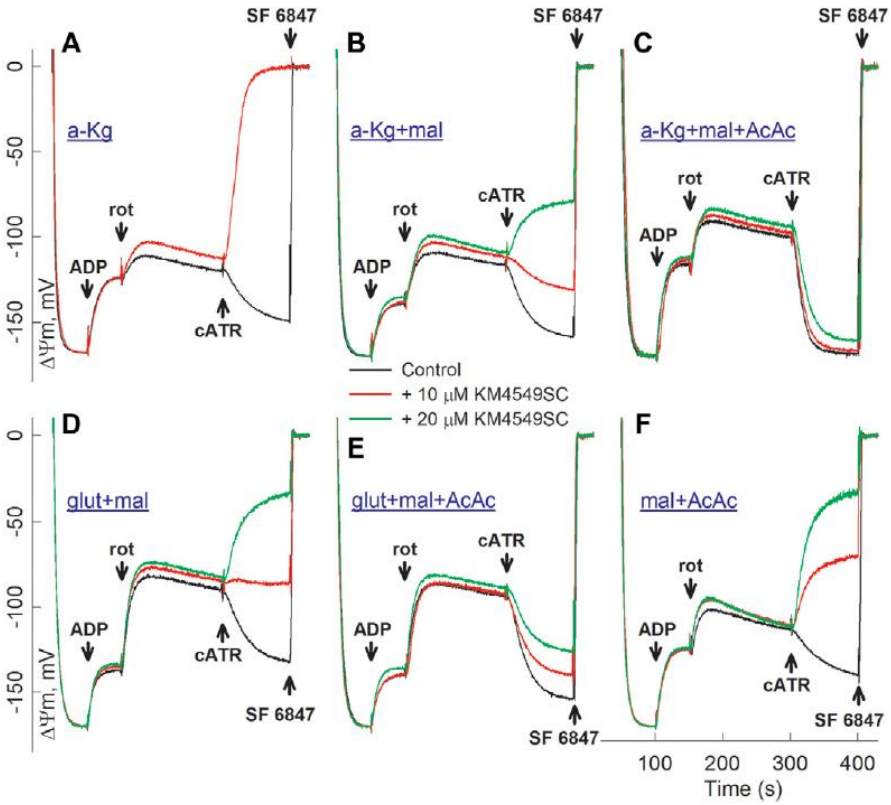

Figure 11.7. Reconstructed time courses of safranine O signal calibrated to $\Delta\Psi m$ in isolated mouse liver mitochondria supported by various substrates as indicated in the panels. The effect of cATR (2 μM) on $\Delta\Psi m$ treated with rotenone (rot, 1 μM) in the absence or presence of KM4549SC in 10 (red traces) or 20 μM (green traces) concentrations is shown. ADP (2 mM) was added where indicated. Control traces are shown in black. At the end of each experiment 1 μM SF 6847 was added to achieve complete depolarization. Each panel shares the same 'x' axis as shown in panel F.

11.9 The effect of the succinate-CoA ligase inhibitor KM4549SC on ANT directionality in rotenone-treated isolated mitochondria

At this point we considered whether a genuine inhibition of succinate-CoA ligase could have an impact on the effect of cATR-induced alterations in $\Delta\Psi m$ in respiration-

impaired mitochondria. To elucidate this, we used KM4549SC (LY266500, 2-(3-Chloro-4-fluorophenyl)-3(2H)-isothiazolone, PubChem CID: 615184), an inhibitor of succinate-CoA ligase (Hunger-Glaser et al., 1999). As shown in figure 11.7, $\Delta\Psi$m was measured by safranine O fluorescence in mouse liver mitochondria and calibrated as described in (Chinopoulos et al., 2010). Additions were as described in figure 11.5. It is evident that KM4549SC reverted the cATR-induced repolarizations (black traces, control) to depolarizations (red and green traces, depending on the concentration of the inhibitor as indicated in the figure) shown in panels A, B, D, and F. In panels C and E the inhibitor did not lead to a cATR-induced depolarization due to the presence of AcAc, which increases [NAD^+] in the mitochondrial matrix, supporting succinyl-CoA production by KGDHC (Kiss et al., 2013), (Kiss et al., 2014). In the experiments shown in panel F, AcAc was also present, but glutamate or α-ketoglutarate were absent.

12 Catabolism of GABA, succinic semialdehyde or gamma-hydroxybutyrate through the GABA shunt impair mitochondrial substrate-level phosphorylation

In (Ravasz et al., 2017) we examined the effect of metabolites catabolized through the GABA shunt on mSLP. The rationale for this is that GABA, succinic semialdehyde or GHB being catablized through the shunt lead to elevation in matrix succinate concentration, thus shifting the equilibrium of the reversible reaction catalyzed by succinate-CoA ligase towards ATP (or GTP) hydrolysis.

12.1 GABA shunt: general considerations

Despite that the participation of GABA in diverse biological processes implies different downstream effectors responsive to this molecule, its metabolism is rather uniform among all tissues: GABA is metabolized through the so-called ‘GABA shunt’, a pathway representing an alternative route for converting α-ketoglutarate to succinate in the citric-acid cycle circumventing succinate-CoA ligase (Machiyama et al., 1970), (Balazs et al., 1970), and figure 12.1. The ensuing succinate from catabolism of GABA through the GABA shunt might be of sufficient flux to force the reaction of succinate-CoA ligase towards ATP (or GTP) hydrolysis, abolishing mitochondrial SLP (Chinopoulos et al., 2010).

12.2 The GABA shunt and relevant reactions pertinent to the experimental design

In order to better outline the rationale of the experiments elaborated below, we depict first the GABA shunt and relevant reactions, transporters and inhibitors pertaining to the study published in (Ravasz et al., 2017).

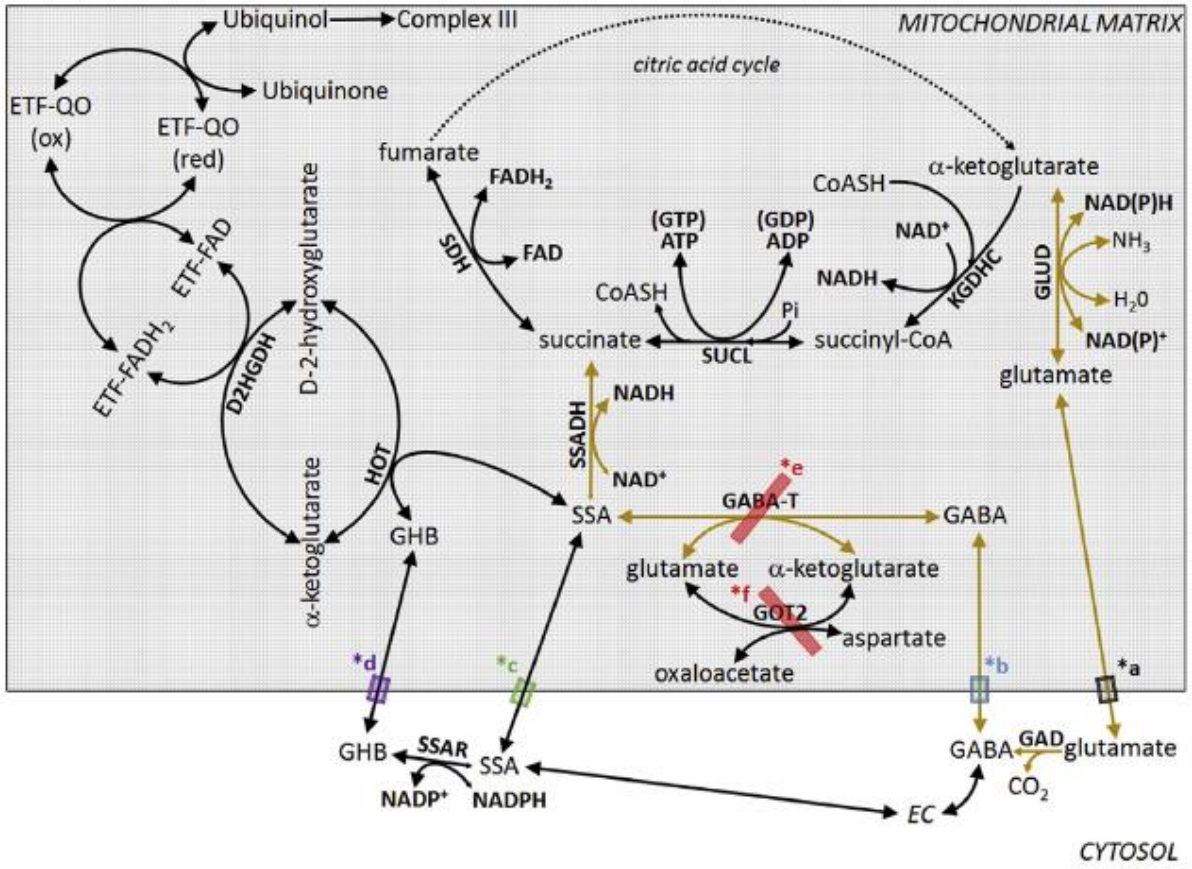

*Figure 12.1. The GABA shunt (outlined by arrows in gold color) and pertinent reactions. SUCL: succinate-CoA ligase; KGDHC: α-ketoglutarate dehydrogenase complex; GLUD: glutamate dehydrogenase; GAD: glutamate decarboxylase; GABA: γ-aminobutyrate; GABA-T: γ-aminobutyrate aminotransferase; GOT2: mitochondrial aspartate aminotransferase; SSAR: succinic semialdehyde reductase; GHB: γ-hydroxybutyrate; SSA: succinic semialdehyde; SSADH: succinic semialdehyde dehydrogenase; HOT: hydroxyacid-oxoacid transhydrogenase; D2HGDH: D-2-hydroxyglutarate dehydrogenase; ETF: electron-transferring flavoprotein; ETF-QO: electron-transferring flavoprotein quinone oxidoreductase; SDH: succinate dehydrogenase. *a: glutamate transporters; *b: putative mitochondrial GABA transporter; *c: putative mitochondrial SSA transporter; *d: putative mitochondrial GHB transporter; *e: inhibitors for GABA-T used in this study: vigabatrin and AOAA; *f: inhibitor for GOT2 in this study: AOAA.*

As shown in figure 12.1, GABA can be derived from glutamate by glutamate decarboxylase (GAD), encoded by either *GAD65* or *GAD67* (Soghomonian and Martin, 1998). Since GAD is a cytosolic enzyme, glutamate needs to be exported from mitochondria; this may occur through well-characterized transporters (depicted as a black semi-transparent box *a), reviewed elsewhere (Sluse, 1996), (Monne and Palmieri, 2014). GABA may also arise by metabolism of putrescine (Sequerra et al., 2007) or homocarnosine (Pisano et al., 1961), or enter the cytoplasm from the extracellular space (EC). In any case, in order for GABA to undergo further transamination it must first enter the mitochondrial matrix. The transport of GABA across the inner mitochondrial membrane (depicted by a blue semi-transparent box *b) has been proposed to occur by "diffusion of a species with no net charge, at rates which are able to maintain maximum activity of the GABA shunt" (Brand and Chappell, 1974). However, in plants, a mitochondrial GABA permease has been identified, termed AtGABP (Michaeli et al., 2011). No such protein has been identified in animals, but a BLASTp homology search yielded a highly homologous (94%) predicted protein termed 'amino acid permease BAT1 (partial)' with a sequence ID: XP_019577258.1 expressed in *Rhinolophus sinicus* (Chinese rufous horseshoe bat), as well as some other

proteins from other species but with low homology (below 35%). In mice and humans there is 23-31% homology of AtGABP to an 'epithelial-stromal interaction protein 1', and no homologous proteins were identified in tissues from rats and guinea pigs. Thus, although several isoforms of plasmalemmal GABA transporters have been identified (Zhou and Danbolt, 2013), their reversibility documented (Pin and Bockaert, 1989), (Bernath, 1992), (Belhage et al., 1993), (Minchin and Iversen, 1974), and GABA is known to permeate murine mitochondria (Brand and Chappell, 1974) and become intramitochondrially metabolized (Salganicoff and De Robertis, 1963), the means of GABA entry to mitochondria remains speculative. Once in the matrix, GABA transaminates with α-ketoglutarate to form glutamate and succinic semialdehyde (SSA) by the mitochondrial GABA transaminase (GABA-T). Succinic semialdehyde will get dehydrogenated by succinate semialdehyde dehydrogenase (SSADH) yielding succinate and NADH, and thus enter the citric acid cycle. SSADH is also the enzyme responsible for further metabolism of aldehyde 4-hydroxy-2-nonenal, an intermediate known to induce oxidant stress (Malaspina et al., 2009). Glutamate and α-ketoglutarate are in equilibrium with oxaloacetate and aspartate through a mitochondrial aspartate aminotransferase (GOT2). In our study we used the GABA-T inhibitors vigabatrin and aminooxyacetic acid (Brand and Chappell, 1974), (Wallach, 1961). The latter compound is also known to inhibit GOT2 (as well as other pyridoxal phosphate-dependent enzymes) (Kauppinen et al., 1987), (Wu and Roberts, 1974). Regarding SSA, there are three possible scenarios for its appearance in the matrix: i) from the extracellular space (EC), transported through the inner mitochondrial membrane by a protein (depicted by a green semi-transparent box *c) that is yet to be characterized (Kim et al., 2011); ii) by the action of hydroxyacid-oxoacid transhydrogenase (HOT), encoded by *ADHFE1*, transhydrogenating β-hydroxybutyrate (GHB) and α-ketoglutarate to D-2-hydroxyglutarate and SSA; or iii) by succinic semialdehyde reductase (SSAR, encoded by *AKR7A2*), converting GHB to SSA in the cytosol (Kaufman et al., 1979), (Hearl and Churchich, 1985), (Hoffman et al., 1980), (Picklo et al., 2001) and the latter getting transported into the matrix; however, the equilibrium of the SSAR reaction is strongly favoured towards GHB formation. The first evidence regarding the existence of HOT came from (Kaufman et al., 1988b), and its gene identified in (Kardon et al., 2006). Later on, this enzyme was isolated and characterized from rat tissues (Kaufman et al., 1988a). Subsequently, the existence of human HOT has been demonstrated in homogenates of human liver and fibroblasts (Struys et al., 2005a), (Struys et al., 2005b). HOT is not the only enzyme interconverting D-2-hydroxyglutarate and α-ketoglutarate; D-2-hydroxyglutarate dehydrogenase (D2HGDH) localized in mitochondria (Wanders and Mooyer, 1995), (Achouri et al., 2004) also performs such an interconversion, but this is coupled to the electron transfer flavoprotein (ETF) system, eventually donating electrons to complex III through ubiquinone. D-2-Hydroxyglutarate is formed as a degradation product of L-hydroxylysine (Lindahl et al., 1967) and possibly also from δ-aminolaevulinate (Chalmers et al., 1980). Interestingly, isocitrate dehydrogenase (IDH) 1 and 2 mutations confer a novel enzymatic activity that facilitates reduction of α-ketoglutarate to D-2-hydroxyglutarate impeding oxidative decarboxylation of isocitrate (Dang et al., 2009), (Pietrak et al., 2011). The accumulation of D-2-hydroxyglutarate due to IDH mutations has been implicated in tumorigenesis (Losman and Kaelin, 2013); however, accumulation of D-2-hydroxyglutarate in glutaric acidurias is associated with encephalopathy and cardiomyopathy, but not tumors (Struys, 2006). In our hands, addition of D-2-hydroxyglutarate to isolated mitochondria did not yield any appreciable $\Delta\Psi$m, as anticipated that it would occur due to the ETF system. This metabolite is known to permeate the cell membrane through a sodium-dicarboxylate cotransporter ($NaDC_3$) and an organic anion transporter (OAT1) (Hagos et al., 2008) but a mitochondrial transport mechanism is yet to be described. GHB is a neurotransmitter (Roth, 1970) and a psychoactive drug, and it is used in the treatment of alcohol withdrawal (Andresen et al., 2011), (Crunelli et al., 2006), (Leone et al., 2010). GHB is also synthesized outside the CNS (Nelson et al., 1981). FDA placed GHB in Schedule I of the Controlled

Substances Act, since 2000. GHB permeates the plasma membrane through monocarboxylate transporters (MCTs) (Cui and Morris, 2009), (Wang et al., 2006). Although it is still controversial whether mitochondrial- and plasma membranes share at least some MCT isoforms (Halestrap, 2013), (Perez-Escuredo et al., 2016) -though MCT2 and MCT4 were recently reported to localize in mitochondria in addition to the plasma membrane (Hussien and Brooks, 2011) - it is very likely that GHB crosses the inner mitochondrial membrane through one or more mitochondrial MCT (purple semi-transparent box *d).

12.3 GABA, SSA and GHB energize mitochondria in aerobic conditions

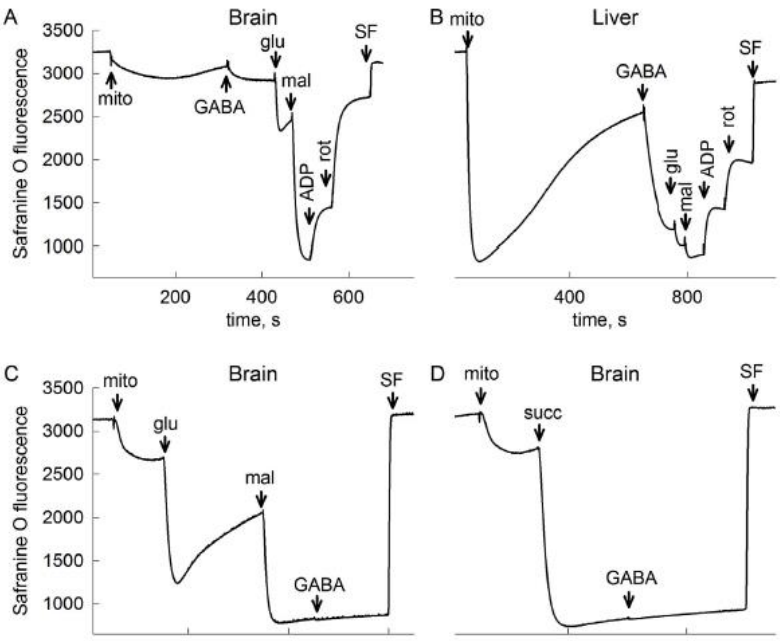

Figure 12.2. The effect of GABA on membrane potential of isolated brain (A, C, D, E) and liver (B, F) mitochondria. Reconstructed time-courses of safranine O fluorescence (arbitrary fluorescence) indicating ΔΨm. Mitochondria (mito) were added where indicated; 0.25 mg for brain, 0.5 mg for liver. GABA (1 mM), glutamate (glu, 5 mM), malate (mal, 5 mM), succinate (succ, 5 mM), ADP (2 mM), rotenone (rot, 1 μM), SF6847 (SF, 1 μM) was added where indicated. In the experiments depicted by the blue traces in panels E and F vigabatrin (VGBT, 0.3 mM) was present in the medium prior to addition of mitochondria. In the experiment depicted by the green trace in panel F aminooxyacetic acid (AOAA, 0.1 mM) was present in the medium prior to addition of mitochondria. Panels to the right share the same y-axis with panels to the left. Each trace is representative of at least four independent experiments.

The use of GABA and SSA as bioenergetic substrates has been addressed in a limited type of tissues, almost exclusively rat brain mitochondria (Walsh and Clark, 1976), (Cunningham et al., 1980), (Tunnicliff et al., 1977), (Loscher et al., 1989). From these studies it was inferred that the "free" mitochondria (a mixture from neuronal and astrocytic origin) exhibit a higher rate of GABA metabolism than synaptic mitochondria (Walsh and Clark, 1976). This is in agreement with later studies showing that GABA is mostly metabolized in astrocytes, not neurons (Schousboe and Waagepetersen, 2007). In order to verify that in our hands and for the type of mitochondria that we prepared (Percoll-purified mouse brain and crude liver), GABA and SSA can be metabolized, we investigated the effect of exogenously adding these compounds on mitochondrial membrane potential ($\Delta\Psi$m) and compared it to that obtained from 'classical' substrates. As shown in figure 12.2A for brain and 12.2B for liver, mitochondria (mito) were added in the suspension without exogenously added substrates, and safranine O fluorescence was recorded. Brain mitochondria do not exhibit a significant pool of endogenous substrates, thus, they develop only a minor $\Delta\Psi$m. On the other hand, liver mitochondria contain endogenous substrates to a higher extent and this is reflected by a more significant polarization, which however, gradually subsides as these endogenous substrates are consumed. Addition of GABA to both types of mitochondria leads

to a further polarization, which is quantitatively higher in liver. Further addition of glutamate (5 mM) and malate (5 mM) leads to an even further polarization, implying that addition of GABA did not lead to achievement of maximum $\Delta\Psi m$. Subsequent addition of ADP, rotenone and SF6847 yielded the expected rise in safranine O fluorescence, implying anticipated responses in decreasing $\Delta\Psi m$. By adding GABA after the sequential addition of glutamate and malate (panel12.2C) or succinate (panel 12.2D) to isolated brain mitochondria, no further polarization was recorded implying that the electron transport chain generating $\Delta\Psi m$ has been saturated with reducing equivalents, NADH (through SSADH) and/or $FADH_2$ (through SDH). Similar traces were obtained from liver mitochondria. Next, we questioned if the GABA-induced polarization is genuinely due to the GABA shunt, eventually entering the citric acid cycle as succinate. To check this, we used vigabatrin, a specific inhibitor of GABA-T. Vigabatrin (VGBT, 0.3 mM), abolished the GABA-induced $\Delta\Psi m$ generation in both brain (panel 12.2E, blue trace) and liver (panel 12.2F, blue trace) mitochondria. Likewise, by adding the alternative GABA-T inhibitor, aminooxyacetic acid (AOAA, 0.1 mM, green trace panel 12.2F), GABA-induced $\Delta\Psi m$ generation was ameliorated. The results of the above experiments are in agreement with those obtained in (Brand and Chappell, 1974), (Wallach, 1961) and (Cunningham et al., 1980), showing that GABA supports mitochondrial respiration, and its oxidation is sensitive to GABA-T inhibition. To address the possibility that the GABA-induced polarization does not stem from supporting α-ketoglutarate to glutamate conversion by GABA-T, in turn leading to NAD(P)H formation from glutamate to α-ketoglutarate conversion by GLUD, we tested the effect of SSA on the membrane potential of isolated mitochondria. As shown in panel 12.3A for brain, and panel 12.3B for liver mitochondria, addition of SSA (1 mM) in the absence of exogenously added substrates lead to generation of $\Delta\Psi m$. Because the subsequent addition of glutamate and malate did not lead to any further polarization, we concluded that SSA conferred the maximum $\Delta\Psi m$ achievable. Thus, GABA generates $\Delta\Psi m$ by transamination to SSA, which is subsequently dehydrogenated by SSADH, entering the citric acid cycle as succinate. At this junction, the question arose if $\Delta\Psi m$ generation was due to NADH production by SSADH, or $FADH_2$ production supported by succinate, or both. To address this, we added either rotenone (red traces) or atpenin A5 (lilac trace) or both (orange trace) after SSA and recorded the changes in $\Delta\Psi m$. When rotenone or atpenin A5 were added alone, there were no changes in safranine O fluorescence, implying that in the first case $FADH_2$ production from SDH was supporting $\Delta\Psi m$, and in the latter case, NADH production from SSADH was responsible for the generation of reducing equivalents. When both complex I and II inhibitors were present, $\Delta\Psi m$ collapsed, and the same effect was observed by inhibiting complex III with stigmatellin (stigm, 1 μM, cyan trace). This implies that $\Delta\Psi m$ generated by SSA is supported by both $FADH_2$ production through SDH, and NADH through SSADH. As expected, the SSA-mediated $\Delta\Psi m$ generation was insensitive to GABA-T inhibitors, shown in figures 12.3C and 12.3D, for brain and liver mitochondria, respectively. We attempted to inhibit SSADH using 4-hydroxybenzaldehyde (Cash et al., 1978) or disulfiram (Ryzlak and Pietruszko, 1988) however both compounds were strongly uncoupling mitochondria (not shown).

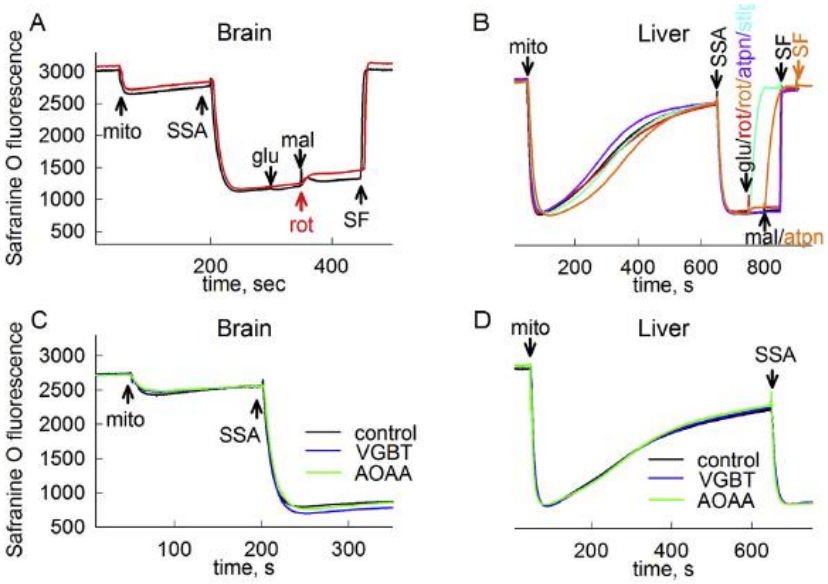

Figure 12.3. The effect of SSA on membrane potential of isolated brain (A, C) and liver (B, D) mitochondria. Reconstructed time-courses of safranine O fluorescence (arbitrary fluorescence) indicating $\Delta\Psi m$. Mitochondria (mito) were added where indicated; 0.25 mg for brain, 0.5 mg for liver. SSA (1 mM), glutamate (glu, 1 mM), malate (mal, 1 mM), rotenone (rot, 1 μM), atpenin A5 (atpn, 2 μM), SF6847 (SF, 1 μM) was added where indicated. In the experiments depicted by the blue traces in panels C and D, vigabatrin (VGBT, 0.3 mM), and in those depicted by green traces, aminooxyacetic acid (AOOA, 0.1 mM) was present in the medium prior to addition of mitochondria. Panels to the right share the same y-axis with panels to the left. In panels A and B, red traces, rotenone was added in lieu of glutamate and malate. In panel B, lilac trace, atpenin A5 was added in lieu of rotenone, and in the orange trace both rotenone and atpenin A5 were present in lieu of glutamate and malate. In the same panel, cyan trace, stigmatellin (stigm, 1 μM) was added where indicated. Each trace is representative of at least four independent experiments.

To further address the contribution of SSA in yielding NADH through SSADH, we recorded the effect of the substrate on NADH autofluorescence in permeabilized or intact mitochondria. As shown in figure 12.4A for brain, and 12.4B for liver, mitochondria were added when indicated, and NADH autofluorescence was recorded. After approximately 100 sec mitochondria were permeabilized by alamethicin, yielding a minor decrease in the signal. Further addition of NAD^+ did not lead to any appreciable changes. Subsequent addition of 10 mM malonate ensures that SDH was fully inhibited. Then, addition of 1 mM SSA yielded a strong increase in NADH concentration. Despite the fact that atpenin A5 has been branded as a specific inhibitor of SDH, we wished to verify that it does not affect SSADH activity either. Indeed, by including 2 μM atpenin A5 and repeating the experiments (red traces, panels A and B), traces were nearly identical to those obtained in the absence of this SDH inhibitor (black traces, figures 12.4A and 12.4B). What is also evident by comparing figure panels 12.4A and 12.4B is that the extent of NADH production by SSA is nearly 10 times higher in liver than brain mitochondria. Since liver mitochondria were double the amount of brain mitochondria for these experiments, it is inferred that SSADH activity in liver is approximately 5 times higher than that in brain mitochondria. This finding is at odds with those reported by Chambliss et al, showing that the liver activity for SSADH was about 2/3 of that in rat brain (Chambliss et al., 1995). Perhaps this is due to the different choice of laboratory animal (rat in Chambliss et al, mice in this study). As expected, addition of succinate after SSA, did not yield any further increase in NADH autofluorescence. In order to demonstrate that NADH can be generated by SSA in intact mitochondria, the following experiment was performed: as shown in figure 12.4C, liver mitochondria were added when indicated, and NADH autofluorescence was recorded.

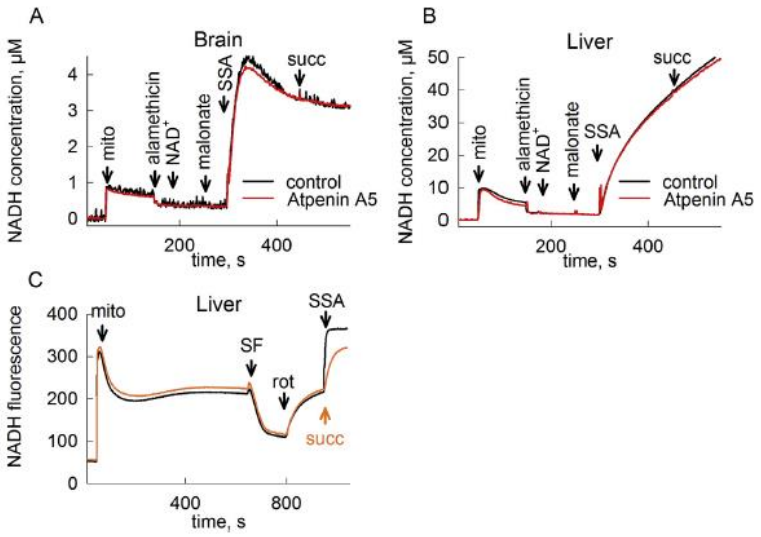

A small amount of the uncoupler (40 nM SF6847) was subsequently added in order to reach the maximum oxidized state of NADH/NAD^+ pools and this was reflected by a decrease in the signal. Subsequent addition of rotenone blocked complex I, thus regenerating some amount of the NADH pool. Then, addition of either SSA (figure 12.4C, black trace) or succinate (figure 12.4C, orange trace) yielded an increase in intramitochondrial NADH fluorescence, but with different

Figure 12.4. The effect of SSA on NADH autofluorescence in permeabilized brain (A) and liver (B) and intact liver (C) mitochondria. Reconstructed time-courses of calibrated (A, B) and uncalibrated (C) NADH autofluorescence. Mitochondria (mito) were added where indicated; 0.25 mg for brain, 0.5 mg for liver. Alamethicin (20 μg), NAD^+ (1 mM), malonate (10 mM) SSA (1 mM), rotenone (rot, 1 μM), succinate (succ, 1 mM), SF6847 (SF, 40 nM) was added where indicated. In the experiments depicted by the red traces in panels A and B, 2 μM atpenin A5 was present in the medium prior to addition of mitochondria. Panel B shares the same y-axis with panel A. Each trace is representative of at least four independent experiments.

kinetics. In the case of SSA, the increase in NADH is due to SSADH activity, while in the case of succinate is probably due to downstream dehydrogenases of the citric acid cycle, thus the timing of NADH increase is more gradual. The pool of NAD^+ for the dehydrogenases in the absence of a functional complex I due to rotenone could be mitochondrial diaphorases, as described previously (Kiss et al., 2014). Regarding GHB, the catabolism of this molecule by mitochondria was addressed by (Kaufman et al., 1988b) and (Gibson and Nyhan, 1989). As shown in figure 12.1, GHB transhydrogenates with α-ketoglutarate to SSA and D-hydroxyglutarate by HOT. However, HOT exhibits a very strong tissue-specific expression; most notably, HOT is scarcely expressed in the brain (Kim et al., 2007), (Kaufman et al., 1988b), a phenomenon that may contribute to the lingering neurologically-related effects of GHB acting on specific receptors (Bay et al., 2014), as it is catabolized very slowly. On the other hand, HOT is abundantly expressed in the liver (Kaufman et al., 1988b). Thus, exogenously added GHB to mitochondria isolated from brain should not lead to any appreciable bioenergetic effects; such effects should be observed if liver mitochondria are used instead. Indeed, as shown in figure 12.5A, addition of 5 mM GHB before addition of 5 μM α-ketoglutarate (red trace) or addition of 50 μM α-ketoglutarate before GHB (black trace, because freshly purified brain mitochondria are devoid of endogenous substrates and HOT requires both GHB and α-ketoglutarate to generate D-hydroxyglutarate and SSA) did not lead to a significant gain of $\Delta\Psi m$ in Percoll-purified brain mitochondria. Further addition of malate (1 mM) led to full polarization which was abolished by rotenone (1 μM), implying that these mitochondria were entirely competent to generate $\Delta\Psi m$ by substrates other than GHB. In contrast, addition of GHB to isolated liver mitochondria (figure 12.5B) before endogenous substrates were fully consumed (thus, minor amounts of α-ketoglutarate were expected to exist in the mitochondrial matrix) led to a considerable polarization compared to vehicle; further addition of a minute amount of α-ketoglutarate (5 μM) led to a further gain of $\Delta\Psi m$. As expected, the concomitant presence of GABA-T inhibitors (figure 12.5B) vigabatrin (VGBT, blue trace) or aminooxyacetic acid (AOAA, green trace) did not affect the GHB-induced polarization in liver mitochondria, compared to control (black trace).

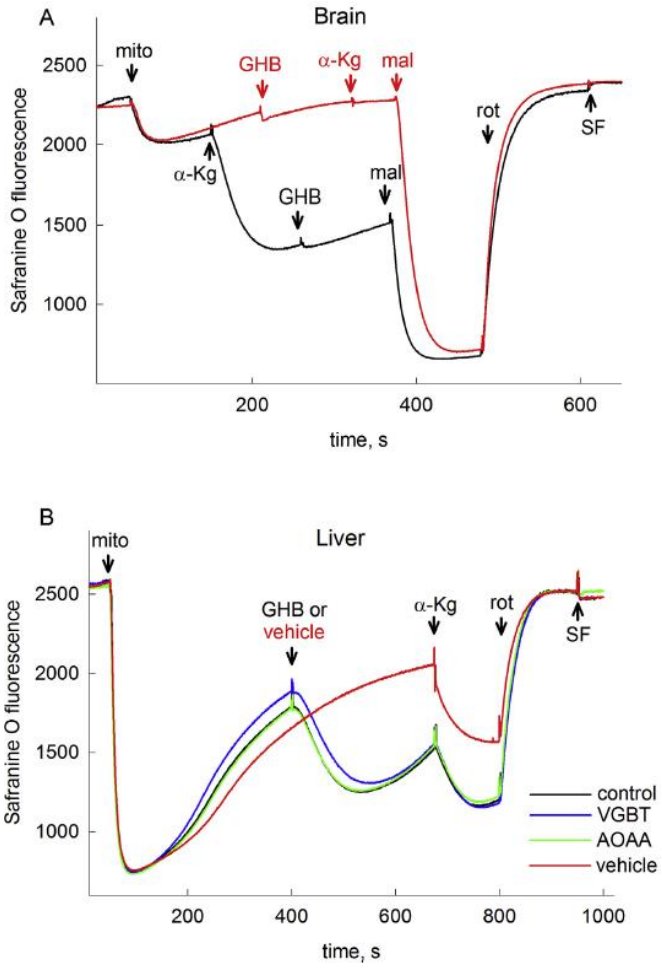

Figure 12.5. The effect of GHB on membrane potential of isolated brain (A) and liver (B) mitochondria. Reconstructed time-courses of safranine O fluorescence (arbitrary fluorescence) indicating $\Delta\Psi m$. Mitochondria (mito) were added where indicated; 0.25 mg for brain, 0.5 mg for liver. GHB (5 mM), α-ketoglutarate (α-Kg, 50 or 5 μM), malate (mal, 1 mM), rotenone (rot, 1 μM), SF6847 (SF, 1 μM) was added where indicated. In the experiments depicted by the blue traces in panel B, vigabatrin (VGBT, 0.3 mM), and in those depicted by green trace, aminooxyacetic acid (AOOA, 0.1 mM) was present in the medium prior to addition of mitochondria. Red trace is a vehicle control for GHB. Each trace is representative of at least four independent experiments.

12.4 GABA, SSA and GHB abolish mitochondrial SLP in anoxia

In order to interrogate the effects of GABA, SSA and GHB on SLP in intact mitochondria, we employed the biosensor test developed by us (Chinopoulos et al., 2010). The results of this test are shown in figure 12.6 for GABA, figure 12.7 for SSA and figure 12.8 for GHB. As shown in figure 12.6A for brain and 12.6B for liver, mitochondria respired on glutamate and malate (black trace), or glutamate and malate plus GABA (red trace) and allowed to fully polarize (solid traces). State 3 respiration was initiated by 2 mM ADP. The presence of GABA did not increase the rates of respiration, consistent with the findings of figures 12.2C and 12.2D showing no further polarization by GABA, in the presence of glutamate and malate. In an air-tight chamber, mitochondria consume the entire amount of oxygen and this is verified by recording 'zero' levels of dissolved oxygen (dashed traces). Anoxia also coincided with the onset of an additional depolarization leading to a clamp of $\Delta\Psi m$ at around -100 mV. At this membrane potential, F_0-F_1 ATP synthase operated in reverse mode, i.e. pumping protons out of the matrix at the expense of matrix ATP hydrolysis. In mitochondria respiring on substrates supporting SLP, as in these experiments, i.e. glutamate and malate, inhibition of the ANT by cATR conferred a moderate repolarization, implying that the translocase was still operating in the forward mode. In contrast, mitochondria fueled by glutamate and malate plus GABA, reacted to cATR with a depolarization during the anoxic period. The effect of GABA, reverting the cATR induced changes from repolarization to depolarization implying abolition of SLP was antagonized by the GABA-T inhibitors vigabatrin (VGBT, 0.3 mM, blue traces in figures 12.6C for brain and 12.6D for liver) and aminooxyacetic acid (AOAA, 0.1 mM green traces in figures 12.6E for brain and 12.6F for liver). It is also notable that AOAA diminished state 3 respiration, which is expected because it is an inhibitor of pyridoxal phosphate-dependent enzymes (Kauppinen et al., 1987), (Wu and Roberts, 1974), (Schousboe and Waagepetersen, 2006), most participating in several bioenergetic pathways.

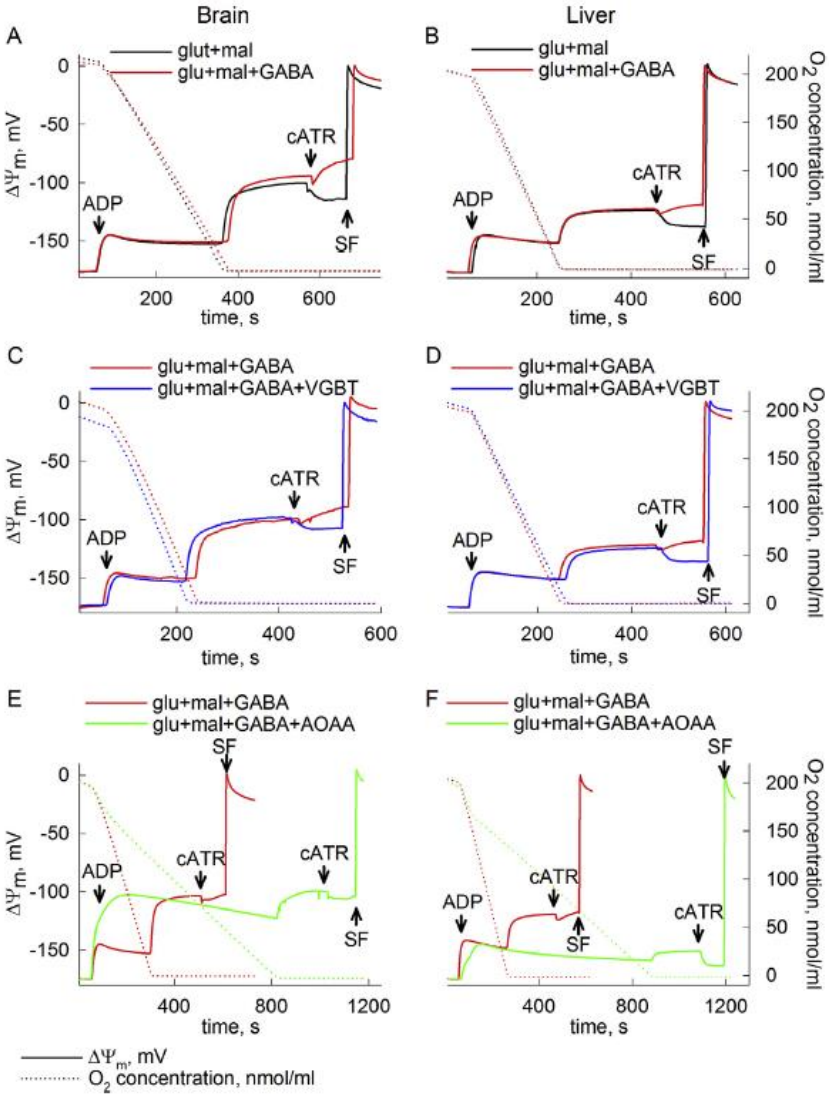

From the above experiments we concluded that GABA metabolism through the GABA shunt led to an increase in succinate formation, which favored the reversible reaction catalyzed by succinate-CoA ligase towards ATP (or GTP) hydrolysis, thus abolishing SLP. Regarding the effect of SSA on SLP, the results of these experiments are shown in figure 12.7. As shown in figure 12.7A for brain and 12.7B for liver, mitochondria respired on glutamate and malate (black trace), or glutamate and malate plus SSA (red trace) and allowed to fully polarize (solid traces). State 3 respiration was initiated by 2 mM ADP. The presence of SSA affected very minorly the rates of respiration, consistent with the findings of figures 12.3A and 12.3B showing no further polarization by SSA, in

Figure 12.6. The effect of GABA on mitochondrial SLP during anoxia. Reconstructed time courses of safranine O signal calibrated to ΔΨm (solid traces), and parallel measurements of oxygen concentration in the medium (dotted traces) in isolated brain (0.5 mg, A, C, E) and liver (1 mg, B, D, F) mitochondria in the presence of either GABA (5 mM, red traces) or GABA+vigabatrin (VGBT, 0.3 mM, blue traces), or GABA+aminooxyacetic acid (AOAA, 0.1 mM green traces). ADP: 2 mM; carboxyatractyloside (cATR), 1 μM. Substrate concentrations were: glutamate (5 mM) and malate (5 mM). At the end of each experiment 1 μM SF 6847 was added to achieve complete depolarization. Each trace is representative of at least four independent experiments.

the presence of glutamate and malate. However, during the anoxic period the presence of SSA reverted the cATR induced changes from repolarization to depolarization implying abolition of SLP, but unlike in the case of GABA, the GABA-T inhibitors vigabatrin (VGBT, 0.3 mM, blue traces in figures 12.7C for brain and 12.7D for liver) and aminooxyacetic acid (AOAA, 0.1 mM green traces in figures 12.7E for brain and 12.7F for liver) did not ameliorate the effect of SSA. This is expected, because SSA entry to the GABA shunt is after the GABA-T step (see figure 12.1). Regarding the effect of GHB on SLP, the results of these experiments are shown in figure 12.8. As shown in figure 12.8A for brain and 12.8B for liver, mitochondria respired on α-ketoglutarate and malate (black trace), or α- ketoglutarate and malate plus GHB (red trace) and allowed to fully polarize (solid traces). State 3 respiration was initiated by 2 mM ADP. The presence of GHB minorly affected the rates of liver but not brain mitochondrial respiration. In liver mitochondria, during the anoxic period the presence of GHB reverted the cATR induced changes

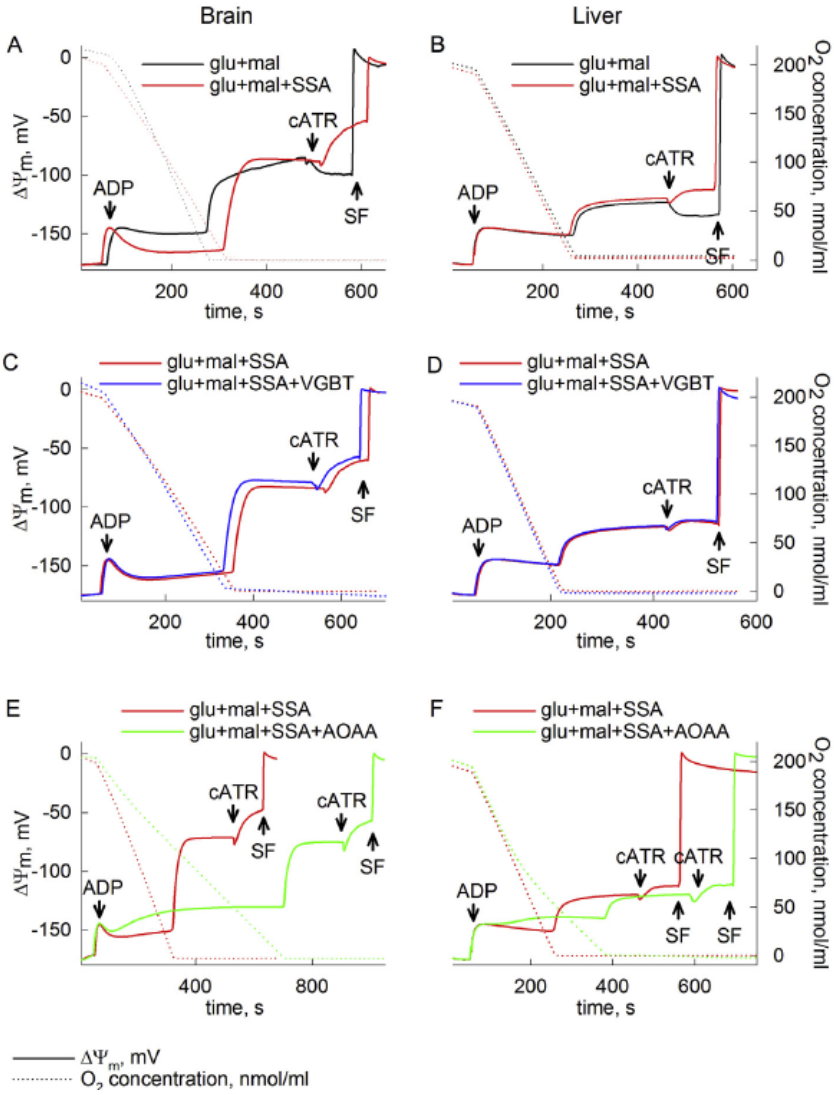

from repolarization to depolarization implying abolition of SLP, but unlike in the case of GABA, vigabatrin (VGBT, 0.3 mM, figure 12.8C blue trace) or aminooxyacetic acid (AOAA, 0.1 mM figure 12.8D, green trace) did not ameliorate the effect of GHB. This is expected, because GHB entry to the GABA shunt does not involve the GABA-T step (see figure 12.1). Unlike liver mitochondria, GHB did not ameliorate SLP in brain mitochondria (figure 12.8A) consistent with the fact that HOT is scarcely expressed in the brain, precluding the formation of an appreciable amount of SSA. From the above experiments we concluded that during anoxia, the beneficial effect of SLP preventing mitochondria from becoming extramitochondrial ATP consumers is abolished by GABA, SSA and GHB.

Figure 12.7. The effect of SSA on mitochondrial SLP during anoxia. Reconstructed time courses of safranine O signal calibrated to ΔΨm (solid traces), and parallel measurements of oxygen concentration in the medium (dotted traces) in isolated brain (0.5 mg, A, C, E) and liver (1 mg, B, D, F) mitochondria in the presence of either SSA (1 mM, red traces) or SSA+vigabatrin (VGBT, 0.3 mM, blue traces), or SSA+aminooxyacetic acid (AOAA, 0.1 mM green traces). ADP: 2 mM; carboxyatractyloside (cATR), 1 μM. Substrate concentrations were: glutamate (5 mM) and malate (5 mM). At the end of each experiment 1 μM SF 6847 was added to achieve complete depolarization. Each trace is representative of at least four independent experiments.

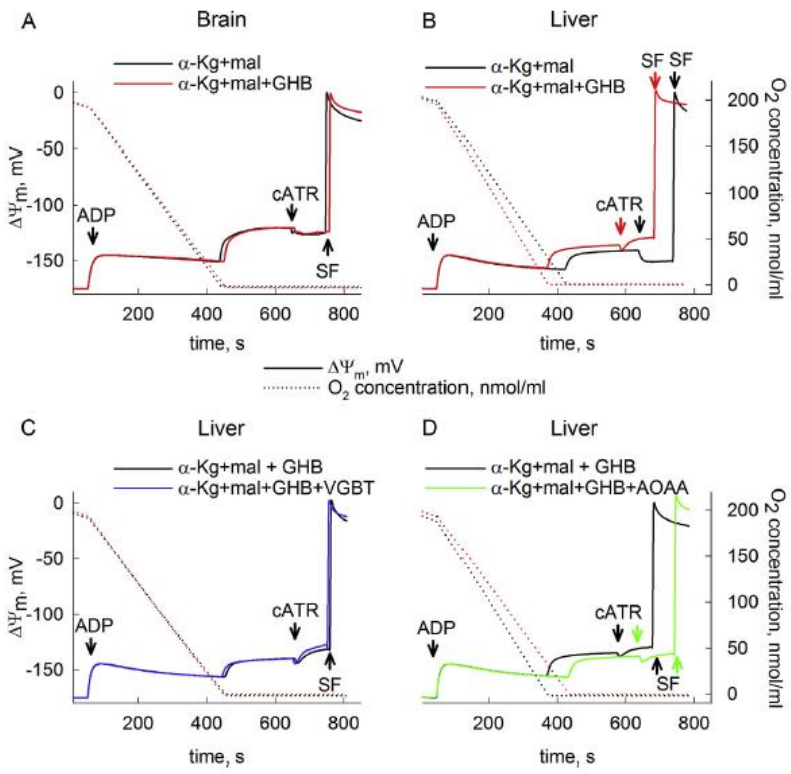

Figure 12.8. The effect of GHB on mitochondrial SLP during anoxia. Reconstructed time courses of safranine O signal calibrated to $\Delta\Psi m$ (solid traces), and parallel measurements of oxygen concentration in the medium (dotted traces) in isolated brain (0.5 mg, A) and liver (1 mg, B, C, D) mitochondria in the presence of either GHB (5 mM, red traces) or GHB+vigabatrin (VGBT, 0.3 mM, blue traces), or GHB+aminooxyacetic acid (AOAA, 0.1 mM green traces). ADP: 2 mM; carboxyatractyloside (cATR), 1 μM. Substrate concentrations were: glutamate (5 mM) and malate (5 mM). At the end of each experiment 1 μM SF 6847 was added to achieve complete depolarization. Each trace is representative of at least four independent experiments.

13 The Effect of 2-Ketobutyrate on Mitochondrial Substrate-Level Phosphorylation

In the mitochondrial matrix, succinyl-CoA can be provided not only by α-ketoglutarate by the reaction catalyzed by KGDHC, but also by threonine, serine and methionine catabolism through the common intermediate, 2-ketobutyrate. However, in this case, 2-ketobutyrate will become succinyl-CoA through propionyl-CoA catabolism, obligatorily passing through an ATP-consuming step substantiated by propionyl-CoA carboxylase.

13.1 2-ketobutyrate catabolism: general considerations

As shown in figure 13.1, a number of metabolites converge to succinyl-CoA such as glutamine, threonine, serine, methionine, valine, isoleucine, thymine, cholesterol and of course others originating upstream from α-ketoglutarate. Dashed arrows imply multiple steps occurring in either inside or outside the mitochondrial matrix. Catabolism of threonine, serine and methionine lead to 2-KB generation which would enter the mitochondrial matrix and get converted to propionyl-CoA by the branched-chain keto-acid dehydrogenase complex (BCKDHC), and then subsequently to D-methylmalonyl-CoA by propionyl-CoA carboxylase (PCC), consuming ATP. In turn, D-methylmalonyl-CoA racemizes to L-methylmalonyl-CoA by methylmalonyl-CoA epimerase (MCEE) and then isomerizes to succinyl-CoA by methylmalonyl-

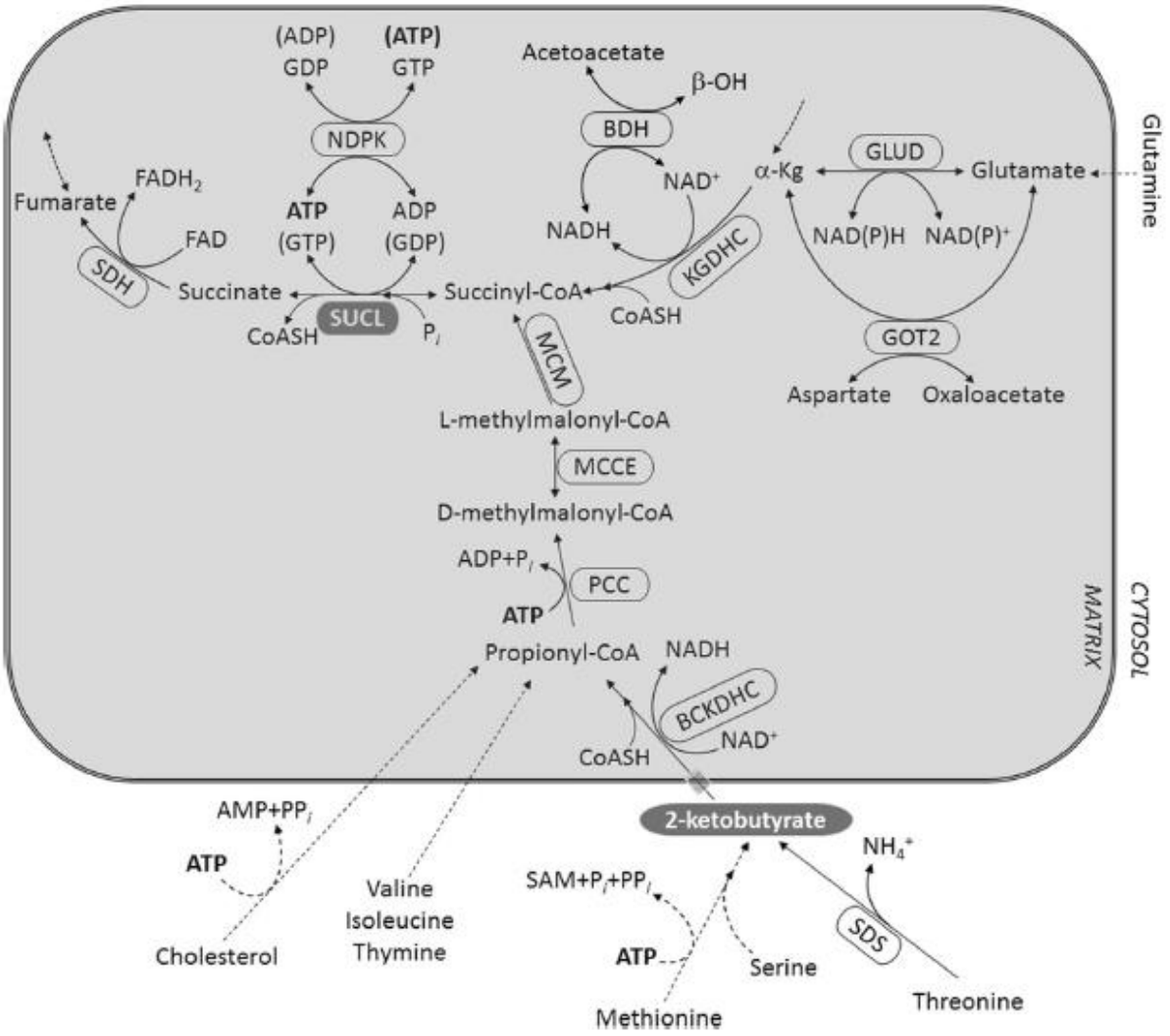

Figure 13.1. Catabolism of metabolites towards succinyl-CoA. BCKDHC: branched-chain keto-acid dehydrogenase; BDH: β-hydroxybutyrate dehydrogenase; GLUD: glutamate dehydrogenase; GOT2: aspartate aminotransferase; KGDHC: ketoglutarate dehydrogenase complex; MCM: methylmalonyl mutase; MCEE: methylmalonyl racemase; NDPK: nucleoside diphosphokinase; PCC: propionyl-CoA carboxylase; SAM: S-adenosylmethionine; SDH: succinate dehydrogenase; SDS: L-serine dehydratase/L-threonine deaminase; SUCL: succinate-coA ligase. Dashed arrows imply multiple steps which may occur inside or outside the mitochondrial matrix. Entrance of 2-KB into the matrix likely occurs through the mitochondrial pyruvate carrier (depicted by a grey semi-transparent cylinder).

CoA mutase (MCM), a B_{12}-dependent enzyme. The aforementioned enzymes reside inside the mitochondrial matrix, and since they process 2-KB it means that this metabolite traverses the inner mitochondrial membrane. To date, a 2-KB-specific carrier has not been identified, though it is known to compete for pyruvate transport through the mitochondrial pyruvate carrier (Bolli et al., 1989), (Paradies and Papa, 1975), (Hutson and Rannels, 1985) and probably the choline carrier (Michel and Bakovic, 2009). The reaction catalyzed by β-hydroxybutyrate dehydrogenase (BDH) is also shown, demonstrating the competition between this enzyme complex and KGDHC for NAD^+, in the presence of excess β-hydroxybutyrate. This phenomenon is exploited in our experimental settings in order to titrate the contribution of KGDHC yielding a-ketoglutarate in mitochondria with an inhibited respiratory chain for the purpose of mSLP. From the above metabolic considerations, we set to investigate if –and to what extent- 2-KB serves as a fuel for mitochondria, and if so, does it impact on mSLP.

13.2 2-KB supports generation of $\Delta\Psi m$ in isolated liver and brain mitochondria by generating both NADH and $FADH_2$

As shown in figures 13.2 and 13.3 for liver and brain mitochondria, respectively, addition of seven 0.5 mM 2-KB pulses to mitochondria totaling 3.5 mM (panel figures 13.2A and 13.3A) conferred a moderate decrease in safranine O fluorescence implying development of $\Delta\Psi m$. In liver mitochondria, $\Delta\Psi m$ was afterwards becoming gradually lost, as opposed to $\Delta\Psi m$ in brain mitochondria that remained stable. Subsequent addition of succinate (succ, 5 mM) led to maximum polarization. Further addition of the complex I inhibitor rotenone (rot, 1 μM) yielded no (liver mitochondria) or a very small depolarization implying intact operation of complexes III and IV.

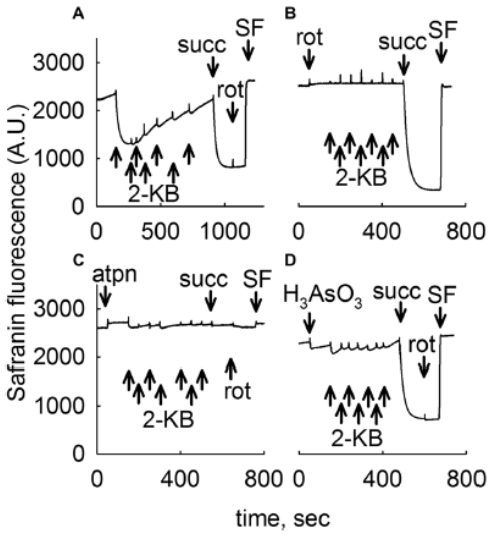

Figure 13.2. 2-KB as a metabolic fuel in mouse liver mitochondria. Reconstructed time courses of safranine O signal in isolated mouse liver mitochondria. The effect of 2-KB pulses (indicated by arrows signifying 0.5 mM each, thus a total of 3.5 mM 2-KB added) is shown. Whenever indicated, succinate (5 mM) or rotenone (1 μM) or atpenin (atpn 1 μM), or arsenite (H_3AsO_3, 1 mM) was added. At the end of each experiment 250 nM SF 6847 was added to achieve complete depolarization (an increase in safranine O fluorescence signal implies depolarization). Wherever single graphs are presented, they are representative of at least 4 independent experiments.

At the end of the experiment the uncoupler SF 6847 (SF, 250 nM) was added in order to achieve a complete loss of $\Delta\Psi m$ indicating maximum safranine O fluorescence. However, addition of rotenone (figure panels 13.2B and 13.3B for liver and brain, respectively), or the complex II inhibitor atpenin (atpn, 1 μM, figure panels 13.2C and 13.3C for liver and brain, respectively) or the dehydrogenases inhibitor arsenite (H_3AsO_3 1 mM, figure panels 13.2D and 13.3D for liver and brain, respectively) abolished the effect of 2-KB conferring $\Delta\Psi m$ to mitochondria (with the exception of atpenin in brain mitochondria, where a mild decrease in safranine O fluorescence was observed upon addition of 2-KB, figure panel 13.3C). As expected, subsequent addition of succinate (succ) led to development of $\Delta\Psi m$ if mitochondria were challenged by rotenone or arsenite, but not atpenin. Note that prior to the addition of any substrates liver mitochondria exhibit an initial, transient polarization which is attributed to consumption of endogenous substrates, most likely acyl carnitines. This transient depolarization proceeds to a complete loss of $\Delta\Psi m$ within ~1 hour. From the above results we deduced that 2-KB affords $\Delta\Psi m$ to mitochondria by mechanisms involving both complex I (fueled by NADH, some originating from BCKDHC, an arsenite-sensitive enzyme complex) and complex II (fueled by $FADH_2$).

13.3 2-KB abolishes mSLP conferred by glutamate or pyruvate

mSLP was addressed by interrogating the directionality of the ANT in mitochondria with an inhibited respiratory chain, isolated from mouse liver (figure panels 13.4A and 13.4B) or brain (figure panels 13.4C and 13.4D). As shown in figure 13.4, mitochondria were added where indicated by the closed circles and safranine O fluorescence was recorded reflecting $\Delta\Psi m$. ADP (2 mM) was added where indicated, initiating respiration and causing a mild depolarization due to forward ANT and F_o-F_1 ATP synthase operation.

Subsequently, oxidative phosphorylation was halted by inhibiting complex I with rotenone (rot). This led to a further loss of $\Delta\Psi m$; $\Delta\Psi m$ was now maintained by a reverse-function of F_o-F_1 ATP synthase. Mindful of the directional synchrony of ANT with SUCL reaction (Chinopoulos, 2011a), Inhibition of the ANT by carboxyatractyloside hints on the presence of mSLP: repolarization implies that SUCL operates towards ATP (or GTP) formation thus supporting mSLP, while cATR-induced depolarization means that SUCL was hydrolyzing ATP (or GTP). Substrates were either glutamate and malate (5 mM each) or glutamate and malate and 2 mM β-hydroxybutyrate (β-OH) (figure panels 13.4A and 13.4C) or pyruvate and malate (5 mM each) as indicated in the legends of figure 13.4. Dose-dependent addition of 2-KB (0.5, 2 or 5 mM) converted the cATR-induced changes in safranine O fluorescence from a repolarization to a depolarization, implying dose-dependent inhibition of mSLP by 2-KB (which was complete at 5 mM, or 2 mM if β-hydroxybutyrate was also present). This concentration range of 2-KB was chosen for interrogating mSLP mindful of that used in figures 13.2 and 13.3 verifying catabolism of this metabolite. At the end of each experiment, the uncoupler SF 6847 SF, 250 nM) was added to achieve a completely depolarized state.

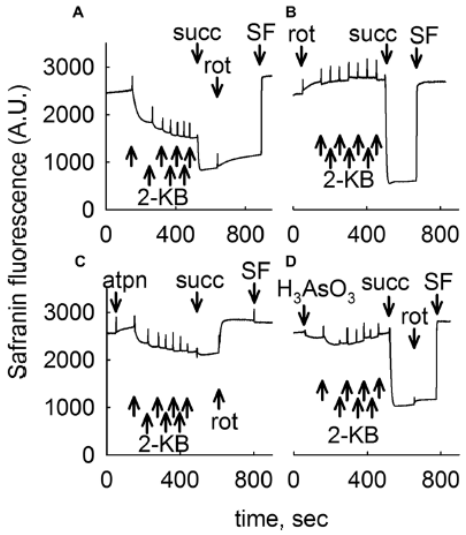

Figure 13.3. -KB as a metabolic fuel in mouse brain mitochondria. Reconstructed time courses of safranine O signal in isolated mouse brain mitochondria. The effect of 2-KB pulses (indicated by arrows signifying 0.5 mM each, thus a total of 3.5 mM 2-KB added) is shown. Whenever indicated, succinate (5 mM) or rotenone (1 μM) or atpenin (atpn 1 μM), or arsenite (H_3AsO_3, 1 mM) was added. At the end of each experiment 250 nM SF 6847 was added to achieve complete depolarization (an increase in safranine O fluorescence signal implies depolarization). Wherever single graphs are presented, they are representative of at least 4 independent experiments.

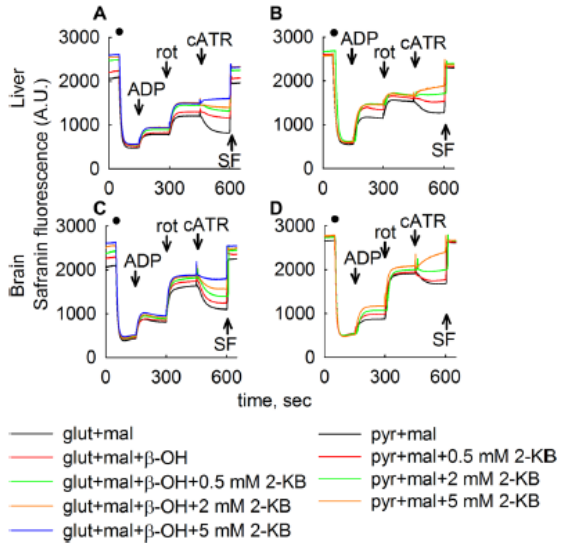

Figure 13.4. 2-KB abolishes mSLP. Reconstructed time courses of safranine O signal in isolated mouse liver (A, B) or brain (C, D) mitochondria. Mitochondria were added where indicated by the closed circles. ADP (2 mM) was added where indicated. The effect of cATR (2 μM) on $\Delta\Psi m$ treated with rotenone (rot, 1 μM) in the absence or dose-dependent presence of 2-KB as indicated in the legends is shown. Control traces are shown in black. At the end of each experiment 250 nM SF 6847 was added to achieve complete depolarization (an increase in safranine O fluorescence signal implies depolarization). Wherever single graphs are presented, they are representative of at least 4 independent experiments.

14 Exclusive neuronal expression of SUCLA2 in the human brain

In (Dobolyi et al., 2015b) we investigated the cell-specific expression of succinate-CoA ligase subunits; we published that the ATP-forming subunit SUCLA2 of succinate-CoA ligase is expressed exclusively in the neurons of the human brain. This is not observesd in the brains of laboratory rodents.

14.1 Subunit composition, tissue-dependent expression and functional considerations of succinate CoA ligase

Succinyl-CoA ligase ([SUCL], also known as succinyl coenzyme A synthetase [SCS], or succinate thiokinase [STK]) is a heterodimeric enzyme, composed of an invariant α subunit encoded by *SUCLG1* and a substrate-specific β subunit, encoded by either *SUCLA2* or *SUCLG2*. This dimer combination results in either an ATP-forming (EC 6.2.1.5) or a GTP-forming SUCL (EC 6.2.1.4). GTP-forming SUCL may support ATP formation in the matrix through the concerted action with a mitochondrial isoform of a nucleotide diphosphate kinase known as nm23-H4; this kinase complexes with either ATP- or GTP forming SUCL (Kadrmas et al., 1991), (Kowluru et al., 2002). Considering the extensive involvement of succinyl-CoA ligase in vital biochemical pathways, it is not surprising that its deficiency leads to serious pathology. The disease phenotype matches the tissue-specific expression of its subunits: A-SUCL-β is highly expressed in skeletal muscle, brain and heart, while G-SUCL-β is barely detected in brain and muscle, but strongly expressed in liver and kidney J. Biol. Chem. 279:36621. Accordingly, mutations in *SUCLA2* (MIM ID#612073) results in Leigh's or a Leigh-like syndrome with onset of severe hypotonia in early childhood, muscular atrophy and sensorineural hearing impairment often leading to death during childhood. Neuroimaging findings include basal ganglia involvement, especially affecting the putamen and the caudate nuclei (Carrozzo et al., 2007), demyelination and atrophy (Ostergaard et al., 2007b). *SUCLA2* deficient patients show no abnormalities related to liver functions. Mutations in the α subunit-encoding *SUCLG1* gene have been reported in 16 patients (Ostergaard et al., 2007a), (Ostergaard et al., 2010) and they are associated with a phenotype similar to that seen in patients with *SUCLA2* deficiency, or a fatal infantile lactic acidosis. Mutations in the *SUCLG2* gene have not been reported so far, and may be incompatible with life. SUCL deficiency is associated with mtDNA depletion, characterized by a massive reduction of mitochondrial DNA content. Relevant to this, we have proposed that the mSLP biosensor test can be used to predict the severity of neurometabolic disorders stemming from mtDNA depletion (Chinopoulos, 2020c). Three main clinical presentations of mtDNA depletion syndrome (MDS) are known: i) myopathic, ii) encephalomyopathic and iii) hepatocerebral, depending on the tissues affected and their residual mitochondrial DNA levels (Rotig and Poulton, 2009). *SUCLA2* deficiency is associated with the encephalomyopathic tier. mtDNA depletion (15–40% residual amount) was found in the muscle samples of such patients (Ostergaard, 2008). However, mtDNA depletion was found in fibroblasts from patients with *SUCLA2* deficiencies of only two out of four patients in one study (Carrozzo et al., 2007), while in (Miller et al., 2011) mtDNA depletion was evident only after serum deprivation which could be ameliorated by supplementation of deoxyribonucleosides. Data on brain biopsies from *SUCLA2* deficiency patients are not available. In the most comprehensive study in terms of extensive biopsies from patients with MDS, samples were collected from muscle, liver, blood or fibroblasts, but not brain (Navarro-Sastre et al., 2012). Yet, in *SUCLA2* deficiency it is the brain that seems to be the most vulnerable tissue, as *SUCLG2* and *nm23-H4* are only weakly expressed (Milon et al., 1997), (Lambeth et al., 2004). SUCL forms a physical complex with nm23-H4, the lack of which hinders the kinase function leading to a defect in the last step of the mitochondrial nucleotide salvage pathway (Elpeleg et al., 2005), thus causing mtDNA depletion (Ostergaard et al., 2007a). Fibroblasts and skeletal muscle are

homogeneous tissues (despite the different categories of muscle fiber types); however, the brain consists of several different cell types, the major categories being neurons and glial cells. There is an obvious gap of knowledge regarding the pathophysiology of *SUCLA2* deficiency in the brain, the organ that suffers the most from this inborn error of metabolism. Analysis of expression of SUCLA2 in the human brain has been reported only once, but in that report cell- or region-specific expression was not investigated (Lambeth et al., 2004). In (Dobolyi et al., 2015b), we published that SUCLA2 is expressed exclusively in the neurons of the human brain.

14.2 The specificity of SUCLA2 and SUCLG2 immunoreactivity in human tissues

The specificity of SUCLA2 immunoreactivity was validated using human fibroblasts from a control subject versus those from a patient suffering from a complete deletion in *SUCLA2* gene. The specificity of SUCLG2 immunoreactivity was validated using HEK293 cells, see figure 14.1. The mitochondrial network was selectively stained by loading cells with Mitotracker Orange (MTO, 1 μM, red) prior to fixation, see panels A2 (control fibroblasts), B2 (SUCLA2-deficient fibroblasts) and C2 (HEK293 cells). Normal human fibroblasts were strongly labeled with the procedure of SUCLA2 immunostaining (panel A1, green), and there was a robust co-localization with the decoration obtained by MTO (panel A3, yellow). In contrast, fibroblasts derived from the patient lacking *SUCLA2* did not show SUCLA2 immunolabeling (panel B1), while the mitochondrial network outlined by MTO was unremarkable (panel B2, red), and accordingly there was no SUCLA2 immunoreactivity-MTO co-localization (panel B3). For validating the antibody raised against SUCLG2 we immunolabeled HEK293 cells which exhibit a very high expression of this protein (Tanner et al., 2007); confocal images of G-SUCL-β immunolabeling in these cells are shown in panel C1 (green). MTO labeling was intense (panel C2, red), and the extent of co-localization was also evident, shown in panel C3 (yellow). The scale bar is 20 μm.

14.3 SUCLA2 immunoreactivity and absence of SUCLG2 immunoreactivity in the human frontal and temporal cortical samples

SUCLA2 antibody labeled a large number of cells in both the frontal and temporal cortex with no visible difference between the male and female human brain (Fig. 14.2A). The labeled cells were numerous in all layers of the cortices except layer I. The labeled cells demonstrated different morphologies. A number of large pyramidal cells were labeled but smaller cells also showed SUCLA2 immunoreactivity. In general, SUCLA2 immunoreactivity was present within the cell bodies as well as the proximal dendrites but not in the nuclei (Fig. 14.2A, B). The same procedure but for SUCLG2 immunoreactivity applied for HEK293 cells or using more concentrated or more diluted antiserum resulted in no specific cellular labeling in the human frontal and temporal cortical samples (Fig. 14.2C), in accordance to the original report by the group of Lambeth (Lambeth et al., 2004). It is to be noted that *SUCLG2* for humans exhibits transcript variants. However, all transcripts are identical in the region 1-396, except in position 220 (see supplemental figure 14.S.1). The antibody that we used to identify SUCLG2 (Abcam, Cat No # ab96172) was raised by immunizing rabbits with a recombinant fragment corresponding to a region within the N terminal amino acids 1-204 of human SUCLG2. Therefore, it should not be able to distinguish among transcript variants.

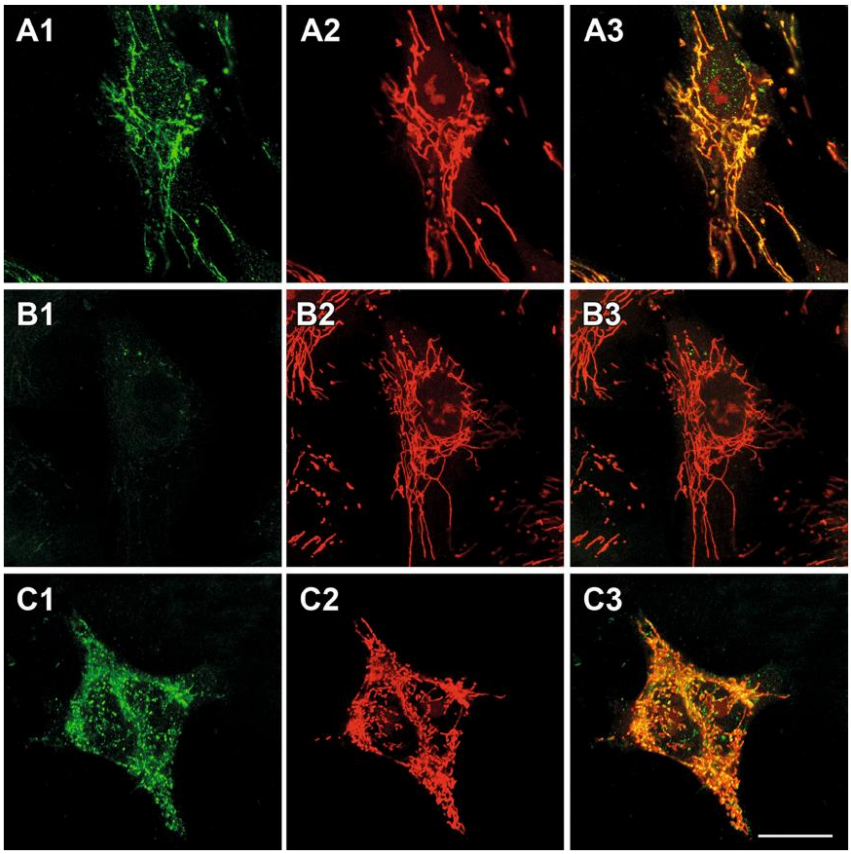

Figure 14.1. Co-immunolabeling of human fibroblasts (SUCLA2) and HEK293 cells (SUCLG2) with Mitotracker Orange (MTO). A1: SUCLA2 immunoreactivity in normal human fibroblasts. Intracellular structures resembling mitochondria are intensely labeled. A2: MTO labeling outlining the mitochondrial network in normal human fibroblasts. A3: Merged image of SUCLA2 immunodecoration with MTO labeling. B1: Specific labeling for SUCLA2 is absent in fibroblasts derived from the patient lacking SUCLA2. B2: MTO staining outlining the mitochondrial network in the fibroblasts obtained from the patient lacking SUCLA2. B3: Merged image of SUCLA2 immunodecoration with MTO labeling, revealing lack of co-localization. C1: SUCLG2 labels HEK293 cells. C2: MTO labeling outlining the mitochondrial network in HEK293 cells. A3: Merged image of SUCLG2 immunodecoration with MTO labeling in HEK293 cells. Scale bar = 20 μm.

14.4 The mitochondrial localization of SUCLA2 immunoreactivity

The labeling of SUCLA2 within the neurons is punctate with a cellular localization resembling that of mitochondria, suggesting the presence of SUCLA2 immunoreactivity in this organelle (Fig. 14.3A1, B1). Although *in situ* mitochondria are normally filamentous, cellular stress as it maybe the case during handling of the specimen or simply postmortem delay will cause mitochondrial fragmentation, yielding a punctate appearance. To identify the mitochondrial presence of SUCLA2, co-localization studies were performed for F_0-F_1 ATP synthase subunit d. The distribution of F_0-F_1 ATP synthase subunit d delineated the expected distribution of mitochondria (Fig. 14.3A2, B2). Furthermore, an almost complete co-localization of SUCLA2 and F_0-F_1 ATP synthase subunit d and the absence of singly labeled structures indicate the exclusively mitochondrial localization of SUCLA2 (Fig. 14.3A3, B3).

14.5 Identification of cell types containing SUCLA2 immunoreactivity in the human temporal cortex

The distribution of SUCLA2-immunoreactive cells is similar to that of neurons: they are present in all layers of the temporal cortex but their density is small in layer I (Fig. 14.4A1, B1). SUCLA2 immunoreactivity was present in 88% of cells identified as neuron based on its larger, less irregular

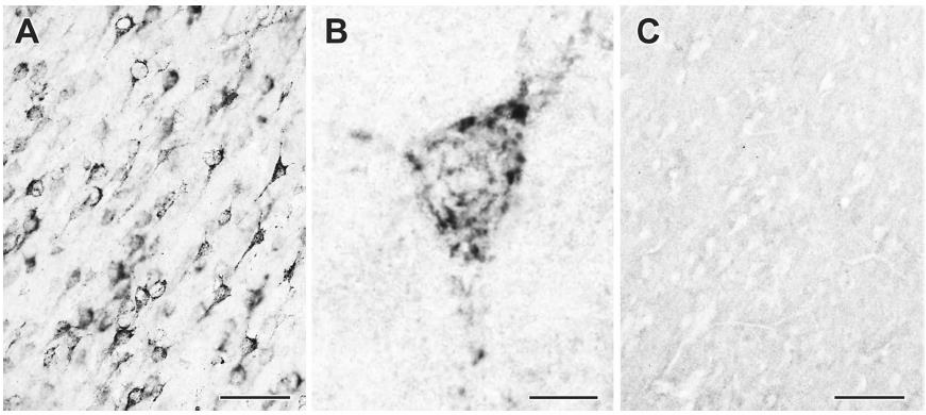

Figure 14.2. Immunolabeling for SUCLA2 but not SUCLG2 in the human temporal cortex. A: SUCLA2-immunoreactive cells with DAB visualization are evenly distributed in layer V. of the human temporal cortex. B: a large magnification picture demonstrates distribution of SUCLA2 immunoreactivity that resembles to that of mitochondria within a labeled cell. C: SUCLG2 immunoreactivity is absent in the human temporal cortex. Scale bars = 50 μm for A and C, and 10 μm for B.

shape in Nissl staining (Fig. 14.4A2). In contrast, dark Nissl-labeled cells, possibly glial cells do not contain SUCLA2 at all (Fig. 14.4A2). Unfortunately, labeling with NeuN (clone BBS/NC/VI-H14) or neuron-specific enolase used for the immunocytochemical identification of neurons did not label our human brain sections consistently to confirm the neuronal location of SUCLA2 immunoreactivity. Instead, we used glial markers to confirm the absence of SUCLA2 immunoreactivity in these cell types. Indeed, a lack of co-localization of SUCLA2 and S100, an astrocyte marker suggested that SUCLA2 was absent in astrocytes (Fig. 14.4B, C). In addition, the glial marker GFAP also showed a different distribution from SUCLA2-immunoreactive cells and did not co-localize with SUCLA2 immunoreactivity (Fig. 14.5).

14.6 The presence of SUCLA2 but not SUCLG2 mRNA in the human temporal cortex

A single band appeared on gels following RT-PCR using all primer pairs specific to *SUCLA2* and *SUCLG2* when cDNA from human fibroblasts were used (Fig. 14.6A). However, when human temporal cortical cDNA was used, the same molecular weight products appeared only with *SUCLA2* primers albeit with a smaller bandwidth. In contrast, *SUCLG2* primers produced extremely faint bands. It must be noted that a cDNA clone containing a complete ORF for *SUCLG2* obtained from the human hippocampus appears in the literature (Strausberg et al., 2002). In our RT-PCR experiments very weak signals may well originate from *SUCLG2* mRNA of lymphocytes, endothelial cells or pericytes of vessels present in the specimen. The lengths of the PCR products were consistent with the lengths calculated from the position of the corresponding primer pair (Fig. 14.6A). PCR reactions without cDNA template were always included, and we did not detect bands in these negative controls.

14.7 The distribution of mRNA expression of SUCLA2 in the human temporal cortex

In situ hybridization histochemistry revealed the distribution of mRNA of *SUCLA2* (Fig. 14.6B), whereas that of SUCLG2 was not detected in the human temporal cortex (Fig. 14.6C), in agreement with the immunohistochemistry and RT-PCR results shown above, and the earlier results by the group of Lambeth (Lambeth et al., 2004). This result also verifies that the absence of G-SUCL-β immunoreactivity is genuine, and does not reflect a technical limitation of the antibody in our immunohistochemistry and/or Western blotting protocols. The two antisense probes for *SUCLA2* resulted in identical hybridization patterns. In the temporal cortex, all layers contained *SUCLA2* mRNA whereas the corpus callosum did

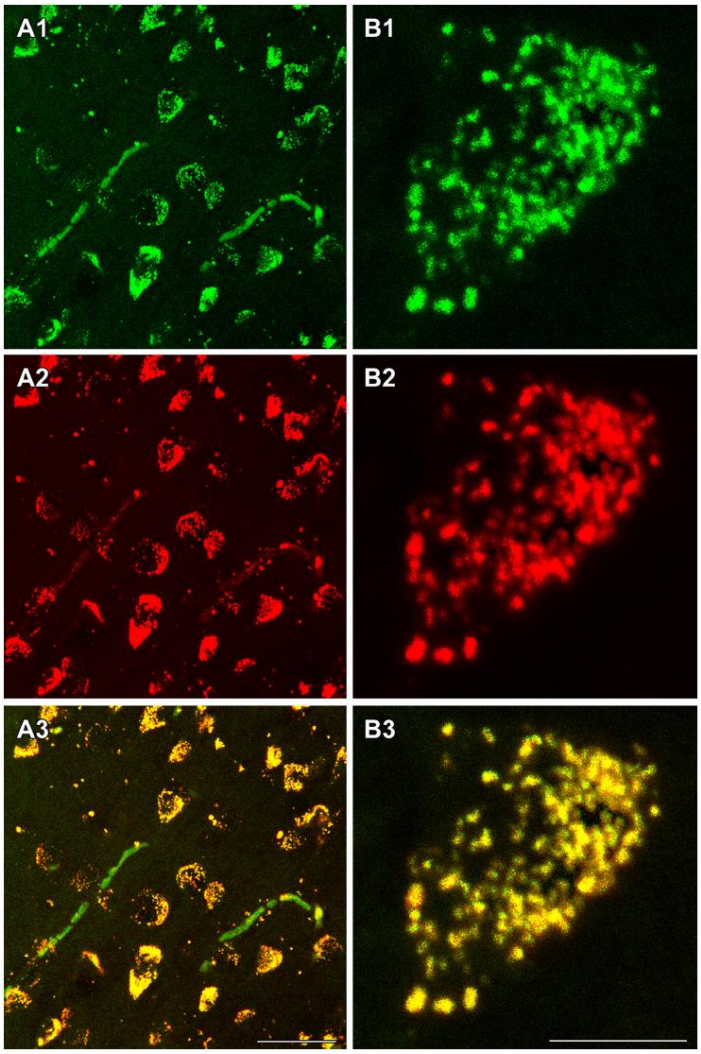

Figure 14.3. The mitochondrial localization of SUCLA2 based on its co-localization with the d subunit of the F_0-F_1 ATP synthase. A1: SUCLA2 immunoreactivity in the human temporal cortex visualized by FITC-tyramide amplification immunofluorescence. Red blood cells in some capillaries are labeled because of their endogenous peroxidase activity. B1: a high magnification confocal image demonstrates the localization of SUCLA2 within a SUCLA2-positive cell. A2: Distribution of the immunoreactivity of the mitochondrial marker F_0-F_1 ATP synthase subunit d in the same field as A1. B2: F_0-F_1 ATP synthase subunit d immunoreactivity in the same field as B1. A3: Yellow color indicates co-localization of SUCLA2 and F_0-F_1 ATP synthase subunit d. An almost complete absence of singly labeled structures can be observed except for the red blood cells. B3: The co-localization of SUCLA2 and F_0-F_1 ATP synthase subunit d is predominant even within a cell at high magnification. Scale bars = 50 μm for A1-3 and 20 μm for B1-3.

not show any labeling. The intensity of labeling was the highest in the pyramidal layers containing large pyramidal cells (Fig. 14.6B). The intensity of labeling was lower in layer VI and in the superficial layers. In particular, layer I contained only a small number of cells expressing *SUCLA2*. In the human temporal cortical brain sections labeled for SUCLA2 mRNA, Nissl-labeled cells as well as S100-immunoreactive cells were present. The distribution of Nissl-labeled neurons (Fig. 14.7A) was similar to that of SUCLA2-expressing cells, whereas S100-immunoreactive glial cells had a more even distribution pattern (Fig. 14.7B). Furthermore, high magnification pictures indicated that over 90% of Nissl-labeled neurons exhibited *SUCLA2* mRNA (Fig. 14.7C) while 95% of *SUCLA2* mRNA-expressing cells were identified as neurons based on Nissl labeling in the human temporal cortex. In contrast, the distribution of SUCLA2 mRNA-expressing cells was different from that of S100-immunoreactive cells in high magnification pictures (Fig. 14.7D) and *SUCLA2* mRNA-expressing cells showed less than 5% co-localization with S100 immunoreactivity.

14.8 SUCLA2 and SUCLG2 immunoreactivities in homogenates from various brain regions

The antibody directed against SUCLA2 worked in immunohistochemistry protocols only from fresh human brain specimens. However, the antibody recognized reliably SUCLA2 in samples that have been preserved in our Brain Tissue Bank for prolonged periods of time which were processed for Western blotting. This provided the opportunity to examine the presence of SUCLA2 from several brain regions. As shown in figure 14.8 panel A, homogenate samples obtained from three different donors (Tables 1A and B) from temporal cortex, caudate nucleus, putamen, frontal cortex, white matter and

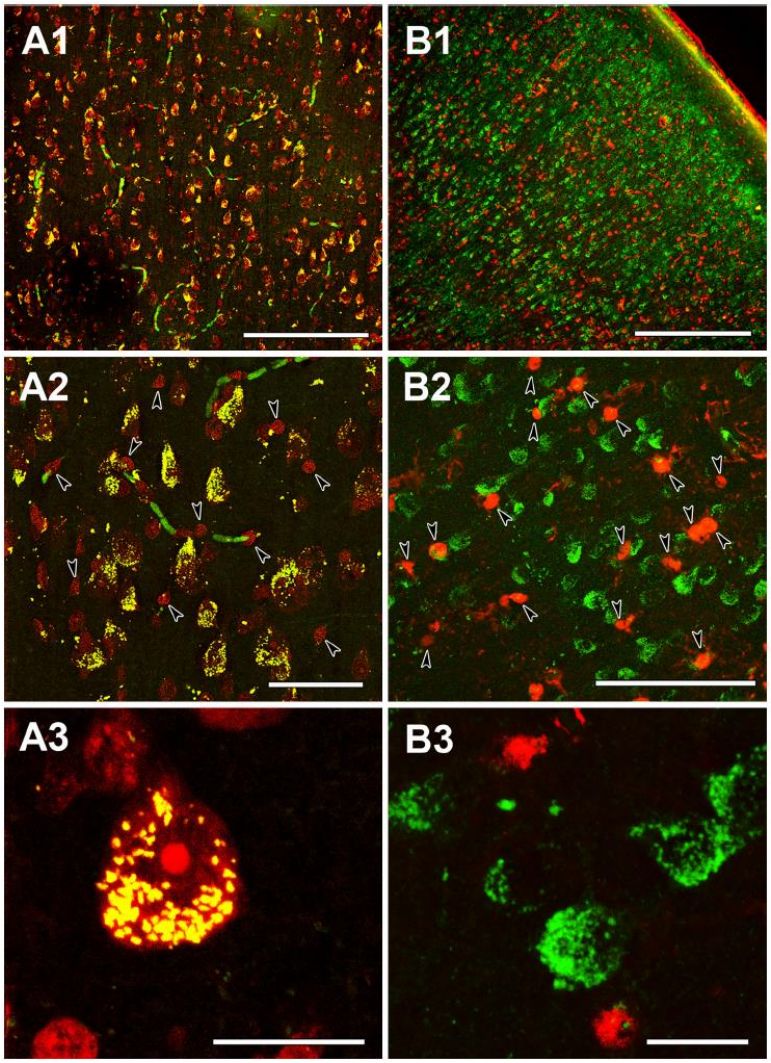

cerebellar cortex tested positive for SUCLA2 immunoreactivity. Even though white matter does not contain neuronal cell bodies it still exhibited significant SUCLA2 immunoreactivity, probably originating from the mitochondria found along the axons. 'MB' signifies mouse brain homogenates from four different animals (numbered as 1, 2, 3 and 4). In this and the other panels of figure 14.8, β-actin immunoreactivity served as a loading control for all lanes. The specificity of the SUCLA2 antibody is certified by the blot shown in panel B, where there was no immunoreactivity from fibroblasts of a patient suffering from complete deletion of the *SUCLA2* gene. SUCLG2 immunoreactivity (panel A) was extremely weak in the human brain samples, as compared to the mouse brain samples, in accordance with the results of previous Western blot experiments (Kiss et al., 2013). As for the case of RT-PCR results,

Figure 14.4. The neuronal localization of SUCLA2 immunoreactivity in the human temporal cortex. A1: The distribution of SUCLA2-positive cells is similar to that of Nissl-labeled cells (red), both present throughout the temporal cortex. A2: A higher magnification image reveals that essentially all large Nissl-labeled cells with irregular shape demonstrate SUCLA2 immunolabeling (yellow cells). In contrast, small, intensely labeled round-shape cells do not exhibit SUCLA2 immunoreactivity and remain red (arrowheads). Some blood vessels are labeled green because of the peroxidase activity of the red blood cells present in the vessels in the non-perfused human tissue. A3: A high magnification confocal microscopy image demonstrating the punctuate location of SUCLA2 immunoreactivity within the cytosol of Nissl-labeled neurons whereas small glial cells do not exhibit SUCLA2 immunoreactivity. B1: The distribution of the glial marker S100 (red) is different from that of SUCLA2-positive cells (green). B2: A higher magnification image demonstrates lack of co-localization between SUCLA2 and S100. Glial cells labeled with S100 are indicated by arrowheads. B3: High magnification confocal picture shows that SUCLA2 and S100 are located in different cell types. Scale bars: 200 μm for A1, 50 μm for A2, 20 μm for A3, 500 μm for B1, 50 μm for B2, and 20 μm for B3.

such weak SUCLG2 immunoreactivity in human brain homogenates may originate from trapped lymphocytes, endothelial cells or pericytes from vessels present in the specimen, and not being genuine to neurons or glial cells. Although there are no tissues available with null expression of SUCLG2 (as in the case for the fibroblasts from the patient suffering from complete deletion of the SUCLA2 gene), the fact that the bands obtained from mouse tissues and the human specimens appeared at the exact same molecular weight affords a reasonable degree of assurance that SUCLG2 immunoreactivity is indeed

genuine. In the rat brain, streptozotocin-induced diabetes upregulates GTP-forming succinyl CoA ligase activity more than 10 times (Jenkins and Weitzman, 1986). Mindful of this, and assuming that diabetes may upregulate SUCLG2 expression in the human brain, we compared SUCLG2 (and SUCLA2) immunoreactivity in brain tissue homogenates from four controls versus four patients that suffered from diabetes mellitus for several years (Tables 1C and D). The results are shown in panel C of figure 14.8: SUCLG2 immunoreactivity was not increased in the samples from the diabetic patients as compared to those from control subjects, also verified by densitometric analysis of the bands. This result affords further c redibility to the claim that *SUCLG2* is not expressed in the human brain to a significant extent.

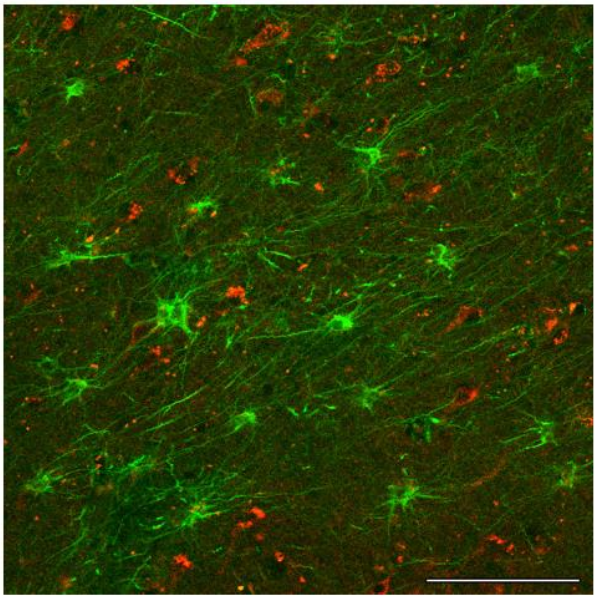

Figure 14.5. The different cellular localization of SUCLA2 and GFAP. SUCLA2 labels a number of evenly distributed cells with punctuate appearance (red). GFAP-positive glial cells (green) possessing the characteristic glial processes are also evenly distributed. These glial cells, however, are not labeled by SUCLA2 whereas SUCLA2 cells are not labeled by GFAP. Scale bar: 100 μm

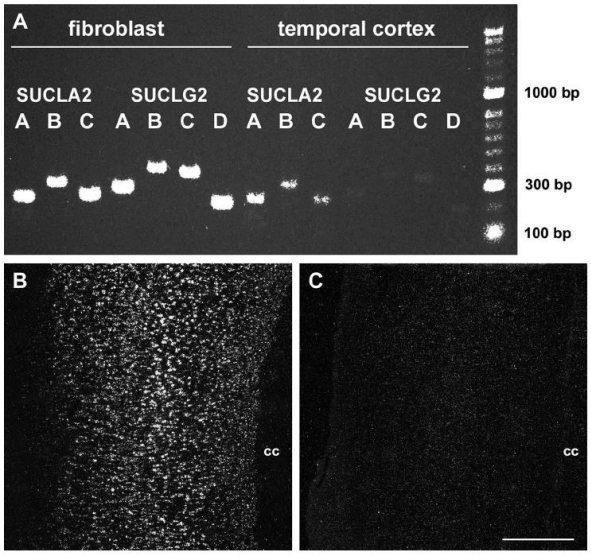

Figure 14.6. An RT-PCR experiment demonstrates the expression of SUCLA2 but not SUCLG2 mRNA in the human temporal cortex by showing PCR products run on gel. The appearance of appropriate bands on the gel for primer pairs A-C for SUCLA2 (235, 309, and 242 bp, respectively) and primer pairs A-D for SUCLG2 (279, 387, 366, and 211 bp, respectively) in human fibroblasts indicate SUCLA2 and SUCLG2 expression in this cell type. In contrast, when the template of the PCR reaction was cDNA prepared from freshly dissected surgical human temporal cortex samples, only SUCLA2 but not SUCLG2 resulted in visible bands. B and C: Dark-field photomicrographs of human temporal cortex labeled with in situ hybridization histochemistry for SUCLA2 (B), and SUCLG2 (C). The white dots represent labeled cells. All cortical layers but not the corpus callosum (cc) is labeled for SUCLA2 (B). The intensity of labeling is highest in layers III-V whereas layers I, II, and VI contains less intensely labeled cell. In contrast, SUCLG2 labeling above the background is absent in all layers of the cerebral cortex (C). Scale bar = 1 mm.

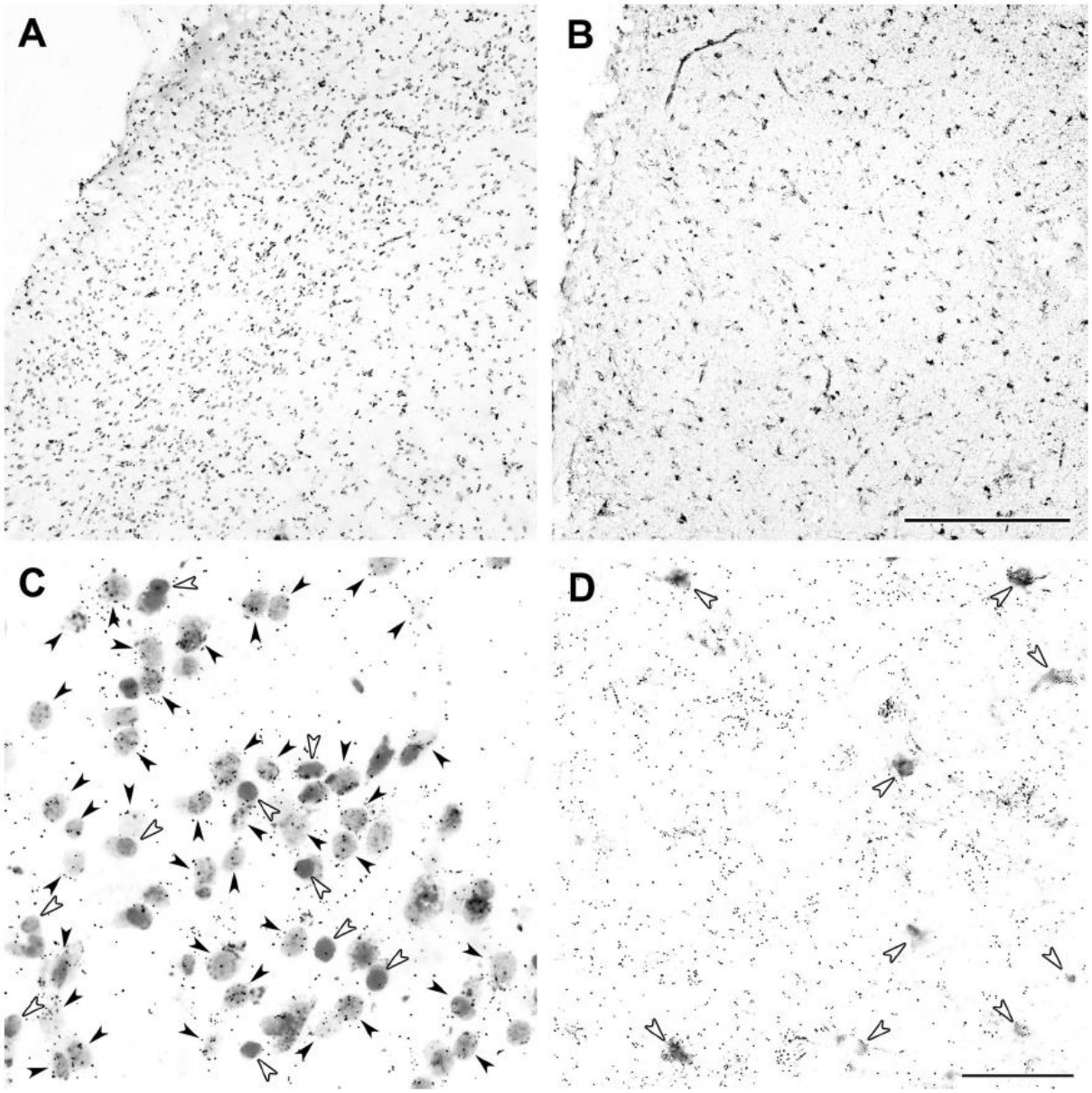

Figure 14.7. The selective SUCLA2 mRNA expression in neurons based on double labeling with in situ hybridization histochemistry for SUCLA2 and neuronal or glial markers. The distribution of Nissl-labeled cells (A) and S100-immunoreactive astrocytes (B) is shown in the human temporal cortex. The tiny autoradiography grains of the in situ hybridization signal are not visible at this low magnification. High magnification pictures demonstrate the location of autoradiography grains representing SUCLA2 mRNA in relation to Nissl-labeled cells (C), and S100-immunoreactive astrocytes (D). Black arrowheads indicate double labeled cells. Based on the larger size and fainter Nissl labeling, these cells are neurons. Above these cells, the number of autoradiography grains is more than 4. In contrast, the darker, smaller and circular-shaped glial cells indicated by white arrowheads in C are not labeled for SUCLA2 mRNA. Also, mRNA expression of SUCLA2 is absent in S100-immunoreactive astrocytes (white arrowheads) in D. Scale bars = 500 μm for A, B, and 50 μm for C, D.

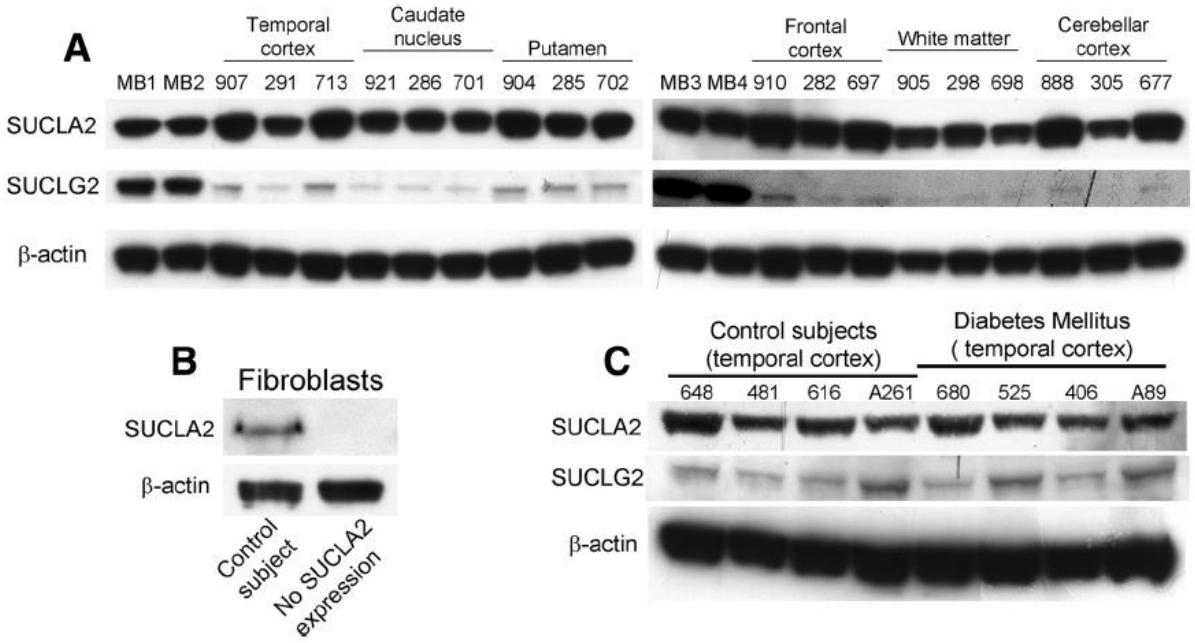

Figure 14.8. Immunoreactivities of the substrate-specific β subunit encoded by either SUCLA2 or SUCLG2 in tissue homogenates. ***A****: MB signifies mouse brain (whole brain homogenates from four different animals 1, 2, 3 and 4). All other alphanumeric titles signify human brain samples obtained from regions as indicated in the panels.* ***B****: Immunoreactivity of the substrate-specific β subunit encoded by SUCLA2 in human fibroblasts from a healthy donor and a patient with a complete deletion of SUCLA2. C: Immunoreactivities of the substrate-specific β subunit encoded by either SUCLA2 or SUCLG2 in human temporal cortex samples from control subjects versus those that suffered from diabetes mellitus. For all lanes of all panels, immunoreactivity of β-actin was used as a loading control.*

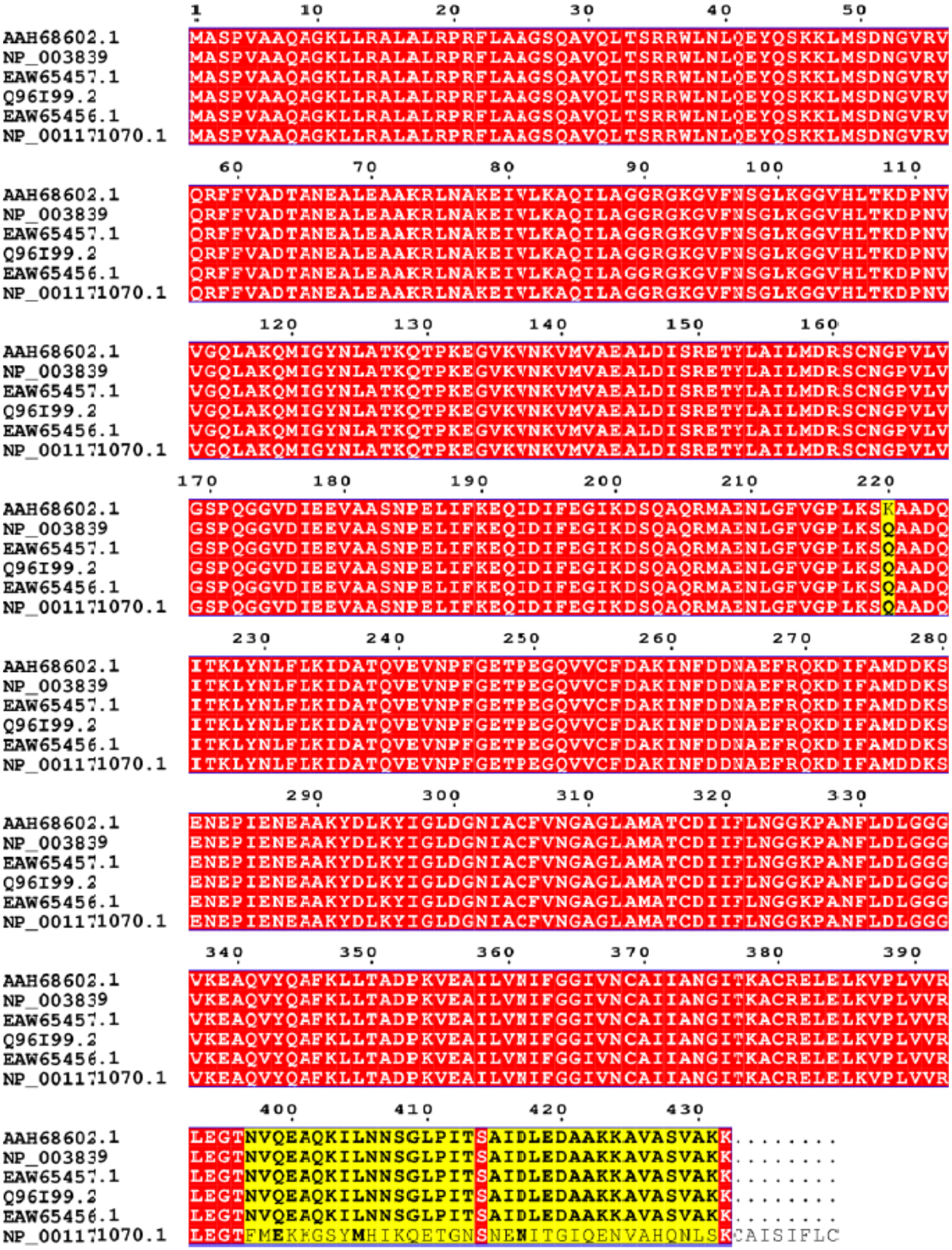

Figure 14.S.1. : multiple sequence alignment of SUCLG2 [Homo Sapiens] versions and transcript variants performed by Multalin; output generated by ESPript.

15 SUCLG2 outlines the human cerebral microvasculature

In (Dobolyi et al., 2015b) we showed that SUCLG2 is very weakly expressed in the adult human brain. In the subsequent study published in (Dobolyi et al., 2015a) we reported that SUCLG2 exist only in cells forming the vasculature or its contents in the adult human brain.

15.1 The specificity of SUCLG2 immunoreactivity in human fibroblast cultures

We have used a novel antibody directed against the human SUCLG2 protein that does not distinguish among various isoforms, different than that we used in (Dobolyi et al., 2015b). The specificity of SUCLG2 immunoreactivity was validated using human fibroblast cells, see figure 15.1. The mitochondrial network was selectively stained by loading cells with Mitotracker Orange (MTO, 1 μM) prior to fixation (panel a). Fibroblasts were subsequently labeled with the procedure of SUCLG2 immunostaining (panel b), and there was a co-localization with the decoration obtained by MTO (panel c). Note that only a minority of the mitochondrial network was stained by the SUCLG2 antiserum, as opposed to SUCLA2 immunoreactivity in the same cells, in which the majority of the mitochondrial network was stained (Dobolyi et al., 2015b).

15.2 SUCLA2 and SUCLG2 labeling in the human cerebral cortex

SUCLA2 immunoreactivity appeared in cells located throughout the cerebral cortex (Fig. 15.2a). The cellular distribution of SUCLA2 labeling suggested that SUCLA2 immunoreactivity is restricted to mitochondria (see figure 15.3a), exactly as described by us previously (Dobolyi et al., 2015b). Furthermore, the distribution of SUCLA2-immunoreactive cells corresponded to that of neurons in accordance with the previously described neuronal expression of this protein. In these sections, the walls of large blood vessels were also labeled with SUCLA2, see upper left corner of figure panel 15.2a. The distribution of SUCLA2 immunoreactivity differed markedly from that of myelin basic protein as the latter one was striking in the white matter and labeled radially arranged structures in accordance with the established localization of myelinated fibers within the cortex (Fig. 15.2b). Indeed, double labeling confirmed the absence of co-localization between SUCLA2 and myelin basic protein (Fig. 15.2c, 15.3b). The distribution of Iba1-labeled microglial cells was relatively even within the examined brain section corresponding to the role of this cell type in immune defense (Fig. 15.2e). Microglial cells had small somata and several processes (Fig. 15.3a). Thus, the morphology of SUCLA2 and Iba1-labeled cells was different. Consistent with this, no co-localization of these markers were found in any cortical regions examined (Fig. 15.3a). SUCLG2 immunoreactivity was found in all layers of the human cerebral cortex. Its distribution was, however, characteristic of blood vessels suggesting endothelial and/or pericytic localization. However, we must note that perivascular staining due to the presence of SUCLG2 in astrocyte end-feet is a viable possibility. The distribution of SUCLG2 immunoreactivity was clearly different from that of myelin basic protein (Fig. 15.2b) and Iba1-positive microglia (Fig. 15.2e), which was also confirmed by double labeling (Fig. 15.2f). Analysis of high magnification images revealed that SUCLG2 immunoreactivity present in structures resembling mitochondria appeared in capillary-forming cells. This is best depicted in the lower left corner (two white arrowheads) and upper right corner (single white arrowhead) of figure panel 15.3d; note the SUCLG2 decoration pattern forming a tubular structure around the red blood cells (stained green because of the immunohistochemical procedure) in a longitudinal (lower left corner) and cross-section (upper right corner) mode delineating a capillary. No

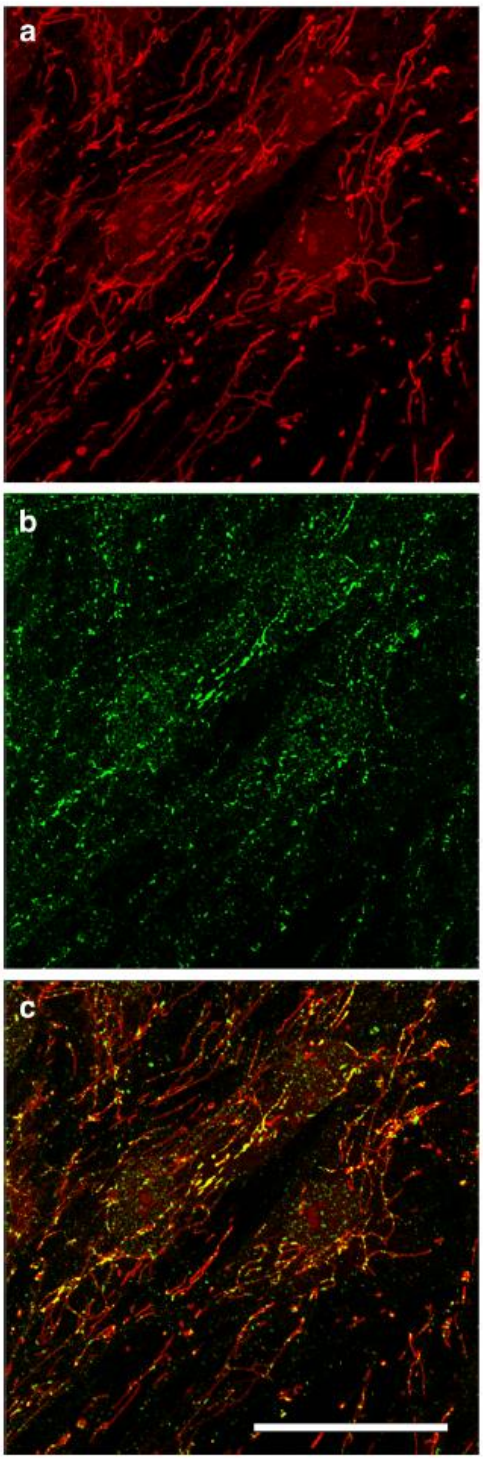

co-localization was found between SUCLG2 and the microglia marker Iba1 (Fig. 15.3c) and oligodendroglial marker myelin basic protein (Fig. 15.3d). On the other hand, SUCLG2 expression has been demonstrated in microglial cells of post-mortem brains of Alzheimer's disease patients and age-matched controls (Ramirez et al., 2014). In humans, SUCLG2 exhibits transcript variants. However, the possibility that the human glial transcript variant of SUCLG2 is not recognized by existing antibodies has been ruled out in (Dobolyi et al., 2015b): all transcripts are identical in the region 1-396, except in position 220 (Dobolyi et al., 2015b). The antibody used in (Dobolyi et al., 2015b) to identify SUCLG2 was raised by immunizing rabbits with a recombinant fragment corresponding to a region within the N terminal amino acids 1-204 of human SUCLG2 which is common among all transcript variants. Furthermore, in (Dobolyi et al., 2015b) PCR and *in situ* hybridization for all known variants have been performed for human brain material; SUCLG2 mRNA was deduced to be very scarce in the human brain, while the same probes tested robustly positive in human fibroblasts.

Figure 15.1. Co-labeling of human fibroblasts (SUCLG2) with Mitotracker Orange (MTO). a: MTO labeling outlining the mitochondrial network in normal human fibroblasts. b: SUCLG2 immunoreactivity in normal human fibroblasts. Intracellular structures resembling mitochondria are intensely labeled c: Merged image of SUCLG2 immunodecoration with MTO labeling. Scale bar = 13 μm.

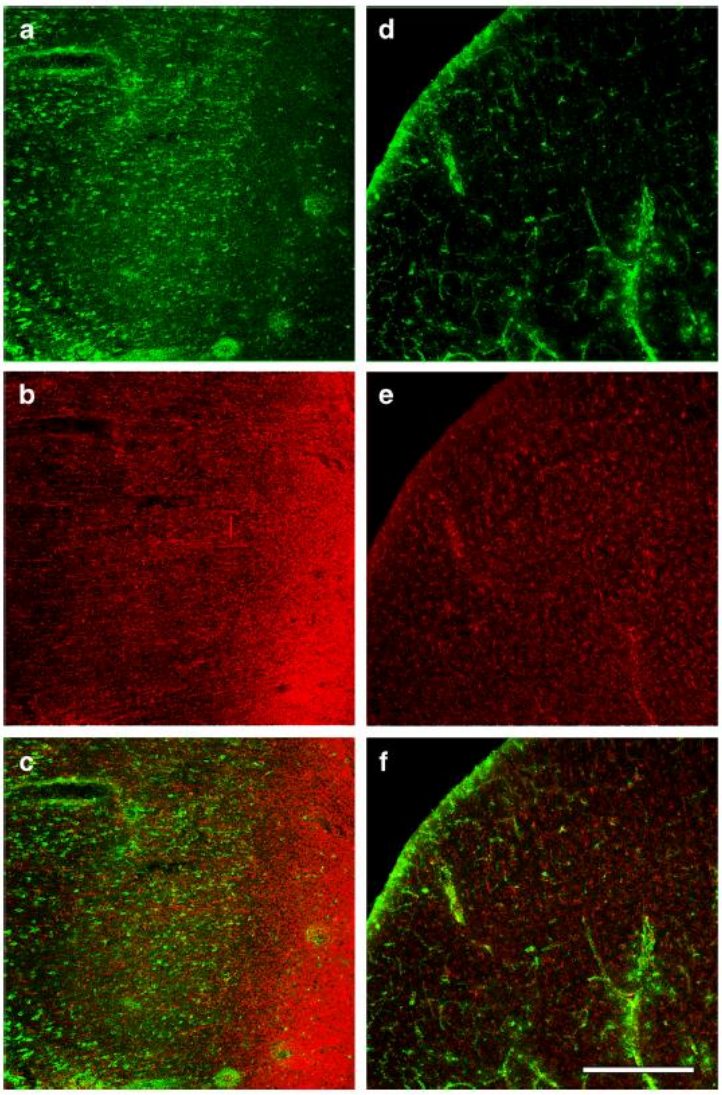

Figure 15.2. Immunocytochemical identification of succinyl CoA ligase subunits, oligodendroglia, and microglia in the human cerebral cortex. The distribution of SUCLA2 (a), myelin basic protein (b), SUCLG2 (d) and Iba1 (e) immunoreactivities are shown in low magnification. c: Double labeling (panels a and b combined) show somewhat overlapping but still fundamentally different distributions of SUCLA2 and myelin basic protein. f: Double labeling (panels d and e combined) demonstrate the distinct distributions of SUCLG2 and Iba1 in the cerebral cortex. Scale bar = 500 μm.

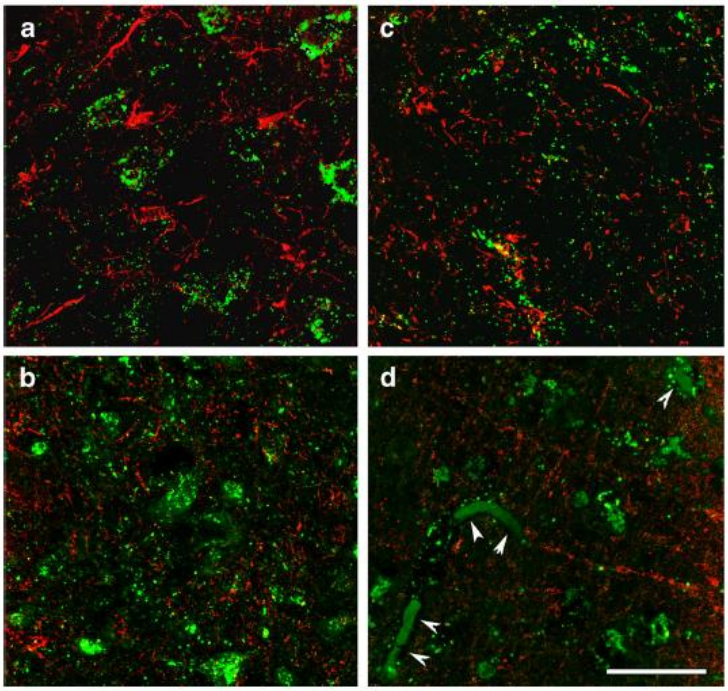

Figure 15.3. High magnification confocal images demonstrate that SUCLA2 immunoreactivity (green in a and b) is present in neurons but not in Iba1-positive microglia cells (red in a) and in oligodendroglial cells labelled with basic myelin protein (red in b). In turn, SUCLG2 immunoreactivity (green in c and d) does not co-localize with Iba1 (red microglia cells in c) and cells labelled with basic myelin protein (red oligodendroglial cells in d). The arrowheads in d point to red blood cells within vessels labelled non-specifically due to their internal peroxidase content. Scale bar = 20 μm.

16 Exclusive neuronal detection of KGDHC-specific subunits in the adult human brain cortex despite pancellular protein lysine succinylation

In (Dobolyi et al., 2015b) and (Dobolyi et al., 2015a) we published that succinate CoA ligase exists only in the neurons of the adult human brain, which begged the question: if the enzyme processing succinyl-CoA exhibits cell-specific expression, does the enzyme producing succinyl CoA follow the same pattern? this enzyme is the α-ketoglutarate dehydrogenase complex (KGDHC). In the work published in (Dobolyi et al., 2020) we investigated exactly that and showed that KGDHC-specific subunits are also absent from glial in the adult human brain cortex.

16.1 KGDHC in the human brain; relation to physiological and pathological states

Mindful of KGDHC's involvement in a multitude of biochemical processes it is not surprising that its deficiency leads to pathology, particularly in the brain: indeed, a decline in KGDHC activity is associated with Alzheimer's disease (Gibson et al., 1998), (Butterworth and Besnard, 1990), (Mastrogiacoma et al., 1996), (Terwel et al., 1998), (Bubber et al., 2005), Parkinson's disease (Gibson et al., 2003), Huntington's chorea (Naseri et al., 2015), Wernicke-Korsakoff syndrome (Butterworth et al., 1993) and progressive supranuclear palsy (Albers et al., 2000), (Park et al., 2001). A reduction of KGDHC activity is not generally paralleled by all other enzymes of the citric acid cycle (Bubber et al., 2005), (Gibson et al., 2010), (Bubber et al., 2011). The reason for this selective vulnerability is incompletely understood, but it is likely to be at least partially due to the ability of KGDHC of both producing and affected by reactive oxygen species (Tretter and Adam-Vizi, 2004), (Starkov et al., 2004). The molecular mechanism(s) linking KGDHC to neurodegeneration are largely unknown; it has been proposed that a decrease in complex activity diminishes glucose uptake and/or metabolism in the brain -a hallmark of Alzheimer's disease- initiating a sequence of events culminating in neurodegeneration (Chen and Zhong, 2013), (Sang et al., 2018). Laboratory mice modeling neurodegenerative diseases cross-bread with those exhibiting KGDHC subunit-specific genetic modifications yielded considerable insight regarding pathophysiology (Dumont

et al., 2009) but stopped short in offering a breakthrough regarding therapy or even prevention strategy in humans. In most neurodegenerative disorders specific regions of the brain are involved, thus, lack of knowledge on KGDHC expression and activity in a cell-specific manner may well underlie the lack of progress regarding identifying suitable therapeutic targets. In (Dobolyi et al., 2020) we reported that KGDHC-specific components were detected in neurons but not glia. However, protein lysine succinylation was pancellularly evident. The latter finding was unexpected because succinylation requires succinyl-CoA, the product of KGDHC, while glia cannot obtain it from succinate-CoA ligase as they also lack this enzyme (Dobolyi et al., 2015b), (Dobolyi et al., 2015a). Potential sources of extramitochondrial succinyl-CoA have been reviewed in (Chinopoulos, 2021), and are currently under investigation.

16.2 Antibody selection for detecting all known KGDHC subunit human isoforms

KGDHC consists of multiple copies of three subunits: oxoglutarate dehydrogenase (OGDH) or oxoglutarate dehydrogenase-like protein (OGDHL), dihydrolipoyl succinyltransferase (DLST), and dihydrolipoyl dehydrogenase (DLD). OGDHL exhibits 3 isoforms Q9ULD0-1, Q9ULD0-2 and Q9ULD0-3; OGDH 3 isoforms: Q02218-1, Q02218-2 and Q02218-3; DLST 2 isoforms: P36957-1 and P36957-2; and DLD 3 isoforms: P09622-1, P09622-2 and P09622-3. By knowing the amino acid sequence of each isoform we could select antibodies raised using epitopes recognizing all isoforms, see Tables 16.1A and B. Whenever the same antibody is used for more than one isoform, this is because the epitope is within a 100% aligning region between the isoforms. More antibodies were probed that yielded no staining and these were excluded from this study.

Table 16.1A: Antibodies used for detecting all known human KGDHC subunit isoforms

Subunit	Isoform	Antibody used
OGDHL	Q9ULD0-1	Atlas Antibodies, Cat# HPA052497, RRID:AB_2681853
	Q9ULD0-2	Proteintech Group, Cat# 17110-1-AP, RRID:AB_2156767
	Q9ULD0-3	Proteintech Group, Cat# 17110-1-AP, RRID:AB_2156767
OGDH	Q02218-1	Proteintech Group, Cat# 15212-1-AP, RRID:AB_2156759
	Q02218-2	Proteintech Group, Cat# 15212-1-AP, RRID:AB_2156759
	Q02218-3	Atlas Antibodies, Cat# HPA020347, RRID:AB_1854773
DLST	P36957-1	Cell Signaling Technology, Cat# 11954, RRID:AB_2732907
	P36957-2	Cell Signaling Technology, Cat# 11954, RRID:AB_2732907
DLD	P09622-1	Abcam, Cat# ab133551, RRID:AB_2732908
	P09622-2	Abcam, Cat# ab133551, RRID:AB_2732908
	P09622-3	Abcam, Cat# ab133551, RRID:AB_2732908

Table 16.1B: Antibodies directed against other targets used in this study

Target	Antibody used
GFAP	Santa Cruz Biotech, Cat# sc-33673, RRID:AB_627673
Aldhl1	Abcam, Cat# ab177463, RRID: AB_2811300
Myelin Basic Protein	Abcam, Cat# ab24567, RRID:AB_448144
Olig2	Abcam, Cat# ab109186, RRID: AB_10861310
IBA1	Abcam, Cat# ab107159, RRID:AB_10972670
Succinyl lysine	NovoPro, Cat# 106768, RRID:AB_2732922
VDAC1	Abcam, Cat# ab154856, RRID:AB_2687466
SUCLG1	Abcam, Cat# ab97867, RRID:AB_10678848

SUCLG2	Atlas Antibodies, Cat# HPA046705, RRID:AB_2679762
SUCLA2	Proteintech Group, Cat# 12627-1-AP, RRID:AB_2271200
β-actin	Abcam, Cat# ab6276, RRID:AB_2223210

16.3 Antibody validation

Antibodies directed against KGDHC subunit isoforms were validated by the following protocols: i) >99% co-localization with mitotracker orange (a dye that stains exclusively mitochondria) in human fibroblasts; ii) decrease in immunocytochemical staining of siRNA –but not scramble RNA- treated human cell lines silencing genes that code KGDHC subunit isoforms and decorated by the same antibodies; iii) emergence of only one band at the expected molecular weight in Western blots probing purified, recombinant proteins and human brain homogenate samples. As shown in figure 16.1, normal human fibroblasts were treated with the antibodies indicated on the left and detected with secondary antibodies conjugated with Alexa 647 fluorophore (left panels, green); their mitochondrial network was selectively stained by loading cells with Mitotracker Orange (MTO, 1 μM, middle panels, red) prior to fixation. Co-localization of Alexa 647 and MTO staining is shown in the panels to the right. From the right-hand panels It is evident that except for antibody HPA052497 directed against isoform 1 of OGDHL (Q9ULD0-1), all other antibodies yielded >99% of co-localization with the mitochondrial network. Regarding Q9ULD0-1, at this junction it cannot be distinguished if the lack of co-localization of the antibody with MTO is due to lack of specificity, or Q9ULD0-1 is not sufficiently expressed in human fibroblasts. Nonetheless, the robust co-localization of all other antibodies with MTO in these confocal images proved that the antigens are located within mitochondria. Next, to investigate if the intramitochondrial decoration is due to antigens belonging to the intended proteins against which the KGDHC-subunit and isoform specific antibodies were raised, cell lines were transfected with either siRNA directed against individual subunits belonging to KGDHC or scramble RNA, and subsequently co-stained with the same antibodies and MTO. For these experiments, cancer cell lines (HeLa and COS-7) were used instead of fibroblasts because the former exhibit much higher transfection efficiencies than the latter. COS-7 is a cell line originating from monkey kidney tissue but it was probed for OGDHL isoforms 2 and 3 which are identical to those expressed in humans. Other cell lines tested did not yield a sufficiently clear mitochondrial network for co-localization studies (not shown). As shown in figure 16.2, HeLa cells were treated with the antibodies indicated on the left and decorated with secondary antibodies conjugated with Alexa 647 fluorophore (left panels, green); their mitochondrial network was selectively stained by loading cells with MTO (1 μM, middle panels, red) prior to fixation. Co-localization of Alexa 647 and MTO staining is shown in the panels to the right. The robust co-localization of all antibodies (except HPA052497) with MTO in these confocal images proved that the antigens are located within mitochondria of HeLa cells as well. As shown in the top rows of figures 16.3-16.8, cells were treated with siRNA directed against the respective protein, and in the bottom rows with scramble RNA. Alexa 647 decoration is shown in panels to the left, while MTO staining is shown in the panels to the right. It is evident that the mitochondrial staining for KGDHC subunits shown in siRNA-treated cells (top-left images) appears weaker than the scramble RNA-treated cells (bottom-left panels); furthermore, in some

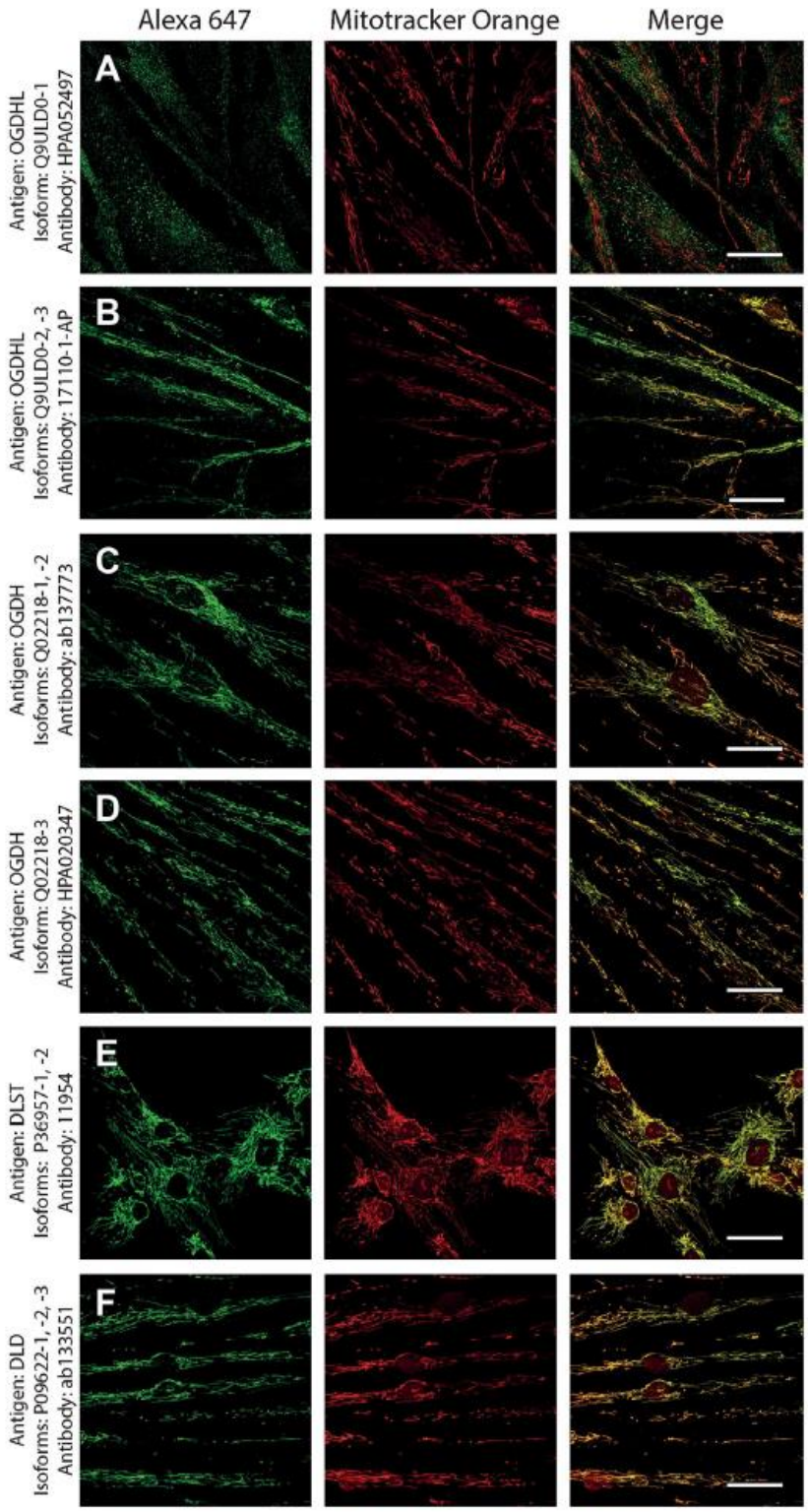

Figure 16.1. OGDHL, OGDH, DLST and DLD immunolabeling (labelling by Alexa 647) in human fibroblasts in relation to mitotracker orange (MTO). Mag: 20x.

instances (top left panels in figures 16.5, 16.6 and 16.8) the mitochondrial network of siRNA-treated cells is more fragmented than those treated with the scramble RNA. The decrease in staining together with the alterations in mitochondrial network in siRNA-treated but not scramble RNA-treated cells strongly argue that the antibodies used are specific for the intended KGDHC subunit proteins. It must be noted that in some panels immunoreactivity with siRNA may appear similar to immunoreactivity without any intervention, however, by semi-quantitating emitted light intensity of the signal minus the background, immunoreactivity presented for siRNA is consistently lower than that for scramble RNA. Subsequently, to afford further assurance that the antibodies used exhibit monospecificity for the intended proteins -which cannot be addressed by immunocytochemistry- and they yield reproducible results from a sufficiently high number of tissues, we performed western blotting analysis on purified, recombinant proteins (Nemeria et al., 2014), (Ambrus et al., 2016) and 63 human brain homogenates obtained from 11 cadaveric brain donors. All antibodies are directed against short stretches of amino acid sequences (which was important for selecting isoform-specific antibodies), thus they were expected to perform equally well in western blotting protocols where protein folding is lost due to the presence of strong detergents. Antibody-selling company policies prohibit the publication of the epitopes (to which the authors of (Dobolyi et al., 2020) disagree). As shown in figure 16.9, recombinant proteins (shown on the left-most lane) and the brain

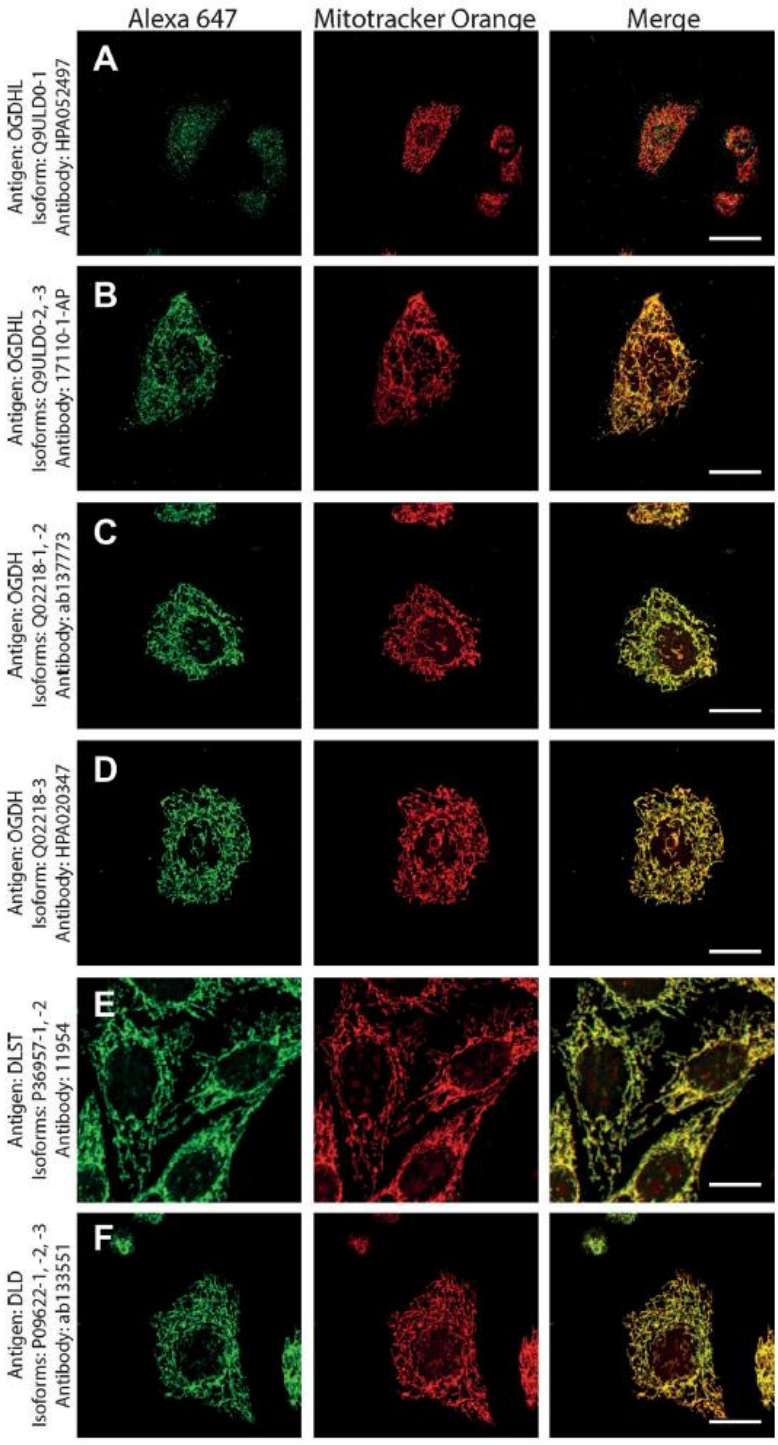

Figure 16.2. OGDHL, OGDH, DLST and DLD immunolabeling (labelling by Alexa 647) in HeLa cells in relation to mitotracker orange (MTO). Mag: 40x.

homogenates were probed for SUCLG1, SUCLG2, SUCLA2, OGDH, DLST, DLD, β-actin and VDAC1. Antibodies directed against OGDHL isoforms were not suitable for western blotting. Since the number of the homogenates used was higher than the number of lanes per gel that could be loaded, samples loaded in the last four lanes of each gel was also loaded in the first four lanes of the next gel. β-actin and VDAC1 served as loading markers for total tissue homogenate and mitochondrial content, respectively. SUCLG1, SUCLG2, SUCLA2 correspond to subunits of succinate-CoA ligase, the enzyme following KGDHC in the citric acid cycle. On the top lane, each three-digit number represents a brain homogenate sample from a brain donor. The exact brain location from where these homogenates originated is shown in table 2 (shown in (Dobolyi et al., 2020), table 2 is too large to be included in the present dissertation format). As shown in the cropped scanned western blots, the antibodies raised against OGDH, DLST and DLD yielded a band which appeared at the same molecular weight as the recombinant protein. Antibodies for SUCLG1, SUCLG2 and SUCLA2 have been validated elsewhere (Dobolyi et al., 2015a), (Dobolyi et al., 2015b), (Chinopoulos et al., 2019). Scanned images of whole blots appear in the supplemental material in (Dobolyi et al., 2020) (material is too large to appear in print in the current dissertation format). In supplemental figure 1 appearing in (Dobolyi et al., 2020) it is shown that antibodies yielded -in the vast majority of cases- a single band at the expected molecular weight; when the blots were "overexposed" several new bands appeared that were much fainter than the band corresponding to the intended protein. From the results shown in western blots and confocal imaging of immunocytochemistry we concluded that the antibodies raised against KGDHC components are specific

to the intended proteins. However, it must be emphasized that this did not apply for those raised against OGDHL isoforms.

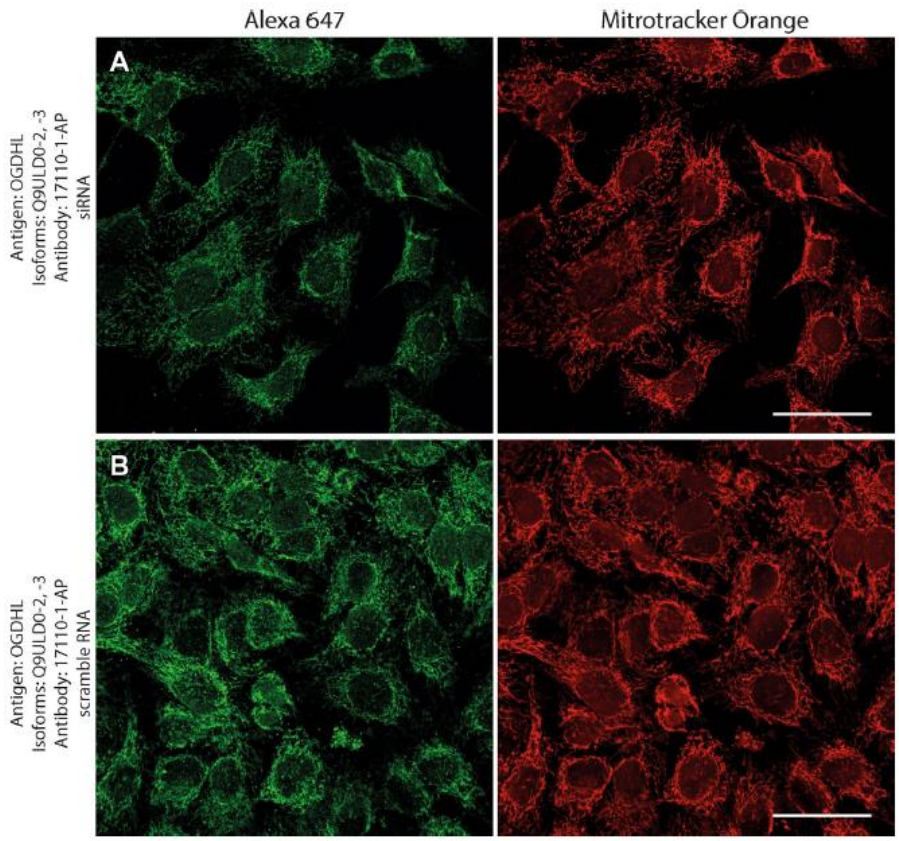

Figure 16.3. Effect of siRNA vs scramble RNA directed against OGDHL isoforms 2 and 3 on OGDHL immunostaining in HeLa cells in relation to mitotracker orange (MTO). Mag: 20x.

16.4 KGDHC subunit- and isoform-specific immunoreactivity in human brain cortex and cell types identification by co-staining with neuronal and/or glial markers

By using the above validated antibodies, we performed immunohistochemistry in human cerebral cortical material obtained from neurosurgical interventions. Frontal and temporal cortical samples did not show any visible difference in their labeling pattern for any antibody. The distribution of OGDH subunits investigated with antibodies specific to different OGDHL and OGDH isoforms were similar (Figures 16.10 and 16.11, respectively). Labeled cells were scarce in layer I of the cerebral cortex. In contrast, a high number of labeled cells were present in all other layers of the cerebral cortex. The labeling was absent in the nuclei of the cells while it was punctate with occasional filamentous appearance in the perikarya. Although *in situ* mitochondria are filamentous, a largely punctate appearance emerged likely because of the multiple amplification steps. Furthermore, immunohistochemistry protocols of signal amplification almost always lead to diminished spatial resolution. Thus, KGDHC staining in the human cerebral cortical tissue did not completely match the filamentous mitochondrial network commonly observed in cultured fibroblasts and cell lines but its appearance was still indicative of mitochondrial localization. To identify the type of cells labeled with the different OGDH subtypes, double labeling was performed. A fluorescent Nissl dye allowed the analysis of cellular morphology, which suggested the presence of all OGDH subtypes in neurons. In addition, a high number of smaller cells, also labeled with fluorescent Nissl dye were also present but did not contain OGDH. Since the smaller size and the even distribution of these cells suggested that they may be glial cells, we performed double labeling with antibodies recognizing different OGDH subtypes and the astrocyte markers GFAP (Figures 16.10 and 16.11) and Aldhl1 (Figure 16.12). The results of these doubly labeling studies indicated the absence of OGDH immunoreactivity in astrocytes. Double labelling of OGDH subunits with the oligondendrocyte markers Olig2 (Figure 16.12) and myelin basic protein

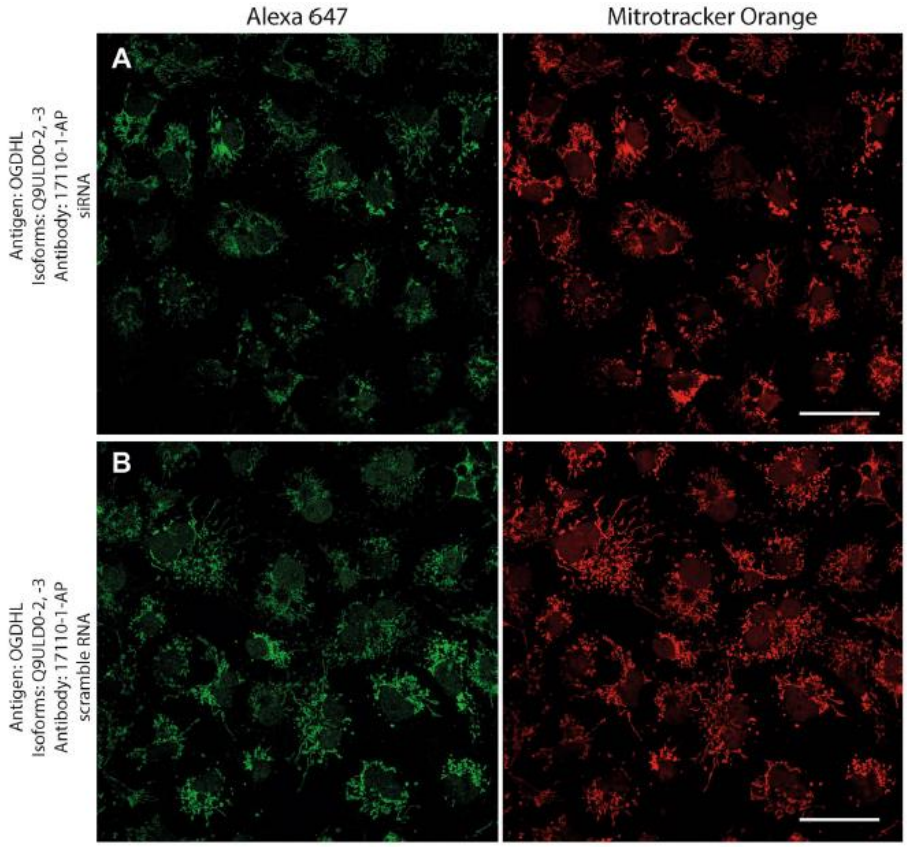

Figure 16.4. Effect of siRNA vs scramble RNA directed against OGDHL isoforms 2 and 3 on OGDHL immunostaining in COS-7 cells in relation to mitotracker orange (MTO). Mag: 20x.

(Figure 16.13), or the microglial marker IBA1 (Figure 16.13) also precluded localization of this KGDHC-specific subunit in oligodendroglia and microglia cells, respectively. Other subunits of KGDHC were examined in similar manner. DLST exhibited a distribution and localization resembling that of OGDH (Figure 16.14). In contrast, DLD was abundant in layer I as well as the deep layers of both the frontal and temporal cortices (Figure 16.15A). Double labeling with the fluorescent Nissl dye suggested that all cells contain DLD (Figure 16.15B). Indeed, astrocytes labeled with GFAP were shown to also localize DLD in them (Figure 16.15C).

16.5 Comparison of immunohistochemistry results obtained in this study from KGDHC subunit staining and those published in the Human Protein Atlas

The Tissue Atlas branch of the Human Protein Atlas aims to map the distribution of all human proteins in major tissues and organs, including the brain (Uhlen et al., 2015). The Tissue Atlas profiles proteins by antibodies in a qualitative manner. More specifically, antibodies are labeled with 3,3'-diaminobenzidine (DAB) yielding a brown discoloration of the stained cell. The section is furthermore counterstained with hematoxylin and cells are identified by visualizing their microscopical characteristics. With this approach the spatial distribution, cell type specificity and approximate relative abundance of proteins can be estimated, in the respective tissues. In table 3 (table 3 is shown in (Dobolyi et al., 2020), it is too large to be included in the present dissertation format), data from the Human Protein Atlas on brain tissues is shown when using KGDHC subunit- and isoform-specific antibodies. The Atlas categorizes staining as ‘high’, ‘medium’ or ‘low’, recognizing ‘glial’ and ‘neuronal’ staining. As shown in table 3 (table 3 is shown in (Dobolyi et al., 2020), it is too large to be included in the present dissertation format), in the human cortex OGDH, OGDHL and DLST are mostly expressed in neurons (medium or high staining), and they exhibit a low expression in glia. DLD staining is medium for both neurons and glia. It must be emphasized that visual identification of neurons versus glia by DAB followed by hematoxylin counterstain is prone to high false-positive and false-negative results. In the present work cells were identified by Nissl, GFAP, IBA1 and basic myelin protein, affording a very high level of assurance regarding correct cell

identification and categorization. Nevertheless, there is an obvious agreement between our data and those amassed by the Human Protein Atlas, namely that KGDHC specific subunits are expressed in neurons and little (if at all) in cortical glia.

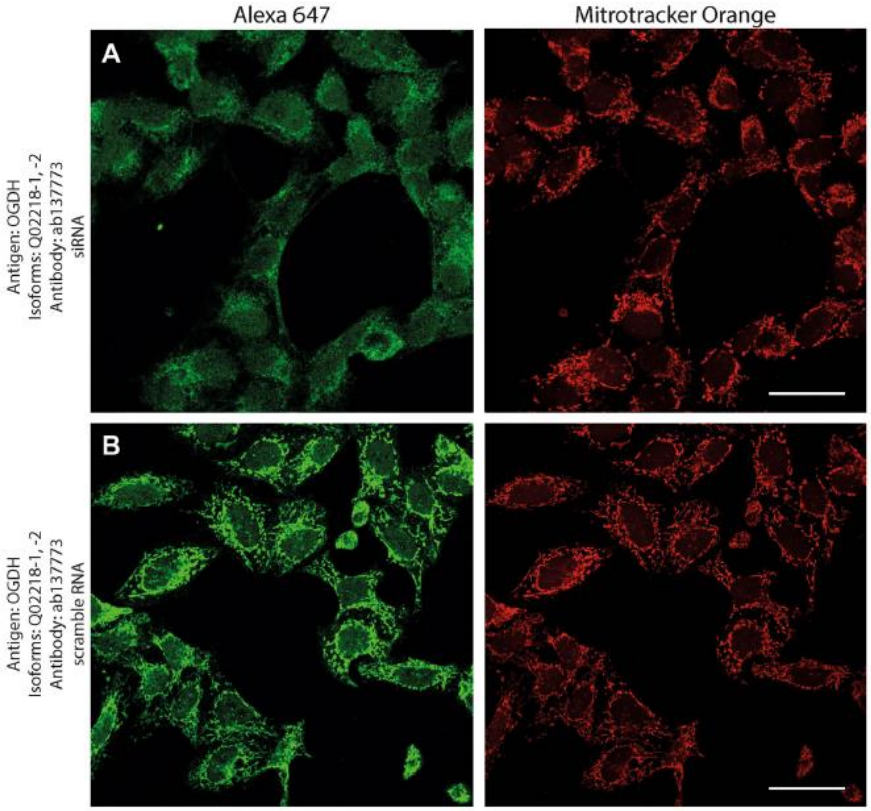

Figure 16.5. Effect of siRNA vs scramble RNA directed against OGDH isoforms 1 and 2 on OGDH immunostaining in HeLa cells in relation to mitotracker orange (MTO). Mag: 20x.

16.6 Correlation of immunohistochemistry results obtained in this study from KGDHC subunit staining and RNA-Seq data published in the Allen Brain Atlas

The Allen Brain Atlas is an integrated spatio-temporal portal for exploring the central nervous system (Sunkin et al., 2013). It entails RNA-Seq data from intact nuclei derived from frozen human brain specimens obtained from middle temporal gyri. Specifically, 15,928 nuclei from 8 human tissue donors ranging in age from 24-66 years were analyzed. As shown in figure 16.16A, RNA-Seq data for *OGDH, OGDHL, DLST and DLD* (indicated on the left) are shown as a function of cell subtype (indicated in the x-axis). These data are pooled exclusively from the exons. It is immediately apparent that, in non-neuronal cells –thus including glia- expression of KGDHC components is much less than that in glutamatergic + GABAergic cells, *i.e.* collectively neuronal cells. For comparisons, RNA-Seq data for GFAP and Olig2 (glial markers), SLC17A7 (Solute Carrier Family 1 (Glutamate Transporter), Member 7; it transports L-glutamate; glutamatergic neuron marker), GAD1: Glutamate Decarboxylase isoform 1; GABA-ergic neuronal marker and SUCLA2 (component of ATP-forming succinate CoA ligase, neuronal marker) are also presented. On the other hand, in figure 16.16B, RNA-Seq data from introns only are presented, and there it is apparent that gene elements coding for KGDHC components are essentially the same between neuronal vs non-neuronal cells; this practically means that in non-neuronal cells (such as glia) genes coding for KGDHC components are embedded in intronic regions as a result of some genetic regulation.

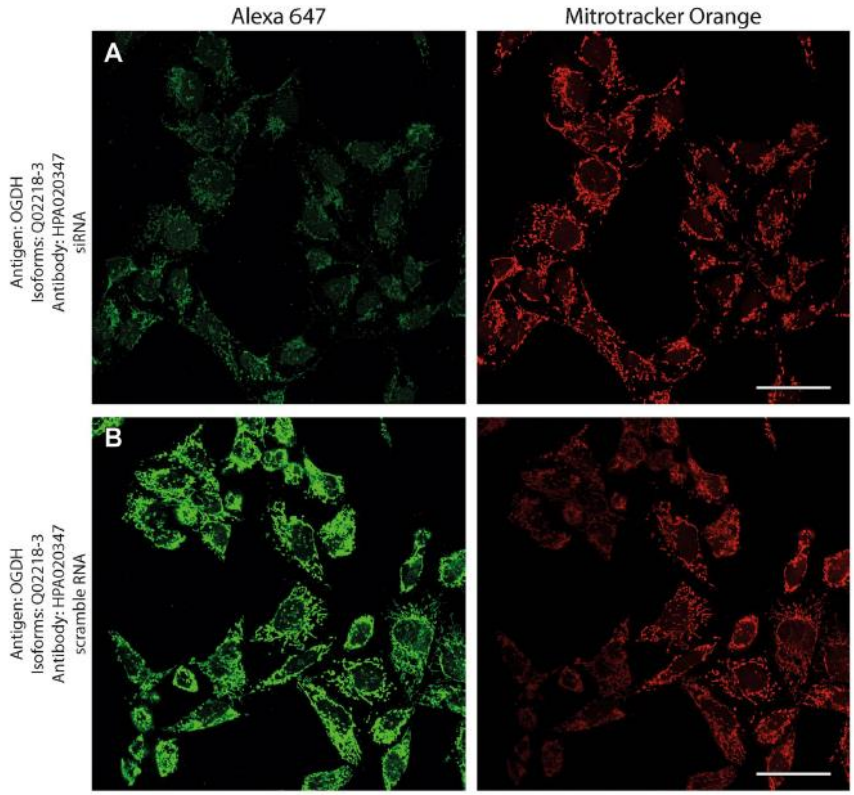

Figure 16.6. Effect of siRNA vs scramble RNA directed against OGDH isoform 3 on OGDH immunostaining in HeLa cells in relation to mitotracker orange (MTO). Mag: 20x.

16.7 Protein lysine succinylation is pancellularly evident in the human brain

All cells in the examined cerebral cortices were immune-positive for protein lysine succinylation as demonstrated by the lack of cells singly labelled with the fluorescent Nissl dye (Figure 16.17). The localization in astrocytes was also confirmed by double labeling with GFAP as indeed all GFAP-positive glial cells contained immunolabeling for protein lysine succinylation as well (Figure 16.17). The specificity of the labeling was confirmed by the absence of signal when the antibody was pre-incubated with succinylated Wheat Germ Agglutinin (WGA, figure panels 16.18B, D) but not WGA without succinylation figure panels 16.18A, C). Specificity of the anti-succinyllysine antibody was further assured by a similar methodology but in Western blots of homogenized brains. As shown in Figure 16.18, panels E-H, WB for 12 brain homogenates was performed. In the same gels, wheat germ agglutinin (WGA) and succinylated WGA were loaded where indicated. In panel E, blots were probed with anti-succinyllysine antibody; the blot shown in panel F was treated with anti-succinyllysine antibody plus WGA; the blot shown in panel G was treated with anti-succinyllysine antibody plus succinylated WGA; and the blot strip shown in panel H depicts the result of probing for β-actin, as loading control. It is evident that incubation of the anti-succinyllysine antibody with succinylated WGA but not WGA yields very little staining. WGA contains endogenous succinylated sites (Zhang, Y. et al., 2017b), thus, a band is visible in the respective lane.

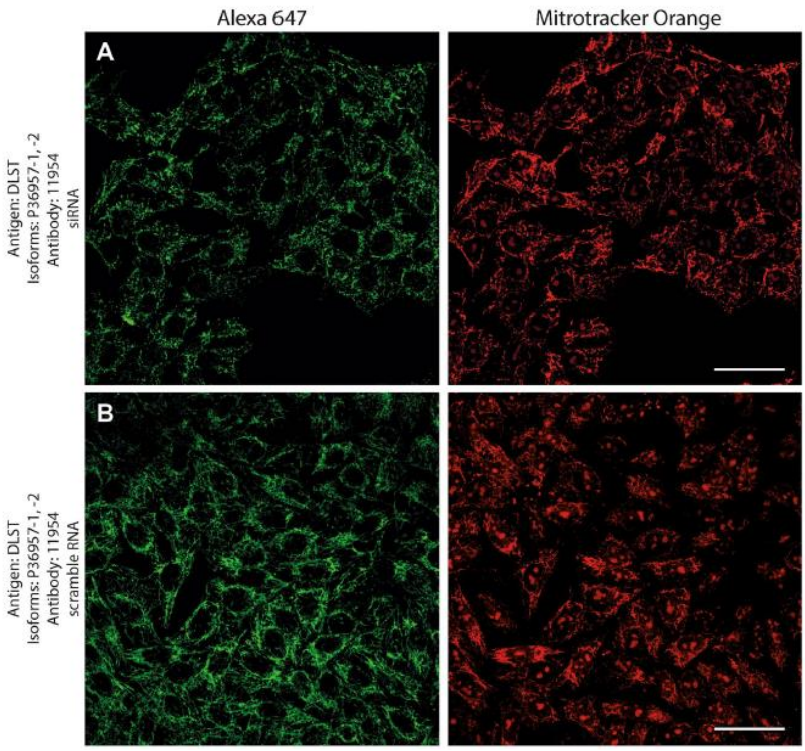

Figure 16.7. Effect of siRNA vs scramble RNA directed against DSLT isoforms 1 and 2 on DSLT immunostaining in HeLa cells in relation to mitotracker orange (MTO). Mag: 20x.

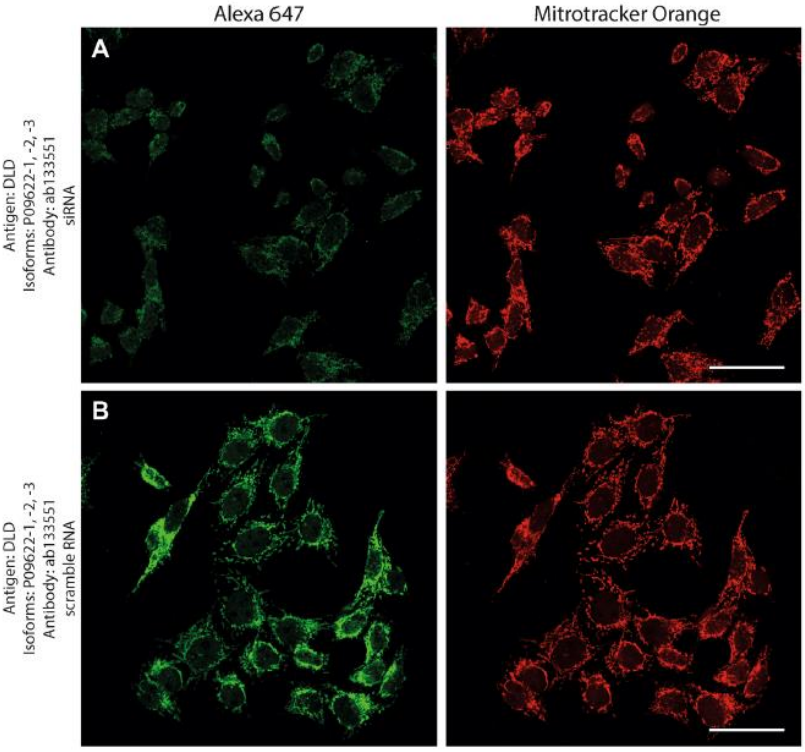

Figure 16.8. Effect of siRNA vs scramble RNA directed against DLD isoforms 1, 2 and 3 on DLD immunostaining in HeLa cells in relation to mitotracker orange (MTO). Mag: 20x.

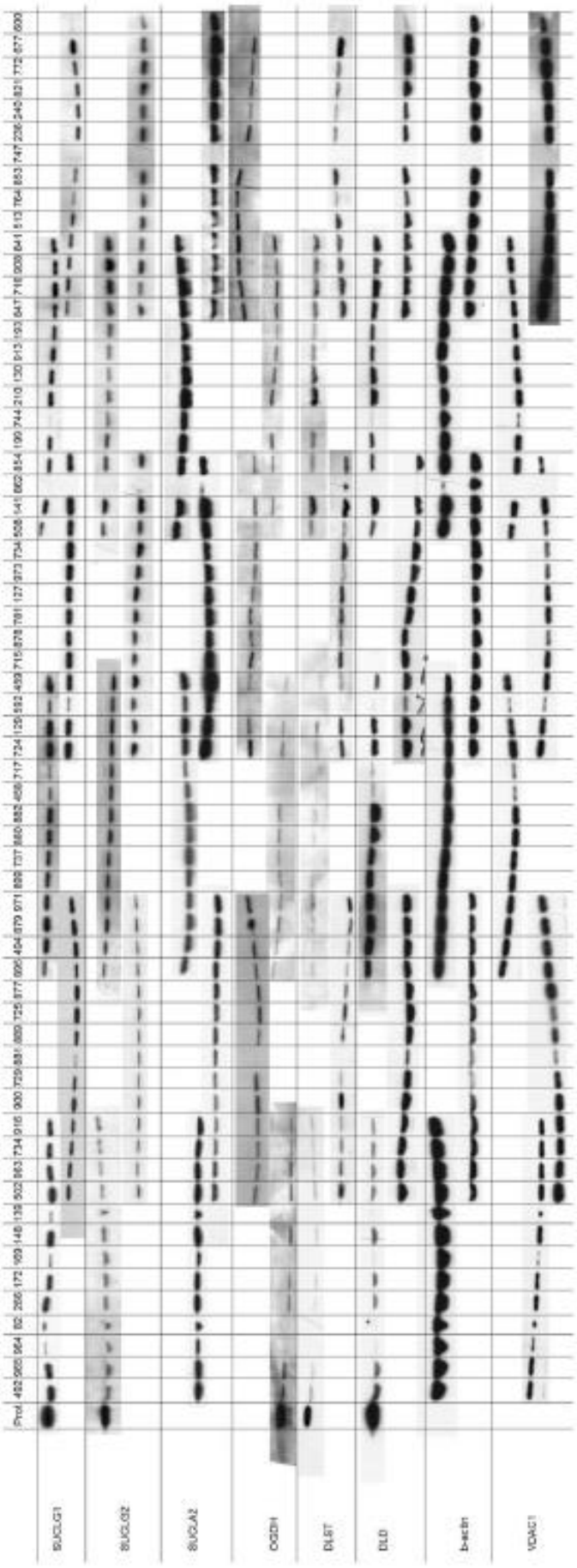

Figure 16.9. Immunoreactivities of the proteins indicated on the left in brain tissue homogenates (indicated on the top; individual samples coded by a three-digit number obtained from brain regions as detailed in table 2 shown in (Dobolyi et al., 2020), it is too large to be included in the present dissertation format). The most-left lane includes purified, recombinant proteins (Prot.) for OGDH, DLST and DLD.

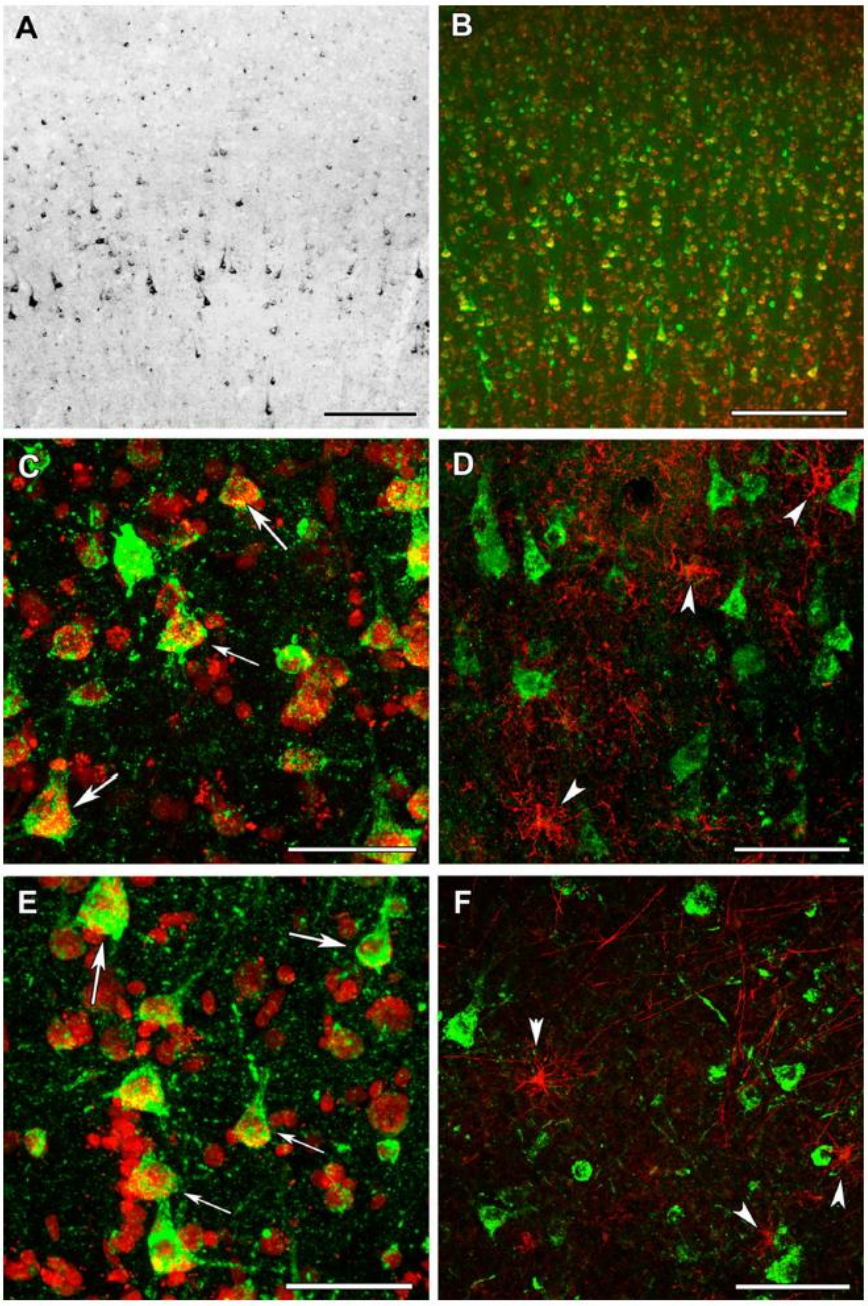

Figure 16.10. OGDHL immunolabeling in the human cerebral cortex in relation to neuronal and glial markers. A: OGDHL isoform 1-immunoreactive cells are present the cerebral cortex, with higher density in the deep layers. B: OGDHL isoform 1 (green) and fluorescent Nissl staining (red) show many double-labeled yellow cells in the cerebral cortex. C: A higher magnification confocal image of a cerebral cortical section double stained with OGDHL isoform 1 (green) and fluorescent Nissl staining (red) demonstrates that larger, neuronal cells (some of them indicated with white arrow) are double labeled. Several small cells are also present, which are not labeled with OGDHL isoform 1. Please, observe the dot-like intracellular labeling pattern of OGDHL subunit 1 immunoreactivity. D: A cerebral cortical section double labeled with OGDHL isoform 1 (green) and the established astrocyte marker glial fibrillary acidic protein (GFAP; red) shows only single labeled cells positive for OGDHL isoform 1 or for GFAP demonstrating that astrocytes are not labeled with OGDHL isoform 1. Some of the single labeled astrocytes are pointed to by white arrowheads. E: A confocal image of a cerebral cortical section double stained with OGDHL isoform 2/3 (green) and fluorescent Nissl staining (red) demonstrates that larger, neuronal cells (some of them indicated with white arrow) are double labeled. Several small cells not labeled with OGDHL isoform 2/3 are also present. Note the dot-like intracellular labeling pattern of OGDHL subunit 2/3 immunoreactivity. F: A cerebral cortical section double labeled with OGDHL isoform 2/3 (green) and GFAP (red) shows cells labeled either with OGDHL or with GFAP demonstrating that astrocytes are not labeled with OGDHL isoform 2/3. Some of the single labeled astrocytes are pointed to by white arrowheads. Scale bars = 200 µm for A, 300 µm for B, 100 µm for C-F.

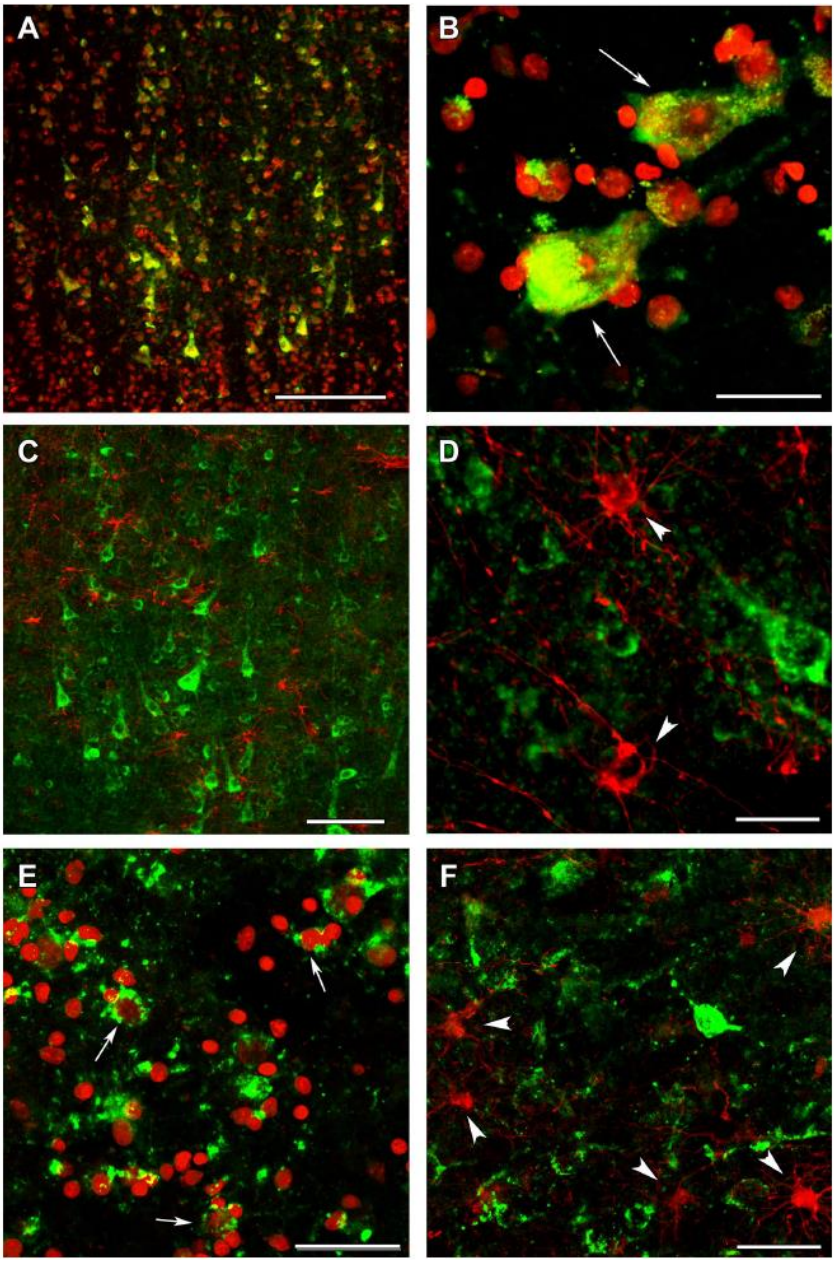

Figure 16.11. OGDH immunolabeling in the human cerebral cortex in relation to neuronal and glial markers. A: OGDH isoform 1/2 (green) immunolabeling and fluorescent Nissl staining (red) show many double-labeled yellow cells in the cerebral cortex. B: A high magnification confocal image of a cerebral cortical section double stained with OGDH isoform 1/2 (green) and fluorescent Nissl staining (red) demonstrates that larger, neuronal cells indicated with white arrow are double labeled. Several small cells are also present, which are not labeled with OGDH isoform 1/2. Note the dot-like intracellular labeling pattern of OGDH subunit 1/2 immunoreactivity. C: A cerebral cortical section double labeled with OGDH isoform 1/2 (green) and the established astrocyte marker glial fibrillary acidic protein (GFAP; red) shows only single labeled cells positive for OGDH isoform 1/2 or for GFAP demonstrating that astrocytes are not labeled with OGDH isoform 1. D: A high magnification confocal image shows separate single OGDH isoform 1/2 and GFAP-positive (red, pointed to by arrowheads) cells. E: A confocal image of a cerebral cortical section double stained with OGDH isoform 3 (green) and fluorescent Nissl staining (red) demonstrates that larger, neuronal cells (some of them indicated with white arrow) are double labeled. Several small cells not labeled with OGDH isoform 3 are also present. F: A cerebral cortical section double labeled with OGDH isoform 3 (green) and GFAP (red) shows cells labeled either with OGDH isoform 3 or with GFAP demonstrating that astrocytes are not labeled with OGDH isoform 3. Some of the single labeled astrocytes are pointed to by white arrowheads. Scale bars = 200 µm for A, 30 µm for B, 100 µm for C, 25 µm for D, and 50 µm for E and F.

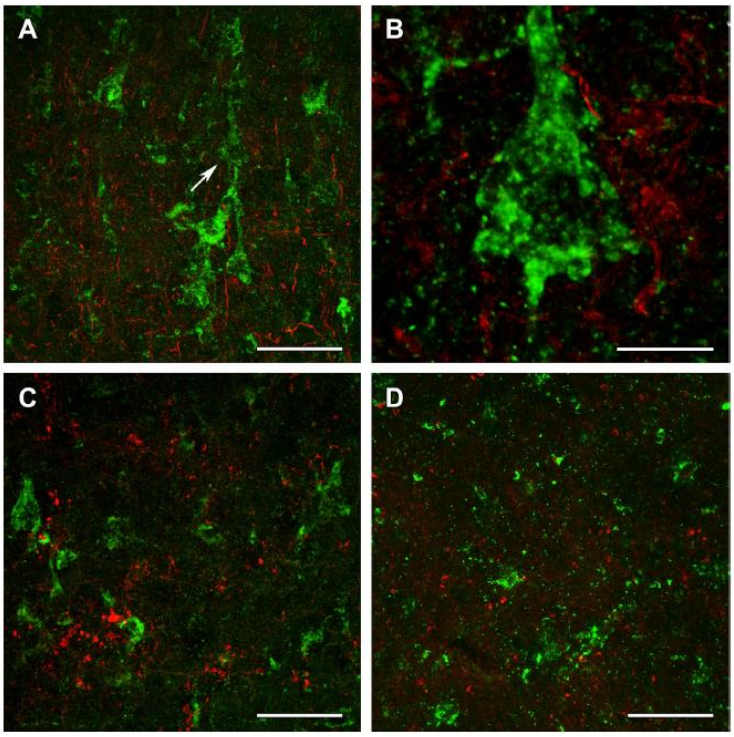

Figure 16.12. OGDHL and OGDH immunolabeling in the human cerebral cortex in relation to glial markers. A: OGDHL-immunoreactive (green) cells as well as ALDHL1-positive (red) astrocytes are both present in the cerebral cortex without any visible colocalization. B: A high magnification confocal image of the area pointed to by the white arrow in A demonstrates that OGDHL-ir cells are not labeled with Aldhl1 and in turn, Aldhl1-ir astrocytes do not contain OGDHL immunoreactivity. C: Aldhl1 (red) is also absent in OGDH-ir cells and their processes (green). D: The image demonstrates the lack of colocalization between OGDHL immunoreactivity (green) and the oligodendrocyte marker Olig2 (red). Scale bars = 50 µm for A, C, and D, and 10 µm for B.

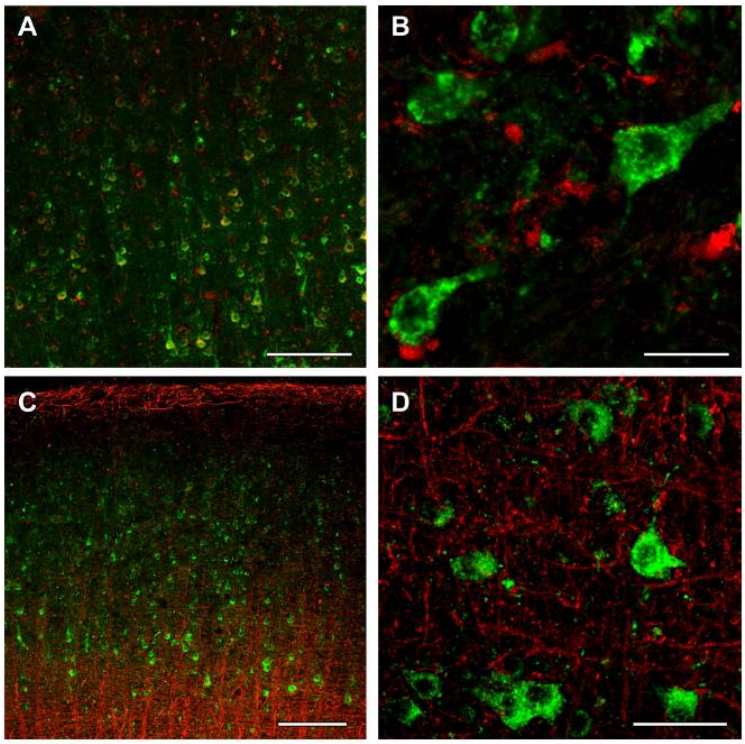

Figure 16.13. OGDH immunolabeling in the human cerebral cortex in relation to microglia and oligodendrocyte markers. A: OGDH isoform 1/2 (green) and Iba1 (red) immunolabeling suggest a distinct distribution of OGDH-containing cells and microglia. In low magnification OGDH- and IBA1- co-immunoreactivity may appear, but this notion is rejected in high magnification microphotographs. B: A high magnification, optically 1 µm thick confocal image of a cerebral cortical section double stained with OGDH isoform 1/2 (green) and Iba1 (red) demonstrates that larger, neuronal cells are single labeled for OGDH isoform 1/2. Several small cells are IBA1-positive. These cells are not labeled with OGDH isoform 1/2 suggesting that that microglial cells are negative for OGDH isoform 1/2. C: A cerebral cortical section double labeled with OGDH isoform 1/2 (green) and the established oligodendrocyte marker myelin basic protein (MBP; red). The latter shows the typical distribution of myelinated fibers in the cerebral cortex. D: A high magnification confocal image shows the lack of co-localization between OGDH isoform 1/2 and MBP-positive structures (red). Scale bars = 200 µm for A and C, 25 µm for B, and 50 um for D.

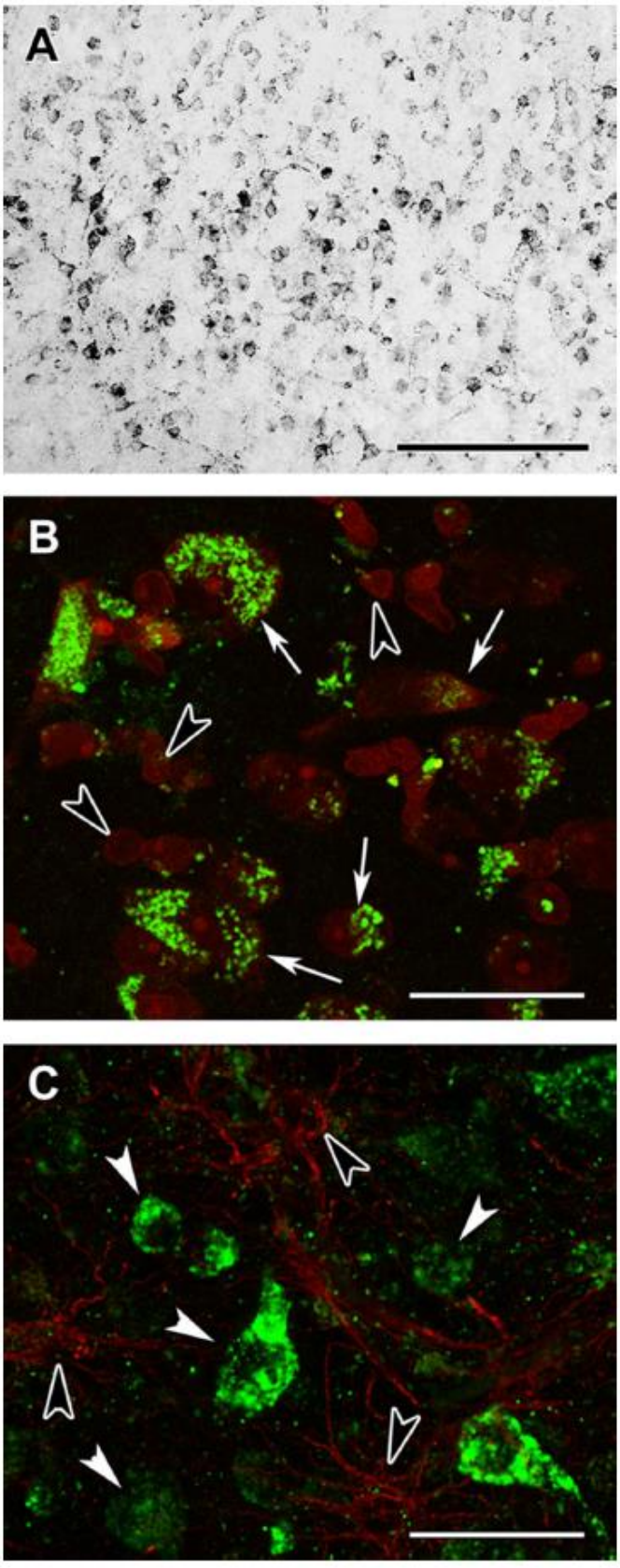

Figure 16.14. DLST immunolabeling in the human cerebral cortex in relation to neuronal and glial markers. A: DLST-immunoreactive (DLST-ir) cells are present in the cerebral cortex. B: DLST (green) and fluorescent Nissl staining (red) show that many cells are double-labeled in the cerebral cortex. Arrows point to double labeled neurons while black arrowheads point to single-labeled, DLST-immunonegative cells. Please, note the dot-like distribution of DLST immunolabeling in the double labeled neurons. C: A cerebral cortical section double labeled with DLST (green) and the established astrocyte marker glial fibrillary acidic protein (GFAP; red) to show the lack of double labeling suggesting that astrocytes are devoid of DLST. White arrowheads point to single labeled (DLST-ir) neurons while black arrowheads point to single labeled (GFAP-ir) astrocytes. Scale bars = 300 µm for A, and 30 µm for B and C.

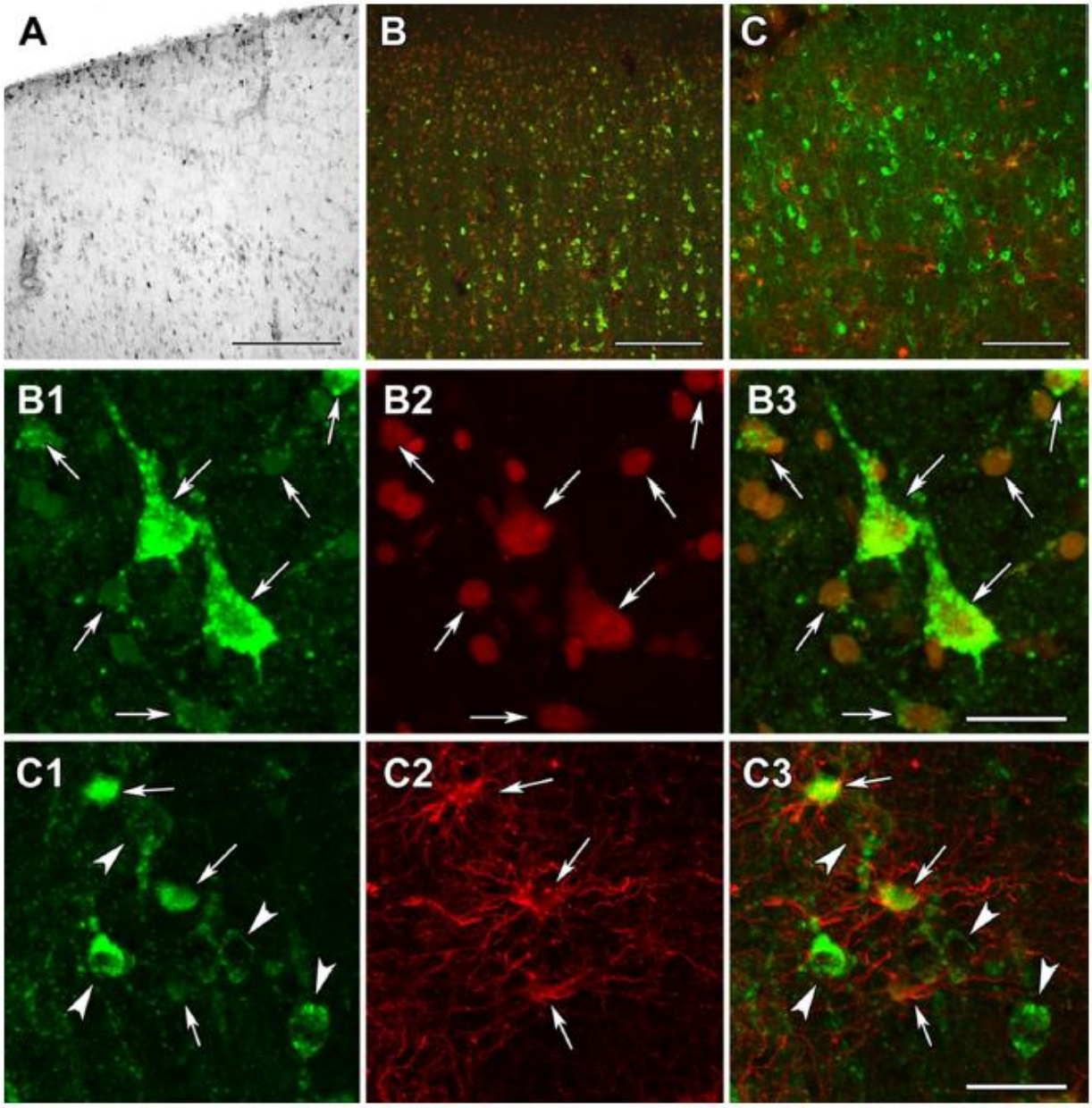

Figure 16.15. DLD immunolabeling in the human cerebral cortex in relation to neuronal and glial markers. A: DLD-immunoreactive (DLD-ir) cells are present in layer 1 and also in deep layers of the cerebral cortex. The density of labeled cells is particularly high in layer 1 and the pyramidal layers. B: DLD (green) and fluorescent Nissl staining (red) show that most cells are yellow, that is double-labeled in the cerebral cortex. C: A cerebral cortical section double labeled with DLD (green) and the established astrocyte marker glial fibrillary acidic protein (GFAP; red) to show that most astrocyte contain DLD. B1-3: A high magnification confocal image of the cerebral cortical section double labeled with DLD (green) and fluorescent Nissl staining (red) demonstrates double labeling of the cells. The arrows point to some of the double-labeled cells. B1 shows the green channel, B2 the red channel, and B3 the merged figure. C1-3: A high magnification confocal image of the cerebral cortical section double labeled with DLD (green) and GFAP (red) demonstrates the presence of DLD in astrocytes (arrows). The arrowheads in turn point to neurons, which contain DLD but do not express GFAP. C1 shows the green channel, B2 the red channel, and B3 the merged figure. Scale bars = 300 µm for A, 200 µm for B, 100 µm for C, and 20 µm for B1-3 and C1-3.

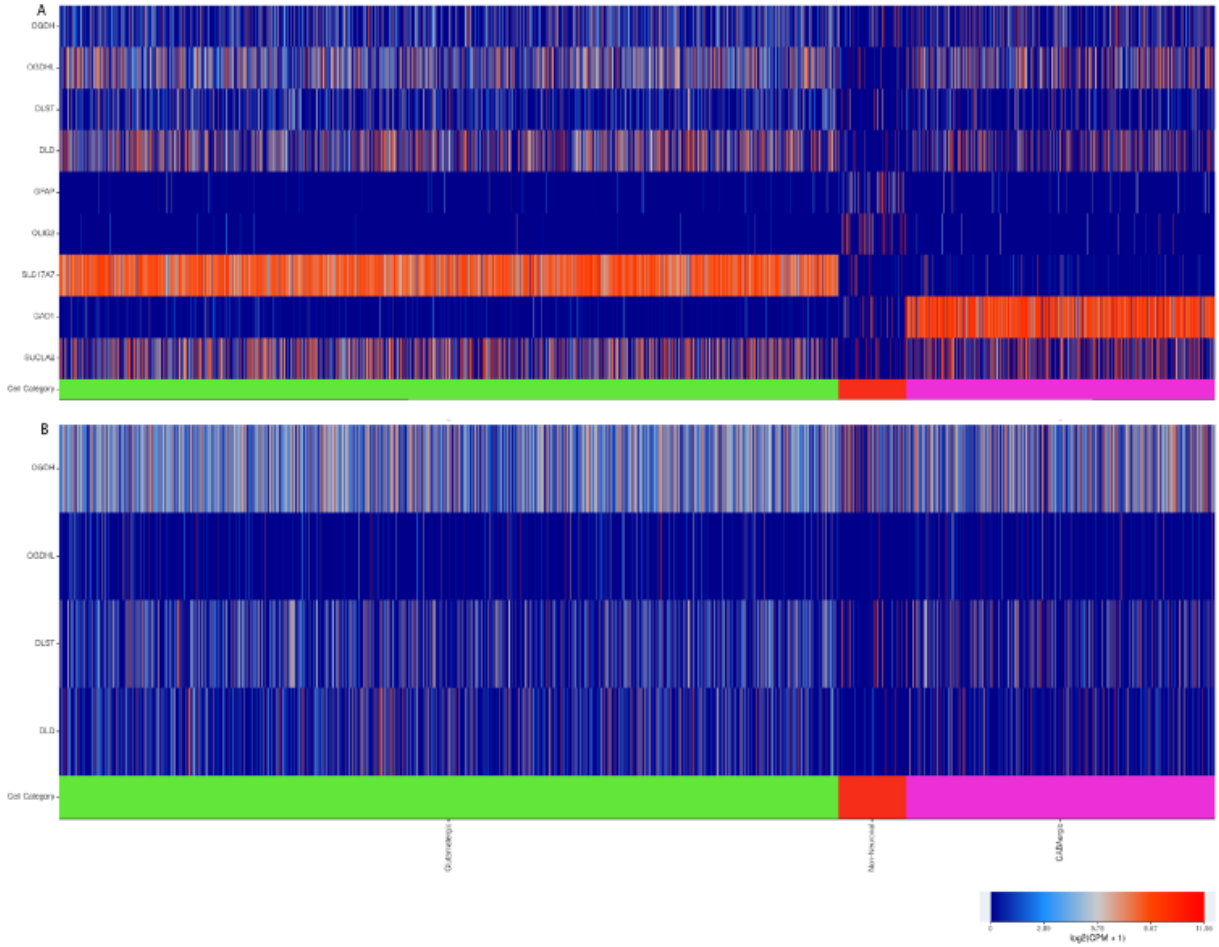

Figure 16.16. RNA-Seq data obtained from the Allen Brain Atlas, looking at the expression of genes indicated in the laft, as a function of cell types. A: genes found only in exons. B: genes found only in introns. Image credit: Allen Institute. http://celltypes.brain-map.org/rnaseq/human

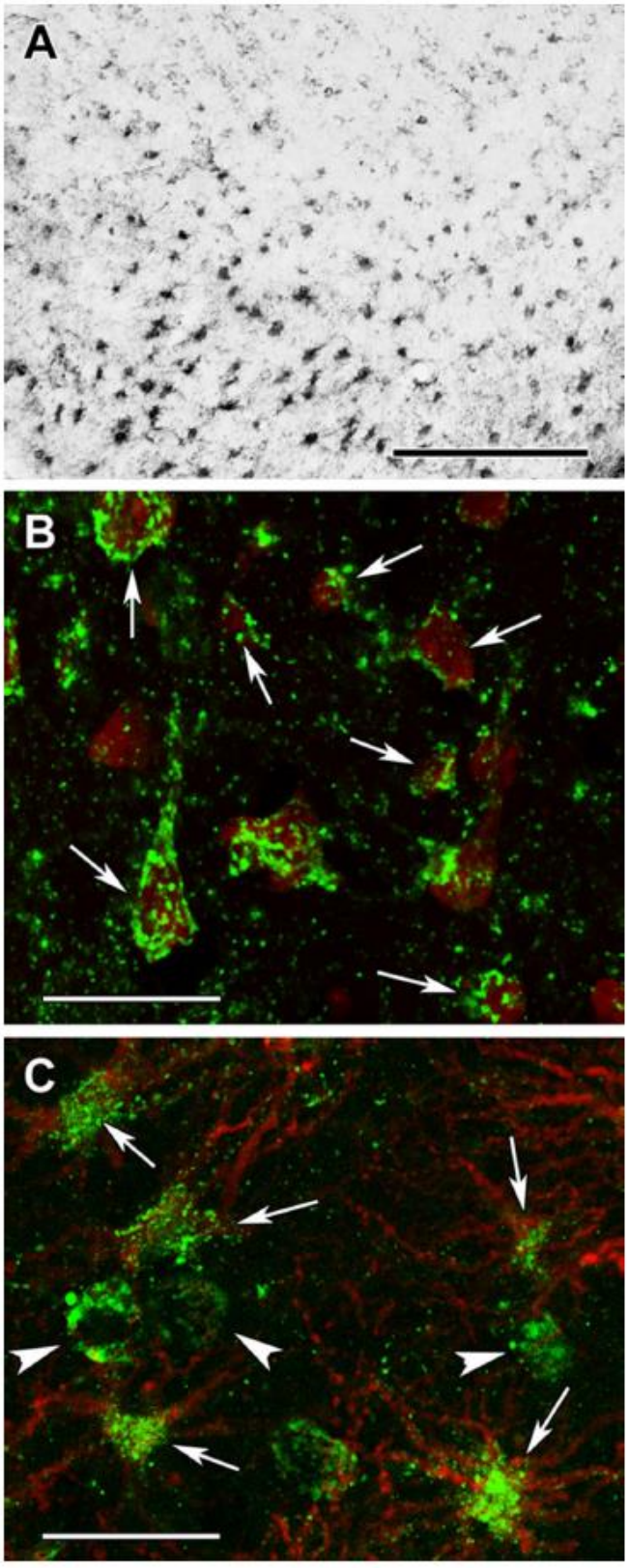

Figure 16.17. succinyl-lysine immunolabeling in the human cerebral cortex in relation to neuronal and glial markers. A: succinyl-lysine -immunoreactive (SUCCLYS-ir) cells are present in the cerebral cortex. B: succinyl-lysine (green) and fluorescent Nissl staining (red) show that essentially all cells are double-labeled in the cerebral cortex. Arrows point to some of these double labeled cells. Please, note the dot-like distribution of succinyl-lysine immunolabeling in the double labeled cells. C: A cerebral cortical section double labeled with succinyl-lysine (green) and the established astrocyte marker glial fibrillary acidic protein (GFAP; red) to show the double labeling of astrocytes. White arrowheads point to single labeled (SUCCLYS-ir) neurons. Scale bars = 300 µm for A, and 30 µm for B and C.

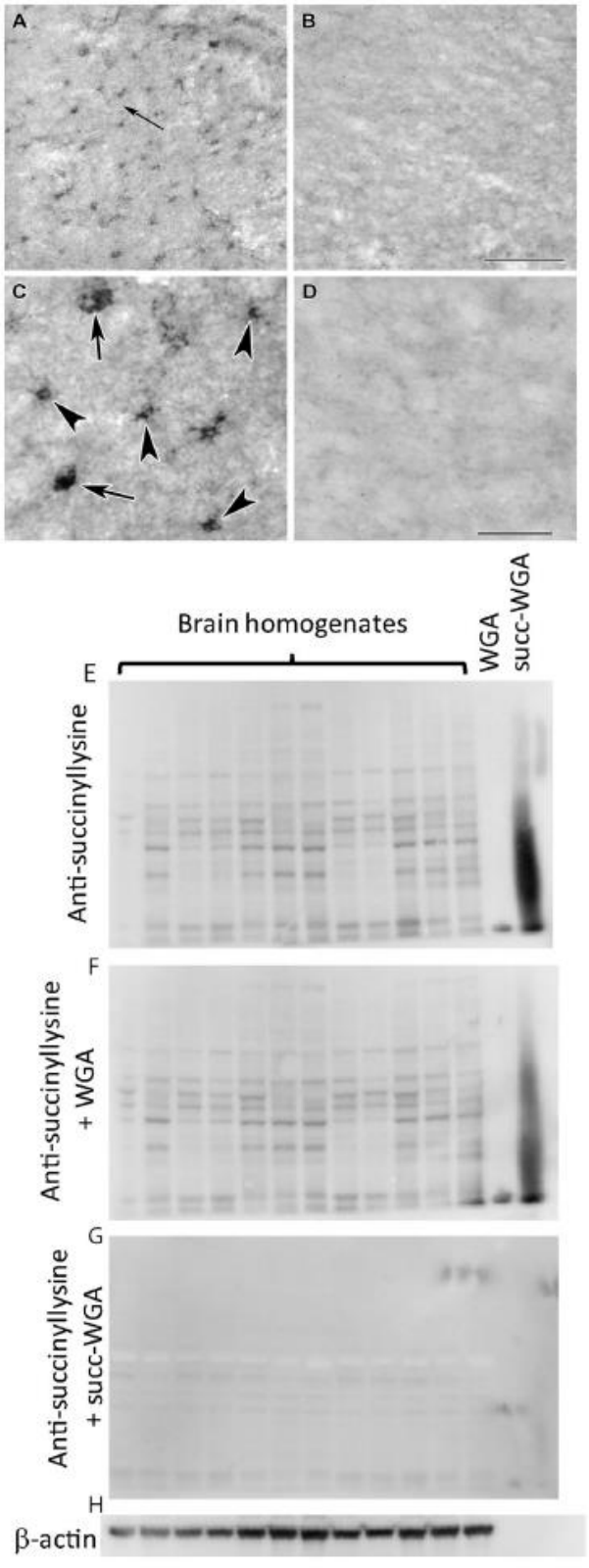

Figure 16.18. Testing of the specificity of the anti-succinyl-lysine antibody by absorption in the human cerebral cortex. A: Preincubation of the anti-succinyl-lysine antibody with wheat germ agglutinin does not prevent immunolabeling. The arrow indicated the area magnified in panel C. B: Following preincubation of the anti-succinyl-lysine antibody with succinylated wheat germ agglutinin eliminates specific immunolabeling in a section adjacent to the one shown in panel A. C, D: Higher magnification images demonstrate the effect of preabsorption with succinylated wheat germ agglutinin. Note the different types of labelled cells in C. Scale bars = 200 µm for A and B, and 50 µm for C and D. E: Western blot loaded with 12 brain homogenates, WGA-loaded lane and succinylated-WGA, where indicated, treated with anti-succinyllysine. F: same as for panel E, treated with WGA plus anti-succinyllysine. G: Same as for panel E but treated with succinylated-WGA plus anti-succinyllysine. H: β-actin as loading control.

DISCUSSION

Cyclophilin D regulates matrix adenine nucleotide levels

In (Chinopoulos et al., 2011) we demonstrated that in intact mitochondria, changes in ATP synthesis or hydrolysis rates of the F_0F_1-ATP synthase due to CYPD binding does not translate to changes in ADP-ATP flux rates. This was due to an imposing role of the ANT. Apparently, the ADP-ATP exchange rates by the ANT are slower than the ADP-ATP interconversions by the F_0F_1-ATP synthase, an assumption which is afforded by the more than twice larger flux control coefficient of ANT (0.63 for WT, 0.66 for CYPD KO) than that of the F_0F_1-ATP synthase (0.29 for WT, 0.3 for CYPD KO), for adenine nucleotide flux rates. This is also supported by early findings showing that the ANT is the step with the highest flux control coefficient in the phosphorylation of externally added ADP to energized mitochondria (Duee and Vignais, 1969b). However, one could argue that a 30% change in F_0F_1-ATP synthase activity which exhibits a ~0.3 flux control coefficient, would alter adenine nucleotide exchange rates in intact mitochondria by 0.3x0.3=0.09, i.e. 9%. To this we must stress that the flux control coefficient applies for infinitesimally small changes in the percent change in the steady state rate of the pathway; if changes are large (e.g. 30%), the flux control coefficient decreases by a factor of ~5, or more (Brand et al., 1993), (Hafner et al., 1990). Thereby, a 30% change in F_0F_1-ATP synthase activity translates to a 0.3x0.3x0.2=0.018 or less, i.e. 1.8% difference in adenine nucleotide exchange rates in intact mitochondria. This is in good agreement with the predictions of the kinetic modeling, suggesting that a 30% increase in F_0F_1-ATP synthase activity yields a 1.38-1.7% increase in ADP-ATP exchange rate mediated by the ANT in fully polarized or fully depolarized mitochondria. Yet, in substrate-energized mitochondria an increase in ATP synthesis rate by relieving the inhibition of the F_0F_1-ATP synthase by CYPD was reflected by an increase in respiration rates during arsenolysis; likewise, in ATP-energized mitochondria with a non-functional respiratory chain, abolition of CYPD or its inhibition by cyclosporin A resulted in an accelerated ATP hydrolysis rate, allowing intact mitochondria to maintain a higher membrane potential. Our findings in (Chinopoulos et al., 2011) imply that the modulation of F_0F_1-ATP synthase activity by CYPD comprises an “in-house” mechanism of regulating matrix adenine nucleotide levels, that does not transduce outside mitochondria, without evoking a functional correlation between CYPD and ANT due to a possible direct link (Bernardi, 1992). This was the first documented example of an intramitochondrial mechanism of adenine nucleotide level regulation, that is not reflected in the extramitochondrial compartment. Furthermore, we speculate that cyclosporin A or *ppif* genetic ablation delays pore opening by providing a more robust $\Delta\Psi m$. It is well established that the lower the $\Delta\Psi m$, the higher the probability for pore opening (Petronilli et al., 1993a), (Bernardi, 1992), (Petronilli et al., 1993b), (Scorrano et al., 1997). In energized mitochondria, abolition of CYPD or its inhibition by cyclosporin A would lead to an accelerated ATP synthesis, while in sufficiently depolarized mitochondria would result in accelerated proton pumping by ATP hydrolysis. However, an alternative explanation relates to matrix P_i which is a product of ATP hydrolysis by a reversed F_0F_1-ATP synthase, and inhibits PTP (Basso et al., 2008). It is therefore also reasonable to speculate that in de-energized mitochondria an increase in matrix P_i concentration could mediate the effect of cyclosporin A or CYPD genetic ablation in delaying PTP opening (Basso et al., 2008).

mSLP dictates ANT directionality

In (Chinopoulos et al., 2010) we demonstrated that during respiratory chain inhibition or submaximal uncoupling, when mitochondria not only stop synthesizing ATP but work as ATP consumers, F_0F_1-ATPase is able to work in reverse without the concomitant reversal of ANT. This phenomenon was demonstrated on three levels: i) Computational modeling suggested that changes in E_{rev_ANT} and in E_{rev_ATPase} define a

ΔΨm range ("B" space), in which F_0F_1-ATPase runs in reverse, whereas the forward function of ANT is maintained. Under these conditions, ΔΨm supported by the ATP-hydrolyzing F_0F_1-ATPase is in a range more negative than the E_{rev_ANT}, thereby ANT would not reverse. ii) Experiments with isolated mitochondria indicated that this phenomenon could indeed exist when respiration of mitochondria is impaired, or submaximally uncoupled and suggested that matrix substrate-level phosphorylation could be critical in providing ATP for the reversed F_0F_1-ATPase. iii) Data obtained with cultured cells supported the suggestion that also *in situ* mitochondria are likely to exhibit reversal of F_0F_1-ATPase but not of ANT, albeit the contribution of ATP provision by *SUCLA2*-mediated substrate level phosphorylation *in situ* has not been pinpointed. It is clear from both the model and the experiments with *in vitro* and *in situ* mitochondria that when depolarization is severe enough i.e., when ΔΨm is less negative than the E_{rev_ANT}, a condition observed in the presence of adequate amount of an uncoupler, mitochondria could consume extramitochondrial ATP translocated from the cytosol by the ANT.

Cytosolic ATP consumption by mitochondria under impaired respiration was reported for isolated nerve terminals challenged with rotenone and FCCP (Akerman and Nicholls, 1981). This phenomenon is also characteristic for oxidative stress (Chinopoulos et al., 1999) when inhibition of α-ketoglutarate dehydrogenase (Tretter and Adam-Vizi, 2000), a key Krebs cycle enzyme, limits the NADH availability and as a result, the respiratory function of mitochondria. It is a novel concept emerging from our study that matrix substrate-level phosphorylation could be an endogenous rescue mechanism supporting the reverse operation of F_0F_1-ATPase, with the benefit of maintaining ΔΨm at a suboptimal level, where mitochondria are depolarized, but not sufficiently for the ANT to reverse. This would assist in preserving of the ATP pool produced by glycolysis, which is evidently crucial for the survival chances of cells due to maintaining the function of the vital ATP-dependent transporters, such as Na^+/K^+-ATPase and Ca^{2+}-ATPases. Cells could be saved as long as matrix substrate-level phosphorylation is able to provide ATP for the F_0F_1-ATPase in impaired mitochondria. The importance of succinate thiokinase can be better appreciated by the severe phenotype observed in patients suffering from *SUCLA2* (or *SUCLG1*) deficiencies (Ostergaard, 2008). However, it would be difficult to attribute the phenotype exclusively to the provision of ATP by succinate thiokinase versus other very important metabolic branches, such as the maintenance of the citric acid cycle (Kaufman et al., 1953), ketone metabolism (Ottaway et al., 1981), or heme synthesis (Labbe et al., 1965). Nonetheless, it is to note that increasing mitochondrial substrate-level phosphorylation can rescue respiratory growth of an ATP synthase-deficient yeast (Schwimmer et al., 2005). It is also noteworthy to mention that recent experiments by the group of Balaban (Phillips et al., 2009) pointed succinyl-CoA synthetase as a target activated by matrix P_i, contributing to the anaerobic provision of ATP in mitochondria. This would obviously have the implication of providing ATP for the consuming F_0F_1-ATPase, thereby maintaining a moderate ΔΨm that -if more negative than E_{rev_ANT}- could contribute to sparing cytosolic ATP pools. Along these lines, a beneficial by-product is the provision of matrix P_i from matrix ATP hydrolysis, that could activate succinyl-CoA synthetase towards extra ATP formation. The finding of Balaban's group is a strong support of our concept, suggesting the importance of succinyl-CoA synthase in providing ATP in impaired mitochondria.

Furthermore, our results are in line with and can explain the repeatedly reported observation that inhibition of the respiratory chain of *in situ* mitochondria failed to activate in all cells the cytosolic ATP sensing mechanisms activated by a drop in [ATP] levels (Sasaki et al., 2001), (Karschin et al., 1998), (Trapp and Ballanyi, 1995), (Ballanyi et al., 1996). It may well be possible that the energy depletion protocols used did not permit ANT reversal in all cells. Accordingly, application of uncouplers to cells invariably led to opening of plasmalemmal K(ATP) channels, in line with sufficient loss of $\Delta\Psi m$ leading to ANT reversal (Sasaki et al., 2001).

The ability of mitochondria to enter the "B" space could be essential for the survival of cells when respiration is impaired in some, but not all *in situ* mitochondria. This scenario is known to exist in pathological conditions, when the mitochondrial DNA (mtDNA) pool of individual cells is heteroplasmic (Taivassalo et al., 1999),(Schnopp et al., 1996), (Coskun et al., 2004), (Wallace et al., 1988). It is reasonable to assume that the substrate-level phosphorylation by SUCL in respiration deficient mitochondria could act as a quality-control switch mechanistically involved in gene shifting of heteroplasmic mtDNA towards wild-type.

Mitochondria have been incriminated in diverse pathologies as ATP consumers. Admittedly, when these circumstances involve strong uncoupling or compromise of the integrity of the inner mitochondrial membrane or other –yet to be identified- conditions all characterized by absence of a *pmf*, F_1-ATPase would do what it does best: hydrolyze ATP. But in respiration-impaired mitochondria with intact inner mitochondrial membranes, if the reverse operation of F_0-F_1 ATP synthase is sustained by ATP provided by matrix substrate-level phosphorylation, $\Delta\Psi m$ will be maintained at a value not more negative than Erev_ATPase, while if only cytosolic ATP reserves are being used, the maximum $\Delta\Psi m$ value attainable cannot be more negative than that of Erev_ANT, imposing very slow reversal ATP-ADP exchange rates on the translocase. Apparently, the most crucial (though not solitary) determinant of cytosolic ATP consumption by intact mitochondria is the value of $\Delta\Psi m$; like Pythagoras said: "All Is Number".

Mitochondrial substrate-level phosphorylation (mSLP) and relevance to cancer

The results shown so far argue that mSLP can rescue mitochondria of normal cells experiencing hypoxia from becoming ATP sinks. By the same token, mSLP can "rescue" cancer cells growing under adverse micronenvironmental conditions, encompassing hypoxia. Relevant to this, evidence supporting tumor cells thriving by exploiting non-oxidative branches of metabolism while at the same time perform glutaminolysis (glutamine catabolism would obligatorily pass through succinate CoA ligase), are overwhelming. Although tumors are highly heterogeneous structures encompassing many different cell types with different properties, the metabolic characteristic of non-oxidative catabolism of glutamine is a "common denominator" for many tumor types. Below, evidence is examined pertaining to brain tumors and in particular glioblastoma (formerly referred to as glioblastoma multiforme, GBM), especially because cell-specific expression of enzymes supporting mSLP in normal adult human brain cells is also being covered in this dissertation.

Glioblastoma: general considerations

Glioblastoma carries the highest mortality rate among primary brain tumors and remains largely unmanageable. Life expectancy following diagnosis is only about 12-14 months. This has changed little for decades despite continuing research (Ahmadloo et al., 2013; Alexander and Cloughesy, 2017; Fisher and Buffler, 2005; Krex et al., 2007; Lawrence et al., 2011; Stupp et al., 2009). Indeed, a recent reevaluation found that overall survival for GBM is woefully similar to that reported by Cushing almost a century ago (Fatehi et al., 2018). A defining characteristic of GBM is the 'secondary structures of Scherer', which include diffuse parenchymal growth invasion over the subpial surface, along white matter tracks, and through the Virchow-Robin spaces (Kleihues and Ohgaki, 1999; Scherer, 1940; Shelton et al., 2010c; Zagzag et al., 2008);(Laws et al., 1993). The highly invasive nature of GBM makes most current therapies ineffective (Perry et al., 2017); (Krex et al., 2007); (Cuddapah et al., 2014); (Chang et al., 2005). Although the introduction of the toxic alkylating agent, temozolomide, has improved progression free survival slightly, quality of life has also remained poor for most GBM patients especially

for those receiving radiation alone (Taphoorn et al., 2005); (Flechl et al., 2012); (Stupp et al., 2009). GBM contains a plethora of morphologically diverse neoplastic cell types that express neural, glial, and myeloid/mesenchymal markers (Huysentruyt et al., 2011; Karsy et al., 2012; Morantz et al., 1979; Roggendorf et al., 1996; Rubinstein, 1972; Seyfried, 2001; Wood and Morantz, 1979; Yuan et al., 2004). Abnormalities in the number, structure, and function of mitochondria in GBM cells are well-recognized. Several groups have documented GBM cells with reduced or increased numbers of morphologically abnormal mitochondria with laminations and aberrant or absent cristae (Arismendi-Morillo and Castellano-Ramirez, 2008; Deighton et al., 2014; Feichtinger et al., 2014; Katsetos et al., 2013; Oudard et al., 1997; Scheithauer and Bruner, 1987; Seyfried et al., 2017; Sipe et al., 1973). Some mitochondria in human GBM cells contain few if any cristae (Arismendi-Morillo and Castellano-Ramirez, 2008). A multitude of findings support the notion that OxPhos is defective in GBM (Dahlberg et al., 2017) (Bartesaghi et al., 2015) (Feichtinger et al., 2014). Based on the concept that mitochondrial structure determines mitochondrial function (Lehninger, 1964), these multiple mitochondrial abnormalities, which are of genetic and/or environmental origin, would be expected to compromise effective energy production through OxPhos (Seyfried et al., 2015; Seyfried et al., 2014; Seyfried and Shelton, 2010). In view of the documented abnormalities in GBM mitochondria, alternative energy source(s) to OxPhos must be in place to maintain cell viability. Accumulating evidence indicates that glucose and glutamine are the primary fuels used for driving the rapid growth of most tumors, including GBM (Yang, C. et al., 2009) (DeBerardinis et al., 2007). Abundant levels of glucose and glutamine are also available in cyst fluid that is often present in GBM and could be used as fuel for the growing tumor cells (Dahlberg et al., 2017). Other potential metabolic fuels in the tumor microenvironment, e.g., acetate and branched chain amino acids, are either not present in sufficient quantities to drive growth through fermentation or exert non-metabolic effects that are yet to be understood (Seyfried et al., 2017) (Jaworski et al., 2016).. Glucose drives tumor growth through aerobic fermentation (Warburg effect), whereas glutamine drives tumor growth through glutaminolysis (DeBerardinis and Cheng, 2010; Flavahan et al., 2013; Rhodes et al., 1983; Yang et al., 2017). Metabolism of glucose and glutamine is also responsible for the high antioxidant capacity of the tumor cells thus making them resistant to chemo-and radiotherapies (Amores-Sanchez and Medina, 1999);(Seyfried et al., 2017; Xu et al., 2005). It remains unclear, however, whether glutamine is used primarily as a substrate for citric acid cycle anaplerosis and lipid synthesis, or if it is also used as a major substrate for energy production through mitochondrial substrate level phosphorylation (mSLP). In (Chinopoulos and Seyfried, 2018) we reviewed and outlined a framework for how provision of high-energy phosphates through mSLP could compensate for the loss of energy production through both glycolysis and OxPhos in GBM. The information is derived form a broad range of experimental materials including human glioma tissue, validated preclinical models of GBM, and from cultured glioma cell lines.

Role of glucose and glycolysis in GBM energy metabolism and mSLP

Warburg originally proposed that cancer originated from an irreversible damage to cellular respiration that was followed by a gradual increase in fermentation, i.e. glucose metabolized through glycolysis, leading to excessive formation of lactate (Warburg, 1956). The increased fermentation, which was present even in saturating partial pressures of oxygen, was necessary to compensate for a loss of energy through OxPhos. Aerobic fermentation is also a metabolic hallmark of GBM (Kirsch et al., 1972) (Oudard et al., 1997) (Rhodes et al., 1983) (Roslin et al., 2003). Despite the evidence mentioned above showing that mitochondria are abnormal in GBM tumor tissue, some investigators have claimed that mitochondria and OxPhos are normal in GBM and other brain tumor types based mostly, but not exclusively, on *in vitro* studies of oxygen consumption rates in tumor cells (Yang et al., 2014) (Ward and

Thompson, 2012) (Maximchik et al., 2016) (Elstrom et al., 2004) (Marin-Valencia et al., 2012) (Janiszewska et al., 2012; Wise et al., 2008);(Zhou et al., 2011) (Pike et al., 2011). It is not clear how these findings can be reconciled in light of the abnormalities reported in the number, structure, and function of GBM mitochondria obtained from GBM tissue sections. Discrepancies between *in vivo* and *in vitro* studies related to mitochondrial structure and function were not discussed in most of these studies. Warburg also proposed that oxygen consumption could be similar in tumor cells and normal cells, but that ATP output from respiration would be less in the former than in the latter. Despite the widely held view that oxygen consumption in cultured cells is a biomarker for OxPhos activity, many studies have since established that oxygen consumption is not linked to OxPhos ATP output in various tumor cell lines (Pacini and Borziani, 2016) (Leznev et al., 2013) (Hall et al., 2013) (Ramanathan et al., 2005) (Arcos et al., 1969). It is not possible, however, to exclude a complete absence of OxPhos in tumor cells, as Hall et al showed that coupling was reduced by about 50% even in an "extreme-case" of V600EBRAF-induced OxPhos dysfunction in melanoma cells (Hall et al., 2013). It is important to emphasize, however, that a ~50% reduction in OxPhos would dissipate the protonmotive force and cause reversal of the F_o-F_1 ATP synthase (Chinopoulos C. 2011a, Chinopoulos C. 2011b). The F_o-F_1 ATP synthase generally operates in forward mode (i.e. generating ATP) only when mitochondria are sufficiently polarized. It would not be possible for the F_o-F_1 ATP synthase to generate ATP under a loss of ETC operation on the order of 45-50%, and would actually hydrolyze ATP, pumping protons out of the matrix. Reversal of the ATP synthase is what affords mitochondrial substrate level phosphorylation the critical role of providing ATP directly within the matrix when OxPhos becomes inhibited or impaired. Furthermore, the possibility of an inverse relationship between OxPhos efficiency and tumor aggression has been reported (Solaini et al., 2011). It is also documented that estimates of mitochondrial OxPhos efficiency can differ between *in vivo* and *in vitro* environments (Suarez et al., 1991) (Kiebish et al., 2009). Viewed collectively, these studies indicate that oxygen consumption alone cannot be used as a measure of normal respiration in cultured cells including GBM cells. Another misconception comes from findings that aerobic glycolysis is required not only for GBM cell proliferation, but also for proliferation of non-transformed cells grown *in vitro*, thus giving the impression that aerobic glycolysis is a normal phenomenon of cell proliferation (Vander Heiden et al., 2009). This phenomenon does not, however, occur in proliferating non-transformed cells grown *in vivo*, e.g., regenerating liver cells and normal colon cells, which use fatty acids and butyrate as fuel, respectively (Hague et al., 1997; Thevananther, 2010; Warburg, 1956). While it is well recognized that biochemical pathways are reprogramed in GBM and in other cancers (Vander Heiden et al., 2009; Ward and Thompson, 2012), it remains unclear how GBM cells would generate sufficient energy with the documented abnormalities in their mitochondria. A re-analysis of how tumor cells obtain energy and metabolites for growth can help elucidate the origin of energy synthesis in GBM. The rate of glycolysis is increased in GBM, which is necessary for supporting growth under hypoxic conditions that commonly occur in the interior of the tumor mass (Roslin et al., 2003), shuttling glycolytic intermediates for building blocks of new cells. The up-regulation of this pathway is due in part to hypoxia-induced stabilization of HIF-1α, which amplifies the transcription of genes encoding glucose transporters and glycolytic enzymes (Semenza, 2010). Oncogenic signaling pathways, including PI3K, can activate HIF-1α under normoxic conditions (Plas and Thompson, 2005). Mutations in tumor suppressor proteins such as the von Hippel-Lindau tumor suppressor gene product (VHL) (Kaelin, 2008), succinate dehydrogenase (SDH) (Selak et al., 2005) and fumarate hydratase (FH) can also activate HIF-1α (King et al., 2006). Due to the cellular heterogeneity of GBM, it is likely that individual cells harbor one or more of these mutations (Soeda et al., 2015). It should also be recognized that the up-regulation of oncogenes in GBM and most other cancers is necessary to facilitate substrate level phosphorylation when OxPhos becomes unable to maintain the differentiated state (Seyfried et al., 2014). Relevant to this, dysregulated tumor cell growth and oncogene expression are often abolished when the cancer nucleus is placed in a cytoplasm containing normal mitochondria or when normal mitochondria replace tumor

mitochondria in the cytoplasm (Kaipparettu et al., 2013; Seyfried, 2015) (Seyfried, 2012a) (Seyfried, 2012b). These findings indicate that normal mitochondrial functions can down-regulate oncogenic signaling pathways restoring normal metabolic programing regardless of the genetic abnormalities present in the tumor cells. Indeed, recent findings of cancer driver mutations in normal cells seriously challenge the role of somatic mutations in the origin of cancer (Martincorena et al., 2018). The enhanced use of glucose is thought to provide essential intermediates for tumor cell growth and proliferation by diverting metabolites into the pentose phosphate pathway (PPP) (Icard and Lincet, 2012), as well as providing intermediates for lipid synthesis, the hexosamine pathway, and the synthesis of uridine diphosphate (UDP)-glucose (Vander Heiden et al., 2009). More recently, it was shown that breast cancer cells could maintain rapid growth and proliferation by diverting 3-phosphoglycerate from glycolysis to generate serine and glycine through phosphoglycerate dehydrogenase (PHGDH) (Possemato et al., 2011). Interestingly, suppression of PHGDH expression decreased cell proliferation, but did not affect intracellular serine levels. On the other hand, reduced PHGDH expression was associated with reduced levels of α-ketoglutarate (Possemato et al., 2011), the main precursor for mSLP. This mechanism also appears to operate in GBM (Liu et al., 2013). It should also be recognized that blood glucose levels are directly correlated with GBM growth, i.e., the higher the blood glucose, the faster the growth and less the survival, while the lower the blood glucose, the slower the growth and the greater the survival (Seyfried et al., 2003) (McGirt et al., 2008) (Derr et al., 2009) (Mayer et al., 2014) (Tieu et al., 2015). In tumor cells, glycolytic intermediates escape 'leak-down' towards pyruvate formation and subsequent entry into the mitochondria, being shunted towards subsidiary pathways by the preferential expression of the dimeric M2 isoform of pyruvate kinase (PKM2). Pyruvate kinase (PK) catalyzes the rate-limiting, ATP-generating 'pay-off' step of glycolysis in which phosphoenolpyruvate (PEP) is converted to pyruvate (Mazurek et al., 2005). Multiple isoenzymes of PK exist in mammals. The type L is found in liver and kidneys, the type R in erythrocytes, type M1 in muscle and brain, and type M2 in embryonic and adult stem cells (Mazurek et al., 2005). GBM cells appear to switch from the PKM1 to PKM2 isoform (Desai et al., 2014). Unlike PKM1, which promotes glycolysis and rapid energy generation, PKM2 may attain a dimeric form that exhibits low affinity to its substrate PEP rendering it inactive at physiological PEP concentrations (Christofk et al., 2008). The high GBM cellular heterogeneity makes it difficult to deduce with certainty, which cells exhibit the dimeric vs tetrameric PKM2 form (Desai et al., 2014) (Marin-Valencia et al., 2012) (Soeda et al., 2015). Preferential expression of PKM2 over PKM1 is mediated by modulating exon splicing, promoted by the oncoprotein MYC (David et al., 2010). HIF-1α also induces transcription of PKM2, but not PKM1, and PKM2 serves as a co-transcriptional activator of HIF-1α, mediated by the proline hydroxylase PHD3 (Luo et al., 2011). A major paradox regarding PKM2 is that cells expressing it produce more glucose-derived pyruvate than PKM1-expressing cells, despite the diminished activity of the M2 isoenzyme compared to M1. However, there are many ways for forming pyruvate bypassing pyruvate kinase, reviewed in (Chinopoulos, 2020b). The fate of pyruvate in GBM is mostly conversion to lactate, by lactate dehydrogenase (LDH), rather than entry into mitochondria. LDH is a tetramer composed of two different subunits, LDHA and LDHB, which can assemble into five different combinations (Markert et al., 1975). Augmented expression of MYC-mediated LDHA is a hallmark of many tumors, the majority of which are highly glycolytic and are associated with a poor prognosis (Dang et al., 2008; Koukourakis et al., 2009). LDHA is the predominant isoform in GBM and most other malignant cancers (Li et al., 2016; Moreno-Sanchez et al., 2009). The association of LDHB with cancer is more complex (Doherty and Cleveland, 2013), and is not likely to play a major role in GBM growth. LDHA catabolizes pyruvate to lactate producing NAD^+, which is necessary to drive glycolysis by GAPDH (Li et al., 2016) (Dawson et al., 1964). The reaction catalyzed by the cytosolic malate dehydrogenase (MDH1) was also recently shown to contribute to NAD^+ provision (Gaude et al., 2018). Furthermore, lactate acidifies the tumor microenvironment (Fantin et al., 2006; Gillies et al., 2008), which enhances the activity of several pro-invasive factors (Gimenez-Roqueplo et al., 2008; Parks et al.,

2013). Recent studies show, however, that it is carbonic anhydrase, and not LDH, that is mostly responsible for tumor-induced acidification (Swietach et al., 2014). Nonetheless, lactate efflux provokes a local inflammatory response attracting macrophages that secrete cytokines and growth factors promoting tumor cell growth and metastasis (Estrella et al., 2013) (Seyfried, 2001). The importance of LDHA activity in acidifying the microenvironment and creating a local inflammatory response, together with the provision of NAD^+ for GAPDH regarding tumor survival, is reflected by the fact that LDHA inhibitors are becoming promising antitumor agents (Li et al., 2016) (Doherty and Cleveland, 2013) (Billiard et al., 2013). Relevant to this, downregulation of LDHA in gliomas with mutations in IDH appeared responsible for slow growth and better prognosis (Chesnelong et al., 2014). This was probably mediated by increased methylation of the LDHA promoter, because silencing of LDHA in brain tumor stem cells (BTSCs) exhibiting mutations in IDH was associated with slower growth (Chesnelong et al., 2014). Fantin et al and Li et al also found that silencing LDHA could reduce tumor progression (Li et al., 2016). Furthermore, Zhang et al showed that additional epigenetic reprogramming, including immune-related genes, are likely to be involved in the pathogenesis of gliomas exhibiting mutations in IDH (Zhang et al., 2016). IDH mutant glioma cells acquire resistance to natural killer (NK) cells through epigenetic silencing of NKG2D ligands.

Role of pyruvate dehydrogenase complex and pyruvate carboxylase in GBM and mSLP

Physiologically, pyruvate has three fates following entry into the mitochondria in normal cells, i) conversion to oxaloacetate by pyruvate carboxylase (PC), ii) conversion to acetyl CoA by the pyruvate dehydrogenase complex (PDHC), iii) transamination with glutamate to α-ketoglutarate and alanine by a mitochondrial alanine aminotransferase (ALT2). In GBM cells, however, both PDHC and PC are usually down regulated (Cheng et al., 2011b; Yuen et al., 2016). HIF-1α, MYC, and other tyrosine kinases activate pyruvate dehydrogenase kinases (PDKs), which phosphorylate and thus inactivate the mitochondrial pyruvate dehydrogenase complex (Papandreou et al., 2006). Pyruvate carboxylase activity is suppressed in several cancer cell types (Chang and Morris, 1973), including glioma cells (Portais et al. 1993). Accordingly, pyruvate carboxylase is induced only when tumors grow in a glutamine-independent manner (Cheng et al., 2011a). Inhibition of mitochondrial pyruvate catabolism is critical for tumor survival. Inhibition of PDK1 activates PDHC- with dichloroacetate (DCA), a drug used for the treatment of hereditary lactic acidosis. This then results in suppression of tumor growth *in vitro* and *in vivo* (Michelakis et al., 2008). In GBM, due to the high cellular heterogeneity, pyruvate metabolism through PDHC and PC exhibit cell-dependent variability (Marin-Valencia et al., 2012). However, the consensus is that PDHC, an NAD^+ and CoASH-requiring enzyme complex, and PC, an ATP-hydrolyzing enzyme, are down regulated in cancer mitochondria. From these considerations, it is evident that pyruvate metabolism by mitochondria is limited in GBM, and that the high glycolytic rate may not generate adequate amounts of ATP due to a hindered pay-off phase. Accordingly, the high glycolytic rate seen in GBM is needed more for rapid synthesis of growth metabolites than for ATP synthesis. Relevant to this, no alternative cytosolic pathways are known that could generate sufficient ATP to replace energy loss through glycolysis and OxPhos.

Role of citrate metabolism in GBM in relation to mSLP

Acetyl-CoA is required for the cytosolic synthesis of fatty acids, cholesterol, and isoprenoid synthesis (Wakil et al., 1957). Acetyl-CoA cannot be directly exported to the cytoplasm but instead must first condense with oxaloacetate to form citrate through citrate synthase. Citrate is then converted to either isocitrate by aconitase, or is exported to the cytosol where it is catabolized to acetyl-CoA and

oxaloacetate by ATP-citrate lyase (ACL), at the expense of a high-energy phosphate bond provided by ATP. Acetyl CoA is subsequently carboxylated to malonyl CoA also at the expense of a high-energy phosphate bond provided by ATP, initiating lipogenesis (Stryer, 1995). The importance of ACL is not only to catabolize citrate for the purpose of yielding acetyl CoA, the building block for lipid synthesis in the cytoplasm, but also to decrease the concentration of citrate, which is a major negative allosteric modulator of phosphofructokinase, a rate-limiting step of glycolysis (Stryer, 1995). Akt facilitates the appearance of acetyl CoA in the cytosol by phosphorylating and activating ACL (Berwick et al., 2002). Pharmacologic inhibition or silencing of ACL or acetyl-CoA carboxylase or fatty acid synthase decreases proliferation of cancer cells (Swinnen et al., 2006), and especially GBM (Lin et al., 2010) (Lee et al., 2012) (Poteet et al., 2013). It is important to mention however, that ACL is likely to have little importance in GBM, as GBM cells can acquire fatty acids from the microenvironment thus bypassing an essential need for fatty acid synthesis (Ta and Seyfried, 2015). However, many cancer cells exhibit a down regulation in the activity of PDHC, which results in diminished provision of acetyl CoA in the mitochondrial matrix. In aggregate, it can be deduced that in GBM mitochondria, up-regulations of ACL and acetyl CoA carboxylase demand an adequate pool of cytosolic ATP.

Role of Isocitrate dehydrogenase in GBM in relation to mSLP

Isocitrate dehydrogenase (IDH) exhibits three isoforms IDH1, IDH2, and IDH3. IDH1 and IDH2 are homodimeric enzymes found in the cytoplasm and mitochondria, respectively and produce NADPH. IDH1 and IDH2 are highly homologous but structurally and functionally distinct from the intra-mitochondrial IDH3, which produces NADH (Stryer, 1995). Many GBM cells exhibit reductive carboxylation of α-ketoglutarate to isocitrate by reversal of IDH and further isomerisation to citrate by aconitase, a pathway that was described in the early metabolic literature, (Ochoa, 1948), and has been investigated as a way to produce citrate for the purpose of lipogenesis from α-ketoglutarate derived from glutamine (Wise et al., 2011). Furthermore, specific mutations in IDH1 and IDH2 are linked to tumorigenesis, in particular, GBM and acute myeloid leukemia (AML) (Yan et al., 2009), but not other tumors (Bleeker et al., 2009). It was shown that these mutations confer to IDH1 and IDH2 the ability to convert α-ketoglutarate to 2-hydroxyglutarate (2-HG) in a NADPH-dependent manner (Dang et al., 2009) (Ohka et al., 2014). Conversion of α-ketoglutarate to 2-HG could lower ATP production, as α-ketoglutarate would be needed as a substrate for mitochondrial substrate level phosphorylation (mSLP) (see below). As also discussed above, reduced α-ketoglutarate levels and LDHA silencing could explain in part the more favorable prognosis for those GBM patients harboring IDH mutations (Chesnelong et al., 2014).

Role of glutamine metabolism in GBM in relation to mSLP

Substantial evidence exists documenting an important role for glutaminolysis and glutamine in cancer and specifically in GBM (DeBerardinis and Cheng, 2010; Medina, 2001; Newsholme and Board, 1991; Yuneva, 2008) (Oizel et al., 2017) (Liu et al., 2017) (Maus and Peters, 2017) (Lemberg et al., 2018; Zhang et al., 2014). It has also been reported that glutaminases may be excellent targets for pheochromocytomas/paragangliomas (Sarkadi et al., 2020). Since the 1950s, it was recognized that tumors require large amounts of glutamine for growth and survival (hence the inclusion of glutamine in most culture media). The high-affinity glutamine transporter Slc1a5 (ASCT2) is upregulated in multiple types of cancer including GBM and has been implicated in mediating net glutamine uptake (Sidoryk et al., 2004) (Fuchs and Bode, 2005). Even in the early studies, it was deduced that the high rate of glutamine consumption could not be fully accounted by protein synthesis because it exceeded the need

for essential amino acids by an order of magnitude (Eagle et al., 1956). Several decades later, it was recognized that glutamine is a major energy source in tumor cells including GBM (Rossignol et al., 2004) (Reitzer et al., 1979). The inter-conversion of glutamine and glutamate is bidirectional in normal cells, with glutamine synthetase catalyzing glutamine formation. In tumors, however, overexpression of glutaminases and/or suppression of glutamine synthetase favor the forward reaction toward glutamate (Perez-Gomez et al., 2005). Glutaminase activity correlates well with tumor growth rates in vivo (Knox et al., 1969), especially for GBM (Shelton et al., 2010b) (Panosyan et al., 2016). Glutaminase activity is critically important for GBM, as glutaminase and glutamate levels are elevated following treatment with mTOR kinase inhibitor (Perez-Gomez et al., 2005). Glutamine-derived glutamate also facilitates GBM invasion (Takano et al., 2001). We also proposed that the most invasive cells of GBM are derived from neoplastic microglia/macrophages, which depend heavily on glutamine for growth (Huysentruyt et al., 2011). Moreover, a decrease in glutaminase activity diminishes growth rates of many tumor cells including the metastatic VM-M3 GBM model (Shelton et al., 2010b). Implantation of tumor tissue triggers a rapid increase in muscle glutamine output and a drop in muscle glutamine stores in rodents (Parry-Billings et al., 1991). A similar burden has been suggested to occur in human tumors (Souba, 1993). The consistency of high glutamine uptake in many tumors led to the development of glutamine PET tracers showing promise for the imaging of glutaminolysis (Wang et al., 2010) (Qu et al., 2012). Although glutamine, like glucose, is a major energy metabolite for GBM, the mechanism by which glutamine generates energy remains unclear especially in tumor cells with abnormalities in the number, structure and function of their mitochondria. Some have suggested that GBM cells predominantly oxidize acetate rather than glutamine for growth (Marin-Valencia et al., 2012; Mashimo et al., 2014). As both acetate and glutamine pass through the common KGDHC ->SUCL->SDH pathway, it remains to be resolved how acetate, but not-glutamine, is catabolized to citric acid cycle intermediates. Relevant to this, acetate has been implicated as an epigenetic regulator of posttranslational protein modification, and might actually have therapeutic potential in cancer management (Jaworski et al., 2016). Thus, the role of acetate in GBM metabolism remains unclear. The fate of glutamine in normal and tumor cells varies widely. An active synthesis of nitrogen-containing compounds, specifically nucleotides and non-essential amino acids (NEAAs), is required for tumor growth. Glutamine is the obligate nitrogen donor in at least three independent steps for purine synthesis including phosphoribosylpyrophosphate amidotranferase, phosphoribosylformylglycinamidine synthetase, and GMP synthetase. Glutamine is also important in two independent enzymatic steps for pyrimidine synthesis, carbamoyl phosphate synthetase II and CTP synthetase (Ahluwalia et al., 1990); (Young and Ajami, 2001). Glutamine-derived glutamate is the primary nitrogen donor for the synthesis of NEAAs including asparagine (Ahluwalia et al., 1990). This is interesting because asparagine is considered a growth metabolite for GBM and other tumors (Knott et al., 2018; Panosyan et al., 2017). The glutamine:fructose-6-phosphate amidotransferase reaction transfers the amide nitrogen of glutamine to form glucosamine-6-phosphate, a precursor for N-linked and O-linked glycosylation needed for hexosamine synthesis (DeBerardinis and Cheng, 2010). Although some have considered that glutamine can be metabolized to lactate through the malic enzyme to produce NADPH for lipid biosynthesis (Qu et al., 2012), other findings indicate that little glutamine is metabolized to lactate in GBM and other cells (Ta and Seyfried, 2015). In addition to the above reactions, glutamine also participates in the synthesis of glutathione through glutathione cysteine ligase, thus playing a major role in the maintenance of cellular redox homeostasis (Le et al., 2012); (Amores-Sanchez and Medina, 1999). Glutathione (GSH) is comprised of glutamate, cysteine, and glycine. Glutamate contributes to the uptake of cystine (Sato et al., 1999). Cystine can then be converted to cysteine inside the cell and used in GSH synthesis (Stryer, 1995). In addition, glutamine induces synthesis of manganese superoxide dismutase (MnSOD) (Aiken et al., 2008), another powerful antioxidant system in mitochondria of GBM (Ria et al., 2001; Shwetha et al., 2016). Hence, glucose and glutamine metabolism can protect GBM from oxidative stress thus making GBM resistant to radio- and

chemotherapy (Seyfried et al., 2017). It is our view that glutamine not only provides nitrogen for synthesis of nucleotides and NEAAs, but also provides α-ketoglutarate to serve as a precursor for ATP synthesis through substrate level phosphorylation in the citric acid cycle. The availability of α-ketoglutarate may occur either through the glutamate dehydrogenase (GLUD1) reaction or through the transamination reaction (DeBerardinis and Cheng, 2010). Indeed, cells from GBM and other cancers rely on either GLUD1-mediated glutamate deamination (Sato et al., 1999), or transamination (Weinberg et al., 2010), thus providing α-ketoglutarate to the cycle. In at least one study, glutamate derived by transamination was suggested to be the major route (Moreadith and Lehninger, 1984). Furthermore, selective inhibition of glutamate transamination with aminooxyacetic acid hindered tumor growth in the absence of nonspecific toxicity of complete inhibition of glutamine metabolism involving GLUD1 (Wise et al., 2008). Oncogenic signals originating from Myc and perhaps also Ras induce all of the above pathways involved in glutamine entry and ensuing glutaminolysis in tumor cells (DeBerardinis et al., 2007) (Weinberg et al., 2010). Overall, it can be concluded that the mitochondria in GBM cells strongly depend on glutamine as a source of α-ketoglutarate that can be used for energy production through mSLP.

Role of the α-ketoglutarate dehydrogenase complex in GBM in relation to mSLP

The α-ketoglutarate dehydrogenase complex (KGDHC) consists of multiple copies of three subunits: α-ketoglutarate dehydrogenase (OGDH), dihydrolipoyl succinyltransferase (DLST), and dihydrolipoyl dehydrogenase (DLD). It catalyzes the conversion of α-ketoglutarate, CoASH and NAD+ to succinyl-CoA, NADH and CO_2. The PDHC and the KGDHC compete for the same pool of CoASH and NAD+ (Kiselevsky et al., 1990). Even a small decrease in KGDHC activity will lead to a considerable decrease in substrate-level phosphorylation in the mitochondrial matrix (Chinopoulos et al., 2010) (Kiss et al., 2013) (Kiss et al., 2014). Hence, the diversion of α-ketoglutarate to 2-hydroxyglutarate could explain in part the improved overall survival of GBM patients containing the IDH mutations, as this diversion would reduce ATP synthesis through mSLP thus reducing tumor growth. Apart from tumor metabolism under ischemia and/or hypoxia there is mounting evidence of pronounced conversion of α-ketoglutarate to succinate (Hochachka et al., 1975), implying that KGDHC remains operational (Chinopoulos, 2013). However, during anoxia, when the ability of Complex I to oxidize NADH to NAD^+ is impaired, the question arises as to the origin of NAD^+ for the KGDHC reaction. Under these conditions we reported that mitochondrial diaphorases oxidize matrix NADH supplying NAD^+ to KGDHC (Kiss et al., 2014) (Ravasz et al., 2018). Additional means for NAD^+ provision in the matrix during anoxia are reviewed by the applicant in (Chinopoulos, 2020a) and are currently under investigation. Furthermore, we showed that Complex III of the respiratory chain mediated re-oxidation of the reducible substrates for the diaphorases using endogenous quinones (Kiss et al., 2014). Regarding KGDHC and cancer, it can be deduced that in hypoxia/anoxia, when the rate of NADH oxidation by complex I is reduced, mitochondrial diaphorases use endogenous quinones to regenerate NAD^+ for the KGDHC reaction. This raises the possibility that downstream provision of succinyl CoA by KGDHC maintains substrate-level phosphorylation yielding ATP or GTP in the mitochondrial matrix. We propose that mSLP provides the majority of energy needed to drive GBM growth.

Role of succinate dehydrogenase in relation to mSLP

Succinate dehydrogenase (SDH), also known as respiratory Complex II, is an integral mitochondrial inner membrane protein complex that oxidizes succinate to fumarate and transfers two electrons to

coenzyme Q (CoQ). SDH is composed of four subunits: SDHA, SDHB, SDHC and SDHD. The assembly of SDH requires two factors, SDH assembly factor 1 (SDHAF1) and SDHAF2 (Bardella et al., 2011). Mutations in some of its subunits or its assembly factors was shown to cause paragangliomas and pheochromocytomas (Bardella et al., 2011). In these tumors, the resulting inhibition of SDH increases mitochondrial and cytosolic succinate levels, inhibiting α-ketoglutarate dependent prolyl hydroxylases (PHDs), thus causing stabilization of HIF-1α (Kurelac et al., 2011). HIF-1α mediates much of the genetic alterations of enzyme and transporter expressions mentioned above. In this sense, succinate has been considered a pro-inflammatory 'oncometabolite' (Selak et al., 2005) (Tannahill et al., 2013) (Tretter et al., 2016). Succinate and fumarate also inhibit other α-ketoglutarate-dependent dioxygenases, including the Jumonji-C histone demethylases (JHDMs) and the TET family of 5-methylcytosine hydroxylases, resulting in genome-wide alterations of histone and DNA methylation and epigenetic dysregulation (Xiao et al., 2012). In other words, extranuclear mitochondrial abnormalities would underlie these nuclear epigenetic changes. Although SDH mutations have not been reported in GBM, an increase in mRNA coding for SDH subunits has been shown in human GBM cells (Kim et al., 2015). This is most relevant regarding mSLP, because the accumulation of succinate, as it may occur by high flux through SUCL will on one hand mediate HIF-1α stabilization and inhibition of JHDMs and TET 5-methylcytosine hydroxylases aggravating epigenetic dysregulation, but on the other hand it may push the reversible SUCL reaction towards ATP (or GTP) consumption. Relevant to this, succinate accumulation also occurs in ischemia and in all likelihood it originates from mSLP (Chinopoulos, 2019). It is also interesting that the interaction of SIRT5 (a lysine desuccinylase) with cardiolipin can influence SDH activity and the efficiency of the electron transport chain (Zhang, Y. et al., 2017a). The cardiolipin abnormalities we found in murine GBM might therefore influence SIRT5 function leading to enhancement of glutaminolysis and mSLP (Kiebish et al., 2008; Wang et al., 2018).

Role of fumarate hydratase in relation to mSLP

Fumarate hydratase (FH) converts fumarate to malate in a reversible manner. Homozygous null mutations in the FH gene are associated with multiple cutaneous and uterine leiomyomatas and aggressive forms of renal cell cancer (Alam et al., 2003). Although fumarate has also been hypothesized to inhibit PHDs, stabilization of HIF-1α was not required for tumorigenesis in $FH^{-/-}$ mice (Adam et al., 2011). Fumarate is an electrophilic unsaturated dicarboxylic acid, and as such it has the ability to bind reactive thiol residues of proteins in a process termed protein succination (Alderson et al., 2006). *Succination* must not to be confused with *succinylation*, the latter being a posttranslational modification of lysine residues using succinyl-CoA (Weinert et al., 2013). Several targets of fumarate have now been identified, and they include the negative regulator of NRF2, Keap1 (Ooi et al., 2011), aconitase (Ternette et al., 2013), and glutathione (Sullivan et al., 2013). As such, fumarate has also achieved the status of an 'oncometabolite' (Yang et al., 2012). To the best of my knowledge, FH and its role in GBM have not yet been addressed. However, it is anticipated that accumulation of fumarate, as it may occur by high flux through SUCL performing substrate-level phosphorylation followed by the action SDH will mediate excessive succinations, potentially contributing to tumor progression through increased glutaminolysis (Wang et al., 2018).

Role of Adenine Nucleotide Translocase (ANT) and F_0-F_1 ATP synthase in GBM in relation to mSLP

As it has been extensively addressed in our laboratory, substrate-level phosphorylation substantiated by succinyl CoA ligase generating ATP, assists respiration-impaired mitochondria exhibiting diminished

values of $\Delta\Psi m$ to retain high matrix ATP levels, sparing cells from cytosolic/nuclear ATP consumption (Chinopoulos, 2011b); (Chinopoulos, 2011a). This concept is inherently related to tumor metabolism generally, and to GBM metabolism specifically, as the likelihood is high that GBM mitochondria exhibit diminished values of $\Delta\Psi m$ due to cristolysis and respiratory inhibition. Pinpointing the component(s) of the respiratory chain exhibiting defects leading to a decrease in respiratory capacity is a daunting task. This task is further complicated by the fact that the exact site of the defect in the respiratory chain will dictate whether a cell can be rescued by provision of substrates supporting mSLP (Chinopoulos, 2018). In any case, respiratory arrest and ensuing decrease in $\Delta\Psi m$ would result in consumption of matrix ATP by the reverse-operating F_0-F_1 ATP synthase. The generation of matrix ATP by succinyl CoA ligase is instrumental in rescuing cancer cells from cytosolic ATP consumption. On the same line of thought, the ATPase inhibitory factor 1 (IF1) exhibits stark changes in expression among various types of human carcinomas (Sanchez-Arago et al., 2013), and has been linked to energy metabolism reprogramming, signaling the oncogenic phenotypes of cancer (Formentini et al., 2012). The critical information that can be obtained from this consideration is that substrate-level phosphorylation substantiated by succinyl CoA ligase generating ATP in the matrix, assists respiration-impaired mitochondria that exhibit diminished values of $\Delta\Psi m$ in avoiding cytosolic ATP consumption, thus sparing cells from cytosolic/nuclear ATP depletion. This concept is inherently related to tumor metabolism because cancer mitochondria frequently exhibit diminished values of $\Delta\Psi m$, a concept associated with the reverse-operation of the F_0-F_1 ATP synthase and the consumption of matrix ATP. From the considerations outlined above, we have arrived to the following conclusions regarding GBM metabolism: 1. The net balance of cytosolic ATP production is low despite having a high rate of glycolysis due to diminished production by the pay-off phase substantiated by the reaction catalyzed by PKM2. 2. ATP is needed in the cytosol not only for maintenance of membrane ion pumps, but also for ATP-consuming reactions of fatty acid synthesis. 3. The mitochondrial F_0-F_1 ATP synthase becomes an ATP consumer in pumping protons out of the matrix due to defects in the electron transport chain (ETC). Consequently, little ATP is generated from either glycolysis or OxPhos, which increases the danger of mitochondria becoming net ATP consumers. 4. The branch of the citric acid cycle towards citrate formation becomes diminished due to lack of intramitochondrial catabolism of pyruvate. On the other hand, the rate of glutamine catabolism towards the citric acid cycle becomes high. 5. The obligate metabolites formed by this pathway are α-ketoglutarate, succinyl-CoA, and succinate. 6. This metabolite trio implies that formation of ATP (or GTP) through succinate-CoA ligase-mediated substrate-level phosphorylation is high. Maintenance of a high matrix ATP/ADP ratio also assures that the adenine nucleotide translocase provides ATP to the cytosol while also preventing the F_0-F_1 ATP synthase from draining cytosolic ATP reserves. The concomitant formation of succinate is efficiently shuttled outside the mitochondria but can also be metabolized to fumarate and malate, the latter supporting exchange of other metabolites across the inner mitochondrial membrane.

Convergence of metabolites towards succinyl-CoA and mSLP

There are a number of metabolites that catabolize towards the citric acid cycle through succinyl-CoA, thus leading to ATP (or GTP) formation through succinate-CoA ligase including the amino acids valine, isoleucine, methionine, histidine, threonine, glutamine, glutamate, and also propionate (Todesco et al., 1991) (Laurent et al., 1995) (Wong et al., 2006) (Snyder et al., 2015) and thymine (Stryer, 1995), and odd-chain fatty acids (OC-FAs). Except for glutamate and glutamine, however, the catabolism of all other metabolites 'expend' one or more high-energy phosphates during metabolic inter-conversions before becoming succinyl-CoA. Support for mSLP can also come from conversion to glutamate (such as proline and arginine) or from other metabolites that catabolize towards α-ketoglutarate (such as glycine, serine,

sarcosine, dimethylglycine through pyruvate and fatty acids or leucine through Acetyl-CoA). However, the concentrations of these metabolites in the plasma or in the microenvironment are far lower than that of glutamine, and are therefore unlikely to make a major contribution to mSLP (Chinopoulos and Seyfried, 2018). In addition to the pathways converging towards succinyl-CoA, there are two more ways for producing high-energy phosphates at the substrate-level: First through the mitochondrial phosphoenolpyruvate carboxykinase (PEPCKm), inter-converting PEP and GDP to oxaloacetate and GTP (GTP, GDP, ADP and ADP can inter-convert through nucleoside diphosphate kinase isoforms, NMEs), and second, through the mono-functional C1-tetrahydrofolate synthase (MTHFD1L) inter-converting ADP, phosphate and 10- formyltetrahydrofolate to ATP, formate and tetrahydrofolate (THF). However, the PEPCKm reaction is strongly favored towards PEP formation (thus consuming GTP) in a process called pyruvate recycling pathway (Chinopoulos, 2013) (Freidmann et al., 1971) (Cohen, 1987) (Rognstad and Katz, 1972) (Cerdan et al., 1990) (Haberg et al., 1998; Kunnecke et al., 1993) (Bakken et al., 1997a) (Bakken et al., 1997b). For this pathway, PEP enters mitochondria through a phosphate/phosphoenolpyruvate antiporter (McCoy and Doeg, 1975), a protein with isoforms in members C, D and E of the solute carrier family 35 (Venter et al., 2001) (Gerhard et al., 2004) (Ota et al., 2004) (Skarnes et al., 2011). Finally, carboxylation of pyruvate by pyruvate carboxylase yielding oxaloacetate is a thermodynamically reversible reaction, however, backflow towards pyruvate leading to ATP production may occur only at a very low rate (Freidmann et al., 1971) (McClure et al., 1971a) (Barden et al., 1972; McClure et al., 1971b). Consumption of one ATP in the reaction catalyzed by pyruvate carboxylase is also the reason why metabolites that converge to pyruvate (glycine, serine, sarcosine and dimethylglycine) do not yield net ATP (or GTP) from mSLP. To date, the contribution of MTHFD1L on yielding ATP through substrate-level phosphorylation has not been adequately addressed.

Interactions between oxidative decarboxylation, provision of reducing equivalents, reductive carboxylation, and mSLP

From the above considerations it is evident that only catabolism of glutamine or glutamate may lead to net ATP (or GTP) production through mSLP; this is entirely consistent with the extremely high dependence of many tumors including GBM on glutamine. However, this prompts considering the following two concepts: i) reductive carboxylation of glutamine towards citrate which exits mitochondria and is destined for fatty acid synthesis has been well-documented to occur in cancers (Gaude et al., 2018), and especially in GBM (DeBerardinis et al., 2007) (Ta and Seyfried, 2015) and ii) oxidative decarboxylation of glutamine/glutamate towards mSLP substantiated by succinate-CoA ligase demands stable provision of NAD^+ for KGDHC. Reductive carboxylation vs oxidative decarboxylation of glutamine/glutamate will 'branch-out' at the level of α-ketoglutarate; in the former case it will become isocitrate by the $NADP^+$-dependent IDH2 and then citrate through reversal of aconitase; in the latter case α-ketoglutarate will become succinyl-CoA by KGDHC and thus follow mSLP. Although both pathways start from α-ketoglutarate, they are not mutually exclusive; flux of glutamine/glutamate towards α-ketoglutarate is sufficiently high to support both pathways (Pike Winer and Wu, 2014). Interestingly, it was recently shown that in cancer cell lines, the degree of OxPhos defects conferred by mtDNA mutations dictates whether α-ketoglutarate follows oxidative decarboxylation or reductive carboxylation (Chen et al., 2018) (Chinopoulos, 2018). On the other hand, regarding oxidative decarboxylation in the absence of OxPhos during which the ability of Complex I in providing NAD^+ is impaired, it has been shown that intra-mitochondrial diaphorases can contribute to the matrix NAD^+ pool (Kiss et al., 2014). This reaction was, however, demonstrated only in isolated mitochondria in artificial conditions. It is currently not known how mitochondria *in situ* regenerate NAD^+ in the absence of OxPhos; it is not even known if a residual, minimal remaining function of Complex I during

hypoxia/anoxia is sufficient for providing NAD^+ for KGDHC for supporting mSLP, in view of the fact that overall respiration has ceased. Apart from mitochondrial diaphorases, there are other pathways that can adopt this role; the malate-aspartate shuttle can operate in reverse (Bremer and Davis, 1975) (Chouchani et al., 2014) and lead to a decrease in the matrix NADH/NAD^+ ratio. For example, conditions that can led to excessive NADH oxidation in the cytosol may lead to increased formation of oxaloacetate in the same compartment that will in turn lead to transamination with glutamate to aspartate and α-ketoglutarate; this will cause the exchange of cytosolic α-ketoglutarate with mitochondrial malate, shifting the equilibrium of MDH2 towards NADH oxidation, thus yielding NAD^+ in the matrix. Furthermore, salvage reactions that can lead to NAD^+ formation could also play a role (Yang and Sauve, 2016). Moreover, there are other potential intra-mitochondrial reactions that can lead to a decrease in matrix NADH/NAD^+ ratio, such as those participating in THF metabolism (Yang and Vousden, 2016). The group of Vamsi Mootha has published a compendium of 342 reactions utilizing NAD(P)H, termed the NAD(P)ome (Goodman et al., 2018). Hence, there are likely several mechanisms by which cancer cells can obtain NAD^+ in low-oxygen, hyper-reducing conditions.

The Warburg theory revisited in light of mSLP

It is our view that SUCL can provision ATP (and/or GTP) thus 'bailing-in' cancer mitochondria from a reverse-operating F_0-F_1 ATP synthase when ETC function(s) are impaired, but can also assist glycolysis in providing high-energy phosphates for energy-consuming processes. Relevant to this, computer modeling of cancer metabolism predicted that a repression of SUCL would cause a significant reduction in growth rate, relative to known chemotherapeutic targets (Khazaei et al., 2012). It has also not escaped our attention that mSLP could represent the “missing link” in Warburg’s central theory that OxPhos insufficiency with compensatory fermentation is the origin of cancer. In addition to cytoplasmic substrate level phosphorylation, i.e., aerobic fermentation or the Warburg effect, mSLP could also compensate for insufficient or defective OxPhos.

Considerations for Controlling GBM Cell Growth in relation to mSLP

It is widely recognized that glucose and glutamine are the major energy metabolites that drive GBM growth and invasion. Glucose and glutamine become the major fermentable fuels for heterogeneous GBM cells due to the inability of OxPhos to meet energy demands, and for growth in hypoxic environments. Recent findings indicate that glutamine is the major fuel for GBM cells with mesenchymal molecular subtype, whereas glucose in the major fuel for GBM cells with proliferative subtype (Oizel et al., 2017). According to the considerations examined above, control of GBM cell growth could involve the simultaneous targeting of substrate level phosphorylation reactions in the cytoplasm (glycolysis) and in the mitochondria (glutaminolysis). A parsimonious consideration would be to restrict availability of glucose and glutamine to the tumor cells in order to down-regulate both glycolysis and glutaminolysis simultaneously. This approach was shown to kill GBM and HeLa cells *in vitro* (Mathews et al., 2014; Shelton, 2010), as would be predicted from ‘ensemble’ modeling of cancer metabolism (Khazaei et al., 2012). No cell can grow without energy regardless of its genetic composition. Since ketone bodies can replace glucose as an energy source, prior studies show that glucose levels could be significantly reduced without harmful effects after first transitioning the body to therapeutic ketosis (Drenick et al., 1972; Seyfried et al., 2015; Seyfried et al., 2017). This fact was mentioned in the work of Cahill and Veech and was demonstrated in nine persons that received insulin injection after fasting for two months (Drenick et al., 1972) (Cahill and Veech, 2003). Indeed, the blood glucose level in one person in the insulin group reached a as low as 9 mg/dl (0.5 mmoles/liter) without evidence of a hypoglycemic response (Drenick

et al., 1972). These findings suggest that the glucose needed for GBM cell growth could be majorly restricted under therapeutic ketosis. Ketone bodies also possess anti-inflammatory potential through reduction of reactive oxygen species and increase of glutathione peroxidase activity in normal brain cells (Veech, 2004) (Seyfried and Mukherjee, 2005). Some studies have shown that GBM and other malignant brain tumors may have a reduced ability to utilize ketone bodies due in part to diminished activity of succinyl-CoA:3-ketoacid coenzyme A transferase 1 (OXCT1), which is essential for metabolism of ketone bodies (Zhou et al., 2007) (Fredericks and Ramsey, 1978) (Maurer et al., 2011). Glucose restriction under therapeutic ketosis or calorie restriction will down-regulate the entire glycolytic pathway from glucose to pyruvate (Marsh et al., 2008). Glycolytic downregulation will not only deprive tumor cells of growth metabolites, but will also reduce LDHA activity and lactate production thus reducing angiogenesis and inflammation in the tumor microenvironment (Husain et al., 2013; Marsh et al., 2008; Mukherjee, P. et al., 2004; Mukherjee et al., 2002; Mulrooney et al., 2011; Urits et al., 2012; Vergati et al., 2017). Glucose restriction should also reduce the metabolites needed for serine-derived one-carbon metabolism, which would further reduce tumor cell anti-oxidant capacity and growth (Meiser and Vazquez, 2016; Semenza, 2017; Zhang, K. et al., 2017). It has been reported that calorie restriction and restricted ketogenic diets, which lower blood glucose and elevate blood ketone bodies are pro-apoptotic against murine glioblastoma, neural stem cell tumors (Mukherjee et al., 2002), (Mukherjee, P. et al., 2004), (Shelton et al., 2010a), (Mukherjee et al., 2019) potentially also beneficial to patients with breast cancers (Seyfried et al., 2020b). Glucose targeting would also reduce metabolites generated through the pentose phosphate pathway that would be needed for the synthesis of glutathione and growth metabolites. From the biochemical point of view, catabolism of ketone bodies obligatorily bypasses mSLP. The ketone bodies acetoacetate and β-hydroxybutyrate enter mitochondria and eventually the citric acid cycle as succinate, bypassing mSLP. This is because formation of succinate is not through SUCL, but through succinyl-CoA:3-ketoacid coenzyme A transferase 1 (OXCT1). By doing so, catabolism of both acetoacetate and β-hydroxybutyrate do not lead to the formation of high-energy phosphates through mSLP. Furthermore, β-hydroxybutyrate is expected to decrease mSLP through glutamine/glutamate even further because it increases NADH/NAD^+ ratio, thus hindering KGDHC operation (Kiss et al., 2013) (Kiss et al., 2014). It is also essential to target glucose and glutamine together, as glutamine can be synthesized from glucose-derived glutamate through the glutamine synthetase activity (Tardito et al., 2015). Hence, the simultaneous restriction of glucose and glutamine, while under therapeutic ketosis, could halt growth of GBM cells that are more dependent on substrate level phosphorylation than on OxPhos for survival.

KGDHC on mSLP

KGDHC is at a cross-road of biochemical pathways and as such, impacts greatly on the overall cell metabolism. It is therefore not surprising that diminished KGDHC activity of transgenic mice results in alterations of glucose utilization, a hallmark of metabolic abnormality, albeit depending on the model (Shi et al., 2009), (Nilsen et al., 2011). Yet, extensive work on transgenic mice for two of the three subunits of KGDHC failed to pinpoint the exact mechanism(s) responsible. In view of this gap of information, the most important aim of our study published in (Kiss et al., 2013) was to address the impact of a decreased KGDHC activity on matrix substrate-level phosphorylation in isolated and *in situ* mitochondria with diminished $\Delta\Psi m$ values achieved by respiratory inhibition. The rationale of this aim is many-fold: i) it is a textbook definition that provision of succinyl-CoA through KGDHC is much higher than that originating from propionyl-CoA metabolism; ii) matrix substrate-level phosphorylation provides ATP in the matrix parallel to that by oxidative phosphorylation (Johnson et al., 1998), (Lambeth et al., 2004), (Nicholls and Bernson, 1977); iii) succinyl-CoA ligase does not require oxygen to produce

ATP, and it is even activated during hypoxia (Phillips et al., 2009); iv) in ischemia and/or hypoxia, there is mounting evidence of pronounced conversion of α-ketoglutarate to succinate, implying that KGDHC is operational (Chinopoulos, 2013), (Pisarenko et al., 1988), (Taegtmeyer, 1978), (Weinberg et al., 2000b), (Weinberg et al., 2000a); v) brains from patients with autopsy-confirmed Alzheimer's disease exhibited significant decreases in the activities of the enzymes in the first part of the citric acid cycle (pyruvate dehydrogenase complex, - 41%), isocitrate dehydrogenase, - 27%), and KGDHC, - 57%), while

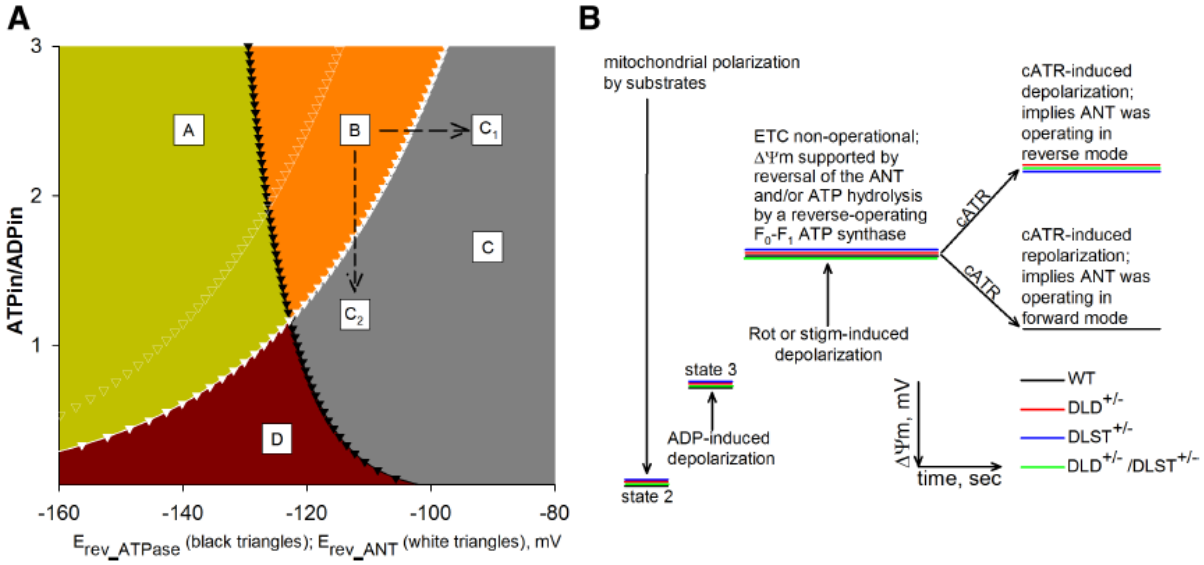

*Figure 7.1. **A**: Computational estimation of Erev_ANT and Erev_ATPase. A: ATPase forward, ANT forward; B: ATP reverse, ANT forward; C, C_1, C_2: ATPase reverse, ANT reverse; D: ATPase forward, ANT reverse. Black solid triangles represent Erev_ATPase; white solid triangles represent Erev_ANT. Values were computed for [ATP]out = 1.2 mM, [ADP]out = 10 µM, Pin = 0.01 M, n = 3.7 (2.7 plus 1 for the electrogenic ATP^{4-}/ADP^{3-} exchange of the ANT), pHi = 7.38, and pHo = 7.25. White open triangles represent Erev_ANT values computed for [ATP]out = 1.4 mM, and all other parameters as above. Traces have been computed by Erev estimator. **B**: Cartoon graph of all safranine O-related measurement from all kinds of mitochondria and conditions, shown in figure 7.2.*

enzyme activities of the second half of the cycle were increased: succinate dehydrogenase, + 44% and malate dehydrogenase, + 54%) (Bubber et al., 2005), (Gibson et al., 2010). It is as though reactions after the succinyl-CoA ligase step were upregulated in order to remove succinate and shift the equilibrium towards ATP formation, given the diminished succinyl-CoA provision; vi) ΔΨm values in neurons are far from being static; in physiological conditions ΔΨm is regulated between -108 mV and -158 mV by concerted increases in ATP demand and Ca^{2+}-dependent metabolic activation (Gerencser et al., 2012), a range that would assign mitochondrial phosphorylation within the "A", "B," or "C" space of figure 7.1A (no conditions have been described that are suitable for the "D" space (Chinopoulos, 2011a)); the implications of the latter statement is that even under physiological conditions, mitochondria are not only ATP producers, but could also be consumers of ATP arising from the cytosol and/or the matrix, depending on their ΔΨm and matrix ATP/ADP ratio pair of values.

Mindful of the above considerations and the results of the work shown in (Kiss et al., 2013), the scenario that could be unfolding in the presence of diminished KGDHC activity, is the following: (1) KGDHC exhibits a high flux control coefficient for producing reducing equivalents in the citric acid cycle also implying that provision of succinyl-CoA would be diminished when the enzyme complex is partially inhibited (especially because metabolism of propionyl-CoA yields only small amounts of succinyl-CoA); (2) in turn, this would lead to a decreased production of ATP in the mitochondrial matrix from substrate-

level phosphorylation. This was reflected in the smaller ATP efflux rates in isolated mitochondria from $DLD^{+/-}$, $DLST^{+/-}$ and $DLD^{+/-}/DLST^{+/-}$ double transgenic mice compared to WT littermates, in the absence of respiratory inhibitors. (3) The diminished production of ATP in the mitochondrial matrix from substrate-level phosphorylation results in a decrease in matrix ATP/ADP ratio, which is also a term in equation 3 defining Erev_ANT, thereby shifting its values to the left in the computed graph of figure 7.1A. (4) Since $\Delta\Psi m$ of mitochondria varies within a wide range even under physiological conditions, the likelihood of the organelles becoming extramitochondrial ATP consumers increases with shifting Erev_ANT values towards more negative potentials. Here we have demonstrated the consumption of extramitochondrial ATP by mitochondria of $DLD^{+/-}$, $DLST^{+/-}$ and $DLD^{+/-}/DLST^{+/-}$ double transgenic mice provided with substrates supporting substrate-level phosphorylation, by clamping $\Delta\Psi m$ in a depolarized range due to targeted respiratory inhibition; using the same substrates and their combinations, consumption of extramitochondrial ATP was not observed in isolated mitochondria of WT mice; likewise cytosolic ATP was consumed by *in situ* neuronal somal mitochondria of $DLD^{+/-}$ and $DLST^{+/-}$, but not WT mice. (5) In addition to the fact that KGDHC-deficient mitochondria exhibit diminished ATP output when fully polarized, excessive reliance of submaximally polarized mitochondria on extramitochondrial ATP poses an overall metabolic stress. This renders the cell less capable of dealing with unrelated circumstantial challenges predisposing to neurodegenerative diseases, as it is already shown to occur *in situ* (Chinopoulos et al., 1999), (Tretter and Adam-Vizi, 2000) or *in vivo* (Yang, L. et al., 2009), (Klivenyi et al., 2004), (Browne and Beal, 2002).

Mitochondrial diaphorases and mSLP

We have highlighted above the critical importance of matrix substrate-level phosphorylation in maintaining ANT operation in the forward mode (Chinopoulos et al., 2010) thereby preventing mitochondria from becoming cytosolic ATP consumers during respiratory arrest (Chinopoulos and Adam-Vizi, 2010a), (Chinopoulos, 2011b), (Chinopoulos, 2011a). Subsequently, we showed that succinyl-CoA provision by KGDHC prevented isolated or *in situ* mitochondria with a dysfunctional electron transport chain to be dependent on extramitochondrial ATP (Kiss et al., 2013). Relevant to this, mounting evidence support the pronounced conversion of α-ketoglutarate to succinate in ischemia and/or hypoxia, implying KGDHC operability (Chinopoulos, 2013). The question arises as to which metabolic pathway(s) could provide NAD^+ for KGDHC during respiratory arrest, when the electron transport chain is dysfunctional and complex I cannot oxidize NADH. Of course, a rotenone-mediated block in complex I can be by-passed by succinate or α-glycerophosphate (Estabrook and Sacktor, 1958), substrates that generate $FADH_2$; however, succinate disfavors substrate-level phosphorylation by the reversible succinyl-CoA ligase due to mass-action, while α-glycerophosphate 'steals' endogenous ubiquinones from the diaphorases. In (Kiss et al., 2014) we considered mitochondrial diaphorases and a finite pool of oxidizable quinones as potential sources of NAD^+ generated within the mitochondrial matrix during respiratory arrest caused by anoxia or poisons of electron transport chain, illustrated in figure 8.7.

The results presented above support the notion that a mitochondrial diaphorase, likely encoded by NQO1, mediated NAD^+ regeneration in the mitochondrial matrix during respiratory arrest by anoxia or inhibition of complex I by rotenone. Inexorably, the classical diaphorase inhibitor dicoumarol suffers from potential specificity problems acting as a mitochondrial uncoupler in addition to inhibiting other enzymes such as NADH:cytochrome b5 reductase. We have compared the cATR-induced effects on $\Delta\Psi m$ in mitochondria during respiratory arrest by rotenone or anoxia from wild-type versus cytochrome b5 reductase isoform 2 knock-out mice, and results were indistinguishable. Furthermore, we titrated

dicoumarol and other diaphorase inhibitors, and used them at concentrations at which their uncoupling activity was negligible. Finally, none of the diaphorase inhibitors nor any of the diaphorase substrates had an effect on pigeon liver mitochondria, where DT-diaphorase activity was absent. On the other hand, pigeon liver mitochondria did show robust cATR-induced repolarizations during respiratory arrest, pointing to alternative mechanisms for providing NAD^+ in the matrix. The absence of diaphorase activity in pigeon liver is not astounding; 1-4% of the human population exhibit a polymorphic version of NQO1 that deprives them of NAD(P)H: quinone oxidoreductase activity (Traver et al., 1997).

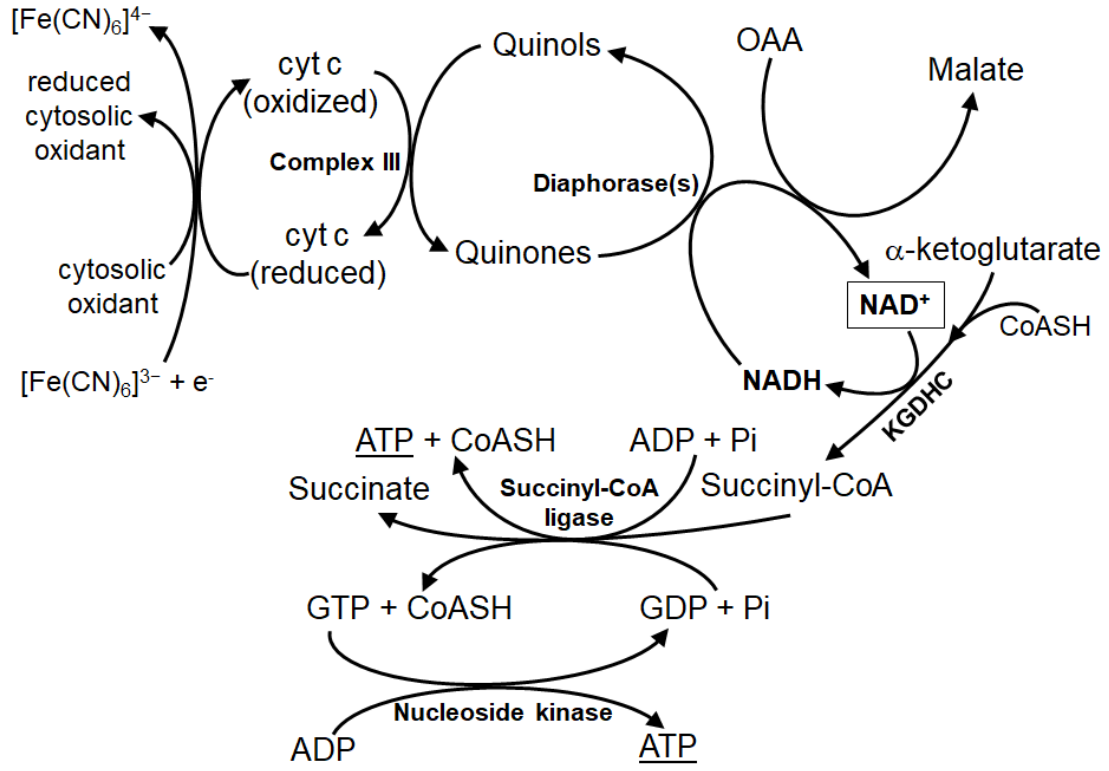

Figure 8.7. Illustration of the pathway linking ATP production by the succinyl-CoA ligase reaction to KGDHC activity, diaphorase activity, re-oxidation of diaphorase substrates by complex III, re-oxidation of cytochrome c, and re-reduction of a cytosolic oxidant.

It may well be possible that pigeons exhibit the same or similar polymorphic version of NQO in a much higher percentage of their population. We also sought for the pathway(s) responsible for providing oxidized substrates to the diaphorase(s). Although various coenzyme Q analogues are maintained in reduced form by the DT-diaphorase (Beyer et al., 1996), their availability is finite (Lenaz et al., 1985) and likely requires means of re-oxidation. Such a pathway has been demonstrated in the mitochondrial matrix; even within the earlier publications by Ernster *et al* it was noted that electrons provided by diaphorase substrates enter the electron transport chain at the level of cytochrome b (Conover and Ernster, 1962), which belongs to complex III. Later on, this concept has been entertained by the group of Iaguzhinskii, examining the stimulatory effect of various diaphorase substrates during cyanide-resistant respiration of isolated mitochondria (Kolesova et al., 1991), (Kolesova et al., 1993), (Kolesova et al., 1987), (Kolesova et al., 1989). Consistent with this, protection in an ischemia model by menadione was abolished by the complex III inhibitor myxothiazol (Yue et al., 2001). In the same line of work, the cytotoxicity caused by complex I inhibition by rotenone but not that caused by complex III inhibition by antimycin could be prevented by coenzyme Q_1 or menadione (Chan et al., 2002). Furthermore, also consistent with the substrate selectivity of NQOs in HepG2 cells where NQO1 expression is very high (Cresteil and Jaiswal, 1991), both idebenone and CoQ_1, but not CoQ_{10} partially restored cellular ATP

levels under conditions of impaired complex I function, in an antimycin-sensitive manner (Haefeli et al., 2011). Cytoprotection from rotenone but not antimycin by CoQ_1, mediated by NQO1 has also been shown in primary hepatocytes (Chan et al., 2002) and lymphocytes (Dedukhova et al., 1986). Menadione had even been shown to support mitochondrial respiration with an inhibited complex I but not complex III before DT-diaphorase was discovered (Colpa-Boonstra and Slater, 1958). This was later confirmed to occur through oxidation of NADH by the intramitochondrial DT diaphorase (Conover and Ernster, 1962). Our results clearly show that the re-oxidization of substrate(s) being used by the diaphorases for generation of NAD^+ during respiratory arrest by rotenone or anoxia is mediated by complex III. In the process, complex III oxidizes cytochrome c (see figure 8.7). Therefore, the finiteness of the reducible amount of cytochrome c would contribute to the finiteness of the oxidizable pool of diaphorase substrates. Indeed, addition of ferricyanide led to cATR-induced repolarization in the presence of complex IV inhibition by cyanide, but not in the presence of complex III inhibition by stigmatellin. However, the question arises, as to what could oxidize cytochrome c naturally, when oxygen is not available. An attractive candidate is p66Shc, a protein residing in the intermembrane space of mitochondria known to oxidize cytochrome c (Giorgio et al., 2005).

In summary, our results point to the importance of mitochondrial diaphorase(s) in providing NAD^+ for KGDHC during anoxia yielding succinyl CoA, that in turn supports ATP production through substrate-level phosphorylation. Additionally, the realization of diaphorase(s) as NAD^+ providers renders them a likely target for cancer prevention, as they may be the means for energy-harnessing in solid tumors with anoxic/hypoxic centers. Finally, since diaphorases are upregulated by dietary nutrients such as sulforaphane (Chapple et al., 2012) through the Nrf2 pathway (Rushmore and Kong, 2002) and a gamut of dietary elements -mainly quinones of plant origin- are substrates for this enzyme (Gomez-Diaz et al., 2003), this may be a convenient way for increasing matrix NAD^+/NADH ratios which play a role in the activation of the mitochondrial NAD^+-dependent deacetylase sirtuin-3 (Sack and Finkel, 2012), a major metabolic sensor.

NQO1 and mSLP

The results presented in (Ravasz et al., 2018) can be visualized in the illustration shown in figure 9. As shown in figure 9, rotenone (thick red line) prevents the oxidation of NADH to NAD^+ and the reduction of ubiquinone (Q) to ubiquinol (QH_2) by complex I, implied by dashed grey arrows. The ability of complex II, electron-transferring-flavoprotein dehydrogenase (ETFDH), glycerol-3-phosphate dehydrogenase (GPDH) and dihydroorotate dehydrogenase (DHODH) reducing Q to QH_2 remain intact. Likewise, complex III can still support oxidation of QH_2 to Q. Complexes III and IV are able to pump protons outside the matrix, but the extent of their proton pumping capacity under these conditions is minimal. This is probably because the flux of electron flow in this ETC segment is weak due to a diminished provision of ubiquinol to complex III as mitochondrial diaphorase activity is too small to produce adequate amounts of QH_2. This interpretation is supported by the findings that addition of quinones to rotenone-treated mitochondria led to a very small gain in respiration rates and $\Delta\Psi m$. Provision of ubiquinol (QH_2) to complex III may occur by complex II and/or ETFDH and/or DHODH and/or GPDH and/or Nqo1 and/or other mitochondrial diaphorases. It is not known if provision of more water-soluble quinols (QH_2') could occur through ETFDH and/or DHODH and/or GPDH. If through Nqo1, then there is concomitant oxidation of NADH to NAD^+. If other diaphorases provided QH_2', these could either use NADH or some other electron donor (e^-D). In any case, QH_2 and QH_2' can be re-oxidized to Q and Q' respectively, by complex III (Kolesova et al., 1991), (Kolesova et al., 1993), (Kolesova et al., 1987), (Kolesova et al., 1989). Alternatively, oxidation of QH_2' to Q' may be redox-coupled to Q/QH_2, implied by the double line brown arrow. The possibility of complex III reducing cytochrome c or some other cytosolic oxidant has been

addressed in (Kiss et al., 2014) and (Giorgio et al., 2005). If MNQ is Q', mostly Nqo1 can catalyze its reduction. If idebenone (or its analogues), menadione, mitoquinone or duroquinone is Q', other diaphorases can perform this catalysis that are coupled to either NADH or e^-D oxidation. In either case, when a suitable Q' and a mitochondrial diaphorase are concomitantly present, regeneration of NAD^+ can occur allowing for the KGDHC reaction to proceed yielding succinyl-CoA. In turn, succinyl-CoA and ADP (or GDP) can be converted to succinate and ATP (or GTP) by succinate-CoA ligase (SUCL). Overall, bypassing an inhibited complex I with a suitable quinone leads to generation of high-energy phosphates in the mitochondrial matrix through mSLP.

Implications regarding NQO1 and other mitochondrial diaphorases on non-oxidative mitochondrial bioenergetics; relevance to mitochondrial pathologies

The most important observations of the work published in (Ravasz et al., 2018) are: i) provision of mitochondrial NAD^+ during complex I inhibition was preferentially supported by Nqo1 diaphorase activity when MNQ was the substrate ultimately supporting mSLP, and ii) mouse liver mitochondria harbor other than Nqo1 dicoumarol-sensitive diaphorases capable of oxidizing NADH or other electron donors, when suitable quinones are available. Regarding MNQ, this is a naturally occurring napthoquinone found in garden balsam, *Impatiens Balsamina L* (Little et al., 1948) but has also been synthesized over 100 years ago by Thiele and Winter https://doi.org/10.1002/0471264180.or019.03. MNQ has been recently added to a list of "complex I bypass factors" as a result of an effort to explore tool compounds for investigating tissues with an impaired complex I (Vafai et al., 2016). Complex I deficiency can be due to several mutations in structural subunits or assembly factors (Rodenburg, 2016), (Vafai and Mootha, 2012) or Parkinson's disease (Greenamyre et al., 2001), for which a number of mouse models exist (Irwin et al., 2013). "Complex I bypass" is a strategy followed for treating complex I deficiency in an attempt to rescue oxidative phosphorylation by recruiting complex I-independent pathways. Several redox-active quinones are known to possess such an activity, namely idebenone and its analogues, menadione (vitamin K3), mitoquinone (mitoQ) and duroquinone (Jaber and Polster, 2015), (Shneyvays et al., 2005), (Isaev et al., 2004), (Kelso et al., 2001), (Ghosh et al., 2011). Among them, idebenone (2-(10-hydroxydecyl)-5,6-dimethoxy-3-methyl-cyclohexa-2,5-diene-1,4-dione) has been extensively researched and is approved for the treatment of Leber's Hereditary Optic Neuropathy (LHON), a genetic disorder most commonly attributed to mutations in mitochondrial DNA encoding complex I subunits (La Morgia et al., 2014). Idebenone is more hydrophilic than ubiquinone (Suno and Nagaoka, 1984), and it is a substrate for NQO1 (Haefeli et al., 2011), glycerol-3-phosphate dehydrogenase, complexes II and III, but not complex I (James et al., 2005), (Esposti et al., 1996). Current consensus is that complex II, mitochondrial glycerol-3-phosphate dehydrogenase and cytosolic NQO1 reduce idebenone to idebenol which is subsequently oxidized by complex III (Esposti et al., 1996). However, this consensus ignores the possibility that idebenone -and in all likelihood- other quinones are reduced by mitochondrial NQO1 and/or other matrix diaphorases. Our results unequivocally showed that idebenone and duroquinone supported mSLP from glutamate implying that there was NAD^+ regeneration in the matrix of intact, isolated mouse liver mitochondria; this occurred in the absence of exogenous pyridine nucleotides and a cytosolic diaphorase, and it was due to a dicoumarol-sensitive mitochondrial diaphorase activity; furthermore, MNQ was preferentially reduced by Nqo1, yielding matrix NAD^+. Regeneration of NAD^+ in the matrix of mitochondria with an inhibited complex I allowed KGDHC reaction to occur, eventually providing high-energy phosphates through mSLP (Kiss et al., 2013). This can at least partly explain why short-chain quinones exhibit ATP rescue abilities under conditions of a defective complex I (Erb et al., 2012). At this junction it is important to consider that the potential benefit of quinones protecting mitochondria and the cells that harbor them may not be solely due to

mSLP, but also from acting as ROS scavengers. Indeed, it has been reported that in rat liver cells, $CoQ1H_2$ formation from CoQ1 by NQO1 was acting as a ROS scavenger at sufficiently high concentrations, affording cytoprotection independent from restoring ATP levels (Chan et al., 2002).

Regarding mitochondrial diaphorases responsible for NAD^+ regeneration not being Nqo1, these cannot be Nqo2 either because this isoform uses dihydronicotinamide riboside (NRH) and not NAD(P)H as an electron donor (Wu et al., 1997). They could still be responsible though for the respective quinol oxidation driving complex III and IV activity supporting respiration and mitochondrial membrane potential. As already pointed out by Ernster and colleagues, the mitochondrial DT-diaphorase and complex III exhibit different preferences and affinities for quinones and corresponding quinols, respectively (Conover and Ernster, 1962), (Ernster et al., 1962). Thus, it is important to consider not only which diaphorase oxidizes NADH, but also which quinone is reduced. As we have shown previously, addition of an exogenous redox-active quinone to isolated, respiration-inhibited mitochondria is not a requirement for demonstrating KGDHC-mediated provision of succinyl-CoA to succinate-CoA ligase and the presence of a diaphorase inhibitor abolishes mSLP (Kiss et al., 2014). This means that endogenous quinones are available and sufficient to sustain diaphorase activity. It is standard practice to include menadione or other vitamin K analogues in the chow of laboratory mice; it may well be possible that these or some other quinones that interconverted in the mouse liver mitochondria accounted for the redundancy of adding quinones exogenously. Perhaps this is why HepG2 cells did not exhibit an appreciable mSLP, since standards cell growth media do not contain vitamin K analogues or other quinones. In rodent mitochondria only CoQ1, CoQ9 and CoQ10 have been identified (Albano et al., 2002), (Tang et al., 2004). Nqo1 is able to reduce CoQ1, but CoQ9 and CoQ10 are very poor diaphorase substrates (Chan et al., 2002), (Dragan et al., 2006), (Haefeli et al., 2011), (Beyer et al., 1996). Thus, CoQ1 could be a candidate quinone for matrix diaphorases. On the other hand, CoQ1 concentration is much lower than that of CoQ9 and CoQ10; it cannot be excluded that there is some other, yet to be identified quinone in mitochondria with a sufficiently high hydrophilicity rendering it a suitable substrate for matrix diaphorases. Alternatively, endogenous quinones may participate in coupled redox reactions leading to a sequential reduction from the less concentrated, hydrophilic quinone utilized by the matrix-soluble diaphorases to the more concentrated, lipophilic quinone embedded in the inner mitochondrial membrane. The possibility of a yet to be identified mitochondrial quinone and the concept of coupled redox reactions of endogenous quinones (enzymatic or non-enzymatic) are non-mutually exclusive postulations. It is also important to emphasize that matrix diaphorases reducing quinones are responsible for oxidizing only a fraction of matrix NADH pools (Kiss et al., 2014); thus, other, non-diaphorase mediated, perhaps quinone-independent reactions are responsible for providing NAD^+ to KGDHC when complex I is inhibited. Relevant to this, the group of Mootha have recently assembled a compendium of reactions producing or consuming NAD(P)H or NA(D)H, or using them as a redox co-factor in liver cells (Goodman et al., 2018). Because several of those localize to the mitochondrial matrix, it would be interesting to explore if they contribute –and to what extent- to NAD^+ provision for KGDHC when complex I is inhibited.

Our results contribute to the understanding of the dynamic regulation of nicotinamide adenine dinucleotide metabolism in mitochondria (Stein and Imai, 2012). NAD^+-boosting strategies in particular, are rapidly becoming intense areas of research involving a wide spectrum of diseases, ranging from diabetes to cancer (Canto et al., 2015), (Yang and Sauve, 2016). More specifically and in the field of cancer, NQO1 has been implicated in cancer therapy (Oh and Park, 2015) through multiple, but opposing processes: i) as it catalyzes a two-electron reduction of quinones avoiding the production of highly reactive, semiquinone intermediates (Iyanagi and Yamazaki, 1970b), inhibition of the enzyme may divert quinones towards a one-electron transfer by the cytochrome P_{450} system forming free radicals (Bachur et al., 1979), (Manoj et al., 2010) that oxidatively damage NQO1-expressing cancer cells (Fiorillo et al.,

2017); ii) on the other hand, NQO1 converts certain quinones to cytotoxic agents, thus, its induction could be beneficial for cancer treatment; iii) more recently, NQO1 has been shown to inhibit proteasomal degradation of p53 and p33ING1b, proteins that are critical for tumor repression (Garate et al., 2008), (Asher et al., 2002). Relevant to this, NQO1 expression is induced by Nrf2 (Jaiswal, 2004), a transcription factor that is being increasingly recognized to favor survival of malignant cells (Menegon et al., 2016), (Sporn and Liby, 2012). To this list of processes, inhibition of NQO1 and other mitochondrial diaphorases as a chemotherapeutic strategy could be added because it abolishes mSLP, a process by which cancer cells are likely to rely upon in order to harness energy during adverse conditions of the tumor microenvironment (Chinopoulos and Seyfried, 2018), (Seyfried et al., 2020a).

Sucla2/g2 transgenic mice

Mitochondrial diseases are collectively considered as a major cause of encephalomyopathies and other multisystem maladies (Schaefer et al., 2008), (Elliott et al., 2008), (Schaefer et al., 2004). A considerable fraction of this pool of diseases encompass mtDNA depletion (Graham, 2012). A number of animal models have been generated to model mtDNA depletion by specifically deleting genes important for mtDNA replication (Fernandez-Canon et al., 2002), (Kimura et al., 2003), (Hance et al., 2005), (Tyynismaa et al., 2005), (Akman et al., 2008), (Martinez-Azorin et al., 2008), (Lopez et al., 2009), (Viscomi et al., 2009), though only one study has addressed the role of succinate-CoA ligase (Donti et al., 2014). In the latter work by Donti et al, tissues from Sucla2$^{-/-}$ mice were examined at an embryonic stage, because -like in our study- no viable homozygote offsprings were born. Nevertheless, accordance to a large extent is observed between the results obtained by Donti et al and our study, despite the fact that there, embryonic tissues of Sucla2$^{-/-}$ mice were examined as opposed to here where we investigated tissues from Sucla2$^{+/-}$ heterozygote adult mice, those engineered to lack one Suclg2 allele, as well as Sucla2$^{+/-}$ /Suclg2$^{+/-}$ double heterozygotes. Among the striking similarities are the varying degrees of mtDNA alterations, the reciprocal increase in Suclg2 expression when Sucla2 levels are decreased, elevations in methylmalonyl esters and a mild increase in succinate dehydrogenase activity. However, unlike in (Donti et al., 2014), we did not observe alterations in the activities of other than complex II ETC components, or any changes in mitochondrial respiration, or SLP.

The most important results of our work published in (Kacso et al., 2016) are those obtained by the comparisons of wild type to Sucla2 $^{+/-}$ mice. These can be categorized to: i) rebound increase in Suclg2 expression and associated GTP-forming activity; ii) lack of effect on bioenergetic parameters including substrate-level phosphorylation; iii) moderate mtDNA decrease; iv) elevation of short- and long-chain carnitine esters in the blood of heterozygote mice. It is important to emphasize that the rebound increase in Suclg2 expression in Sucla2 $^{+/-}$ mice seemed to occur mostly in heart mitochondria, also in brain mitochondria but only from the older (6-12 months old) mice, and not in liver mitochondria. Furthermore, the increase in GTP-forming activity also seemed heart-specific, as well as the changes in complex II activity observed in Sucla2 $^{+/-}$ / Suclg2 $^{+/-}$ mice. Obviously, the molecular mechanisms responsible for these rebound effects are tissue-specific and appear to be operational in the heart and at least some brain-specific cells, but not in the liver. The elucidation of such molecular mechanisms maybe of great value in setting an example of gene-gene interactions of similar nature.

On the same line, regarding the rebound increase in Suclg2 expression and associated GTP-forming activity in Sucla2 heterozygote mice, the concept of 'complementation' between Sucla2 and Suclg2 and -as an extension of this- ATP- and GTP-forming activity has been proposed earlier (Miller et al., 2011). This has been observed in embryonic tissues of Sucla2$^{-/-}$ mice (Donti et al., 2014), but not in fibroblasts from patients exhibiting mutations in *SUCLA2* (Miller et al., 2011). However, as it is evident from our

results this complementation is sufficient to alleviate only some of the biochemical abnormalities of the Sucla2 heterozygous mice. Indeed, mitochondrial respiration, ΔΨm, ETC/CS activities and substrate-level phosphorylation were virtually identical between WT and Sucla2 $^{+/-}$ mice, while there was mild mtDNA depletion but significant alterations in blood carnitine esters. The alterations in mtDNA should be attributed to alterations in the activity of succinate-CoA ligase with caution; it has been recently reported that GABA transaminase is essential for mitochondrial nucleoside metabolism and thus is important for mtDNA maintenance, and it co-immunoprecipitates with SUCLG1, SUCLG2 and SUCLA2 (Besse et al., 2015). The alterations in the carnitine esters concern those with both short- and long-chain. However, the levels of free carnitine in four heterozygous human carriers for *SUCLA2* mutations were not significantly elevated, compared to reference values (values were 25, 27, 29 and 37, with reference values of 24-64 mmol/l).

Finally, regarding the rebound increase in Suclg2 expression in Sucla2$^{+/-}$ mice, it is noteworthy to emphasize that the concomitant loss of one *Suclg2* allele yielding Sucla2$^{+/-}$/Suclg2$^{+/-}$ double transgenic mice was not sufficient to impose a considerable decrease in Suclg2 expression or GTP-forming succinate-CoA ligase activity. Apparently, the translational or post-translational mechanism(s) mediating this effect (as there was no change in *Suclg2* transcript, reported in (Donti et al., 2014)), supersede those occurring at the gene level, and merit further consideration. In aggregate, in (Kacso et al., 2016) we profiled the metabolism of two transgenic mouse models for beta subunit components of succinate-CoA ligase; the results presented as well as the availability of these transgenic mouse colonies to the scientific community is of value in the pursuit for understanding succinate-CoA ligase deficiency.

LPS-induced inflammation, itaconate and mSLP

Itaconate is a molecule exhibiting promiscuous pharmacological properties. Apart from being a substrate and a weak competitive inhibitor of SDH, it can be also metabolized to itaconyl-CoA by succinate-CoA ligase (Booth et al., 1952), (Adler et al., 1957), (Wang et al., 1961), inhibit (methyl)isocitrate lyase (Patel and McFadden, 1978), (McFadden and Purohit, 1977), inhibit propionyl-CoA carboxylase in isocitrate lyase-negative bacteria (Berg et al., 2002) and impair fructose 2,6-bisphosphate synthesis in rat liver (Sakai et al., 2004). The experimental observations shown above are associated with its interaction with SDH and succinate-CoA ligase, as well as the concept that succinate-CoA ligase (while operating opposite to SLP) and the α-ketoglutarate dehydrogenase complex share the same CoA pool.

In (Kiss et al., 2014) we reported that by inducing *Irg1* in BMDM and RAW-264.7 cells with LPS, which is expected to lead to an increase in endogenous itaconate production (Michelucci et al., 2013), (Strelko et al., 2011), *in situ* matrix SLP is also abolished. This is in accordance to recent findings showing that LPS increased succinate levels (Tannahill et al., 2013), (Mills and O'Neill, 2014). In the latter studies this was attributed to i) increased glutamine uptake in LPS-activated macrophages and subsequent anaplerosis of α-ketoglutarate into the citric acid cycle leading to elevated succinate production, and ii) LPS-induced upregulation of the 'GABA shunt', a pathway that eventually also led to increased levels of succinate. However, the possibility of LPS inducing *Irg1* resulting in itaconate production, which in turn subsequently inhibits SDH and favours itaconyl CoA production leading to a 'CoA trap' abolishing SLP, has been overlooked. Our findings shown in (Nemeth et al., 2016) imply that the latter scenarios are also likely to unfold; moreover, they are not at odds with the possibilities of increased glutamine uptake leading to elevated succinate production by anaplerosis, or the upregulation of the GABA shunt. The likelihood of the mechanism operating in cells of macrophage lineage proposed hereby is supported by our results on exogenously added itaconate to isolated mitochondria; there, in isolated mouse liver

mitochondria with an inhibited respiratory chain, itaconate dose-dependently reverted the cATR-induced repolarization to a depolarization, thus implying an abolition of SLP. Because this effect could be reproduced by malonate, it cannot be determined if it was due to i) succinate build-up shifting succinate-CoA ligase equilibrium towards ATP (or GTP) utilization, or to ii) favouring itaconyl-CoA formation hydrolysing ATP (or GTP) for the thioesterification, or due to iii) an ensuing 'CoA trap' in the form of itaconyl-CoA which could negatively affect the upstream supply of succinyl-CoA from the α-ketoglutarate dehydrogenase complex, in turn diminishing ATP (or GTP) formation through SLP by succinate-CoA ligase. In support of ii) and iii), the succinate-CoA ligase inhibitor KM4549SC which does not inhibit SDH exerted a similar effect as itaconate on $\Delta\Psi m$ of respiration-inhibited mitochondria. Regarding the impact of ATP (or GTP) hydrolysis caused by itaconyl-CoA formation *versus* the sequestration of CoA negatively affecting the upstream supply of succinyl-CoA from the α-ketoglutarate dehydrogenase complex and in turn the reaction catalyzed by succinate-CoA ligase towards SLP, the latter concept is probably more important: the catalytic efficiency of succinate-CoA ligase with itaconate is likely to be smaller than that for succinate; indeed, bacterial succinate-CoA ligases exhibit 2- to 10-fold higher K_m values for itaconate compared to those for succinate (Nolte et al., 2014). Furthermore, biosynthesis of one CoA molecule requires the expenditure of four ATP molecules (Theodoulou et al., 2014). Therefore, the itaconate-induced sequestration of CoA in the form of itaconyl-CoA (which metabolizes very slowly in mammalian cells) decreasing the upstream supply of succinyl-CoA from the α-ketoglutarate dehydrogenase complex and in turn affecting the reaction catalyzed by succinate-CoA ligase towards formation of ATP (or GTP) results in a more pronounced effect diminishing SLP, than that of hydrolysing ATP (or GTP) for the thioesterification of itaconate by succinate-CoA ligase.

The significance of our findings lie on the notion that, in order to mount an immune defence, cells of macrophage lineage may lose their capacity of mitochondrial SLP for producing itaconate. Having said that, the question arises as of what would be the consequences of mitochondrial SLP inhibition during infection i*n vivo*? This is difficult to address, primarily because that would have been done through induction of *Irg1* through LPS (or an appropriate infection), a manoeuvre that inherently induces concomitant alterations in glycolysis and oxidative phosphorylation. Under these conditions, it would be challenging to decipher which bioenergetic (or any other) effects are attributed to glycolysis and/or oxidative phosphorylation and/or mitochondrial substrate-level phosphorylation. Limitations in oxygen availability (that could greatly upregulate glycolysis and diminish oxidative phosphorylation) where substrate-level phosphorylation by succinate-CoA ligase is afforded a much more prominent role regarding mitochondrial bioenergetics (Chinopoulos et al., 2010), (Kiss et al., 2013), (Chinopoulos, 2011b), (Chinopoulos, 2011a), (Weinberg et al., 2000a), could only occur in macrophages infiltrating oxygen-depleted tissues (i.e. infections with hypoxic cores, or rapidly expanding solid tumors). In such environments, production of itaconate by infiltrating macrophages would have dual, but opposing roles: itaconate would decrease the survival of the infective microbes (or the tumor cells, should they rely on SLP for energy harnessing in view of a pertaining hypoxia) but on the other hand it would also decrease the ability of the macrophage producing it to cope under the same bioenergetic stress of hypoxia, as discussed elsewhere (Chinopoulos et al., 2010), (Kiss et al., 2013), (Chinopoulos, 2011b), (Chinopoulos, 2011a), (Weinberg et al., 2000a). Regarding the potential consequences of mitochondrial SLP inhibition during infection, it is also worth mentioning those for the infective organism. Inhibition of SLP of the infective organism could be detrimental; indeed, apart from the antimicrobial properties of itaconate (due to its effect on the glyoxylate shunt), mitochondrial substrate level phosphorylation mediated by succinate-CoA ligase is essential for growth of procyclic *Trypanosoma brucei* (Bochud-Allemann and Schneider, 2002) and likely other microbes relying on this oxygen-independent pathway. Internalization of macrophage-produced itaconate by the microbe would inhibit its SLP and decrease its chances for survival, thus thwarting the infection.

GABA shunt and mSLP

Apart from the main observation in the work published in (Ravasz et al., 2017), i.e. that molecules catabolized through the GABA shunt ultimately impair SLP, it is important to dwell on ramifications of these pathways. Specifically, it makes sense to ponder on the following concept: the reaction catalyzed by SSADH is strongly favored towards succinate formation (Cash et al., 1977), (Blaner and Churchich, 1979). However, *in organello*, conditions maybe met where SSA concentration is sufficiently low so that succinate could get diverted towards SSA formation, oxidizing NADH in the process. This is not an implausible scenario: it is well known that in isolation, the mitochondrial malate dehydrogenase reaction strongly favors NADH oxidation towards formation of malate from oxaloacetate; yet, under physiological conditions within the mitochondrial matrix, oxaloacetate concentration is so low that the reaction is pulled towards NADH formation (Li et al., 2011). Thus, mindful of the possibility that SSADH reaction could operate in reverse, addition of succinate to mitochondria will lead to NADH oxidation by this enzyme. By the same token, any substrate combination that yields succinate, would also follow NADH oxidation through the SSADH branch of metabolism. This notion exerts a considerable impact on a large body of work regarding succinate and NADH/NAD^+ pools addressing the so-called 'reverse electron transport', RET. RET is a $\Delta\Psi$m- and NADH/NAD^+ ratio-dependent phenomenon (Murphy, 2009), in which succinate-supported mitochondria exhibit electron flow from complex II to complex I involving coenzyme Q (Hinkle et al., 1967). RET is associated with reactive oxygen species formation (ROS) (Tretter and Adam-Vizi, 2007a), and thus, it is a putative pharmacological target for many pathological situations involving ROS. On the basis of the results presented in this study, it is at least prudent to consider that NADH oxidation by SSADH, a nearly ubiquitous enzyme, will be confounding in interpreting RET-related experiments in which mitochondria are fueled by succinate, and the NADH/NAD^+ ratio is a critical determinant of the measured variable. Still on the same line of thought but considering the thermodynamically favored SSADH reaction flow, the consequences on ROS formation by succinate originating from SSA obligatorily connected to an increase in NADH/NAD^+ ratio can be 'dissected' from the status of complex I using rotenone. To put this more simply, the effect(s) of succinate on ROS as a function of an increased level of NADH (by using SSA) could be addressed in the presence of inhibited complex I.

An additional ramification of the results outlined in this study stems from the large quantitative difference of GABA-induced polarization between brain and liver mitochondria. Because SSA conferred a full $\Delta\Psi$m in both types of tissues, it is unlikely that this variance is due to a differential SSADH activity, despite the fact that we report a higher activity of the enzyme in mouse liver compared to mouse brain, at odds with what has been reported by (Chambliss et al., 1995). We presume that it is due to either a differential expression of the GABA transport mechanism (which is yet to be identified), and/or a difference in GABA-T expression among the two tissues.

The results shown in (Ravasz et al., 2017) argue that GABA, SSA and GHB impair mitochondrial SLP during anoxia. An important exception is the lack of effect of GHB in brain, most likely due to the very low HOT expression, the enzyme responsible for GHB catabolism towards the citric acid cycle. Otherwise, the implications of the results presented in this work extend to a multitude of tissues, because the expression of enzymes participating in the GABA shunt appear to be widespread (Gladkevich et al., 2006), (Garry et al., 1987), (White and Sato, 1978), (Minuk, 1993), and not limited to the CNS. Furthermore, in some cells GABA meta bolism is an inducible system (Stuckey et al., 2005), (Bhat et al., 2010), (Tannahill et al., 2013). It is therefore, reasonable to assume that in those cells where GABA shunt is active, mitochondrial SLP is impaired.

2-ketobutyrate and mSLP

The most important observation of the work published in (Bui et al., 2019) is the abolition of mSLP by 2-KB in isolated mitochondria with an inhibited respiratory chain. This is likely attributed to ATP expenditure by PCC, even though 2-KB supports succinate-CoA ligase by providing succinyl-CoA. As a word of caution though, the effect of BCKDHC stealing NAD^+ from KGDHC (when glutamate and malate were the main fuels) could also contribute to abrogation of mSLP. The decrease in NAD^+ provision to KGDHC with the aim of diminishing mSLP is the strategy followed by including β-hydroxybutyrate in the media (supporting NADH generation by β-hydroxybutyrate dehydrogenase) relying on the fact that KGDHC activity is important for mSLP (Kiss et al., 2013). The effect of 2-KB inhibiting pyruvate oxidation has been published before (Gibson et al., 1975), albeit this was only observed at very high 2-KB concentrations (20 mM). This was attributed to a weak inhibitory action of 2-KB on the pyruvate dehydrogenase complex (Kanzaki et al., 1969), (Blass and Lewis, 1973).

Our work identifies 2-KB (or metabolites converging towards this molecule) as abrogating mSLP in a physiological manner. In human neutrophils, value ranges of 0.01-0.07 fmol/cell have been reported (Muhling et al., 2003); mindful that the volume of a human neutrophil is ~ 299 μm^3 (Ting-Beall et al., 1993), 2-KB cytosolic concentration must be 0.033 - 0.232 mM. In blood plasma and urine, 2-KB concentration is <0.01 mM but can be elevated ten- or hundred-fold in certain disease states (Yang and Roth, 1985), (Lee et al., 1998), (Bouatra et al., 2013), thus, the flux of 2-KB production by several metabolites may indeed reach a threshold upon which mSLP is affected. This can be exploited in a number of metabolic settings in order to interrogate mSLP as part of the citric acid cycle (Chinopoulos, 2013), further benefitted by it being membrane-permeable. However, it must be emphasized that 2-KB is also a substrate for lactate dehydrogenase being converted to α-hydroxybutyrate (Sullivan et al., 2015), thus, the effect of 2-KB in whole cells or tissues may not only be attributed to the mechanisms outlined in the present study. By the same token, the effects of 2-KB described in (Sullivan et al., 2015) could be partially ascribed to its ability of negating mSLP. Finally, since the catabolism of other metabolites converging to succinyl-CoA (except those originating from α-Kg) besides threonine, serine and methionine also require expenditure of one (such as in case of valine, isoleucine, thymine) or two (such as with cholesterol) molecules of ATP, it is expected that they will also lead to abolition of mSLP.

SUCLA2 expression in adult human brain

In (Dobolyi et al., 2015b) we investigated the cell-specific expression of *SUCLA2* and *SUCLG2* in the human brain. The most important observation was that A-SUCL-β was present exclusively in neurons, and not in other cell types. An obvious pathophysiological implication for astrocytes lacking A-SUCL-β and therefore being incapable of ATP provision by matrix substrate-level phosphorylation, is that their mitochondria are more likely to engage in cytosolic ATP consumption (Chinopoulos et al. 2010) than neuronal mitochondria, during natural fluctuations of their membrane potentials (Gerencser et al. 2012). As an extension of this, astrocytic mitochondria should be more vulnerable than neuronal mitochondria in terms of relying on -in house- ATP reserves during energy crisis, such as during brain ischemia (Chinopoulos and Adam-Vizi, 2010), (Chinopoulos 2011b), (Chinopoulos 2011a). To this end, the weak expression of nm23-H4 (Milon et al. 1997), together with the lack of G-SUCL-β expression in astrocytes preclude the possibility of matrix ATP formation through GTP transphosphorylation.

Furthermore, the notion that both ATP- and GTP-forming succinyl-CoA ligase activity should exhibit an extremely low -if any- rate in human astrocytes, hints at peculiarities of the directionality of citric acid cycle in these cells (Chinopoulos, 2013). Although the citric acid cycle is branded as a "cycle", it does not

necessarily operate as one (Chinopoulos, 2013). It is well known, that astrocytes produce and release large quantities of succinate (Westergaard et al. 1994). Succinate can be the end-product of a 'backflux' citric acid cycle (Brekke et al. 2012), commencing from pyruvate that is converted to oxaloacetate by pyruvate carboxylase. Pyruvate carboxylase is mostly expressed in liver and kidneys being part of gluconeogenesis, but it is also found in the astrocytes of the brain (Shank et al. 1985), (Yu et al. 1983), playing an important role in lipogenesis and synthesis of neurotransmitters (Wallace et al. 1998), (Sonnewald and Rae 2010).

Another relevant concept to our findings is that GABA uptake in the neuropil occurs through the GABA transporter GAT-3, which is exclusively expressed in astrocytes (Minelli et al. 1996), as well as GAT-1 and -2, which are found both in astrocytic processes and other neuronal- and non-neuronal elements (Conti et al. 1998), (Conti et al. 1999). GABA metabolism in the astrocytes proceeds through GABA transaminase (which also requires α-ketoglutarate) yielding succinate semialdehyde (and glutamate) that is in turn processed by succinate semialdehyde dehydrogenase yielding succinate which enters the citric acid cycle, thus effectively by-passing the 'missing' succinyl-CoA ligase, since neither *SUCLA2* nor *SUCLG2* is expressed in these cells.

Finally, in the absence of either ATP- or GTP-forming succinyl-CoA ligase, succinyl-CoA emerging from the α-ketoglutarate dehydrogenase complex in astrocytic mitochondria could be further processed towards heme and/or ketone body metabolism, pathways which are fully operational in astrocytes (Lopes-Cardozo et al. 1986), (Dringen et al. 2007), or serve as cofactor for lysine succinylation (Zhang et al. 2011), a wide-spread post-translational modification; this would also prevent a 'coenzyme A trap' in the form of succinyl-CoA.

In aggregate, our findings presented in this paper have strong physiological implications regarding the differential metabolism of neurons versus astrocytes in the human brain and pathological implications related to the impact of SUCLA2 deficiency on brain functions. Furthermore, our study pinpoints SUCLA2 as a reliable marker for neuronal mitochondria. By the same token, any report on the function or activity of ATP-forming succinyl CoA ligase in brain tissue should not apply for the whole brain, only for neurons. Finally, and in the same line, intracellular pathological manifestations of the brain caused by SUCLA2 deficiency, such as mtDNA depletion, should only be sought in neurons.

SUCLG2 expression in the microvasculature of the adult human brain

The work published in (Dobolyi et al., 2015a) is a follow-up on the lead provided by our previous work showing that SUCLG2 is very weakly expressed in the human brain, and it is not found in either neurons or astrocytes (Dobolyi et al., 2015b). There, the most important finding was that SUCLG2 expression was further confirmed to be absent from microglia and oligodendroglia, but it was detected in cells forming the microvasculature, most likely endothelial cells and/or pericytes. An additional finding was that SUCLG2 staining in human fibroblasts covered only a small fraction of the mitochondrial network. On the other hand, SUCLA2 staining covered the majority of mitochondria in the same cells (Dobolyi et al., 2015b). Triple-colocalization study of SUCLG2, SUCLA2 and mitotracker orange in the same cell was performed later on by us, published in (Chinopoulos et al., 2019).

KGDHC subunits expression in the adult human brain

The two most important observations of the work published in (Dobolyi et al., 2020) are that i) we detected KGDHC-specific subunits immunoreactivity in neurons but not glia of the human brain, and ii) protein lysine succinylations were pancellularly observed, thus, in glia, succinyl-CoA is probably a product of an enzyme other than KGDHC. Furthermore, to the best of our knowledge, our work is the first to demonstrate protein lysine succinylation in the adult human cortex. DLD subunit was found also in non-neuronal cells, but this is probably due to its participation in the pyruvate dehydrogenase complex, branched-chain alpha-keto acid dehydrogenase complex and the glycine cleavage system. Regarding the finding that KGDHC-specific components were not observed in cells staining positive with glial markers, it is important to emphasize that our immunohistochemistry protocols included several amplification steps. This implies that if KGDHC-specific components are expressed in human glia they are probably at least two orders of magnitude less abundant than those expressed in neurons, precluding the possibility of an appreciable KGDHC activity in the former cell types. The group of John P Blass have also published the absence of KGDHC immunoreactivity from glia in the adult human brain; however, out of perhaps abundance of caution they reported it as "*surprisingly, convincing immunoreactivity was not found in glia*" (Ko et al., 2001), even though KGDHC immunoreactivity was completely absent from all of their microphotographs. In (Dobolyi et al., 2020) we investigated glial cells exhibiting GFAP, Aldhl1, myelin-basic protein, Olig2 and IBA1, identifying astrocytes, oligodendrocytes and microglia. However, the human brain harbors hundreds (if not thousands) of cell types and subtypes. The Human Brain Project aims to identify and catalogue all these cells (Amunts et al., 2016). Thus, it cannot be excluded that some glial subtypes exhibit KGDHC-specific components to a detectable level. This is supported by RNA-Seq data obtained from the Allen Brain Atlas, in which positive "hits" were scarce but still visible in non-neuronal cells. The notion that glia of the adult human brain may not exhibit KGDHC (nor succinyl-CoA ligase) activity, thus precluding operation of the citric acid cycle as we know it calling for reconsideration of a textbook definition of a universal metabolic pathway should not come as a great surprise: mice engineered to lack cytochrome c oxidase in astrocytic mitochondria *in vivo* were fully viable in the absence of any signs of glial or neuronal loss even at one year of age (Supplie et al., 2017). Notably though, KGDHC (detected immunologically by using an antibody generated using the whole complex as an epitope) has been reported in astrocytes of cerebrum and cerebellum of newborn mice (Waagepetersen et al., 2006). Furthermore, in (Calingasan et al., 1994), it was shown that in 3-month old male Fischer 344/Brown Norway F1 hybrid rats immunohistochemistry for KGDHC (using an anti-rabbit IgG for KGDHC, no further information is provided), KGDHC stained neurons much more intensely than glia in several brain areas. Perhaps KGDHC is absent (or at least present at an extremely small level) in human glia so as to assist the glutamate-glutamine cycle by preventing glutamate catabolism through the citric acid cycle (which necessitates KGDHC activity), instead being shuttled towards glutamine formation. By the same token, uptaken glutamate from the EC would be shuttled towards GABA metabolism, also known to operate in glia cells. Relevant to this, in a human embryonic kidney cell line even a mild reduction (~30%) in KGDHC activity elevated the GABA shunt (Shi et al., 2009).

Regarding the observation of pancellular lysine succinylation in the adult human cortex in view of the fact that glia may not exhibit KGDHC nor succinyl-CoA ligase activity implies that these cells must obtain succinyl-CoA from some other metabolic pathway. In mammals, this high-energy metabolite can be generated only through KGDHC, succinyl-CoA ligase, catabolism of valine, isoleucine, methionine, thymine, odd-number chain fatty acids (and perhaps propionate) and through the reaction catalyzed by OXCT1. Since glia may not exhibit KGDHC nor succinyl-CoA ligase components, provision of succinyl-CoA is ensured only by the remaining pathways. Mindful of the remaining pathways generating succinyl-CoA inside the matrix, it is still a mystery how can there be extramitochondrial protein lysine succinylations, and this has been reviewed in (Chinopoulos, 2021), where the concept of pathways participating in peroxisomal fatty acid oxidation leading to succinyl-CoA production potentially supporting succinylation of extramitochondrial proteins, is scrutinized.

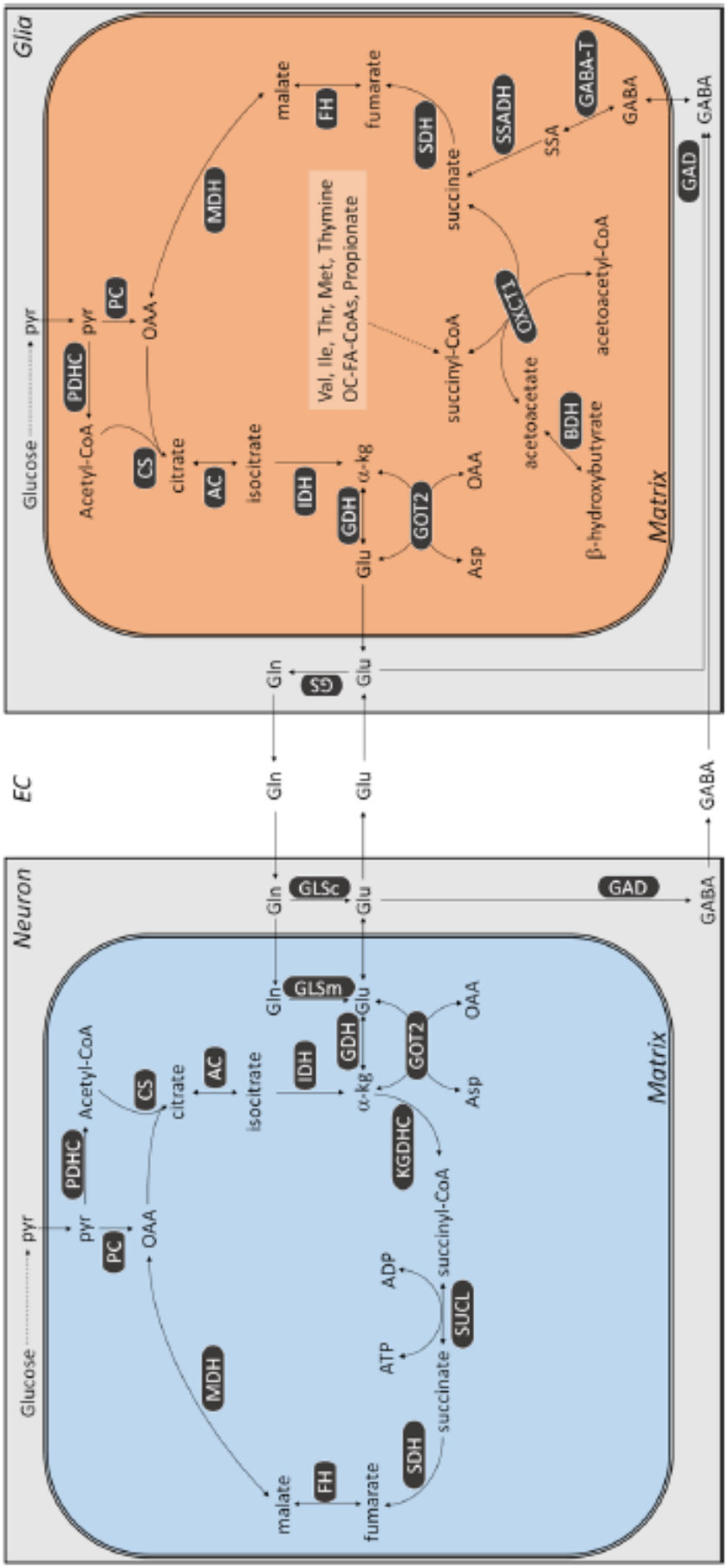

Figure 16.19. Metabolic considerations of a neuronal mitochondrion (blue box) and a glial mitochondrion (orange box) pertinent to KGDHC. AC: aconitase; BDH: β-hydroxybutyrate dehydrogenase; CS: citrate synthase; FH: fumarase; GAD: glutamate decarboxylase; GABA-T: GABA aminotransferase; GDH: glutamate dehydrogenase; GLSc: glutaminase (cytosolic); GLSm: glutaminase (mitochondrial); GOT2: aspartate aminotransferase; IDH: isocitrate dehydrogenase; KGDHC: ketoglutarate dehydrogenase complex; MDH: malate dehydrogenase (mitochondrial); OXCT1: Succinyl-CoA:3-Oxoacid CoA-Transferase; PC: pyruvate carboxylase; PDHC: pyruvate dehydrogenase complex; SDH: succinate dehydrogenase; SSADH: Succinic Semialdehyde Dehydrogenase; SUCL: succinyl-CoA ligase.

Nevertheless, mindful of our previously published work showing that adult human glia lack succinate-CoA ligase, the segment of the citric acid cycle from α-ketoglutarate to succinate could only be connected through the GABA shunt, a pathway which is known to take place in glia (Minelli et al., 1996), (Conti et al., 1998), (Conti et al., 1999). However, succinyl-CoA is still being made since protein lysine succinylations were detected in glial

mitochondria as well. Thus, we propose the following metabolism pertinent to KGDHC in neurons versus glia: as shown in figure 16.19, neuronal mitochondria (blue box) perform the citric acid cycle as described in textbooks. They also receive glutamine (Gln) from the extracellular space (EC), which originated from glia as part of the so-called “glutamate-glutamine cycle” between neurons and glia (Sonnewald and Schousboe, 2016). Some neurons will also extrude GABA to the EC which can be taken up by the glia. Glial mitochondria (orange box), on the other hand, will also take up glutamate from the EC, which has been released by neurons and further process it by transamination or use it for forming GABA. Succinyl-CoA in glia can only be produced from valine, isoleucine, methionine, thymine, odd-number chain fatty acids and perhaps propionate (multiple reactions, omitted for clarity), and from the reaction catalyzed by OXCT1, an enzyme participating in ketone bodies catabolism; relevant to this, ketone bodies metabolism is known to occur in human astrocytes (Thevenet et al., 2016).

ABBREVIATIONS

1,2-NQ	1,2-naphthoquinone
1,4-NQ	1,4-naphthoquinone
2-HG	2-hydroxyglutarate
2-KB	2-ketobutyrate
A+R	antimycin A with rotenone
AC	aconitase
AcAc	acetoacetate
ACL	ATP-citrate lyase
α-Kg	α-ketoglutarate
ALT2	mitochondrial alanine aminotransferase
AML	acute myeloid leukemia
ANT	adenine nucleotide translocase
AOAA	aminooxyacetic acid
AP5A	P1,P5-di(adenosine-) pentaphosphate
asp	aspartate
atpn	atpenin A5
BCECF	2',7'-bis(carboxyethyl)-5,6-carboxyfluorescein
BCKDHC	branched-chain keto-acid dehydrogenase complex
BDH	β-hydroxybutyrate dehydrogenase
BKA	bongkrekic acid
BMDM	bone marrow-derived macrophages
βOH, bOH	β-hydroxybutyrate
BQ	p-benzoquinone
cADC	cis-aconitate decarboxylase
cATR	carboxyatractyloside
CBQ	2-chloro-1,4-benzoquinone
CBQ	2-chloro-1,4-benzoquinone
CCCP	carbonyl cyanide 3-chlorophenylhydrazone
CCIN	alpha-Cyano-4-hydroxycinnamate

CHAPS	3-[(3-Cholamidopropyl)dimethylammonio]-1-propanesulfonate
CoA	coenzyme A
CoQ	coenzyme Q
COX	cytochrome oxidase
Cyb5r2	NADH:cytochrome b5 reductase isoform 2
CypD	cyclophilin D
cys A	cyclosporin A
DAB	3,3-diaminobenzidine
DCA	dichloroacetate
DCBQ	2,6-dichloro-1,4-benzoquinone
DCIP	2,6-dichloroindophenol
DHODH	dihydroorotate dehydrogenase
DIC	dicoumarol
diOH-flavone	7,8-dihydroxyflavone hydrate
DLD	dihydrolipoyl dehydrogenase
DLST	dihydrolipoyl succinyltransferase
DMBQ	2,6-dimethylbenzoquinone
DMEM	Dulbecco's Modified Eagle Medium
DNP	2,4-dinitrophenol
DQ	duroquinone
$\Delta\Psi m$	mitochondrial membrane potential
EC	extracellular space
ECAR	extracellular acidification rate
EDTA	ethylenediaminetetraacetic acid
EGTA	ethylene glycol-bis(2-aminoethylether)-N,N,N?,N?-tetraacetic acid
Erev_ANT	Reversal potential of the ANT
Erev_ATPase	Reversal potential of the F0-F1 ATPase
ETF	electron transfer flavoprotein
ETFDH	electron-transferring-flavoprotein dehydrogenase
FC	Fold change

FCCP	carbonyl cyanide 4-(trifluoromethoxy)phenylhydrazone
FerrCyan	$K_3[Fe(CN)_6]$
FH	fumarate hydratase
GABA	γ-Aminobutyric acid
GABA-T	GABA transaminase
GAD	glutamate decarboxylase
GBM	glioblastoma (multiforme)
GHB	β-hydroxybutyrate
gln	glutamine
glut	glutamate
GPDH	glycerol-3-phosphate dehydrogenase
GSH	glutathione (reduced form)
HBTB	Human Brain Tissue Bank
HOT	hydroxyacid-oxoacid transhydrogenase
HPLC	High Performance Liquid Chromatography
IDB	idebenone
IDH	Isocitrate dehydrogenase
IF1, IF-1	Inhibitor protein
Irg1	immunoresponsive gene 1
JC-1	5,5',6,6'-tetrachloro-1,1',3,3'-tetraethylbenzimidazolcarbocyanine iodide
JHDM	Jumonji-C histone demethylase
KGDHC	ketoglutarate dehydrogenase complex
KO	knock out
LDH	lactate dehydrogenase
LPS	lipopolysaccharide
mal	malate
MBQ	methyl-p-benzoquinone
MBQ	methyl-p-benzoquinone
MCEE	methylmalonyl-CoA epimerase
MCM	methylmalonyl-CoA mutase

M-CSF	Macrophage colony-stimulating factor
MCT	monocarboxylate transporter
MDH	malate dehydrogenase
MgG, MgGr	magnesium green
MGTK	methylglutaconase, methylglutaconyl-CoA hydratase
mito	mitochondria
mitoQ	mitoquinone
MND	menadione
MNQ	2-methoxy-1,4-naphtoquinone
MnSOD	Manganese Superoxide Dismutase
mPTP	mitochondrial permeability transition pore
mSLP	mitochondrial substrate-level phosphorylation
MS-MS	electrospray ionization-tandem mass spectrometry
mtDNA	mitochondrial DNA
MTO	Mitotracker Orange
NEAAs	non-essential amino acids
NK	natural killer
NQO	NAD(P)H:quinone oxidoreductase
OAT1	organic anion transporter
OC-FAs	odd-chain fatty acids
OCR	oxygen consumption rate
OGDH	oxoglutarate dehydrogenase
OGDHL	oxoglutarate dehydrogenase-like protein
olgm	oligomycin
OXCT1	succinyl-CoA:3-ketoacid coenzyme A transferase 1
OxPhos	oxidative phosphorylation
PBS	phosphate-buffered saline
PC	pyruvate carboxylase
PCC	propionyl-CoA carboxylase
PDHC	pyruvate dehydrogenase complex

PDK	pyruvate dehydrogenase kinase
PEP	phosphoenolpyruvate
PEPCK	phosphoEnolPyruvate CarboxyKinase
PHD	prolyl hydroxylase
PHGDH	phosphoglycerate dehydrogenase
PK	pyruvate kinase
PKM2	dimeric M2 isoform of pyruvate kinase
pmf	protonmotive force
PPP	pentose phosphate pathway
PTP	permeability transition pore
pyr	pyruvate
RCR	respiratory control ratio
RIPA	radioimmunoprecipitation assay
ROS	reactive oxygen species
rot	rotenone
SDH	succinate dehydrogenase
SDHAF	SDH assembly factor
SF 6847	tyrphostin 9, RG-50872, Malonaben, 3,5-di-tert-butyl-4-hydroxybenzylidenemalononitrile, 2,6-di-t-butyl-4-(2',2'-dicyanovinyl)phenol
siRNA	short-interfering RNA
SLP	substrate-level phosphorylation
SSA	succinic semialdehyde
SSADH	succinate semialdehyde dehydrogenase
SSAR	succinic semialdehyde reductase
stigm	stigmatellin
succ	succinate
SUCL	Succinate-CoA Ligase
TCA	tricarboxylic acid (cycle)
TIPM	thioglycollate-induced peritoneal macrophages
TLR	Toll-like receptor

TMPD	N,N,N,N-Tetramethyl-p-phenylenediamine
TMRM	tetramethylrhodamine, methyl ester, perchlorate
TPP	tetraphenylphosphonium
TRAM-34	triarylmethane-34
UDP	uridine diphosphate
VGBT	vigabatrin
VHL	von Hippel-Lindau tumor suppressor gene
WGA	wheat germ agglutinin
WT	wild type
ε	extinction coefficient

ACKNOWLEDGEMENTS

It is a great pleasure for me to be given the opportunity to thank all the people listed below; each and every one of them played a significant role in my professional advances, and even though most of them don't know nor ever met each other, they are all very close to me.

Foremost, I would like to thank Prof. Ádám Veronika, who has practically taken me under her wing the moment I stepped foot in her department. Prof. Ádám arranged for my international exposure to the world of science even when I was a TDK student; she further ensured that I could continue my PhD studies by waiving my tuition fees once it became clear that I was unable to pay the amount; offered me a position right after my postdoc; and throughout all these years afforded me with the freedom to pursue my curiosity in research. She is the role model of the lab leader and mentor that I strive to be with my own students and apprentices.

I am also indebted to Prof. Tretter László for inviting me to join prof. Ádám department; I owe to him incredibly much, mindful his undiminished attention to all of my questions and concerns in the lab, and for passing to me the incurable "Puskin street infection"!

I am thankful to Prof. Gary Fiskum, my mentor during my postdoctoral studies in Baltimore. With him I not only advanced in science, but also in science politics and grant writing.

I also wish to thank Dr. Krish Chandrasekaran "Chandra" for including me in his projects regarding bilobalide and N-acetylaspartate biosynthesis.

I am indebted to Dr. Anatoly Starkov for practically all the advanced knowledge that I have acquired regarding mitochondriology.

I am also very thankful to Dr. Akos Gerencser, with whom we started our PhD studies together at the Puskin street and we still interact to this day regarding his ingenious mitochondrial imaging algorithms.

Furthermore, I wish to express my gratitude to Prof. Volodymyr Gerzanich who was the one to teach me electrophysiology without anything in return; Dr. Bill Shuttleworth and Prof. John Connor for boosting my patch-clamping skills by showing me the combined image-patch methodology in brain slices.

In addition, I am indebted to Prof. László Csanády for working out the binding equations for the ANT activity assay, Dr. Attila Ambrus for providing purified proteins for antibody validations, Dr. Eugeniy Metelkin and Prof. Oleg Demin for the computer modelling, Prof. Giovanni Manfredi and Dr. Hibiki Kawamata for genetically modified cell lines and being such excellent collaborators to this day, Dr. Kiebish and his team for lipidomic and proteomic analysis, Dr. Janos Lábár for electron microscopy, Prof. Kathleen Kinnally for mitoplast pach-clamp analysis, Prof. Roza Kucharczyk for the genetically-modified yeast mitochondrial projects, Prof. Molnár Mária Judit and Dr. Gál Anikó for the human muscle specimens, Prof. Patocs Attila for the cancer cell lines and other collaborative projects, Prof. Ann Saada and Dr. Elsebet Ostergaard for the patient fibroblasts with rare diseases, Prof. Dobolyi Árpád for immunohistochemistry of human brains, Prof. Palkovits Miklos for providing access to the Human Tissue Brain Bank, Dr. Bagó Atttila for the fresh human brain specimens, Prof. Attila Mocsai and Dr. Daniel Csete for the murine macrophages, Dr. Iordan Iordanov and Dr. Beata Torocsik for the molecular biology work, Dr. Andoni Echaniz-Laguna and Dr. Bénédicte Mousson de Camaret for work related to the ANT1-deficient cells, Prof. Araki and Prof. Nakahara for help regarding transgenic mice generation, Prof. Thomas Seyfried for extremely insightful comments and suggestions regarding mitochondria and cancer, Prof. Dora Zelena and Dr. Otto Pinter for work related to murine behaviour, Ms. Erzsebet Oszwald for excellent immunocytochemistry protocols, Prof. Krasimir Kolev for collaboration regarding cyclophilin D and platelet adhesion, Prof. Alena Zikova and Dr. Carolina Hierro-Yap for mSLP work in Trypanosomas, Dr. Anna Stepanova for bioinformatic analysis, and Prof. Erich Gnaiger and Oroboros instruments for lending to us the Next-Generation O2k prototypes.

Furthermore, I am indebted to my colleagues Dr. Judit Dóczi and Dr. Dóra Ravasz with whom I have the pleasure of working throughout the past several years, as well as my past and current PhD students and senior colleagues Drs. Gergely Kiss, Csaba Konrad, Gergely Kacso, Beata Nemeth, David Bui, Gergely Pallag, Krisztina Paal and Sara Nazarian.

Finally, I am thankful to my spouse, Ildikó for her undiminished love and support and for keeping my standards of discipline very high.

BIBLIOGRAPHY

Abramov, A.Y., Duchen, M.R., 2005. The role of an astrocytic NADPH oxidase in the neurotoxicity of amyloid beta peptides. Philos Trans R Soc Lond B Biol Sci 360(1464), 2309-2314.

Abramov, A.Y., Duchen, M.R., 2008. Mechanisms underlying the loss of mitochondrial membrane potential in glutamate excitotoxicity. Biochim Biophys Acta 1777(7-8), 953-964.

Achouri, Y., Noel, G., Vertommen, D., Rider, M.H., Veiga-Da-Cunha, M., Van Schaftingen, E., 2004. Identification of a dehydrogenase acting on D-2-hydroxyglutarate. Biochem J 381(Pt 1), 35-42.

Adam-Vizi, V., Ligeti, E., 1984. Release of acetylcholine from rat brain synaptosomes by various agents in the absence of external calcium ions. J Physiol 353, 505-521.

Adam, J., Hatipoglu, E., O'Flaherty, L., Ternette, N., Sahgal, N., Lockstone, H., Baban, D., Nye, E., Stamp, G.W., Wolhuter, K., Stevens, M., Fischer, R., Carmeliet, P., Maxwell, P.H., Pugh, C.W., Frizzell, N., Soga, T., Kessler, B.M., El-Bahrawy, M., Ratcliffe, P.J., Pollard, P.J., 2011. Renal cyst formation in Fh1-deficient mice is independent of the Hif/Phd pathway: roles for fumarate in KEAP1 succination and Nrf2 signaling. Cancer Cell 20(4), 524-537.

Adler, J., Wang, S.F., Lardy, H.A., 1957. The metabolism of itaconic acid by liver mitochondria. J Biol Chem 229(2), 865-879.

Ahluwalia, G.S., Grem, J.L., Hao, Z., Cooney, D.A., 1990. Metabolism and action of amino acid analog anti-cancer agents. Pharmacol.Ther. 46(2), 243-271.

Ahmadloo, N., Kani, A.A., Mohammadianpanah, M., Nasrolahi, H., Omidvari, S., Mosalaei, A., Ansari, M., 2013. Treatment outcome and prognostic factors of adult glioblastoma multiforme. J Egypt Natl Canc Inst 25(1), 21-30.

Aiken, K.J., Bickford, J.S., Kilberg, M.S., Nick, H.S., 2008. Metabolic regulation of manganese superoxide dismutase expression via essential amino acid deprivation. J Biol Chem 283(16), 10252-10263.

Akerboom, T.P., Bookelman, H., Tager, J.M., 1977. Control of ATP transport across the mitochondrial membrane in isolated rat-liver cells. FEBS Lett 74(1), 50-54.

Akerman, K.E., Nicholls, D.G., 1981. Calcium transport by intact synaptosomes. Influence of ionophore A23187 on plasma-membrane potential, plasma-membrane calcium transport, mitochondrial membrane potential, respiration, cytosolic free-calcium concentration and noradrenaline release. Eur J Biochem 115(1), 67-73.

Akerman, K.E., Wikstrom, M.K., 1976. Safranine as a probe of the mitochondrial membrane potential. FEBS Lett 68(2), 191-197.

Akman, H.O., Dorado, B., Lopez, L.C., Garcia-Cazorla, A., Vila, M.R., Tanabe, L.M., Dauer, W.T., Bonilla, E., Tanji, K., Hirano, M., 2008. Thymidine kinase 2 (H126N) knockin mice show the essential role of balanced deoxynucleotide pools for mitochondrial DNA maintenance. Hum Mol Genet 17(16), 2433-2440.

Alam, N.A., Rowan, A.J., Wortham, N.C., Pollard, P.J., Mitchell, M., Tyrer, J.P., Barclay, E., Calonje, E., Manek, S., Adams, S.J., Bowers, P.W., Burrows, N.P., Charles-Holmes, R., Cook, L.J., Daly, B.M., Ford, G.P., Fuller, L.C., Hadfield-Jones, S.E., Hardwick, N., Highet, A.S., Keefe, M., MacDonald-Hull, S.P., Potts, E.D., Crone, M., Wilkinson, S., Camacho-Martinez, F., Jablonska, S., Ratnavel, R., MacDonald, A., Mann,

R.J., Grice, K., Guillet, G., Lewis-Jones, M.S., McGrath, H., Seukeran, D.C., Morrison, P.J., Fleming, S., Rahman, S., Kelsell, D., Leigh, I., Olpin, S., Tomlinson, I.P., 2003. Genetic and functional analyses of FH mutations in multiple cutaneous and uterine leiomyomatosis, hereditary leiomyomatosis and renal cancer, and fumarate hydratase deficiency. Hum.Mol.Genet. 12(11), 1241-1252.

Alarcon, C., Wicksteed, B., Prentki, M., Corkey, B.E., Rhodes, C.J., 2002. Succinate is a preferential metabolic stimulus-coupling signal for glucose-induced proinsulin biosynthesis translation. Diabetes 51(8), 2496-2504.

Albano, C.B., Muralikrishnan, D., Ebadi, M., 2002. Distribution of coenzyme Q homologues in brain. Neurochem Res 27(5), 359-368.

Albers, D.S., Augood, S.J., Park, L.C., Browne, S.E., Martin, D.M., Adamson, J., Hutton, M., Standaert, D.G., Vonsattel, J.P., Gibson, G.E., Beal, M.F., 2000. Frontal lobe dysfunction in progressive supranuclear palsy: evidence for oxidative stress and mitochondrial impairment. J Neurochem 74(2), 878-881.

Alderson, N.L., Wang, Y., Blatnik, M., Frizzell, N., Walla, M.D., Lyons, T.J., Alt, N., Carson, J.A., Nagai, R., Thorpe, S.R., Baynes, J.W., 2006. S-(2-Succinyl)cysteine: a novel chemical modification of tissue proteins by a Krebs cycle intermediate. Arch Biochem Biophys 450(1), 1-8.

Alexander, B.M., Cloughesy, T.F., 2017. Adult Glioblastoma. J Clin Oncol 35(21), 2402-2409.

Alexandre, A., Reynafarje, B., Lehninger, A.L., 1978. Stoichiometry of vectorial H+ movements coupled to electron transport and to ATP synthesis in mitochondria. Proc Natl Acad Sci U S A 75(11), 5296-5300.

Altschuld, R.A., Jung, D.W., Phillips, R.M., Narayan, P., Castillo, L.C., Whitaker, T.E., Hensley, J., Hohl, C.M., Brierley, G.P., 1994. Evidence against norepinephrine-stimulated efflux of mitochondrial Mg2+ from intact cardiac myocytes. Am J Physiol 266(3 Pt 2), H1103-1111.

Ambrus, A., Wang, J., Mizsei, R., Zambo, Z., Torocsik, B., Jordan, F., Adam-Vizi, V., 2016. Structural alterations induced by ten disease-causing mutations of human dihydrolipoamide dehydrogenase analyzed by hydrogen/deuterium-exchange mass spectrometry: Implications for the structural basis of E3 deficiency. Biochim Biophys Acta 1862(11), 2098-2109.

Amores-Sanchez, M.I., Medina, M.A., 1999. Glutamine, as a precursor of glutathione, and oxidative stress. Mol Genet Metab 67(2), 100-105.

Amunts, K., Ebell, C., Muller, J., Telefont, M., Knoll, A., Lippert, T., 2016. The Human Brain Project: Creating a European Research Infrastructure to Decode the Human Brain. Neuron 92(3), 574-581.

Andresen, H., Aydin, B.E., Mueller, A., Iwersen-Bergmann, S., 2011. An overview of gamma-hydroxybutyric acid: pharmacodynamics, pharmacokinetics, toxic effects, addiction, analytical methods, and interpretation of results. Drug Test Anal 3(9), 560-568.

Aprille, J.R., 1993. Mechanism and regulation of the mitochondrial ATP-Mg/P(i) carrier. J.Bioenerg.Biomembr. 25(5), 473-481.

Araki, M., Nakahara, M., Muta, M., Itou, M., Yanai, C., Yamazoe, F., Miyake, M., Morita, A., Araki, M., Okamoto, Y., Nakagata, N., Yoshinobu, K., Yamamura, K., Araki, K., 2014. Database for exchangeable gene trap clones: pathway and gene ontology analysis of exchangeable gene trap clone mouse lines. Dev Growth Differ 56(2), 161-174.

Arcos, J.C., Tison, M.J., Gosch, H.H., Fabian, J.A., 1969. Sequential alterations in mitochondrial inner and outer membrane electron transport and in respiratory control during feeding of amino azo dyes; stability of phosphorylation. Correlation with swelling-contraction changes and tumorigenesis threshold. Cancer Res 29(6), 1298-1305.

Arismendi-Morillo, G.J., Castellano-Ramirez, A.V., 2008. Ultrastructural mitochondrial pathology in human astrocytic tumors: potentials implications pro-therapeutics strategies. Journal of electron microscopy 57(1), 33-39.

Arnold, S., Kadenbach, B., 1997. Cell respiration is controlled by ATP, an allosteric inhibitor of cytochrome-c oxidase. Eur J Biochem 249(1), 350-354.

Asher, G., Lotem, J., Cohen, B., Sachs, L., Shaul, Y., 2001. Regulation of p53 stability and p53-dependent apoptosis by NADH quinone oxidoreductase 1. Proc Natl Acad Sci U S A 98(3), 1188-1193.

Asher, G., Lotem, J., Kama, R., Sachs, L., Shaul, Y., 2002. NQO1 stabilizes p53 through a distinct pathway. Proc Natl Acad Sci U S A 99(5), 3099-3104.

Aureliano, M., Crans, D.C., 2009. Decavanadate (V10 O28 6-) and oxovanadates: oxometalates with many biological activities. J Inorg Biochem 103(4), 536-546.

Austin, J., Aprille, J.R., 1984. Carboxyatractyloside-insensitive influx and efflux of adenine nucleotides in rat liver mitochondria. J Biol Chem 259(1), 154-160.

Awapara, J., Landua, A.J., Fuerst, R., Seale, B., 1950. Free gamma-aminobutyric acid in brain. J Biol Chem 187(1), 35-39.

Azzu, V., Parker, N., Brand, M.D., 2008. High membrane potential promotes alkenal-induced mitochondrial uncoupling and influences adenine nucleotide translocase conformation. Biochem J 413(2), 323-332.

Bachur, N.R., Gordon, S.L., Gee, M.V., Kon, H., 1979. NADPH cytochrome P-450 reductase activation of quinone anticancer agents to free radicals. Proc Natl Acad Sci U S A 76(2), 954-957.

Bajic, D., Koike, M., Albsoul-Younes, A.M., Nakajima, S., Nakajima, Y., 2002. Two different inward rectifier K+ channels are effectors for transmitter-induced slow excitation in brain neurons. Proc Natl Acad Sci U S A 99(22), 14494-14499.

Bakken, I.J., Sonnewald, U., Clark, J.B., Bates, T.E., 1997a. [U-13C]glutamate metabolism in rat brain mitochondria reveals malic enzyme activity. Neuroreport 8(7), 1567-1570.

Bakken, I.J., White, L.R., Aasly, J., Unsgard, G., Sonnewald, U., 1997b. Lactate formation from [U-13C]aspartate in cultured astrocytes: compartmentation of pyruvate metabolism. Neurosci.Lett. 237(2-3), 117-120.

Balazs, R., Machiyama, Y., Hammond, B.J., Julian, T., Richter, D., 1970. The operation of the gamma-aminobutyrate bypath of the tricarboxylic acid cycle in brain tissue in vitro. Biochem J 116(3), 445-461.

Ballanyi, K., Doutheil, J., Brockhaus, J., 1996. Membrane potentials and microenvironment of rat dorsal vagal cells in vitro during energy depletion. J Physiol 495 (Pt 3), 769-784.

Bando, Y., Aki, K., 1992. One- and two-electron oxidation-reduction properties of lipoamide dehydrogenase. J Nutr Sci Vitaminol (Tokyo) Spec No, 453-456.

Barbour, R.L., Chan, S.H., 1981. Characterization of the kinetics and mechanism of the mitochondrial ADP-atp carrier. J Biol Chem 256(4), 1940-1948.

Bardella, C., Pollard, P.J., Tomlinson, I., 2011. SDH mutations in cancer. Biochim.Biophys.Acta 1807(11), 1432-1443.

Barden, R.E., Fung, C.H., Utter, M.F., Scrutton, M.C., 1972. Pyruvate carboxylase from chicken liver. Steady state kinetic studies indicate a "two-site" ping-pong mechanism. Journal of Biological Chemistry 247(4), 1323-1333.

Bartesaghi, S., Graziano, V., Galavotti, S., Henriquez, N.V., Betts, J., Saxena, J., Minieri, V., A, D., Karlsson, A., Martins, L.M., Capasso, M., Nicotera, P., Brandner, S., De Laurenzi, V., Salomoni, P., 2015. Inhibition of oxidative metabolism leads to p53 genetic inactivation and transformation in neural stem cells. Proc Natl Acad Sci U S A 112(4), 1059-1064.

Basso, E., Petronilli, V., Forte, M.A., Bernardi, P., 2008. Phosphate is essential for inhibition of the mitochondrial permeability transition pore by cyclosporin A and by cyclophilin D ablation. J Biol Chem 283(39), 26307-26311.

Baukrowitz, T., Hwang, T.C., Nairn, A.C., Gadsby, D.C., 1994. Coupling of CFTR Cl- channel gating to an ATP hydrolysis cycle. Neuron 12(3), 473-482.

Bay, T., Eghorn, L.F., Klein, A.B., Wellendorph, P., 2014. GHB receptor targets in the CNS: focus on high-affinity binding sites. Biochem Pharmacol 87(2), 220-228.

Beard, D.A., 2005. A biophysical model of the mitochondrial respiratory system and oxidative phosphorylation. PLoS Comput Biol 1(4), e36.

Belhage, B., Hansen, G.H., Schousboe, A., 1993. Depolarization by K+ and glutamate activates different neurotransmitter release mechanisms in GABAergic neurons: vesicular versus non-vesicular release of GABA. Neuroscience 54(4), 1019-1034.

Berg, I.A., Filatova, L.V., Ivanovsky, R.N., 2002. Inhibition of acetate and propionate assimilation by itaconate via propionyl-CoA carboxylase in isocitrate lyase-negative purple bacterium Rhodospirillum rubrum. FEMS Microbiol Lett 216(1), 49-54.

Bernardi, P., 1992. Modulation of the mitochondrial cyclosporin A-sensitive permeability transition pore by the proton electrochemical gradient. Evidence that the pore can be opened by membrane depolarization. J Biol Chem 267(13), 8834-8839.

Bernath, S., 1992. Calcium-independent release of amino acid neurotransmitters: fact or artifact? Prog Neurobiol 38(1), 57-91.

Berwick, D.C., Hers, I., Heesom, K.J., Moule, S.K., Tavare, J.M., 2002. The identification of ATP-citrate lyase as a protein kinase B (Akt) substrate in primary adipocytes. J.Biol.Chem 277(37), 33895-33900.

Besse, A., Wu, P., Bruni, F., Donti, T., Graham, B.H., Craigen, W.J., McFarland, R., Moretti, P., Lalani, S., Scott, K.L., Taylor, R.W., Bonnen, P.E., 2015. The GABA transaminase, ABAT, is essential for mitochondrial nucleoside metabolism. Cell Metab 21(3), 417-427.

Beyer, R.E., Segura-Aguilar, J., Di Bernardo, S., Cavazzoni, M., Fato, R., Fiorentini, D., Galli, M.C., Setti, M., Landi, L., Lenaz, G., 1996. The role of DT-diaphorase in the maintenance of the reduced antioxidant form of coenzyme Q in membrane systems. Proc Natl Acad Sci U S A 93(6), 2528-2532.

Bhat, R., Axtell, R., Mitra, A., Miranda, M., Lock, C., Tsien, R.W., Steinman, L., 2010. Inhibitory role for GABA in autoimmune inflammation. Proc Natl Acad Sci U S A 107(6), 2580-2585.

Bianchet, M.A., Faig, M., Amzel, L.M., 2004. Structure and mechanism of NAD[P]H:quinone acceptor oxidoreductases (NQO). Methods Enzymol 382, 144-174.

Billiard, J., Dennison, J.B., Briand, J., Annan, R.S., Chai, D., Colon, M., Dodson, C.S., Gilbert, S.A., Greshock, J., Jing, J., Lu, H., McSurdy-Freed, J.E., Orband-Miller, L.A., Mills, G.B., Quinn, C.J., Schneck, J.L., Scott, G.F., Shaw, A.N., Waitt, G.M., Wooster, R.F., Duffy, K.J., 2013. Quinoline 3-sulfonamides inhibit lactate dehydrogenase A and reverse aerobic glycolysis in cancer cells. Cancer Metab 1(1), 19.

Bisetto, E., Di Pancrazio, F., Simula, M.P., Mavelli, I., Lippe, G., 2007. Mammalian ATPsynthase monomer versus dimer profiled by blue native PAGE and activity stain. Electrophoresis 28(18), 3178-3185.

Blaner, W.S., Churchich, J., 1979. Succinic semialdehyde dehydrogenase. Reactivity of lysyl residues. J Biol Chem 254(6), 1794-1798.

Blass, J.P., Lewis, C.A., 1973. Kinetic properties of the partially purified pyruvate dehydrogenase complex of ox brain. Biochem J 131(1), 31-37.

Blau, H.M., Chiu, C.P., Webster, C., 1983. Cytoplasmic activation of human nuclear genes in stable heterocaryons. Cell 32(4), 1171-1180.

Bleeker, F.E., Lamba, S., Leenstra, S., Troost, D., Hulsebos, T., Vandertop, W.P., Frattini, M., Molinari, F., Knowles, M., Cerrato, A., Rodolfo, M., Scarpa, A., Felicioni, L., Buttitta, F., Malatesta, S., Marchetti, A., Bardelli, A., 2009. IDH1 mutations at residue p.R132 (IDH1(R132)) occur frequently in high-grade gliomas but not in other solid tumors. Hum.Mutat. 30(1), 7-11.

Block, M.R., Boulay, F., Brandolin, G., Dupont, Y., Lauquin, G.J., Vignais, P.V., 1986. Fluorescent probes of the mitochondrial ADP/ATP carrier protein. Methods Enzymol 125, 639-649.

Bochud-Allemann, N., Schneider, A., 2002. Mitochondrial substrate level phosphorylation is essential for growth of procyclic Trypanosoma brucei. J Biol Chem 277(36), 32849-32854.

Bolli, R., Nalecz, K.A., Azzi, A., 1989. Monocarboxylate and alpha-ketoglutarate carriers from bovine heart mitochondria. Purification by affinity chromatography on immobilized 2-cyano-4-hydroxycinnamate. J Biol Chem 264(30), 18024-18030.

Booth, A.N., Taylor, J., Wilson, R.H., Deeds, F., 1952. The inhibitory effects of itaconic acid in vitro and in vivo. J Biol Chem 195(2), 697-702.

Bose, S., French, S., Evans, F.J., Joubert, F., Balaban, R.S., 2003. Metabolic network control of oxidative phosphorylation: multiple roles of inorganic phosphate. J Biol Chem 278(40), 39155-39165.

Bouatra, S., Aziat, F., Mandal, R., Guo, A.C., Wilson, M.R., Knox, C., Bjorndahl, T.C., Krishnamurthy, R., Saleem, F., Liu, P., Dame, Z.T., Poelzer, J., Huynh, J., Yallou, F.S., Psychogios, N., Dong, E., Bogumil, R., Roehring, C., Wishart, D.S., 2013. The human urine metabolome. PLoS One 8(9), e73076.

Boyer, P.D., 2001. Toward an adequate scheme for the ATP synthase catalysis. Biochemistry (Mosc) 66(10), 1058-1066.

Brand, M.D., Chappell, J.B., 1974. Permeability of mitochondria from rat brain and rat liver to GABA. J Neurochem 22(1), 47-51.

Brand, M.D., Harper, M.E., Taylor, H.C., 1993. Control of the effective P/O ratio of oxidative phosphorylation in liver mitochondria and hepatocytes. Biochem J 291 (Pt 3), 739-748.

Brand, M.D., Vallis, B.P., Kesseler, A., 1994. The sum of flux control coefficients in the electron-transport chain of mitochondria. Eur J Biochem 226(3), 819-829.

Brandolin, G., Marty, I., Vignais, P.V., 1990. Kinetics of nucleotide transport in rat heart mitochondria studied by a rapid filtration technique. Biochemistry 29(41), 9720-9727.

Bremer, J., Davis, E.J., 1975. Studies on the active transfer of reducing equivalents into mitochondria via the malate-aspartate shuttle. Biochim Biophys Acta 376(3), 387-397.

Bround, M.J., Bers, D.M., Molkentin, J.D., 2020. A 20/20 view of ANT function in mitochondrial biology and necrotic cell death. J Mol Cell Cardiol 144, A3-A13.

Brown, M.R., Sullivan, P.G., Dorenbos, K.A., Modafferi, E.A., Geddes, J.W., Steward, O., 2004. Nitrogen disruption of synaptoneurosomes: an alternative method to isolate brain mitochondria. J Neurosci Methods 137(2), 299-303.

Browne, S.E., Beal, M.F., 2002. Toxin-induced mitochondrial dysfunction. Int Rev Neurobiol 53, 243-279.

Bubber, P., Haroutunian, V., Fisch, G., Blass, J.P., Gibson, G.E., 2005. Mitochondrial abnormalities in Alzheimer brain: mechanistic implications. Ann Neurol 57(5), 695-703.

Bubber, P., Hartounian, V., Gibson, G.E., Blass, J.P., 2011. Abnormalities in the tricarboxylic acid (TCA) cycle in the brains of schizophrenia patients. Eur Neuropsychopharmacol 21(3), 254-260.

Budd, S.L., Nicholls, D.G., 1996. A reevaluation of the role of mitochondria in neuronal Ca2+ homeostasis. J Neurochem 66(1), 403-411.

Bui, D., Ravasz, D., Chinopoulos, C., 2019. The Effect of 2-Ketobutyrate on Mitochondrial Substrate-Level Phosphorylation. Neurochem Res 44(10), 2301-2306.

Butterworth, R.F., Besnard, A.M., 1990. Thiamine-dependent enzyme changes in temporal cortex of patients with Alzheimer's disease. Metab Brain Dis 5(4), 179-184.

Butterworth, R.F., Kril, J.J., Harper, C.G., 1993. Thiamine-dependent enzyme changes in the brains of alcoholics: relationship to the Wernicke-Korsakoff syndrome. Alcohol Clin Exp Res 17(5), 1084-1088.

Byczkowski, J., Zychlinski, L., Tluczkiewicz, J., 1979. Interaction of vanadate with respiratory chain of rat liver and wheat seedling mitochondria. Int J Biochem 10(12), 1007-1011.

Cahill, G.F., Jr., Veech, R.L., 2003. Ketoacids? Good medicine? Trans Am Clin Climatol Assoc 114, 149-161; discussion 162-143.

Calingasan, N.Y., Baker, H., Sheu, K.F., Gibson, G.E., 1994. Distribution of the alpha-ketoglutarate dehydrogenase complex in rat brain. J Comp Neurol 346(3), 461-479.

Calingasan, N.Y., Ho, D.J., Wille, E.J., Campagna, M.V., Ruan, J., Dumont, M., Yang, L., Shi, Q., Gibson, G.E., Beal, M.F., 2008. Influence of mitochondrial enzyme deficiency on adult neurogenesis in mouse models of neurodegenerative diseases. Neuroscience 153(4), 986-996.

Campanella, M., Casswell, E., Chong, S., Farah, Z., Wieckowski, M.R., Abramov, A.Y., Tinker, A., Duchen, M.R., 2008. Regulation of mitochondrial structure and function by the F1Fo-ATPase inhibitor protein, IF1. Cell Metab 8(1), 13-25.

Cantley, L.C., Jr., Josephson, L., Warner, R., Yanagisawa, M., Lechene, C., Guidotti, G., 1977. Vanadate is a potent (Na,K)-ATPase inhibitor found in ATP derived from muscle. J Biol Chem 252(21), 7421-7423.

Canto, C., Menzies, K.J., Auwerx, J., 2015. NAD(+) Metabolism and the Control of Energy Homeostasis: A Balancing Act between Mitochondria and the Nucleus. Cell Metab 22(1), 31-53.

Carrozzo, R., Dionisi-Vici, C., Steuerwald, U., Lucioli, S., Deodato, F., Di Giandomenico, S., Bertini, E., Franke, B., Kluijtmans, L.A., Meschini, M.C., Rizzo, C., Piemonte, F., Rodenburg, R., Santer, R., Santorelli, F.M., van Rooij, A., Vermunt-de Koning, D., Morava, E., Wevers, R.A., 2007. SUCLA2 mutations are associated with mild methylmalonic aciduria, Leigh-like encephalomyopathy, dystonia and deafness. Brain 130(Pt 3), 862-874.

Carrozzo, R., Verrigni, D., Rasmussen, M., de Coo, R., Amartino, H., Bianchi, M., Buhas, D., Mesli, S., Naess, K., Born, A.P., Woldseth, B., Prontera, P., Batbayli, M., Ravn, K., Joensen, F., Cordelli, D.M., Santorelli, F.M., Tulinius, M., Darin, N., Duno, M., Jouvencel, P., Burlina, A., Stangoni, G., Bertini, E., Redonnet-Vernhet, I., Wibrand, F., Dionisi-Vici, C., Uusimaa, J., Vieira, P., Osorio, A.N., McFarland, R., Taylor, R.W., Holme, E., Ostergaard, E., 2016. Succinate-CoA ligase deficiency due to mutations in SUCLA2 and SUCLG1: phenotype and genotype correlations in 71 patients. J Inherit Metab Dis 39(2), 243-252.

Cash, C., Ciesielski, L., Maitre, M., Mandel, P., 1977. Purification and properties of rat brain succinic semialdehyde dehydrogenase. Biochimie 59(3), 257-268.

Cash, C.D., Maitre, M., Ossola, L., Mandel, P., 1978. Purification and properties of two succinate semialdehyde dehydrogenases from human brain. Biochim Biophys Acta 524(1), 26-36.

Cerdan, S., Kunnecke, B., Seelig, J., 1990. Cerebral metabolism of [1,2-13C2]acetate as detected by in vivo and in vitro 13C NMR. Journal of Biological Chemistry 265(22), 12916-12926.

Chalmers, R.A., Lawson, A.M., Watts, R.W., Tavill, A.S., Kamerling, J.P., Hey, E., Ogilvie, D., 1980. D-2-hydroxyglutaric aciduria: case report and biochemical studies. J Inherit Metab Dis 3(1), 11-15.

Chambliss, K.L., Zhang, Y.A., Rossier, E., Vollmer, B., Gibson, K.M., 1995. Enzymatic and immunologic identification of succinic semialdehyde dehydrogenase in rat and human neural and nonneural tissues. J Neurochem 65(2), 851-855.

Chan, T.S., Teng, S., Wilson, J.X., Galati, G., Khan, S., O'Brien, P.J., 2002. Coenzyme Q cytoprotective mechanisms for mitochondrial complex I cytopathies involves NAD(P)H: quinone oxidoreductase 1(NQO1). Free Radic Res 36(4), 421-427.

Chance, B., Mela, L., 1966. Hydrogen ion concentration changes in mitochondrial membranes. J Biol Chem 241(20), 4588-4599.

Chang, L.O., Morris, H.P., 1973. Enzymatic and immunological studies on pyruvate carboxylase in livers and liver tumors. Cancer Res. 33(9), 2034-2041.

Chang, S.M., Parney, I.F., Huang, W., Anderson, F.A., Jr., Asher, A.L., Bernstein, M., Lillehei, K.O., Brem, H., Berger, M.S., Laws, E.R., Glioma Outcomes Project, I., 2005. Patterns of care for adults with newly diagnosed malignant glioma. JAMA 293(5), 557-564.

Chapple, S.J., Siow, R.C., Mann, G.E., 2012. Crosstalk between Nrf2 and the proteasome: therapeutic potential of Nrf2 inducers in vascular disease and aging. Int J Biochem Cell Biol 44(8), 1315-1320.

Chen, Q., Kirk, K., Shurubor, Y.I., Zhao, D., Arreguin, A.J., Shahi, I., Valsecchi, F., Primiano, G., Calder, E.L., Carelli, V., Denton, T.T., Beal, M.F., Gross, S.S., Manfredi, G., D'Aurelio, M., 2018. Rewiring of Glutamine Metabolism Is a Bioenergetic Adaptation of Human Cells with Mitochondrial DNA Mutations. Cell Metab 27(5), 1007-1025 e1005.

Chen, Z., Zhong, C., 2013. Decoding Alzheimer's disease from perturbed cerebral glucose metabolism: implications for diagnostic and therapeutic strategies. Prog Neurobiol 108, 21-43.

Cheng, T., Sudderth, J., Yang, C., Mullen, A.R., Jin, E.S., Mates, J.M., DeBerardinis, R.J., 2011a. Pyruvate carboxylase is required for glutamine-independent growth of tumor cells. Proc.Natl.Acad.Sci.U.S.A 108(21), 8674-8679.

Cheng, T., Sudderth, J., Yang, C., Mullen, A.R., Jin, E.S., Mates, J.M., Deberardinis, R.J., 2011b. Pyruvate carboxylase is required for glutamine-independent growth of tumor cells. Proc Natl Acad Sci U S A.

Cherubini, E., Gaiarsa, J.L., Ben-Ari, Y., 1991. GABA: an excitatory transmitter in early postnatal life. Trends Neurosci 14(12), 515-519.

Chesnelong, C., Chaumeil, M.M., Blough, M.D., Al-Najjar, M., Stechishin, O.D., Chan, J.A., Pieper, R.O., Ronen, S.M., Weiss, S., Luchman, H.A., Cairncross, J.G., 2014. Lactate dehydrogenase A silencing in IDH mutant gliomas. Neuro Oncol 16(5), 686-695.

Chess, D.J., Khairallah, R.J., O'Shea, K.M., Xu, W., Stanley, W.C., 2009. A high-fat diet increases adiposity but maintains mitochondrial oxidative enzymes without affecting development of heart failure with pressure overload. Am J Physiol Heart Circ Physiol 297(5), H1585-1593.

Chinopoulos, C., 2011a. The "B Space" of mitochondrial phosphorylation. J.Neurosci.Res. 89(12), 1897-1904.

Chinopoulos, C., 2011b. Mitochondrial consumption of cytosolic ATP: not so fast. FEBS Lett. 585(9), 1255-1259.

Chinopoulos, C., 2013. Which way does the citric acid cycle turn during hypoxia? The critical role of alpha-ketoglutarate dehydrogenase complex. J.Neurosci.Res. 91(8), 1030-1043.

Chinopoulos, C., 2018. OXPHOS Defects Due to mtDNA Mutations: Glutamine to the Rescue! Cell Metab 27(6), 1165-1167.

Chinopoulos, C., 2019. Succinate in ischemia: Where does it come from? Int J Biochem Cell Biol 115, 105580.

Chinopoulos, C., 2020a. Acute sources of mitochondrial NAD(+) during respiratory chain dysfunction. Exp Neurol 327, 113218.

Chinopoulos, C., 2020b. From Glucose to Lactate and Transiting Intermediates Through Mitochondria, Bypassing Pyruvate Kinase: Considerations for Cells Exhibiting Dimeric PKM2 or Otherwise Inhibited Kinase Activity. Front Physiol 11, 543564.

Chinopoulos, C., 2020c. Quantification of mitochondrial DNA from peripheral tissues: Limitations in predicting the severity of neurometabolic disorders and proposal of a novel diagnostic test. Mol Aspects Med 71, 100834.

Chinopoulos, C., 2021. The Mystery of Extramitochondrial Proteins Lysine Succinylation. Int J Mol Sci 22(11).

Chinopoulos, C., Adam-Vizi, V., 2010a. Mitochondria as ATP consumers in cellular pathology. Biochim Biophys Acta 1802(1), 221-227.

Chinopoulos, C., Adam-Vizi, V., 2010b. Mitochondrial Ca2+ sequestration and precipitation revisited. FEBS J 277(18), 3637-3651.

Chinopoulos, C., Batzios, S., van den Heuvel, L.P., Rodenburg, R., Smeets, R., Waterham, H.R., Turkenburg, M., Ruiter, J.P., Wanders, R.J.A., Doczi, J., Horvath, G., Dobolyi, A., Vargiami, E., Wevers, R.A., Zafeiriou, D., 2019. Mutated SUCLG1 causes mislocalization of SUCLG2 protein, morphological alterations of mitochondria and an early-onset severe neurometabolic disorder. Mol Genet Metab 126(1), 43-52.

Chinopoulos, C., Gerencser, A.A., Doczi, J., Fiskum, G., Adam-Vizi, V., 2004. Inhibition of glutamate-induced delayed calcium deregulation by 2-APB and La3+ in cultured cortical neurones. J Neurochem 91(2), 471-483.

Chinopoulos, C., Gerencser, A.A., Mandi, M., Mathe, K., Torocsik, B., Doczi, J., Turiak, L., Kiss, G., Konrad, C., Vajda, S., Vereczki, V., Oh, R.J., Adam-Vizi, V., 2010. Forward operation of adenine nucleotide translocase during F0F1-ATPase reversal: critical role of matrix substrate-level phosphorylation. FASEB J. 24(7), 2405-2416.

Chinopoulos, C., Kiss, G., Kawamata, H., Starkov, A.A., 2014. Measurement of ADP-ATP exchange in relation to mitochondrial transmembrane potential and oxygen consumption. Methods Enzymol 542, 333-348.

Chinopoulos, C., Konrad, C., Kiss, G., Metelkin, E., Torocsik, B., Zhang, S.F., Starkov, A.A., 2011. Modulation of F0F1-ATP synthase activity by cyclophilin D regulates matrix adenine nucleotide levels. FEBS J 278(7), 1112-1125.

Chinopoulos, C., Seyfried, T.N., 2018. Mitochondrial Substrate-Level Phosphorylation as Energy Source for Glioblastoma: Review and Hypothesis. ASN Neuro 10, 1759091418818261.

Chinopoulos, C., Starkov, A.A., Fiskum, G., 2003. Cyclosporin A-insensitive permeability transition in brain mitochondria: inhibition by 2-aminoethoxydiphenyl borate. J Biol Chem 278(30), 27382-27389.

Chinopoulos, C., Starkov, A.A., Grigoriev, S., Dejean, L.M., Kinnally, K.W., Liu, X., Ambudkar, I.S., Fiskum, G., 2005. Diacylglycerols activate mitochondrial cationic channel(s) and release sequestered Ca(2+). J Bioenerg Biomembr 37(4), 237-247.

Chinopoulos, C., Tretter, L., Adam-Vizi, V., 1999. Depolarization of in situ mitochondria due to hydrogen peroxide-induced oxidative stress in nerve terminals: inhibition of alpha-ketoglutarate dehydrogenase. J Neurochem 73(1), 220-228.

Chinopoulos, C., Vajda, S., Csanady, L., Mandi, M., Mathe, K., Adam-Vizi, V., 2009. A novel kinetic assay of mitochondrial ATP-ADP exchange rate mediated by the ANT. Biophys J 96(6), 2490-2504.

Choi, S.W., Gerencser, A.A., Nicholls, D.G., 2009. Bioenergetic analysis of isolated cerebrocortical nerve terminals on a microgram scale: spare respiratory capacity and stochastic mitochondrial failure. J Neurochem 109(4), 1179-1191.

Chouchani, E.T., Pell, V.R., Gaude, E., Aksentijevic, D., Sundier, S.Y., Robb, E.L., Logan, A., Nadtochiy, S.M., Ord, E.N., Smith, A.C., Eyassu, F., Shirley, R., Hu, C.H., Dare, A.J., James, A.M., Rogatti, S., Hartley, R.C., Eaton, S., Costa, A.S., Brookes, P.S., Davidson, S.M., Duchen, M.R., Saeb-Parsy, K., Shattock, M.J., Robinson, A.J., Work, L.M., Frezza, C., Krieg, T., Murphy, M.P., 2014. Ischaemic accumulation of succinate controls reperfusion injury through mitochondrial ROS. Nature 515(7527), 431-435.

Christofk, H.R., Vander Heiden, M.G., Wu, N., Asara, J.M., Cantley, L.C., 2008. Pyruvate kinase M2 is a phosphotyrosine-binding protein. Nature 452(7184), 181-186.

Clark, J.B., Land, J.M., 1979. Inhibitors of mitochondrial enzymes. Pharmacol Ther 7(2), 351-373.

Climent, F., Bartrons, R., Pons, G., Carreras, J., 1981. Effect of vanadate on phosphoryl transfer enzymes involved in glucose metabolism. Biochem Biophys Res Commun 101(2), 570-576.

Cohen, S.M., 1987. Effects of insulin on perfused liver from streptozotocin-diabetic and untreated rats: 13C NMR assay of pyruvate kinase flux. Biochemistry 26(2), 573-580.

Colpa-Boonstra, J.P., Slater, E.C., 1958. The possible role of vitamin K in the respiratory chain. Biochim Biophys Acta 27(1), 122-133.

Conover, T.E., Ernster, L., 1960. Mitochondrial oxidation of extra-mitochondrial TPNH1 mediated by purified DT diaphorase. Biochem Biophys Res Commun 2, 26-30.

Conover, T.E., Ernster, L., 1962. DT diaphorase. II. Relation to respiratory chain of intact mitochondira. Biochim Biophys Acta 58, 189-200.

Conover, T.E., Ernster, L., 1963. DT diaphorase. IV. Coupling of extramitochondrial reduced pyridine nucleotide oxidation to mitochondrial respiratory chain. Biochim Biophys Acta 67, 268-280.

Conti, F., Melone, M., De Biasi, S., Minelli, A., Brecha, N.C., Ducati, A., 1998. Neuronal and glial localization of GAT-1, a high-affinity gamma-aminobutyric acid plasma membrane transporter, in human cerebral cortex: with a note on its distribution in monkey cortex. J Comp Neurol 396(1), 51-63.

Conti, F., Zuccarello, L.V., Barbaresi, P., Minelli, A., Brecha, N.C., Melone, M., 1999. Neuronal, glial, and epithelial localization of gamma-aminobutyric acid transporter 2, a high-affinity gamma-aminobutyric acid plasma membrane transporter, in the cerebral cortex and neighboring structures. J Comp Neurol 409(3), 482-494.

Cordes, T., Michelucci, A., Hiller, K., 2015. Itaconic Acid: The Surprising Role of an Industrial Compound as a Mammalian Antimicrobial Metabolite. Annu Rev Nutr 35, 451-473.

Corkey, B.E., Duszynski, J., Rich, T.L., Matschinsky, B., Williamson, J.R., 1986. Regulation of free and bound magnesium in rat hepatocytes and isolated mitochondria. J Biol Chem 261(6), 2567-2574.

Coskun, P.E., Beal, M.F., Wallace, D.C., 2004. Alzheimer's brains harbor somatic mtDNA control-region mutations that suppress mitochondrial transcription and replication. Proc Natl Acad Sci U S A 101(29), 10726-10731.

Coty, W.A., Pedersen, P.L., 1974. Phosphate transport in rat liver mitochondria. Kinetics and energy requirements. J Biol Chem 249(8), 2593-2598.

Crane, R.K., Lipmann, F., 1953. The effect of arsenate on aerobic phosphorylation. J Biol Chem 201(1), 235-243.

Cresteil, T., Jaiswal, A.K., 1991. High levels of expression of the NAD(P)H:quinone oxidoreductase (NQO1) gene in tumor cells compared to normal cells of the same origin. Biochem Pharmacol 42(5), 1021-1027.

Crinson, M., Nicholls, P., 1992. Routes of electron transfer in beef heart cytochrome c oxidase: is there a unique pathway used by all reductants? Biochem Cell Biol 70(5), 301-308.

Cross, R.L., Muller, V., 2004. The evolution of A-, F-, and V-type ATP synthases and ATPases: reversals in function and changes in the H+/ATP coupling ratio. FEBS Lett 576(1-2), 1-4.

Crunelli, V., Emri, Z., Leresche, N., 2006. Unravelling the brain targets of gamma-hydroxybutyric acid. Curr Opin Pharmacol 6(1), 44-52.

Cuddapah, V.A., Robel, S., Watkins, S., Sontheimer, H., 2014. A neurocentric perspective on glioma invasion. Nat Rev Neurosci 15(7), 455-465.

Cui, D., Morris, M.E., 2009. The drug of abuse gamma-hydroxybutyrate is a substrate for sodium-coupled monocarboxylate transporter (SMCT) 1 (SLC5A8): characterization of SMCT-mediated uptake and inhibition. Drug Metab Dispos 37(7), 1404-1410.

Cunningham, J., Clarke, D.D., Nicklas, W.J., 1980. Oxidative metabolism of 4-aminobutyrate by rat brain mitochondria: inhibition by branched-chain fatty acid. J Neurochem 34(1), 197-202.

Dahlberg, D., Struys, E.A., Jansen, E.E., Morkrid, L., Midttun, O., Hassel, B., 2017. Cyst Fluid From Cystic, Malignant Brain Tumors: A Reservoir of Nutrients, Including Growth Factor-Like Nutrients, for Tumor Cells. Neurosurgery 80(6), 917-924.

Dahout-Gonzalez, C., Nury, H., Trezeguet, V., Lauquin, G.J., Pebay-Peyroula, E., Brandolin, G., 2006. Molecular, functional, and pathological aspects of the mitochondrial ADP/ATP carrier. Physiology (Bethesda) 21, 242-249.

Dang, C.V., Kim, J.W., Gao, P., Yustein, J., 2008. The interplay between MYC and HIF in cancer. Nat.Rev.Cancer 8(1), 51-56.

Dang, L., White, D.W., Gross, S., Bennett, B.D., Bittinger, M.A., Driggers, E.M., Fantin, V.R., Jang, H.G., Jin, S., Keenan, M.C., Marks, K.M., Prins, R.M., Ward, P.S., Yen, K.E., Liau, L.M., Rabinowitz, J.D., Cantley, L.C., Thompson, C.B., Vander Heiden, M.G., Su, S.M., 2009. Cancer-associated IDH1 mutations produce 2-hydroxyglutarate. Nature 462(7274), 739-744.

David, C.J., Chen, M., Assanah, M., Canoll, P., Manley, J.L., 2010. HnRNP proteins controlled by c-Myc deregulate pyruvate kinase mRNA splicing in cancer. Nature 463(7279), 364-368.

Davies, D.R., Hol, W.G., 2004. The power of vanadate in crystallographic investigations of phosphoryl transfer enzymes. FEBS Lett 577(3), 315-321.

Dawson, D.M., Goodfriend, T.L., Kaplan, N.O., 1964. LACTIC DEHYDROGENASES: FUNCTIONS OF THE TWO TYPES RATES OF SYNTHESIS OF THE TWO MAJOR FORMS CAN BE CORRELATED WITH METABOLIC DIFFERENTIATION. Science 143(3609), 929-933.

DeBerardinis, R.J., Cheng, T., 2010. Q's next: the diverse functions of glutamine in metabolism, cell biology and cancer. Oncogene 29(3), 313-324.

DeBerardinis, R.J., Mancuso, A., Daikhin, E., Nissim, I., Yudkoff, M., Wehrli, S., Thompson, C.B., 2007. Beyond aerobic glycolysis: transformed cells can engage in glutamine metabolism that exceeds the requirement for protein and nucleotide synthesis. Proc.Natl.Acad.Sci.U.S.A 104(49), 19345-19350.

Dedukhova, V.I., Kirillova, G.P., Mokhova, E.N., Rozovskaia, I.A., Skulachev, V.P., 1986. [Effect of menadione and vicasol on mitochondrial energy during inhibition of initiation sites of the respiration chain]. Biokhimiia 51(4), 567-573.

Degrandi, D., Hoffmann, R., Beuter-Gunia, C., Pfeffer, K., 2009. The proinflammatory cytokine-induced IRG1 protein associates with mitochondria. J Interferon Cytokine Res 29(1), 55-67.

Deighton, R.F., Le Bihan, T., Martin, S.F., Gerth, A.M., McCulloch, M., Edgar, J.M., Kerr, L.E., Whittle, I.R., McCulloch, J., 2014. Interactions among mitochondrial proteins altered in glioblastoma. Journal of neuro-oncology 118(2), 247-256.

Demin, O.V., Gorianin, II, Kholodenko, B.N., Westerhoff, H.V., 2001. [Kinetic modeling of energy metabolism and generation of active forms of oxygen in hepatocyte mitochondria]. Mol Biol (Mosk) 35(6), 1095-1104.

Demin, O.V., Westerhoff, H.V., Kholodenko, B.N., 1998. Mathematical modelling of superoxide generation with the bc1 complex of mitochondria. Biochemistry (Mosc) 63(6), 634-649.

Derr, R.L., Ye, X., Islas, M.U., Desideri, S., Saudek, C.D., Grossman, S.A., 2009. Association between hyperglycemia and survival in patients with newly diagnosed glioblastoma. J Clin Oncol 27(7), 1082-1086.

Dervartanian, D.V., Veeger, C., 1964. Studies on Succinate Dehydrogenase. I. Spectral Properties of the Purified Enzyme and Formation of Enzyme-Competitive Inhibitor Complexes. Biochim Biophys Acta 92, 233-247.

Desai, S., Ding, M., Wang, B., Lu, Z., Zhao, Q., Shaw, K., Yung, W.K., Weinstein, J.N., Tan, M., Yao, J., 2014. Tissue-specific isoform switch and DNA hypomethylation of the pyruvate kinase PKM gene in human cancers. Oncotarget 5(18), 8202-8210.

Dobolyi, A., Bago, A., Palkovits, M., Nemeria, N.S., Jordan, F., Doczi, J., Ambrus, A., Adam-Vizi, V., Chinopoulos, C., 2020. Exclusive neuronal detection of KGDHC-specific subunits in the adult human brain cortex despite pancellular protein lysine succinylation. Brain Struct Funct 225(2), 639-667.

Dobolyi, A., Bago, A.G., Gal, A., Molnar, M.J., Palkovits, M., Adam-Vizi, V., Chinopoulos, C., 2015a. Localization of SUCLA2 and SUCLG2 subunits of succinyl CoA ligase within the cerebral cortex suggests the absence of matrix substrate-level phosphorylation in glial cells of the human brain. J.Bioenerg.Biomembr. 47(1-2), 33-41.

Dobolyi, A., Ostergaard, E., Bago, A.G., Doczi, T., Palkovits, M., Gal, A., Molnar, M.J., Adam-Vizi, V., Chinopoulos, C., 2015b. Exclusive neuronal expression of SUCLA2 in the human brain. Brain Struct.Funct. 220(1), 135-151.

Doherty, J.R., Cleveland, J.L., 2013. Targeting lactate metabolism for cancer therapeutics. J.Clin.Invest 123(9), 3685-3692.

Dolce, V., Fiermonte, G., Runswick, M.J., Palmieri, F., Walker, J.E., 2001. The human mitochondrial deoxynucleotide carrier and its role in the toxicity of nucleoside antivirals. Proc Natl Acad Sci U S A 98(5), 2284-2288.

Dominguez-Ramirez, L., Gomez-Puyou, A., de Gomez-Puyou, M.T., 2006. A hinge of the endogeneous ATP synthase inhibitor protein: the link between inhibitory and anchoring domains. Proteins 65(4), 999-1007.

Dong, H., Shertzer, H.G., Genter, M.B., Gonzalez, F.J., Vasiliou, V., Jefcoate, C., Nebert, D.W., 2013. Mitochondrial targeting of mouse NQO1 and CYP1B1 proteins. Biochem Biophys Res Commun 435(4), 727-732.

Donti, T.R., Stromberger, C., Ge, M., Eldin, K.W., Craigen, W.J., Graham, B.H., 2014. Screen for abnormal mitochondrial phenotypes in mouse embryonic stem cells identifies a model for succinyl-CoA ligase deficiency and mtDNA depletion. Dis Model Mech 7(2), 271-280.

Dragan, M., Dixon, S.J., Jaworski, E., Chan, T.S., O'Brien P, J., Wilson, J.X., 2006. Coenzyme Q(1) depletes NAD(P)H and impairs recycling of ascorbate in astrocytes. Brain Res 1078(1), 9-18.

Drenick, E.J., Alvarez, L.C., Tamasi, G.C., Brickman, A.S., 1972. Resistance to symptomatic insulin reactions after fasting. J Clin Invest 51(10), 2757-2762.

Duchen, M.R., Leyssens, A., Crompton, M., 1998. Transient mitochondrial depolarizations reflect focal sarcoplasmic reticular calcium release in single rat cardiomyocytes. J Cell Biol 142(4), 975-988.

Duee, E.D., Vignais, P.V., 1969a. Kinetics and specificity of the adenine nucleotide translocation in rat liver mitochondria. J Biol Chem 244(14), 3920-3931.

Duee, E.D., Vignais, P.V., 1969b. Kinetics of phosphorylation of intramitochondrial and extramitochondrial adenine nucleotides as related to nucleotide translocation. J Biol Chem 244(14), 3932-3940.

Dummler, K., Muller, S., Seitz, H.J., 1996. Regulation of adenine nucleotide translocase and glycerol 3-phosphate dehydrogenase expression by thyroid hormones in different rat tissues. Biochem J 317 (Pt 3), 913-918.

Dumont, M., Ho, D.J., Calingasan, N.Y., Xu, H., Gibson, G., Beal, M.F., 2009. Mitochondrial dihydrolipoyl succinyltransferase deficiency accelerates amyloid pathology and memory deficit in a transgenic mouse model of amyloid deposition. Free Radic Biol Med 47(7), 1019-1027.

Duyckaerts, C., Sluse-Goffart, C.M., Fux, J.P., Sluse, F.E., Liebecq, C., 1980. Kinetic mechanism of the exchanges catalysed by the adenine-nucleotide carrier. Eur J Biochem 106(1), 1-6.

Dzeja, P.P., Bortolon, R., Perez-Terzic, C., Holmuhamedov, E.L., Terzic, A., 2002. Energetic communication between mitochondria and nucleus directed by catalyzed phosphotransfer. Proc Natl Acad Sci U S A 99(15), 10156-10161.

Eagle, H., Oyama, V.I., Levy, M., Horton, C.L., Fleischman, R., 1956. The growth response of mammalian cells in tissue culture to L-glutamine and L-glutamic acid. J.Biol.Chem 218(2), 607-616.

Edlund, C., Elhammer, A., Dallner, G., 1982. Distribution of newly synthesized DT-diaphorase in rat liver. Biosci Rep 2(11), 861-865.

Eliasson, M., Bostrom, M., DePierre, J.W., 1999. Levels and subcellular distributions of detoxifying enzymes in the ovarian corpus luteum of the pregnant and non-pregnant pig. Biochem Pharmacol 58(8), 1287-1292.

Elliott, H.R., Samuels, D.C., Eden, J.A., Relton, C.L., Chinnery, P.F., 2008. Pathogenic mitochondrial DNA mutations are common in the general population. Am J Hum Genet 83(2), 254-260.

Elpeleg, O., Miller, C., Hershkovitz, E., Bitner-Glindzicz, M., Bondi-Rubinstein, G., Rahman, S., Pagnamenta, A., Eshhar, S., Saada, A., 2005. Deficiency of the ADP-forming succinyl-CoA synthase activity is associated with encephalomyopathy and mitochondrial DNA depletion. Am J Hum Genet 76(6), 1081-1086.

Elstrom, R.L., Bauer, D.E., Buzzai, M., Karnauskas, R., Harris, M.H., Plas, D.R., Zhuang, H., Cinalli, R.M., Alavi, A., Rudin, C.M., Thompson, C.B., 2004. Akt stimulates aerobic glycolysis in cancer cells. Cancer Res 64(11), 3892-3899.

Erb, M., Hoffmann-Enger, B., Deppe, H., Soeberdt, M., Haefeli, R.H., Rummey, C., Feurer, A., Gueven, N., 2012. Features of idebenone and related short-chain quinones that rescue ATP levels under conditions of impaired mitochondrial complex I. PLoS One 7(4), e36153.

Ernster, L., Danielson, L., Ljunggren, M., 1962. DT diaphorase. I. Purification from the soluble fraction of rat-liver cytoplasm, and properties. Biochim Biophys Acta 58, 171-188.

Ernster, L., Lee, I.Y., Norling, B., Persson, B., 1969. Studies with ubiquinone-depleted submitochondrial particles. Essentiality of ubiquinone for the interaction of succinate dehydrogenase, NADH dehydrogenase, and cytochrome b. Eur J Biochem 9(3), 299-310.

Esposti, M.D., Ngo, A., Ghelli, A., Benelli, B., Carelli, V., McLennan, H., Linnane, A.W., 1996. The interaction of Q analogs, particularly hydroxydecyl benzoquinone (idebenone), with the respiratory complexes of heart mitochondria. Arch Biochem Biophys 330(2), 395-400.

Estabrook, R.W., Sacktor, B., 1958. alpha-Glycerophosphate oxidase of flight muscle mitochondria. J Biol Chem 233(4), 1014-1019.

Estrella, V., Chen, T., Lloyd, M., Wojtkowiak, J., Cornnell, H.H., Ibrahim-Hashim, A., Bailey, K., Balagurunathan, Y., Rothberg, J.M., Sloane, B.F., Johnson, J., Gatenby, R.A., Gillies, R.J., 2013. Acidity generated by the tumor microenvironment drives local invasion. Cancer Res. 73(5), 1524-1535.

Everts, B., Amiel, E., van der Windt, G.J., Freitas, T.C., Chott, R., Yarasheski, K.E., Pearce, E.L., Pearce, E.J., 2012. Commitment to glycolysis sustains survival of NO-producing inflammatory dendritic cells. Blood 120(7), 1422-1431.

Fabiato, A., Fabiato, F., 1979. Calculator programs for computing the composition of the solutions containing multiple metals and ligands used for experiments in skinned muscle cells. J Physiol (Paris) 75(5), 463-505.

Faig, M., Bianchet, M.A., Winski, S., Hargreaves, R., Moody, C.J., Hudnott, A.R., Ross, D., Amzel, L.M., 2001. Structure-based development of anticancer drugs: complexes of NAD(P)H:quinone oxidoreductase 1 with chemotherapeutic quinones. Structure 9(8), 659-667.

Fantin, V.R., St-Pierre, J., Leder, P., 2006. Attenuation of LDH-A expression uncovers a link between glycolysis, mitochondrial physiology, and tumor maintenance. Cancer Cell 9(6), 425-434.

Fatehi, M., Hunt, C., Ma, R., Toyota, B.D., 2018. Persistent Disparities in Survival for Patients with Glioblastoma. World Neurosurg.

Faustin, B., Rossignol, R., Rocher, C., Benard, G., Malgat, M., Letellier, T., 2004. Mobilization of adenine nucleotide translocators as molecular bases of the biochemical threshold effect observed in mitochondrial diseases. J Biol Chem 279(19), 20411-20421.

Feichtinger, R.G., Weis, S., Mayr, J.A., Zimmermann, F., Geilberger, R., Sperl, W., Kofler, B., 2014. Alterations of oxidative phosphorylation complexes in astrocytomas. Glia 62(4), 514-525.

Ferguson, S.J., 2000. ATP synthase: what dictates the size of a ring? Curr Biol 10(21), R804-808.

Fernandez-Canon, J.M., Baetscher, M.W., Finegold, M., Burlingame, T., Gibson, K.M., Grompe, M., 2002. Maleylacetoacetate isomerase (MAAI/GSTZ)-deficient mice reveal a glutathione-dependent nonenzymatic bypass in tyrosine catabolism. Mol Cell Biol 22(13), 4943-4951.

Fiermonte, G., De Leonardis, F., Todisco, S., Palmieri, L., Lasorsa, F.M., Palmieri, F., 2004. Identification of the mitochondrial ATP-Mg/Pi transporter. Bacterial expression, reconstitution, functional characterization, and tissue distribution. J Biol Chem 279(29), 30722-30730.

Figueira, T.R., Melo, D.R., Vercesi, A.E., Castilho, R.F., 2012. Safranine as a fluorescent probe for the evaluation of mitochondrial membrane potential in isolated organelles and permeabilized cells. Methods Mol Biol 810, 103-117.

Fiorillo, M., Sotgia, F., Sisci, D., Cappello, A.R., Lisanti, M.P., 2017. Mitochondrial "power" drives tamoxifen resistance: NQO1 and GCLC are new therapeutic targets in breast cancer. Oncotarget 8(12), 20309-20327.

Fisher, P.G., Buffler, P.A., 2005. Malignant gliomas in 2005: where to GO from here? Jama 293(5), 615-617.

Flatmark, T., 1967. Multiple molecular forms of bovine heart cytochrome c. V. A comparative study of their physicochemical properties and their reactions in biological systems. J Biol Chem 242(10), 2454-2459.

Flavahan, W.A., Wu, Q., Hitomi, M., Rahim, N., Kim, Y., Sloan, A.E., Weil, R.J., Nakano, I., Sarkaria, J.N., Stringer, B.W., Day, B.W., Li, M., Lathia, J.D., Rich, J.N., Hjelmeland, A.B., 2013. Brain tumor initiating cells adapt to restricted nutrition through preferential glucose uptake. Nat Neurosci 16(10), 1373-1382.

Flechl, B., Ackerl, M., Sax, C., Dieckmann, K., Crevenna, R., Gaiger, A., Widhalm, G., Preusser, M., Marosi, C., 2012. Neurocognitive and sociodemographic functioning of glioblastoma long-term survivors. Journal of neuro-oncology 109(2), 331-339.

Forman, N.G., Wilson, D.F., 1983. Dependence of mitochondrial oxidative phosphorylation on activity of the adenine nucleotide translocase. J Biol Chem 258(14), 8649-8655.

Formentini, L., Sanchez-Arago, M., Sanchez-Cenizo, L., Cuezva, J.M., 2012. The mitochondrial ATPase inhibitory factor 1 triggers a ROS-mediated retrograde prosurvival and proliferative response. Mol.Cell 45(6), 731-742.

Fredericks, M., Ramsey, R.B., 1978. 3-Oxo acid coenzyme A transferase activity in brain and tumors of the nervous system. J Neurochem 31(6), 1529-1531.

Freeman, H.C., Hugill, A., Dear, N.T., Ashcroft, F.M., Cox, R.D., 2006. Deletion of nicotinamide nucleotide transhydrogenase: a new quantitive trait locus accounting for glucose intolerance in C57BL/6J mice. Diabetes 55(7), 2153-2156.

Freidmann, B., Goodman, E.H., Jr., Saunders, H.L., Kostos, V., Weinhouse, S., 1971. An estimation of pyruvate recycling during gluconeogenesis in the perfused rat liver. Arch.Biochem.Biophys. 143(2), 566-578.

Fuchs, B.C., Bode, B.P., 2005. Amino acid transporters ASCT2 and LAT1 in cancer: partners in crime? Semin.Cancer Biol. 15(4), 254-266.

Gadsby, D.C., Nakao, M., 1989. Steady-state current-voltage relationship of the Na/K pump in guinea pig ventricular myocytes. J Gen Physiol 94(3), 511-537.

Gaikwad, A., Long, D.J., 2nd, Stringer, J.L., Jaiswal, A.K., 2001. In vivo role of NAD(P)H:quinone oxidoreductase 1 (NQO1) in the regulation of intracellular redox state and accumulation of abdominal adipose tissue. J Biol Chem 276(25), 22559-22564.

Gajewski, C.D., Yang, L., Schon, E.A., Manfredi, G., 2003. New insights into the bioenergetics of mitochondrial disorders using intracellular ATP reporters. Mol Biol Cell 14(9), 3628-3635.

Garate, M., Wong, R.P., Campos, E.I., Wang, Y., Li, G., 2008. NAD(P)H quinone oxidoreductase 1 inhibits the proteasomal degradation of the tumour suppressor p33(ING1b). EMBO Rep 9(6), 576-581.

Garedew, A., Henderson, S.O., Moncada, S., 2010. Activated macrophages utilize glycolytic ATP to maintain mitochondrial membrane potential and prevent apoptotic cell death. Cell Death Differ 17(10), 1540-1550.

Garry, D.J., Coulter, H.D., McIntee, T.J., Wu, J.Y., Sorenson, R.L., 1987. Immunoreactive GABA transaminase within the pancreatic islet is localized in mitochondria of the B-cell. J Histochem Cytochem 35(8), 831-836.

Gaude, E., Schmidt, C., Gammage, P.A., Dugourd, A., Blacker, T., Chew, S.P., Saez-Rodriguez, J., O'Neill, J.S., Szabadkai, G., Minczuk, M., Frezza, C., 2018. NADH Shuttling Couples Cytosolic Reductive Carboxylation of Glutamine with Glycolysis in Cells with Mitochondrial Dysfunction. Mol Cell 69(4), 581-593 e587.

Gerencser, A.A., Adam-Vizi, V., 2005. Mitochondrial Ca2+ dynamics reveals limited intramitochondrial Ca2+ diffusion. Biophys J 88(1), 698-714.

Gerencser, A.A., Chinopoulos, C., Birket, M.J., Jastroch, M., Vitelli, C., Nicholls, D.G., Brand, M.D., 2012. Quantitative measurement of mitochondrial membrane potential in cultured cells: calcium-induced de- and hyperpolarization of neuronal mitochondria. J Physiol 590(12), 2845-2871.

Gerencser, A.A., Mark, K.A., Hubbard, A.E., Divakaruni, A.S., Mehrabian, Z., Nicholls, D.G., Polster, B.M., 2009a. Real-time visualization of cytoplasmic calpain activation and calcium deregulation in acute glutamate excitotoxicity. J Neurochem 110(3), 990-1004.

Gerencser, A.A., Neilson, A., Choi, S.W., Edman, U., Yadava, N., Oh, R.J., Ferrick, D.A., Nicholls, D.G., Brand, M.D., 2009b. Quantitative microplate-based respirometry with correction for oxygen diffusion. Anal Chem 81(16), 6868-6878.

Gerhard, D.S., Wagner, L., Feingold, E.A., Shenmen, C.M., Grouse, L.H., Schuler, G., Klein, S.L., Old, S., Rasooly, R., Good, P., Guyer, M., Peck, A.M., Derge, J.G., Lipman, D., Collins, F.S., Jang, W., Sherry, S., Feolo, M., Misquitta, L., Lee, E., Rotmistrovsky, K., Greenhut, S.F., Schaefer, C.F., Buetow, K., Bonner, T.I., Haussler, D., Kent, J., Kiekhaus, M., Furey, T., Brent, M., Prange, C., Schreiber, K., Shapiro, N., Bhat, N.K., Hopkins, R.F., Hsie, F., Driscoll, T., Soares, M.B., Casavant, T.L., Scheetz, T.E., Brown-stein, M.J., Usdin, T.B., Toshiyuki, S., Carninci, P., Piao, Y., Dudekula, D.B., Ko, M.S., Kawakami, K., Suzuki, Y., Sugano, S., Gruber, C.E., Smith, M.R., Simmons, B., Moore, T., Waterman, R., Johnson, S.L., Ruan, Y., Wei, C.L., Mathavan, S., Gunaratne, P.H., Wu, J., Garcia, A.M., Hulyk, S.W., Fuh, E., Yuan, Y., Sneed, A., Kowis, C., Hodgson, A., Muzny, D.M., McPherson, J., Gibbs, R.A., Fahey, J., Helton, E., Ketteman, M., Madan, A., Rodrigues, S., Sanchez, A., Whiting, M., Madari, A., Young, A.C., Wetherby, K.D., Granite, S.J., Kwong, P.N., Brinkley, C.P., Pearson, R.L., Bouffard, G.G., Blakesly, R.W., Green, E.D., Dickson, M.C., Rodriguez, A.C., Grimwood, J., Schmutz, J., Myers, R.M., Butterfield, Y.S., Griffith, M., Griffith, O.L., Krzywinski, M.I., Liao, N., Morin, R., Palmquist, D., Petrescu, A.S., Skalska, U., Smailus, D.E., Stott, J.M., Schnerch, A., Schein, J.E., Jones, S.J., Holt, R.A., Baross, A., Marra, M.A., Clifton, S., Makowski, K.A., Bosak, S., Malek, J., 2004. The status, quality, and expansion of the NIH full-length cDNA project: the Mammalian Gene Collection (MGC). Genome Res. 14(10B), 2121-2127.

Ghosh, A., Bera, S., Ghosal, S., Ray, S., Basu, A., Ray, M., 2011. Differential inhibition/inactivation of mitochondrial complex I implicates its alteration in malignant cells. Biochemistry (Mosc) 76(9), 1051-1060.

Gibson, G.E., Jope, R., Blass, J.P., 1975. Decreased synthesis of acetylcholine accompanying impaired oxidation of pyruvic acid in rat brain minces. Biochem J 148(1), 17-23.

Gibson, G.E., Kingsbury, A.E., Xu, H., Lindsay, J.G., Daniel, S., Foster, O.J., Lees, A.J., Blass, J.P., 2003. Deficits in a tricarboxylic acid cycle enzyme in brains from patients with Parkinson's disease. Neurochem Int 43(2), 129-135.

Gibson, G.E., Starkov, A., Blass, J.P., Ratan, R.R., Beal, M.F., 2010. Cause and consequence: mitochondrial dysfunction initiates and propagates neuronal dysfunction, neuronal death and behavioral abnormalities in age-associated neurodegenerative diseases. Biochim Biophys Acta 1802(1), 122-134.

Gibson, G.E., Xu, H., Chen, H.L., Chen, W., Denton, T.T., Zhang, S., 2015. Alpha-ketoglutarate dehydrogenase complex-dependent succinylation of proteins in neurons and neuronal cell lines. J Neurochem 134(1), 86-96.

Gibson, G.E., Zhang, H., Sheu, K.F., Bogdanovich, N., Lindsay, J.G., Lannfelt, L., Vestling, M., Cowburn, R.F., 1998. Alpha-ketoglutarate dehydrogenase in Alzheimer brains bearing the APP670/671 mutation. Ann Neurol 44(4), 676-681.

Gibson, K.M., Nyhan, W.L., 1989. Metabolism of [U-14C]-4-hydroxybutyric acid to intermediates of the tricarboxylic acid cycle in extracts of rat liver and kidney mitochondria. Eur J Drug Metab Pharmacokinet 14(1), 61-70.

Gillies, R.J., Robey, I., Gatenby, R.A., 2008. Causes and consequences of increased glucose metabolism of cancers. J Nucl Med 49 Suppl 2, 24S-42S.

Gilliham, M., Tyerman, S.D., 2016. Linking Metabolism to Membrane Signaling: The GABA-Malate Connection. Trends Plant Sci 21(4), 295-301.

Gimenez-Roqueplo, A.P., Burnichon, N., Amar, L., Favier, J., Jeunemaitre, X., Plouin, P.F., 2008. Recent advances in the genetics of phaeochromocytoma and functional paraganglioma. Clinical and experimental pharmacology & physiology 35(4), 376-379.

Giorgio, M., Migliaccio, E., Orsini, F., Paolucci, D., Moroni, M., Contursi, C., Pelliccia, G., Luzi, L., Minucci, S., Marcaccio, M., Pinton, P., Rizzuto, R., Bernardi, P., Paolucci, F., Pelicci, P.G., 2005. Electron transfer between cytochrome c and p66Shc generates reactive oxygen species that trigger mitochondrial apoptosis. Cell 122(2), 221-233.

Giorgio, V., Bisetto, E., Soriano, M.E., Dabbeni-Sala, F., Basso, E., Petronilli, V., Forte, M.A., Bernardi, P., Lippe, G., 2009. Cyclophilin D modulates mitochondrial F0F1-ATP synthase by interacting with the lateral stalk of the complex. J Biol Chem 284(49), 33982-33988.

Giorgio, V., Petronilli, V., Ghelli, A., Carelli, V., Rugolo, M., Lenaz, G., Bernardi, P., 2012. The effects of idebenone on mitochondrial bioenergetics. Biochim Biophys Acta 1817(2), 363-369.

Giuditta, A., Strecker, H.J., 1959. Alternate pathways of pyridine nucleotide oxidation in cerebral tissue. J Neurochem 5, 50-61.

Giuditta, A., Strecker, H.J., 1961. Purification and some properties of a brain diaphorase. Biochim Biophys Acta 48, 10-19.

Giuditta, A., Strecker, H.J., 1963. Brain NADH-tretraazolium reductase activity, lipomide dehydrogenase and activating lipids. Biochim Biophys Acta 67, 316-318.

Gladkevich, A., Korf, J., Hakobyan, V.P., Melkonyan, K.V., 2006. The peripheral GABAergic system as a target in endocrine disorders. Auton Neurosci 124(1-2), 1-8.

Gomez-Diaz, C., Buron, M.I., Alcain, F.J., Gonzalez-Ojeda, R., Gonzalez-Reyes, J.A., Bello, R.I., Herman, M.D., Navas, P., Villalba, J.M., 2003. Effect of dietary coenzyme Q and fatty acids on the antioxidant status of rat tissues. Protoplasma 221(1-2), 11-17.

Gonzalez-Billault, C., Demandt, E., Wandosell, F., Torres, M., Bonaldo, P., Stoykova, A., Chowdhury, K., Gruss, P., Avila, J., Sanchez, M.P., 2000. Perinatal lethality of microtubule-associated protein 1B-deficient mice expressing alternative isoforms of the protein at low levels. Mol Cell Neurosci 16(4), 408-421.

Goodman, R.P., Calvo, S.E., Mootha, V.K., 2018. Spatiotemporal compartmentalization of hepatic NADH and NADPH metabolism. J Biol Chem 293(20), 7508-7516.

Gopal, D., Wilson, G.S., Earl, R.A., Cusanovich, M.A., 1988. Cytochrome c: ion binding and redox properties. Studies on ferri and ferro forms of horse, bovine, and tuna cytochrome c. J Biol Chem 263(24), 11652-11656.

Gordon, J.A., 1991. Use of vanadate as protein-phosphotyrosine phosphatase inhibitor. Methods Enzymol 201, 477-482.

Graham, B.H., 2012. Diagnostic challenges of mitochondrial disorders: complexities of two genomes. Methods Mol Biol 837, 35-46.

Greenamyre, J.T., Sherer, T.B., Betarbet, R., Panov, A.V., 2001. Complex I and Parkinson's disease. IUBMB Life 52(3-5), 135-141.

Gropp, T., Brustovetsky, N., Klingenberg, M., Muller, V., Fendler, K., Bamberg, E., 1999. Kinetics of electrogenic transport by the ADP/ATP carrier. Biophys J 77(2), 714-726.

Gungor, O., Ozkaya, A.K., Gungor, G., Karaer, K., Dilber, C., Aydin, K., 2016. Novel mutation in SUCLA2 identified on sequencing analysis. Pediatr Int 58(7), 659-661.

Haberg, A., Qu, H., Bakken, I.J., Sande, L.M., White, L.R., Haraldseth, O., Unsgard, G., Aasly, J., Sonnewald, U., 1998. In vitro and ex vivo 13C-NMR spectroscopy studies of pyruvate recycling in brain. Dev.Neurosci. 20(4-5), 389-398.

Haefeli, R.H., Erb, M., Gemperli, A.C., Robay, D., Courdier Fruh, I., Anklin, C., Dallmann, R., Gueven, N., 2011. NQO1-dependent redox cycling of idebenone: effects on cellular redox potential and energy levels. PLoS One 6(3), e17963.

Hafner, R.P., Brown, G.C., Brand, M.D., 1990. Analysis of the control of respiration rate, phosphorylation rate, proton leak rate and protonmotive force in isolated mitochondria using the 'top-down' approach of metabolic control theory. Eur J Biochem 188(2), 313-319.

Hagen, T., Lagace, C.J., Modica-Napolitano, J.S., Aprille, J.R., 2003. Permeability transition in rat liver mitochondria is modulated by the ATP-Mg/Pi carrier. Am J Physiol Gastrointest Liver Physiol 285(2), G274-281.

Hagos, Y., Krick, W., Braulke, T., Muhlhausen, C., Burckhardt, G., Burckhardt, B.C., 2008. Organic anion transporters OAT1 and OAT4 mediate the high affinity transport of glutarate derivatives accumulating in patients with glutaric acidurias. Pflugers Arch 457(1), 223-231.

Hague, A., Singh, B., Paraskeva, C., 1997. Butyrate acts as a survival factor for colonic epithelial cells: further fuel for the in vivo versus in vitro debate. Gastroenterology 112(3), 1036-1040.

Haile, D.J., Rouault, T.A., Harford, J.B., Kennedy, M.C., Blondin, G.A., Beinert, H., Klausner, R.D., 1992. Cellular regulation of the iron-responsive element binding protein: disassembly of the cubane iron-sulfur cluster results in high-affinity RNA binding. Proc Natl Acad Sci U S A 89(24), 11735-11739.

Halestrap, A.P., 2013. Monocarboxylic acid transport. Compr Physiol 3(4), 1611-1643.

Halestrap, A.P., Brenner, C., 2003. The adenine nucleotide translocase: a central component of the mitochondrial permeability transition pore and key player in cell death. Curr Med Chem 10(16), 1507-1525.

Hall, A., Meyle, K.D., Lange, M.K., Klima, M., Sanderhoff, M., Dahl, C., Abildgaard, C., Thorup, K., Moghimi, S.M., Jensen, P.B., Bartek, J., Guldberg, P., Christensen, C., 2013. Dysfunctional oxidative phosphorylation makes malignant melanoma cells addicted to glycolysis driven by the (V600E)BRAF oncogene. Oncotarget 4(4), 584-599.

Hamman, H.C., Haynes, R.C., Jr., 1983. Elevated intramitochondrial adenine nucleotides and mitochondrial function. Arch Biochem Biophys 223(1), 85-94.

Hance, N., Ekstrand, M.I., Trifunovic, A., 2005. Mitochondrial DNA polymerase gamma is essential for mammalian embryogenesis. Hum Mol Genet 14(13), 1775-1783.

Hansen, G.M., Markesich, D.C., Burnett, M.B., Zhu, Q., Dionne, K.M., Richter, L.J., Finnell, R.H., Sands, A.T., Zambrowicz, B.P., Abuin, A., 2008. Large-scale gene trapping in C57BL/6N mouse embryonic stem cells. Genome Res 18(10), 1670-1679.

Harris, D.A., Rosing, J., van de Stadt, R.J., Slater, E.C., 1973. Tight binding of adenine nucleotides to beef-heart mitochondrial ATPase. Biochim Biophys Acta 314(2), 149-153.

Harris, E.J., Achenjang, F.M., 1977. Energy-dependent uptake of arsenite by rat liver mitochondria. Biochem J 168(1), 129-132.

Hartung, K.J., Bohme, G., Kunz, W., 1983. Involvement of intramitochondrial adenine nucleotides and inorganic phosphate in oxidative phosphorylation of extramitochondrially added adenosine-5'-diphosphate. Biomed Biochim Acta 42(1), 15-26.

Hartwick, R.A., Brown, P.R., 1975. The performance of microparticle chemically-bonded anion-exchange resins in the analysis of nucleotides. J Chromatogr 112, 650-662.

Hearl, W.G., Churchich, J.E., 1985. A mitochondrial NADP+-dependent reductase related to the 4-aminobutyrate shunt. Purification, characterization, and mechanism. J Biol Chem 260(30), 16361-16366.

Heinrich, R., Rapoport, T.A., 1974. A linear steady-state treatment of enzymatic chains. General properties, control and effector strength. Eur J Biochem 42(1), 89-95.

Heldt, H.W., Klingenberg, M., Milovancev, M., 1972. Differences between the ATP-ADP ratios in the mitochondrial matrix and in the extramitochondrial space. Eur J Biochem 30(3), 434-440.

Heldt, H.W., Pfaff, E., 1969. Adenine nucleotide translocation in mitochondria. Quantitative evaluation of the correlation between the phosphorylation of endogenous and exogenous ADP in mitochondria. Eur J Biochem 10(3), 494-500.

Hillier, S., Charnetzky, W.T., 1981. Glyoxylate bypass enzymes in Yersinia species and multiple forms of isocitrate lyase in Yersinia pestis. J Bacteriol 145(1), 452-458.

Hilz, H., Knappe, J., Ringelmann, E., Lynen, F., 1958. [Methylglutaconase, a new hydrase participating in the metabolism of various carboxylic acids]. Biochem Z 329(6), 476-489.

Hinkle, P.C., Butow, R.A., Racker, E., Chance, B., 1967. Partial resolution of the enzymes catalyzing oxidative phosphorylation. XV. Reverse electron transfer in the flavin-cytochrome beta region of the respiratory chain of beef heart submitochondrial particles. J Biol Chem 242(22), 5169-5173.

Hochachka, P.W., Owen, T.G., Allen, J.F., Whittow, G.C., 1975. Multiple end products of anaerobiosis in diving vertebrates. Comp Biochem Physiol B 50(1), 17-22.

Hoebe, K., Du, X., Georgel, P., Janssen, E., Tabeta, K., Kim, S.O., Goode, J., Lin, P., Mann, N., Mudd, S., Crozat, K., Sovath, S., Han, J., Beutler, B., 2003. Identification of Lps2 as a key transducer of MyD88-independent TIR signalling. Nature 424(6950), 743-748.

Hoentjen, F., Sartor, R.B., Ozaki, M., Jobin, C., 2005. STAT3 regulates NF-kappaB recruitment to the IL-12p40 promoter in dendritic cells. Blood 105(2), 689-696.

Hoffman, P.L., Wermuth, B., von Wartburg, J.P., 1980. Human brain aldehyde reductases: relationship to succinic semialdehyde reductase and aldose reductase. J Neurochem 35(2), 354-366.

Hunger-Glaser, I., Brun, R., Linder, M., Seebeck, T., 1999. Inhibition of succinyl CoA synthetase histidine-phosphorylation in Trypanosoma brucei by an inhibitor of bacterial two-component systems. Mol Biochem Parasitol 100(1), 53-59.

Husain, Z., Huang, Y., Seth, P., Sukhatme, V.P., 2013. Tumor-derived lactate modifies antitumor immune response: effect on myeloid-derived suppressor cells and NK cells. J Immunol 191(3), 1486-1495.

Hussien, R., Brooks, G.A., 2011. Mitochondrial and plasma membrane lactate transporter and lactate dehydrogenase isoform expression in breast cancer cell lines. Physiol Genomics 43(5), 255-264.

Hutson, S.M., Rannels, S.L., 1985. Characterization of a mitochondrial transport system for branched chain alpha-keto acids. J Biol Chem 260(26), 14189-14193.

Huysentruyt, L.C., Akgoc, Z., Seyfried, T.N., 2011. Hypothesis: are neoplastic macrophages/microglia present in glioblastoma multiforme? ASN Neuro 3(4).

Icard, P., Lincet, H., 2012. A global view of the biochemical pathways involved in the regulation of the metabolism of cancer cells. Biochim.Biophys.Acta 1826(2), 423-433.

Irwin, M.H., Parameshwaran, K., Pinkert, C.A., 2013. Mouse models of mitochondrial complex I dysfunction. Int J Biochem Cell Biol 45(1), 34-40.

Isaev, N.K., Stelmashook, E.V., Ruscher, K., Andreeva, N.A., Zorov, D.B., 2004. Menadione reduces rotenone-induced cell death in cerebellar granule neurons. Neuroreport 15(14), 2227-2231.

Iskander, K., Gaikwad, A., Paquet, M., Long, D.J., 2nd, Brayton, C., Barrios, R., Jaiswal, A.K., 2005. Lower induction of p53 and decreased apoptosis in NQO1-null mice lead to increased sensitivity to chemical-induced skin carcinogenesis. Cancer Res 65(6), 2054-2058.

Issartel, J.P., Dupuis, A., Lunardi, J., Vignais, P.V., 1991. Fluoroaluminum and fluoroberyllium nucleoside diphosphate complexes as probes of the enzymatic mechanism of the mitochondrial F1-ATPase. Biochemistry 30(19), 4726-4733.

Iyanagi, T., Yamazaki, I., 1970a. One-electron-transfer reactions in biochemical systems. V. Difference in the mechanism of quinone reduction by the NADH dehydrogenase and the NAD(P)H dehydrogenase (DT-diaphorase). Biochim Biophys Acta 216(2), 282-294.

Iyanagi, T., Yamazaki, I., 1970b. One-electron-transfer reactions in biochemical systems. V. Difference in the mechanism of quinone reduction by the NADH dehydrogenase and the NAD(P)H dehydrogenase (DT-diaphorase). Biochim.Biophys.Acta 216(2), 282-294.

Jaber, S., Polster, B.M., 2015. Idebenone and neuroprotection: antioxidant, pro-oxidant, or electron carrier? J Bioenerg Biomembr 47(1-2), 111-118.

Jaberi, E., Chitsazian, F., Ali Shahidi, G., Rohani, M., Sina, F., Safari, I., Malakouti Nejad, M., Houshmand, M., Klotzle, B., Elahi, E., 2013. The novel mutation p.Asp251Asn in the beta-subunit of succinate-CoA ligase causes encephalomyopathy and elevated succinylcarnitine. J Hum Genet 58(8), 526-530.

Jackson, J.B., 1991. The proton-translocating nicotinamide adenine dinucleotide transhydrogenase. J Bioenerg Biomembr 23(5), 715-741.

Jacobus, W.E., Moreadith, R.W., Vandegaer, K.M., 1982. Mitochondrial respiratory control. Evidence against the regulation of respiration by extramitochondrial phosphorylation potentials or by [ATP]/[ADP] ratios. J Biol Chem 257(5), 2397-2402.

Jaiswal, A.K., 2004. Nrf2 signaling in coordinated activation of antioxidant gene expression. Free Radic Biol Med 36(10), 1199-1207.

James, A.M., Cocheme, H.M., Smith, R.A., Murphy, M.P., 2005. Interactions of mitochondria-targeted and untargeted ubiquinones with the mitochondrial respiratory chain and reactive oxygen species. Implications for the use of exogenous ubiquinones as therapies and experimental tools. J Biol Chem 280(22), 21295-21312.

Janiszewska, M., Suva, M.L., Riggi, N., Houtkooper, R.H., Auwerx, J., Clement-Schatlo, V., Radovanovic, I., Rheinbay, E., Provero, P., Stamenkovic, I., 2012. Imp2 controls oxidative phosphorylation and is crucial for preserving glioblastoma cancer stem cells. Genes Dev 26(17), 1926-1944.

Jault, J.M., Allison, W.S., 1994. Hysteretic inhibition of the bovine heart mitochondrial F1-ATPase is due to saturation of noncatalytic sites with ADP which blocks activation of the enzyme by ATP. J Biol Chem 269(1), 319-325.

Jaworski, D.M., Namboodiri, A.M., Moffett, J.R., 2016. Acetate as a Metabolic and Epigenetic Modifier of Cancer Therapy. J Cell Biochem 117(3), 574-588.

Jenkins, T.M., Weitzman, P.D., 1986. Distinct physiological roles of animal succinate thiokinases. Association of guanine nucleotide-linked succinate thiokinase with ketone body utilization. FEBS Lett 205(2), 215-218.

Jin, Z., Mendu, S.K., Birnir, B., 2013. GABA is an effective immunomodulatory molecule. Amino Acids 45(1), 87-94.

Johnson, J.D., Mehus, J.G., Tews, K., Milavetz, B.I., Lambeth, D.O., 1998. Genetic evidence for the expression of ATP- and GTP-specific succinyl-CoA synthetases in multicellular eucaryotes. J Biol Chem 273(42), 27580-27586.

Johnson, M.T., Yang, H.S., Magnuson, T., Patel, M.S., 1997. Targeted disruption of the murine dihydrolipoamide dehydrogenase gene (Dld) results in perigastrulation lethality. Proc Natl Acad Sci U S A 94(26), 14512-14517.

Joyal, J.L., Hagen, T., Aprille, J.R., 1995. Intramitochondrial protein synthesis is regulated by matrix adenine nucleotide content and requires calcium. Arch Biochem Biophys 319(1), 322-330.

Jung, D.W., Panzeter, E., Baysal, K., Brierley, G.P., 1997. On the relationship between matrix free Mg2+ concentration and total Mg2+ in heart mitochondria. Biochim Biophys Acta 1320(3), 310-320.

Kacser, H., Burns, J.A., 1979. MOlecular democracy: who shares the controls? Biochem Soc Trans 7(5), 1149-1160.

Kacso, G., Ravasz, D., Doczi, J., Nemeth, B., Madgar, O., Saada, A., Ilin, P., Miller, C., Ostergaard, E., Iordanov, I., Adams, D., Vargedo, Z., Araki, M., Araki, K., Nakahara, M., Ito, H., Gal, A., Molnar, M.J., Nagy, Z., Patocs, A., Adam-Vizi, V., Chinopoulos, C., 2016. Two transgenic mouse models for beta-

subunit components of succinate-CoA ligase yielding pleiotropic metabolic alterations. Biochem J 473(20), 3463-3485.

Kadenbach, B., Arnold, S., 1999. A second mechanism of respiratory control. FEBS Lett 447(2-3), 131-134.

Kadrmas, E.F., Ray, P.D., Lambeth, D.O., 1991. Apparent ATP-linked succinate thiokinase activity and its relation to nucleoside diphosphate kinase in mitochondrial matrix preparations from rabbit. Biochim.Biophys.Acta 1074(3), 339-346.

Kaelin, W.G., Jr., 2008. The von Hippel-Lindau tumour suppressor protein: O2 sensing and cancer. Nat.Rev.Cancer 8(11), 865-873.

Kaipparettu, B.A., Ma, Y., Park, J.H., Lee, T.L., Zhang, Y., Yotnda, P., Creighton, C.J., Chan, W.Y., Wong, L.J., 2013. Crosstalk from non-cancerous mitochondria can inhibit tumor properties of metastatic cells by suppressing oncogenic pathways. PLoS One 8(5), e61747.

Kamo, N., Muratsugu, M., Hongoh, R., Kobatake, Y., 1979. Membrane potential of mitochondria measured with an electrode sensitive to tetraphenyl phosphonium and relationship between proton electrochemical potential and phosphorylation potential in steady state. J Membr Biol 49(2), 105-121.

Kanzaki, T., Hayakawa, T., Hamada, M., Fukuyoshi, Y., Koike, M., 1969. Mammalian alpha-keto acid dehydrogenase complexes. IV. Substrate specificities and kinetic properties of the pig heart pyruvate and 2-oxyoglutarate dehydrogenase complexes. J Biol Chem 244(5), 1183-1187.

Karch, J., Bround, M.J., Khalil, H., Sargent, M.A., Latchman, N., Terada, N., Peixoto, P.M., Molkentin, J.D., 2019. Inhibition of mitochondrial permeability transition by deletion of the ANT family and CypD. Sci Adv 5(8), eaaw4597.

Kardon, T., Noel, G., Vertommen, D., Schaftingen, E.V., 2006. Identification of the gene encoding hydroxyacid-oxoacid transhydrogenase, an enzyme that metabolizes 4-hydroxybutyrate. FEBS Lett 580(9), 2347-2350.

Karschin, A., Brockhaus, J., Ballanyi, K., 1998. KATP channel formation by the sulphonylurea receptors SUR1 with Kir6.2 subunits in rat dorsal vagal neurons in situ. J Physiol 509 (Pt 2), 339-346.

Karsy, M., Gelbman, M., Shah, P., Balumbu, O., Moy, F., Arslan, E., 2012. Established and emerging variants of glioblastoma multiforme: review of morphological and molecular features. Folia Neuropathol 50(4), 301-321.

Katsetos, C.D., Anni, H., Draber, P., 2013. Mitochondrial dysfunction in gliomas. Semin Pediatr Neurol 20(3), 216-227.

Kaufman, E.E., Nelson, T., Fales, H.M., Levin, D.M., 1988a. Isolation and characterization of a hydroxyacid-oxoacid transhydrogenase from rat kidney mitochondria. J Biol Chem 263(32), 16872-16879.

Kaufman, E.E., Nelson, T., Goochee, C., Sokoloff, L., 1979. Purification and characterization of an NADP+-linked alcohol oxido-reductase which catalyzes the interconversion of gamma-hydroxybutyrate and succinic semialdehyde. J Neurochem 32(3), 699-712.

Kaufman, E.E., Nelson, T., Miller, D., Stadlan, N., 1988b. Oxidation of gamma-hydroxybutyrate to succinic semialdehyde by a mitochondrial pyridine nucleotide-independent enzyme. J Neurochem 51(4), 1079-1084.

Kaufman, S., Gilvarg, C., Cori, O., Ochoa, S., 1953. Enzymatic oxidation of alpha-ketoglutarate and coupled phosphorylation. J Biol Chem 203(2), 869-888.

Kauppinen, R.A., Sihra, T.S., Nicholls, D.G., 1987. Aminooxyacetic acid inhibits the malate-aspartate shuttle in isolated nerve terminals and prevents the mitochondria from utilizing glycolytic substrates. Biochim Biophys Acta 930(2), 173-178.

Kawamata, H., Starkov, A.A., Manfredi, G., Chinopoulos, C., 2010. A kinetic assay of mitochondrial ADP-ATP exchange rate in permeabilized cells. Anal Biochem 407(1), 52-57.

Kay, L., Nicolay, K., Wieringa, B., Saks, V., Wallimann, T., 2000. Direct evidence for the control of mitochondrial respiration by mitochondrial creatine kinase in oxidative muscle cells in situ. J Biol Chem 275(10), 6937-6944.

Kelso, G.F., Porteous, C.M., Coulter, C.V., Hughes, G., Porteous, W.K., Ledgerwood, E.C., Smith, R.A., Murphy, M.P., 2001. Selective targeting of a redox-active ubiquinone to mitochondria within cells: antioxidant and antiapoptotic properties. J Biol Chem 276(7), 4588-4596.

Khazaei, T., McGuigan, A., Mahadevan, R., 2012. Ensemble modeling of cancer metabolism. Front Physiol 3, 135.

Kholodenko, B.N., 1984. Control of mitochondrial oxidative phosphorylation. J Theor Biol 107(2), 179-188.

Kiebish, M.A., Han, X., Cheng, H., Chuang, J.H., Seyfried, T.N., 2008. Cardiolipin and electron transport chain abnormalities in mouse brain tumor mitochondria: lipidomic evidence supporting the Warburg theory of cancer. Journal of lipid research 49(12), 2545-2556.

Kiebish, M.A., Han, X., Cheng, H., Seyfried, T.N., 2009. In vitro growth environment produces lipidomic and electron transport chain abnormalities in mitochondria from non-tumorigenic astrocytes and brain tumours. ASN Neuro 1(3).

Kim, J., Han, J., Jang, Y., Kim, S.J., Lee, M.J., Ryu, M.J., Kweon, G.R., Heo, J.Y., 2015. High-capacity glycolytic and mitochondrial oxidative metabolisms mediate the growth ability of glioblastoma. Int J Oncol 47(3), 1009-1016.

Kim, J.Y., Tillison, K.S., Zhou, S., Lee, J.H., Smas, C.M., 2007. Differentiation-dependent expression of Adhfe1 in adipogenesis. Arch Biochem Biophys 464(1), 100-111.

Kim, K.J., Pearl, P.L., Jensen, K., Snead, O.C., Malaspina, P., Jakobs, C., Gibson, K.M., 2011. Succinic semialdehyde dehydrogenase: biochemical-molecular-clinical disease mechanisms, redox regulation, and functional significance. Antioxid Redox Signal 15(3), 691-718.

Kimura, A., Naka, T., Nakahama, T., Chinen, I., Masuda, K., Nohara, K., Fujii-Kuriyama, Y., Kishimoto, T., 2009. Aryl hydrocarbon receptor in combination with Stat1 regulates LPS-induced inflammatory responses. J Exp Med 206(9), 2027-2035.

Kimura, T., Takeda, S., Sagiya, Y., Gotoh, M., Nakamura, Y., Arakawa, H., 2003. Impaired function of p53R2 in Rrm2b-null mice causes severe renal failure through attenuation of dNTP pools. Nat Genet 34(4), 440-445.

Kindmark, H., Kohler, M., Brown, G., Branstrom, R., Larsson, O., Berggren, P.O., 2001. Glucose-induced oscillations in cytoplasmic free Ca2+ concentration precede oscillations in mitochondrial membrane potential in the pancreatic beta-cell. J Biol Chem 276(37), 34530-34536.

King, A., Selak, M.A., Gottlieb, E., 2006. Succinate dehydrogenase and fumarate hydratase: linking mitochondrial dysfunction and cancer. Oncogene 25(34), 4675-4682.

Kirsch, W.M., Schulz, Q., Van Buskirk, J., Nakane, P., 1972. Anaerobic energy metabolism in brain tumors. Prog Exp Tumor Res 17, 163-191.

Kiselevsky, Y.V., Ostrovtsova, S.A., Strumilo, S.A., 1990. Kinetic characterization of the pyruvate and oxoglutarate dehydrogenase complexes from human heart. Acta Biochim.Pol. 37(1), 135-139.

Kiss, G., Konrad, C., Doczi, J., Starkov, A.A., Kawamata, H., Manfredi, G., Zhang, S.F., Gibson, G.E., Beal, M.F., Adam-Vizi, V., Chinopoulos, C., 2013. The negative impact of alpha-ketoglutarate dehydrogenase complex deficiency on matrix substrate-level phosphorylation. FASEB J. 27(6), 2392-2406.

Kiss, G., Konrad, C., Pour-Ghaz, I., Mansour, J.J., Nemeth, B., Starkov, A.A., Adam-Vizi, V., Chinopoulos, C., 2014. Mitochondrial diaphorases as NAD(+) donors to segments of the citric acid cycle that support substrate-level phosphorylation yielding ATP during respiratory inhibition. FASEB J. 28(4), 1682-1697.

Kleihues, P., Ohgaki, H., 1999. Primary and secondary glioblastomas: from concept to clinical diagnosis. Neuro Oncol 1(1), 44-51.

Klingenberg, M., 1980. The ADP-ATP translocation in mitochondria, a membrane potential controlled transport. J Membr Biol 56(2), 97-105.

Klingenberg, M., 2008. The ADP and ATP transport in mitochondria and its carrier. Biochim Biophys Acta 1778(10), 1978-2021.

Klingenberg, M., Rottenberg, H., 1977. Relation between the gradient of the ATP/ADP ratio and the membrane potential across the mitochondrial membrane. Eur J Biochem 73(1), 125-130.

Klivenyi, P., Starkov, A.A., Calingasan, N.Y., Gardian, G., Browne, S.E., Yang, L., Bubber, P., Gibson, G.E., Patel, M.S., Beal, M.F., 2004. Mice deficient in dihydrolipoamide dehydrogenase show increased vulnerability to MPTP, malonate and 3-nitropropionic acid neurotoxicity. J Neurochem 88(6), 1352-1360.

Knott, S.R.V., Wagenblast, E., Khan, S., Kim, S.Y., Soto, M., Wagner, M., Turgeon, M.O., Fish, L., Erard, N., Gable, A.L., Maceli, A.R., Dickopf, S., Papachristou, E.K., D'Santos, C.S., Carey, L.A., Wilkinson, J.E., Harrell, J.C., Perou, C.M., Goodarzi, H., Poulogiannis, G., Hannon, G.J., 2018. Asparagine bioavailability governs metastasis in a model of breast cancer. Nature 554(7692), 378-381.

Knox, W.E., Horowitz, M.L., Friedell, G.H., 1969. The proportionality of glutaminase content to growth rate and morphology of rat neoplasms. Cancer Res. 29(3), 669-680.

Ko, L.W., Sheu, K.F., Thaler, H.T., Markesbery, W.R., Blass, J.P., 2001. Selective loss of KGDHC-enriched neurons in Alzheimer temporal cortex: does mitochondrial variation contribute to selective vulnerability? J Mol Neurosci 17(3), 361-369.

Kolesova, G.M., Kapitanova, N.G., Iaguzhinskii, L.S., 1987. [Stimulation by quinones of cyanide-resistant respiration in rat liver and heart mitochondria]. Biokhimiia 52(5), 715-719.

Kolesova, G.M., Karnaukhova, L.V., Iaguzhinskii, L.S., 1991. [Interaction of menadione and duroquinone with Q-cycle during DT-diaphorase function]. Biokhimiia 56(10), 1779-1786.

Kolesova, G.M., Karnaukhova, L.V., Segal, N.K., Iaguzhinskii, L.S., 1993. [The effect of inhibitors of the Q-cycle on cyano-resistant oxidation of malate by rat liver mitochondria in the presence of menadione]. Biokhimiia 58(10), 1630-1640.

Kolesova, G.M., Vishnivetskii, S.A., Iaguzhinskii, L.S., 1989. [A study of the mechanism of cyanide resistant oxidation of succinate from rat liver mitochondria in the presence of menadione]. Biokhimiia 54(1), 103-111.

Koli, A.K., Yearby, C., Scott, W., Donaldson, K.O., 1969. Purification and properties of three separate menadione reductases from hog liver. J Biol Chem 244(4), 621-629.

Kolisek, M., Zsurka, G., Samaj, J., Weghuber, J., Schweyen, R.J., Schweigel, M., 2003. Mrs2p is an essential component of the major electrophoretic Mg2+ influx system in mitochondria. EMBO J 22(6), 1235-1244.

Koukourakis, M.I., Giatromanolaki, A., Winter, S., Leek, R., Sivridis, E., Harris, A.L., 2009. Lactate dehydrogenase 5 expression in squamous cell head and neck cancer relates to prognosis following radical or postoperative radiotherapy. Oncology 77(5), 285-292.

Kowluru, A., Tannous, M., Chen, H.Q., 2002. Localization and characterization of the mitochondrial isoform of the nucleoside diphosphate kinase in the pancreatic beta cell: evidence for its complexation with mitochondrial succinyl-CoA synthetase. Arch.Biochem.Biophys. 398(2), 160-169.

Kramer, R., 1980. Influence of divalent cations on the reconstituted ADP, ATP exchange. Biochim Biophys Acta 592(3), 615-620.

Kramer, R., 1986. Reconstitution of ADP/ATP translocase in phospholipid vesicles. Methods Enzymol 125, 610-618.

Krawczyk, C.M., Holowka, T., Sun, J., Blagih, J., Amiel, E., DeBerardinis, R.J., Cross, J.R., Jung, E., Thompson, C.B., Jones, R.G., Pearce, E.J., 2010. Toll-like receptor-induced changes in glycolytic metabolism regulate dendritic cell activation. Blood 115(23), 4742-4749.

Kreiter, J., Beitz, E., Pohl, E.E., 2020. A Fluorescence-Based Method to Measure ADP/ATP Exchange of Recombinant Adenine Nucleotide Translocase in Liposomes. Biomolecules 10(5).

Krex, D., Klink, B., Hartmann, C., von Deimling, A., Pietsch, T., Simon, M., Sabel, M., Steinbach, J.P., Heese, O., Reifenberger, G., Weller, M., Schackert, G., German Glioma, N., 2007. Long-term survival with glioblastoma multiforme. Brain 130(Pt 10), 2596-2606.

Kunnecke, B., Cerdan, S., Seelig, J., 1993. Cerebral metabolism of [1,2-13C2]glucose and [U-13C4]3-hydroxybutyrate in rat brain as detected by 13C NMR spectroscopy. NMR Biomed. 6(4), 264-277.

Kurelac, I., Romeo, G., Gasparre, G., 2011. Mitochondrial metabolism and cancer. Mitochondrion. 11(4), 635-637.

Kvitvang, H.F., Andreassen, T., Adam, T., Villas-Boas, S.G., Bruheim, P., 2011. Highly sensitive GC/MS/MS method for quantitation of amino and nonamino organic acids. Anal Chem 83(7), 2705-2711.

La Morgia, C., Carbonelli, M., Barboni, P., Sadun, A.A., Carelli, V., 2014. Medical management of hereditary optic neuropathies. Front Neurol 5, 141.

Labbe, R.F., Kurumada, T., Onisawa, J., 1965. The role of succinyl-CoA synthetase in the control of heme biosynthesis. Biochim Biophys Acta 111(2), 403-415.

Lakhani, R., Vogel, K.R., Till, A., Liu, J., Burnett, S.F., Gibson, K.M., Subramani, S., 2014. Defects in GABA metabolism affect selective autophagy pathways and are alleviated by mTOR inhibition. EMBO Mol Med 6(4), 551-566.

Lambeth, D.O., 2002. What is the function of GTP produced in the Krebs citric acid cycle? IUBMB Life 54(3), 143-144.

Lambeth, D.O., Tews, K.N., Adkins, S., Frohlich, D., Milavetz, B.I., 2004. Expression of two succinyl-CoA synthetases with different nucleotide specificities in mammalian tissues. J Biol Chem 279(35), 36621-36624.

Lamperti, C., Fang, M., Invernizzi, F., Liu, X., Wang, H., Zhang, Q., Carrara, F., Moroni, I., Zeviani, M., Zhang, J., Ghezzi, D., 2012. A novel homozygous mutation in SUCLA2 gene identified by exome sequencing. Mol Genet Metab 107(3), 403-408.

Laurent, C., Simoneau, C., Marks, L., Braschi, S., Champ, M., Charbonnel, B., Krempf, M., 1995. Effect of acetate and propionate on fasting hepatic glucose production in humans. Eur J Clin Nutr 49(7), 484-491.

Lawrence, Y.R., Blumenthal, D.T., Matceyevsky, D., Kanner, A.A., Bokstein, F., Corn, B.W., 2011. Delayed initiation of radiotherapy for glioblastoma: how important is it to push to the front (or the back) of the line? Journal of neuro-oncology.

Laws, E.R., Jr., Goldberg, W.J., Bernstein, J.J., 1993. Migration of human malignant astrocytoma cells in the mammalian brain: Scherer revisited. Int J Dev Neurosci 11(5), 691-697.

Le, A., Lane, A.N., Hamaker, M., Bose, S., Gouw, A., Barbi, J., Tsukamoto, T., Rojas, C.J., Slusher, B.S., Zhang, H., Zimmerman, L.J., Liebler, D.C., Slebos, R.J., Lorkiewicz, P.K., Higashi, R.M., Fan, T.W., Dang, C.V., 2012. Glucose-independent glutamine metabolism via TCA cycling for proliferation and survival in B cells. Cell Metab 15(1), 110-121.

Lee, C.P., Gu, Q., Xiong, Y., Mitchell, R.A., Ernster, L., 1996. P/O ratios reassessed: mitochondrial P/O ratios consistently exceed 1.5 with succinate and 2.5 with NAD-linked substrates. FASEB J 10(2), 345-350.

Lee, D.H., Lee, T.H., Jung, C.H., Kim, Y.H., 2012. Wogonin induces apoptosis by activating the AMPK and p53 signaling pathways in human glioblastoma cells. Cell Signal 24(11), 2216-2225.

Lee, S.H., Kim, S.O., Chung, B.C., 1998. Gas chromatographic-mass spectrometric determination of urinary oxoacids using O-(2,3,4,5,6-pentafluorobenzyl)oxime-trimethylsilyl ester derivatization and cation-exchange chromatography. J Chromatogr B Biomed Sci Appl 719(1-2), 1-7.

Lee, Y., Sohn, W.J., Kim, D.S., Kwon, H.J., 2004. NF-kappaB- and c-Jun-dependent regulation of human cytomegalovirus immediate-early gene enhancer/promoter in response to lipopolysaccharide and bacterial CpG-oligodeoxynucleotides in macrophage cell line RAW 264.7. Eur J Biochem 271(6), 1094-1105.

Lehninger, A.L., 1964. The Mitochondrion: Molecular Basis of Structure and Function. W.A. Benjamin, INC., New York.

Lemasters, J.J., Hackenbrock, C.R., 1979. Continuous measurement of adenosine triphosphate with firefly luciferase luminescence. Methods Enzymol 56, 530-544.

Lemberg, K.M., Vornov, J.J., Rais, R., Slusher, B.S., 2018. We're Not "DON" Yet: Optimal Dosing and Prodrug Delivery of 6-Diazo-5-oxo-L-norleucine. Mol Cancer Ther 17(9), 1824-1832.

Lenaz, G., Fato, R., Degli Esposti, M., Rugolo, M., Parenti Castelli, G., 1985. The essentiality of coenzyme Q for bioenergetics and clinical medicine. Drugs Exp Clin Res 11(8), 547-556.

Leone, M.A., Vigna-Taglianti, F., Avanzi, G., Brambilla, R., Faggiano, F., 2010. Gamma-hydroxybutyrate (GHB) for treatment of alcohol withdrawal and prevention of relapses. Cochrane Database Syst Rev(2), CD006266.

Letko, G., Kuster, U., Duszynski, J., Kunz, W., 1980. Investigation of the dependence of the intramitochondrial [ATP]/[ADP] ratio on the respiration rate. Biochim Biophys Acta 593(2), 196-203.

Levy, S.E., Chen, Y.S., Graham, B.H., Wallace, D.C., 2000. Expression and sequence analysis of the mouse adenine nucleotide translocase 1 and 2 genes. Gene 254(1-2), 57-66.

Leyssens, A., Nowicky, A.V., Patterson, L., Crompton, M., Duchen, M.R., 1996. The relationship between mitochondrial state, ATP hydrolysis, [Mg2+]i and [Ca2+]i studied in isolated rat cardiomyocytes. J Physiol 496 (Pt 1), 111-128.

Leznev, E.I., Popova, II, Lavrovskaja, V.P., Evtodienko, Y.V., 2013. Comparison of oxygen consumption rates in minimally transformed BALB/3T3 and virus-transformed 3T3B-SV40 cells. Biochemistry (Mosc) 78(8), 904-908.

Li, J., Zhu, S., Tong, J., Hao, H., Yang, J., Liu, Z., Wang, Y., 2016. Suppression of lactate dehydrogenase A compromises tumor progression by downregulation of the Warburg effect in glioblastoma. Neuroreport 27(2), 110-115.

Li, X., Wu, F., Beard, D.A., 2013. Identification of the kinetic mechanism of succinyl-CoA synthetase. Biosci.Rep. 33(1), 145-163.

Li, X., Wu, F., Qi, F., Beard, D.A., 2011. A database of thermodynamic properties of the reactions of glycolysis, the tricarboxylic acid cycle, and the pentose phosphate pathway. Database (Oxford) 2011, bar005.

Lienhard, G.E., Secemski, II, 1973. P 1 ,P 5 -Di(adenosine-5')pentaphosphate, a potent multisubstrate inhibitor of adenylate kinase. J Biol Chem 248(3), 1121-1123.

Ligeti, E., Brandolin, G., Dupont, Y., Vignais, P.V., 1985. Kinetics of Pi-Pi exchange in rat liver mitochondria. Rapid filtration experiments in the millisecond time range. Biochemistry 24(16), 4423-4428.

Lin, Y.C., Hung, C.M., Tsai, J.C., Lee, J.C., Chen, Y.L., Wei, C.W., Kao, J.Y., Way, T.D., 2010. Hispidulin potently inhibits human glioblastoma multiforme cells through activation of AMP-activated protein kinase (AMPK). J Agric Food Chem 58(17), 9511-9517.

Lind, C., Cadenas, E., Hochstein, P., Ernster, L., 1990. DT-diaphorase: purification, properties, and function. Methods Enzymol 186, 287-301.

Lind, C., Hojeberg, B., 1981. Biospecific adsorption of hepatic DT-diaphorase on immobilized dicoumarol. II. Purification of mitochondrial and microsomal DT-diaphorase from 3-methylcholanthrene-treated rats. Arch Biochem Biophys 207(1), 217-224.

Lindahl, G., Lindstedt, G., Lindstedt, S., 1967. Metabolism of 2-amino-5-hydroxyadipic acid in the rat. Arch Biochem Biophys 119(1), 347-352.

Little, J.E., Sproston, T.J., Foote, M.W., 1948. Isolation and antifungal action of naturally occurring 2-methoxy-1,4-naphthoquinone. J Biol Chem 174(1), 335-342.

Liu, J., Guo, S., Li, Q., Yang, L., Xia, Z., Zhang, L., Huang, Z., Zhang, N., 2013. Phosphoglycerate dehydrogenase induces glioma cells proliferation and invasion by stabilizing forkhead box M1. Journal of neuro-oncology 111(3), 245-255.

Liu, Y., Su, W.W., Wang, S., Li, P.B., 2012. Naringin inhibits chemokine production in an LPS-induced RAW 264.7 macrophage cell line. Mol Med Rep 6(6), 1343-1350.

Liu, Z., Wang, J., Li, Y., Fan, J., Chen, L., Xu, R., 2017. MicroRNA-153 regulates glutamine metabolism in glioblastoma through targeting glutaminase. Tumour Biol 39(2), 1010428317691429.

Long, D.J., 2nd, Jaiswal, A.K., 2000. NRH:quinone oxidoreductase2 (NQO2). Chem Biol Interact 129(1-2), 99-112.

Lopez, L.C., Akman, H.O., Garcia-Cazorla, A., Dorado, B., Marti, R., Nishino, I., Tadesse, S., Pizzorno, G., Shungu, D., Bonilla, E., Tanji, K., Hirano, M., 2009. Unbalanced deoxynucleotide pools cause mitochondrial DNA instability in thymidine phosphorylase-deficient mice. Hum Mol Genet 18(4), 714-722.

Lord, K.A., Reed, G.H., 1990. Vanadyl(IV) complexes with pyruvate kinase: activation of the enzyme and electron paramagnetic resonance properties of ternary complexes with the protein. Arch Biochem Biophys 281(1), 124-131.

Loscher, W., Honack, D., Gramer, M., 1989. Use of inhibitors of gamma-aminobutyric acid (GABA) transaminase for the estimation of GABA turnover in various brain regions of rats: a reevaluation of aminooxyacetic acid. J Neurochem 53(6), 1737-1750.

Losman, J.A., Kaelin, W.G., Jr., 2013. What a difference a hydroxyl makes: mutant IDH, (R)-2-hydroxyglutarate, and cancer. Genes Dev 27(8), 836-852.

Lou, P.H., Hansen, B.S., Olsen, P.H., Tullin, S., Murphy, M.P., Brand, M.D., 2007. Mitochondrial uncouplers with an extraordinary dynamic range. Biochem J 407(1), 129-140.

Luo, W., Hu, H., Chang, R., Zhong, J., Knabel, M., O'Meally, R., Cole, R.N., Pandey, A., Semenza, G.L., 2011. Pyruvate kinase M2 is a PHD3-stimulated coactivator for hypoxia-inducible factor 1. Cell 145(5), 732-744.

Maas, E., Bisswanger, H., 1990. Localization of the alpha-oxoacid dehydrogenase multienzyme complexes within the mitochondrion. FEBS Lett 277(1-2), 189-190.

Maas, R.R., Marina, A.D., de Brouwer, A.P., Wevers, R.A., Rodenburg, R.J., Wortmann, S.B., 2016. SUCLA2 Deficiency: A Deafness-Dystonia Syndrome with Distinctive Metabolic Findings (Report of a New Patient and Review of the Literature). JIMD Rep 27, 27-32.

Machiyama, Y., Balazs, R., Hammond, B.J., Julian, T., Richter, D., 1970. The metabolism of gamma-aminobutyrate and glucose in potassium ion-stimulated brain tissue in vitro. Biochem J 116(3), 469-481.

Maerki, F., Martius, C., 1961. [Vitamin K reductase, from cattle and ratliver]. Biochem Z 334, 293-303.

Malaspina, P., Picklo, M.J., Jakobs, C., Snead, O.C., Gibson, K.M., 2009. Comparative genomics of aldehyde dehydrogenase 5a1 (succinate semialdehyde dehydrogenase) and accumulation of gamma-hydroxybutyrate associated with its deficiency. Hum Genomics 3(2), 106-120.

Mannella, C.A., Pfeiffer, D.R., Bradshaw, P.C., Moraru, II, Slepchenko, B., Loew, L.M., Hsieh, C.E., Buttle, K., Marko, M., 2001. Topology of the mitochondrial inner membrane: dynamics and bioenergetic implications. IUBMB Life 52(3-5), 93-100.

Manoj, K.M., Gade, S.K., Mathew, L., 2010. Cytochrome P450 reductase: a harbinger of diffusible reduced oxygen species. PLoS One 5(10), e13272.

Marin-Valencia, I., Yang, C., Mashimo, T., Cho, S., Baek, H., Yang, X.L., Rajagopalan, K.N., Maddie, M., Vemireddy, V., Zhao, Z., Cai, L., Good, L., Tu, B.P., Hatanpaa, K.J., Mickey, B.E., Mates, J.M., Pascual, J.M., Maher, E.A., Malloy, C.R., Deberardinis, R.J., Bachoo, R.M., 2012. Analysis of tumor metabolism reveals mitochondrial glucose oxidation in genetically diverse human glioblastomas in the mouse brain in vivo. Cell Metab 15(6), 827-837.

Maritius, C., Strufe, R., 1954. [Phylloquinone reductase; preliminary report]. Biochem Z 326(1), 24-25.

Markert, C.L., Shaklee, J.B., Whitt, G.S., 1975. Evolution of a gene. Multiple genes for LDH isozymes provide a model of the evolution of gene structure, function and regulation. Science 189(4197), 102-114.

Marsh, J., Mukherjee, P., Seyfried, T.N., 2008. Akt-dependent proapoptotic effects of dietary restriction on late-stage management of a phosphatase and tensin homologue/tuberous sclerosis complex 2-deficient mouse astrocytoma. Clin Cancer Res 14(23), 7751-7762.

Martincorena, I., Fowler, J.C., Wabik, A., Lawson, A.R.J., Abascal, F., Hall, M.W.J., Cagan, A., Murai, K., Mahbubani, K., Stratton, M.R., Fitzgerald, R.C., Handford, P.A., Campbell, P.J., Saeb-Parsy, K., Jones, P.H., 2018. Somatic mutant clones colonize the human esophagus with age. Science 362(6417), 911-917.

Martinez-Azorin, F., Calleja, M., Hernandez-Sierra, R., Farr, C.L., Kaguni, L.S., Garesse, R., 2008. Over-expression of the catalytic core of mitochondrial DNA (mtDNA) polymerase in the nervous system of Drosophila melanogaster reduces median life span by inducing mtDNA depletion. J Neurochem 105(1), 165-176.

Martius, C., Nitz-Litzow, D., 1953. [The mechanism of action of dicumarol and related compounds]. Biochim Biophys Acta 12(1-2), 134-140.

Mashimo, T., Pichumani, K., Vemireddy, V., Hatanpaa, K.J., Singh, D.K., Sirasanagandla, S., Nannepaga, S., Piccirillo, S.G., Kovacs, Z., Foong, C., Huang, Z., Barnett, S., Mickey, B.E., DeBerardinis, R.J., Tu, B.P., Maher, E.A., Bachoo, R.M., 2014. Acetate is a bioenergetic substrate for human glioblastoma and brain metastases. Cell 159(7), 1603-1614.

Massey, V., 1960. The identity of diaphorase and lipoyl dehydrogenase. Biochim Biophys Acta 37, 314-322.

Mastrogiacoma, F., Lindsay, J.G., Bettendorff, L., Rice, J., Kish, S.J., 1996. Brain protein and alpha-ketoglutarate dehydrogenase complex activity in Alzheimer's disease. Ann Neurol 39(5), 592-598.

Mathews, E.H., Stander, B.A., Joubert, A.M., Liebenberg, L., 2014. Tumor cell culture survival following glucose and glutamine deprivation at typical physiological concentrations. Nutrition 30(2), 218-227.

Matilainen, S., Isohanni, P., Euro, L., Lonnqvist, T., Pihko, H., Kivela, T., Knuutila, S., Suomalainen, A., 2015. Mitochondrial encephalomyopathy and retinoblastoma explained by compound heterozygosity of SUCLA2 point mutation and 13q14 deletion. Eur J Hum Genet 23(3), 325-330.

Matlib, M.A., Shannon, W.A., Jr., Srere, P.A., 1977. Measurement of matrix enzyme activity in isolated mitochondria made permeable with toluene. Arch Biochem Biophys 178(2), 396-407.

Maurer, G.D., Brucker, D.P., Bahr, O., Harter, P.N., Hattingen, E., Walenta, S., Mueller-Klieser, W., Steinbach, J.P., Rieger, J., 2011. Differential utilization of ketone bodies by neurons and glioma cell lines: a rationale for ketogenic diet as experimental glioma therapy. BMC Cancer 11, 315.

Maus, A., Peters, G.J., 2017. Glutamate and alpha-ketoglutarate: key players in glioma metabolism. Amino Acids 49(1), 21-32.

Maximchik, P.V., Kulikov, A.V., Zhivotovsky, B.D., Gogvadze, V.G., 2016. Cellular Energetics as a Target for Tumor Cell Elimination. Biochemistry (Mosc) 81(2), 65-79.

Mayer, A., Vaupel, P., Struss, H.G., Giese, A., Stockinger, M., Schmidberger, H., 2014. Strong adverse prognostic impact of hyperglycemic episodes during adjuvant chemoradiotherapy of glioblastoma multiforme. Strahlenther Onkol 190(10), 933-938.

Mazurek, S., Boschek, C.B., Hugo, F., Eigenbrodt, E., 2005. Pyruvate kinase type M2 and its role in tumor growth and spreading. Semin.Cancer Biol. 15(4), 300-308.

McClure, W.R., Lardy, H.A., Kneifel, H.P., 1971a. Rat liver pyruvate carboxylase. I. Preparation, properties, and cation specificity. Journal of Biological Chemistry 246(11), 3569-3578.

McClure, W.R., Lardy, H.A., Wagner, M., Cleland, W.W., 1971b. Rat liver pyruvate carboxylase. II. Kinetic studies of the forward reaction. Journal of Biological Chemistry 246(11), 3579-3583.

McCoy, G.D., Doeg, K.A., 1975. Characterization of the phosphoenolpyruvate inhibition of mitochondrial protein synthesis. Journal of Biological Chemistry 250(9), 3510-3514.

McFadden, B.A., Purohit, S., 1977. Itaconate, an isocitrate lyase-directed inhibitor in Pseudomonas indigofera. J Bacteriol 131(1), 136-144.

McGirt, M.J., Chaichana, K.L., Gathinji, M., Attenello, F., Than, K., Ruiz, A.J., Olivi, A., Quinones-Hinojosa, A., 2008. Persistent outpatient hyperglycemia is independently associated with decreased

survival after primary resection of malignant brain astrocytomas. Neurosurgery 63(2), 286-291; discussion 291.

McMillin, J.B., Pauly, D.F., 1988. Control of mitochondrial respiration in muscle. Mol Cell Biochem 81(2), 121-129.

Medina, M.A., 2001. Glutamine and cancer. The Journal of nutrition 131(9 Suppl), 2539S-2542S; discussion 2550S-2531S.

Meiser, J., Vazquez, A., 2016. Give it or take it: the flux of one-carbon in cancer cells. FEBS J 283(20), 3695-3704.

Menegon, S., Columbano, A., Giordano, S., 2016. The Dual Roles of NRF2 in Cancer. Trends Mol Med 22(7), 578-593.

Metelkin, E., Demin, O., Kovacs, Z., Chinopoulos, C., 2009. Modeling of ATP-ADP steady-state exchange rate mediated by the adenine nucleotide translocase in isolated mitochondria. FEBS J 276(23), 6942-6955.

Metelkin, E., Goryanin, I., Demin, O., 2006. Mathematical modeling of mitochondrial adenine nucleotide translocase. Biophys J 90(2), 423-432.

Michaeli, S., Fait, A., Lagor, K., Nunes-Nesi, A., Grillich, N., Yellin, A., Bar, D., Khan, M., Fernie, A.R., Turano, F.J., Fromm, H., 2011. A mitochondrial GABA permease connects the GABA shunt and the TCA cycle, and is essential for normal carbon metabolism. Plant J 67(3), 485-498.

Michel, V., Bakovic, M., 2009. The solute carrier 44A1 is a mitochondrial protein and mediates choline transport. FASEB J 23(8), 2749-2758.

Michelakis, E.D., Webster, L., Mackey, J.R., 2008. Dichloroacetate (DCA) as a potential metabolic-targeting therapy for cancer. Br.J.Cancer 99(7), 989-994.

Michelucci, A., Cordes, T., Ghelfi, J., Pailot, A., Reiling, N., Goldmann, O., Binz, T., Wegner, A., Tallam, A., Rausell, A., Buttini, M., Linster, C.L., Medina, E., Balling, R., Hiller, K., 2013. Immune-responsive gene 1 protein links metabolism to immunity by catalyzing itaconic acid production. Proc Natl Acad Sci U S A 110(19), 7820-7825.

Miller, C., Wang, L., Ostergaard, E., Dan, P., Saada, A., 2011. The interplay between SUCLA2, SUCLG2, and mitochondrial DNA depletion. Biochim Biophys Acta 1812(5), 625-629.

Mills, E., O'Neill, L.A., 2014. Succinate: a metabolic signal in inflammation. Trends Cell Biol 24(5), 313-320.

Milon, L., Rousseau-Merck, M.F., Munier, A., Erent, M., Lascu, I., Capeau, J., Lacombe, M.L., 1997. nm23-H4, a new member of the family of human nm23/nucleoside diphosphate kinase genes localised on chromosome 16p13. Hum Genet 99(4), 550-557.

Minchin, M.C., Iversen, L.L., 1974. Release of (3H)gamma-aminobutyric acid from glial cells in rat dorsal root ganglia. J Neurochem 23(3), 533-540.

Minelli, A., DeBiasi, S., Brecha, N.C., Zuccarello, L.V., Conti, F., 1996. GAT-3, a high-affinity GABA plasma membrane transporter, is localized to astrocytic processes, and it is not confined to the vicinity of GABAergic synapses in the cerebral cortex. J Neurosci 16(19), 6255-6264.

Minuk, G.Y., 1993. Gamma-aminobutyric acid and the liver. Dig Dis 11(1), 45-54.

Miyadera, H., Shiomi, K., Ui, H., Yamaguchi, Y., Masuma, R., Tomoda, H., Miyoshi, H., Osanai, A., Kita, K., Omura, S., 2003. Atpenins, potent and specific inhibitors of mitochondrial complex II (succinate-ubiquinone oxidoreductase). Proc Natl Acad Sci U S A 100(2), 473-477.

Mogilevskaya, E., Bagrova, N., Plyusnina, T., Gizzatkulov, N., Metelkin, E., Goryacheva, E., Smirnov, S., Kosinsky, Y., Dorodnov, A., Peskov, K., Karelina, T., Goryanin, I., Demin, O., 2009. Kinetic modeling as a tool to integrate multilevel dynamic experimental data. Methods Mol Biol 563, 197-218.

Monne, M., Palmieri, F., 2014. Antiporters of the mitochondrial carrier family. Curr Top Membr 73, 289-320.

Mookerjee, S.A., Goncalves, R.L.S., Gerencser, A.A., Nicholls, D.G., Brand, M.D., 2015. The contributions of respiration and glycolysis to extracellular acid production. Biochim Biophys Acta 1847(2), 171-181.

Morantz, R.A., Wood, G.W., Foster, M., Clark, M., Gollahon, K., 1979. Macrophages in experimental and human brain tumors. Part 2: studies of the macrophage content of human brain tumors. J. Neurosurg 50(3), 305-311.

Morava, E., Steuerwald, U., Carrozzo, R., Kluijtmans, L.A., Joensen, F., Santer, R., Dionisi-Vici, C., Wevers, R.A., 2009. Dystonia and deafness due to SUCLA2 defect; Clinical course and biochemical markers in 16 children. Mitochondrion 9(6), 438-442.

Moreadith, R.W., Lehninger, A.L., 1984. The pathways of glutamate and glutamine oxidation by tumor cell mitochondria. Role of mitochondrial NAD(P)+-dependent malic enzyme. J.Biol.Chem 259(10), 6215-6221.

Morel, F., Lauquin, G., Lunardi, J., Duszynski, J., Vignais, P.V., 1974. An appraisal of the functional significance of the inhibitory effect of long chain acyl-CoAs on mitochondrial transports. FEBS Lett 39(2), 133-138.

Moreno-Sanchez, R., Devars, S., Lopez-Gomez, F., Uribe, A., Corona, N., 1991. Distribution of control of oxidative phosphorylation in mitochondria oxidizing NAD-linked substrates. Biochim Biophys Acta 1060(3), 284-292.

Moreno-Sanchez, R., Rodriguez-Enriquez, S., Saavedra, E., Marin-Hernandez, A., Gallardo-Perez, J.C., 2009. The bioenergetics of cancer: is glycolysis the main ATP supplier in all tumor cells? BioFactors (Oxford, England) 35(2), 209-225.

Muhling, J., Fuchs, M., Campos, M.E., Gonter, J., Engel, J.M., Sablotzki, A., Menges, T., Weiss, S., Dehne, M.G., Krull, M., Hempelmann, G., 2003. Quantitative determination of free intracellular alpha-keto acids in neutrophils. J Chromatogr B Analyt Technol Biomed Life Sci 789(2), 383-392.

Mukherjee, B., Patra, B., Mahapatra, S., Banerjee, P., Tiwari, A., Chatterjee, M., 2004. Vanadium--an element of atypical biological significance. Toxicol Lett 150(2), 135-143.

Mukherjee, P., Abate, L.E., Seyfried, T.N., 2004. Antiangiogenic and proapoptotic effects of dietary restriction on experimental mouse and human brain tumors. Clin Cancer Res 10(16), 5622-5629.

Mukherjee, P., Augur, Z.M., Li, M., Hill, C., Greenwood, B., Domin, M.A., Kondakci, G., Narain, N.R., Kiebish, M.A., Bronson, R.T., Arismendi-Morillo, G., Chinopoulos, C., Seyfried, T.N., 2019. Therapeutic

benefit of combining calorie-restricted ketogenic diet and glutamine targeting in late-stage experimental glioblastoma. Commun Biol 2, 200.

Mukherjee, P., El-Abbadi, M.M., Kasperzyk, J.L., Ranes, M.K., Seyfried, T.N., 2002. Dietary restriction reduces angiogenesis and growth in an orthotopic mouse brain tumour model. Br J Cancer 86(10), 1615-1621.

Mulrooney, T.J., Marsh, J., Urits, I., Seyfried, T.N., Mukherjee, P., 2011. Influence of Caloric Restriction on Constitutive Expression of NF-kappaB in an Experimental Mouse Astrocytoma. PLoS One 6(3), e18085.

Murphy, M.P., 2009. How mitochondria produce reactive oxygen species. Biochem J 417(1), 1-13.

Murthy, M.S., Pande, S.V., 1985. Microcompartmentation of transported carnitine, acetylcarnitine and ADP occurs in the mitochondrial matrix. Implications for transport measurements and metabolism. Biochem J 230(3), 657-663.

Naseri, N.N., Xu, H., Bonica, J., Vonsattel, J.P., Cortes, E.P., Park, L.C., Arjomand, J., Gibson, G.E., 2015. Abnormalities in the tricarboxylic Acid cycle in Huntington disease and in a Huntington disease mouse model. J Neuropathol Exp Neurol 74(6), 527-537.

Navarro-Sastre, A., Tort, F., Garcia-Villoria, J., Pons, M.R., Nascimento, A., Colomer, J., Campistol, J., Yoldi, M.E., Lopez-Gallardo, E., Montoya, J., Unceta, M., Martinez, M.J., Briones, P., Ribes, A., 2012. Mitochondrial DNA depletion syndrome: new descriptions and the use of citrate synthase as a helpful tool to better characterise the patients. Mol Genet Metab 107(3), 409-415.

Nelson, T., Kaufman, E., Kline, J., Sokoloff, L., 1981. The extraneural distribution of gamma-hydroxybutyrate. J Neurochem 37(5), 1345-1348.

Nemeria, N.S., Ambrus, A., Patel, H., Gerfen, G., Adam-Vizi, V., Tretter, L., Zhou, J., Wang, J., Jordan, F., 2014. Human 2-oxoglutarate dehydrogenase complex E1 component forms a thiamin-derived radical by aerobic oxidation of the enamine intermediate. J Biol Chem 289(43), 29859-29873.

Nemeth, B., Doczi, J., Csete, D., Kacso, G., Ravasz, D., Adams, D., Kiss, G., Nagy, A.M., Horvath, G., Tretter, L., Mocsai, A., Csepanyi-Komi, R., Iordanov, I., Adam-Vizi, V., Chinopoulos, C., 2016. Abolition of mitochondrial substrate-level phosphorylation by itaconic acid produced by LPS-induced Irg1 expression in cells of murine macrophage lineage. FASEB J 30(1), 286-300.

Newsholme, E.A., Board, M., 1991. Application of metabolic-control logic to fuel utilization and its significance in tumor cells. Adv Enzyme Regul 31, 225-246.

Nicholls, D.G., 2006. Simultaneous monitoring of ionophore- and inhibitor-mediated plasma and mitochondrial membrane potential changes in cultured neurons. J Biol Chem 281(21), 14864-14874.

Nicholls, D.G., Bernson, V.S., 1977. Inter-relationships between proton electrochemical gradient, adenine-nucleotide phosphorylation potential and respiration, during substrate-level and oxidative phosphorylation by mitochondria from brown adipose tissue of cold-adapted guinea-pigs. Eur J Biochem 75(2), 601-612.

Nilsen, L.H., Shi, Q., Gibson, G.E., Sonnewald, U., 2011. Brain [U-13 C]glucose metabolism in mice with decreased alpha-ketoglutarate dehydrogenase complex activity. J Neurosci Res 89(12), 1997-2007.

Nogueira, C., Meschini, M.C., Nesti, C., Garcia, P., Diogo, L., Valongo, C., Costa, R., Videira, A., Vilarinho, L., Santorelli, F.M., 2015. A novel SUCLA2 mutation in a Portuguese child associated with "mild" methylmalonic aciduria. J Child Neurol 30(2), 228-232.

Nolte, J.C., Schurmann, M., Schepers, C.L., Vogel, E., Wubbeler, J.H., Steinbuchel, A., 2014. Novel characteristics of succinate coenzyme A (Succinate-CoA) ligases: conversion of malate to malyl-CoA and CoA-thioester formation of succinate analogues in vitro. Appl Environ Microbiol 80(1), 166-176.

Nosek, M.T., Aprille, J.R., 1992. ATP-Mg/Pi carrier activity in rat liver mitochondria. Arch Biochem Biophys 296(2), 691-697.

Nosek, M.T., Dransfield, D.T., Aprille, J.R., 1990. Calcium stimulates ATP-Mg/Pi carrier activity in rat liver mitochondria. J Biol Chem 265(15), 8444-8450.

Nury, H., Dahout-Gonzalez, C., Trezeguet, V., Lauquin, G.J., Brandolin, G., Pebay-Peyroula, E., 2006. Relations between structure and function of the mitochondrial ADP/ATP carrier. Annu Rev Biochem 75, 713-741.

O'Reilly, C.M., Fogarty, K.E., Drummond, R.M., Tuft, R.A., Walsh, J.V., Jr., 2003. Quantitative analysis of spontaneous mitochondrial depolarizations. Biophys J 85(5), 3350-3357.

Ochoa, S., 1948. Biosynthesis of tricarboxylic acids by carbon dioxide fixation; enzymatic mechanisms. J.Biol.Chem 174(1), 133-157.

Offner, F.F., 1991. Ion flow through membranes and the resting potential of cells. J Membr Biol 123(2), 171-182.

Oh, E.T., Park, H.J., 2015. Implications of NQO1 in cancer therapy. BMB Rep 48(11), 609-617.

Ohka, F., Ito, M., Ranjit, M., Senga, T., Motomura, A., Motomura, K., Saito, K., Kato, K., Kato, Y., Wakabayashi, T., Soga, T., Natsume, A., 2014. Quantitative metabolome analysis profiles activation of glutaminolysis in glioma with IDH1 mutation. Tumour Biol 35(6), 5911-5920.

Ohno-Shosaku, T., Yamamoto, C., 1992. Identification of an ATP-sensitive K+ channel in rat cultured cortical neurons. Pflugers Arch 422(3), 260-266.

Oizel, K., Chauvin, C., Oliver, L., Gratas, C., Geraldo, F., Jarry, U., Scotet, E., Rabe, M., Alves-Guerra, M.C., Teusan, R., Gautier, F., Loussouarn, D., Compan, V., Martinou, J.C., Vallette, F.M., Pecqueur, C., 2017. Efficient Mitochondrial Glutamine Targeting Prevails Over Glioblastoma Metabolic Plasticity. Clin Cancer Res 23(20), 6292-6304.

Okabe, M., Lies, D., Kanamasa, S., Park, E.Y., 2009. Biotechnological production of itaconic acid and its biosynthesis in Aspergillus terreus. Appl Microbiol Biotechnol 84(4), 597-606.

Ooi, A., Wong, J.C., Petillo, D., Roossien, D., Perrier-Trudova, V., Whitten, D., Min, B.W., Tan, M.H., Zhang, Z., Yang, X.J., Zhou, M., Gardie, B., Molinie, V., Richard, S., Tan, P.H., Teh, B.T., Furge, K.A., 2011. An antioxidant response phenotype shared between hereditary and sporadic type 2 papillary renal cell carcinoma. Cancer Cell 20(4), 511-523.

Ostergaard, E., 2008. Disorders caused by deficiency of succinate-CoA ligase. J Inherit Metab Dis 31(2), 226-229.

Ostergaard, E., Christensen, E., Kristensen, E., Mogensen, B., Duno, M., Shoubridge, E.A., Wibrand, F., 2007a. Deficiency of the alpha subunit of succinate-coenzyme A ligase causes fatal infantile lactic acidosis with mitochondrial DNA depletion. Am J Hum Genet 81(2), 383-387.

Ostergaard, E., Hansen, F.J., Sorensen, N., Duno, M., Vissing, J., Larsen, P.L., Faeroe, O., Thorgrimsson, S., Wibrand, F., Christensen, E., Schwartz, M., 2007b. Mitochondrial encephalomyopathy with elevated methylmalonic acid is caused by SUCLA2 mutations. Brain 130(Pt 3), 853-861.

Ostergaard, E., Schwartz, M., Batbayli, M., Christensen, E., Hjalmarson, O., Kollberg, G., Holme, E., 2010. A novel missense mutation in SUCLG1 associated with mitochondrial DNA depletion, encephalomyopathic form, with methylmalonic aciduria. Eur J Pediatr 169(2), 201-205.

Ota, T., Suzuki, Y., Nishikawa, T., Otsuki, T., Sugiyama, T., Irie, R., Wakamatsu, A., Hayashi, K., Sato, H., Nagai, K., Kimura, K., Makita, H., Sekine, M., Obayashi, M., Nishi, T., Shibahara, T., Tanaka, T., Ishii, S., Yamamoto, J., Saito, K., Kawai, Y., Isono, Y., Nakamura, Y., Nagahari, K., Murakami, K., Yasuda, T., Iwayanagi, T., Wagatsuma, M., Shiratori, A., Sudo, H., Hosoiri, T., Kaku, Y., Kodaira, H., Kondo, H., Sugawara, M., Takahashi, M., Kanda, K., Yokoi, T., Furuya, T., Kikkawa, E., Omura, Y., Abe, K., Kamihara, K., Katsuta, N., Sato, K., Tanikawa, M., Yamazaki, M., Ninomiya, K., Ishibashi, T., Yamashita, H., Murakawa, K., Fujimori, K., Tanai, H., Kimata, M., Watanabe, M., Hiraoka, S., Chiba, Y., Ishida, S., Ono, Y., Takiguchi, S., Watanabe, S., Yosida, M., Hotuta, T., Kusano, J., Kanehori, K., Takahashi-Fujii, A., Hara, H., Tanase, T.O., Nomura, Y., Togiya, S., Komai, F., Hara, R., Takeuchi, K., Arita, M., Imose, N., Musashino, K., Yuuki, H., Oshima, A., Sasaki, N., Aotsuka, S., Yoshikawa, Y., Matsunawa, H., Ichihara, T., Shiohata, N., Sano, S., Moriya, S., Momiyama, H., Satoh, N., Takami, S., Terashima, Y., Suzuki, O., Nakagawa, S., Senoh, A., Mizoguchi, H., Goto, Y., Shimizu, F., Wakebe, H., Hishigaki, H., Watanabe, T., Sugiyama, A., Takemoto, M., Kawakami, B., Yamazaki, M., Watanabe, K., Kumagai, A., Itakura, S., Fukuzumi, Y., Fujimori, Y., Komiyama, M., Tashiro, H., Tanigami, A., Fujiwara, T., Ono, T., Yamada, K., Fujii, Y., Ozaki, K., Hirao, M., Ohmori, Y., Kawabata, A., Hikiji, T., Kobatake, N., Inagaki, H., Ikema, Y., Okamoto, S., Okitani, R., Kawakami, T., Noguchi, S., Itoh, T., Shigeta, K., Senba, T., Matsumura, K., Nakajima, Y., Mizuno, T., Morinaga, M., Sasaki, M., Togashi, T., Oyama, M., Hata, H., Watanabe, M., Komatsu, T., Mizushima-Sugano, J., Satoh, T., Shirai, Y., Takahashi, Y., Nakagawa, K., Okumura, K., Nagase, T., Nomura, N., Kikuchi, H., Masuho, Y., Yamashita, R., Nakai, K., Yada, T., Nakamura, Y., Ohara, O., Isogai, T., Sugano, S., 2004. Complete sequencing and characterization of 21,243 full-length human cDNAs. Nat.Genet. 36(1), 40-45.

Ottaway, J.H., McClellan, J.A., Saunderson, C.L., 1981. Succinic thiokinase and metabolic control. Int.J.Biochem. 13(4), 401-410.

Oudard, S., Boitier, E., Miccoli, L., Rousset, S., Dutrillaux, B., Poupon, M.F., 1997. Gliomas are driven by glycolysis: putative roles of hexokinase, oxidative phosphorylation and mitochondrial ultrastructure. Anticancer Res 17(3C), 1903-1911.

Out, T.A., Valeton, E., Kemp, A., Jr., 1976. Role of the intramitochondrial adenine nucleotides as intermediates in the uncoupler-induced hydrolysis of extramitochondrial ATP. Biochim Biophys Acta 440(3), 697-710.

Owens, D.F., Kriegstein, A.R., 2002. Is there more to GABA than synaptic inhibition? Nat Rev Neurosci 3(9), 715-727.

Pacini, N., Borziani, F., 2016. Oncostatic-Cytoprotective Effect of Melatonin and Other Bioactive Molecules: A Common Target in Mitochondrial Respiration. Int J Mol Sci 17(3), 341.

Pagliarini, D.J., Calvo, S.E., Chang, B., Sheth, S.A., Vafai, S.B., Ong, S.E., Walford, G.A., Sugiana, C., Boneh, A., Chen, W.K., Hill, D.E., Vidal, M., Evans, J.G., Thorburn, D.R., Carr, S.A., Mootha, V.K., 2008. A mitochondrial protein compendium elucidates complex I disease biology. Cell 134(1), 112-123.

Palkovits, M., 1973. Isolated removal of hypothalamic or other brain nuclei of the rat. Brain Res 59, 449-450.

Palmieri, F., 2004. The mitochondrial transporter family (SLC25): physiological and pathological implications. Pflugers Arch 447(5), 689-709.

Palmieri, L., Rottensteiner, H., Girzalsky, W., Scarcia, P., Palmieri, F., Erdmann, R., 2001. Identification and functional reconstitution of the yeast peroxisomal adenine nucleotide transporter. EMBO J 20(18), 5049-5059.

Panosyan, E.H., Lasky, J.L., Lin, H.J., Lai, A., Hai, Y., Guo, X., Quinn, M., Nelson, S.F., Cloughesy, T.F., Nghiemphu, P.L., 2016. Clinical aggressiveness of malignant gliomas is linked to augmented metabolism of amino acids. Journal of neuro-oncology 128(1), 57-66.

Panosyan, E.H., Lin, H.J., Koster, J., Lasky, J.L., 3rd, 2017. In search of druggable targets for GBM amino acid metabolism. BMC Cancer 17(1), 162.

Papandreou, I., Cairns, R.A., Fontana, L., Lim, A.L., Denko, N.C., 2006. HIF-1 mediates adaptation to hypoxia by actively downregulating mitochondrial oxygen consumption. Cell Metab 3(3), 187-197.

Paradies, G., Papa, S., 1975. The transport of monocarboxylic oxoacids in rat liver mitochondria. FEBS Lett 52(1), 149-152.

Park, L.C., Albers, D.S., Xu, H., Lindsay, J.G., Beal, M.F., Gibson, G.E., 2001. Mitochondrial impairment in the cerebellum of the patients with progressive supranuclear palsy. J Neurosci Res 66(5), 1028-1034.

Parks, S.K., Chiche, J., Pouyssegur, J., 2013. Disrupting proton dynamics and energy metabolism for cancer therapy. Nat.Rev.Cancer 13(9), 611-623.

Parry-Billings, M., Leighton, B., Dimitriadis, G.D., Curi, R., Bond, J., Bevan, S., Colquhoun, A., Newsholme, E.A., 1991. The effect of tumour bearing on skeletal muscle glutamine metabolism. Int.J.Biochem. 23(9), 933-937.

Passarella, S., Ostuni, A., Atlante, A., Quagliariello, E., 1988. Increase in the ADP/ATP exchange in rat liver mitochondria irradiated in vitro by helium-neon laser. Biochem Biophys Res Commun 156(2), 978-986.

Patel, S.P., Katyare, S.S., 2005. Differences in kinetic properties of cytochrome oxidase in mitochondria from rat tissues. A comparative study. Z Naturforsch C J Biosci 60(9-10), 785-791.

Patel, T.R., McFadden, B.A., 1978. Caenorhabditis elegans and Ascaris suum: inhibition of isocitrate lyase by itaconate. Exp Parasitol 44(2), 262-268.

Pebay-Peyroula, E., Brandolin, G., 2004. Nucleotide exchange in mitochondria: insight at a molecular level. Curr Opin Struct Biol 14(4), 420-425.

Pedersen, P.L., Catterall, W.A., 1979. The use of thin-layer chromatography on poly(ethyleneimine) cellulose to facilitate assays of ATP-ADP exchange, ATP-Pi exchange, adenylate kinase, and nucleoside diphosphokinase activity. Methods Enzymol 55, 283-289.

Perevoshchikova, I.V., Sorochkina, A.I., Zorov, D.B., Antonenko, Y.N., 2009. Safranine O as a fluorescent probe for mitochondrial membrane potential studied on the single particle level and in suspension. Biochemistry (Mosc) 74(6), 663-671.

Perez-Escuredo, J., Van Hee, V.F., Sboarina, M., Falces, J., Payen, V.L., Pellerin, L., Sonveaux, P., 2016. Monocarboxylate transporters in the brain and in cancer. Biochim Biophys Acta 1863(10), 2481-2497.

Perez-Gomez, C., Campos-Sandoval, J.A., Alonso, F.J., Segura, J.A., Manzanares, E., Ruiz-Sanchez, P., Gonzalez, M.E., Marquez, J., Mates, J.M., 2005. Co-expression of glutaminase K and L isoenzymes in human tumour cells. Biochem.J. 386(Pt 3), 535-542.

Perry, J.R., Laperriere, N., O'Callaghan, C.J., Brandes, A.A., Menten, J., Phillips, C., Fay, M., Nishikawa, R., Cairncross, J.G., Roa, W., Osoba, D., Rossiter, J.P., Sahgal, A., Hirte, H., Laigle-Donadey, F., Franceschi, E., Chinot, O., Golfinopoulos, V., Fariselli, L., Wick, A., Feuvret, L., Back, M., Tills, M., Winch, C., Baumert, B.G., Wick, W., Ding, K., Mason, W.P., Trial, I., 2017. Short-Course Radiation plus Temozolomide in Elderly Patients with Glioblastoma. N Engl J Med 376(11), 1027-1037.

Petronilli, V., Azzone, G.F., Pietrobon, D., 1988. Analysis of mechanisms of free-energy coupling and uncoupling by inhibitor titrations: theory, computer modeling and experiments. Biochim Biophys Acta 932(3), 306-324.

Petronilli, V., Cola, C., Bernardi, P., 1993a. Modulation of the mitochondrial cyclosporin A-sensitive permeability transition pore. II. The minimal requirements for pore induction underscore a key role for transmembrane electrical potential, matrix pH, and matrix Ca2+. J Biol Chem 268(2), 1011-1016.

Petronilli, V., Cola, C., Massari, S., Colonna, R., Bernardi, P., 1993b. Physiological effectors modify voltage sensing by the cyclosporin A-sensitive permeability transition pore of mitochondria. J Biol Chem 268(29), 21939-21945.

Pfaff, E., Heldt, H.W., Klingenberg, M., 1969. Adenine nucleotide translocation of mitochondria. Kinetics of the adenine nucleotide exchange. Eur J Biochem 10(3), 484-493.

Pfaff, E., Klingenberg, M., 1968. Adenine nucleotide translocation of mitochondria. 1. Specificity and control. Eur J Biochem 6(1), 66-79.

Phillips, D., Aponte, A.M., French, S.A., Chess, D.J., Balaban, R.S., 2009. Succinyl-CoA synthetase is a phosphate target for the activation of mitochondrial metabolism. Biochemistry 48(30), 7140-7149.

Phillips, R.C., George, P., Rutman, R.J., 1963. Potentiometric Studies of the Secondary Phosphate Ionizations of Amp, Adp, and Atp, and Calculations of Thermodynamic Data for the Hydrolysis Reactions. Biochemistry 2, 501-508.

Phillips, R.C., George, P., Rutman, R.J., 1966. Thermodynamic studies of the formation and ionization of the magnesium(II) complexes of ADP and ATP over the pH range 5 to 9. J Am Chem Soc 88(12), 2631-2640.

Picklo, M.J., Sr., Olson, S.J., Hayes, J.D., Markesbery, W.R., Montine, T.J., 2001. Elevation of AKR7A2 (succinic semialdehyde reductase) in neurodegenerative disease. Brain Res 916(1-2), 229-238.

Pietrak, B., Zhao, H., Qi, H., Quinn, C., Gao, E., Boyer, J.G., Concha, N., Brown, K., Duraiswami, C., Wooster, R., Sweitzer, S., Schwartz, B., 2011. A tale of two subunits: how the neomorphic R132H IDH1 mutation enhances production of alphaHG. Biochemistry 50(21), 4804-4812.

Pike, L.S., Smift, A.L., Croteau, N.J., Ferrick, D.A., Wu, M., 2011. Inhibition of fatty acid oxidation by etomoxir impairs NADPH production and increases reactive oxygen species resulting in ATP depletion and cell death in human glioblastoma cells. Biochim Biophys Acta 1807(6), 726-734.

Pike Winer, L.S., Wu, M., 2014. Rapid analysis of glycolytic and oxidative substrate flux of cancer cells in a microplate. PLoS One 9(10), e109916.

Pin, J.P., Bockaert, J., 1989. Two distinct mechanisms, differentially affected by excitatory amino acids, trigger GABA release from fetal mouse striatal neurons in primary culture. J Neurosci 9(2), 648-656.

Pires-daSilva, A., Nayernia, K., Engel, W., Torres, M., Stoykova, A., Chowdhury, K., Gruss, P., 2001. Mice deficient for spermatid perinuclear RNA-binding protein show neurologic, spermatogenic, and sperm morphological abnormalities. Dev Biol 233(2), 319-328.

Pisano, J.J., Wilson, J.D., Cohen, L., Abraham, D., Udenfriend, S., 1961. Isolation of gamma-aminobutyrylhistidine (homocarnosine) from brain. J Biol Chem 236, 499-502.

Pisarenko, O., Studneva, I., Khlopkov, V., Solomatina, E., Ruuge, E., 1988. An assessment of anaerobic metabolism during ischemia and reperfusion in isolated guinea pig heart. Biochim Biophys Acta 934(1), 55-63.

Plas, D.R., Thompson, C.B., 2005. Akt-dependent transformation: there is more to growth than just surviving. Oncogene 24(50), 7435-7442.

Porpaczy, Z., Sumegi, B., Alkonyi, I., 1983. Association between the alpha-ketoglutarate dehydrogenase complex and succinate thiokinase. Biochim Biophys Acta 749(2), 172-179.

Porter, R.K., 2001. Mitochondrial proton leak: a role for uncoupling proteins 2 and 3? Biochim Biophys Acta 1504(1), 120-127.

Possemato, R., Marks, K.M., Shaul, Y.D., Pacold, M.E., Kim, D., Birsoy, K., Sethumadhavan, S., Woo, H.K., Jang, H.G., Jha, A.K., Chen, W.W., Barrett, F.G., Stransky, N., Tsun, Z.Y., Cowley, G.S., Barretina, J., Kalaany, N.Y., Hsu, P.P., Ottina, K., Chan, A.M., Yuan, B., Garraway, L.A., Root, D.E., Mino-Kenudson, M., Brachtel, E.F., Driggers, E.M., Sabatini, D.M., 2011. Functional genomics reveal that the serine synthesis pathway is essential in breast cancer. Nature 476(7360), 346-350.

Poteet, E., Choudhury, G.R., Winters, A., Li, W., Ryou, M.G., Liu, R., Tang, L., Ghorpade, A., Wen, Y., Yuan, F., Keir, S.T., Yan, H., Bigner, D.D., Simpkins, J.W., Yang, S.H., 2013. Reversing the Warburg effect as a treatment for glioblastoma. J Biol Chem 288(13), 9153-9164.

Preusch, P.C., Smalley, D.M., 1990. Vitamin K1 2,3-epoxide and quinone reduction: mechanism and inhibition. Free Radic Res Commun 8(4-6), 401-415.

Pullman, M.E., Monroy, G.C., 1963. A Naturally Occurring Inhibitor of Mitochondrial Adenosine Triphosphatase. J Biol Chem 238, 3762-3769.

Qu, W., Oya, S., Lieberman, B.P., Ploessl, K., Wang, L., Wise, D.R., Divgi, C.R., Chodosh, L.A., Thompson, C.B., Kung, H.F., 2012. Preparation and characterization of L-[5-11C]-glutamine for metabolic imaging of tumors. J.Nucl.Med. 53(1), 98-105.

Radjendirane, V., Joseph, P., Lee, Y.H., Kimura, S., Klein-Szanto, A.J., Gonzalez, F.J., Jaiswal, A.K., 1998. Disruption of the DT diaphorase (NQO1) gene in mice leads to increased menadione toxicity. J Biol Chem 273(13), 7382-7389.

Ramanathan, A., Wang, C., Schreiber, S.L., 2005. Perturbational profiling of a cell-line model of tumorigenesis by using metabolic measurements. Proc Natl Acad Sci U S A 102(17), 5992-5997.

Ramirez, A., van der Flier, W.M., Herold, C., Ramonet, D., Heilmann, S., Lewczuk, P., Popp, J., Lacour, A., Drichel, D., Louwersheimer, E., Kummer, M.P., Cruchaga, C., Hoffmann, P., Teunissen, C., Holstege, H., Kornhuber, J., Peters, O., Naj, A.C., Chouraki, V., Bellenguez, C., Gerrish, A., International Genomics of Alzheimer's, P., Alzheimer's Disease Neuroimaging, I., Heun, R., Frolich, L., Hull, M., Buscemi, L., Herms, S., Kolsch, H., Scheltens, P., Breteler, M.M., Ruther, E., Wiltfang, J., Goate, A., Jessen, F., Maier, W., Heneka, M.T., Becker, T., Nothen, M.M., 2014. SUCLG2 identified as both a determinator of CSF Abeta1-42 levels and an attenuator of cognitive decline in Alzheimer's disease. Hum Mol Genet 23(24), 6644-6658.

Rashed, M.S., Bucknall, M.P., Little, D., Awad, A., Jacob, M., Alamoudi, M., Alwattar, M., Ozand, P.T., 1997. Screening blood spots for inborn errors of metabolism by electrospray tandem mass spectrometry with a microplate batch process and a computer algorithm for automated flagging of abnormal profiles. Clin Chem 43(7), 1129-1141.

Rasmussen, U.F., Krustrup, P., Kjaer, M., Rasmussen, H.N., 2003. Experimental evidence against the mitochondrial theory of aging. A study of isolated human skeletal muscle mitochondria. Exp Gerontol 38(8), 877-886.

Ravasz, D., Kacso, G., Fodor, V., Horvath, K., Adam-Vizi, V., Chinopoulos, C., 2017. Catabolism of GABA, succinic semialdehyde or gamma-hydroxybutyrate through the GABA shunt impair mitochondrial substrate-level phosphorylation. Neurochem Int 109, 41-53.

Ravasz, D., Kacso, G., Fodor, V., Horvath, K., Adam-Vizi, V., Chinopoulos, C., 2018. Reduction of 2-methoxy-1,4-naphtoquinone by mitochondrially-localized Nqo1 yielding NAD(+) supports substrate-level phosphorylation during respiratory inhibition. Biochim Biophys Acta.

Ray, B.D., Moore, J.M., Rao, B.D., 1990. 31P NMR studies of enzyme-bound substrate complexes of yeast 3-phosphoglycerate kinase: III. Two ADP binding sites and their Mg(II) affinity; effects of vanadate and arsenate on enzymic complexes with ADP and 3-P-glycerate. J Inorg Biochem 40(1), 47-57.

Reed, L.J., Oliver, R.M., 1968. The multienzyme alpha-keto acid dehydrogenase complexes. Brookhaven Symp Biol 21(2), 397-412.

Reed, P.W., 1979. Ionophores. Methods Enzymol 55, 435-454.

Reich, J.G., Rohde, K., 1983. On the relationship between Z delta pH and delta psi as components of the protonmotive potential in Mitchell's chemiosmotic system. Biomed Biochim Acta 42(1), 37-46.

Reisch, A.S., Elpeleg, O., 2007. Biochemical assays for mitochondrial activity: assays of TCA cycle enzymes and PDHc. Methods Cell Biol 80, 199-222.

Reitzer, L.J., Wice, B.M., Kennell, D., 1979. Evidence that glutamine, not sugar, is the major energy source for cultured HeLa cells. J.Biol.Chem 254(8), 2669-2676.

Rhodes, C.G., Wise, R.J., Gibbs, J.M., Frackowiak, R.S., Hatazawa, J., Palmer, A.J., Thomas, D.G., Jones, T., 1983. In vivo disturbance of the oxidative metabolism of glucose in human cerebral gliomas. Ann Neurol 14(6), 614-626.

Ria, F., Landriscina, M., Remiddi, F., Rosselli, R., Iacoangeli, M., Scerrati, M., Pani, G., Borrello, S., Galeotti, T., 2001. The level of manganese superoxide dismutase content is an independent prognostic factor for glioblastoma. Biological mechanisms and clinical implications. Br J Cancer 84(4), 529-534.

Riboldi, E., Porta, C., Morlacchi, S., Viola, A., Mantovani, A., Sica, A., 2013. Hypoxia-mediated regulation of macrophage functions in pathophysiology. Int Immunol 25(2), 67-75.

Roberts, E., Frankel, S., 1950. gamma-Aminobutyric acid in brain: its formation from glutamic acid. J Biol Chem 187(1), 55-63.

Robinson, J.D., Davis, R.L., Steinberg, M., 1986. Fluoride and beryllium interact with the (Na + K)-dependent ATPase as analogs of phosphate. J Bioenerg Biomembr 18(6), 521-531.

Rodenburg, R.J., 2016. Mitochondrial complex I-linked disease. Biochim Biophys Acta 1857(7), 938-945.

Rodriguez-Prados, J.C., Traves, P.G., Cuenca, J., Rico, D., Aragones, J., Martin-Sanz, P., Cascante, M., Bosca, L., 2010. Substrate fate in activated macrophages: a comparison between innate, classic, and alternative activation. J Immunol 185(1), 605-614.

Rodriguez-Zavala, J.S., Moreno-Sanchez, R., 1998. Modulation of oxidative phosphorylation by Mg2+ in rat heart mitochondria. J Biol Chem 273(14), 7850-7855.

Roggendorf, W., Strupp, S., Paulus, W., 1996. Distribution and characterization of microglia/macrophages in human brain tumors. Acta Neuropathol. 92, 288-293.

Rognstad, R., Katz, J., 1972. Gluconeogenesis in the kidney cortex. Quantitative estimation of carbon flow. Journal of Biological Chemistry 247(19), 6047-6054.

Romani, A., Dowell, E., Scarpa, A., 1991. Cyclic AMP-induced Mg2+ release from rat liver hepatocytes, permeabilized hepatocytes, and isolated mitochondria. J Biol Chem 266(36), 24376-24384.

Rosing, J., Slater, E.C., 1972. The value of G degrees for the hydrolysis of ATP. Biochim Biophys Acta 267(2), 275-290.

Roslin, M., Henriksson, R., Bergstrom, P., Ungerstedt, U., Bergenheim, A.T., 2003. Baseline levels of glucose metabolites, glutamate and glycerol in malignant glioma assessed by stereotactic microdialysis. Journal of neuro-oncology 61(2), 151-160.

Rossignol, R., Gilkerson, R., Aggeler, R., Yamagata, K., Remington, S.J., Capaldi, R.A., 2004. Energy substrate modulates mitochondrial structure and oxidative capacity in cancer cells. Cancer Res 64(3), 985-993.

Rossignol, R., Letellier, T., Malgat, M., Rocher, C., Mazat, J.P., 2000. Tissue variation in the control of oxidative phosphorylation: implication for mitochondrial diseases. Biochem J 347 Pt 1, 45-53.

Roth, R.H., 1970. Formation and regional distribution of gamma-hydroxybutyric acid in mammalian brain. Biochem Pharmacol 19(12), 3013-3019.

Rotig, A., Poulton, J., 2009. Genetic causes of mitochondrial DNA depletion in humans. Biochim Biophys Acta 1792(12), 1103-1108.

Rouslin, W., 1987. The mitochondrial adenosine 5'-triphosphatase in slow and fast heart rate hearts. Am J Physiol 252(3 Pt 2), H622-627.

Rouslin, W., Broge, C.W., 1990. Regulation of the mitochondrial adenosine 5'-triphosphatase in situ during ischemia and in vitro in intact and sonicated mitochondria from slow and fast heart-rate hearts. Arch Biochem Biophys 280(1), 103-111.

Rouslin, W., Broge, C.W., 1993. Factors affecting the species-homologous and species-heterologous binding of mitochondrial ATPase inhibitor, IF1, to the mitochondrial ATPase of slow and fast heart-rate hearts. Arch Biochem Biophys 303(2), 443-450.

Rouslin, W., Broge, C.W., 1996. IF1 function in situ in uncoupler-challenged ischemic rabbit, rat, and pigeon hearts. J Biol Chem 271(39), 23638-23641.

Rouslin, W., Broge, C.W., Grupp, I.L., 1990. ATP depletion and mitochondrial functional loss during ischemia in slow and fast heart-rate hearts. Am J Physiol 259(6 Pt 2), H1759-1766.

Rouslin, W., Erickson, J.L., Solaro, R.J., 1986. Effects of oligomycin and acidosis on rates of ATP depletion in ischemic heart muscle. Am J Physiol 250(3 Pt 2), H503-508.

Rouslin, W., Frank, G.D., Broge, C.W., 1995. Content and binding characteristics of the mitochondrial ATPase inhibitor, IF1, in the tissues of several slow and fast heart-rate homeothermic species and in two poikilotherms. J Bioenerg Biomembr 27(1), 117-125.

Rubinstein, L.J., 1972. Tumors of the central nervous system. Armed Forces Institute of Pathology, Washington, D.C.

Rulfs, J., Aprille, J.R., 1982. Adenine nucleotide pool size, adenine nucleotide translocase activity, and respiratory activity in newborn rabbit liver mitochondria. Biochim Biophys Acta 681(2), 300-304.

Rushmore, T.H., Kong, A.N., 2002. Pharmacogenomics, regulation and signaling pathways of phase I and II drug metabolizing enzymes. Curr Drug Metab 3(5), 481-490.

Rutter, G.A., Osbaldeston, N.J., McCormack, J.G., Denton, R.M., 1990. Measurement of matrix free Mg2+ concentration in rat heart mitochondria by using entrapped fluorescent probes. Biochem J 271(3), 627-634.

Ryzlak, M.T., Pietruszko, R., 1988. Human brain "high Km" aldehyde dehydrogenase: purification, characterization, and identification as NAD+ -dependent succinic semialdehyde dehydrogenase. Arch Biochem Biophys 266(2), 386-396.

Saada, A., Bar-Meir, M., Belaiche, C., Miller, C., Elpeleg, O., 2004. Evaluation of enzymatic assays and compounds affecting ATP production in mitochondrial respiratory chain complex I deficiency. Anal Biochem 335(1), 66-72.

Sack, M.N., Finkel, T., 2012. Mitochondrial metabolism, sirtuins, and aging. Cold Spring Harb Perspect Biol 4(12).

Sagi-Eisenberg, R., Gutman, M., 1979. Generation of high delta psi in respiring submitochondrial particles by steady-state accumulation of oxidized N,N,N',N'-tetramethyl-p-phenylenediamine. Eur J Biochem 97(1), 127-132.

Sakai, A., Kusumoto, A., Kiso, Y., Furuya, E., 2004. Itaconate reduces visceral fat by inhibiting fructose 2,6-bisphosphate synthesis in rat liver. Nutrition 20(11-12), 997-1002.

Salganicoff, L., De Robertis, E., 1963. Subcellular distribution of glutamic decarboxylase and gamma-aminobutyric alpha-ketoglutaric transaminase. Life Sci (1962) 2, 85-91.

Salminen, M., Meyer, B.I., Bober, E., Gruss, P., 2000. Netrin 1 is required for semicircular canal formation in the mouse inner ear. Development 127(1), 13-22.

Sanadi, D.R., Gibson, M., Ayengar, P., 1954. Guanosine triphosphate, the primary product of phosphorylation coupled to the breakdown of succinyl coenzyme A. Biochim Biophys Acta 14(3), 434-436.

Sanchez-Arago, M., Formentini, L., Martinez-Reyes, I., Garcia-Bermudez, J., Santacatterina, F., Sanchez-Cenizo, L., Willers, I.M., Aldea, M., Najera, L., Juarranz, A., Lopez, E.C., Clofent, J., Navarro, C., Espinosa, E., Cuezva, J.M., 2013. Expression, regulation and clinical relevance of the ATPase inhibitory factor 1 in human cancers. Oncogenesis. 2, e46.

Sang, S., Pan, X., Chen, Z., Zeng, F., Pan, S., Liu, H., Jin, L., Fei, G., Wang, C., Ren, S., Jiao, F., Bao, W., Zhou, W., Guan, Y., Zhang, Y., Shi, H., Wang, Y., Yu, X., Wang, Y., Zhong, C., 2018. Thiamine diphosphate reduction strongly correlates with brain glucose hypometabolism in Alzheimer's disease, whereas amyloid deposition does not. Alzheimers Res Ther 10(1), 26.

Sarkadi, B., Meszaros, K., Krencz, I., Canu, L., Krokker, L., Zakarias, S., Barna, G., Sebestyen, A., Papay, J., Hujber, Z., Butz, H., Darvasi, O., Igaz, P., Doczi, J., Luconi, M., Chinopoulos, C., Patocs, A., 2020. Glutaminases as a Novel Target for SDHB-Associated Pheochromocytomas/Paragangliomas. Cancers (Basel) 12(3).

Sasaki, N., Sato, T., Marban, E., O'Rourke, B., 2001. ATP consumption by uncoupled mitochondria activates sarcolemmal K(ATP) channels in cardiac myocytes. Am J Physiol Heart Circ Physiol 280(4), H1882-1888.

Sato, H., Tamba, M., Ishii, T., Bannai, S., 1999. Cloning and expression of a plasma membrane cystine/glutamate exchange transporter composed of two distinct proteins. J.Biol.Chem 274(17), 11455-11458.

Schaefer, A.M., McFarland, R., Blakely, E.L., He, L., Whittaker, R.G., Taylor, R.W., Chinnery, P.F., Turnbull, D.M., 2008. Prevalence of mitochondrial DNA disease in adults. Ann Neurol 63(1), 35-39.

Schaefer, A.M., Taylor, R.W., Turnbull, D.M., Chinnery, P.F., 2004. The epidemiology of mitochondrial disorders--past, present and future. Biochim Biophys Acta 1659(2-3), 115-120.

Schafer, D.F., Jones, E.A., 1982. Hepatic encephalopathy and the gamma-aminobutyric-acid neurotransmitter system. Lancet 1(8262), 18-20.

Scheithauer, B.W., Bruner, J.M., 1987. The ultrastructural spectrum of astrocytic neoplasms. Ultrastruct Pathol 11(5-6), 535-581.

Scherer, H.J., 1940. A critical review: The pathology of cerebral gliomas. J. Neurol. Neuropsychiat. 3, 147-177.

Schnopp, N.M., Kosel, S., Egensperger, R., Graeber, M.B., 1996. Regional heterogeneity of mtDNA heteroplasmy in parkinsonian brain. Clin Neuropathol 15(6), 348-352.

Schonfeld, P., 1990. Does the function of adenine nucleotide translocase in fatty acid uncoupling depend on the type of mitochondria? FEBS Lett 264(2), 246-248.

Schousboe, A., Waagepetersen, H.S., 2006. Glial modulation of GABAergic and glutamat ergic neurotransmission. Curr Top Med Chem 6(10), 929-934.

Schousboe, A., Waagepetersen, H.S., 2007. GABA: homeostatic and pharmacological aspects. Prog Brain Res 160, 9-19.

Schwenke, W.D., Soboll, S., Seitz, H.J., Sies, H., 1981. Mitochondrial and cytosolic ATP/ADP ratios in rat liver in vivo. Biochem J 200(2), 405-408.

Schwimmer, C., Lefebvre-Legendre, L., Rak, M., Devin, A., Slonimski, P.P., di Rago, J.P., Rigoulet, M., 2005. Increasing mitochondrial substrate-level phosphorylation can rescue respiratory growth of an ATP synthase-deficient yeast. J Biol Chem 280(35), 30751-30759.

Scorrano, L., Petronilli, V., Bernardi, P., 1997. On the voltage dependence of the mitochondrial permeability transition pore. A critical appraisal. J Biol Chem 272(19), 12295-12299.

Scott, I.D., Nicholls, D.G., 1980. Energy transduction in intact synaptosomes. Influence of plasma-membrane depolarization on the respiration and membrane potential of internal mitochondria determined in situ. Biochem J 186(1), 21-33.

Selak, M.A., Armour, S.M., MacKenzie, E.D., Boulahbel, H., Watson, D.G., Mansfield, K.D., Pan, Y., Simon, M.C., Thompson, C.B., Gottlieb, E., 2005. Succinate links TCA cycle dysfunction to oncogenesis by inhibiting HIF-alpha prolyl hydroxylase. Cancer Cell 7(1), 77-85.

Semenza, G.L., 2010. HIF-1: upstream and downstream of cancer metabolism. Curr Opin Genet Dev 20(1), 51-56.

Semenza, G.L., 2017. Hypoxia-inducible factors: coupling glucose metabolism and redox regulation with induction of the breast cancer stem cell phenotype. EMBO J 36(3), 252-259.

Senior, A.E., Nadanaciva, S., Weber, J., 2000. Rate acceleration of ATP hydrolysis by F(1)F(o)-ATP synthase. J Exp Biol 203(Pt 1), 35-40.

Sequerra, E.B., Gardino, P., Hedin-Pereira, C., de Mello, F.G., 2007. Putrescine as an important source of GABA in the postnatal rat subventricular zone. Neuroscience 146(2), 489-493.

Seyfried, T.N., 2001. Perspectives on brain tumor formation involving macrophages, glia, and neural stem cells. Perspect Biol Med 44(2), 263-282.

Seyfried, T.N., 2012a. Cancer as a Metabolic Disease: On the Origin, Management, and Prevention of Cancer, Cancer as a Metabolic Disease. John Wiley & Sons, Hoboken, NJ, pp. 133-144.

Seyfried, T.N., 2012b. Mitochondria: The ultimate tumor suppressor, Cancer as a Metabolic Disease. John Wiley & Sons, Hoboken, NJ, pp. 195-205.

Seyfried, T.N., 2015. Cancer as a mitochondrial metabolic disease. Frontiers in cell and developmental biology 3, 43.

Seyfried, T.N., Arismendi-Morillo, G., Mukherjee, P., Chinopoulos, C., 2020a. On the Origin of ATP Synthesis in Cancer. iScience 23(11), 101761.

Seyfried, T.N., Flores, R., Poff, A.M., D'Agostino, D.P., Mukherjee, P., 2015. Metabolic therapy: a new paradigm for managing malignant brain cancer. Cancer letters 356(2 Pt A), 289-300.

Seyfried, T.N., Flores, R.E., Poff, A.M., D'Agostino, D.P., 2014. Cancer as a metabolic disease: implications for novel therapeutics. Carcinogenesis 35(3), 515-527.

Seyfried, T.N., Mukherjee, P., 2005. Targeting energy metabolism in brain cancer: review and hypothesis. Nutr Metab (Lond) 2, 30.

Seyfried, T.N., Mukherjee, P., Iyikesici, M.S., Slocum, A., Kalamian, M., Spinosa, J.P., Chinopoulos, C., 2020b. Consideration of Ketogenic Metabolic Therapy as a Complementary or Alternative Approach for Managing Breast Cancer. Front Nutr 7, 21.

Seyfried, T.N., Sanderson, T.M., El-Abbadi, M.M., McGowan, R., Mukherjee, P., 2003. Role of glucose and ketone bodies in the metabolic control of experimental brain cancer. Br J Cancer 89(7), 1375-1382.

Seyfried, T.N., Shelton, L.M., 2010. Cancer as a metabolic disease. Nutr Metab (Lond) 7(1), 7.

Seyfried, T.N., Yu, G., Maroon, J.C., D'Agostino, D.P., 2017. Press-pulse: a novel therapeutic strategy for the metabolic management of cancer. Nutr Metab (Lond) 14, 19.

Shavit, N., San Pietro, A., 1967. K+ -dependent uncoupling of photophosphorylation by nigericin. Biochem Biophys Res Commun 28(2), 277-283.

Shelton, L.M., 2010. Targeting energy metabolism in brain cancer, Biology. Boston College, Chestnut Hill, p. 228.

Shelton, L.M., Huysentruyt, L.C., Mukherjee, P., Seyfried, T.N., 2010a. Calorie restriction as an anti-invasive therapy for malignant brain cancer in the VM mouse. ASN Neuro 2(3), e00038.

Shelton, L.M., Huysentruyt, L.C., Seyfried, T.N., 2010b. Glutamine targeting inhibits systemic metastasis in the VM-M3 murine tumor model. Inter. J. Cancer. 127(10), 2478-2485.

Shelton, L.M., Mukherjee, P., Huysentruyt, L.C., Urits, I., Rosenberg, J.A., Seyfried, T.N., 2010c. A novel pre-clinical in vivo mouse model for malignant brain tumor growth and invasion. Journal of neuro-oncology 99(2), 165-176.

Shi, Q., Risa, O., Sonnewald, U., Gibson, G.E., 2009. Mild reduction in the activity of the alpha-ketoglutarate dehydrogenase complex elevates GABA shunt and glycolysis. J Neurochem 109 Suppl 1, 214-221.

Shin, J.H., Yang, J.Y., Jeon, B.Y., Yoon, Y.J., Cho, S.N., Kang, Y.H., Ryu, D.H., Hwang, G.S., 2011. (1)H NMR-based metabolomic profiling in mice infected with Mycobacterium tuberculosis. J Proteome Res 10(5), 2238-2247.

Shin, S.J., Lee, W.K., Lim, H.W., Park, J., 2000. Characterization of the ATP transporter in the reconstituted rough endoplasmic reticulum proteoliposomes. Biochim Biophys Acta 1468(1-2), 55-62.

Shneyvays, V., Leshem, D., Shmist, Y., Zinman, T., Shainberg, A., 2005. Effects of menadione and its derivative on cultured cardiomyocytes with mitochondrial disorders. J Mol Cell Cardiol 39(1), 149-158.

Shrago, E., Ball, M., Sul, H.S., Baquer, N.Z., McLean, P., 1977. Interrelationship in the regulation of pyruvate dehydrogenase and adenine-nucleotide translocase by palmitoyl-CoA in isolated mitochondria. Eur J Biochem 75(1), 83-89.

Shwetha, S.D., Shastry, A.H., Arivazhagan, A., Santosh, V., 2016. Manganese superoxide dismutase (MnSOD) is a malignant astrocytoma specific biomarker and associated with adverse prognosis in p53 expressing glioblastoma. Pathol Res Pract 212(1), 17-23.

Sidoryk, M., Matyja, E., Dybel, A., Zielinska, M., Bogucki, J., Jaskolski, D.J., Liberski, P.P., Kowalczyk, P., Albrecht, J., 2004. Increased expression of a glutamine transporter SNAT3 is a marker of malignant gliomas. Neuroreport 15(4), 575-578.

Sims, N.R., 1990. Rapid isolation of metabolically active mitochondria from rat brain and subregions using Percoll density gradient centrifugation. J Neurochem 55(2), 698-707.

Sipe, J.C., Herman, M.M., Rubinstein, L.J., 1973. Electron microscopic observations on human glioblastomas and astrocytomas maintained in organ culture systems. The American journal of pathology 73(3), 589-606.

Skarnes, W.C., Rosen, B., West, A.P., Koutsourakis, M., Bushell, W., Iyer, V., Mujica, A.O., Thomas, M., Harrow, J., Cox, T., Jackson, D., Severin, J., Biggs, P., Fu, J., Nefedov, M., de Jong, P.J., Stewart, A.F., Bradley, A., 2011. A conditional knockout resource for the genome-wide study of mouse gene function. Nature 474(7351), 337-342.

Skulachev, V.P., 1998. Uncoupling: new approaches to an old problem of bioenergetics. Biochim Biophys Acta 1363(2), 100-124.

Sluse, F.E., 1996. Mitochondrial metabolite carrier family, topology, structure and functional properties: an overview. Acta Biochim Pol 43(2), 349-360.

Snyder, N.W., Basu, S.S., Worth, A.J., Mesaros, C., Blair, I.A., 2015. Metabolism of propionic acid to a novel acyl-coenzyme A thioester by mammalian cell lines and platelets. Journal of lipid research 56(1), 142-150.

Soboll, S., Akerboom, T.P., Schwenke, W.D., Haase, R., Sies, H., 1980. Mitochondrial and cytosolic ATP/ADP ratios in isolated hepatocytes. A comparison of the digitonin method and the non-aqueous fractionation procedure. Biochem J 192(3), 951-954.

Soboll, S., Scholz, R., Heldt, H.W., 1978. Subcellular metabolite concentrations. Dependence of mitochondrial and cytosolic ATP systems on the metabolic state of perfused rat liver. Eur J Biochem 87(2), 377-390.

Soboll, S., Seitz, H.J., Sies, H., Ziegler, B., Scholz, R., 1984. Effect of long-chain fatty acyl-CoA on mitochondrial and cytosolic ATP/ADP ratios in the intact liver cell. Biochem J 220(2), 371-376.

Soeda, A., Hara, A., Kunisada, T., Yoshimura, S., Iwama, T., Park, D.M., 2015. The evidence of glioblastoma heterogeneity. Sci Rep 5, 7979.

Soghomonian, J.J., Martin, D.L., 1998. Two isoforms of glutamate decarboxylase: why? Trends Pharmacol Sci 19(12), 500-505.

Solaini, G., Sgarbi, G., Baracca, A., 2011. Oxidative phosphorylation in cancer cells. Biochim Biophys Acta 1807(6), 534-542.

Sonnewald, U., Schousboe, A., 2016. Introduction to the Glutamate-Glutamine Cycle. Adv Neurobiol 13, 1-7.

Souba, W.W., 1993. Glutamine and cancer. Ann.Surg. 218(6), 715-728.

Sporn, M.B., Liby, K.T., 2012. NRF2 and cancer: the good, the bad and the importance of context. Nat Rev Cancer 12(8), 564-571.

Srere, P.A., 1969. [1] Citrate synthase: [EC 4.1.3.7. Citrate oxaloacetate-lyase (CoA-acetylating)], Methods in Enzymology. Academic Press, pp. 3-11.

Starkov, A.A., 2013. An update on the role of mitochondrial alpha-ketoglutarate dehydrogenase in oxidative stress. Mol Cell Neurosci 55, 13-16.

Starkov, A.A., Fiskum, G., Chinopoulos, C., Lorenzo, B.J., Browne, S.E., Patel, M.S., Beal, M.F., 2004. Mitochondrial alpha-ketoglutarate dehydrogenase complex generates reactive oxygen species. J Neurosci 24(36), 7779-7788.

Steiger, M.G., Blumhoff, M.L., Mattanovich, D., Sauer, M., 2013. Biochemistry of microbial itaconic acid production. Front Microbiol 4, 23.

Stein, A.M., Kaplan, N.O., 1958. The diaphorases of rat-liver mitochondria. Biochim Biophys Acta 29(2), 452-453.

Stein, L.R., Imai, S., 2012. The dynamic regulation of NAD metabolism in mitochondria. Trends Endocrinol Metab 23(9), 420-428.

Strausberg, R.L., Feingold, E.A., Grouse, L.H., Derge, J.G., Klausner, R.D., Collins, F.S., Wagner, L., Shenmen, C.M., Schuler, G.D., Altschul, S.F., Zeeberg, B., Buetow, K.H., Schaefer, C.F., Bhat, N.K., Hopkins, R.F., Jordan, H., Moore, T., Max, S.I., Wang, J., Hsieh, F., Diatchenko, L., Marusina, K., Farmer, A.A., Rubin, G.M., Hong, L., Stapleton, M., Soares, M.B., Bonaldo, M.F., Casavant, T.L., Scheetz, T.E., Brownstein, M.J., Usdin, T.B., Toshiyuki, S., Carninci, P., Prange, C., Raha, S.S., Loquellano, N.A., Peters, G.J., Abramson, R.D., Mullahy, S.J., Bosak, S.A., McEwan, P.J., McKernan, K.J., Malek, J.A., Gunaratne, P.H., Richards, S., Worley, K.C., Hale, S., Garcia, A.M., Gay, L.J., Hulyk, S.W., Villalon, D.K., Muzny, D.M., Sodergren, E.J., Lu, X., Gibbs, R.A., Fahey, J., Helton, E., Ketteman, M., Madan, A., Rodrigues, S., Sanchez, A., Whiting, M., Madan, A., Young, A.C., Shevchenko, Y., Bouffard, G.G., Blakesley, R.W., Touchman, J.W., Green, E.D., Dickson, M.C., Rodriguez, A.C., Grimwood, J., Schmutz, J., Myers, R.M., Butterfield, Y.S., Krzywinski, M.I., Skalska, U., Smailus, D.E., Schnerch, A., Schein, J.E., Jones, S.J., Marra, M.A., Mammalian Gene Collection Program, T., 2002. Generation and initial analysis of more than 15,000 full-length human and mouse cDNA sequences. Proc Natl Acad Sci U S A 99(26), 16899-16903.

Strelko, C.L., Lu, W., Dufort, F.J., Seyfried, T.N., Chiles, T.C., Rabinowitz, J.D., Roberts, M.F., 2011. Itaconic acid is a mammalian metabolite induced during macrophage activation. J Am Chem Soc 133(41), 16386-16389.

Struys, E.A., 2006. D-2-Hydroxyglutaric aciduria: unravelling the biochemical pathway and the genetic defect. J Inherit Metab Dis 29(1), 21-29.

Struys, E.A., Salomons, G.S., Achouri, Y., Van Schaftingen, E., Grosso, S., Craigen, W.J., Verhoeven, N.M., Jakobs, C., 2005a. Mutations in the D-2-hydroxyglutarate dehydrogenase gene cause D-2-hydroxyglutaric aciduria. Am J Hum Genet 76(2), 358-360.

Struys, E.A., Verhoeven, N.M., Ten Brink, H.J., Wickenhagen, W.V., Gibson, K.M., Jakobs, C., 2005b. Kinetic characterization of human hydroxyacid-oxoacid transhydrogenase: relevance to D-2-hydroxyglutaric and gamma-hydroxybutyric acidurias. J Inherit Metab Dis 28(6), 921-930.

Stryer, L., 1995. Biochemistry. W.H. Freeman & Company.

Stuckey, D.J., Anthony, D.C., Lowe, J.P., Miller, J., Palm, W.M., Styles, P., Perry, V.H., Blamire, A.M., Sibson, N.R., 2005. Detection of the inhibitory neurotransmitter GABA in macrophages by magnetic resonance spectroscopy. J Leukoc Biol 78(2), 393-400.

Stumpf, D.A., McAfee, J., Parks, J.K., Eguren, L., 1980. Propionate inhibition of succinate:CoA ligase (GDP) and the citric acid cycle in mitochondria. Pediatr Res 14(10), 1127-1131.

Stupp, R., Hegi, M.E., Mason, W.P., van den Bent, M.J., Taphoorn, M.J., Janzer, R.C., Ludwin, S.K., Allgeier, A., Fisher, B., Belanger, K., Hau, P., Brandes, A.A., Gijtenbeek, J., Marosi, C., Vecht, C.J., Mokhtari, K., Wesseling, P., Villa, S., Eisenhauer, E., Gorlia, T., Weller, M., Lacombe, D., Cairncross, J.G., Mirimanoff, R.O., European Organisation for, R., Treatment of Cancer Brain, T., Radiation Oncology, G., National Cancer Institute of Canada Clinical Trials, G., 2009. Effects of radiotherapy with concomitant and adjuvant temozolomide versus radiotherapy alone on survival in glioblastoma in a randomised phase III study: 5-year analysis of the EORTC-NCIC trial. Lancet Oncol 10(5), 459-466.

Suarez, R.K., Lighton, J.R., Brown, G.S., Mathieu-Costello, O., 1991. Mitochondrial respiration in hummingbird flight muscles. Proc Natl Acad Sci U S A 88(11), 4870-4873.

Sullivan, L.B., Gui, D.Y., Hosios, A.M., Bush, L.N., Freinkman, E., Vander Heiden, M.G., 2015. Supporting Aspartate Biosynthesis Is an Essential Function of Respiration in Proliferating Cells. Cell 162(3), 552-563.

Sullivan, L.B., Martinez-Garcia, E., Nguyen, H., Mullen, A.R., Dufour, E., Sudarshan, S., Licht, J.D., DeBerardinis, R.J., Chandel, N.S., 2013. The proto-oncometabolite fumarate binds glutathione to amplify ROS-dependent signaling. Mol.Cell 51(2), 236-248.

Sunkin, S.M., Ng, L., Lau, C., Dolbeare, T., Gilbert, T.L., Thompson, C.L., Hawrylycz, M., Dang, C., 2013. Allen Brain Atlas: an integrated spatio-temporal portal for exploring the central nervous system. Nucleic Acids Res 41(Database issue), D996-D1008.

Suno, M., Nagaoka, A., 1984. Inhibition of lipid peroxidation by a novel compound, idebenone (CV-2619). Jpn J Pharmacol 35(2), 196-198.

Supplie, L.M., Duking, T., Campbell, G., Diaz, F., Moraes, C.T., Gotz, M., Hamprecht, B., Boretius, S., Mahad, D., Nave, K.A., 2017. Respiration-Deficient Astrocytes Survive As Glycolytic Cells In Vivo. J Neurosci 37(16), 4231-4242.

Swietach, P., Vaughan-Jones, R.D., Harris, A.L., Hulikova, A., 2014. The chemistry, physiology and pathology of pH in cancer. Philos.Trans.R.Soc.Lond B Biol.Sci. 369(1638), 20130099.

Swinnen, J.V., Brusselmans, K., Verhoeven, G., 2006. Increased lipogenesis in cancer cells: new players, novel targets. Curr.Opin.Clin.Nutr.Metab Care 9(4), 358-365.

Ta, N.L., Seyfried, T.N., 2015. Influence of Serum and Hypoxia on Incorporation of [(14)C]-D-Glucose or [(14)C]-L-Glutamine into Lipids and Lactate in Murine Glioblastoma Cells. Lipids 50(12), 1167-1184.

Taegtmeyer, H., 1978. Metabolic responses to cardiac hypoxia. Increased production of succinate by rabbit papillary muscles. Circ Res 43(5), 808-815.

Tager, J.M., Wanders, R.J., Groen, A.K., Kunz, W., Bohnensack, R., Kuster, U., Letko, G., Bohme, G., Duszynski, J., Wojtczak, L., 1983. Control of mitochondrial respiration. FEBS Lett 151(1), 1-9.

Taivassalo, T., Fu, K., Johns, T., Arnold, D., Karpati, G., Shoubridge, E.A., 1999. Gene shifting: a novel therapy for mitochondrial myopathy. Hum Mol Genet 8(6), 1047-1052.

Takano, T., Lin, J.H., Arcuino, G., Gao, Q., Yang, J., Nedergaard, M., 2001. Glutamate release promotes growth of malignant gliomas. Nature medicine 7(9), 1010-1015.

Tang, P.H., Miles, M.V., Miles, L., Quinlan, J., Wong, B., Wenisch, A., Bove, K., 2004. Measurement of reduced and oxidized coenzyme Q9 and coenzyme Q10 levels in mouse tissues by HPLC with coulometric detection. Clin Chim Acta 341(1-2), 173-184.

Tang, X.D., Tong, Z.Q., 1995. An adenosine triphosphate (ATP)-sensitive K+ channel of rat neocortical neurons is bi-gated by intracellular ATP and voltage: a novel channel gating mechanism? Neurosci Lett 193(2), 93-96.

Tannahill, G.M., Curtis, A.M., Adamik, J., Palsson-McDermott, E.M., McGettrick, A.F., Goel, G., Frezza, C., Bernard, N.J., Kelly, B., Foley, N.H., Zheng, L., Gardet, A., Tong, Z., Jany, S.S., Corr, S.C., Haneklaus, M., Caffrey, B.E., Pierce, K., Walmsley, S., Beasley, F.C., Cummins, E., Nizet, V., Whyte, M., Taylor, C.T., Lin, H., Masters, S.L., Gottlieb, E., Kelly, V.P., Clish, C., Auron, P.E., Xavier, R.J., O'Neill, L.A., 2013. Succinate is an inflammatory signal that induces IL-1beta through HIF-1alpha. Nature 496(7444), 238-242.

Tanner, S., Shen, Z., Ng, J., Florea, L., Guigo, R., Briggs, S.P., Bafna, V., 2007. Improving gene annotation using peptide mass spectrometry. Genome Res 17(2), 231-239.

Taphoorn, M.J., Stupp, R., Coens, C., Osoba, D., Kortmann, R., van den Bent, M.J., Mason, W., Mirimanoff, R.O., Baumert, B.G., Eisenhauer, E., Forsyth, P., Bottomley, A., European Organisation for, R., Treatment of Cancer Brain Tumour, G., Group, E.R., National Cancer Institute of Canada Clinical Trials, G., 2005. Health-related quality of life in patients with glioblastoma: a randomised controlled trial. Lancet Oncol 6(12), 937-944.

Tardito, S., Oudin, A., Ahmed, S.U., Fack, F., Keunen, O., Zheng, L., Miletic, H., Sakariassen, P.O., Weinstock, A., Wagner, A., Lindsay, S.L., Hock, A.K., Barnett, S.C., Ruppin, E., Morkve, S.H., Lund-Johansen, M., Chalmers, A.J., Bjerkvig, R., Niclou, S.P., Gottlieb, E., 2015. Glutamine synthetase activity fuels nucleotide biosynthesis and supports growth of glutamine-restricted glioblastoma. Nat Cell Biol 17(12), 1556-1568.

Tavakoli, S., Zamora, D., Ullevig, S., Asmis, R., 2013. Bioenergetic profiles diverge during macrophage polarization: implications for the interpretation of 18F-FDG PET imaging of atherosclerosis. J Nucl Med 54(9), 1661-1667.

ter Welle, H.F., Slater, E.C., 1967. Uncoupling of respiratory-chain phosphorylation by arsenate. Biochim Biophys Acta 143(1), 1-17.

Terada, H., 1975. Some biochemical and physiochemical properties of the potent uncoupler SF 6847 (3,5-di-tert-butyl-4-hydroxybenzylidenemalononitrile). Biochim Biophys Acta 387(3), 519-532.

Terada, H., 1981. The interaction of highly active uncouplers with mitochondria. Biochim Biophys Acta 639(3-4), 225-242.

Ternette, N., Yang, M., Laroyia, M., Kitagawa, M., O'Flaherty, L., Wolhulter, K., Igarashi, K., Saito, K., Kato, K., Fischer, R., Berquand, A., Kessler, B.M., Lappin, T., Frizzell, N., Soga, T., Adam, J., Pollard, P.J., 2013. Inhibition of mitochondrial aconitase by succination in fumarate hydratase deficiency. Cell Rep. 3(3), 689-700.

Terwel, D., Bothmer, J., Wolf, E., Meng, F., Jolles, J., 1998. Affected enzyme activities in Alzheimer's disease are sensitive to antemortem hypoxia. J Neurol Sci 161(1), 47-56.

Theodoulou, F.L., Sibon, O.C., Jackowski, S., Gout, I., 2014. Coenzyme A and its derivatives: renaissance of a textbook classic. Biochem Soc Trans 42(4), 1025-1032.

Thevananther, S., 2010. Adipose to the rescue: peripheral fat fuels liver regeneration. Hepatology 52(6), 1875-1876.

Thevenet, J., De Marchi, U., Domingo, J.S., Christinat, N., Bultot, L., Lefebvre, G., Sakamoto, K., Descombes, P., Masoodi, M., Wiederkehr, A., 2016. Medium-chain fatty acids inhibit mitochondrial metabolism in astrocytes promoting astrocyte-neuron lactate and ketone body shuttle systems. FASEB J 30(5), 1913-1926.

Tieu, M.T., Lovblom, L.E., McNamara, M.G., Mason, W., Laperriere, N., Millar, B.A., Menard, C., Kiehl, T.R., Perkins, B.A., Chung, C., 2015. Impact of glycemia on survival of glioblastoma patients treated with radiation and temozolomide. Journal of neuro-oncology 124(1), 119-126.

Ting-Beall, H.P., Needham, D., Hochmuth, R.M., 1993. Volume and osmotic properties of human neutrophils. Blood 81(10), 2774-2780.

Todesco, T., Rao, A.V., Bosello, O., Jenkins, D.J., 1991. Propionate lowers blood glucose and alters lipid metabolism in healthy subjects. Am J Clin Nutr 54(5), 860-865.

Tomashek, J.J., Brusilow, W.S., 2000. Stoichiometry of energy coupling by proton-translocating ATPases: a history of variability. J Bioenerg Biomembr 32(5), 493-500.

Toye, A.A., Lippiat, J.D., Proks, P., Shimomura, K., Bentley, L., Hugill, A., Mijat, V., Goldsworthy, M., Moir, L., Haynes, A., Quarterman, J., Freeman, H.C., Ashcroft, F.M., Cox, R.D., 2005. A genetic and physiological study of impaired glucose homeostasis control in C57BL/6J mice. Diabetologia 48(4), 675-686.

Trapp, S., Ballanyi, K., 1995. KATP channel mediation of anoxia-induced outward current in rat dorsal vagal neurons in vitro. J Physiol 487(1), 37-50.

Traver, R.D., Siegel, D., Beall, H.D., Phillips, R.M., Gibson, N.W., Franklin, W.A., Ross, D., 1997. Characterization of a polymorphism in NAD(P)H: quinone oxidoreductase (DT-diaphorase). Br J Cancer 75(1), 69-75.

Traves, P.G., de Atauri, P., Marin, S., Pimentel-Santillana, M., Rodriguez-Prados, J.C., Marin de Mas, I., Selivanov, V.A., Martin-Sanz, P., Bosca, L., Cascante, M., 2012. Relevance of the MEK/ERK signaling pathway in the metabolism of activated macrophages: a metabolomic approach. J Immunol 188(3), 1402-1410.

Tretter, L., Adam-Vizi, V., 2000. Inhibition of Krebs cycle enzymes by hydrogen peroxide: A key role of [alpha]-ketoglutarate dehydrogenase in limiting NADH production under oxidative stress. J Neurosci 20(24), 8972-8979.

Tretter, L., Adam-Vizi, V., 2004. Generation of reactive oxygen species in the reaction catalyzed by alpha-ketoglutarate dehydrogenase. J Neurosci 24(36), 7771-7778.

Tretter, L., Adam-Vizi, V., 2007a. Moderate dependence of ROS formation on DeltaPsim in isolated brain mitochondria supported by NADH-linked substrates. Neurochem Res 32(4-5), 569-575.

Tretter, L., Adam-Vizi, V., 2007b. Uncoupling is without an effect on the production of reactive oxygen species by in situ synaptic mitochondria. J Neurochem 103(5), 1864-1871.

Tretter, L., Mayer-Takacs, D., Adam-Vizi, V., 2007. The effect of bovine serum albumin on the membrane potential and reactive oxygen species generation in succinate-supported isolated brain mitochondria. Neurochem Int 50(1), 139-147.

Tretter, L., Patocs, A., Chinopoulos, C., 2016. Succinate, an intermediate in metabolism, signal transduction, ROS, hypoxia, and tumorigenesis. Biochim Biophys Acta 1857(8), 1086-1101.

Tunnicliff, G., Ngo, T.T., Rojo-Ortega, J.M., Barbeau, A., 1977. The inhibition by substrate analogues of gamma-aminobutyrate aminotransferase from mitochondria of different subcellular fractions of rat brain. Can J Biochem 55(4), 479-484.

Tyynismaa, H., Mjosund, K.P., Wanrooij, S., Lappalainen, I., Ylikallio, E., Jalanko, A., Spelbrink, J.N., Paetau, A., Suomalainen, A., 2005. Mutant mitochondrial helicase Twinkle causes multiple mtDNA deletions and a late-onset mitochondrial disease in mice. Proc Natl Acad Sci U S A 102(49), 17687-17692.

Udenfriend, S., 1950. Identification of gamma-aminobutyric acid in brain by the isotope derivative method. J Biol Chem 187(1), 65-69.

Uhlen, M., Fagerberg, L., Hallstrom, B.M., Lindskog, C., Oksvold, P., Mardinoglu, A., Sivertsson, A., Kampf, C., Sjostedt, E., Asplund, A., Olsson, I., Edlund, K., Lundberg, E., Navani, S., Szigyarto, C.A., Odeberg, J., Djureinovic, D., Takanen, J.O., Hober, S., Alm, T., Edqvist, P.H., Berling, H., Tegel, H., Mulder, J., Rockberg, J., Nilsson, P., Schwenk, J.M., Hamsten, M., von Feilitzen, K., Forsberg, M., Persson, L., Johansson, F., Zwahlen, M., von Heijne, G., Nielsen, J., Ponten, F., 2015. Proteomics. Tissue-based map of the human proteome. Science 347(6220), 1260419.

Urits, I., Mukherjee, P., Meidenbauer, J., Seyfried, T.N., 2012. Dietary restriction promotes vessel maturation in a mouse astrocytoma. J. Oncology Article ID 264039, 10.

Vafai, S.B., Mevers, E., Higgins, K.W., Fomina, Y., Zhang, J., Mandinova, A., Newman, D., Shaw, S.Y., Clardy, J., Mootha, V.K., 2016. Natural Product Screening Reveals Naphthoquinone Complex I Bypass Factors. PLoS One 11(9), e0162686.

Vafai, S.B., Mootha, V.K., 2012. Mitochondrial disorders as windows into an ancient organelle. Nature 491(7424), 374-383.

Vajda, S., Mandi, M., Konrad, C., Kiss, G., Ambrus, A., Adam-Vizi, V., Chinopoulos, C., 2009. A re-evaluation of the role of matrix acidification in uncoupler-induced Ca2+ release from mitochondria. FEBS J 276(10), 2713-2724.

Valle, V.G., Pereira-da-Silva, L., Vercesi, A.E., 1986. Undesirable feature of safranine as a probe for mitochondrial membrane potential. Biochem Biophys Res Commun 135(1), 189-195.

Vander Heiden, M.G., Cantley, L.C., Thompson, C.B., 2009. Understanding the Warburg effect: the metabolic requirements of cell proliferation. Science 324(5930), 1029-1033.

Vasiliou, V., Ross, D., Nebert, D.W., 2006. Update of the NAD(P)H:quinone oxidoreductase (NQO) gene family. Hum Genomics 2(5), 329-335.

Veech, R.L., 2004. The therapeutic implications of ketone bodies: the effects of ketone bodies in pathological conditions: ketosis, ketogenic diet, redox states, insulin resistance, and mitochondrial metabolism. Prostaglandins Leukot Essent Fatty Acids 70(3), 309-319.

Venter, J.C., Adams, M.D., Myers, E.W., Li, P.W., Mural, R.J., Sutton, G.G., Smith, H.O., Yandell, M., Evans, C.A., Holt, R.A., Gocayne, J.D., Amanatides, P., Ballew, R.M., Huson, D.H., Wortman, J.R., Zhang, Q., Kodira, C.D., Zheng, X.H., Chen, L., Skupski, M., Subramanian, G., Thomas, P.D., Zhang, J., Gabor Miklos, G.L., Nelson, C., Broder, S., Clark, A.G., Nadeau, J., McKusick, V.A., Zinder, N., Levine, A.J., Roberts, R.J., Simon, M., Slayman, C., Hunkapiller, M., Bolanos, R., Delcher, A., Dew, I., Fasulo, D., Flanigan, M., Florea, L., Halpern, A., Hannenhalli, S., Kravitz, S., Levy, S., Mobarry, C., Reinert, K., Remington, K., Abu-Threideh, J., Beasley, E., Biddick, K., Bonazzi, V., Brandon, R., Cargill, M., Chandramouliswaran, I., Charlab, R., Chaturvedi, K., Deng, Z., Di, F.V., Dunn, P., Eilbeck, K., Evangelista, C., Gabrielian, A.E., Gan, W., Ge, W., Gong, F., Gu, Z., Guan, P., Heiman, T.J., Higgins, M.E., Ji, R.R., Ke, Z., Ketchum, K.A., Lai, Z., Lei, Y., Li, Z., Li, J., Liang, Y., Lin, X., Lu, F., Merkulov, G.V., Milshina, N., Moore, H.M., Naik, A.K., Narayan, V.A., Neelam, B., Nusskern, D., Rusch, D.B., Salzberg, S., Shao, W., Shue, B., Sun, J., Wang, Z., Wang, A., Wang, X., Wang, J., Wei, M., Wides, R., Xiao, C., Yan, C., Yao, A., Ye, J., Zhan, M., Zhang, W., Zhang, H., Zhao, Q., Zheng, L., Zhong, F., Zhong, W., Zhu, S., Zhao, S., Gilbert, D., Baumhueter, S., Spier, G., Carter, C., Cravchik, A., Woodage, T., Ali, F., An, H., Awe, A., Baldwin, D., Baden, H., Barnstead, M., Barrow, I., Beeson, K., Busam, D., Carver, A., Center, A., Cheng, M.L., Curry, L., Danaher, S., Davenport, L., Desilets, R., Dietz, S., Dodson, K., Doup, L., Ferriera, S., Garg, N., Gluecksmann, A., Hart, B., Haynes, J., Haynes, C., Heiner, C., Hladun, S., Hostin, D., Houck, J., Howland, T., Ibegwam, C., Johnson, J., Kalush, F., Kline, L., Koduru, S., Love, A., Mann, F., May, D., McCawley, S., McIntosh, T., McMullen, I., Moy, M., Moy, L., Murphy, B., Nelson, K., Pfannkoch, C., Pratts, E., Puri, V., Qureshi, H., Reardon, M., Rodriguez, R., Rogers, Y.H., Romblad, D., Ruhfel, B., Scott, R., Sitter, C., Smallwood, M., Stewart, E., Strong, R., Suh, E., Thomas, R., Tint, N.N., Tse, S., Vech, C., Wang, G., Wetter, J., Williams, S., Williams, M., Windsor, S., Winn-Deen, E., Wolfe, K., Zaveri, J., Zaveri, K., Abril, J.F., Guigo, R., Campbell, M.J., Sjolander, K.V., Karlak, B., Kejariwal, A., Mi, H., Lazareva, B., Hatton, T., Narechania, A., Diemer, K., Muruganujan, A., Guo, N., Sato, S., Bafna, V., Istrail, S., Lippert, R., Schwartz, R., Walenz, B., Yooseph, S., Allen, D., Basu, A., Baxendale, J., Blick, L., Caminha, M., Carnes-Stine, J., Caulk, P., Chiang, Y.H., Coyne, M., Dahlke, C., Mays, A., Dombroski, M., Donnelly, M., Ely, D., Esparham, S., Fosler, C., Gire, H., Glanowski, S., Glasser, K., Glodek, A., Gorokhov, M., Graham, K., Gropman, B., Harris, M., Heil, J., Henderson, S., Hoover, J., Jennings, D., Jordan, C., Jordan, J., Kasha, J., Kagan, L., Kraft, C., Levitsky, A., Lewis, M., Liu, X., Lopez, J., Ma, D., Majoros, W., McDaniel, J., Murphy, S., Newman, M., Nguyen, T., Nguyen, N., Nodell, M., 2001. The sequence of the human genome. Science 291(5507), 1304-1351.

Vergati, M., Krasniqi, E., Monte, G.D., Riondino, S., Vallone, D., Guadagni, F., Ferroni, P., Roselli, M., 2017. Ketogenic Diet and Other Dietary Intervention Strategies in the Treatment of Cancer. Curr Med Chem 24(12), 1170-1185.

Vignais, P.V., 1976. Molecular and physiological aspects of adenine nucleotide transport in mitochondria. Biochim Biophys Acta 456(1), 1-38.

Vignais, P.V., Vignais, P.M., Defaye, G., 1971. Gummiferin, an inhibitor of the adenine-nucleotide translocation. Study of its binding properties to mitochondria. FEBS Lett 17(2), 281-288.

Vignais, P.V., Vignais, P.M., Doussiere, J., 1975. Functional relationship between the ADP/ATP-carrier and the F1-ATPase in mitochondria. Biochim Biophys Acta 376(2), 219-230.

Viscomi, C., Spinazzola, A., Maggioni, M., Fernandez-Vizarra, E., Massa, V., Pagano, C., Vettor, R., Mora, M., Zeviani, M., 2009. Early-onset liver mtDNA depletion and late-onset proteinuric nephropathy in Mpv17 knockout mice. Hum Mol Genet 18(1), 12-26.

Voss, A.K., Thomas, T., Gruss, P., 1998. Compensation for a gene trap mutation in the murine microtubule-associated protein 4 locus by alternative polyadenylation and alternative splicing. Dev Dyn 212(2), 258-266.

Vozza, A., Blanco, E., Palmieri, L., Palmieri, F., 2004. Identification of the mitochondrial GTP/GDP transporter in Saccharomyces cerevisiae. J Biol Chem 279(20), 20850-20857.

Waagepetersen, H.S., Hansen, G.H., Fenger, K., Lindsay, J.G., Gibson, G., Schousboe, A., 2006. Cellular mitochondrial heterogeneity in cultured astrocytes as demonstrated by immunogold labeling of alpha-ketoglutarate dehydrogenase. Glia 53(2), 225-231.

Wadkins, C.L., 1960. Stimulation of adenosine triphosphatase activity of mitochondria and submitochondrial particles by arsenate. J Biol Chem 235, 3300-3303.

Wakil, S.J., Porter, J.W., Gibson, D.M., 1957. Studies on the mechanism of fatty acid synthesis. I. Preparation and purification of an enzymes system for reconstruction of fatty acid synthesis. Biochim.Biophys.Acta 24(3), 453-461.

Wallace, D.C., Zheng, X.X., Lott, M.T., Shoffner, J.M., Hodge, J.A., Kelley, R.I., Epstein, C.M., Hopkins, L.C., 1988. Familial mitochondrial encephalomyopathy (MERRF): genetic, pathophysiological, and biochemical characterization of a mitochondrial DNA disease. Cell 55(4), 601-610.

Wallach, D.P., 1961. Studies on the GABA pathway. I. The inhibition of gamma-aminobutyric acid-alpha-ketoglutaric acid transaminase in vitro and in vivo by U-7524 (amino-oxyacetic acid). Biochem Pharmacol 5, 323-331.

Walsh, J.M., Clark, J.B., 1976. Studies on the control of 4-aminobutyrate metabolism in 'synaptosomal' and free rat brain mitochondria. Biochem J 160(2), 147-157.

Wanders, R.J., Mooyer, P., 1995. D-2-hydroxyglutaric acidaemia: identification of a new enzyme, D-2-hydroxyglutarate dehydrogenase, localized in mitochondria. J Inherit Metab Dis 18(2), 194-196.

Wang, J.B., Erickson, J.W., Fuji, R., Ramachandran, S., Gao, P., Dinavahi, R., Wilson, K.F., Ambrosio, A.L., Dias, S.M., Dang, C.V., Cerione, R.A., 2010. Targeting mitochondrial glutaminase activity inhibits oncogenic transformation. Cancer Cell 18(3), 207-219.

Wang, Q., Darling, I.M., Morris, M.E., 2006. Transport of gamma-hydroxybutyrate in rat kidney membrane vesicles: Role of monocarboxylate transporters. J Pharmacol Exp Ther 318(2), 751-761.

Wang, S.F., Adler, J., Lardy, H.A., 1961. The pathway of itaconate metabolism by liver mitochondria. J Biol Chem 236, 26-30.

Wang, Y.Q., Wang, H.L., Xu, J., Tan, J., Fu, L.N., Wang, J.L., Zou, T.H., Sun, D.F., Gao, Q.Y., Chen, Y.X., Fang, J.Y., 2018. Sirtuin5 contributes to colorectal carcinogenesis by enhancing glutaminolysis in a deglutarylation-dependent manner. Nat Commun 9(1), 545.

Warburg, O., 1956. On the origin of cancer cells. Science 123(3191), 309-314.

Ward, P.S., Thompson, C.B., 2012. Metabolic reprogramming: a cancer hallmark even warburg did not anticipate. Cancer Cell 21(3), 297-308.

Weinberg, F., Hamanaka, R., Wheaton, W.W., Weinberg, S., Joseph, J., Lopez, M., Kalyanaraman, B., Mutlu, G.M., Budinger, G.R., Chandel, N.S., 2010. Mitochondrial metabolism and ROS generation are essential for Kras-mediated tumorigenicity. Proc.Natl.Acad.Sci.U.S.A 107(19), 8788-8793.

Weinberg, J.M., Venkatachalam, M.A., Roeser, N.F., Nissim, I., 2000a. Mitochondrial dysfunction during hypoxia/reoxygenation and its correction by anaerobic metabolism of citric acid cycle intermediates. Proc Natl Acad Sci U S A 97(6), 2826-2831.

Weinberg, J.M., Venkatachalam, M.A., Roeser, N.F., Saikumar, P., Dong, Z., Senter, R.A., Nissim, I., 2000b. Anaerobic and aerobic pathways for salvage of proximal tubules from hypoxia-induced mitochondrial injury. Am J Physiol Renal Physiol 279(5), F927-943.

Weinert, B.T., Scholz, C., Wagner, S.A., Iesmantavicius, V., Su, D., Daniel, J.A., Choudhary, C., 2013. Lysine succinylation is a frequently occurring modification in prokaryotes and eukaryotes and extensively overlaps with acetylation. Cell Rep. 4(4), 842-851.

Werber, M.M., Peyser, Y.M., Muhlrad, A., 1992. Characterization of stable beryllium fluoride, aluminum fluoride, and vanadate containing myosin subfragment 1-nucleotide complexes. Biochemistry 31(31), 7190-7197.

White, H.L., Sato, T.L., 1978. GABA-transaminases of human brain and peripheral tissues--kinetic and molecular properties. J Neurochem 31(1), 41-47.

Wibom, C., Surowiec, I., Moren, L., Bergstrom, P., Johansson, M., Antti, H., Bergenheim, A.T., 2010. Metabolomic patterns in glioblastoma and changes during radiotherapy: a clinical microdialysis study. J Proteome Res 9(6), 2909-2919.

Wibom, R., Lundin, A., Hultman, E., 1990. A sensitive method for measuring ATP-formation in rat muscle mitochondria. Scand J Clin Lab Invest 50(2), 143-152.

Williams, C.H., Jr., Gibbs, R.H., Kamin, H., 1959. A microsomal TPNH-neotetrazolium diaphorase. Biochim Biophys Acta 32, 568-569.

Williamson, J.R., Corkey, B.E., 1979. Assay of citric acid cycle intermediates and related compounds--update with tissue metabolite levels and intracellular distribution. Methods Enzymol 55, 200-222.

Willke, T., Vorlop, K.D., 2001. Biotechnological production of itaconic acid. Appl Microbiol Biotechnol 56(3-4), 289-295.

Wilson, D.F., Erecinska, M., Schramm, V.L., 1983. Evaluation of the relationship between the intra- and extramitochondrial [ATP]/[ADP] ratios using phosphoenolpyruvate carboxykinase. J Biol Chem 258(17), 10464-10473.

Wilson, D.F., Nelson, D., Erecinska, M., 1982. Binding of the intramitochondrial ADP and its relationship to adenine nucleotide translocation. FEBS Lett 143(2), 228-232.

Wilson, D.F., Owen, C.S., Erecinska, M., 1979. Quantitative dependence of mitochondrial oxidative phosphorylation on oxygen concentration: a mathematical model. Arch Biochem Biophys 195(2), 494-504.

Winder, W.W., Baldwin, K.M., Terjung, R.L., Holloszy, J.O., 1975. Effects of thyroid hormone administration on skeletal muscle mitochondria. Am J Physiol 228(5), 1341-1345.

Winkler, H.H., Lehninger, A.L., 1968. The atractyloside-sensitive nucleotide binding site in a membrane preparation from rat liver mitochondria. J Biol Chem 243(11), 3000-3008.

Winski, S.L., Koutalos, Y., Bentley, D.L., Ross, D., 2002. Subcellular localization of NAD(P)H:quinone oxidoreductase 1 in human cancer cells. Cancer Res 62(5), 1420-1424.

Wise, D.R., DeBerardinis, R.J., Mancuso, A., Sayed, N., Zhang, X.Y., Pfeiffer, H.K., Nissim, I., Daikhin, E., Yudkoff, M., McMahon, S.B., Thompson, C.B., 2008. Myc regulates a transcriptional program that stimulates mitochondrial glutaminolysis and leads to glutamine addiction. Proc.Natl.Acad.Sci.U.S.A 105(48), 18782-18787.

Wise, D.R., Ward, P.S., Shay, J.E., Cross, J.R., Gruber, J.J., Sachdeva, U.M., Platt, J.M., DeMatteo, R.G., Simon, M.C., Thompson, C.B., 2011. Hypoxia promotes isocitrate dehydrogenase-dependent carboxylation of alpha-ketoglutarate to citrate to support cell growth and viability. Proc.Natl.Acad.Sci.U.S.A 108(49), 19611-19616.

Wisniewski, E., Kunz, W.S., Gellerich, F.N., 1993. Phosphate affects the distribution of flux control among the enzymes of oxidative phosphorylation in rat skeletal muscle mitochondria. J Biol Chem 268(13), 9343-9346.

Wojtczak, L., Schonfeld, P., 1993. Effect of fatty acids on energy coupling processes in mitochondria. Biochim Biophys Acta 1183(1), 41-57.

Wojtczak, L., Zaluska, H., 1967. The inhibition of translocation of adenine nucleotides through mitochondrial membranes by oleate. Biochem Biophys Res Commun 28(1), 76-81.

Wojtczak, L., Zaluska, H., Wroniszewska, A., Wojtczak, A.B., 1972. Assay for the intactness of the outer membrane in isolated mitochondria. Acta Biochim Pol 19(3), 227-234.

Wolff, J.R., Joo, F., Dames, W., 1978. Plasticity in dendrites shown by continuous GABA administration in superior cervical ganglion of adult rat. Nature 274(5666), 72-74.

Wong, J.M., de Souza, R., Kendall, C.W., Emam, A., Jenkins, D.J., 2006. Colonic health: fermentation and short chain fatty acids. J Clin Gastroenterol 40(3), 235-243.

Wood, G.W., Morantz, R.A., 1979. Immunohistologic evaluation of the lymphoreticular infiltrate of human central nervous system tumors. J. Natl. Cancer Inst. 62(3), 485-491.

Wosilait, W.D., Nason, A., 1954. Pyridine nucleotide-quinone reductase. I. Purification and properties of the enzyme from pea seeds. J Biol Chem 206(1), 255-270.

Wosilait, W.D., Nason, A., Terrell, A.J., 1954. [Pyridine nucleotide-quinone reductase. II. Role in electron transport]. J Biol Chem 206(1), 271-282.

Wu, F., Yang, F., Vinnakota, K.C., Beard, D.A., 2007. Computer modeling of mitochondrial tricarboxylic acid cycle, oxidative phosphorylation, metabolite transport, and electrophysiology. J Biol Chem 282(34), 24525-24537.

Wu, F., Zhang, E.Y., Zhang, J., Bache, R.J., Beard, D.A., 2008. Phosphate metabolite concentrations and ATP hydrolysis potential in normal and ischaemic hearts. J Physiol 586(17), 4193-4208.

Wu, J.Y., Roberts, E., 1974. Properties of brain L-glutamate decarboxylase: inhibition studies. J Neurochem 23(4), 759-767.

Wu, K., Knox, R., Sun, X.Z., Joseph, P., Jaiswal, A.K., Zhang, D., Deng, P.S., Chen, S., 1997. Catalytic properties of NAD(P)H:quinone oxidoreductase-2 (NQO2), a dihydronicotinamide riboside dependent oxidoreductase. Arch Biochem Biophys 347(2), 221-228.

Xaus, J., Comalada, M., Valledor, A.F., Lloberas, J., Lopez-Soriano, F., Argiles, J.M., Bogdan, C., Celada, A., 2000. LPS induces apoptosis in macrophages mostly through the autocrine production of TNF-alpha. Blood 95(12), 3823-3831.

Xiao, M., Yang, H., Xu, W., Ma, S., Lin, H., Zhu, H., Liu, L., Liu, Y., Yang, C., Xu, Y., Zhao, S., Ye, D., Xiong, Y., Guan, K.L., 2012. Inhibition of alpha-KG-dependent histone and DNA demethylases by fumarate and succinate that are accumulated in mutations of FH and SDH tumor suppressors. Genes Dev. 26(12), 1326-1338.

Xiao, W., Wang, L., Xiao, R., Wu, M., Tan, J., He, Y., 2011. Expression profile of human immune-responsive gene 1 and generation and characterization of polyclonal antiserum. Mol Cell Biochem 353(1-2), 177-187.

Xu, L., Shen, S., Ma, Y., Kim, J.K., Rodriguez-Agudo, D., Heuman, D.M., Hylemon, P.B., Pandak, W.M., Ren, S., 2012. 25-Hydroxycholesterol-3-sulfate attenuates inflammatory response via PPARgamma signaling in human THP-1 macrophages. Am J Physiol Endocrinol Metab 302(7), E788-799.

Xu, R.H., Pelicano, H., Zhou, Y., Carew, J.S., Feng, L., Bhalla, K.N., Keating, M.J., Huang, P., 2005. Inhibition of glycolysis in cancer cells: a novel strategy to overcome drug resistance associated with mitochondrial respiratory defect and hypoxia. Cancer research 65(2), 613-621.

Yan, H., Parsons, D.W., Jin, G., McLendon, R., Rasheed, B.A., Yuan, W., Kos, I., Batinic-Haberle, I., Jones, S., Riggins, G.J., Friedman, H., Friedman, A., Reardon, D., Herndon, J., Kinzler, K.W., Velculescu, V.E., Vogelstein, B., Bigner, D.D., 2009. IDH1 and IDH2 mutations in gliomas. N.Engl.J.Med. 360(8), 765-773.

Yang, C., Ko, B., Hensley, C.T., Jiang, L., Wasti, A.T., Kim, J., Sudderth, J., Calvaruso, M.A., Lumata, L., Mitsche, M., Rutter, J., Merritt, M.E., DeBerardinis, R.J., 2014. Glutamine oxidation maintains the TCA cycle and cell survival during impaired mitochondrial pyruvate transport. Mol Cell 56(3), 414-424.

Yang, C., Sudderth, J., Dang, T., Bachoo, R.M., McDonald, J.G., DeBerardinis, R.J., 2009. Glioblastoma cells require glutamate dehydrogenase to survive impairments of glucose metabolism or Akt signaling. Cancer Res 69(20), 7986-7993.

Yang, L., Shi, Q., Ho, D.J., Starkov, A.A., Wille, E.J., Xu, H., Chen, H.L., Zhang, S., Stack, C.M., Calingasan, N.Y., Gibson, G.E., Beal, M.F., 2009. Mice deficient in dihydrolipoyl succinyl transferase show increased vulnerability to mitochondrial toxins. Neurobiol Dis 36(2), 320-330.

Yang, L., Venneti, S., Nagrath, D., 2017. Glutaminolysis: A Hallmark of Cancer Metabolism. Annu Rev Biomed Eng.

Yang, M., Soga, T., Pollard, P.J., Adam, J., 2012. The emerging role of fumarate as an oncometabolite. Front Oncol. 2, 85.

Yang, M., Vousden, K.H., 2016. Serine and one-carbon metabolism in cancer. Nat Rev Cancer 16(10), 650-662.

Yang, W., Roth, K.S., 1985. Defect in alpha-ketobutyrate metabolism: a new inborn error. Clin Chim Acta 145(2), 173-182.

Yang, Y., Sauve, A.A., 2016. NAD(+) metabolism: Bioenergetics, signaling and manipulation for therapy. Biochim Biophys Acta 1864(12), 1787-1800.

Ylikallio, E., Page, J.L., Xu, X., Lampinen, M., Bepler, G., Ide, T., Tyynismaa, H., Weiss, R.S., Suomalainen, A., 2010. Ribonucleotide reductase is not limiting for mitochondrial DNA copy number in mice. Nucleic Acids Res 38(22), 8208-8218.

Young, V.R., Ajami, A.M., 2001. Glutamine: the emperor or his clothes? J.Nutr. 131(9 Suppl), 2449S-2459S.

Yuan, X., Curtin, J., Xiong, Y., Liu, G., Waschsmann-Hogiu, S., Farkas, D.L., Black, K.L., Yu, J.S., 2004. Isolation of cancer stem cells from adult glioblastoma multiforme. Oncogene 23(58), 9392-9400.

Yue, Y., Krenz, M., Cohen, M.V., Downey, J.M., Critz, S.D., 2001. Menadione mimics the infarct-limiting effect of preconditioning in isolated rat hearts. Am J Physiol Heart Circ Physiol 281(2), H590-595.

Yuen, C.A., Asuthkar, S., Guda, M.R., Tsung, A.J., Velpula, K.K., 2016. Cancer stem cell molecular reprogramming of the Warburg effect in glioblastomas: a new target gleaned from an old concept. CNS Oncol 5(2), 101-108.

Yuneva, M., 2008. Finding an "Achilles' heel" of cancer: the role of glucose and glutamine metabolism in the survival of transformed cells. Cell cycle (Georgetown, Tex 7(14), 2083-2089.

Zagzag, D., Esencay, M., Mendez, O., Yee, H., Smirnova, I., Huang, Y., Chiriboga, L., Lukyanov, E., Liu, M., Newcomb, E.W., 2008. Hypoxia- and vascular endothelial growth factor-induced stromal cell-derived factor-1alpha/CXCR4 expression in glioblastomas: one plausible explanation of Scherer's structures. The American journal of pathology 173(2), 545-560.

Zeng, W., Liu, P., Pan, W., Singh, S.R., Wei, Y., 2015. Hypoxia and hypoxia inducible factors in tumor metabolism. Cancer letters 356(2 Pt A), 263-267.

Zhang, J., Fan, J., Venneti, S., Cross, J.R., Takagi, T., Bhinder, B., Djaballah, H., Kanai, M., Cheng, E.H., Judkins, A.R., Pawel, B., Baggs, J., Cherry, S., Rabinowitz, J.D., Thompson, C.B., 2014. Asparagine plays a critical role in regulating cellular adaptation to glutamine depletion. Mol Cell 56(2), 205-218.

Zhang, K., Xu, P., Sowers, J.L., Machuca, D.F., Mirfattah, B., Herring, J., Tang, H., Chen, Y., Tian, B., Brasier, A.R., Sowers, L.C., 2017. Proteome Analysis of Hypoxic Glioblastoma Cells Reveals Sequential Metabolic Adaptation of One-Carbon Metabolic Pathways. Mol Cell Proteomics 16(11), 1906-1921.

Zhang, X., Rao, A., Sette, P., Deibert, C., Pomerantz, A., Kim, W.J., Kohanbash, G., Chang, Y., Park, Y., Engh, J., Choi, J., Chan, T., Okada, H., Lotze, M., Grandi, P., Amankulor, N., 2016. IDH mutant gliomas escape natural killer cell immune surveillance by downregulation of NKG2D ligand expression. Neuro Oncol 18(10), 1402-1412.

Zhang, Y., Bharathi, S.S., Rardin, M.J., Lu, J., Maringer, K.V., Sims-Lucas, S., Prochownik, E.V., Gibson, B.W., Goetzman, E.S., 2017a. Lysine desuccinylase SIRT5 binds to cardiolipin and regulates the electron transport chain. J Biol Chem 292(24), 10239-10249.

Zhang, Y., Wang, G., Song, L., Mu, P., Wang, S., Liang, W., Lin, Q., 2017b. Global analysis of protein lysine succinylation profiles in common wheat. BMC Genomics 18(1), 309.

Zhang, Z., Tan, M., Xie, Z., Dai, L., Chen, Y., Zhao, Y., 2011. Identification of lysine succinylation as a new post-translational modification. Nat Chem Biol 7(1), 58-63.

Zhao, Q., Yang, X.L., Holtzclaw, W.D., Talalay, P., 1997. Unexpected genetic and structural relationships of a long-forgotten flavoenzyme to NAD(P)H:quinone reductase (DT-diaphorase). Proc Natl Acad Sci U S A 94(5), 1669-1674.

Zhou, W., Mukherjee, P., Kiebish, M.A., Markis, W.T., Mantis, J.G., Seyfried, T.N., 2007. The calorically restricted ketogenic diet, an effective alternative therapy for malignant brain cancer. Nutr Metab (Lond) 4, 5.

Zhou, Y., Danbolt, N.C., 2013. GABA and Glutamate Transporters in Brain. Front Endocrinol (Lausanne) 4, 165.

Zhou, Y., Zhou, Y., Shingu, T., Feng, L., Chen, Z., Ogasawara, M., Keating, M.J., Kondo, S., Huang, P., 2011. Metabolic alterations in highly tumorigenic glioblastoma cells: preference for hypoxia and high dependency on glycolysis. J Biol Chem 286(37), 32843-32853.

Zhu, L., Zhao, Q., Yang, T., Ding, W., Zhao, Y., 2015. Cellular metabolism and macrophage functional polarization. Int Rev Immunol 34(1), 82-100.

Zolkiewska, A., Czyz, A., Duszynski, J., Wojtczak, L., 1993. Continuous recording of intramitochondrial pH with fluorescent pH indicators: novel probes and limitations of the method. Acta Biochim Pol 40(2), 241-250.

Zsurka, G., Gregan, J., Schweyen, R.J., 2001. The human mitochondrial Mrs2 protein functionally substitutes for its yeast homologue, a candidate magnesium transporter. Genomics 72(2), 158-168.